UNIVERSITAT DE
BARCELONA

Targeting metabolic reprogramming associated to cancer cells: search of novel targets and combined therapies in cancer treatment

Miriam Tarrado Castellarnau

PROGRAMA DE DOCTORAT EN BIOTECNOLOGIA
Departament de Bioquímica i Biologia Molecular
Facultat de Biologia

Targeting metabolic reprogramming associated to cancer cells: search of novel targets and combined therapies in cancer treatment

Memòria presentada per na **Míriam Neus Tarrado Castellarnau** per optar al grau de Doctora per la Universitat de Barcelona

Marta Cascante Serratosa

Directora i tutora

Pedro Ramon de Atauri Carulla

Codirector

Míriam Neus Tarrado Castellarnau

Doctoranda

Targeting metabolic reprogramming associated to cancer cells: search of novel targets and combined therapies in cancer treatment

Míriam Tarrado Castellarnau

PhD Thesis

2015

Index

1. Introduction

1. INTRODUCTION

1.1. Cancer

Multifactorial diseases are the final result of the interaction between genetic susceptibility and environmental factors in which a clear hereditary pattern is not found. This complexity causes difficulties in the risk evaluation, diagnosis and treatment of these diseases. Cancer, one of the most prevalent multifactorial diseases, is characterised by the lost of physiological control and the malignant transformation of cells that acquire functional and genetic abnormalities, leading to tumour development and progression. In some cases, cancer cells have the ability to invade other tissues resulting in metastasis, the major cause of death from cancer. According to the most recent data released by the World Health Organisation (WHO) in 2012, more than 14 million of new cancer cases were diagnosed, and 8.2 million cancer deaths and 32.4 million people living with cancer (within 5 years of diagnosis) were registered worldwide. The most common cancers by primary site location were lung, prostate and colorectal in men, and breast, colorectal and cervix uteri in women [1].

1.1.1. Colorectal cancer

Colorectal cancer (CRC) is a global leading cause of cancer-related mortality being the third most common cancer in men and the second in women worldwide [1]. Fortunately, systematic risk population screening programmes facilitate early detection and treatment reducing its incidence and mortality rate. The American Joint Committee on Cancer (AJCC) TNM staging system establishes four different stages of tumour progression (I to IV) depending on the primary tumour extent (T), the regional lymph node involvement (N) and the absence or presence of distant metastasis (M) [2]. Cancer staging systems help oncologists to evaluate disease prognosis, treatment suitability and the possibilities of patients to be enrolled in specific clinical trials,

contributing to fight CRC. However, further studies are required to identify new biomarkers to predict CRC outcome, help to understand its evolution and find the most suitable treatment.

1.1.1.1. Definition of TNM staging system

Intestinal colon walls are divided into four layers; serosa, muscularis propria, submucosa and mucosa, which is the innermost layer and where colonic epithelium renews by itself. Mutations affecting this self-renewal process can distress intestinal development triggering DNA repair or apoptotic mechanisms. Accumulation of mutations can induce adenoma formation and ultimately lead to malignancy. The definition of TNM according to the cancer staging manual of the AJCC [2] is as follows:

Primary tumour (T):

- TX: Primary tumour cannot be assessed
- T0: No evidence of primary tumour
- Tis: Carcinoma *in situ*: intraepithelial or invasion of lamina propria
- T1: Tumour invades submucosa
- T2: Tumour invades muscularis propria
- T3: Tumour invades through the muscularis propria into the subserosa, or into non-peritonealised pericolic or perirectal tissues
- T4: Tumour directly invades other organs or structures, and/or perforates visceral peritoneum

Regional lymph nodes (N):

- NX: Regional lymph nodes cannot be assessed
- N0: No regional lymph nodes metastasis
- N1: Metastasis in 1 to 3 regional lymph nodes
- N2: Metastasis in 4 or more regional lymph nodes

Distant metastasis (M):

- MX: Distant metastasis cannot be assessed
- M0: No distant metastasis
- M1: Distant metastasis

Table 1.1. TNM stage grouping for colorectal cancer.

Stage	T	N	M
0	Tis	N0	M0
I	T1-2	N0	M0
IIA	T3	N0	M0
IIB	T4	N0	M0
IIIA	T1-2	N1	M0
IIIB	T3-4	N1	M0
IIIC	T1-4	N2	M0
IV	T1-4	N0-2	M1

1.1.2. Lung cancer

Lung cancer remains the most common cancer in the world, both in term of new cases (1.8 million cases, 12.9% of total) and deaths (1.6 million deaths, 19.4%), with one of the lowest cure rate worldwide [1]. In early stages of the disease, surgery is the common choice while chemotherapy is the main treatment for advanced lung cancer. However, the currently available chemotherapeutic treatments exhibit modest efficacy due to their side effects and drug resistance [3]. Alone or in combination with radiotherapy, platinum derivatives such as cisplatin and carboplatin are the most commonly used agents in conventional chemotherapy [4, 5]. Therefore, the search for new synthetic or natural drugs with low systemic toxicity and high efficiency holds great promise to decrease the morbidity and mortality of lung cancer.

1.2. Cancer characteristics

Tumour cells present common biological capabilities sequentially acquired during the development of cancer that are considered essential to drive malignancy and known as the hallmarks of cancer [6]. These hallmark capabilities include sustaining proliferative signalling, evading growth suppressors, avoiding immune destruction, enabling replicative immortality, activating invasion and metastasis, inducing angiogenesis, resisting cell death and reprogramming cellular metabolism. In addition, there are two consequential characteristics of tumourigenesis that enable the acquisition of the hallmarks of cancer. The most prominent is the development of genomic instability and mutability, which endow tumour cells with genetic alterations that can orchestrate tumour progression. The second one involves the tumour-promoting inflammation by innate immune cells, which serve to support multiple hallmark capabilities [6].

Non-transformed cells tightly regulate the mitogenic signalling that command cell growth and division in order to maintain a balance between cell proliferation and death. Therefore, the dysregulation of the signalling pathways that regulate the progression through cell cycle, cell survival and metabolism may lead to malignant transformation. It is worth noting that neoplastic transformation requires not only the alteration of proliferative stimuli but also the disruption of mechanisms that prevent unrestrained proliferation such as programmed cell death (apoptosis) or negative-feedback signalling [7]. Likewise, the cooperating activation of oncogenes (genes that promote cell growth, proliferation and survival) and/or inactivation of tumour suppressor genes (genes that restrain cell growth and proliferation, promote DNA repair or trigger apoptosis) are involved in tumour development [7, 8]. Oncogenes can be activated through several mechanisms including upregulated transcriptional expression, increased stability of mutant proteins, altered functionality of proteins and abnormal recruitment or subcellular localisation of gene products through interaction with aberrantly expressed or mutant binding partners [7, 9]. The products of oncogenes comprise transcription factors (e.g. c-MYC), growth factor receptors (e.g. EGFR), signal transduction proteins (e.g. RAS and PI3K), serine-threonine protein kinases (e.g. Akt, mTOR, CDK4 and CDK6) and inhibitors of apoptosis (e.g. BCL2) [9]. On

the other hand, tumour suppressor genes encode proteins that inhibit cell division and cell proliferation (e.g. RB, p53, p16^{INK4a}, PTEN), stimulate cell death (e.g. caspase 8 and p53) and repair damaged DNA (e.g. MSH2, MSH6, ATM and ATR) [10].

1.3. Cell cycle

Cell cycle is a set of organised and monitored events responsible of proper cell division into two daughter cells. It is a high energy demanding process that requires an encompassed and ordered series of events to guarantee the correct duplication and segregation of the genome. This process involves four sequential phases; G1, S, G2, and M [11] (Figure 1.1). Cells can enter the first gap phase (G1) from the quiescent state G0 or, if they are proliferating, after completing cytokinesis. The progression
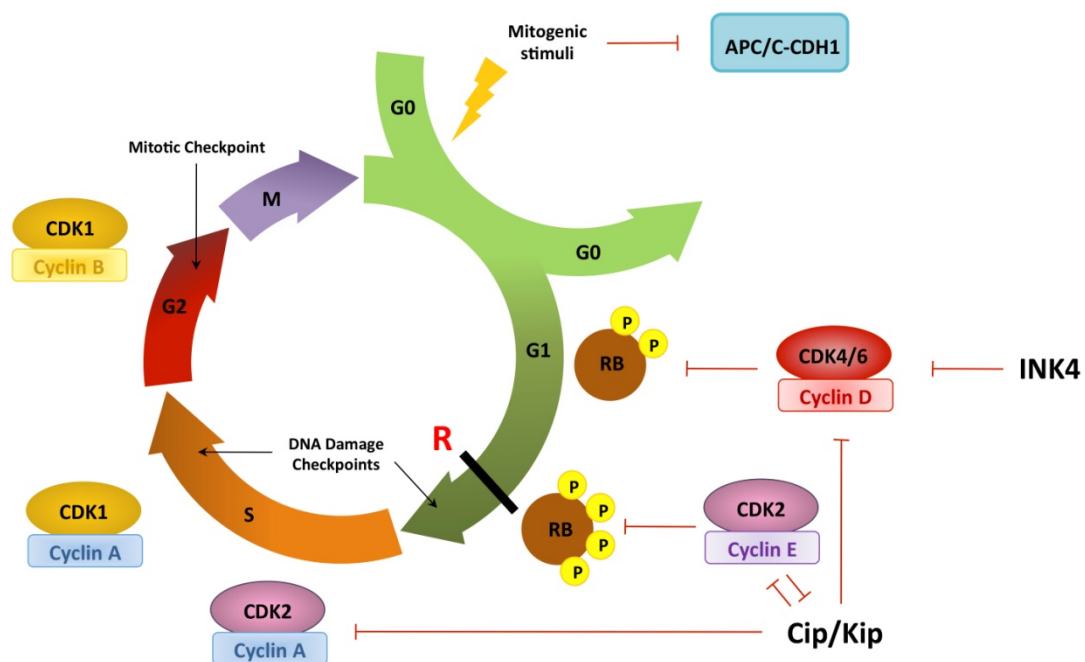
Figure 1.1. Cell cycle overview. Cell cycle is divided in four sequential phases; G1, S, G2, and M. Cells can enter the first gap phase (G1) from the quiescent state G0 or after completing cytokinesis. The Restriction point (R) is a G1 phase checkpoint at which mammalian cells commit to enter the synthesis (S) phase and become independent of mitogenic stimuli. Once S phase is successfully completed, cells are able to enter the second gap phase (G2) in preparation for mitosis (M), where each cell generates two genomically stable daughter cells. The CDK/cyclin complexes are the principal regulators of cell cycle and are regulated by activation through the binding to specific cyclins, by inhibition through the union to inhibitors (INK4 and Cip/Kip families) and by positive or negative phosphorylation/dephosphorylation events.

through G1 is mitogen-dependent up to the Restriction point (R) [12], after which cells can proliferate independently of mitogenic stimuli and are committed to enter the synthesis (S) phase, when DNA replication occurs. R prevents cells from entering the cell cycle, allowing them to return to G0, until a certain level of mitogen signalling events is achieved. Before undergoing division, cells have to assess whether there is an adequate metabolic status to initiate and complete cell cycle properly [13]. Cell cycle checkpoints are sensor mechanisms within the cell that supervise the adequate progression through cell cycle, preventing the transition to the next phase until the previous one is successfully concluded. The activation of one checkpoint induces cell cycle arrest until the problem is solved, if it is possible, or may enter senescence or undergo apoptosis if the repair is not successful [14]. Once the chromosomes are correctly duplicated, cells can enter G2, another gap phase to prepare for the mitosis (M), where the cell generates two genomically stable daughter cells. Abrogation of cell cycle checkpoints is associated with many diseases including cancer [15].

1.3.1. Canonical cell cycle regulation

Cyclin-dependent kinases (CDK) are the catalytic subunits of a family of mammalian heterodimeric serine/threonine protein kinases [16, 17] that play an important role both in eukaryotic cell cycle progression and in transcriptional regulation [18, 19]. CDK activity requires binding to specific cyclins, the regulatory subunits of the heterodimeric complexes, and is regulated by the union to inhibitors and by positive or negative phosphorylation events [20-22]. However, since CDKs are constitutively expressed and only bind to specific cyclins, the activation of the CDK-cyclin complexes governing the transitions between cell cycle phases depends on the availability of the regulatory subunits. Thereby, cell machinery regulates cyclin oscillatory changes by controlling their synthesis and degradation at specific times, leading to the orchestrated progression of the cell cycle [22, 23]. In quiescent cells, cyclins are subjected to ubiquitination and proteasome degradation [24]. However, mitogenic stimuli inactivate the E3 ubiquitin ligases that target cyclins for degradation, leading to their accumulation and activating cell division (Figure 1.1). There are two E3 ubiquitin

ligase complexes, APC/C (anaphase-promoting complex or cyclosome) and SCF (SKP1/CUL-1/F-box protein), that distinctively recognise degradation motifs, such as D (destruction) or KEN (lysine, glutamate, asparagine) boxes [25], in cyclins and other cell-cycle proteins, regulating their sequential ubiquitin-dependent degradation and allowing them to drive the cell cycle by peaking at different phases [26-28].

There are twenty different CDK (CDK1-20) that have been identified in mammals. All of them have been reported to interact with specific cyclins (CDK1-14) or include cycling-binding domains in their structure (CDK15-20) [29]. However, only four of them drive cell cycle events; CDK1, 2, 4 and 6 (and perhaps CDK3 and CDK5) [30-33]. CDK7-11 are involved in transcriptional regulation with some implications in cell cycle control while CDK12 and 13 play a role in alternative splicing [34, 35]. The cyclin partners associated with and the functions of the other seven members of the CDK structural family have yet to be identified [29, 36].

The interphase cyclin dependent kinases CDK4 and CDK6 control cell cycle re-entry and progression through G1 phase. They are activated by D-type cyclins (D1, D2 and D3) forming CDK4/6-cyclin D complexes. In response to mitogenic signalling through pathways like the RAS/RAF/MAPK, cells synthesise D-type cyclins that bind CDK4 and CDK6, becoming active complexes with capacity to phosphorylate the members of the retinoblastoma (RB) protein family including pRB, p107 and p130 (Figures 1.1 and 1.2). RB members are transcriptional regulators that repress transcription of several genes involved in DNA replication by the binding and inactivation of transcription factors such as those of the E2F family, and the recruitment of repressor complexes such as histone deacetylases and chromosomal remodelling SWI/SNF complexes [37, 38]. The protein complexes E2F are heterodimers composed by a protein E2F (E2F-1 to 6) and a protein from the DP family (DP-1 and DP-2) [39, 40]. Therefore, the phosphorylation of RB proteins by CDK4/6-cyclin D complexes leads to their partial inactivation and relieve the transcriptional repression mediated by the RB-E2F complex, allowing both the transcription of E-type cyclins (E1 and E2), which bind and activate CDK2, and surpassing the Restriction point [41]. Immediately, CDK2-cyclin E complexes completely inactivate RB proteins by hyperphosphorylation, allowing E2F activation, that directs the transient transcription of genes required for entering the S phase

(Figure 1.2). Active CDK2-cyclin E also phosphorylates proteins involved in histone modification, DNA replication and repair, centrosome duplication and maturation, and its own inhibitor p27^{Kip1} [17, 36, 42]. CDK3 might also participate in inactivation of pRB, this kinase is highly related to CDK2 and CDK1 and interacts with A-type and E-type cyclins, being involved in G1 progression, transition to S phase and DNA repair [43]. CDK5 is activated by p35 and p39 although can also bind D-type and E-type cyclins, forming complexes whose activity is still unclear [43].
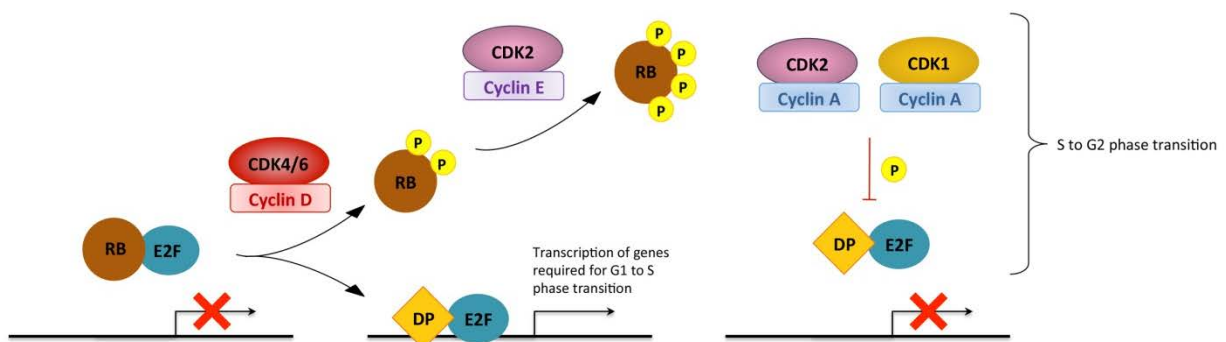
Figure 1.2. Transcription regulation by CDKs. Active CDK4/6-cyclin D and CDK2-cyclin E complexes sequentially phosphorylate the members of the retinoblastoma (RB) protein family, relieving the transcriptional repression mediated by the RB-E2F complex and allowing the transcription of genes required for surpassing the Restriction point. In turn, CDK2-cyclin A and CDK1-cyclin A complexes phosphorylate the E2F and DP dimer, triggering its release from the DNA to allow S phase transition to G2 and promoting the formation of RB-E2F complexes.

Once in S phase, in order to avoid the re-replication of DNA, the CDK2-cyclin E complexes are inactivated through degradation of cyclin E by the ubiquitin ligase SCF-related complexes via the proteasome-mediated pathway [26, 44]. At the same time, the full inactivation of pRB permits the transcription of A-type (A1 and A2) and B-type (B1, B2 and B3) cyclins. Free CDK2 binds to cyclin A resulting in active CDK2-cyclin A complexes which phosphorylate E2F and DP, releasing the dimer from the DNA [45] and consequently, downregulating E2F activity to allow S phase transition to G2. At the end of the S phase, the mitotic CDK1 is associated with cyclin A and phosphorylates a wide range of proteins [36] including E2F, thus promoting the formation of RB-E2F complexes (Figure 1.2). During G2, A-type cyclins are degraded by ubiquitin-mediated proteolysis while B-type cyclins are actively synthesised and able to bind free CDK1.

CDK1-cyclin B complexes are essential for initiating mitosis and can phosphorylate a broad spectrum of proteins involved in regulatory and structural processes required for mitosis such as nuclear envelope breakdown, chromosomal condensation, fragmentation of the Golgi apparatus, formation of the spindle and attachment of chromosomes to it [36, 43]. Exiting mitosis requires the inactivation of CDK1-cyclin B, which is carried out by the ubiquitin-dependent proteolysis of B-type cyclins by the APC/C-CDC20 complex [46, 47].

The kinase activity of CDKs is not only regulated by the interaction with activating subunits (cyclins) as mentioned above, but also by the binding to negative regulators (CDK inhibitors, CKI) and the phosphorylation/dephosphorylation events. There are two families of CKI: INK4 proteins (p16^{INK4a}, p15^{INK4b}, p18^{INK4c} and p19^{INK4d}) that bind specifically to CDK4 and CDK6 but not to other CDKs preventing their union to D-type cyclins, and the Cip/Kip family (p21^{Cip1}, p27^{Kip1} and p57^{Kip2}) which form heterotrimeric complexes with the cyclin D-, cyclin E- and cyclin A-dependent kinases complexes [42] (Figure 1.1). CDK4/6-cyclin D complexes facilitate G1 progression not only by partial phosphorylation of pRB but also by the sequestration of p21^{Cip1} and p27^{Kip1}, releasing CDK2-cyclin E from these inhibitors and promoting CDK2 kinase activity [42, 48]. Moreover, the active CDK2-cyclin E complexes can phosphorylate their own inhibitor p27^{Kip1} triggering its degradation by the SCF ubiquitin ligase [49, 50] and their consequential self-activation. It has been reported that p27^{Kip1} binding to CDK4/6-cyclin D complexes is essential for their formation, and that this association do not affect their kinase activity [42] except in quiescent cells (G0), where p27^{Kip1} union to CDK4/6-cyclin D is in an inhibitory mode [48]. Cell cycle arrest is commanded by anti-mitogenic signals, such as TGF-β, resulting in D-type cyclins synthesis stop, INK4 binding to CDK4/6 and, as a result, forcing the redistribution of p27^{Kip1} to CDK2-cyclin E, preventing pRB phosphorylation and thus repressing transcription [48]. DNA damage and metabolic stress activate p53, which induces p21^{Cip1} transcription causing the inhibition of both CDK2 and CDK4 activities, resulting in G1 arrest in mammalian cells [51-54]. Phosphorylation and dephosphorylation events also control the CDK activity as binding to cyclins is not enough to activate CDK-cyclin complexes. The formation of the complex exposes the threonine residue in the T-loop of the CDK subunit to the CDK7-

cyclin H-Mat1 complex (CDK Activating Kinase, CAK) allowing its phosphorylation [14, 20]. The role of CAK is to activate CDKs complexes and it does not require phosphorylation to be active. CAK is inhibited by phosphorylation of cyclin H by CDK8-cyclin C [36]. In addition, CAK is involved in promoter clearance and progression of transcription as it is part of the general transcription factor TFIIH [43]. Once a CDK-cyclin complex is formed, it can be activated by CAK or inactivated by the WEE1 and MYT1 kinases that phosphorylate adjacent threonine and tyrosine residues (Thr14/Tyr15 in CDK1) in the CDK subunit. These inhibitory phosphorylations can be reversed by CDC25 phosphatases (CDC25A, CDC25B and CDC25C) [36].

There are other kinases families with important roles in cell cycle apart from CDKs: Aurora kinases, Polo-like kinases, SAC kinases, NIMA-related kinases and Checkpoint kinases CHK1 and CHK2. Aurora kinases (Aurora A, B and C) contribute to mitosis entry by assisting the establishment of the proper chromosome structures, building of the bipolar mitotic spindle, centrosome separation and microtubule dynamics, ensuring an accurate cell division. Polo-like kinases (PLK1-5) are less studied; PLK1 play a significant role in entering mitosis, with major functions in centrosome maturation and cytokinesis while PLK4 is essential in centriole duplication. PLK1 is the most studied member of the family and it is only found (along with PLK4) in proliferating cells whereas PLK2, 3 and 5 are also expressed in non-dividing cells. It is worth mentioning that Aurora A and PLK1 expression is also regulated by the APC/C-CDH1 complex [47, 55]. The Spindle Assembly Checkpoint (SAC) is a signalling pathway that inhibits anaphase start until chromosomes are correctly attached to the mitotic spindle, ensuring accurate segregation of sister chromatids. The SAC kinases BUB1 and BUBR1 participate in this proper chromosome-spindle attachment, while the SAC kinase MPS1 is involved in the regulation of APC/C, the centrosome duplication and cytokinesis [56]. NIMA (Never-in-mitosis *Aspergillus*)-related kinases (NEK) is a family of eleven serine/threonine kinases (NEK1-11) generally implicated in microtubule organisation [16, 43]. Finally, Checkpoint kinases CHK1 and CHK2 are key signal transducers of the genome integrity checkpoints that are activated by genotoxic insults. Once active, CHK1 and CHK2 phosphorylate downstream effectors which further propagate the checkpoint signalling leading to one response mechanism such as switching to

damage-induced transcription, DNA repair, cell cycle arrest, apoptosis or chromatin remodelling [57, 58].

As mentioned above, proper transition between cell cycle phases requires the strictly regulated degradation of cell cycle progression proteins. The activity of SCF and APC/C, the two ubiquitin ligase complexes that control the sequential degradation of these proteins, is precisely regulated to ensure or to prevent the timely degradation of the key cell cycle regulators based on signalling stimuli [47]. SCF is activated in G1, S and early M phases by SKP2, β-TrCP and Fbw7, while APC/C is functional from M to G1 by the action of CDC20 (this association requires the phosphorylation of APC/C by CDKs) and CDH1 (its phosphorylation prevents its union with APC/C) [26, 59, 60]. Therefore, in order to effectively activate cell cycle progression, mitogenic stimuli not only have to induce the synthesis of cyclins but also have to lead to the inactivation of the APC/C-CDH1 complex by CDH1 phosphorylation [46, 61]. The status of SCF substrates and its modular assembly manage the activity of this ubiquitin ligase complex in a non cell-cycle-regulated manner. Interestingly, the blocking activities of cell cycle progression are overcome by SCF degradation of its substrates such as p21^{Cip1}, p27^{Kip1}, p57^{Kip2}, cyclin E, Wee1 and Emi1 [26, 47, 59]. However, exiting mitosis requires the APC/C complexes-mediated destruction of mitotic cyclins for the beginning of telophase and for preparing the next cycle. In addition, APC/C complexes also degrade most cell cycle progression activators (PLK1, E2-C, SKP2, CDC25A, CDK1, Tome-1, Hsl1, Aurora kinases A and B, TPX2, FOXM1, CDC6 and germinin), proteins related to chromosome segregation (NEK2, cyclin A, securin, cyclin B), and eventually its own activators CDC20 and CDH1 to prepare for the next cycle [26, 28, 47, 56, 62].

The classic consideration that each cell cycle phase is driven by specific CDKs is been challenged by some genetic studies in mice that reveal that interphase CDKs (CDK2, CDK4 and CDK6) are not essential for the mammalian cell cycle of most cell types [36, 62, 63]. Mice lacking Cdk4, Cdk6 or Cdk2 are viable, suggesting a possible compensatory role between cyclin dependent kinases [64]. In fact, the knockout of CDK loci in the mouse germline showed that interphase CDKs are only required for the proliferation of specific cell types. For instance, Cdk2 is necessary for completion of prophase I during meiotic cell division in both male and female germ cells but is not

required for proliferation in mitotic cells [65, 66] and cell cycle regulation mediated by p21^{Cip1} and p27^{Kip1} [67]. Cdk4 is essential for postnatal proliferation of specialised endocrine cells types such as pancreatic β-cells and pituitary lactotrophs [64]. In addition, defects in the erythroid lineage are reported in Cdk6-deficient and double mutant lacking Cdk4 and Cdk6 mice [68]. By contrast, Cdk1 mutant mice embryos are not able to develop beyond the two-cell stage, indicating that the mitotic kinase Cdk1 is essential for cell division in the embryo and that interphase Cdks cannot compensate for its absence [62]. Moreover, Cdk1 is sufficient to drive the mammalian cell cycle in all cell types, undergoing organogenesis and developing to midgestation [69]. All these data show the complexity of the CDK-dependent regulation of the cell cycle and the variability that exists between different cell lines depending on its origin. Thus, when cell proliferation is not an option but an obligation, like in embryonic development, interphase CDKs are less important, whereas in situations where proliferation has to be only a response to specific mitogenic stimuli these CDKs play their canonical role governing the entry in the cycle and the progression through G1 phase.

1.3.2. Cell cycle defects and cancer

The portrait of the cell cycle molecular machinery is necessary to outline the importance of its regulation and relationship with neoplasic transformation. Indeed, genes that have a role in the cell cycle control (checkpoints, regulation of transcription or cell cycle progression) are frequently altered in cancer, underlying the unscheduled proliferation in tumour pathogenesis (Figure 1.3).

As it has been described, cell cycle progression in mammalian cells is regulated by different mechanisms: the CDK-dependent pathways, which include the vast number of proteins that modulate the activity of CDK complexes and directly act over the cycle machinery, the metabolic adaptations and the redox-dependent signalling. All of them enable cell cycle initiation, progression and completion by establishing a complex network of interactions. Accordingly, the study of cell cycle regulation has led to the development of new mathematical models for the characterisation of CDK-dependent

control of the cell cycle [70-72]. In addition, most of the key players of cell cycle progression are proposed and tested as anti-cancer targets with different success (see Section 1.7.1). Interestingly, inhibition not only of oncogenes but also of well-known tumour suppressor genes such as checkpoint kinases has shown good results in impairing cancer cell proliferation [43].
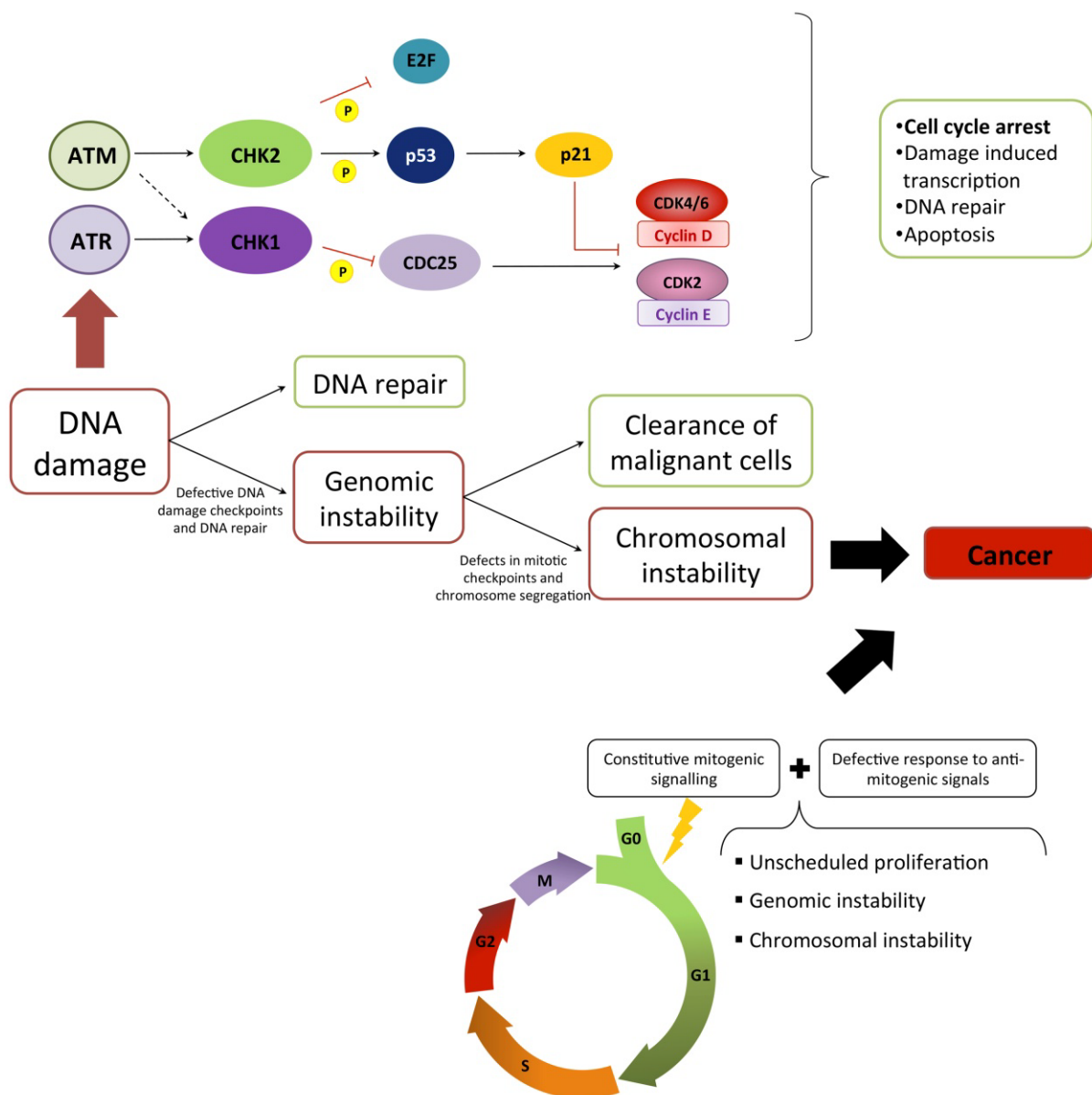
Figure 1.3. Cell cycle defects and cancer. Genes that have a role in the cell cycle control such as checkpoints, regulation of transcription or cell cycle progression are frequently altered in cancer. Misregulated CDKs can induce constitutive mitogenic signalling and defective response to anti-mitogenic signals, while defects in checkpoints and DNA repair processes can lead to unscheduled proliferation and genomic and chromosomal instability. ATM, ataxia-telangiectasia-mutated; ATR, ATM and Rad 3-related.

Overexpression of CDKs and cyclins and loss of CKI and pRB expression are often reported in human neoplasias [17, 38]. These tumour-associated modifications commonly result from chromosome alterations (amplifications and translocations of oncogenes and deletions of tumour suppressors) or epigenetic inactivation (methylation of tumour suppressor promoters). Misregulated CDKs can induce constitutive mitogenic signalling and defective responses to anti-mitogenic signals, leading to unscheduled proliferation and genomic and chromosomal instability [50, 62] (Figure 1.3). Indeed, most of human tumours show defects in G1 to S transition control. Accordingly, the CDKs involved in this transition, CDK4, 6 and 2, are altered in more than 80-90% of tumours, being the misregulation of their activity a selective step during tumour development [38, 43, 73].

The high percentage of tumours including altered CDK activity led researchers to postulate therapeutic strategies against cancer directly targeting these proteins [74-76]. Indeed, there is a broad range of drugs frequently used in chemotherapy targeting CDK activities [17, 75, 76]. These molecules target both cell cycle machinery and transcriptional CDKs inducing cell cycle arrest and cell death (see Section 1.7.1). In particular, CDK4 and CDK6 are promising targets for inhibiting cell cycle progression since their dysregulation is implicated in a wide range of human cancers, and preclinical and clinical data indicate that the inhibition of cyclin D-dependent kinase activity have therapeutic benefits [17, 41, 77-85]. In addition, metabolic studies reported that inhibition of CDK4 and CDK6 disturbs the balance between the oxidative and the non-oxidative branches of the pentose phosphate pathway, which has been previously described as one of the most robust tumour metabolic adaptations [86]. Moreover, it has been reported that some human tumour cell lines display a selective dependence on interphase CDKs [62]. Consequently, therapeutic strategies must take into account these specific requirements when designing the CDK inhibition treatment. Following that statement, it has been demonstrated that mice expressing a mutant form of cyclin D1 that bound to its kinase targets Cdk4 and Cdk6 without activating their catalytic activity were resistant to mammary tumour development induced by the *c-neu/erbB*-2 (*ErbB-2*) oncogene [81, 82]. Accordingly, downregulation of Cdk4 expression in *ErbB*-2-induced mammary tumour cells abrogates tumour formation

when re-inoculated into mammary fat pads [82]. Moreover, Cdk2-null mice and those with hemizygous disruption of Cdc25A are also protected from *ErbB*-2-induced mammary tumourigenesis [87, 88], indicating that Cdk2 and active Cdk4-cyclin D1 complexes are required for *ErbB*-2-driven mammary oncogenesis. However, cyclin D1 ablation has no effect on breast tumour development induced by *c-Myc* or *Wnt1* oncogenes [89]. This fact along with the results that demonstrate that Cdk1 is sufficient to drive the mammalian cell cycle [69] and those that suggest that cells lacking interphase CDKs are able to normally complete the proliferation cycle, point out the compensatory role that other kinases may play to enable cell cycle progression [64, 65, 67]. Therefore, it is essential to accurately depict tumour cell characteristics to choose the most suitable therapy for each kind of tumour. In *ERBB2*-positive breast tumours, pharmacological specific inhibition of interphase CDKs could be a good strategy as it might preferentially target breast cancer cells [78]. Likewise, in *RAS*-induced tumours CDK4 seems to be the best target while the inactivation of CDK2 activity may possibly be a good therapeutic approach in *c-MYC*-induced tumours [43, 90-92].

Mutations in DNA damage checkpoint, mainly in the ATM (ataxia-telangiectasia-mutated)-CHK2-p53 pathway, can result in CDK hyperactivity, cell cycle progression in presence of damaged DNA, genomic instability and ultimately, cancer [58, 62] (Figure 1.3). In fact, genome instability has been reported as an enabling characteristic that facilitates the acquisition of the hallmarks of cancer highlighting its significance in cancer development [6]. The mitotic checkpoint prevents chromosome mis-segregation, aneuploidy and genome instability, which are common characteristics of many human cancers [93]. Either defects in this checkpoint, the mitotic kinases (CDK1, Aurora and PLK kinases) or the spindle assembly checkpoint (SAC) pathway can end in apoptosis or abnormal chromosome content. Therefore, novel anticancer strategies propose taking advantage of the characteristic genome instability of tumour cells to activate their apoptosis under conditions that do not affect normal cells [93, 94].

It is worth noting that uncontrolled tumour cell proliferation involves a metabolic reprogramming in order to fulfil the augmented demand of energy and macromolecules [95]. The dependencies on specific metabolic substrates such as

glucose or glutamine exhibited by tumour cells are determined by their alterations in oncogenes and tumour suppressor genes. For instance, c-MYC-transformed cells display addiction to glutamine as a bioenergetic substrate and are sensitive to inhibitors of glutaminolysis [96].

1.4. Metabolic reprogramming of tumour cells

Metabolism is the term that is used to describe the integrated network of chemical reactions involved in sustaining growth, proliferation and survival of cells and organisms. These reactions are catalysed by tightly regulated enzymes, sensing environmental cues and providing energy, reducing power and macromolecules to supply the cellular needs. Metabolic reactions can be classified into catabolic pathways that produce energy (adenosine triphosphate, ATP) through the breakdown of molecules, and anabolic pathways that synthesise molecules through energy-consuming processes. The metabolic network is regulated by signalling pathways that respond to the specific cellular needs which, in turn, vary depending on the cell type and proliferative state.

In particular, tumour cells switch their core metabolism to meet the increased requirements of cell growth and division. Indeed, tumour metabolic reprogramming involves the enhancement of key metabolic pathways such as glycolysis, pentose phosphate pathway (PPP), glutaminolysis and lipid, nucleic acid and amino acid metabolism [95] (Figure 1.4). Thus, key oncogenic pathways converge to adapt the metabolism of carbohydrates, proteins, lipids and nucleic acids to the dynamic tumour microenvironment, where nutrient and oxygen concentrations are spatially and temporally heterogeneous [97, 98]. Then, the study of the tumour metabolic reprogramming and its connection with oncogenic signalling will lead to the identification of new targets for cancer therapy.
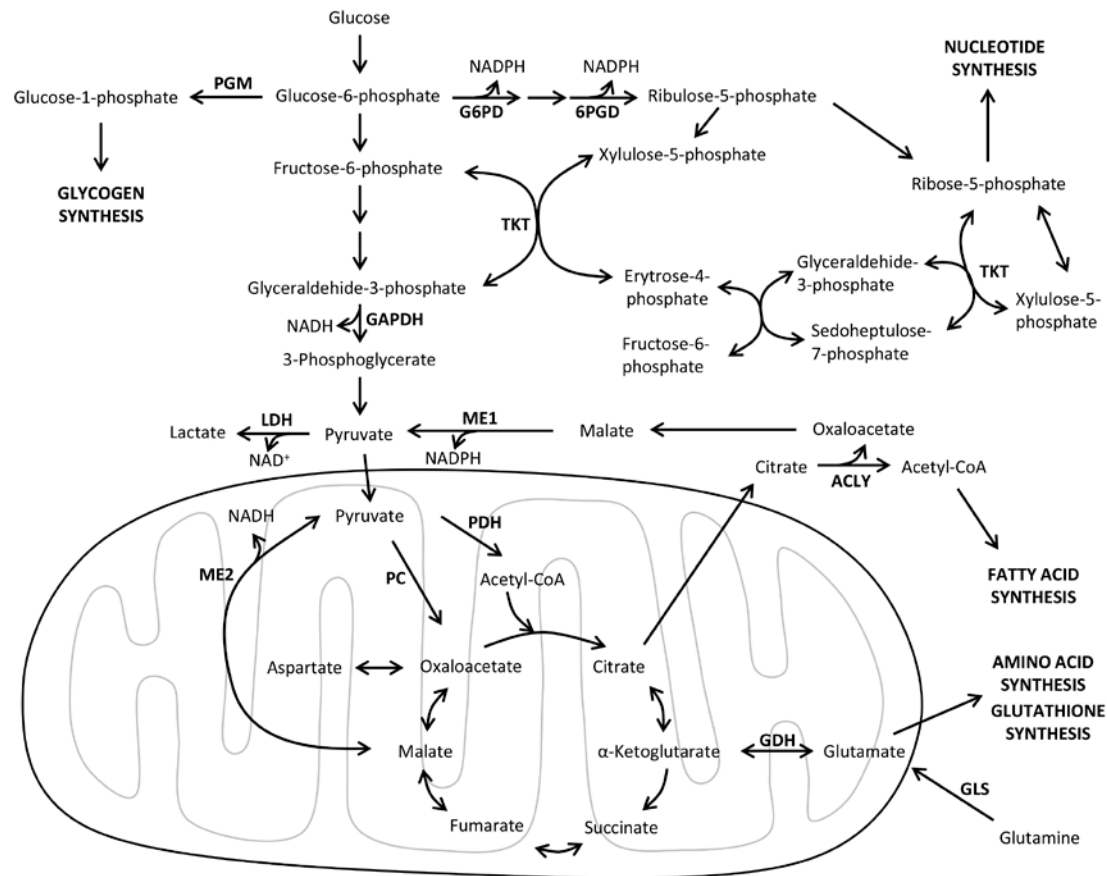
Figure 1.4. Major metabolic pathways involved in tumour metabolic reprogramming. An overview of the main catabolic and anabolic metabolic pathways supporting tumour cell growth and survival. Enzymes are shown in **bold**. 6PGD, 6-phosphogluconate dehydrogenase; ACLY, ATP citrate lyase; CoA, coenzyme A; GLS, glutaminase; GDH, glutamate dehydrogenase; G6PD, glucose-6-phosphate dehydrogenase; GAPDH, glyceraldehyde-3-phosphate dehydrogenase; LDH, lactate dehydrogenase; ME1, malic enzyme 1 cytoplasmic form; ME2, malic enzyme 2 mitochondrial form; NAD$^+$, nicotinamide adenine dinucleotide oxidised form; NADH, nicotinamide adenine dinucleotide reduced form; NADPH, nicotinamide adenine dinucleotide phosphate reduced form; PC, pyruvate carboxylase; PDH, pyruvate dehydrogenase; PGM, phosphoglucomutase.

1.4.1. Glycolysis and the Warburg effect

Glycolysis pathway metabolises glucose and other sugars into pyruvate in an oxygen-independent manner to generate energy in the form of ATP and intermediates, which are used as precursors for the biosynthesis of macromolecules [99]. Under physiologic oxygen concentrations, pyruvate enters the mitochondria to be oxidised through an oxygen-dependent process known as oxidative phosphorylation (OXPHOS), which

couples the oxidation of metabolites and the electron transport chain (ETC) with ATP production, being also a source of reactive oxygen species (ROS) [97].

The first metabolic phenotype observed in tumour cells was described by Otto Warburg as a shift from oxidative phosphorylation to aerobic glycolysis to generate ATP even in presence of oxygen, which is known as the Warburg effect [100, 101]. Therefore, cancer cells convert most incoming glucose to lactate rather than entering in the mitochondria to be oxidised through oxidative phosphorylation [102]. Initially, it was believed that the Warburg effect resulted from defects in the mitochondrial function of cancer cells. However, this effect is also exhibited by tumour cells with intact and functional mitochondria, suggesting that their preference for glycolysis might confer benefits on them such as reduced levels of ROS, high production of metabolic intermediates for macromolecular biosynthesis and acidification of extracellular microenvironment due to lactate excretion [103, 104]. It is worth noting that the ATP produced per molecule of glucose catabolised through glycolysis is considerably less efficient than through oxidative phosphorylation (2 versus 31-38 molecules of ATP [105], respectively), causing tumour cells to greatly increase both the rate of glucose uptake and glycolysis to sustain their increased energetic, biosynthetic and redox needs [106]. Conveniently, the high glycolytic rates displayed by cancer cells allow their visualisation by ^{18}F-deoxyglucose positron emission tomography (FDG-PET) and assist tumour detection, prevention and treatment [107].

Over the past decade, numerous studies and reviews have supported the hypothesis that the Warburg effect can be explained by the alterations in multiple signalling pathways resulting from mutations in oncogenes and tumour suppressor genes. In effect, the enhanced glycolytic rate can be justified through the overexpression of glucose transporters and several key glycolytic enzymes mediated by specific activated oncogenes (e.g. *PI3K* and *c-MYC*) and transcription factors (e.g. HIF1), contributing to the acquisition of the Warburg effect and maintaining tumour cell growth and survival [98, 104, 108]. Likewise, loss-of-function mutations in tumour suppressor *TP53* (encoding p53) also contribute to the Warburg effect, since they prevent p53-mediated transcriptional repression of glucose transporters GLUT1 and GLUT4, activation of cytochrome c oxidase assembly protein (SCO2) expression which

promotes OXPHOS, and upregulation of TP53-induced glycolysis and apoptosis regulator (TIGAR) expression which reduces the intracellular concentration of the glycolytic activator fructose-2,6-bisphosphate [97, 109].

Interestingly, the metabolic switch in tumour cells has a key role in the establishment of many other cancer hallmarks [95]. In fact, some metabolic enzymes have been described as multifaceted proteins which can directly regulate transcription, glucose homeostasis and resistance to cell death [110, 111]. Therefore, the targeting of multifunctional metabolic enzymes may restore the tumour cells susceptibility to cell death, offering new options for cancer therapy. For example, GAPDH is one of the key glycolytic enzymes that exhibits a variety of functions unrelated to its classical role in energy production [112].

1.4.1.1. Key roles of glyceraldehyde-3-phosphate dehydrogenase as a multifunctional enzyme

Glyceraldehyde-3-phosphate dehydrogenase (GAPDH, EC 1.2.1.12) is an essential regulator of glycolysis ubiquitously overexpressed in 21 cancer classes, being one of the three glycolytic genes overexpressed in colorectal cancer, along with enolase and pyruvate kinase [113, 114]. This fact advises against its widely extended use as a housekeeping gene. GAPDH catalyses the phosphorylation and oxidation of glyceraldehyde-3-phosphate to 1,3-bisphosphoglycerate coupled with the reduction of NAD+ to NADH. GAPDH is constituted by four identical subunits of 37 kDa and has binding sequences for coenzymes NAD+ and NADH and for nucleic acids. In fact, GAPDH is one of the multifaceted glycolytic enzymes that contributes to cell survival and resistance to cell death [111], becoming a promising biomarker in cancer research. Moreover, GAPDH expression is regulated by transcription factors which are frequently altered in cancer such as HIF-1α, p53 or AP-1. In addition, *GAPDH* gene has insulin (IRE) and hypoxia response elements (HRE) in its promoter [115]. As a multifunctional enzyme, GAPDH is involved in endocytosis, membrane fusion, vesicle secretion, transcription coactivation, cell cycle regulation, tRNA transport, mRNA stabilisation and DNA repair and replication [112, 115, 116]. Paradoxically, GAPDH also plays

important roles activating apoptosis by nuclear translocation upon cellular stress, and protecting from caspase-independent cell death (CICD) by autophagic removal of damaged mitochondria [116].

Interestingly, due to its glycolytic role, GAPDH may also play a part in metabolic reprogramming, one of the hallmarks of cancer [6] and a suitable target for cancer therapy as tumour cells require an increased use of the metabolic pathways to sustain their energetic and biosynthetic needs. As described before, aerobic glycolysis with high lactate production is one of the main phenotypic characteristics of tumour metabolism [100]. This phenomenon gives advantage to cancer cells by an increased production of NADH and an acidification of the microenvironment due to lactate excretion, favouring tumour invasion [104]. In addition, the high rate of glucose uptake and the increased glycolytic flux in cancer cells meet the requirements for maintaining the energy status, the biosynthesis of macromolecules and the maintenance of cellular redox balance [97]. Consequently, GAPDH is likely to be a key enzyme implicated in tumourigenesis and cancer progression.

1.4.2. Pentose phosphate pathway

Pentose phosphate pathway (PPP) is one of the main metabolic pathways that enables tumour cell proliferation by regulating the flux of carbons between nucleic acid synthesis and lipogenesis to support DNA replication and RNA production. Nucleic acids are composed by combinations of four different nucleotides which in turn are constituted by an organic base (purine, in the case of the nucleotides adenine and guanine, or pyrimidine, in the case of cytosine, thymine, and uracil), a pentose (ribose for RNA or deoxyribose for DNA) and one or more phosphate groups. The pentose phosphate is mainly obtained through the PPP, which also generates nicotinamide adenine dinucleotide phosphate (NADPH). NADPH is an essential cofactor for providing reducing equivalents for lipid and amino acid biosynthesis, and for modulating oxidative stress through the maintenance of the reduced glutathione (GSH) pool [117]. The association between upregulation of PPP and tumour cell proliferation is been

extensively studied, as PPP plays a pivotal role in allowing tumour cells to meet their anabolic demands and counteract oxidative stress [118-120].

The PPP is divided into the oxidative branch and the non-oxidative branch (Figure 1.5). The oxidative branch catalyses the irreversible transformation of glucose-6-phosphate into ribose-5-phosphate (R5P), yielding NADPH. The non-oxidative branch is a reversible pathway that interconverts R5P and glycolytic intermediaries. The enzymes that mainly regulate the PPP are glucose-6-phosphate dehydrogenase (G6PD) in the oxidative branch and transketolase (TKT) in the non-oxidative branch [121-123]. Several oncogenic signalling pathways promote G6PD activation by posttranslational mechanisms [117], while the tumour suppressor p53 directly inhibits G6PD and the PPP [119]. Proliferating cells increase G6PD activity during late G1 and S phases [124], while the activation of the SCF ubiquitin ligase by its interaction with the protein-β-transduction repeat-containing protein (β-TrCP) allows the recognition of PFKFB3 and its proteasome degradation during S phase [60, 125], promoting the shuttling of the glycolytic substrates through the PPP, increasing the production of NADPH and R5P to allow S phase progression.
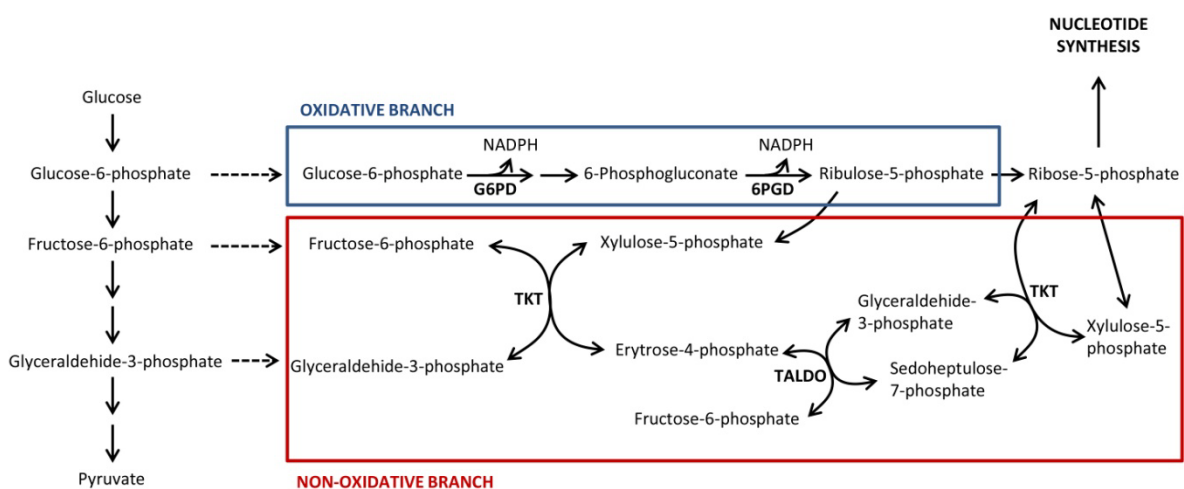
Figure 1.5. Oxidative and non-oxidative branches of the pentose phosphate pathway. The irreversible oxidative branch of the pentose phosphate pathway (PPP) catalyses the conversion of glucose-6-phosphate into ribose-5-phosphate producing NADPH, while the reversible non-oxidative branch can either recycle the excess of pentoses or synthesise ribose form glycolytic intermediaries. The main enzymes involved in the regulation of the PPP are glucose-6-phosphate dehydrogenase (G6PD) in the oxidative branch and transketolase (TKT) in the non-oxidative branch. NADPH, nicotinamide adenine dinucleotide phosphate reduced form; 6PGD, 6-phosphogluconate dehydrogenase; TALDO, transaldolase.

1.4.3. Lipid metabolism

Triacylglycerides, phosphoglycerides, sterols and sphingolipids are hydrophobic or amphipathic molecules known as lipids. Fatty acids are long hydrocarbon chains with a carboxy-terminal group that constitute the main component of triacylglycerides and phosphoglycerides, being also present in sphingolipids and sterol esters. While triacylglycerides are used as energy storage units, phosphoglycerides, sterols and sphingolipids are major structural components of plasma membranes. Lipids are also involved in signal transduction and participate in the regulation of cell growth, proliferation, differentiation, survival, apoptosis, membrane homeostasis, motility and drug resistance [126, 127].

Tumour metabolic reprogramming involves an increase in lipid biosynthesis to supply the building blocks for membrane formation and sustain the high proliferative rate of tumour cells. Distinctively, tumour cells mainly activate and thrive on *de novo* lipid biosynthesis, while most non-transformed cells rely on extracellular lipids. This augmented lipogenesis is reflected in an upregulation of many lipogenic enzymes such as ATP citrate lyase (ACLY), fatty acid synthase (FASN) and acetyl-CoA carboxylase (ACC) [128]. The acetyl groups for fatty acids biosynthesis are provided by mitochondrial citrate, which is exported to the cytosol where ACLY catalyses its conversion into acetyl-CoA and oxaloacetate [129]. Then, malate dehydrogenase (MDH) and malic enzyme (ME) can produce pyruvate from oxaloacetate, yielding NADPH which in turn can be used for fatty acid biosynthesis. In addition, lipid biosynthesis is also connected to pentose phosphate pathway through the consumption of the NADPH generated in the oxidative branch of the PPP. Next, acetyl-CoA is converted to malonyl-CoA by ACC, and both acetyl and malonyl groups are condensed through a cyclical series of reactions by FASN, resulting in long-chain saturated fatty acids, predominantly palmitate. Further elongation and desaturation of *de novo* synthesised saturated fatty acids can be obtained through the action of elongases and desaturases [126, 130]. On the other hand, the mitochondrial degradation of fatty acids through β-oxidation releases large amounts of ATP and generates ROS through the TCA cycle and the oxidative phosphorylation [126, 127].

Sterol regulatory element-binding proteins (SREBPs) are the main transcription factors regulating the expression of most of enzymes involved in the synthesis of fatty acids and cholesterol. In turn, SREBPs are negatively regulated by tumour suppressors such as p53, pRB and AMPK, and activated by oncogenes such as PI3K and Akt. For instance, besides promoting glycolysis, Akt upregulates the expression of the lipogenic enzymes through activation and nuclear translocation of SREBP, and positively regulates ACLY by direct phosphorylation, linking enhanced glycolysis with increased lipogenesis [130, 131]. Therefore, targeting lipogenic pathways is thought to be a promising strategy for cancer therapy, as lipogenic enzymes are found to be upregulated or activated in tumour cells to satisfy their increased demand for lipids [127, 128].

1.4.4. Amino acids metabolism

Amino acids are organic compounds containing a specific side chain and both amino and carboxyl groups that enable them undergo polymerisation to form proteins. In addition, amino acids can be metabolised as a source of carbon and nitrogen for biosynthesis. There are 20 different amino acids, 11 of which can be endogenously synthesised by mammal cells while the remainder are known as essential amino acids, and must be obtained from external sources. In fact, amino acids have a pivotal role in supporting proliferative metabolism and are required for cell survival. It is not surprising, then, that cells have developed an amino acid sensing system through mechanistic target of rapamycin (mTOR) signalling to determine whether there are sufficient amino acids available for protein biosynthesis. Specifically, leucine, glutamine and arginine act as critical signalling molecules that activate mTOR pathway [132, 133]. In response to amino acid deficiency, inhibition of mTOR act to rapidly suppress protein synthesis and induce autophagy, in order to maintain a free amino acid pool which may be required during prolonged amino acid limitation [134].

Non-essential aminoacids can be synthesised from glycolytic intermediates such as 3-phosphoglycerate which is the precursor for serine, or pyruvate that can be converted to alanine. In addition, TCA intermediates like oxaloacetate and α-ketoglutarate can

synthesise aspartate, asparagine and glutamate. Moreover, glutamate can be converted to L-glutamate-5-semialdehyde (GSA) and 1-pyrroline-5-carboxylate (P5C), which are further converted to ornithine and proline, respectively [135]. Next, ornithine can enter the urea cycle and produce arginine. Also, serine can generate cysteine and glycine [136].

Highly proliferating cells, like tumour cells, consume essential and non-essential amino acids from external sources since the capacity of endogenous synthesis is not sufficient to fulfil their amino acidic increased needs [137]. However, amino acids are hydrophilic molecules that require selective transport proteins to cross the cell membrane. Reasonably, four amino acid transporters (SLC1A5, SLC7A5, SLC7A11 and SLC6A14) have been found to be overexpressed in cancer cells to increase the uptake of amino acids and meet their growing demands [137].

In tumour cells, the consumption of some amino acids (specially non-essential amino acids) greatly exceeds the requirements for protein biosynthesis, indicating their use as intermediates in metabolism by providing one carbon units, replenishing the TCA cycle or synthesising fatty acids, nucleotides and other amino acids [136]. For example, glutamine, glycine and aspartate are required for nucleotide biosynthesis, while serine and glycine play an essential role in a one-carbon metabolism, generating precursors for the biosynthesis of lipids, nucleotides and proteins, regulating the redox status and participating in protein and nucleic acid methylation [138, 139]. The net conversion of serine to glycine can be catalysed either by the cytosolic or mitochondrial serine hydroxymethyltransferase (SHMT1 and SHMT2, respectively). The metabolic activity of SHMT2 has been shown to strongly correlate with the rates of proliferation across the NCI60 cancer cell collection [140]. Interestingly, SHMT2 has been suggested as fundamental to sustain cancer metabolism by fuelling heme biosynthesis and therefore oxidative phosphorylation [141].

It is worth noting that the reactions catalysing the degradation of proline produce significant amounts of ROS. The first step of proline degradation is catalysed by the mitochondrial proline dehydrogenase (PRODH), which is a tumour suppressor that inhibits proliferation and induces apoptosis [135, 142]. This mitochondrial enzyme is

linked to the electron transport chain through complex III, being shown as a source for ATP and ROS generation. In addition, P5C and proline can act as a redox couple, carrying reducing potential into and oxidising potential out of the mitochondria by the combined activities of the mitochondrial PRODH and the cytosolic form of P5C reductase (PYCR) that preferably uses NADPH [135, 142, 143].

It is worth noting that glutamine is the amino acid presenting the most prominent role in tumour metabolism, and some tumour cells have been reported to exhibit dependence on this amino acid [96, 144].

1.4.5. Mitochondrial metabolism

Mitochondrial function is essential for cancer cells as it is involved in numerous crucial cellular processes such as ATP generation, regulation of programmed cell death, and regulation of signal transduction pathways through ROS production, cytosolic calcium levels modulation and small metabolites trafficking. Indeed, impairment of mitochondrial function and reduction of mitochondrial biogenesis greatly suppresses tumour formation, growth and proliferation [130, 145, 146]. Conversely, enhancement of mitochondrial biogenesis is advantageous for tumour cells [130, 147]. On the other hand, alterations in mitochondrial function can lead to several diseases including cardiovascular dysfunctions, muscular degeneration and cancer [145, 148].

In the presence of oxygen, oxidative phosphorylation (OXPHOS) is the most efficient mechanism for synthesising ATP. OXPHOS is coupled to the oxidation of reduced nicotinamide adenine dinucleotide (NADH) and flavin adenine dinucleotide (FADH$_2$) through the electron transport chain. The mitochondrial respiratory chain, located in the mitochondrial inner membrane, comprises four complexes (I to IV) that are responsible for the oxidation of the reducing equivalents in the form of NADH or FADH$_2$ and the reduction of molecular oxygen (final electron acceptor) to water. This process is coupled to the pumping of protons into the mitochondrial intermembrane space, resulting in a proton gradient that is used by the ATPase (complex V) to produce ATP [149] (Figure 1.6).
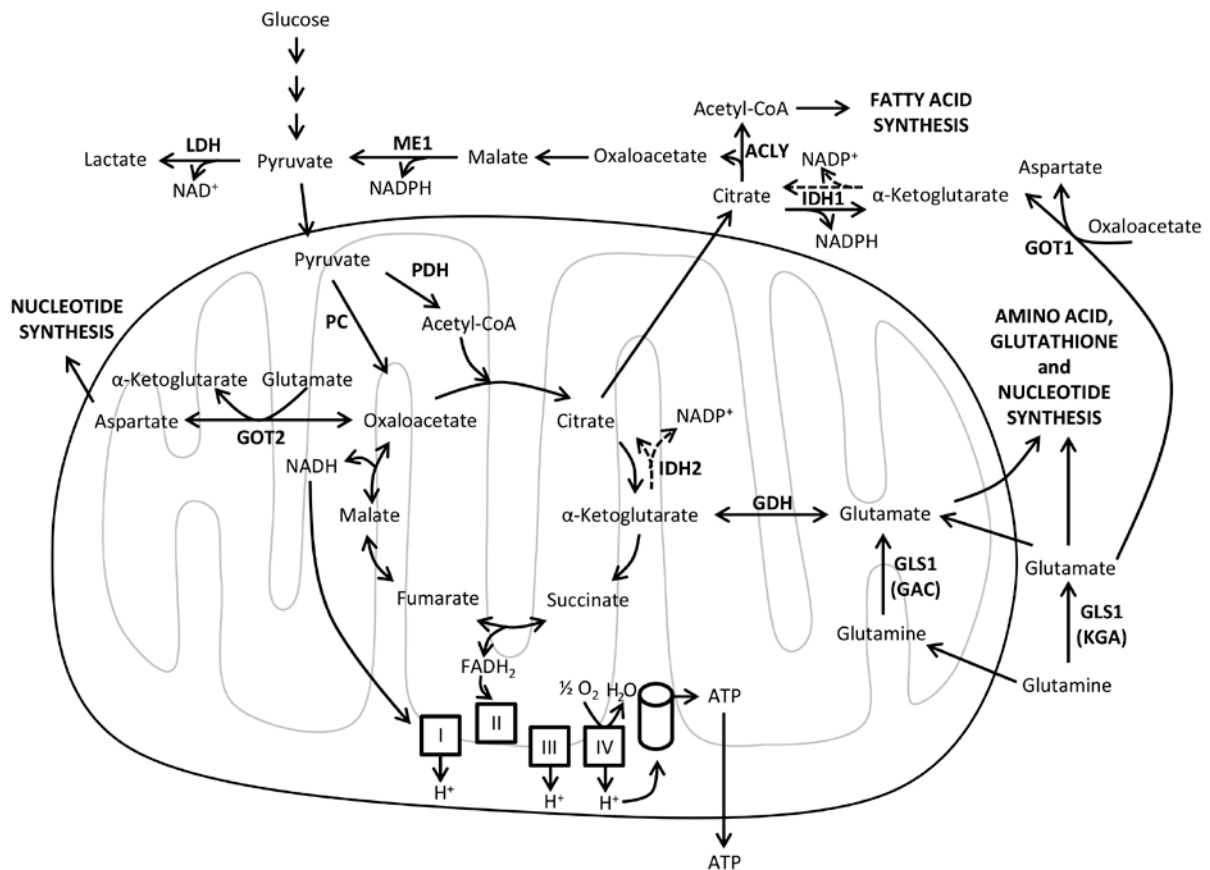
Figure 1.6. Mitochondrial metabolism. Schematic representation of the biosynthetic and bioenergetic reactions of the TCA cycle and the oxidative phosphorylation (OXPHOS). OXPHOS is coupled to the oxidation of NADH and FADH$_2$, which are produced in the TCA cycle, via the electron transport chain (ETC, also known as the mitochondrial respiratory chain). The ETC comprises four complexes (I to IV) that transfer electrons generating a gradient of protons in the mitochondrial intermembrane space (H$^+$), which is used by the ATPase (complex V) to produce ATP. Reductive carboxylation of α-ketoglutarate by IDH1 and IDH2 produces citrate (dashed arrows). ACLY, ATP citrate lyase; ATP, adenosine triphosphate; CoA, coenzyme A; FADH$_2$, flavin adenine dinucleotide reduced form; GAC, glutaminase C; GDH, glutamate dehydrogenase; GLS1, glutaminase 1; GOT1, glutamic-oxaloacetic transaminase 1 cytoplasmic form; GOT2, glutamic-oxaloacetic transaminase 2 mitochondrial form; IDH1, isocitrate dehydrogenase cytoplasmic form; IDH2, isocitrate dehydrogenase mitochondrial form; KGA, kidney (K-type) glutaminase; LDH, lactate dehydrogenase; ME1, malic enzyme 1 cytoplasmic form ; ME2, malic enzyme 2 mitochondrial form; NAD$^+$, nicotinamide adenine dinucleotide oxidised form; NADH, nicotinamide adenine dinucleotide reduced form; NADP$^+$, nicotinamide adenine dinucleotide phosphate oxidised form; NADPH, nicotinamide adenine dinucleotide phosphate reduced form; PC, pyruvate carboxylase; PDH, pyruvate dehydrogenase.

Among the metabolic pathways that take place in the mitochondria, the TCA cycle is a route of pivotal importance for the entire cellular metabolism and, in particular, for oxidative metabolism. Remarkably, TCA cycle provides precursors for the biosynthesis

of lipids, nucleic acids and proteins, as well as reducing equivalents (NADH and FADH$_2$) for ATP production (Figure 1.6). Genetic studies have found mutations in several genes that encode enzymes of the TCA cycle including citrate synthase, aconitase, isocitrate dehydrogenase, succinate dehydrogenase and fumarate hydratase, which lead to the dysfunction of the TCA cycle and are associated with some tumour types [148, 150, 151].

1.4.5.1. Glutamine metabolism

Glutamine is the most abundant amino acid in plasma and in intracellular pools, being consumed at greatly higher rates than other amino acids by tumour cells [144]. Glutamine plays several cellular key roles as a nitrogen donor for nucleotide and protein synthesis, a carbon source for energy production and lipid biosynthesis, and a precursor for some non-essential amino acids and antioxidant GSH biosynthesis [144, 152]. Despite being traditionally considered a non-essential amino acid, glutamine is crucial for the proliferation of most cells and the viability of some tumour cells that have developed glutamine dependence [153].

The expression levels of oncogenes and tumour suppressors are decisive to regulate glutamine metabolism [151, 154], while tumour genetics can direct cellular dependence on glutamine for survival [152]. In fact, tumour cells overexpressing c-MYC reprogram their mitochondrial metabolism to depend on glutamine for the maintenance of cell viability, mitochondrial integrity and TCA cycle anaplerosis, triggering cellular addiction to glutamine and displaying increased sensitivity to glutamine deprivation [96, 155].

In addition to glycolysis, many tumour cells also rely on glutamine to fulfil their bioenergetic and metabolic needs. Indeed, glutamine catabolism is the source of many precursors for major anaplerotic processes such as the TCA cycle. Cells requiring *de novo* lipid biosynthesis, like tumour cells, divert citrate from the TCA cycle to produce lipogenic acetyl-CoA. The depletion of citrate from the TCA cycle creates a need for anaplerotic replenishment of the cycle, which can be provided through oxidative

metabolism of glutamine. Oxidation of glutamine in the mitochondria begins with its conversion to glutamate catalysed by glutaminase (GLS). Glutaminase is a pivotal enzyme in the regulation of glutamine metabolism in tumour cells which has recently gathered some attention as a promising target for cancer therapy [156-158]. There are three mammalian glutaminase isoforms; kidney (K-type) glutaminase (KGA) and glutaminase C (GAC) are encoded by *GLS* and referred to as GLS1, while liver (L-type) glutaminase (LGA) is encoded by *GLS2* and usually known as GLS2 [159]. Glutamate can be converted to α-ketoglutarate by either glutamate dehydrogenase (GDH) or transaminases, to feed the TCA cycle (Figure 1.6). In addition, glutamate can serve as a precursor of GSH and non-essential amino acids such as aspartate, alanine, proline and arginine. α-ketoglutarate levels are determinant for the regulation of HIF1α degradation through prolyl hydroxylase (PHD) sensing pathway [132, 160]. Furthermore, glutaminolysis and α-ketoglutarate production are also involved in the activation of mTOR signalling [133, 161]. Glutamine carbons can exit the TCA cycle in the form of malate, which can be converted to pyruvate by malic enzyme (ME) with NADPH generation [162]. Both glutamine-derived NADPH and GSH production allow tumour cells to reduce the oxidative stress associated with mitochondrial respiration and rapid cell proliferation.

It is worth noting that glutamine utilisation as a respiratory substrate through the TCA cycle produces NADH and $FADH_2$ that provide electrons for the mitochondrial electron transport chain to generate ATP (Figure 1.6). Remarkably, glycolytic contribution to total ATP synthesis in tumour cells differs widely depending on cell type, from over 60% to less than 1%, with a mean contribution of 17±18% in the tested cell lines [163]. These results are confirmed by a flux balance analysis across the NCI-60 cell lines [140, 164] which shows that oxidative phosphorylation contributes to 70-84% of the total cellular ATP production [165]. Therefore, oxidative metabolism is the major energetic source in many cancer cell lines.

Together, glucose and glutamine are the two principal nutrients to coordinately fuel the proliferation of tumour cells by supplying not only ATP but also key precursors for protein, lipid and nucleic acid biosynthesis (Figures 1.4 and 1.6). In fact, some cancer cells can switch their carbon source in response to nutrient availability. For example,

glucose withdrawal increases GDH activity in c-MYC-transformed glioblastoma cells [166], while glutaminase silencing and consequent impairment of glutamine oxidative metabolism induce a compensatory anaplerotic mechanism catalysed by pyruvate carboxylase (PC) that enables the use of glucose-derived pyruvate for anaplerosis [167]. However, the metabolic compensation adopted by tumour cells renders them absolutely dependent on the new upregulated pathways, opening new opportunities for cancer combined therapies. Therefore, the metabolic flexibility and compensatory abilities exhibited by some tumour cells have to be carefully considered when designing cancer therapies based on targeting metabolism.

1.4.5.2. Glutamine reductive carboxylation

There are two different glutamine-dependent pathways for fatty acid biosynthesis. On the one hand, cells can oxidatively metabolise glutamine-derived α-ketoglutarate to citrate in the TCA cycle and subsequently transport it to the cytosol to generate oxaloacetate and lipogenic acetyl-CoA [129]. In addition, malate produced from glutamine in the TCA cycle can generate pyruvate through the action of malic enzyme, which can be further metabolised to lipogenic acetyl-CoA. On the other hand, α-ketoglutarate obtained from glutamine can be directly converted to citrate by reductive carboxylation, especially in tumour cells under hypoxic conditions or when mitochondrial respiration is impaired to sustain cell growth under these circumstances [168-171]. This reaction takes advantage of the reversible activity catalysed by isocitrate dehydrogenase. The cytosolic $NADP^+$/NADPH-dependent isocitrate dehydrogenase 1 (IDH1) is the main enzyme catalysing the reversible reductive carboxylation of α-ketoglutarate to isocitrate and $NADP^+$ [168] (Figure 1.6). Indeed, reductive carboxylation of glutamine provides a glucose-independent pathway to generate acetyl-CoA for biosynthesis, allowing cells to conserve glucose for the production of biosynthetic precursors that are specifically generated from glucose [168].

1.4.6. Redox status and cell cycle progression

A fundamental objective of the metabolism is to maintain an appropriate redox status, together with the appropriate supply of energy and metabolic precursors for biosynthetic processes. Reactive oxygen species (ROS) are a group of molecules that include species that possess an increased reactivity compared to that of molecular oxygen, and include superoxide (O_2^-), hydrogen peroxide (H_2O_2), hydroxyl radical ($\cdot OH$) and singlet oxygen ($^1O_2$). Endogenous production of ROS does not only arise from the mitochondrial metabolism, but can also come from other organelles such as the peroxisome or through the NADPH oxidase (NOX) complex [172, 173].

Moderate levels of ROS can act as intracellular messengers regulating intensity and duration of cell signalling pathways [174-176]. Non-radical oxidants as H_2O_2, unlike more reactive free radicals such as O_2^-, $\cdot OH$ or $^1O_2$, modulate the redox status of cysteine residues in kinases, phosphatases and other regulatory factors controlling redox-dependent signal transduction [175, 177, 178]. To prevent oxidative damage, ROS generation is modulated by highly efficient enzymes such glutathione peroxidase, peroxiredoxin, superoxide dismutase or catalase [179]. For example, superoxide dismutase catalyse the dismutation of O_2^- into molecular oxygen (O_2) and H_2O_2, while glutathione peroxidase catalyses the reduction of H_2O_2 to water, oxidising reduced glutathione (GSH) to GSSG. In turn, glutathione reductase recycles oxidised glutathione to its reduced form, using electrons from the NADPH. The main sources of NADPH are the oxidative branch of PPP, the cytosolic form of the malic enzyme and NADP-dependent isocitrate dehydrogenase [97]. Recently, the reaction catalysed by methylenetetrahydrofolate dehydrogenase has been proposed as an additional and relevant source of NADPH [180, 181]. Also, as discussed before, a significant role associated to redox homeostasis has been suggested for the metabolism of proline [143].

ROS levels are used by the cell to sense the oxidative stress and mediate the adequate responses. However, some controversy seems to be on the effect of ROS on the progression of cell cycle. For instance, H_2O_2 can both halt and promote the cell cycle, while O_2^- has been shown to provoke or prevent apoptosis, depending on the cell type

[182]. These discrepancies may arise from the dual role of ROS that regulate contradictory mechanisms in a dose-dependent manner. High ROS levels imply high risk of DNA and cellular damage, triggering the suppression of DNA replication, cell cycle arrest and, finally, apoptosis [183-185]. On the other hand, it has also been reported that moderate increases in ROS are required for cell cycle re-entry after quiescence and for G1 phase progression [176, 186, 187]. Therefore, when redox-dependent signalling effects are addressed, fine evaluation of ROS concentration is required in order to identify its role unequivocally.

Intracellular ROS levels show a cyclic distribution through the cell cycle [188] (Figure 1.7). The cell cycle transition from quiescence to division (G0 to G1) is the only one that is not dependent on CDK-cyclin complexes, but rather regulated by redox-dependent signalling [176]. Indeed, growth factor induction of proliferation requires H_2O_2 formation to activate SOS/RAS/RAF/ERK and PI3K/Akt kinase cascades. Moreover, it has been described that redox-dependent signalling pathways mediating G0 to G1 transition converge on interphase CDKs regulators such as $p16^{INK4a}$, $p27^{Kip1}$ and cyclin D1 [48, 189-191]. High oxidative stress induces $p21^{Cip1}$ activation and $p16^{INK4a}$ and $p27^{Kip1}$ accumulation through p38 MAPK activation and forkhead box O (FOXO) transcription factors, respectively. These proteins lead to CDK-cyclin D sequestration, cell cycle arrest and, subsequently, senescence. However, antioxidant treatment of proliferating cells reduces ROS levels to a minimum and leads to a decrease in cyclin D1 levels, an accumulation of $p27^{Kip1}$ and the hypophosphorylation of pRB that also ends in cell cycle arrest in G1 phase [187, 192]. Therefore, moderate ROS formation is essential for G1 progression and cell proliferation, but higher or lower levels lead to the opposite effect. In fact, ROS act over $p16^{INK4a}$, $p21^{Cip1}$, $p27^{Kip1}$ and p53 regulating transcription and activity of D-type cyclins, which are essential for G1 progression [176, 186]. Moreover, moderate ROS levels have been described to favour cyclin accumulation by inducing APC/C-CDH1 dissociation which also enables cell cycle progression [187].

The key event regulating G1 to S transition is pRB hyperphosphorylation, mediated by CDK-cyclin complexes in response to growth stimuli and ROS. When intracellular redox potential is higher than −207 mV (the redox potential of the reaction of

phosphorylation of the pRB), pRB is dephosphorylated and cell cycle is arrested [193]. It has been reported that at the G1/S boundary, mitochondria are able to undergo a transition to a fused hyperpolarised state maximising ATP production, which is necessary to S transition. Failure to achieve this increased bioenergetic state leads to a G1/S checkpoint that involves the sequential activation of AMPK, p53 and ultimately the downregulation of E cyclins [194].
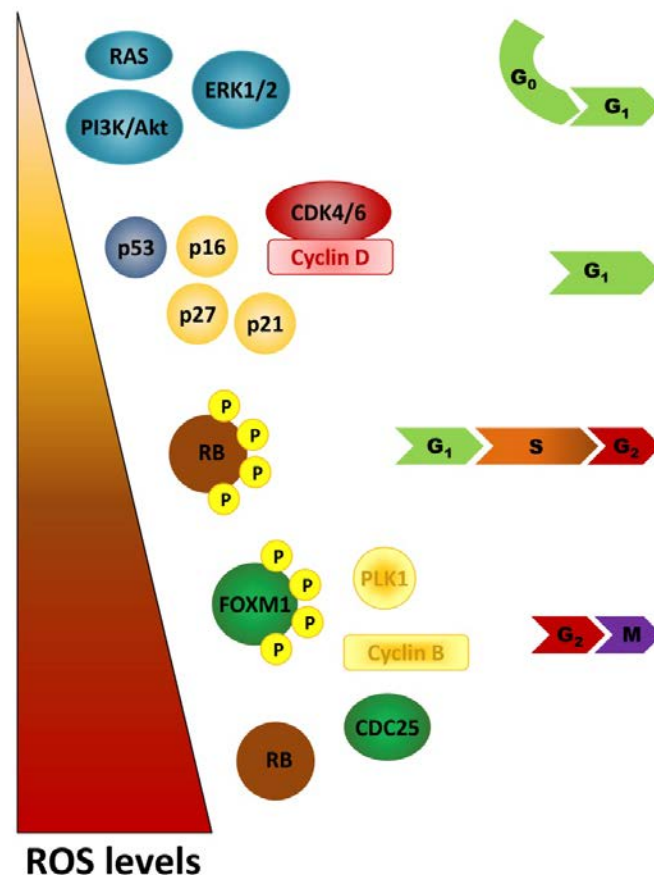
Figure 1.7. ROS cycle within the cell cycle. ROS levels increased gradually towards a more oxidising environment as cells in G1 phase progressed through the cell cycle. A tight regulation of ROS levels is essential to drive cell cycle progression, linking oxidative metabolic processes with cell cycle functions and regulators.

In synchronised cells, the ROS levels increase throughout the cell cycle, peaking in G2/M phase [176, 187] (Figure 1.7). This shift in the cellular redox potential may enhance cyclin B, PLK1, Aurora A and CDC25B expression through the transcription factor FOXM1 [195]. However, given that the proteins of the CDC25 phosphatase family remove inhibitory phosphates from CDK1-cyclin B complex, the increase in the

oxidative levels in G2 phase may also be moderated in order to prevent the oxidation and inhibition of their active sites [196]. Thus, redox-dependent signalling allows cells to complete its cycle of division.

1.4.7. Metabolic control of cell cycle

There is a growing awareness that cell cycle progression is coordinated with intracellular metabolism. In fact, cell cycle entry is an energetically demanding process that requires high metabolic activity to fuel the rapid increase of the cell mass [13]. As early as in 1974, it was established that the availability of nutrients is a key factor for cell proliferation, being glucose availability a metabolic checkpoint in cell cycle linked to the progression from G1 to S phase, when most biosynthetic reactions occur [12]. However, even though the knowledge on the core cell cycle players and regulatory mechanisms has considerably increased in the last 40 years, the links between cell cycle machinery, nutrient availability, biosynthetic intermediates and energetic balance remain incompletely understood [197-199]. It has been only recently, with the finding that the activities of 6-phosphofructo-2-kinase/fructose-2,6-bisphosphatase, isoform 3 (PFKFB3) and glutaminase 1 (GLS1) are regulated by an ubiquitin ligase (anaphase-promoting complex or cyclosome, APC/C), that has become clear that the process of ubiquitination not only orchestrates the periodic transcriptional regulation of cyclins and other cell cycle regulators, but also is crucial in the metabolic regulation of cell cycle [197, 200-202].

In consequence, it is of great interest to elucidate how the core cell cycle machinery is integrated with the metabolic signalling and the role it plays in driving the cell cycle to ensure the efficient use of energy and substrates.

1.5. Oncogenic regulation of the metabolic reprogramming

Tumour metabolic reprogramming is a direct result of the re-engineering of intracellular signalling pathways that are altered by mutations in oncogenes and tumour suppressor genes. In fact, most cancers harbour activating mutations of

oncogenes and/or inactivating mutations of tumour suppressor genes which determine the tumour metabolic phenotype and support tumourigenesis by giving to transformed cells a proliferative advantage over non-malignant cells. Several oncogenes including c-MYC, hypoxia inducible factor 1 (HIF1), phosphoinositide-3-kinase (PI3K), protein kinase B (PBK or Akt) and the mechanistic target of rapamycin (mTOR), have been known to be involved in the regulation of tumour metabolic reprogramming [9, 97, 151].

1.5.1. MYC as a master regulator of tumourigenesis

The *c-MYC* oncogene (hereafter referred to as *MYC*) belongs to the *MYC* family of genes together with *MYCN* and *MYCL*. However, *MYC* is the only isoform ubiquitously expressed in a broad range of tissues, while *MYCN* and *MYCL* are normally only expressed during development [203]. MYC is a multi-functional transcription factor that exerts control over cell proliferation, cell cycle progression, cell growth, metabolism, apoptosis, differentiation and stress response through transcriptional regulation of its target genes [203, 204]. In fact, MYC binds to the promoter of 10-15% of all known genes, regulating both genes encoding proteins and those encoding non-coding RNA products of several functional classes [203, 205]. *MYC* expression is dysregulated in many human cancers by either chromosomal translocation or gene amplification. In addition, the expression and stability of MYC protein and *MYC* mRNA can also be dysregulated, promoting tumourigenesis through unrestricted cell proliferation, inhibition of cell differentiation, metabolic adaptation, angiogenesis, reduction of cell adhesion and genomic instability [203, 204, 206, 207].

To function as a transcription factor, MYC protein heterodimerises with its binding partner MAX, forming an activated complex that recognises E box sequences (CACGTG) and induces the transcription of targets genes. MYC can also act as transcriptional repressor by binding to MIZ1 or Sp1 transcription factors and interfering with their transcriptional activity [208]. It is worth noting that multiple genes that are repressed by MYC encode negative regulators of cell proliferation such as *CDKN2B* (encoding

p15[INK4b]), *CDKN2C* (p18[INK4c]), *CDKN1A* (p21[Cip1]), *CDKN1B* (p27[Kip1]), and *CDKN1C* (p57[Kip2]) [208]. MAX can also bind to MAD1, MXI1, MAD3, MAD4 and MNT or form homodimers, repressing the transcriptional activation of MYC target genes [209].

1.5.1.1. MYC and metabolism

MYC is known to enhance glycolysis through the activation of glycolytic genes (such as *HK2*, *GAPDH*, *ENO1* and *PK*, among others) and glucose transporters (*SLC2A1*, *SLC2A2* and *SLC2A4*) [210, 211]. In addition, MYC promoted lactate production and export, increasing target gene expression of *LDHA* and the lactate transporter *MCT1* [207, 212, 213]. Figure 1.8 illustrates the main metabolic pathways regulated by MYC.

On the other hand, transformed cells exhibit increased MYC-dependent glutaminolysis and glutamine dependency [96, 214]. Indeed, MYC has been described as the main oncoprotein responsible for inducing a transcriptional program that promotes glutaminolysis and triggers cellular addiction to glutamine as a bioenergetic substrate [96]. This glutamine addiction leads tumour cells to reprogram intermediate metabolism for the maintenance of mitochondrial tricarboxylic acid (TCA) cycle integrity [96]. Moreover, high levels of MYC promote mitochondrial biogenesis and function, both increasing the rate of oxygen consumption and the energy production required for rapid cell proliferation [206, 215-217]. High glutaminolysis rate results in the robust production of NADPH, which is needed to fulfil the requirements for cell proliferation [96, 162]. In conditions of low glucose and oxygen availability, MYC-induced glutamine catabolism is important for cell survival [157]. Furthermore, cells with supraphysiological levels of MYC are more sensitive to inhibition of mitochondrial oxidative metabolism [218]. Moreover, MYC is also found to contribute to increase glutamine uptake by upregulation of the expression of glutamine transporters (ASCT2 [SLC1A5] and SLC7A5) [147, 214]. Importantly, MYC enhances glutaminolysis by transcriptionally repressing miR-23a and miR-23b (microRNA-23a/b), resulting in greater expression of their target protein, glutaminase (GLS1) [214]. In fact, GLS1 is the first enzyme in the glutaminolysis and catalyses the conversion of glutamine to
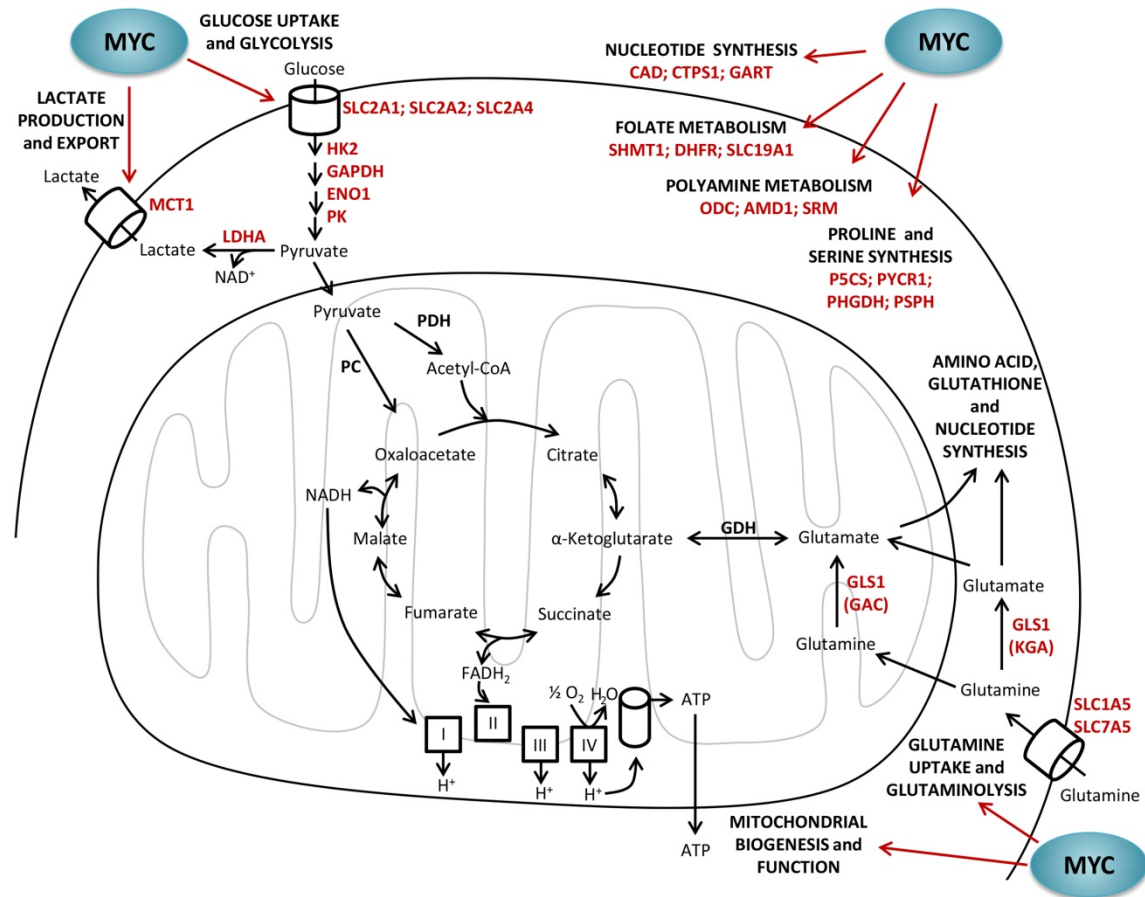
Figure 1.8. Metabolic regulation by MYC. MYC has a pivotal role in the metabolic reprogramming of tumour cells by enhancing glucose uptake and glycolysis, lactate production and export, glutamine uptake and glutaminolysis, mitochondrial biogenesis and oxidative phosphorylation, and nucleotide, folate, polyamine, proline and serine synthesis. AMD1, adenosylmethionine decarboxylase; ATP, adenosine triphosphate; CAD, carbamoyl-phosphate synthase/aspartate carbamoyltransferase/dihydroorotase; CoA, coenzyme A; CTPS1, cytidine triphospate synthase 1; DHFR, dihydrofolate reductase; $FADH_2$, flavin adenine dinucleotide reduced form; GAC, glutaminase C; GART, phosphoribosylglycinamide formyltransferase, phosphoribosylglycinamide synthetase, phosphoribosylaminoimida-zole synthetase; GDH, glutamate dehydrogenase; GLS1, glutaminase 1; KGA, kidney (K-type) glutaminase; LDHA, lactate dehydrogenase A; MCT1, monocarboxylate transporter/SLC16A1 solute carrier family 16 member 1; NAD^+, nicotinamide adenine dinucleotide oxidised form; NADH, nicotinamide adenine dinucleotide reduced form; $NADP^+$, nicotinamide adenine dinucleotide phosphate oxidised form; NADPH, nicotinamide adenine dinucleotide phosphate reduced form; ODC, ornithine decarboxylase; P5CS, Δ^1-pyrroline-5-carboxylate synthetase; PHGDH, phosphoglycerate dehydrogenase; PC, pyruvate carboxylase; PDH, pyruvate dehydrogenase; PSPH, phosphoserine phosphatase; PYCR1, Δ^1-pyrroline-5-carboxylate reductase 1; SHMT1, serine hydroxymethyltransferase 1; SLC1A5, solute carrier family 1 (neutral amino acid transporter) member 5; SLC2A1, solute carrier family 2 (facilitated glucose transporter) member 1; SLC2A2, solute carrier family 2 (facilitated glucose transporter) member 2; SLC2A4, solute carrier family 2 (facilitated glucose transporter) member 4; SLC7A5, solute carrier family 7 (amino acid transporter light chain, L system) member 5; SLC19A1, solute carrier family 19 (folate transporter) member 1; SRM, spermidine synthase.

glutamate for its oxidation in the TCA cycle and also for protein or glutathione synthesis. It is worth mentioning that MYC can stimulate the use of the TCA cycle to generate intermediates for macromolecular synthesis using both glucose and glutamine as carbon source [152, 157]. However, it has been reported that cells presenting high MYC levels greatly rely on mitochondrial oxidative phosphorylation and increase glutaminolysis by 2- to 4-fold, while only moderately increasing glycolysis by 1.2-fold [219].

Additionally, MYC has been shown to activate nucleotide biosynthesis by inducing several gens involved in nucleotide metabolism including *carbamoyl-phosphate synthase / aspartate carbamoyltransferase / dihydroorotase* (*CAD*), *CTP synthase 1* (*CTPS*) and *ornithine decarboxylase* (*ODC*) [210, 213, 220, 221]. Polyamine biosynthesis is also regulated by MYC since ornithine decarboxylase (ODC) (the rate-limiting enzyme in polyamine production) [220], adenosylmethionine decarboxylase (AMD1) and spermidine synthase (SRM) have E boxes in their regulatory region and are enhanced in MYC-expressing cells [213]. Furthermore, polyamines stimulate MYC transcription in a positive feedback loop [222, 223].

Moreover, MYC can redirect glycolytic flux from 3-phosphoglycerate for the synthesis of serine and glycine involving folate metabolism, which are essential for purine and thymidylate biosynthesis [147, 213, 224, 225]. MYC is also implicated in proline metabolism regulation by transcriptionally repressing proline oxidase/proline dehydrogenase (POX/PRODH) expression through upregulation of miR-23b*, and increasing the expression of the enzymes of proline biosynthesis pathway (P5C synthase, P5CS and P5C reductase 1, PYCR1) [135].

1.5.1.2. MYC and cell cycle

The network of MYC target genes suggests its implication in the fulfilment of the metabolic requirements for cell cycle entry [198, 218]. In fact, one of the earliest observations after *MYC* discovery was its ability to promote cell proliferation and inhibit cell differentiation [210]. Remarkably, MYC overexpression in quiescent cells is

sufficient to trigger cell cycle entry, reduce the requirement for growth factors, block cell cycle exit, and increase cell size [226, 227]. MYC promotes cell cycle progression by regulation of pivotal cell cycle control genes through transcriptional induction of CDKs and cyclins, and repression of CIP/KIP proteins. MYC mediates the increase of active cyclin-CDK complexes levels not only by upregulation of *CDK1*, *CDK2*, *CDK4* (one of the principal MYC target genes [228]), *CDK6*, *CCND1* (encoding cyclin D1), *CCND2* (cyclin D2), *CCND3* (cyclin D3), *CCNE1* (cyclin E1), *CCNE2* (cyclin E2), *CCNA2* (cyclin A2) and *CCNB1* (cyclin B1), but also by induction of CDC25A (CDKs phosphatase) and CDK activating kinase complex (CAK, through enhanced mRNA translation of its subunits, CDK7, cyclin H and MAT1), and repression of the CDK inhibitory kinase *WEE1* through miR-221 activation [203, 207, 210, 226, 229]. Moreover, MYC abrogates the transcription of cell cycle checkpoint genes *GADD45* and *GADD153* [203, 229], and impairs the activity of the CDK inhibitors p27^{Kip1}, p21^{Cip1} and p15^{INK4b} through several mechanisms [203, 207, 210, 226]. One of the most studied mechanisms for p21^{Cip1} and p15^{INK4b} MYC-mediated repression is the binding to MIZ1 and the blocking of its transcriptional activity [210, 226]. In contrast, MYC antagonises p27^{Kip1} function by several parallel mechanisms such as induction of miR-221 and miR-222, activation of E2F transcription factors, increase of CDK4/6-cyclin D and CDK2-cyclin E complexes levels, and enhancement of the expression of several components of the SCF ubiquitin ligase complex [203, 226]. Last but not least, MYC further stimulates cell cycle progression by inducing genes directly involved in DNA replication including *MCM* (minichromosome maintenance), *ORC* (origin recognition complex), *CDC6* (cell division cycle 6), *TERT* (telomerase reverse transcriptase) and the genes encoding three subunits of the APC/C (*ANAPC5*, *CDC16* and *CDC23*) [226].

1.5.1.3. MYC regulation

Given its pivotal role on cell fate, *MYC* expression is tightly regulated at transcriptional, post-transcriptional and post-translational levels in non-transformed cells. Accordingly, dysregulation of *MYC* expression is one of the most common abnormalities in human diseases, being MYC overexpression frequently found in most human cancers.

Remarkably, *MYC* oncogenic activation results from insertional mutagenesis, chromosomal translocation and gene amplification mechanisms, while most oncogenes are activated by mutations in their coding sequence [203].

MYC protein presents extremely short half-life (in the order of 20-30 minutes [230]) in the absence of mitogenic signals, but is transiently stabilised upon cell cycle entry and RAS activation, allowing its accumulation [231, 232]. RAS promotes MYC stability through RAF/MEK/ERK kinase cascade and via glycogen synthase kinase-3β (GSK-3β) inhibition by the PI3K/Akt pathway [231, 233]. MYC turnover is regulated by the ubiquitin proteasome pathway [230, 234] and is dependent on the phosphorylation of two highly conserved residues located near the N-terminal region of *MYC*, Thr58 and Ser62. These phosphorylation sites exert opposing control effects on MYC degradation [231]. ERK (extracellular receptor kinase) phosphorylates MYC on Ser62, promoting its protein accumulation, while phosphorylation of Thr58, which is mediated by GSK-3β but dependent on prior Ser62 phosphorylation, triggers MYC proteasomal degradation [231-233, 235]. Therefore, MYC phosphorylation at Ser62 has two opposite roles; MYC stabilisation and accumulation, and activation of the subsequent phosphorylation at Thr 58, triggering MYC degradation. Interestingly, proteasome inhibition studies reveal that the accumulated poly-ubiquitinated MYC only exhibits phosphorylation on Thr58 [233, 235]. Since phosphorylation on Ser62 is required prior to Thr58 phosphorylation, the Ser62 phosphate is removed before MYC ubiquitination by protein phosphatase 2A (PP2A) action, contributing to MYC degradation [231, 233, 235].

In non-transformed cells, growth stimuli lead to RAS activation and MYC protein synthesis. However, when mitogenic signalling ends, RAS and PI3K activities decline and release GSK-3β from its negative regulation, activating its kinase activity and thus promoting MYC degradation by phosphorylation on Thr58 [235]. The ordered phosphorylation of Ser62 and Thr58 followed by Ser62 dephosphorylation allows a tight control of MYC protein levels. Hence, the disruption of the physiological regulation of MYC expression can lead to malignancy.

1.5.2. HIF1

The hypoxia inducible factors HIF1, HIF2 and HIF3 are the principal regulators of the transcriptional homeostatic responses to situations of limited availability of oxygen. HIF1 is ubiquitously expressed while HIF2 and HIF3 are only expressed in certain tissues [236]. Only HIF1 and HIF2 are further discussed in this section since HIF3 function is less well understood. The HIF factors are formed by an oxygen-dependent HIFα subunit and a constitutively expressed HIFβ subunit. HIF activity is tightly regulated by cycles of synthesis and oxygen-dependent proteasomal degradation. Indeed, HIFα subunits are continuously synthesised and their stability is regulated by oxygen availability [236]. Under normoxic conditions, HIFα subunits are hydroxylated on proline residues in the oxygen-dependent degradation (ODD) domain by prolyl hydroxylase enzymes (PHDs) and subsequently ubiquitinated by the tumour suppressor protein von Hippel-Lindau (VHL) prior to their degradation in the proteasome [236, 237] (Figure 1.9). Under hypoxic conditions, the reduced molecular oxygen levels decrease the activity of PHDs, which are further inactivated through the oxidation of the ferrous ion within their active sites by ROS released from inefficient mitochondrial respiration [238], thus preventing their interaction with VHL [237]. Consequently, stable HIFα subunits form heterodimers with HIFβ subunits and translocate to the nucleus, where they bind to specific consensus sequences (hypoxia response element, HRE) in the promoter of hypoxia-responsive genes for the transcriptional activation of the cellular adaptation to hypoxia [239].

1.5.2.1. Hypoxia and cancer

Solid tumours frequently develop hypoxia when highly proliferating tumour cells outgrow their vascular network, resulting in tumours with limited oxygen diffusion. In order to adapt to the hypoxic microenvironment and support cell survival, cells principally initiate response mechanisms through HIF stabilisation and accumulation, favouring angiogenesis, invasion and metabolic reprogramming [240, 241]. Accordingly, HIF levels are increased in many human cancers and correlate with poor

clinical prognosis [241]. It is worth mentioning that tumour cells can exhibit augmented levels of HIF1α under normoxic conditions, a phenomenon known as pseudohypoxia [240]. For example, induction of RAS or SRC oncogenic signalling promotes normoxic HIF1α accumulation through prolyl hydroxylation inhibition [242].

1.5.2.2. Regulation of HIF by prolyl hydroxylases

In humans, there are three different members of the prolyl hydroxylase family; PHD1, PHD2 and PHD3. However, only PHD2 has been confirmed to be involved in the oxygen regulation of HIF1α, while PHD1 and PHD3 display only partial additive effects on HIF1α stability [243]. These enzymes are good oxygen sensors since their affinity for oxygen is low with K_m values from 230 to 250 μM, slightly above the concentration of oxygen in the air (200 μM) [244]. PHDs require α-ketoglutarate, oxygen and a prolyl residue as substrates, iron and ascorbate as cofactors, to produce a hydroxyl-prolyl residue, succinate and CO_2 [160]. Prolyl hydroxylation is required for the recognition and binding of VHL to the ODD domain, which recruits an ubiquitin ligase complex [239] (Figure 1.9). Chemical inhibitors of the activity of PHD, such as iron chelators (e.g. desferrioxamine, DFO) or competitors of α-ketoglutarate for binding at the hydroxylase (e.g. dimethyloxalylglycine, DMOG), prevent the hydroxylation of HIFα subunits, causing their accumulation and promoting the expression of HIF target genes [245]. Remarkably, the use of α-ketoglutarate as an electron donor in the reaction of hydroxylation results in its oxidation into succinate, which is an end product whose accumulation can inhibit PHD activity even in the presence of oxygen [246]. In fact, deficiency of succinate dehydrogenase has been demonstrated to increase succinate levels and competitively inhibit PHDs under normoxia, leading to HIF1α stabilisation in a pseudo-hypoxic phenotype [246]. Interestingly, PHD activity can be rescued by artificially increasing cellular α-ketoglutarate levels both in normoxia, reversing the succinate-mediated HIF1α stabilisation [247], and hypoxia, resulting in the destabilisation of HIF1α and reversing the hypoxic phenotype [248]. Therefore, PHD activity is regulated not only by oxygen availability, but also by the availability of α-ketoglutarate, a metabolite which plays a central role in numerous metabolic

processes and is closely connected to amino acid metabolism [160]. In fact, both intracellular α-ketoglutarate levels and PHD activity are highly dependent on amino acid availability, while amino acids ability to induce mTORC1 signalling requires PHD enzymatic activity [249].
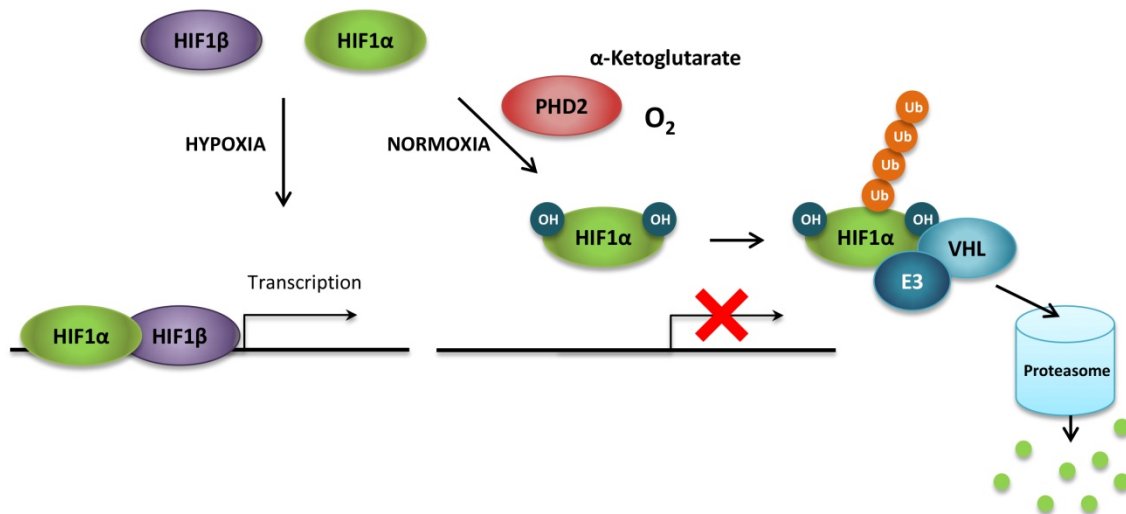
Figure 1.9. HIF1α regulation under normoxia. In the presence of oxygen and α-ketoglutarate, HIF1α subunits are hydroxylated on proline residues in the oxygen-dependent degradation (ODD) domain by prolyl hydroxylases (principally prolyl hydroxylase 2, PHD2). Prolyl hydroxylation is required for the binding of the von Hippel-Lindau protein (VHL), which recruits an ubiquitin ligase complex (E3) that ubiquitinates HIF1α. Ubiquitination marks HIF1α for proteasomal-mediated degradation. Ub, ubiquitin; OH, hydroxylation.

It is worth noting that, in addition to the principal mechanism regulating HIF1α stability in response to oxygen availability involving PHD and VHL, there are also oxygen-independent pathways regulating the synthesis and degradation of HIF1α, which involve RACK1 (receptor for activated C kinase 1) protein binding to HIF1α, recruitment of an ubiquitin ligase complex and consequent HIF1α proteasome-mediated degradation [239, 250].

1.5.2.3. HIF transcriptional targets

HIF1α and HIF2α present overlap in their ability to activate target genes involved in angiogenesis, metastasis and invasion, while HIF1α alone regulate several glycolytic

and apoptotic genes and HIF2α preferentially promote the transcription of certain genes such as *vascular endothelial growth factor* (*VEGF*) or *transforming growth factor α* (*TGFα*) [236, 240, 245, 251].

HIF1 activation increases oxygen and nutrients supply to tumours through angiogenesis and erythropoiesis stimulation by *VEGF* and *erythropoietin* (*EPO*) upregulation, respectively [98]. In addition, HIF1 enhances glycolysis and lactate production by transactivating glucose transporters and glycolytic enzymes, while actively inhibits oxidative phosphorylation by inducing *pyruvate dehydrogenase kinase 1* (*PDHK1*), which phosphorylates and inhibits pyruvate dehydrogenase (PDH), thus preventing pyruvate from entering the TCA cycle [252]. Furthermore, HIF1 enhances electron transport chain efficiency through *cytochrome c oxidase subunit IV, isoform 2* (*COX4I2*) induction, which replaces the less efficient isoform 1 (COX4I1), resulting in increased ATP production and reduced ROS generation [253]. In addition to the catabolic process of anaerobic glycolysis, HIF1 also endorses anabolic processes such as glycogen synthesis by upregulating the enzymes involved in its biosynthetic pathway [254-256].

1.5.2.4. HIF1 effects on MYC

There is a complex interplay between HIF1 and MYC proteins concerning glucose metabolism and mitochondrial function [212, 237, 257]. Both HIF1 and MYC share common metabolic target genes such as *SLC2A1* glucose transporter, *HK*, *phosphofructokinase* (*PFK*), *pyruvate kinase* (*PK*) or *LDH*, among others [212]. In contrast, *SLC2A3* glucose transporter is a specific HIF1 target gene [212]. On the other hand, HIF1 and MYC have opposing effects on cell proliferation, mitochondrial biogenesis and DNA repair [257]. HIF1 impairs mitochondrial biogenesis and oxygen consumption by inhibiting MYC-mediated transcription and inducing MYC degradation [216], while regulates cell cycle and DNA repair genes by functionally counteracting MYC through displacement of the inhibitory MYC binding in the *CDKN1A* promoter [258] and of the activating MYC binding from *MSH2* and *MSH6* promoters [259]. Remarkably, HIF1 directly inhibits MYC through induction of MXI1, which binds to MAX

and represses MYC transcriptional activity, and by promotion of MYC proteasomal degradation [216, 260]. Indeed, HIF increases MYC phosphorylation at Thr58, triggering MYC ubiquitination, and decreases the de-ubiquitinating enzyme USP28, promoting MYC proteasome-dependent degradation [261]. On the other hand, MYC induces MCM3 and MCM5 proteins [226] which in turn inhibit HIF1 activity by stimulating HIF1α hydroxylation, ubiquitination and degradation [262, 263]. However, prolonged hypoxic conditions reduced MCM mRNA expression in a HIF1-dependent manner, indicating that MCM and HIF1 display antagonistic functions [262, 263]. Interestingly, HIF1 and MYC present sirtuin-mediated shared regulation mechanisms since sirtuin 1 (SIRT1) works in conjunction with both transcription factors while SIRT6 inhibit their transcriptional activity via effects on chromatin [264]. Moreover, dual deficiency of oxygen and glucose suppresses HIF signalling [265] and enhances MYC degradation in cancer cells as an adaptive response to survive under conditions of deficient energy sources [266].

1.5.3. The PI3K/Akt pathway

Overactivation of phosphoinositide-3-kinase (PI3K)/Akt signalling is commonly observed in human cancers, as it is essential for cell proliferation, growth, survival and metabolic reprogramming [267]. PI3Ks are a family of lipid kinases that integrate prosurvival signals such as growth factors, cytokines, hormones and other environmental cues, translating them into intracellular signals that activate Akt-dependent and Akt-independent downstream signalling pathways [267]. Akt is a serine-threonine protein kinase that is regulated mainly following PI3K activation and through sequential phosphorylation at Thr308 and Ser473 [268, 269]. Since constitutive activation of Akt is frequently found in human tumours, being a central node in the PI3K signalling pathway, it is potentially interesting to molecularly target components of the Akt pathway for cancer therapy [269].

Forkhead box O (FOXO) transcription factors are direct targets of Akt that modulate cellular differentiation, cell cycle, growth, survival, apoptosis, metabolism, DNA repair,

resistance to oxidative stress and tumour suppressor pathways [270-274]. Four different FOXO proteins are encoded in mammalian cells; FOXO1, FOXO3a and FOXO4, which are ubiquitously expressed, and FOXO6 which is expressed predominantly in neural cells [275, 276]. As transcription factors, FOXO proteins activate or repress the transcription of their target genes through nuclear translocation regulated by post-translational modifications such as phosphorylation, acetylation and ubiquitination [277]. The principal mechanism of FOXO transcriptional regulation is FOXO phosphorylation by Akt which impairs its DNA binding activity and promotes its interaction with the chaperone protein 14-3-3, resulting in nuclear exclusion, cytoplasmic accumulation and ubiquitin-proteasome pathway-dependent degradation, thus promoting cell survival [278, 279]. In contrast, FOXO proteins are activated and released from 14-3-3 in the presence of oxidative stress through Jun N-terminal kinase (JNK) signalling [270, 272, 280, 281] (Figure 1.10).
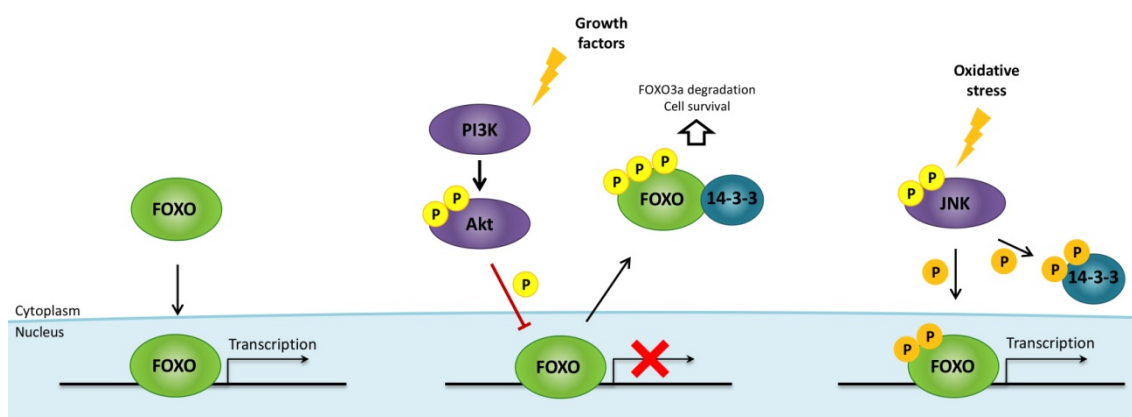
Figure 1.10. FOXO regulation by growth factors and oxidative stress. Growth factors activate PI3K/Akt pathway, resulting in FOXO factors phosphorylation, impairment of FOXO binding activity to DNA and promotion of FOXO interaction with the chaperone protein 14-3-3, which in turn causes FOXO nuclear exclusion, cytoplasmic accumulation and ubiquitin-proteasome pathway-dependent degradation. Oxidative stress activates Jun N-terminal kinase (JNK) signalling, which phosphorylates both FOXO (at other regulatory sites than Akt) and 14-3-3 proteins, triggering the release of FOXO factors, their nuclear translocation and their transcriptional activity. Akt/PBK, protein kinase B; FOXO, forkhead box O; P, phosphate; PI3K, phosphoinositide-3-kinase.

FOXM1 transcription factor is a crucial regulator of cell proliferation and cell cycle progression that is overexpressed in many types of cancer. Cell differentiation, angiogenesis, senescence, DNA damage repair and tissue homeostasis are regulated by

FOXM1, conferring oncogene-like properties to this forkhead subfamily member [282]. Recent studies have reported that FOXO3a represses FOXM1 expression and that they both compete for binding to similar DNA sequences, sharing numerous target genes but being antagonists [277, 283-285]. It is worth noting that FOXO3a and FOXM1 proteins are indirect targets of several conventional and widely used cytotoxic chemotherapeutic drugs such as cisplatin or gefitinib, which mediate their effects through FOXO3a activation and FOXM1 indirect repression via PI3K/Akt signalling pathway inhibition [286-291]. The dysregulation of the PI3K/Akt/FOXO3a axis leads to drug resistance since inhibition of FOXO3a and/or overexpression of FOXM1 enhances DNA repair, as well as cell maintenance, proliferation and survival [277, 282].

A hallmark of most cancers where the PI3K pathway is hyperactivated (caused by RAS, PTEN or PI3K mutations) is inactivation of FOXO proteins [269, 281], postulating FOXO family members to be tumour suppressors [292]. In contrast, PI3K depletion results in a significant activation of FOXO transcription factors, induction of apoptosis, decrease of cell viability and G1 cell cycle arrest with inhibition of CDK4/6, cyclin D and accumulation of p27^{Kip1} [293]. Indeed, *in vivo* models of loss of FOXO function exhibit spontaneous tumour formation, while FOXO overexpression can inhibit tumourigenesis [272, 291, 292, 294-296]. Even though FOXO transcription factors are considered to be tumour suppressors, genetic inactivation of FOXO is not often found in human cancers, being predominantly repressed through overactivation of the PI3K/Akt pathway caused by mutations in RAS, PTEN or PI3K oncogenes [292]. Therefore, the search for compounds that promote activation and relocalisation of FOXO from the cytoplasm to the nucleus is a promising therapeutic approach for cancer treatment and overcome of drug resistance [295].

1.5.3.1. FOXO effects on MYC, HIF1α and mTOR

Activated PI3K/Akt pathway stimulates cell growth and proliferation, and stabilise MYC through inhibition of GSK3β by preventing MYC phosphorylation at Thr58 [235]. Active PI3K and MYC specifically cooperate in dysregulation of cell growth and proliferation, since both regulate a common set of cellular processes [297]. Conversely, activation of

FOXO transcription factors following inhibition of PI3K/Akt signalling represses multiple MYC target genes including those involved in cell proliferation and mitochondrial activity, blocking MYC-mediated cell proliferation and transformation, and reducing ROS production [298, 299]. In addition, FOXO3a induces the expression of the MAD/MXD family of transcriptional repressors, although MXI1 is the only member that is its direct target. Indeed, MXI1 is necessary for efficient inhibition of MYC transcriptional activity [300]. Furthermore, FOXO3a activation considerably reduces MYC protein levels by enhancing phosphorylation of MYC at Thr58, which triggers its proteasomal degradation [299]. Interestingly, FOXO3a-mediated regulation of MYC at different levels enables both acute inhibition of mitochondrial gene expression by MYC degradation and sustained inhibition through MXI1 antagonistic effects [301]. Therefore, the inhibition of the transcriptional activity of FOXO proteins by Akt-mediated phosphorylation is required for MYC-induced cell proliferation and transformation [298].

FOXO3a is induced under hypoxic conditions as a direct target gene of HIF1 to mediate the hypoxic repression of nuclear-encoded genes with mitochondrial function by directly antagonising MYC at their promoters, resulting in reduced mitochondrial mass, oxygen consumption and ROS production [302, 303]. Additionally, FOXO3a promote cell survival both in hypoxic tumour cells and hypoxic tumour tissue *in vivo*, in contrast with its role as a tumour suppressor under normoxic conditions [292, 302]. On the other hand, FOXO3a prevents HIF1α stabilisation by blocking the hypoxia-induced ROS increase [299], and inhibits HIF1α activity through stimulation of CITED2 expression, also reducing HIF1α-induced apoptosis during hypoxic stress, promoting cell survival [303].

In response to energy stress, FOXO proteins inhibit the mechanistic target of rapamycin complex 1 (mTORC1) signalling through induction of *BCL2/adenovirus E1B 19kDa interacting protein 3* (*BNIP3*) expression, which in turn negatively regulates the mTORC1 activator RHEB and the BCL2 pro-survival family members, resulting in energy stress-induced apoptosis [304]. In addition, mTORC1 inhibition upregulates FOXO3a expression and nuclear accumulation through *FOXO3a* demethylation [305]. Conversely, mTOR complex 2 (mTORC2) phosphorylates the Class IIa histone

deacetylases (HDACs) in an Akt-independent manner, resulting in FOXO acetylation, release of MYC proteins from FOXO-mediated repression and the consequent conferral of resistance to PI3K and Akt Inhibitors [306].

1.5.4. mTOR

The mechanistic target of rapamycin (mTOR, formerly mammalian TOR) is a conserved cytoplasmic serine-threonine protein kinase that acts as a central cell growth regulator by sensing mitogens, energy and amino acids. mTOR pathway regulates cell survival and growth through modulation of some pivotal cellular processes including protein synthesis, ribosome biogenesis, autophagy and metabolism [307]. In fact, the dysregulation of mTOR-dependent cellular homeostasis maintenance is associated with several human diseases such as cancer and considerable research efforts have been made to efficiently inhibit mTOR signalling [308, 309].

mTOR forms two functionally and structurally different multiprotein complexes named mTOR complex 1 (mTORC1) and 2 (mTORC2). mTORC1 activity is regulated by growth factors, oxygen and nutrient availability. Activation of PI3K/Akt and RAS/RAF/ERK pathways by growth factors results in Akt- and ERK-mediated phosphorylation and inactivation of the heterodimer tuberous sclerosis 1 (TSC1)/TSC2, which is a GTPase-activating protein (GAP) that negatively regulates mTORC1 through inhibition of the RAS homolog enriched in brain (RHEB) GTPase [310]. Remarkably, intracellular amino acids are necessary for the activation of mTORC1 since they activate the mechanism by which mTORC1 is able to interact with and be activated by RHEB [132].

Activated mTORC1 signalling cascade initiates with the direct phosphorylation of the regulators of translation eukaryotic translation initiation factor 4E (eIF4E)-binding protein 1 (4E-BP1) and S6 kinase 1 (S6K1), which promote protein synthesis [311]. In addition, mTORC1 regulates lipid homeostasis through activation of the transcription factors sterol regulatory element-binding protein 1/2 (SREBP1/2), which in turn control the expression of genes involved in fatty acid, triglyceride, phospholipid and cholesterol synthesis [307, 312]. Interestingly, mTORC1 also promotes mitochondrial

biogenesis and the expression of genes involved in oxidative metabolism [313, 314]. On the other hand, mTORC2 pathway regulation and function remain poorly understood. mTORC2 signalling is independent of nutrient availability but is sensitive to PI3K signalling [307]. mTORC2 directly activates Akt through phosphorylation of the Ser473 residue, which in turn activate mTORC1, both situating mTOR upstream and downstream of Akt [315]. It is worth noting that acute rapamycin treatment specifically inhibits mTOR when it is part of mTORC1 but not mTORC2 [307, 308].

1.5.4.1. mTOR regulation by hypoxia and MYC

Hypoxic oxygen levels inhibit mTORC1 by activating the TSC1/TSC2 complex through two different pathways. On the one hand, hypoxia reduces cellular ATP levels and triggers 5'-AMP-activated protein kinase (AMPK) activation, which positively regulates TSC1/TSC2 in a HIF1-independent manner [316]. On the other hand, hypoxia activates TSC1/TSC2 by the transcriptional induction of *regulated in development and DNA damage responses 1* (*REDD1*) gene, antagonising other pathways that promote growth through TSC1/TSC2 inhibition via Akt [317, 318]. Hypoxia can also negatively regulate mTORC1 through the hypoxia-inducible protein BNIP3 binding to RHEB, which inhibits the ability of RHEB to activate mTORC1 [319]. Conversely, MYC acts as a strong and direct repressor for *TSC2* expression by binding to its promoter, resulting in mTORC1 activation [320]. In addition, mTORC1 downstream effector S6K1 phosphorylates the eukaryotic initiation factor eIF4B, enhancing MYC translation efficiency and positively regulating glutaminase (GLS) and glutamate dehydrogenase (GDH) [321, 322]. Moreover, glutaminolysis and α-ketoglutarate production, in response to glutamine and leucine [133], also mediate mTORC1 activation [161].

In summary, mTOR, PI3K, HIF and MYC are key regulators of cellular metabolism that are frequently altered in cancer, collaborating in both synergistic and antagonistic ways. A better understanding of the relationship between these pathways as well as the identification of other key players in the regulation of the tumour metabolic reprogramming are fundamental challenges for the development of new strategies for cancer treatment.

1.6. Study and characterisation of tumour metabolism

Metabolic reprogramming is one of the hallmarks of cancer that enable tumour cells to fulfil their needs for energy and building blocks for biosynthesis in order to sustain their increased proliferation rate [6]. In addition, the metabolic switch in tumour cells is associated to drug resistance in cancer therapy. Consequently, the study of tumour metabolism is of crucial importance to develop and implement selective cancer therapeutics that slow tumour growth and progression, improve treatment response, and overcome therapeutic resistance.

1.6.1. Metabolomics

The characterisation of tumour cells has been traditionally focused on genomics, transcriptomics and proteomics, while in the past decade metabolomics has emerged as a powerful tool for the study of tumour phenotype. Fan et al. defined metabolomics as a systematic analysis of metabolite structures, concentrations, pathways and fluxes, and molecular interactions within and among cells, organs, and organisms as a function of their environment [323]. In fact, the metabolome is the closest representative of the phenotype as the end-product of the cellular processes. Metabolism is commonly studied from an integrate perspective in combination with the information from gene and protein expression in order to consider the entire metabolic network and its regulations. To this end, computational systems biology integrates experimental and computational approaches to predict and describe the complex behaviour of biological systems [324, 325].

To date, there are several specific metabolite extraction methods as well as different analytical chemical tools to obtain metabolic information. Depending on the metabolites of interest and the nature of the samples, the main analytical techniques used for the metabolome analysis are nuclear magnetic resonance (NMR) spectroscopy, gas or liquid chromatography coupled with mass spectrometry (GC/MS

and LC/MS, respectively), direct-infusion mass spectrometry (DIMS), Fourier transform infrared spectroscopy (FTIR) and capillary electrophoresis (CE) [324, 326].

However, metabolomics only provides a static view of the cell metabolic profile in a specific moment. In order to complete the dynamic picture of the phenotype, the emerging field known as fluxomics addresses both the required analyses of the metabolic flux distributions and the functional interactions of the metabolome with the environment and the genome [324, 327]. Thus, fluxomics complements metabolomics and contributes to gain a comprehensive understanding of the metabolism in different contexts such as tumour metabolic reprogramming.

1.6.2. Fluxomics

Fluxomics has become an essential approach to examine the metabolic production and consumption rates in a biological system. So far, to identify the flux distribution within the metabolic network of a cell, flux balance analysis (FBA) and ^{13}C metabolic flux analysis (^{13}C-MFA) are applied.

1.6.2.1. Flux balance analysis

FBA is one of the most used mathematical approaches for the prediction of metabolic flux distributions at steady state using an optimisation criterion to select a distribution of fluxes from the feasible space delimited by the metabolic reactions and the restrictions imposed over them. These constraints involve the equation of stoichiometric modelling used, inequality constraints obtained from irreversibility of metabolic reactions and information about maximum and minimum rates, and equality constraints used for introducing input data in the model. On the other hand, the resulting flux distribution depends on the specific objective function selected, such as the maximisation of biomass production or ATP production. To confirm that the objective function chosen is a good representation, the comparison and adjust with the experimental data are required [328, 329].

1.6.2.2. ^{13}C metabolic flux analysis

Based on isotope labelling technology, ^{13}C-MFA provides additional constraints to the stoichiometric equations used in the metabolite balancing of the model, which reduce the space of possible distributions of fluxes. Indeed, ^{13}C-MFA is widely used to quantify changes in the fluxes of metabolic pathways that result from interventions from the environment and the genome [330, 331]. The information obtained from ^{13}C-MFA is of great importance for the characterisation of the physiological properties of the biological system under study, which lead to the detection of the metabolic pathways that are affected by specific environmental and genetic factors and thus, the identification of new metabolic targets.

1.6.2.2.1. ^{13}C-assited metabolomics experiments

The proper selection of the isotopic tracers is of pivotal importance to improve the quality of the ^{13}C-MFA results. Thus, algorithms for the rational selection of tracers have been developed to select the optimal tracer for determining the fluxes of interest, also for parallel labelling experiments [332]. In fact, the tracer selection determines which isotopomers will be formed and the sensitivity of the isotopomer measurements with respect to flux changes [331]. For tracer-based metabolomics experiments, cells are incubated for a specified period of time with ^{13}C-labelled substrates, which are metabolised to ^{13}C-labelled metabolites. The metabolic pathway followed by a specific tracer can be determined through the analysis of the position and the number of ^{13}C atoms of the newly synthesised metabolites. Therefore, the different mass isotopomers (also known as isotopologues, isomers with a specific number of ^{13}C substitutions) and positional isotopomers (also known as isotopomers, isomers with ^{13}C substitutions in a specific carbon position) obtained from the distribution of ^{13}C of a specifically labelled precursor give information about the metabolic pathways through which they have been synthesised [333]. The theoretical number of ^{13}C mass isotopomers from a specific metabolite with n carbons is n+1, while the number of possible positional isotopomers is 2^n. For example, three-carbon metabolites such as lactate or pyruvate can potentially present n+1=3+1=4 mass

isotopomers (m0, m1, m2 and m3, according to the number of ^{13}C) and $2^n=2^3=8$ positional isotopomers (for m0, $^{12}C_1$-$^{12}C_2$-$^{12}C_3$; for m1, $^{13}C_1$-$^{12}C_2$-$^{12}C_3$, $^{12}C_1$-$^{13}C_2$-$^{12}C_3$, $^{12}C_1$-$^{12}C_2$-$^{13}C_3$; for m2, $^{13}C_1$-$^{13}C_2$-$^{12}C_3$, $^{12}C_1$-$^{13}C_2$-$^{13}C_3$, $^{13}C_1$-$^{12}C_2$-$^{13}C_3$; and for m3, $^{13}C_1$-$^{13}C_2$-$^{13}C_3$). It is worth noting that GC/MS analysis give information about mass isotopomers while NMR spectroscopy can determine the positional isotopomer distribution of the metabolites.

The most widely used ^{13}C tracers are ^{13}C-glucose and ^{13}C-glutamine for their ability to precisely and accurately estimate fluxes in central carbon metabolism. More concretely, $[1,2-^{13}C_2]$-glucose provides the most precisely estimated fluxes for glycolysis, the pentose phosphate pathway, and the overall metabolic network. In the case of ^{13}C-glutamine tracers, the ideal isotopic tracer for the analysis of the TCA cycle fluxes is $[U-^{13}C_5]$-glutamine [334]. In addition, ^{13}C-based metabolic experiments can be performed with using a single tracer or a combination of tracers optimised to minimise the confidence intervals of the metabolic flux network under study. When a combination of tracers is used, such as $[1,2-^{13}C_2]$-glucose and $[U-^{13}C_5]$-glutamine, the experiments can be conducted in single labelling involving the use of a mixture of the different tracers in the same experiment, or in parallel labelling, using a different tracer for each experiment. The parallel labelling experiments are usually started at the same time and experimental conditions to minimise the biological variability. The resulting data from the parallel experiments with different tracers are integrated into a single flux model using ^{13}C-MFA [332, 335]. It is worth mentioning that parallel labelling experiments present numerous advantages compared to single tracer experiments, such as high observability of the global network, more efficient use of the tracers improving specific fluxes precision, reduction of the length of the labelling experiments to achieve the isotopic steady-state by introducing multiple points of entry of the tracers, validation of the biochemical network models by placing more stringent constraints on the network model assumptions, and improvement of the performance of ^{13}C-MFA in systems where the number of measurements is limited [335-337].

1.6.2.2.2. Mass isotopomer distribution analysis

The mass isotopomer distribution of newly synthesised ^{13}C-labelled metabolites in combination with the measurements of metabolic extracellular fluxes can be used to estimate some intracellular fluxes or the ratio between some of them. In fact, label
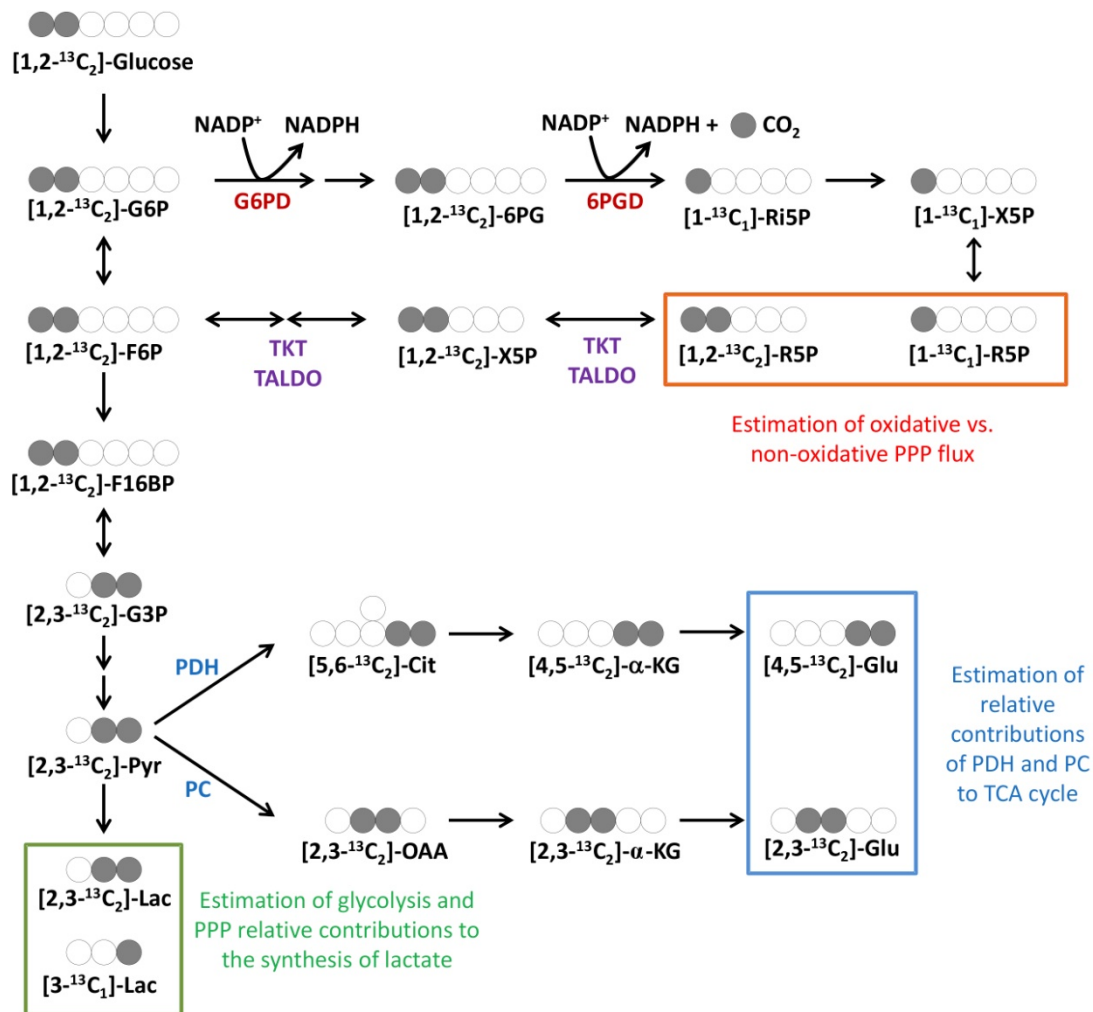
Figure 1.11. ^{13}C-assisted metabolomics experiments using [1,2-^{13}C$_2$]-glucose. The use of [1,2-^{13}C$_2$]-glucose allows estimating the performance of several major metabolic pathways such as pentose phosphate pathway (PPP), glycolysis or tricarboxylic acid (TCA) cycle. The contribution of the oxidative and the non-oxidative PPP branches to ribose-5-phosphate (R5P) production, required for the synthesis of nucleotides, can be estimated by determining the mass isotopomer distribution of RNA ribose through quantifying the percentage of R5P molecules containing one ^{13}C atom (m1 ribose, [1-^{13}C$_1$]-R5P) or two ^{13}C atoms (m2 ribose, [1,2-^{13}C$_2$]-R5P). Also, the mass isotopomer distribution of lactate (Lac) gives information about the relative contribution of glycolysis and PPP to the synthesis of lactate, since [2,3-^{13}C$_2$]-Lac (m2 lactate) is produced by direct glycolysis while [3-^{13}C$_1$]-Lac (m1 lactate) is produced by a combination of glycolysis and PPP pathways, where [1-^{13}C$_1$]-R5P is reintroduced into glycolysis

propagation has been largely used to study the reactions associated with metabolic pathways, allowing the discrimination of the relevant metabolic pathways and the comparison of flux distributions among two or more experimental conditions by checking the label propagation from the labelled substrates to different metabolic products. Mass isotopomer distribution analysis (MIDA) is a comparative analysis of tracer-based metabolomic data that use simple analytical formulas based on previous knowledge of the reactions within the metabolic network to characterise the metabolic flux distribution without bioinformatics resources [324]. For instance, the analysis of the label propagation from $[1,2-^{13}C_2]$-glucose to ribose can determine the approximate contribution of the oxidative and non-oxidative branches of the PPP to the synthesis of ribose, since the metabolism of $[1,2-^{13}C_2]$-glucose-6-phosphate through the oxidative branch yields m1 ribose ($[1-^{13}C_1]$-ribose) while the metabolism of $[1,2-^{13}C_2]$-fructose-6-phosphate through the non-oxidative branch yields m2 ribose ($[1,2-^{13}C_2]$-ribose) (Figure 1.11) [338]. In addition, combining lactate mass isotopomer distribution and concentration measurements, the relative contribution of glycolysis, PPP and other pathways to the synthesis of lactate can be estimated as described in Section 3.32.1. Likewise, the analysis of label propagation from $[1,2-^{13}C_2]$-glucose to glutamate can estimate the approximate relative contribution of pyruvate dehydrogenase (PDH) and pyruvate carboxylase (PC) to TCA cycle [339]. It is worth noting that the flux values estimated using MIDA can be introduced in the metabolic flux analysis as constraints.

---

through the non-oxidative PPP giving m1 labelled glycolytic intermediates (for simplicity, glycolytic intermediates corresponding to this process are not shown in the figure). Pyruvate entry into the mitochondria (from labelled glucose) can also be estimated by analysing the mass isotopomer distribution of glutamate (Glu). According to the pathway used to shunt pyruvate into the TCA cycle, the positional isotopomer distribution of glutamate will differ. Entry of pyruvate via pyruvate dehydrogenase (PDH) yields $[4,5-^{13}C_2]$-Glu, while entry via pyruvate carboxylase (PC) yields $[2,3-^{13}C_2]$-Glu. Details about the procedures used to determine the mass isotopomer distribution of all these metabolites are described in Section 3.29. For clarity purposes, only the main isotopomers are represented. G6P, glucose-6-phosphate; G6PD, glucose-6-phosphate dehydrogenase; 6PG, 6-phosphogluconate; 6PGD, 6-phosphogluconate dehydrogenase; Ri5P, ribulose-5-phosphate; X5P, xylulose-5-phosphate; TKT, transketolase; TALDO, transaldolase; F6P, fructose-6-phosphate; F16BP, fructose-1,6-bisphosphate; G3P, glyceraldehyde-3-phosphate; Pyr, pyruvate; Cit, citrate; OAA, oxalacetate; α-KG, α-ketoglutarate.

1.7. Strategies for cancer therapy

1.7.1. Targeting the cell cycle in cancer therapy

The main role played by the dysregulation of the cell cycle in tumourigenesis has led to the development of several strategies for cancer therapy that target different components of the cell cycle machinery (Table 1.1). Given the importance of CDK-cyclin complexes in conducting the cycle, their inhibition has been addressed as a promising strategy for cancer therapy [340-343] leading to the description of a wide number of drugs targeting CDK inhibition. The structural knowledge of cell cycle kinases has allowed the development of inhibitors of CDKs with potential therapeutic effects that have been used in clinical trials. Unfortunately, until now none of these molecules have been approved for its commercial use as anticancer drugs. CDK small-molecule inhibitors developed to date can be divided into two groups, the broad-range inhibitors or pan-CDK inhibitors (flavopiridol, olomoucine, R-roscovitine, kenpaullone, SNS-032, AT7519, AG-024322, R547, ZK 304709 and BAY 1000394) and the highly selective CDK inhibitors (Fascaplysin, Ryuvidine, Purvalanol A, NU2058, BML-259, SU 9516, PD-0332991, P276-00, Dinaciclib and AZD5438). The first generation of pan-CDK inhibitors such as flavopiridol, olomoucine or R-roscovitine, despite showing good results in pre-clinical tests [344-348], did not meet the expectations displaying low activity and/or toxicity in clinical trials [342, 343, 349-353]. These results reinforced the interest in searching for new compounds targeting CDKs more specifically, and led to a second generation of more potent CDK inhibitors that mainly interact with the catalytic active site of the kinases competing with ATP or blocking its binding [354-357]. However, some clinical trials with promising pre-clinical results (such as AG-024322 or AZD5438) were discontinued after phase I due to the inability to effectively discriminate from other treatment options or to poor clinical tolerance [358]. Also, it is worth noting that certain tumour types might display a different sensitivity to CDK inhibition depending on its pathogenic spectrum of mutations. This consideration can be of greater importance when evaluating a new CDK inhibitor undergoing clinical trials [62].

Metabolites have also been used as activators of CKI in certain tumours highlighting the existing interconnection between different kinds of cell cycle regulators. For instance, CKI p21^{Cip1} activates apoptosis in response to cisplatin in human ovarian adenocarcinoma SKOV3 cells [359], induces programmed cell death in presence of sodium butyrate in human breast adenocarcinoma MCF7 cells [360], and induces apoptosis in response to C6 ceramide in hepatoma cells [361]. On the other hand, the treatment with antimetabolites of folate or folate synthesis blockers in human colorectal carcinoma HCT116 and in human lung carcinoma A549 cell lines induces apoptosis due to mutations in p21^{Cip1}. These treatments cause a strong depletion of the purine and ATP pools resulting in metabolic stress. Under these conditions, p53 activates p21^{Cip1}-mediated metabolic arrest or apoptosis triggered by PUMA in the absence of p21^{Cip1}. Therefore, in p21^{Cip1}-active cell lines, metabolite deprivation induces p21^{Cip1}-dependent cell cycle arrest and, in absence of DNA damage, an anti-apoptotic response; however, when p21^{Cip1} is inactivated apoptosis is induced by PUMA [53]. Mutations in p21^{Cip1} have also been reported to mediate an apoptotic effect in response to methotrexate [362]. In addition, metabolic stress caused by nutrient withdrawal can lead to the activation of the autophagy gene product ATG7 and p53-mediated p21^{Cip1} activation, inducing cell cycle G1 phase arrest. In absence of ATG7, starved cells fail to undergo cell cycle arrest and there is no accumulation of p21^{Cip1}. With prolonged nutrient deprivation, the lack of ATG7 causes an increase of ROS and DNA damage which, in turn, activates CHK2 and p53-mediated transcription of pro-apoptotic genes [54].

Other strategies aiming cancer cell proliferation impairment are focused on the inhibition of the proteins that collaborate with CDK in the regulation of the progression through the different phases of the cycle. In this regard, the key role played by CDC7 kinase on the regulation of S-phase progression has led in the last years most major pharmaceutical companies worldwide such as Pfizer, Roche, Novartis, Sanofi-Aventis, Nerviano Medical Sciences or Bristol Myers Squibb (BMS) to design CDC7 inhibitors [363]. These inhibitors showed antitumour activity in pre-clinical trials, thus Nerviano (NMS-1116354) and BMS (XL-413/BMS-863233) compounds entered phase I-II clinical trials from 2009. Both molecules are ATP-competitor inhibitors of CDC7 and are

showing promising effects on the treatment of solid tumours impairing DNA replication and inducing apoptosis without causing significant toxicity [363, 364].

Table 1.1. Cell cycle regulators as therapeutic targets. Numerous pharmacological inhibitors of key regulators of the cell cycle have been developed for cancer therapy. When the inhibitors affect more than one CDK, bolded ones are the most specific targets.

Drug	Specific Target (Impaired Mechanism)	Studies	References
Flavopiridol	CDK1, CDK2, **CDK4**, CDK6, CDK7, **CDK9**, GSK3β (Canonical Cell Cycle Regulation)	Clinical Trials	[349-351]
Olomoucine	CDK1, CDK2, CDK5; ERK1 (Canonical Cell Cycle Regulation)	Pre-clinical	[343, 352]
Seliciclib	**CDK1**, **CDK2**, CDK4, **CDK5**, CDK6, **CDK7**, **CDK9** (Canonical Cell Cycle Regulation)	Clinical Trials	[352, 353]
Kenpaullone	CDK1, CDK2, CDK5, GSK3β (Canonical Cell Cycle Regulation)	Pre-clinical	[365]
SNS-032	CDK2, CDK7, CDK9 (Canonical Cell Cycle Regulation)	Clinical Trials	[366, 367]
AT7519	CDK1, **CDK2**, **CDK4**, **CDK5**, CDK6, **CDK9**, GSK3β (Canonical Cell Cycle Regulation)	Clinical Trials	[368]
AG-024322	CDK1, CDK2, CDK4 (Canonical Cell Cycle Regulation)	Clinical Trials Discontinued (2007)	[342, 369]
R547	CDK1, CDK2, CDK4 (Canonical Cell Cycle Regulation)	Clinical Trials	[370, 371]
ZK 304709	CDK1, CDK2, CDK4, CDK7, CDK9 (Canonical Cell Cycle Regulation)	Clinical Trials	[372, 373]
BAY 1000394	CDK1, CDK2, CDK4, CDK9 (Canonical Cell Cycle Regulation)	Clinical Trials	[374]
Fascaplysin	CDK4, CDK6 (Canonical Cell Cycle Regulation)	Pre-clinical	[354]
Ryuvidine	CDK4 (Canonical Cell Cycle Regulation)	Pre-clinical	[343, 375]
Purvalanol A	**CDK2**, CDK4, **CDK5** (Canonical Cell Cycle Regulation)	Pre-clinical	[376]
NU2058	CDK1, CDK2 (Canonical Cell Cycle Regulation)	Pre-clinical	[355]
BML-259	CDK2, CDK5 (Canonical Cell Cycle Regulation)	Pre-clinical	[377]
SU 9516	**CDK1**, **CDK2**, CDK4, PKC, p38, PDGFR, EGFR (Canonical Cell Cycle Regulation)	Pre-clinical	[378]
PD-0332991	CDK4, CDK6 (Canonical Cell Cycle Regulation)	Clinical Trials Clinical development	[84, 379-381]

Drug	Specific Target (Impaired Mechanism)	Studies	References
P276-00	CDK1, **CDK2**, CDK4 (Canonical Cell Cycle Regulation)	Clinical Trials	[343, 357]
Dinaciclib	CDK1, CDK2, CDK5, CDK9 (Canonical Cell Cycle Regulation)	Clinical Trials	[382, 383]
AZD5438	CDK1, CDK2, CDK9 (Canonical Cell Cycle Regulation)	Clinical Trials Discontinued (2009)	[384]
PHA-848125	CDK1, **CDK2**, CDK4, CDK5, CDK7, TRKA (Canonical Cell Cycle Regulation)	Clinical Trials	[385-387]
Terameprocol	CDK1, survivin, VEGFRs (Canonical Cell Cycle Regulation)	Clinical Trials	[342, 388, 389]
Indisulam	Cyclin E (Canonical Cell Cycle Regulation)	Clinical Trials	[342, 390, 391]
NMS-1116354 XL-413/BMS-863233	CDC7 Kinase (Canonical Cell Cycle Regulation)	Clinical Trials	[363, 364]
PF-03814735 Danusertib AT9283	Aurora Kinases (Canonical Cell Cycle Regulation)	Clinical Trials	[392-394]
ENMD-2076	Aurora Kinase A (Canonical Cell Cycle Regulation)	Clinical Trials	[395, 396]
Barasertib	Aurora Kinase B (Canonical Cell Cycle Regulation)	Clinical Trials	[397]
GSK461364 BI2536 Rigosertibin TAK-960	PLK1 (Canonical Cell Cycle Regulation)	Clinical Trials	[398-401]
Taxanes & Vinca Alkaloids	Microtubule Dynamics (Cytoskeleton)	Clinical Trials and Therapy	[93, 402]
XL-844 AZD7762	CHK 1/2 (Canonical Cell Cycle Regulation)	Pre-clinical	[403, 404]
Bortezomib	Proteasome (Proteolysis)	Clinical Trials and Therapy	[405]
TCH-013	Proteasome (Proteolysis)	Pre-clinical	[406]
Nutlins	MDM2-p53 (Ubiquitin Ligases-Proteolysis)	Pre-clinical Clinical Trials	[407, 408]
TAME	APC/C (Ubiquitin Ligases-Proteolysis)	Pre-clinical	[409]

Regarding other kinase families with important roles in cell cycle apart from CDKs, aurora kinases inhibitors have been used in clinical trials for the treatment of solid tumours and hematologic malignancies such as leukemia due to their ability to affect chromosome segregation and arrest cell cycle. Several molecules have been designed

to inhibit aurora kinases, some of them are selective for aurora A or aurora B, but most of them are active not only against aurora kinases but also against many other kinases. Phase I and II clinical trials evaluating aurora kinases inhibitors are being conducted. ENMD-2076, a synthetic molecule designed for selectively inhibiting aurora A but not aurora B has been tested with promising results both in phase I clinical trials to treat hematologic malignancies and myeloma, and in phase II clinical trials in patients with platinum-resistant ovarian cancer [395, 396]. On the other hand, barasertib (AZD1152) is a selective inhibitor of aurora B that has been used in phase I and II clinical trials to treat patients with advanced acute myeloid leukemia with a response rate of 25% and manageable adverse effects [397]. Moreover, danusertib (PHA-739358), AT9283 and PF-03814735 are inhibitors of both aurora A and B kinases that have also entered clinical trials [392-394]. Also, regarding polo-like kinases, PLK1 has been also widely accepted as a feasible antitumour target. However, since the inhibition of the other PLKs (PLK2-5) may lead to tumour development, the specificity of PLK1 inhibitors is of paramount importance. Several PLK1 inhibitors such as GSK461364, BI2536, rigosertib or TAK-960 have been tested in phase I trials, obtaining acceptable results and warranting further investigation of PLK1 inhibitors in the future [399-401, 410]. In addition, microtubule-targeted drugs including taxanes and vinca alkaloids are used to treat patients with breast and ovarian cancers [93, 402].

As mentioned above, genome instability and accumulation of mutations are enabling characteristics for the acquisition of the malignant phenotype. They are enhanced by defects in the genome maintenance mechanisms such as DNA repair and cell cycle checkpoint pathways. Consequently, the checkpoint kinase CHK2 is a candidate tumour suppressor that is found altered in some types of cancer, like colon or breast cancer [57]. Mutations in *CHK2* can lead to abnormal activation of CHK2 and increased levels of the pro-apoptotic E2F1 transcription factor. The suprathreshold stabilisation of E2F1 using β-lapachone results in selectively cancer cell death [411]. However, the molecular mechanisms underlying the anticancer activity of β-lapachone have not yet been fully elucidated. Indeed, β-lapachone and several derivatives mediate cancer cell toxicity through ROS formation and DNA damage [412], pointing out the difficulty of isolating a single target for a drug effect. Targeting not only CHK2 but also the other

checkpoint regulator CHK1 and E3 ubiquitin ligases involved in mediate cyclins proteasome degradation have been also proposed as relevant anticancer therapeutic approaches. Preclinical studies have shown that CHK1 and CHK2 inhibitors, such as XL-844 or AZD7762, sensitise different tumour cells to radiation via inhibition of DNA repair and induction of mitotic catastrophe [403, 404]. On the other hand, blocking mitotic exit by affecting CDC20 has been proposed as a cancer therapeutic strategy that might circumvent the resistances arisen around the targeting of the checkpoint machinery [413, 414]. Both strategies are in pre-clinical studies and require further research.

On the other hand, promising results have been obtained for the treatment of cancer with drugs targeting the inhibition of the proteasome-dependent proteolysis. Bortezomib is a proteasome inhibitor used for the treatment of relapsed multiple myeloma, among other cancers, that has shown favourable results [59, 405, 415]. The efficacy of bortezomib has been corroborated in many clinical trials supporting its suitability for cancer treatment. However, due to the intolerance or resistance usually developed to bortezomib, this drug is currently being tested in combination with radiotherapy and with several other drugs such as the histone deacetylase inhibitor vorinostat (MK-0683), or the cytochrome P450 3A4 (CYP3A4) inducers rifampicin and dexamethasone among others, to take advantage of its capacity to sensitise cancer cells to cytotoxic chemotherapy (search for bortezomib or NCT00011778, NCT00773747 and NCT00608907 at www.clinicaltrials.gov/ct2/search). Moreover, the imidazoline scaffold TCH-013 has been described as a new generation proteasome inhibitor that overcomes the resistance to bortezomib and should offer better results in the treatment of cancer patients [406]. Other drugs have been described inhibiting proteolysis by different ways. For instance small molecules blocking the MDM2-p53 interaction lead to the stabilisation and reactivation of the tumour suppressor protein p53. Bortezomib has also been proposed to inhibit p53 degradation in human non-small cell lung cancer cell line H460 [415]. However, more specific antagonists of MDM2 such as nutlins have been described as potential chemotherapeutics [59, 407] and subsequent studies have supported their use in cancer therapy [408]. These results indicated that specific inhibition of the SCF or the APC/C complexes could also

be effective against cancer and have led to new studies of molecules targeting the ubiquitin ligases. An example of these drugs is TAME (tosyl-L-arginine methyl ester), a small molecule that in pre-clinical studies has shown efficient activity preventing APC/C activation by CDC20 and CDH1, leading to arrest of tumour cells in mitosis and triggering tumour cell death [409].

1.7.2. Targeting the metabolic reprogramming in cancer therapy

Development of malignancy comes along with a metabolic reprogramming closely related to the acquisition of most of cancer hallmarks [6, 104]. As described before, one of these metabolic alterations associated to cell malignant transformation is the aerobic glycolysis resulting from the increased metabolism of glucose to lactate even in presence of oxygen (Warburg effect) [416, 417]. Indeed, metabolic properties of tumour cells are significantly different from those of non-transformed cells. Of note, tumour metabolic reprogramming is linked to drug resistance in cancer treatment [418]. Accordingly, metabolic adaptations and redox signalling are also involved in different therapeutic approaches for cancer therapy. The main metabolic pathways that enable cell transformation are glycolysis, PPP, nucleic acid synthesis and lipogenesis. Glycolysis supplies the energy and carbon sources for biosynthesis and cell duplication leading to the formation of lactate, PPP regulates the flux of carbons between nucleic acid synthesis and lipogenesis and the latter two generate the elemental units for genetic material and cell membrane duplication. Moreover, pathways like glutaminolysis have been described essential for many tumours, thus confirming the importance of their role in controlling proliferation [96, 153]. The acquisition of most of cancer hallmarks has been reported to be accompanied by a complete metabolic reprogramming [104]. Interestingly, there is a close relationship between metabolism and redox balance mediated mainly by mitochondrial activity but also by all $NAD(P)^+/NAD(P)H$-dependent reactions [97].

The importance of metabolism in cancer is illustrated by the fact that the first chemotherapeutical agents used in the mid-twentieth century in cancer treatment

were antimetabolites that blocked precisely the nucleotide synthesis: antifolates (aminopterin and methotrexate) and 5-fluorouracil [419, 420]. Methotrexate allosterically inhibits dihydrofolate reductase (DHFR), an enzyme that participates in the tetrahydrofolate synthesis and necessary for the synthesis of nucleotides, while 5-fluorouracil is able to irreversibly interact with thymidylate synthase, which is essential for thymidyne synthesis. From then on, several metabolic pathways and enzymes have been proposed and successfully used as anticancer targets (Table 1.2). Given the fact that one of the main metabolic features of cancer cells is the aerobic glycolysis, numerous studies have been conducted to inhibit this pathway by blocking the enzymes that control it, such as pyruvate kinase [421-425].

Other pre-clinical studies have focused in blocking the synthesis of fatty acid by treatment with fatty acid synthase (FASN) inhibitors such as cerulenin and its chemical analogue C75, orlistat or triclosan and with ATP citrate lyase (ACLY) inhibitors such as SB-204990 [128, 426-428]. Lipid synthesis has also been targeted by activating the metabolic regulator AMPK with acadesine (AICAR, 5-Aminoimidazole-4-carboxamide-1-beta-4-ribofuranoside) or rosiglitazone [429-432]. Since these molecules have shown lipid synthesis-blocking capacity and are able to impair tumour growth, they have entered clinical trials to test their suitability as antitumour drugs (NCT00559624, NCT00369174 and NCT00182052). The other metabolic pathway proposed as potential target against cancer is the PPP. Both the G6PD inhibitor dehydroepiandrosterone (DHEA) and the TKT inhibitor oxythiamine have been reported to have antitumour effects [13, 121, 124, 433]. Remarkably, DHEA entered several clinical trials in order to test its efficacy against different diseases and in the last years it is also being tested in breast cancer patients (NCT00972023 and NCT02000375).

Blocking pyruvate conversion to lactate with dichloroacetate (DCA) presents promising results with minor side effects in early phase clinical trials with glioblastoma patients by suppressing angiogenesis, increasing mitochondrial ROS, inducing apoptosis, blocking HIF1 signalling and activating tumour suppressor p53 [434-436]. In fact, DCA inhibits PDHK leading to the metabolic switch from glycolysis to oxidative phosphorylation through PDH reactivation [434]. Moreover, combined therapies with DCA and conventional cancer therapeutics such as omeprazole and tamoxifen show

synergistic antitumour effects which can overcome drug resistance [437]. Ongoing clinical trials with DCA as a single agent or in combination with other therapeutics are being conducted for patients with recurrent or metastatic solid tumours and head and neck carcinoma (NCT00566410 and NCT01386632).

Table 1.2. Metabolic enzymes as therapeutic targets. Several pharmacological inhibitors of key metabolic enzymes have been developed for cancer therapy.

Drug	Specific Target	Studies	References
Cerulenin/C75 Triclosan Orlistat	FASN	Pre-clinical	[426]
SB-204990	ACLY	Pre-clinical	[427]
Acadesine Rosiglitazone	AMPK activation	Clinical Trials	[429-432]
Dehydroepiandrosterone	G6PD	Clinical Trials	[121, 433]
Oxythiamine	TKT	Pre-clinical	[121, 433]
Dichloroacetate (DCA)	PDHK	Clinical Trials	[436]
968	GLS1	Pre-clinical	[438]
BPTES	GLS1	Pre-clinical	[439]
CB-839	GLS1	Clinical Trials	[156]

There is a growing interest on the development of pharmacological strategies to inhibit tumour glutamine metabolism. The use of amino acid analogues such as acivicin demonstrated severe side effects in clinical trials, aiming for more selective therapeutic strategies [440]. As a result, GLS1 isoform has emerged as a promising target for cancer therapy, and several specific small molecule inhibitors of GLS1 have recently been characterised. Compound 968 and BPTES (bis-2-(5-phenylacetamido-1,2,4-thiadiazol-2-yl)ethyl sulfide) are two allosteric inhibitors of GLS1 that exhibit antitumour activities in numerous pre-clinical studies and in several tumour types [155, 157, 171, 438, 439, 441]. Remarkably, the selective inhibitor of GLS1 known as CB-839 presents *in vitro* antiproliferative activity against acute myeloid leukemia cells [442], a panel of triple-negative breast cancer cell lines, but not estrogen receptor (ER)

or human epidermal growth factor receptor 2 (HER2) positive cell lines, and *in vivo* efficacy in breast cancer xenograft models [156]. In addition, CB-839 has recently entered phase I clinical trials without displaying central nervous system toxicity (NCT02071862 and NCT02071888). In fact, GLS1 inhibition is a good strategy for tumour cells that overexpress MYC and thus present glutamine dependence [96, 153]. It is worth mentioning that, to date, no effective MYC inhibitors have been developed despite the fact that MYC overexpression is frequently found in human cancers [206, 443-445]. However, targeting GLS1 significantly antagonises the growth of tumours presenting MYC overexpression and can be exploited as a novel antitumour therapy [155].

1.7.3. Selenium as a chemotherapeutic agent

The trace element selenium (Se) in various chemical forms is nutritionally essential for humans but has toxic activity at higher levels [446, 447]. To date, the antioxidant and chemopreventive role of different Se agents as a dietary supplement has not been completely elucidated [448]. Se compounds such as sodium selenite (Na_2SeO_3) [449, 450] and methylseleninic acid (CH_3SeO_2H, abbreviated as MSA) have also been studied as potential anticancer agents. MSA is a synthetic precursor of methylselenol (CH_3SeH) which induces several cellular, transcriptional and biochemical responses that differ from those induced by selenium forms that are transformed via hydrogen selenide, such as sodium selenite [451, 452].

As a constituent of the selenocysteine-containing selenoproteins, selenium has a key role in redox regulation and defence against oxidative stress by greatly enhancing the activity of some antioxidant enzyme systems [453]. Several selenoenzymes, including thioredoxin reductase, iodothyronine deiodinase and glutathione peroxidase, may be associated with cancer development and progression by modulating cell proliferation, transformation, migration and protection against oxidative damage [446]. Selenium deficiency has also been linked to cancer development since it was observed that populations with low selenium intake had greater cancer incidence. Numerous studies

and clinical trials have shown that supranutritional doses of individual and mixed selenium compounds inhibit proliferation of cancer cells, induce tumour cell apoptosis, suppress tumour formation and metastasis in animal models and reduce the risk of prostate, lung, breast, and colorectal cancers in humans [453-455]. However, not all selenium compounds have efficacy in chemoprevention, as in a recent large clinical trial (SELECT), selenomethionine was concluded to be ineffective in reducing the risk for prostate cancer development [456].

Using a stable isotope-resolved metabolomic (SIRM) approach, Fan and collaborators [457] reported that several metabolites, including lactate, glutathione and glutamate are depleted in A549 lung cancer cells by selenite but not by selenomethionine, suggesting multiple perturbations of the central metabolic networks. Interestingly, the reduction in glycolysis, tricarboxylic acid cycle (TCA) and pentose phosphate pathway (PPP) fluxes observed is opposite to those observed when phosphoinositide-3-kinase (PI3K) pathway is activated [458], pointing to the hypothesis that Se agents target this signalling pathway. Among the selenium compounds with anticancer properties, it has been reported that MSA is a potent inhibitor of the growth and survival of human umbilical vein endothelial cells (HUVECs) and that this antiproliferative effect could be enacted through the PI3K pathway [459, 460]. Studies with prostate cancer LNCaP, PC-3 (high basal Akt activity) and DU145 cells (low basal Akt activity) have also shown that Akt plays an important role in regulating apoptosis sensitivity to MSA [461]. However, the molecular mechanism of action of MSA is still not fully elucidated.

1.7.4. Combination therapies

Identification of cytotoxic compounds led the development of antitumour therapeutics until in the recent years chemotherapy has advanced into the era of molecularly targeted therapeutics. The bases of molecular targeted cancer therapy are to selectively kill tumour cells while sparing non-malignant cells, and prevent tumour resistance emergence and relapse [462]. However, solid tumours response to targeted monotherapy is limited and frequently associated with the development of drug

resistance. In addition, the design of targeted therapies requires the definition of the activated oncogenic pathways in transformed cells and the availability of selective small-molecule inhibitors directed to these pathways. The modest efficacy of current therapies is also caused by the high degree of tumour clonal and genetic heterogeneity, since inhibition of a single target does not necessarily eradicate the tumour. Therefore, the use of combination therapies of selective agents and/or cytotoxic agents that inhibit two or more molecular targets in a single pathway, or in parallel or compensatory pathways, is an attractive strategy for cancer treatment [463]. Additionally, the simultaneous inhibition of multiple targets or redundant pathways is aimed at improving treatment efficacy and overcoming and/or preventing the emergence of resistance.

Then, in order to select appropriate molecular targets for inhibition or modification, is necessary to first perform a tumour expression profiling to identify its specific oncogenic signatures, and confirm that the target is tumour specific, non-redundant, and able to influence the outcome of tumour progression [462, 464]. However, many oncogenic pathways cannot be directly targeted with small-molecule inhibitors [444]. Remarkably, gene expression analysis can be used as a predictive tool to identify the oncogenic pathways which are dysregulated in a specific tumour, providing a potential basis for guiding the use of pathway-specific drugs and directing combination therapies [464].

2. Objectives

2. OBJECTIVES

The main objective of this thesis is to explore new possibilities for cancer treatment and diagnosis. To this end, we have analysed the links between metabolism and tumour progression, the tumour metabolic reprogramming associated to the dysregulation of cell cycle, and the use of combination therapies for cancer treatment. Hence, in order to accomplish the main objective, the specific objectives of this thesis are:

1. Identification of glyceraldehyde-3-phosphate dehydrogenase (GAPDH) as a potential predictive biomarker for tumour staging and prognosis of human colorectal cancer.

2. Characterisation of metabolic reprogramming and potential metabolic vulnerabilities associated to the inhibition of cyclin-dependent kinases 4 and 6 (CDK4/6) in tumour cells, and identification of combination therapies that increase the efficacy of CDK4/6 inhibition by overcoming adaptive resistance.

3. Determination of the molecular mechanism of action of the selenium compound methylseleninic acid (MSA), and evaluation of its potential as an antitumour agent in combination with conventional chemotherapeutic drugs for cancer therapy.

Successful completion of these objectives will shed new light on the understanding of tumour metabolic reprogramming as well as the mechanisms of action of compounds potentially useful as antitumour agents. This knowledge can be used to develop new strategies complementing conventional and existing chemotherapies, providing new approaches for cancer treatment and diagnosis.

3. Materials and methods

3. MATERIALS AND METHODS

All products were purchased from Sigma-Aldrich Co (St Louis, MO, USA), unless otherwise specified.

3.1. Chemicals

PD0332991, 10058-F4, DMOG and sodium selenite were purchased from Sigma-Aldrich. Methylseleninic acid (MSA) was supplied by Dr Teresa Fan (University of Kentucky, KY, USA). The PI3K inhibitor LY294002 was purchased from Calbiochem (San Diego, CA, USA). The glutaminase inhibitor bis-2-(5-phenylacetamido-1,2,4-thiadiazol-2-yl)ethyl sulfide (BPTES) was kindly provided by Dr Mariia Yuneva (The Francis Crick Institute, London, UK). Stock solutions of 10 mM were prepared with Dulbecco's phosphate buffered saline (PBS), water for cell culture or dimethyl sulfoxide (DMSO), according to the manufacturer's instructions. Antibiotic (10,000 U mL^{-1} penicillin, 10 mg mL^{-1} streptomycin), PBS and Trypsin EDTA solution C (0.05% trypsin – 0.02% EDTA) were obtained from Biological Industries (Kibbutz Beit Haemet, Israel), and fetal bovine serum (FBS) from Invitrogen (Carlsbad, CA, USA).

3.2. Cell culture

All cell lines were purchased from the American Type Culture Collection (ATCC, Manassas, VA, USA), unless otherwise specified. Human colorectal carcinoma HCT116 cells and human breast adenocarcinoma SKBR3 cells were cultured in Dulbecco's modified Eagle medium (Gibco, Thermo Fisher Scientific Inc., Waltham, MA, USA) / Nutrient mixture HAM F12 (Biological Industries) (DMEM/F12, 1:1 mixture) with L-glutamine and 12.5 mM D-glucose. Human lung carcinoma A549 cells were grown in Roswell Park Memorial Institute (RPMI)-1640 medium with L-glutamine and 10 mM D-glucose prepared following the manufacturer's instructions. Human osteosarcoma stably transfected U2foxRELOC cells (a gift from Dr Wolfgang Link), human

osteosarcoma U2OS cells, human large cell lung cancer NCI-H460 cells, human ovary adenocarcinoma OVCAR3 cells, human embryonic kidney 293 (HEK293) cells, human skin BJ fibroblasts and adipocyte-like differentiated 3T3-L1 cells were grown in DMEM with L-glutamine and 25 mM D-glucose. Human breast adenocarcinoma MCF7 cells were cultured in MEM medium without phenol red (Gibco) containing 10 mM D-glucose, 2 mM L-glutamine, 1 mM pyruvate (Biological Industries), 0.01 mg mL^{-1} insulin and 1% non-essential aminoacids (Biological Industries). Media were supplemented with 10% heat-inactivated FBS, penicillin (50 U mL^{-1}) and streptomycin (50 μg mL^{-1}). U2foxRELOC cells, which express a resistance to Geneticin, were incubated with G418 (Gibco) at 100 μg mL^{-1}. 3T3-L1 pre-adipocyte cells were grown in DMEM with 0% FBS, 10% newborn calf serum (NCS) and 0.5% streptomycin/penicillin. Cells were incubated at 37ºC in a humidified atmosphere with 5% CO_2. For hypoxia incubations, the cells were kept in an atmosphere containing 1% oxygen and 5% CO_2 at 37ºC in a hypoxia incubator for the indicated time periods.

3.3. 3T3-L1 differentiation

Pre-adipocyte 3T3-L1 cells were seeded in 96-well-flat-bottomed microtitre plates. Medium was changed two days after confluence with DMEM containing 0% NCS, 10% FBS and induction cocktail (250 μM isobutylmethylxanthine, 1 μM dexamethasone and 0.98 μM insulin). After 72 h, medium was replaced with DMEM containing 10% FBS and 0.98 μM insulin and cells were incubated for 72 h. Then, medium was replaced with DMEM containing 10% FBS. Cells were fully differentiated into adipocytes within 48 h and cell viability assay was performed on them.

3.4. siRNA transfection

HCT116 cell line was transfected using Lipofectamine RNAiMAX (Invitrogen) transfection reagent following the manufacturer's instructions. We tested different concentrations of lipid transfection reagent and siRNA, transfection periods and cell

numbers plated for transfection. The optimised transfection conditions that delivered the best knockdown results were selected by quantitative reverse transcription-polymerase chain reaction (RT-qPCR) and Western blot, while cell population was maintained in a state of exponential growth during all the experiment. Briefly, 5×10^{4} cells/well were seeded in antibiotic-free medium in 6-well flat-bottom tissue culture plates and transfected the next day with a mix (siRNA CDK4/6) containing 30 nM of ON-TARGETplus SMARTpool siRNA against CDK4 (L-003238-00, GE Healthcare Dharmacon Inc., Lafayette, CO, USA) and 30 nM of Silencer Select siRNA against CDK6 (s51, Ambion, Austin, TX, USA) or with a mix (siRNA Control) containing 30 nM of ON-TARGETplus Non-Targeting Control Pool siRNA (D-001810-10, GE Healthcare Dharmacon Inc.) and 30 nM of Silencer Select Negative Control siRNA (4390844, Ambion). After 24 h, culture medium was replaced with fresh medium with antibiotics. The CDK4 siRNA pool includes the sequences: CAAGGUAACCCUGGUGUUU GAGCUCUGCAGCACUCUUA CAGCACAGUUCGUGAGGUG GCACUUACACCCGUGGUUG. The CDK6 siRNA includes the sequence GUUUGUAACAGAUAUCGAU. The sequences contained in the control pool are not detailed by the manufacturer. Cells were analysed 96 h after transfection.

3.5. Cell proliferation and viability assay

Proliferation assays were performed by flow cytometry combining direct cell counting and propidium iodide (PI) staining. 96 h after transfection or as indicated elsewhere, cells were trypsinised and resuspended in 500 µL of a solution containing 450 µL of complete media, 45 µL of Flow-Count Fluorospheres (Beckman Coulter, Brea, CA, USA) and 5 µL of 1 mg mL^{-1} PI. Flow cytometer was adjusted to 1×10^{4} fluorospheres cut-off and total cell number was recorded, allowing discrimination between dead and alive cells. Cell size and volume values were obtained using a Scepter^{TM} Handheld Automated Cell Counter (Merck Millipore, Billerica, MA, USA) which employs the Coulter principle of impedance-based particle detection.

Cell viability was assessed using Hoechst stain (HO33342; 2'-[4-ethoxyphenyl]-5-[4-methyl-1-piperazinyl]-2,5'-bi-1H-benzimidazole trihydrochloride trihydrate), a cell-permeable blue fluorescent dye that stains DNA. This assay was performed when testing drugs that affect mitochondrial respiration. 24 h after seeding 2×10^3 cells/well in 96-well plates, media were replaced with complete fresh media containing the desired concentration of drug, the combination of drugs under study, or vehicle. At the end of the experiment, cells were washed with PBS before adding 100 µL of 0.01% SDS per well. Plates were then stored frozen at -20ºC. To analyse the samples, plates were thawed at 37ºC until fully liquid and 100 µL of 4 µg mL^{-1} HO33342 in stain solution buffer (1 M NaCl, 1 mM EDTA, 10 mM Tris-HCl pH 7.4) were added to each well, minimising light exposure. Tinfoil-covered plates were placed on a shaker and incubated at 37ºC for 1 h. Finally, fluorescence was measured in a fluorescence plate reader (FLUOstar OPTIMA Microplate Reader, BMG LABTECH GmbH, Ortenberg, Germany) at 355 nm excitation and 460 nm emission. Cell viability was assessed and represented as a percentage of viability relative to untreated control cells.

Cell viability assay was also performed using a modified method described by Mosmann [465]. This assay was performed when testing drugs which interact with DNA. Increasing concentrations of the inhibitor were added in sextuplicate in 96-well-flat-bottomed microtitre plates where 2×10^3 cells/well had been seeded 24 h before. In the case of MSA drug sensitivity assay, MSA was added to 3T3-L1 cells once the differentiation process was completed. MSA was depleted after >24 h of treatment, so medium was refreshed every day. After 24, 48 or 72 hours, 1 mg mL^{-1} 3-(4,5-dimethylthiazol-2-yl)-2,5-diphenyltetrazolium bromide (MTT) in PBS was added at a final concentration of 0.5 mg mL^{-1}. After 1 hour, supernatant was removed and the formazan product was dissolved in 100 µL of dimethyl sulfoxide (DMSO). The absorbance was measured on an ELISA plate reader (Tecan Sunrise MR20-301, TECAN, Salzburg, Austria) at 550 nm.

Concentrations that caused 50% of inhibition of cell proliferation (IC$_{50}$) were calculated using Graphpad Prism 6 software (La Jolla, CA, USA).

3.6. Mitochondrial activity per number of cells ratio

Total mitochondrial activity per number of cells was estimated by the conversion of the tetrazolium salt MTT into formazan crystals, as explained in Section 3.5., and the direct cell counting of parallel cultures. The MTT assay principle is that for most viable cells mitochondrial activity is constant and linearly proportional to the number of viable cells. In such case, the ratio of mitochondrial activity per number of cells (determined by cell counting) is constant, independently of the treatment. However, there are some treatments that can have an effect on mitochondrial activity, increasing or decreasing the ratio of mitochondrial activity per number of cells.

3.7. Spheroid formation

10^4 cells were seeded in 24-well ultra low attachment culture plates (Corning, Corning, NY, USA) in complete culture medium containing 0.6% methyl cellulose and the concentration of inhibitor(s) specified in each case, and allowed to grow for 10 days. Spheroid formation was also studied using an alternative method; cells were grown for 10 days in presence of the specified inhibitor(s) in serum-free media supplemented with 20 ng mL^{-1} EGF, 20 ng mL^{-1} bFGF, 10 µg mL^{-1} heparine, B27 (1:50), 5 µg mL^{-1} insulin and 0.5 µg mL^{-1} hydrocortisone. In both cases, at the end of the experiment, spheroids were incubated with 0.5 mg mL^{-1} MTT for 2-3 h until fully stained. Finally, plates were scanned and spheroids were scored by image acquisition and spheroid area and volume quantification with ImageJ software (public domain National Institutes of Health, USA, http://rsbweb.nih.gov/ij/).

3.8. Cell cycle synchronisation

Cells were arrested at the cell cycle G1 phase by double thymidine block [466]. Asynchronously cells were grown to approximately 40% confluence and incubated for 16 h with complete medium containing 2mM thymidine. Then, cells were washed

twice with fresh complete medium and incubated for 9 h with 24 μM deoxycytidine. After two washes with fresh complete medium, cells were incubated with 2mM thymidine for another 16 h. Finally, cells were released from cell cycle G1 phase arrest replacing thymidine with complete medium containing 24 μM deoxycytidine. Cells were collected every 2 h for 24 h and analysed by flow cytometry to identify each cell cycle phase.

3.9. Cell cycle analysis

For HCT116 cells, cell cycle analysis was performed 96 h after transfection or inhibitor treatment. For A549 cells, 5×10^4 cells/well were seeded in 6-well plates and treated 24 h later with MSA for 24, 48 and 72 h. Both adherent and detached cells were collected by centrifugation after trypsinisation, resuspended in 0.5 mL PBS and added dropwise to 4.5 mL 70% (v/v) cold ethanol. Then, cells were centrifuged, washed with PBS and resuspended in PBS containing 0.2 mg mL^{-1} DNAse free RNAse A (Roche, Basel, Switzerland) and incubated for 1 h at 37ºC. Prior to analysis, 0.05 μg mL^{-1} propidium iodide (PI) was added. Fluorescence-activated cell sorter (FACS) analysis was carried out at 488 nm in an Epics XL flow cytometer (Coulter Corporation, Hialeah, FL, USA). Data of 1×10^4 cells were collected and analysed using Multicycle program (Phoenix Flow Systems, San Diego, CA, USA). All experiments were performed three times with three replicates per experiment.

3.10. Apoptosis assay

Cells were seeded and treated as described in the cell cycle analysis assay. After centrifugation, cells were washed and resuspended in binding buffer (10 mM Hepes pH 7.4, 140 mM sodium chloride, 2.5 mM calcium chloride). Annexin V coupled with fluorescein isothiocyanate (FITC) was added according to the Annexin V-FITC kit (Bender System MedSystem, Viena, Austria). Following 30 min of incubation at room temperature in darkness, PI was added at 20 μg mL^{-1} 1 min before FACS analysis.

Experiments were performed in triplicate and repeated three independent times. Data from 2×10^4 cells were collected and analysed in each experiment.

Apoptosis was also assessed in A549 cells using the membrane-permeable fluorescent dye bisbenzimide Hoechst. After 24 h in the absence or presence of $^{72h}IC_{50}$ MSA, cells were harvested by mild trypsinisation, collected by centrifugation and fixed with 3.7% paraformaldehyde for 10 minutes at -20ºC. Cells were washed with PBS, 0.5% Triton X-100 was added for 5 min at 4ºC and cells were stained with 50 ng mL^{-1} Hoechst 33342 dye for 15 min before placing them onto slides and mounting the coverslips with Mowiol 4-88. Chromatin condensation was visualised by fluorescence microscopy.

3.11. Single cell gel electrophoresis (comet assay)

3×10^4 A549 cells/well were seeded in 6-well plates and treated the next day with $^{72h}IC_{50}$ MSA, hydrogen peroxide 100 µM (positive control) and vehicle (negative control). After 24, the comet assay was carried out according to Tice et al. [467]. Briefly, 6×10^5 cells mL^{-1} were mixed with 140 µL of 1% low-melting-point agarose and 70 µL were spread onto pre-coated microscope slides (1% of normal-melting-point agarose). Glass cover slips (Menzel-Glaser, Braunschweig, Germany) were placed on the gels, which were allowed to set at 4ºC. Then, cover slips were removed and cells embedded in agarose were lysed for 1 hour by immersion in 2.5 M NaCl, 100 mM Na$_2$-EDTA, 10 mM Trizma-HCl (pH 10) and 1% Triton X-100 at 4ºC. The slides were placed on a horizontal gel electrophoresis tank and the DNA was allowed to unwind for 40 min in freshly prepared alkaline electrophoresis buffer (300 mM NaOH and 1 mM Na$_2$-EDTA, pH > 13). Electrophoresis was carried out in the same buffer for 30 min at 25 V in an ice bath condition. The slides were rinsed 3×5 min with 400 mM Trizma (pH 7.5) to neutralise the excess alkali, washed in water (10 minutes), stained with 25 µL of 4,6-Diamidino-2-phenylindole (DAPI) (Invitrogen) and covered with a cover. DAPI stained nuclei were evaluated with a Nikon Eclipse TE 300 fluorescence microscope (Nikon, Tokyo, Japan). A total of 100 comets on each gel were visually scored and classified as belonging to one of five classes according to the tail intensity. Each comet class was

given a value between 0 (undamaged) and 4 (maximum damage). Total score was calculated by the following equation: (percentage of cells in class 0×0) + (percentage of cells in class 1×1) + (percentage of cells in class 2×2) + (percentage of cells in class 3×3) + (percentage of cells in class 4×4). Consequently, the total score was in the range from 0 to 400. Experiments were performed in triplicate.

3.12. Measurement of extracellular metabolites

Glucose, lactate, glutamate and glutamine concentrations from cell culture media were determined using a COBAS Mira Plus spectrophotometer (Horiba ABX, Kyoto, Japan) to monitor the production of NAD(P)H in specific reactions for each metabolite at 340 nm wavelength. Glucose concentration was measured using hexokinase (HK) and glucose-6-phosphate dehydrogenase (G6PD) coupled enzymatic reactions (ABX Pentra Glucose HK CP, HORIBA ABX, Montpellier, France). Lactate concentration was determined by lactate dehydrogenase (LDH) reaction, which was carried out at 37ºC by mixing the media samples with 1.55 mg mL^{-1} NAD$^+$ and 87.7 U mL^{-1} LDH (Roche) in 0.2 M hydrazine 12 mM EDTA buffer (pH 9). Glutamate concentration was assessed by conversion to α-ketoglutarate through glutamate dehydrogenase (GDH) reaction in the presence of ADP. This reaction was performed at 37ºC by adding media samples to 2.41 mM ADP, 3.9 mM NAD$^+$ and 39 U mL^{-1} of GDH (Roche) in 0.5 M glycine/0.5 M hydrazine buffer (pH 9). Glutamine concentration was calculated by means of its conversion to glutamate by glutaminase (GLS) and subsequently quantification of glutamate concentration as described above. GLS reaction was carried out by incubating the media samples with 125 mU mL^{-1} GLS in 125 mM acetate buffer (pH 5) for 30 min at 37ºC in agitation.

Non-essential and essential amino acids (alanine, aspartate, asparagine, proline, glycine, serine, arginine, cysteine, threonine, isoleucine, leucine, lysine, methionine, valine, tryptophan, histidine, phenylalanine, tyrosine, glutamate and glutamine) concentrations in cell media were measured by ion-exchange chromatography with a Biochrom 30 amino acid analyser (Pharmacia Biochrom Ltd, Cambridge, UK). As an

internal standard, 70 µL of 150 µM norleucine were added to 500 µL of medium. Then, samples were dried by SpeedVac (Thermo Fisher Scientific Inc.), resuspended in 500 µL of lithium citrate buffer (pH 2.2) and filtrated with 0.22 µm filter. 30 µL of each sample were injected onto the Biochrom 30 lithium system according to the manufacturer's protocol. A set of lithium citrate buffers were used as mobile phase for separation during 115 minutes and post column derivatisation with ninhydrin allowed amino acid detection at 570 and 440 nm. The retention time of the peak on the chart allowed the amino acid identification and the area under the peak correlated with the quantity of amino acid.

In order to calculate the consumption/production rate of each metabolite, media samples were collected at the beginning and at the end of the experiment, and frozen until analysed. At the same time points, cell number was determined for normalisation purposes. All the biochemical assays were carried out under exponential growth conditions. All results are expressed in micromol or nanomol of metabolite consumed or produced per hour and per million cells.

3.13. Estimation of metabolite consumption and production rates

Net fluxes per cell of uptake and release of different metabolites (J_{met}) were estimated from the experimentally measured variation of metabolite concentration in medium and the changes in cell number for 24 h. The estimation was performed by assuming exponential growth and constant uptake or release per cell, which corresponds to solve a simple model of cell growth and metabolite consumption/production:

$$\begin{cases} dN_t/dt = N_t \times \mu \\ dM_t/dt = N_t \times J_{met} \end{cases}$$

where N is the cell number, M is the quantity of metabolite and μ is the growth rate. This simple model for flux estimation was verified to be a good assumption for the

experimental period of time and is equivalent to the model used to measure the consumption and release profiles of 219 medium metabolites across the NCI-60 panel of tumour-derived cell lines [140], which include the HCT116 cell line. Our exchange rates were in tune with those measured for the NCI-60 collection.

3.14. Enzyme activities

96 h after siRNA transfection, HCT116 fresh cultures were rinsed with PBS, incubated for 30 min at 4ºC with lysis buffer (20 mM Tris-HCl pH 7.5, 1 mM dithiothreitol, 1 mM EDTA, 0.2% Triton X-100, 0.02% sodium deoxycholate) supplemented with 1% protease inhibitor cocktail, scraped and collected in 1.5 mL eppendorf tubes. Cell lysates were disrupted by sonication using a titanium probe (VibraCell, Sonics & Materials Inc., Newtown, CT, USA) set at Tune 50 and Output 30, and immediately centrifuged at 12,000 g for 20 min at 4ºC. Supernatants were recovered and the protein content was quantified by the bicinchoninic acid (BCA) kit (Pierce Biotechnology, Rockford, IL, USA). Specific enzyme activities were determined by spectrophotometry (COBAS Mira Plus, Horiba ABX) by monitoring NAD(P)H increment or decrement at 340 nm wavelength. Enzymatic activities were normalised by protein content in the supernatant.

3.14.1. Glucose-6-phosphate dehydrogenase (G6PD, EC 1.1.1.49)

G6PD specific activity was determined by incubation of the protein extracts with 0.5 mM $NADP^+$ in 50 mM Tris-HCl (pH 7.6) at 37ºC. Reaction was initiated by the addition of glucose-6-phosphate at a final concentration of 2 mM.

3.14.2. Transketolase (TKT, EC 2.2.1.1)

TKT specific activity was measured by incubation of the protein extracts with 5 mM

$MgCl_2$, 0.2 U mL^{-1} triose phosphate isomerase, 0.2 mM NADH and 0.1 mM thiamine pyrophosphate in 50 mM Tris-HCl (pH 7.6) at 37ºC. The reaction was initiated by the addition of a substrate mixture containing ribose-5-phosphate and xylulose-5-phosphate. The substrate mixture was previously prepared by dissolving 50 mM ribose-5-phosphate in 50 mM Tris-HCl (pH 7.6) in the presence of 0.1 U mL^{-1} ribulose-5-phosphate-3-epimerase and 1.7 mU mL^{-1} phosphoriboisomerase in continuous agitation at 37ºC for 1 h.

3.15. PDH activity

PDH activity was measured with the Pyruvate dehydrogenase (PDH) Enzyme Activity Microplate Assay kit (Abcam, Cambridge, UK) according to the manufacturer's instructions. Briefly, HCT116 cells transfected with CDK4/6 or Control siRNA for 96 h were collected, counted and resuspended in the corresponding volume of PBS to adjust the sample protein concentration to 15 mg mL^{-1}. Then, samples were solubilised with Detergent (9:1), incubated on ice for 10 minutes and centrifuged at 1000 g for 10 minutes at 4ºC. The supernatants were diluted in Assay Buffer to the appropriated concentration within the linear working range for the assay, loaded to each well of the microplate and incubated at room temperature for 3 h. For the measurement, the wells were emptied and 200 µL of Assay Solution were added. The absorbance was measured at 450 nm using a kinetic program with readings every 25 seconds for 30 minutes. PDH activity was normalised by protein content in the supernatant, determined by the bicinchoninic acid (BCA) assay.

3.16. Intracellular glutathione quantification

Total glutathione content was determined by glutathione reductase enzymatic method. Fresh cells were lysed with 5% 5-sulfosalicylic acid solution, vortexed and disrupted by two freezing/thawing cycles in liquid N_2 and 37ºC water bath. For each

sample, 50 µL of cell lysate were separated for subsequent protein quantification by BCA assay. Cell extracts were incubated at 4ºC for 10 min and centrifuged at 10,000 g for 10 min. For glutathione quantification, a working solution containing 15 U mL^{-1} of glutathione reductase and 40 µg mL^{-1} of 5,5'-Dithiobis(2-nitrobenzoic acid) was prepared in assay buffer (100 mM K$_2$HPO$_4$/KH$_2$PO$_4$, 1 mM EDTA, pH 7.0). Glutathione standards were prepared from a 50 mM oxidised glutathione (GSSG) stock solution. Reaction was initiated by mixing 150 µL of working solution with 10 µL of cell extract (diluted 1:5 or 1:10) or 10 µL of GSSG standard (final concentrations from 0 to 12.5 µM). Next, 50 µL of 0.16 mg mL^{-1} NADPH solution were added to the samples and the increase in absorbance was recorded at 340 nm wavelength. Total glutathione concentration was normalised by protein content.

3.17. Intracellular NADP and NADPH quantification

Intracellular nucleotides NADP and NADPH were quantified using the NADP/NADPH Quantification Kit (MAK038, Sigma-Aldrich), following the manufacturer's instructions. Briefly, fresh cells were washed twice with ice-cold PBS, trypsinised and lysed with 200 µL of NADP/NADPH Extraction Buffer by freeze/thawing for 2 cycles of 20 minutes on dry ice followed by 10 minutes at room temperature. Then, samples were vortexed and centrifuged at 13,000 g for 10 min. For the detection of total NADP, 50 µL of supernatant were transferred to the 96-well plate. To detect only NADPH, NADP was first decomposed by incubating 200 µL of the extracted samples at 60ºC for 30 min before transferring 50 µL of sample to the 96-well plate. For NADPH quantification, a standard curve of 0 (blank), 20, 40, 60, 80, and 100 pmol of NADPH per well standards was generated. 100 µL of Master reaction Mix containing 98 µL of NADP cycling buffer and 2 µL of NADP cycling enzyme Mix were added to each well, mixed and incubated for 5 min at room temperature (to convert NADP to NADPH). Then, 10 µL of NADPH developer were added to each well and samples were incubated for 1 to 4 h at room temperature. The absorbance was measured at 450 nm. NADP and NADPH calculated pmol were normalised by cell number.

3.18. Determination of Intracellular Reactive Oxygen Species (ROS) levels

A549 cells were grown on 6-well plates to 70% confluence, washed once with warm PBS, and incubated with 5 μM 2'-7'-dichlorodihydrofluorescein diacetate (H$_2$DCFDA, Invitrogen) in PBS supplemented with 5.5 mM glucose. After 30 min at 37ºC, PBS was replaced with complete culture medium and incubated for another 50 min at 37ºC. Finally, cells were trypsinised and resuspended thoroughly with 0.4 mL of PBS, H$_2$DCFDA (50 μM) and PI (20 μg mL^{-1}). Intracellular internalised probe reacts with ROS and emits fluorescence when excited at 492 nm. Emitted fluorescence was recorded by flow cytometry at 520 nm using an Epics XL flow cytometer (Coulter Corporation, Hialeah, FL, USA). Data of DCF fluorescence concentrations from 1×10^4 PI negative cells were collected and analysed using Multicycle program (Phoenix Flow Systems, San Diego, CA, USA).

3.19. A549 transient transfection with FOXO3a-GFP reporter plasmid

A549 cells were grown on the surface of cover slips (Menzel-Glaser, Braunschweig, Germany) placed in 6-well plates. When confluence reached 80%, cells were transiently transfected with a previously incubated (30 min) mix containing 2 μg of the green fluorescent protein (GFP)-FOXO3a reporter plasmid and 2 μL of X-tremeGENE HP reagent (Roche) in 200 μL medium.

3.20. FOXO translocation assay

24 hours after seeding U2foxRELOC cells in 6-well plates containing cover slips or 21 hours after transfection in the case of A549 cells, media were replaced with media containing MSA, sodium selenite, LY294002 20 μM (positive control) or vehicle (negative control). After 6 hours of incubation, media were replaced with fresh media containing 1 μM CellTracker Red (Invitrogen) and incubated for 10 minutes. Then,

media were removed and the cover slips containing the cells were washed 3×5 min with PBS, fixed with paraformaldehyde for 15 minutes and washed again 3×5 min with PBS containing 20 mM glycine. The cover slips were then mounted on slides using 20 µL ProLong Gold (Invitrogen). After 16 h, the slides were visualised in a TCS SPE Leica confocal microscope (Leica Microsystems, Wetzlar, Germany) and the intensity of the GFP fluorescence in nuclei and cytoplasm was measured from a minimum of 50 random cells per condition using ImageJ software (public domain National Institutes of Health, USA, http://rsbweb.nih.gov/ij/).

3.21. Time course relocalisation assay and data analysis

The U2foxRELOC-based assay was performed as described previously [468]. All liquid handling for compound treatment, washing, fixing and staining steps was performed by a robotic workstation [469]. Briefly, 1×10^5 cells mL^{-1} were seeded in black-walled clear-bottomed 96-well microplates (BD Biosciences, San Jose, CA, USA) in a final volume of 200 µL per well using a multidrop automatic dispenser. After 12 h, cells were treated with 5 µM MSA for 1.5, 3, 6, 11 or 24 hours and 10 µM LY294002 (positive control) and vehicle (negative control) for 1.5 hours. Cells were washed with PBS, fixed in paraformaldehyde, washed again and stained with DAPI for 20 min at room temperature to define the nucleus. Assay plates were read on the BD Pathway 855 Bioimager (BD Biosciences) equipped with a 488/10 nm EGFP excitation filter, a 380/10 nm DAPI excitation filter, a 515 LP nm EGFP emission filter and a 435 LP nm DAPI emission filter. Images were acquired in the DAPI and GFP channels of each well by using 20Q dry objective. Data was exported from the BD Pathway Bioimager as text files and imported into the data analysis software BD Image Data Explorer (BD Biosciences) for processing. Cells presenting nuclear accumulation of the fluorescent reporter above 60% of the signal obtained from wells treated with 10 µM LY294002 were considered as hits.

3.22. Stable shRNA cell line generation

U2OS and HEK293 stable FOXO3a knockdown cell lines were generated by Effectene (Qiagen, Hilden, Germany) reagent-mediated transfection with three different FOXO3a shRNA constructs originated from the Netherlands Cancer Institute (NKI) shRNA library [470]. FOXO3a shRNA sequences FOXO3a KD#1 (GCAGGCCTCATCTCAGAGCTCTCTTGAA GCTCTGAGATGAGGCCTGC), FOXO3a KD#2 (CTGCGACGGCTGACTGAAATCTCTTGAATTTC AGTCAGCAGTCGCAG) and FOXO3a KD#3 (CCTGATGGGGGAAANANCTCTCTTGAANCTC TGANATGANGCCTGC) were cloned into pRetroSuper vector (NKI, Amsterdam, Netherlands). Empty pRetroSuper vector was used for control cells (Ctrl). Cells were selected in complete medium containing 1 μg mL^{-1} puromycin.

3.23. Immunohistochemical staining

Colorectal tumours were dissected immediately after surgical resection by a pathologist, snap-frozen and stored in liquid nitrogen. Colorectal cancer sections were obtained by vibrotom cuts, desiccated to prevent degradation and kept at ambient laboratory conditions. Tissue specimens (2-5 μm) from 62 samples were placed on slides and fixed with paraformaldehyde. To hydrate the samples and retrieve the antigens, the slides were rinsed in decreasing concentrations of ethanol (3 x 5 min) and heated to 65ºC in 10 mM sodium citrate buffer (pH 6.0) for 5 minutes. After rinsing with Milli-Q water, endogenous peroxidases were inhibited by 3% hydrogen peroxide incubation for 10 minutes. Then, the slides were rinsed in phosphate buffered saline (PBS) and incubated with 3% w/v bovine serum albumin (BSA) in PBS for 15 min to prevent unspecific staining. Slides were incubated at room temperature with a mouse monoclonal anti-GAPDH antibody (sc-47724, Santa Cruz Biotechnology, Santa Cruz, CA, USA) at a concentration of 4 μg mL^{-1} for 1 hour in a humidified chamber, followed by PBS washes (3 x 5 min) and by incubation with secondary antibody (Biotinylated Link, LSAB+-kit, DakoCytomation, Hamburg, Germany) for 25 minutes. Negative controls were incubated with 3% BSA instead of primary antibody. After rinsing with PBS (3 x 5 min), samples were treated with streptavidin-peroxidase (Streptavidin-HRP, LSAB+-kit,

DakoCytomation, Hamburg, Germany) for 25 minutes at room temperature and stained with 3-39-diaminobenzidine (DAB+Chromogen, Dako- Cytomation, Hamburg, Germany) for 20 min. Cover slips were mounted on slides using gelatine. After 24 h, slides were viewed under a LEICA DM 4000 B microscope (Leica Microsystems, Germany) and a monochromatic IEEE-1394 CFW-1312M camera (Scion Corporation, Frederik, MD, USA). GAPDH expression was quantified using ImageJ software (NIH Imaging, USA), measuring relative intensity per area and interpolating into a calibration curve plotted using a grey scale. For each sample, 4 to 15 pictures from different areas were quantified. Samples were processed in groups of 8 with representation of all four stages of tumour progression each time. Values are presented as relative values in arbitrary units (a.u.). This procedure of staining quantification requires 8-bit monochromatic images and quantifies grey intensity within a calibration scale [471, 472] giving a more objective protein expression comparison between samples than classifications by arbitrary scores.

3.24. Total protein extraction from formalin-fixed paraffin-embedded tissues

Extraction of proteins from formalin-fixed paraffin-embedded tissues was performed as described previously [473]. Briefly, slides were deparaffinised by incubation at room temperature in xylene (4 x 2 min), rehydrated with a graded series of ethanol (3 x 5 min), briefly air-dried in a fume hood and weighed. Then, samples were incubated with protein extraction buffer (300 mM Tris–HCl and 2% SDS, pH 8.0) at 90ºC for 75 minutes, sonicated and centrifuged at 16,000 g for 20 min at 4ºC.

3.25. Total protein extraction from cell cultures

5×10^4 HCT116 cells per well were plated in 6-well plates and treated with PD0332991 or vehicle, or transfected with siRNA as detailed in Section 3.4., for 96 h. For A549 cells, 3×10^5 cells per well were seeded in 6-well plates and treated the next day with

MSA, sodium selenite, LY294002 or vehicle at the specified concentrations for 6 and 24 hours. At the end of the treatment, cells were washed twice with ice-cold PBS and incubated for 30 min on ice with RIPA buffer containing 50 mM Tris (pH 8.0), 150 mM sodium chloride, 1% Triton X-100, 0.5% sodium deoxycholate, 0.1% sodium dodecyl sulphate (SDS), 1% protease inhibitor cocktail and 1% phosphatase inhibitor cocktail (Thermo Fisher Scientific Inc.). Cells were scraped, sonicated and centrifuged at 16,000 g for 20 min at 4ºC. Supernatants were recovered and the protein content was quantified by the BCA kit (Pierce Biotechnology).

3.26. Cytosolic and nuclear protein extracts from cell cultures

3×10^5 A549 cells per well were seeded in 6-well plates and treated the next day with MSA, sodium selenite, LY294002 or vehicle at the specified concentrations for 6 h. Then, cells were washed twice with ice-cold PBS and incubated for 10 min on ice with hypotonic buffer containing 20 mM HEPES (pH 7.6), 10 mM NaCl, 1.5 mM $MgCl_2$, 0.2 mM EDTA, 20% (v/v) glycerol, 0.1% (v/v) Triton X-100, 1% protease inhibitor cocktail and 1% phosphatase inhibitor cocktail. Cells were scraped and pipetted into cooled eppendorf tubes and then centrifuged at 1000 rpm in a swinging-bucket centrifuge at 4ºC. Supernatant was the cytoplasmic extract and the pellet contained the nuclei. To extract the nuclear proteins, the pellet was resuspended in five times its volume with hypertonic buffer (hypotonic buffer adding 500 mM NaCl), rocked for 1 h at 4ºC and spinned at maximum speed at 4ºC for 5 min. The nuclear extract was the supernatant. Both cytosolic and nuclear extracts were assayed for protein concentration using the BCA kit.

3.27. Western blot analysis

An equal volume of protein was size-separated by electrophoresis on SDS-polyacrylamide gels and electroblotted onto polyvinylidene fluoride transfer membranes (PVDF) (Bio-Rad Laboratories, Hercules, CA, USA). After 1 h of blocking at

room temperature with 5% skim milk in PBS 0.1% Tween, blots were incubated with the specific primary antibodies overnight at 4ºC. Then, membranes were treated with the appropriate secondary antibody for 1 h at room temperature. All blots were treated with Immobilon ECL Western Blotting Detection Kit Reagent (EMD Millipore, Billerica, MA, USA) and developed after exposure to an autoradiography film (VWR International, Radnor, PA, USA). The primary antibodies used were Phospho-Akt (#9271), Akt (#9272), Phospho-mTOR (#5536), procaspase 3 (#9662), HK2 (#2867) and PDHK1 (#3820) from Cell Signaling (Beverly, MA, USA); PDH (ab110330), GLS1 (ab93434), MYC (ab32072), P-MYC (ab106952), PHD2 (ab4561) and ME2 (ab139686) from Abcam; P-PDH (ABS204) from Millipore (EMD Millipore); GAC (19958-1-AP) and KGA (20170-1-AP) from Proteintech (Chicago, IL, USA); FOXO3a (#06-951) from Upstate (EMD Millipore); Phospho-FOXO3a (sc-101683), Phospho-JNK (sc-6254), FOXM1 (sc-500), Bax (sc-493), CDK4 (sc-260), CDK6 (sc-177), HIF1α (sc-13515), EPAS-1 (HIF2α, sc-28706), KRAS (sc-30), Ub (sc-8017), ERK2 (sc-154), Lamin B (sc-6217) and GAPDH (sc-47724) from Santa Cruz Biotechnology; GDH (GTX105765) from Tebu-Bio (Le-Perray-en-Yvelines, France); Phospho-PRAS40 (#44-1100) from BioSource International (Camarillo, CA, USA); PARP (#556493) and cytochrome c (#556433) from BD Pharmingen (BD Biosciences); p27^{Kip1} (#610242) from BD Transduction Laboratories (BD Biosciences) and β-actin (#69100) form MP Biomedicals (Santa Ana, CA, USA). The secondary antibodies used were anti-mouse (PO260) from Dako (Glostrup, Denmark), anti-rabbit (NA934V) from Amersham Biosciences (GE Healthcare, Little Chalfont, UK) and anti-goat (sc-2020) from Santa Cruz Biotechnology.

3.28. Immunoprecipitation

Whole cell lysates were isolated as described in Section 3.25. To reduce non-specific binding to the Protein A agarose beads (#9863, Cell Signaling), cell lysates were pre-cleared adding Protein A agarose beads (20 µL of 50% bead slurry) to 200 µL cell lysate and incubating on a rotator at 4ºC for 1 h. Then, samples were spinned for 10 minutes at 4ºC. Supernatant protein concentration was measured using the BCA kit. For each sample, 200 µg of protein were incubated with 1 µg of anti-c-Myc antibody (ab32072,

Abcam) with gentle rocking overnight at 4ºC. Protein immunocomplexes were then incubated with 20 µL of 50% bead slurry protein A agarose beads with gentle rocking for 3 h at 4ºC, collected by centrifugation (30 seconds at 4ºC) and washed five times in 500 µL of RIPA buffer containing 1% protease and 1% phosphatase inhibitors. The pellet was resuspended with 20 µL 3X SDS loading buffer, vortexed and centrifuged for 30 seconds. Finally, samples were heated to 100ºC for 5 min, centrifuged for 1 min at 14,000 g and loaded on a SDS-PAGE gel for Western blot analysis.

3.29. RNA extraction, quantification, retrotranscription and Quantitative Reverse Transcription-Polymerase Chain Reaction (qRT-PCR)

RNA was isolated from frozen plates using Trizol reagent (Invitrogen) following the manufacturer's instructions. Briefly, Trizol cell homogenates were mixed with chloroform and centrifuged, obtaining an aqueous phase and an organic phase. In order to precipitate RNA, cold isopropanol was added in the aqueous phase and centrifuged at 12,000 g for 15 min at 4ºC. RNA was purified by several cold 75% ethanol washes and finally resuspended in RNAse free water. RNA was quantified using a Nanodrop (ND 1000 V3.1.0, Thermo Fisher Scientific Inc.). Reverse transcription was carried out with 1 µg RNA at 37ºC for 1 h with the following reagents: Buffer 5x (Invitrogen), dithiothreitol (DTT) 0.1 M (Invitrogen), Random Hexamers (Roche), RNAsin 40 U µL^{-1} (Promega, Fitchburg, WI, USA), dNTPs 40 mM (Bioline, London, UK), M-MLV-RT 200 U µL^{-1} (Invitrogen). Gene expression analysis was performed on an Applied Biosystems 7500 Real-Time PCR System according to the manufacturer's protocol, using Taqman gene specific sequences for *CDK4* (Hs00262861_m1), *CDK6* (Hs01026371_m1), *GLS* (Hs01014019_m1), *SLC7A6* (Hs00938056_m1), *SLC7A5* (Hs00185826_m1), *MAX* (Hs04332980_m1), *PDHK1* (Hs01561850_m1), *PDHK3* (Hs00178440_m1), *ODC1* (Hs00159739_m1), *SAT1* (Hs00161511_m1), *SLC25A13* (Hs01573628_m1), *CCND1* (Hs00765553_m1), *PFKFB4* (Hs00190096_m1), *HK2* (Hs00606086_m1), *ENO2* (Hs00157360_m1), *SLC2A3* (Hs00359840_m1), *SLC3A2* (Hs00374243_m1), *PIK3R3* (Hs00177524_m1), *CDKN1B* (Hs01597588_m1), *GSK3B* (Hs01047719_m1), *EGLN1* (Hs00254392_m1), *FOXO1* (Hs01054576_m1), *FOXO3a*

(Hs00818121_m1), *SLC2A6* (Hs01115485_m1) and *IDH2* (Hs00158033_m1) (Applied Biosystems, Thermo Fisher Scientific Inc.). Reactions were performed in 20 µL volume, using 9 µL of the cDNA mixture and 11 µL of the specific Taqman in Master Mix (Applied Biosystems). Real-Time PCR was conducted according to the following parameters: an initial incubation at 50ºC for 2 min, a denaturalisation at 95ºC for 10 min, followed by 40 cycles at 95ºC and 60ºC for 15 s and 1 min, respectively. Expression was quantified by ΔΔCt method using Cyclophilin A (*PPIA*: Hs99999904_m1, Applied Biosystems) as reference gene.

3.30. Transcriptomic analysis

3.30.1. Microarray analysis (Affymetrix U133 Plus 2.0 array)

Total RNA was isolated from frozen plates using Trizol reagent (Invitrogen) and the RNeasy Mini Kit (Qiagen, Hilden, Germany) according to the manufacturer's protocols. RNA integrity was tested using lab-on-a-chip technology on the BioAnalyzer 2100 (Agilent, Palo Alto, CA, USA). RNA was used to produce biotinylated cRNA that was hybridised to Affymetrix GeneChip® human genome U133 Plus 2.0 arrays following the manufacturer's instructions (Affymetrix Inc., Santa Clara, CA, USA). The Human Genome U133 Plus 2.0 Array chip contains over 55,000 probe sets representing over 47,000 transcripts derived from approximately 39,500 human genes. Comparative transcriptomic analyses between CDK4/6 knockdown and control cells were performed on independent triplicate samples. Raw data were exported to multiple .CEL files.

".CEL" files were uploaded to the R-Project Bioconductor statistical tools package and standardised using the Robust Multi-array Average (RMA) method [474], which consists in three steps: background correction, normalisation to remove systematic errors and biases, and summarisation combining the multiple probe intensities from a probe set. We used the simpleaffy [475] package to compute the RMA expression values (signal intensities (SI) on the base 2 logarithm scale (log_2SI) representing gene expression levels) and the differential gene expression was assessed using the limma [476] package from Bioconductor. Multiple testing adjustment of p-value was

conducted according to Benjamini et al. [477]. As for concentrations and activities of the metabolic profile, a fold change (FC) value is provided based on this normalisation criterion. Fold changes quantifying the differential expression for a probe set were defined as the ratio of normalised intensity values in CDK4/6-inhibited cells relative to normalised intensity values in control cells. FC were calculated by the following formula: if expression was upregulated for CDK4/6 inhibition, $2^{\wedge}(mean\ (CDK4/6$ knockdown replicates in $\log_2 SI))/(2^{\wedge}mean\ (Control\ replicates\ in\ \log_2 SI)$; if expression was downregulated for CDK4/6 inhibition, $-1 \times 2^{\wedge}(mean\ (Control\ replicates\ in\ \log_2 SI))/(2^{\wedge}mean\ (CDK4/6\ knockdown\ replicates\ in\ \log_2 SI)$.

3.30.2. Gene association studies

Association studies were performed looking for the evidence of metabolic mechanisms altered under the inhibition of CDK4 and CDK6 by comparing our genes differentially expressed with gene expression signatures (gene sets) associated with cellular and biological components or functions, or with perturbations linked to metabolism, cancer and/or cell cycle. We applied one method, Gene Set Enrichment Analysis (GSEA) [478], which follows a strategy that do not rely on any arbitrarily predefined threshold to select the set of genes differentially expressed. Instead of using arbitrary cut-offs, the significance of the association is based on aggregating weak evidences. This method was applied over data sets created by merging signatures downloaded from the Molecular Signatures Database (MSigDB v5.0) [478].

3.30.3. Gene Set Enrichment Analysis (GSEA)

GSEA is a computational method that determines whether an a priori defined set of genes shows statistically significant, concordant differences between two phenotypes (CDK4/6 knockdown cells and control cells in our case) [478]. Looking for associations between our gene expression experiments and the gene expression signatures, a Java implementation of the GSEA method and a collection of gene sets provided by the

Broad Institute of MIT and Harvard (http://www.broadinstitute.org/gsea/index.jsp) were used. GSEA was applied to analyse the computed RMA expression values over data sets of signatures listed in Table 3.1. These data sets were downloaded from the Molecular Signatures Database (MSigDB v5.0), which is a database composed of curated gene sets, grouped in various collections and based on high-throughput experiments as well as expert knowledge from literature or databases. A number of gene sets come in pairs: i.e. there are reciprocal gene sets of up (_UP) and down (_DN) regulated genes for a given condition.

Table 3.1. Data sets from the Molecular Signatures Database (MSigDB v5.0) of the Broad Institute of MIT and Harvard (http://www.broadinstitute.org/gsea/index.jsp).

Hallmark gene sets	Coherently expressed signatures from the aggregation of many MSigDB gene sets to represent well-defined biological states or processes. This collection is envisioned as the starting point for exploration of the MSigDB resource and GSEA.
Curated gene sets	From online pathway databases, publications in PubMed and knowledge of domain experts. They include gene sets from *chemical and genetic perturbations*, *canonical pathways*, *BioCarta*, *KEGG* and *Reactome* collections.
GO gene sets	Genes annotated by the same gene ontology (GO) terms. They include gene sets from *GO biological process*, *GO cellular component* and *GO molecular function* collections.
Oncogenic signatures	Defined directly from microarray gene expression data from cancer gene perturbations. They include gene sets from *oncogenic signatures* collection.

3.30.4. Procedure and keys to interpret GSEA enrichment plots

GSEA uses a Kolmogorov-Smirnov style statistic. The application of the GSEA can be followed in the GSEA enrichment plot examples illustrated in Figure 3.1, while the selected options for the analysis are listed in Table 3.2. First, signal to noise ratios were computed for each gene of our RMA expression data from the two phenotypes

analysed: CDK4/6 knockdown cells (indicated as CDK) and control cells (indicated as CONTROL). Then, the resulting list of genes was sorted from most positive to most negative (ranked list metric at the bottom part of GSEA enrichment plots). Genes that appear towards the left (top) of the list are more expressed in the CDK4/6 knockdown phenotype, while genes that appear towards the right (bottom) of the list are more expressed in the control phenotype. Next, GSEA walks down the ranked gene list and computes a running sum. Each time a gene in the gene set is hit (vertical bars), the sum is increased, while each time the gene hit is not in the gene set, the sum is decreased. The resulting enrichment score profile (green line) records the cumulative score. The score at the peak of the plot is the enrichment score (ES) for the gene set.
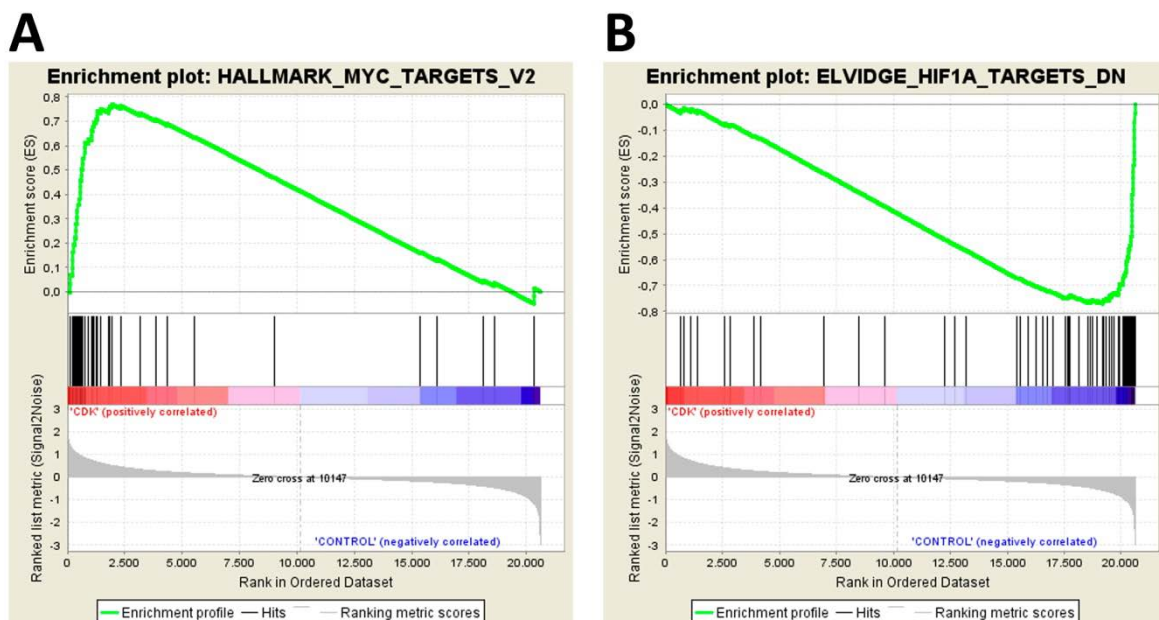
Figure 3.1. Enrichment plot examples. A. Enrichment plot for a positive ES. B. Enrichment plot for a negative ES. The top portion of the plot shows the running ES for the gene set as the analysis walks down the ranked list. The score at the peak of the plot (the score furthest from 0.0) is the ES for the gene set. Gene sets with a distinct peak at the beginning (**A**) or end (**B**) of the ranked list are generally the most interesting. The middle portion of the plot shows where the members of the gene set appear in the ranked list of genes. The leading edge subset of a gene set is the subset of members that contribute most to the ES. For a positive ES (**A**), the leading edge subset is the set of members that appear in the ranked list prior to the peak score. For a negative ES, it is the set of members that appear subsequent to the peak score. The bottom portion of the plot shows the value of the gene ranking metric which measures a gene's correlation with a phenotype. A positive value indicates correlation with the first phenotype (CDK4/6 inhibition) and a negative value indicates correlation with the second phenotype (control).

Table 3.2. Selected options for the Gene Set Enrichment Analysis.

Collapse data set to symbols	True	All probe set identifiers that map to a particular gene were summarised (collapsed) into a single expression vector associated with the corresponding HUGO gene symbol. The data set had 54,675 native features, after collapsing features into gene symbols, there were 20,606 genes.
Permutation type	Gene_set	As recommended when there are fewer than seven samples in any phenotype.
Number of permutations	1000	As recommended by the GSEA team.
Enrichment statistic	Weighted	
Metric for ranking genes	Signal2Noise	Signal to noise ratios (mean divided by variance).
Gene list sorting mode	Real	
Gene list ordering mode	Descending	
Max size: exclude larger sets	500	
Min size: exclude smaller sets	15	

3.30.5. GSEA statistics

In order to determine the significance of the ES, GSEA creates a number of permutations and recalculates the ES for each permutation, and a nominal p-value (NOM p-value) is given. According to the default settings, the number of phenotype permutations involved in the nominal p-value calculation was 1000 (Table 3.2). A normalised enrichment score (NES) was used to rank the enriched gene sets in each phenotype (control and CDK4/6 knockdown). A false discovery rate q-value (FDR q-value) was also computed in order to estimate the probability that a gene set with a given NES was representing a false positive finding. Finally, a family wise-error rate p value was computed in order to estimate the probability that the normalised

enrichment score represents a false positive finding. Gene sets with a FDR q value ≤ 5% were considered significant. Table 3.3 describes the GSEA statistics.

Table 3.3. GSEA statistics definitions.

SIZE	Number of genes in the gene set after filtering out those genes not in the expression data set.
ES	Enrichment score for the gene set; that is, the degree to which this gene set is overrepresented at the top or bottom of the ranked list of genes in the expression data set.
NES	Normalised enrichment score: Enrichment score for the gene set after it has been normalised across the analysed gene sets. NES is used to rank the enriched pathways in each phenotype.
NOM p-value	Nominal p value; that is, the statistical significance of the enrichment score. The nominal p value is not adjusted for gene set size or multiple hypothesis testing; therefore, it is of limited use in comparing gene sets.
FDR q-value	False discovery rate: Estimated probability that the normalised enrichment score represents a false positive finding. The FDR is adjusted for gene set size and multiple hypotheses testing. A FDR cutoff of 5% is selected, as suggested for analyses with small number of samples and use of gene-set permutation.
FWER p-value	Family wise-error rate: A more conservatively estimated probability that the normalised enrichment score represents a false positive finding. Because the goal of GSEA is to generate hypotheses, the GSEA team recommends focusing on the FDR statistic.

3.30.6. Selection of differentially expressed genes

Differentially expressed genes were identified from normalised RMA expression data obtained from the Affymetrix GeneChip arrays comparing CDK4/6 knockdown and control cells. They were selected among those associated to cell cycle machinery or those associated to metabolism. As a preliminary criteria the selection was restricted to those with a |FC| > 1.5 ($\log_2$ FC > 0.585), and for each selected gene, the probe-sets corresponded to those with a p-adjusted value lower than 0.01 and with signal

intensities above 100 ($\geq \log_2 100$). However, exceptions to these criteria were applied. Genes with a differential expression and a lower FC were included when it was estimated that it could help to provide a clearer picture of the effects in a family of genes. Also, some probe-sets corresponding to fundamental genes encoding regulatory proteins or metabolic enzymes presented signal intensities below 100.

3.31. ^{13}C-tracer-based metabolomics

In order to obtain a precise pattern of mass isotopomer enrichments of the central carbon metabolism, CDK4/6 knockdown and control HCT116 cells were incubated in the presence of either 10 mM [1,2-^{13}C$_2$]-glucose or 2 mM [U-^{13}C$_5$]-glutamine under normoxic or hypoxic conditions for 24 h. After the 24 h incubation, media and cell cultured plates were collected and stored at -20ºC and -80ºC, respectively. Media samples were used for extracellular metabolite measurements as detailed at Section 3.12, and for determination of mass isotopomer distributions of glucose, lactate, glutamate, alanine, glycine, aspartate/asparagine, methionine, proline and serine. Cell cultured plates were used for the analysis of mass isotopomer distributions of glycogen, RNA ribose, fatty acids and metabolic intermediates including pyruvate, lactate, alanine, aspartate, glutamate and tricarboxylic acid (TCA) cycle intermediates.

Analyses of ^{13}C-labelled extracellular and intracellular metabolites for mass isotopomer distribution were conducted by gas chromatography coupled to mass spectrometry (GC/MS) using an Agilent 7890A GC (Agilent Technologies, Santa Clara, CA, USA) equipped with a HP-5 capillary column connected to an Agilent 5975C MS (Agilent Technologies). Fatty acids GC/MS analysis was performed employing a GCMS-QP 2012 Shimadzu (Shimadzu Corporation, Kyoto, Japan) equipped with a BPX70 column (SGE Analytical Science, Melbourne, Australia). In all cases, 1 μL of sample was injected using helium as a carrier gas at a flow rate of 1 mL min^{-1}.

Supplementary data for mass isotopomer distribution of the analysed metabolites and the conditions of each ^{13}C-tracer experiment are shown in Appendix I.

Metabolite isolation and derivatisation methods as well as GC/MS detection conditions are described in detail below and summarised in Table 3.4.

3.31.1. Glucose

Glucose was isolated from cell culture media using a tandem set of Dowex-1X8/Dowex-50WX8 ion-exchange columns, with water elution. Then, water was evaporated to dryness under airflow overnight. Isolated glucose was derivatised in two steps; incubation with 100 µL of 2% (v/v) hydroxylamine hydrochloride in pyridine for 30 min at 100ºC and then with 75 µL of acetic anhydride for 60 min at 100ºC. Excess of reagent and solvent was eliminated by evaporation with N_2 flow, and glucose derivative was dissolved in ethyl acetate for GC/MS analysis under chemical ionisation mode. Samples were injected at 250ºC and oven temperature was programmed as follows: 230ºC for 2min, then increased at 10ºC min^{-1} to 260ºC, followed by a 25ºC min^{-1} ramp to 270ºC and hold for 2 min. Detector was run in SIM, recording ion abundance of C1-C6 molecule in the range of 327-336 m/z. Retention time was 3.7 min.

3.31.2. Lactate

For each sample, 1 mL of medium was acidified with hydrochloric acid (HCl) and lactic acid was extracted with 1 mL of ethyl acetate and evaporated to dryness under N_2 flow. Lactate was derivatised to its lactic acid n-propylamide-heptafluorobutyric ester by incubation at 75ºC for 1 h with 200 µL of 2,2-dimethoxypropane and 50 µL of 0.5 N methanolic HCl. 60 µL of n-propylamine were added to the reaction mixture and heated at 100ºC for 1 h. Samples were dried under a stream of N_2. Derivative product was extracted with 1 mL of ethyl acetate and filtered through a glass wool packed Pasteur pipette. Samples were dried under N_2 flow. Then, precipitates were resuspended with 200 µL of dichloromethane and 15 µL of heptafluorobutyric anhydride at room temperature for 10 min. Samples were dried under N_2 flow and

resuspended in dichloromethane for GC/MS analysis under chemical ionisation mode. Samples were injected at 200ºC and oven temperature was programmed as follows: 100ºC for 3 min, then increased at 20ºC min^{-1} to 160ºC and hold for 2 min. Detector was run in SIM recording ion abundance of C1-C3 molecule in the range of 327-332 m/z. Retention time was 5.4 min.

3.31.3. Glutamate

Media were passed through Dowex-50WX8 columns and amino acids were eluted with 10 mL of 2 N ammonium hydroxide. The eluates were left to dry under airflow overnight and then resuspended with 5 mL of Milli-Q water. To further separate glutamate from glutamine, the solutions were passed through Dowex-1X8 columns. Columns were washed with water and glutamate was collected with 10 mL of 0.5 N acetic acid. The acid solutions were evaporated to dryness under airflow overnight. Glutamate was converted to its n-trifluoroacetyl-n-butyl ester by incubation with 200 µL of butanolic HCl at 100ºC for 1 h. Then, samples were dried under a stream of N$_2$ and 100 µL of dichloromethane and 25 µL of trifluoroacetic anhydride were added. After 20 min, samples were dried under a N$_2$ flow and the derivative was dissolved in dichloromethane for GC/MS analysis under electron impact mode, yielding C2-C4 and C2-C5 glutamate fragments. Samples were injected at 250ºC and oven temperature was programmed as follows: 215ºC for 2 min, then increased at 9ºC min^{-1} to 224ºC and at 3ºC min^{-1} to 233ºC and hold for 2 min. Detector was run in SIM mode recording ion abundance in the range of 151-157 m/z for C2-C4 and 197-203 m/z for C2-C5. Retention time was 3.9 min.

3.31.4. Alanine, glycine, aspartate/asparagine, glutamate/glutamine, methionine, proline and serine

Media were passed through Dowex-50WX8 columns and amino acids were eluted with 10 mL of 2 N ammonium hydroxide. The solutions were evaporated to dryness under

airflow overnight. Amino acids were converted to their n-trifluoroacetyl-n-butyl ester by incubation with 200 μL of butanolic HCl at 100ºC for 1 h. The excess of reagent was removed under a stream of N_2 and the precipitate was dissolved in 100 μL of dichloromethane and 25 μL of trifluoroacetic anhydride at room temperature for 20 min. Then, samples were dried under a stream of N_2 and dissolved in dichloromethane for GC/MS analysis under chemical ionisation mode. Samples were injected at 250ºC and oven temperature was programmed as follows: 110ºC for 1 min, then increased at 10ºC min^{-1} to 125ºC, 5ºC min^{-1} to 153ºC, 50ºC min^{-1} to 200ºC, 5ºC min^{-1} to 216ºC and hold for 1 min, and a final 25ºC min^{-1} ramp to 250ºC and hold for 2 min. Detector was run in SIM mode recording ion abundance in the range of 241-246 m/z for C1-C3 alanine (Retention time, RT: 5.3 min), 341-348 m/z for C1-C4 aspartate and asparagine (RT: 11.5 min), 383-390 m/z for C1-C5 glutamate/glutamine (RT: 12.8 min); 227-231 m/z for C1-C2 glycine (RT: 5.7 min), 329-336 m/z for C1-C4SC5 methionine (RT: 10.8 min), 253-259 for C1-C4 methionine (RT: 10.8 min), 295-302 for C1-C5 proline (RT: 9.6 min) and 353-358 for C1-C3 serine (RT: 6.6 min).

3.31.5. Ribose

Ribose from RNA was isolated from the aqueous phase after addition of Trizol reagent to cell cultured plates as described in Section 3.29. Purified RNA was hydrolysed in 2 mL of 2 N HCl at 100ºC for 2 h and the solvent was evaporated to dryness under airflow overnight. RNA ribose was converted to its ribose aldonitrile acetate derivative after treatment at 100ºC for 30 min with 100 μL of hydroxylamine hydrochloride in pyridine (2% v/v) and then 75 μL of acetic anhydride at 100ºC for 1 h. Excess reagent and solvent were removed by evaporation with N_2 flow, and the derivatised ribose was resuspended in ethyl acetate just before GC/MS analysis under chemical ionisation mode. Samples were injected at 250ºC and oven temperature was programmed as follows: 150ºC for 1 min, then increased at 15ºC min^{-1} to 275ºC and finally to 300ºC at 40ºC min^{-1}. Detection was run in SIM recording ion abundance of C1-C5 molecule in the range of 256-261 m/z. Retention time was 5.3 min.

3.31.6. Fatty acids: palmitate and sterate

Fatty acids from cell cultured plates were hydrolysed from the inter- and organic phase obtained from Trizol extract as described in Section 3.29, by adding 500 µL of 100% ethanol and 300 µL of 30% potassium hydroxide. Samples were then incubated at 70ºC overnight, after which free fatty acids were extracted twice with petroleum ether, followed by evaporation to dryness under N_2 flow. Fatty acids were derivatised to its methyl ester derivative by adding 500 µL of methanolic HCl, incubating at 70ºC for 1 h and evaporating under N_2 flow. Fatty acids derivatives were dissolved in hexane for GC/MS analysis under chemical ionisation mode. Samples were injected at 250ºC and oven temperature was programmed as follows: 120ºC for 1 min, then increased at 5ºC min^{-1} to 220ºC and held for 1 min. Detector was run in SIM recording ion abundance in the range of 269-278 m/z for palmitate and of 297-306 m/z for stearate. Retention times were 9.2 min for palmitate and 11.85 min for stearate.

3.31.7. Intracellular metabolic intermediates

Polar intracellular metabolites were extracted from liquid nitrogen-frozen cell cultured plates with the addition of 100% methanol and milli-Q H_2O (1:1) and scraping on ice. Chloroform was added to cell lysates and tubes were placed in a shaker for vigorous agitation at 4ºC for 30 min. Subsequently, samples were centrifuged at 4000 rpm for 15 min and the upper aqueous phase was separated and evaporated to dryness under airflow at room temperature. TCA cycle intermediates and intracellular metabolites were derivatised by adding 50 µL of 2% (v/v) methoxyamine hydrochloride in pyridine to samples and shaking vigorously at 37ºC for 90 min. Next, 30 µL of N-methyl-N-(tert-butyldimethylsilyl)trifluoroacetamide (MBTSTFA) + 1% tert-butyldimetheylchlorosilane (TBDMCS) were added and samples were incubated for 1 h at 55ºC before GC/MS analysis under electron impact mode. Samples were injected at 270ºC and oven temperature was programmed as follows: 100ºC for 3 min, then increased to 165ºC at 10ºC min^{-1}, then at 2.5ºC min^{-1} to 225ºC, at 25ºC min^{-1} to 265ºC and finally at 7.5ºC min^{-1} to 300ºC. Table 3.4 shows the metabolites and m/z ranges monitored by SIM.

Table 3.4. Analysed ^{13}C-labelled extracellular and intracellular metabolites.

ID	Metabolite	Fragment	Source	Extraction	Derivatisation	Gas chromatography Instrument	Mass spectrometry Instrument	Ion source	Ret. time	m/z range
Palm-270	Palmitate	C1 -C10	Cell pellet	Organic extraction of saponified pellet	metil ester	Column model: BPX-70 (30m lenght; 0,25 mm i.d.; 0,25 microm thickness; 70% CyanopropylPolysil phenylene	Shimadzu GCMS-QP 2010 Mass analyser: MS quadrupole	Electron impact ionisation	9.2	269 – 278
Stear-298	Stearate	C1-C10						Electron impact ionisation	11.9	297 – 307
Rib-256	Ribose	C1-C5		Trizol extraction and acid hydrolysis	aldonitrile acetate (acetylation)			Chemical ionisation **Scan polarity:** positive	5.3	255 – 262
Glyc-328	Glycogen (glucose)	C1-C6		Amylase digestion and ion-exchange columns-based extraction, aqueous elution					3.7	327 – 334
Glc-328	Glucose	C1-C6	Medium	Ion-exchange columns-based extraction, aqueous elution					3.7	327 – 334
Lac-328	Lactate	C1-C3		Organic extraction of acidified media	n-propylamide-heptafluoro butynic ester				5.4	327 – 332
Glu/Gln -152	Glutamate	C2-C4		Ion-exchange columns-based extraction, acid and basic elutions	n-trifluoroacetyl-n-butyl-ester			Electron impact ionisation	3.9	151 – 157
Glu/Gln -198	Glutamate	C2-C5							3.9	197 – 203
Ala-242	Alanine	C1-C3		Ion-exchange columns-based extraction, basic elution				Chemical ionisation **Scan polarity:** positive	5.3	241 – 246
Asp/Asn-342	Aspartate+ Asparagine	C1-C4							11.5	341 – 348
Glu/Gln-384	Glutamate Glutamine	C1-C5							12.8	383 – 390
Gly-228	Glycine	C1-C2							5.7	227 – 231
Met-330	Methionine	C1-C4SC5							10.8	329 – 336
Met-254	Methionine	C1-C4							10.8	253 – 259
Pro-296	Proline	C1-C5							9.6	295 – 302
Ser-354	Serine	C1-C3				Agilent 7890AGC with Agilent 5975C MSD **Column model:** HP 5ms (30m lenght; 0.25 mm i.d.; 0.25 microm thickness; (5%-phenyl)-methyl polysiloxane)	Agilent 7890AGC with Agilent 5975C MSD **Mass analyser:** MS quadrupole		6.6	353 – 358
αKG-346	α-Keto glutarate	C1-C5	Cell pellet	Methanol:water: chloroform extraction	2% methoxyamine hydrochloride in pyridine + MBTSTFA + 1% TBDMCS (sylation)			Electron impact ionisation	24.6	345 – 356
Ala-232	Alanine	C2-C3							12.6	231 – 239
Ala-260	Alanine	C1-C3							12.6	259 – 268
Asp-418	Aspartate	C1-C4							28.9	417 – 428
Cit-459	Citrate	C1-C6							37.7	458 – 469
Cit-591	Citrate	C1-C6							37.7	590 – 599
Glu-330	Glutamate	C2-C5							32.6	329 – 338
Glu-432	Glutamate	C1-C5							32.6	431 – 442
Lac-261	Lactate	C1-C3							11.8	260 – 269
Mal-419	Malate	C1-C4							27.6	418 – 428
Pyr-174	Pyruvate	C1-C3							8.2	173 – 181

3.31.8. Glycogen

96 h after transfection, siRNA-treated cells seeded in 6-well plates were processed to quantify the glycogen content and analyse its mass isotopomer distribution. Cell cultures were washed twice with ice-cold PBS, scraped with 80 µL of 0.1 M NaOH and heated at 100ºC for 15 min for protein denaturation. Then, samples were sonicated for 5 min using an ultrasonic bath (Branson 200 Ultrasonic Cleaner, Emerson Industrial Automation, St Louis, MO, USA). 5-10 µL of 1 µg µL^{-1} [U-^{13}C-D$_7$]-glucose were added as recovery standard and internal standard to quantify the glucose released from glycogen. Cell extracts were neutralised with 0.5 M HCl and glycogen was digested by incubation with 1 U mL^{-1} α-amyloglucosidase in 0.4 M acetate buffer with gentle rocking for 20 h at 37ºC. Both glucose released from glycogen and [U-^{13}C-D$_7$]-glucose were isolated from homogenates using a tandem set of Dowex-1X8/Dowex-50WX8 ion-exchange columns, being eluted with water. The glucose eluate was evaporated to dryness under airflow overnight. Glucose was converted to its glucose aldonitrile pentaacetate derivative after treatment for 30 min at 100ºC with 100 µL of hydroxylamine hydrochloride in pyridine (2% v/v) and then with 75 µL of acetic anhydride for 1 h at 100ºC. Excess reagent and solvent were removed by evaporation with N$_2$ flow, and the derivatised glucose was resuspended in ethyl acetate for GC/MS analysis under chemical ionisation mode. Samples were injected at 250ºC and oven temperature was programmed as follows: 230ºC for 2min, then increased at 10ºC min^{-1} to 260ºC, followed by a 25ºC min^{-1} ramp to 270ºC and hold for 2 min. Detector was run in SIM, recording ion abundance of C1-C6 molecule in the range of 327-334 m/z for glucose and 339-345 m/z for the molecular ion (C1-C6) of the aldonitrile pentaacetate of the [U-^{13}C-D$_7$]-glucose used as a recovery standard. Retention time was 3.7 min. Glucose from glycogen was normalised by cell number.

3.32. [U-^{13}C]-glucose tracer experiments

A549 cells were seeded in 10 cm plates and grown in the RPMI medium as described above for 24-36 h before the medium was changed to the RPMI medium with dialysed

FBS and [U-^{13}C]-glucose, and in the absence (Control) or presence of 5 µM MSA. Cells in the tracer medium were grown for another 24 hours before harvest by trypsinisation, followed by 2 washes in excess cold PBS to remove medium components. The final cell pellet obtained from spin at 1700 g, 4ºC for 5 min was flash-frozen in liquid N$_2$ before extraction with ice-cold 10% trichloroacetic acid, as described previously [479] . The polar extracts were aliquoted and lyophilised for analysis by GC-MS and 1D ^{13}C-edited HSQC NMR at 14.1 T, 20ºC using a 5 mm HCN triple resonance cold probe (Agilent Technologies, Santa Clara, CA). For GC/MS analysis, the extracts were derivatised in MTBSTFA before analysis, and for NMR analysis, the extracts were dissolved in 100% D$_2$O, as described previously [480].

3.33. GC/MS data reduction

Spectral data obtained from a mass spectrometer simply represent the distribution of ions of a compound or its fragments with different molecular weights (m/z). The ion clusters around the specific m/z were monitored for each analysed metabolite to determine the fractional distribution of ^{13}C. The areas of peaks for all ions in the cluster were extracted from raw data using MSD5975C Data Analysis (Agilent Technologies) or GCMS Postrun Analysis (Shimadzu) software. A value of each peak area is proportional to the fraction of ions with the same molecular weight. The value for each observed m/z is given by the experimental isotope incorporation, the presence of isotopes in heteroatoms, the presence of natural abundance of ^{13}C in the background and, when corresponds, the ^{12}C isotope impurity in the ^{13}C-labeled precursor used as a tracer (in the case of glucose or glutamine). Also, derivatisation reagents often contain isotopes (e.g. Si isotopes) which contribute to the mass isotopomer distribution of the derivatised compound as well. Correction for all such contributions is necessary before determining the amount of isotope incorporation from artificially ^{13}C labelled substrates and the distribution of mass isotopomers in the compound of interest. This correction was conducted by regression analysis using an in-house developed algorithm. The algorithm used corrects all the previous detailed contributions over the observed spectral intensities of each ion cluster, and provides

the mass isotopomer distribution in the analysed metabolite due to incorporation of ^{13}C atoms from the tracer used as precursor. Results of the mass isotopomers in any of the ion clusters were reported as fractional enrichments of molecule isotopomers, defined as the fraction of molecules having a certain number of isotope substitutions. Thus, they are designated as m0, m1, m2, etc. where the number indicates the number of labelled carbons (^{13}C) in the molecule corrected as described above. It is worth noting that the sum of all mass isotopomers of the ion clusters ($\sum_{i=0}^{i=n} m_i$, where n is the number of carbons in the molecule or fragment) is equal to 1 (or 100%), while the total ^{13}C enrichment is calculated as $\sum_{i=1}^{i=n} m_i$, or 1 (or 100%) minus m0.

3.33.1. Isotopic steady state and total ^{13}C enrichment

Ideally, assuming steady state, the distribution of mass isotopomers would only depend on the distribution of fluxes and the labelled and non-labelled status of the substrates used in the experiment. However, ^{13}C propagation from tracer precursors to products is a dynamical phenomenon. At the beginning, all product metabolites are unlabelled (m0). Progressively, these products are enriched in ^{13}C, with the subsequent decrease in m0. Isotopic steady state [481] is quickly reached for small pools of metabolites but not necessarily for larger pools such as those of fatty acids, glycogen and culture medium metabolites. For these larger pools, unlabelled isotopomers m0 are oversized and might not decrease to the hypothetical value that should be reached at steady state. Accordingly, when isotopic steady state cannot be assumed, the measure of total ^{13}C enrichment ($\Sigma m = \sum_{i=1}^{i=n} m_i$) and the normalisation of the mass isotopomers (m1, m2, m3, etc.) by Σm (m1/Σm, m2/Σm, m3/Σm, etc.), should be used for comparisons.

3.34. Mass isotopomer distribution analysis (MIDA)

The contribution of specific metabolic pathways to the synthesis of certain metabolites can be estimated based on the mass isotopomer results. These calculations are

explained along with the results at Section 4.2. However, the estimation of pathway-specific produced lactate is detailed here, due to its extension.

3.34.1 Contribution of glycolysis, pentose phosphate pathway (PPP) and other pathways to the synthesis of lactate

The amount of lactate produced from glucose via glycolysis, PPP or other pathways can be estimated by combining lactate concentrations and the mass isotopomer distribution of lactate in cell culture media, using $[1,2-^{13}C_2]$-glucose as a tracer. In order to calculate the pathway-specific lactate, we assumed that HCT116 cells produced lactate and did not consume it under the experimental conditions assayed (with glucose and glutamine availability). Therefore, the amount of unlabeled lactate present in the media at the beginning of $[1,2-^{13}C_2]$-glucose incubation is going to contribute to the m0 lactate pool at the end of the experiment. Taking this into account, the absolute mass isotopomer distribution of accumulated lactate in mM at the end of the incubation ($[Lac_{Total}(m0,m1,m2,m3)]_{t=f}$ (mM)) was obtained from the product of the produced lactate concentration ($[Lac]_{t=f}$ (mM), determined as detailed in Section 3.12) and its mass isotopomer distribution ($Lac_{Total}(m0,m1,m2,m3)_{t=f}$ (%)) (Equation 3.1).

$$[Lac_{Total}(m0,m1,m2,m3)]_{t=f} \text{ (mM)} = [Lac]_{t=f} \text{ (mM)} \times Lac_{Total}(m0,m1,m2,m3)_{t=f} \text{ (%)} \qquad (3.1)$$

Then, initial lactate concentration ($[Lac]_{t=i}$ (mM)) was subtracted from the concentration of total m0 lactate ($[Lac_{Total}(m0)]_{t=f}$ (mM)) to obtain the produced lactate ($[Lac_{Prod}(m0)]$ (mM)) without including the initial unlabelled lactate (Equation 3.2). The value of produced lactate in mM that contains one, two or three ^{13}C ($[Lac_{Prod}(m1,m2,m3)]$ (mM)) coincides with the measured values of m1, m2 and m3 in mM in total lactate ($[Lac_{Total}(m1,m2,m3)]_{t=f}$ (mM)).

$$[Lac_{Prod}(m0)] \text{ (mM)} = [Lac_{Total}(m0)]_{t=f} \text{ (mM)} - [Lac]_{t=i} \qquad (3.2)$$

Relative mass isotopomer distribution of produced lactate ($Lac_{Prod}(m0,m1,m2,m3)_{t=f}$ (%)) was recalculated by dividing the absolute mass isotopomer distribution of

produced lactate ($[Lac_{Prod}(m0,m1,m2,m3)]_{t=f}$ (mM)) by total produced lactate ($[Lac_{Prod}]$ (mM)) (Equation 3.3), which in turn was obtained by subtracting initial lactate concentration ($[Lac]_{t=i}$ (mM)) from final lactate concentration ($[Lac]_{t=f}$ (mM)) (Equation 3.4).

$$Lac_{Prod}(m0,m1,m2,m3)_{t=f} \, (\%) = [Lac_{Prod}(m0,m1,m2,m3)]_{t=f} \, (mM) \, / \, [Lac_{Prod}] \, (mM) \qquad (3.3)$$

$$[Lac_{Prod}] \, (mM) = [Lac]_{t=f} \, (mM) - [Lac]_{t=i} \, (mM) \qquad (3.4)$$

The percentage of lactate that comes from glucose through direct glycolysis (glycolytic tax, GT) was obtained from the recalculated mass isotopomer distribution of produced lactate (Equation 3.5).

$$GT = Lact_{Prod}(m2)_{t=f} \, (\%) \times 2 \, / \, Glc(m2)_{t=i} \, (\%) \qquad (3.5)$$

where $Glc(m2)_{t=i}$ (%) is the percentage of $[1,2-^{13}C_2]$-glucose in culture medium at the beginning of the experiment. Then, maximum feasible amount of lactate coming from glycolysis ($[Lac_{ProdGlyc}]$ (mM)) was obtained from the product of GT and produced lactate ($[Lac_{Prod}]$ (mM)) (Equation 3.6).

$$[Lac_{ProdGlyc}] \, (mM) = GT \times [Lac_{Prod}] \, (mM) \qquad (3.6)$$

The Pentose Cycle (PC) parameter is defined as the relative amount of glucose metabolised through glycolysis related to the glucose metabolised through PPP. A detailed description of this parameter and the deduction of the equation can be found in *Lee et al.*, 1998 [482]. To estimate the amount of lactate from glucose coming through PPP, we first calculated the PC parameter using values of mass isotopomer distribution of total lactate (Equation 3.7).

$$PC = (Lac_{Total}(m1)_{t=f} \, / \, Lac_{Total}(m2)_{t=f}) \, / \, (3 + Lac_{Total}(m1)_{t=f} \, / \, Lac_{Total}(m2)_{t=f}) \qquad (3.7)$$

Then, lactate from glucose coming through PPP ($[Lac_{ProdPPP}]$ (mM)) was obtained from the product of PC and the maximum feasible amount of lactate coming from glycolysis ($[Lac_{ProdGlyc}]$ (mM)) (Equation 3.8).

$$[Lac_{ProdPPP}] \, (mM) = PC \times [Lac_{ProdGlyc}] \, (mM) \qquad (3.8)$$

Finally, in order to calculate the amount of lactate produced from other sources than glucose ($[Lac_{ProdOS}]$ (mM)), the maximum lactate produced from glycolysis ($[Lac_{ProdGlyc}]$ (mM)) and lactate coming from glucose through PPP ($[Lac_{ProdPPP}]$ (mM)) were subtracted from produced lactate ($[Lac_{Prod}]$ (mM)) (Equation 3.9).

$$[Lac_{ProdOS}] \text{ (mM)} = [Lac_{Prod}] \text{ (mM)} - [Lac_{ProdGlyc}] \text{ (mM)} - [Lac_{ProdPPP}] \text{ (mM)} \qquad (3.9)$$

3.35. Intracellular metabolic intermediates quantification

Intracellular metabolic intermediates including pyruvate, alanine, malate, aspartate, α-ketoglutarate, glutamate and citrate were extracted and analysed as in Section 3.31.7 with addition of 5 μL of norvaline 1 mg mL^{-1} at each sample before scraping to minimise the differences associated to extraction efficiency. Chromatograms were integrated and areas were normalised by norvaline and cell number, and expressed as relative to control cells.

3.36. Polyamine quantification

Polyamines were extracted from liquid nitrogen-frozen cultured plates with addition of 500 μL of 10 mM acetic acid in methanol/Milli-Q water (1:1) and scraping on ice. Then, 5 μL of 200 mg mL^{-1} 1,6-diaminohexane (a total of 1 μg per sample) were added to each sample as an internal standard and sonicated with titanium probe (3 cycles, 5 seconds per cycle, Tune 50, Output 30). The volume of each sample was measured and 20 μL were taken for protein determination. Samples were then centrifuged at 13,000 rpm at 4ºC and the supernatant was transferred to glass tubes to start the derivatisation. First, pH was adjusted to 11-12 with 2 N NaOH. Then, 1 mL of diethyl ether and 50 μL of ethyl chloroformate were added and tubes were placed in a shaker for vigorous agitation at 4ºC for 20 min. After that, samples were centrifuged at 2500 g for 5 min and the organic phase was collected and evaporated to dryness under N_2 flow. Next, 20 μL of pentaflyoropropylic anhydride and 100 μL of ethyl acetate were added and samples were incubated at 50ºC for 30 min. Finally, samples were dried

under N_2 flow and resuspended with ethyl acetate for GC/MS analysis under electron impact mode. Samples were injected at 260ºC and oven temperature was programmed as follows: 140ºC, then increased to 210ºC at 8ºC min^{-1} and held for 2 min and finally at 20ºC min^{-1} to 320ºC and held for 3.75 min. Retention times were 7.99 min for putrescine, 14.95 min for spermidine and 10.63 for 1,6-diaminohexane.

3.37. Oxygen consumption rate (OCR) and extracellular acidification rate (ECAR)

Oxygen consumption rate (OCR) and extracellular acidification rate (ECAR) were determined using a XF24 Extracellular Flux Analyzer (Seahorse Bioscience, North Billerica, MA, USA). HCT116 cells were transfected with siRNA as explained in Section 3.4, and 72 h after transfection, cells were collected and reseeded at a concentration of 6×10^4 cells per well in 100 µL of complete medium in a XF24-well microplate (Seahorse Bioscience). 150 µL of complete medium were added to the wells 4 h after seeding (once the cells were attached) and plates were incubated at 37ºC and 5% CO_2. After 24 h, only 150 µL of medium were removed from each well (to prevent exposure of the cells to air and potentially drying out) and cells were rinsed with 1 mL of warm XF assay medium (non-buffered, pH 7.4, Seahorse Bioscience) supplemented exclusively with the carbon source indicated in each case (glucose, glutamine or neither glucose nor glutamine). Finally, 400 µL of XF assay medium were added to each well (final volume of 500 µL per well) and plates were incubated at 37ºC for 1 h without CO_2. Previously, the sensor cartridge was incubated overnight with 1 mL of PBS per well at 37ºC. Prior to the start of the Seahorse assay, the four reagent delivery ports (A, B, C and D) of the sensor cartridge were loaded with the assay reagents at 10x final concentration in XF assay medium. Then, the sensor cartridge was equilibrated inside the Seahorse analyser and next, the XF24-well microplate was placed inside the Seahorse as well. Oxygen and proton measurements were carried out over 105 minutes divided into five periods, following the programmed protocol. Within the first period, basal oxygen consumption rate and basal extracellular acidification rate were

determined. Once the measure is complete, the cells from each well were counted to normalise the OCR and ECAR readings.

3.37.1. Mito Stress test

Mitochondrial function and potential were analysed by sequential injection of oligomycin (ATP synthase inhibitor), Carbonyl cyanide 4-(trifluoromethoxy) phenylhydrazone (FCCP, mitochondrial uncoupler) and rotenone and antimycin A (mitochondrial complex I and III inhibitors, respectively). An example of the OCR and ECAR profiles is shown in Figure 3.2. For the different experiments using this test, four types of XF assay media were used: minimal media without glucose and glutamine, media supplemented with 10 mM glucose, media supplemented with 2 mM glutamine and complete media supplemented with 10 mM glucose and 2 mM glutamine.

The sensor cartridge four reagent delivery ports (A, B, C and D) were loaded with the assay reagents at 10x final concentration in XF assay medium as follows:

Position A:

- 55 µL of XF assay medium with 100 mM glucose and 20 mM glutamine (for assays with complete medium).

- 55 µL of XF assay medium with 100 mM glucose (for assays with glutamine deprivation).

- 55 µL of XF assay medium with 20 mM glutamine (for assays with glucose deprivation).

- 55 µL of XF assay medium without glucose and glutamine (for assays with glucose and glutamine deprivation).

Position B: 60 µL of 15 µM Oligomycin.

Position C: 65 µL of 10 µM FCCP.

Position D: 70 µL of 10 µM Antimycin A and 10 µM Rotenone.
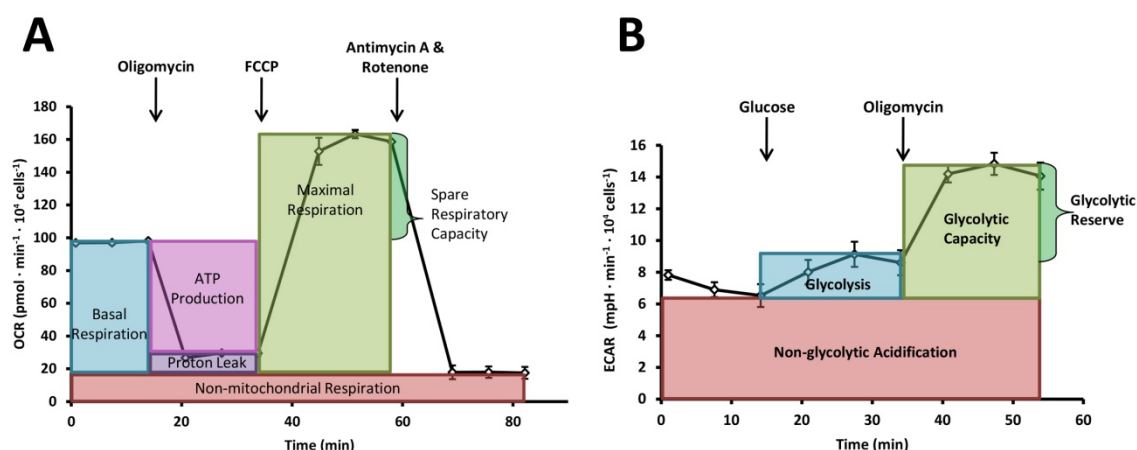
Figure 3.2. OCR and ECAR profiles example. A. Schematic OCR profile after Oligomycin, FCCP and Antimycin A and Rotenone sequential addition. Representative oxygen consumption rates for basal respiration, ATP production-associated respiration, non-ATP linked oxygen consumption (proton leak), maximal respiration, spare respiratory capacity and non-mitochondrial respiration are illustrated. **B.** Schematic ECAR profile after glucose and Oligomycin injection. Representative extracellular acidification rates for glycolysis, glycolytic capacity and glycolytic reserve are illustrated.

3.38. Data analysis and statistical methods

Experiments were carried out at least in triplicate and repeated three times. To evaluate the effects of combined drug treatments the multiple drug-effect analysis of Chou–Talalay [483] was used with the CompuSyn software (ComboSyn, Inc., Paramus, NJ, USA). Combined drug treatments interactions were quantified by determining the Combination Index (CI), where CI<1, CI=1, and CI>1 indicate synergism, additivity, and antagonism, respectively. All data are expressed as mean ± standard deviation (SD). Statistical analyses were conducted using Statgraphics statistical package (Statgraphics Centurion XVI, StatPoint technologies Inc., Warrenton, VA, USA). Fisher's least significant difference (LSD) test was used to identify which were the groups that specifically differed from the others. Outliers were identified by Dixon's Q-test and homogeneity of variances was assessed by Levene's test. Probability of patient survival and disease-free survival were analysed by the univariate product-limit method of Kaplan-Meier. Control and treatment measurements were compared using Kruskal-Wallis, ANOVA and two-tailed independent sample Student's t tests. All data are

expressed as mean ± standard deviation (SD). Differences were considered to be significant at $p < 0.05$ (*), $p < 0.01$ (**) and $p < 0.001$ (***) in Chapter 4.1 and 4.2, and at $p < 0.05$ (*) in Chapter 4.3. Non-significant differences ($p > 0.05$) are indicated in some cases as n.s.

4. Results and discussion

Glyceraldehyde-3-phosphate dehydrogenase is overexpressed in colorectal cancer onset

4.1.1. Introduction

Increasing evidence exists on the significant metabolic reprogramming associated to tumourigenesis and on the glucose metabolic flux distribution alterations displayed by cancer cells, resulting in an enhanced Warburg effect [106]. Moreover, changes in glycolytic enzymes expression such as glyceraldehyde-3-phosphate dehydrogenase (GAPDH) have been described to accompany these metabolic flux alterations [113]. However, despite being an essential regulator of glycolysis, GAPDH has been and is still highly used as a housekeeping marker for gene/protein normalisation. In previous studies we have demonstrated that transketolase-like 1 but not enolase protein levels directly correlated with regional lymph node involvement and inversely with metastasis [471]. In this chapter, given the pivotal role of GAPDH in tumour metabolism [115, 484], our objectives were to demonstrate that GAPDH can no longer be considered as a housekeeping marker and also, to correlate its protein expression with tumour staging and prognosis of colorectal cancer.

To this aim, we have employed an objective computational image analysis quantification method [471] to examine the expression pattern of GAPDH throughout the stages of tumour progression in colorectal cancer. Correlations between GAPDH expression and tumour progression are explored in order to clarify the role of this protein during tumour onset and development. We have identified significant differences in GAPDH expression depending on primary tumour extent, regional lymph node involvement and presence of distant metastasis. Studying the role of GAPDH in malignant transformation can shed new light on the understanding of tumour onset and lead to the design of more efficient personalised therapies.

4.1.2. Results

4.1.2.1. Human tissue specimens and patients information

This study included 62 non-chosen samples from 45 men and 17 women between 33 and 93 years old (average 70 ± 11 years old) with colorectal cancer (CRC) which underwent surgery between November 2000 and October 2001[1]. The Gastroenterology Department of the Hospital Clínic of Barcelona recruited all patients as part of the EPICOLON project, a prospective multicenter, nation-wide, population-based study for the establishment of the incidence and characteristics of inherited and familial colorectal cancer forms in Spain [485]. The EPICOLON project included all newly diagnosed CRC patients in any participating centre during one-year period. Pathological staging was based on the standard of the American Joint Committee on Cancer (AJCC) TNM classification of colon and rectal cancer, which establishes four different stages of tumour progression (I to IV) considering transmural extension (T), lymph node involvement (N) and presence of metastasis (M) [2]. Our study included 9 tumour samples from stage I patients, 21 from stage II, 16 from stage III and 16 from stage IV. Table 4.1.1 lists the demographic, clinical and tumour-related characteristics of the 62 patients included in our cohort. After a 49-month period follow-up, 26 patients had died.

After surgery, patients underwent standard therapeutic and follow-up measures according to recommended guidelines. Postoperative adjuvant treatment with 5-fluorouracil and leucovorin was routinely given to patients with stage II and III tumours, and radiation therapy was indicated in patients with rectal cancer. Postoperative surveillance consisted of medical history, physical examination, and laboratory studies including the monitoring of serum carcinoembryonic antigen (CEA) levels every three months, abdominal ultrasonography or computed tomography every six months, and chest radiograph and total colonoscopy once a year. All tumour recurrences detected during the follow-up were histologically confirmed.

---

[1] Ethics statement: This study obtained the ethics approval from the Hospital Clínic of Barcelona ethics committee and the written informed consent from all patients. All clinical investigation has been conducted according to the principles expressed in the Declaration of Helsinki.

Table 4.1.1. Demographic, clinical and tumour-related characteristics of patients included in the study (n = 62).

Age (years)[a]		**69.5 ± 11.4**
Gender – nº. (%)	Male	**45 (72.6)**
	Female	**17 (27.4)**
Family history of colorectal cancer – nº. (%)		**10 (16.1)**
Fulfilment of revised Bethesda guidelines – nº. (%)		**14 (22.6)**
Tumour location – nº. (%)	Proximal to splenic flexure	**19 (30.6)**
	Distal to splenic flexure	**43 (69.4)**
TNM tumour stage – nº. (%)[b]	I	**9 (14.5)**
	II	**21 (33.9)**
	III	**16 (25.8)**
	IV	**16 (25.8)**
Tumour size (mm)[a]		**43 ± 20**
Differentiation degree – nº. (%)	Well	**6 (9.7)**
	Moderate	**51 (82.2)**
	Poor	**5 (8.1)**
Mucinous carcinoma type – nº. (%)		**10 (16.1)**
Mismatch repair deficiency – nº. (%)[c]		**4 (6.5)**
Synchronous colorectal cancer – nº. (%)		**5 (8.1)**
Synchronous colorectal adenoma – nº. (%)		**23 (37.1)**
Surgical treatment – nº. (%)	Right colectomy	**16 (25.8)**
	Left colectomy	**6 (9.7)**
	Sigmoidectomy	**22 (35.5)**
	Anterior resection	**9 (14.5)**
	Total colectomy	**6 (9.7)**
	Abdominoperineal resection (Miles)	**3 (4.8)**
Chemotherapy – nº. (%)[d]		**35 (56.5)**
Length of follow-up (months)[e]		**49 (40-53)**

[a]Expressed as mean ± standard deviation. [b]TNM staging system: T, primary tumour extent; N, regional lymph node involvement; M, absence or presence of distant metastasis. [c]All four cases correspond to loss of MutL homolog 1 (MLH1) protein expression. [d]All chemotherapeutic regimens included 5-fluoruracil, 5 of them in combination with oxaliplatin and 2 in combination with irinotecan. [e]Expressed as median (range).

123

4.1.2.2. Immunohistochemical detection of GAPDH expression

Tumour samples prepared from paraformaldehyde embedded tissue specimens were immunohistochemically stained as described at Section 3.23. Mouse monoclonal antibody against human GAPDH was proved to be specific by Western blot, presenting a single band at 37kDa (Figure 4.1.1).
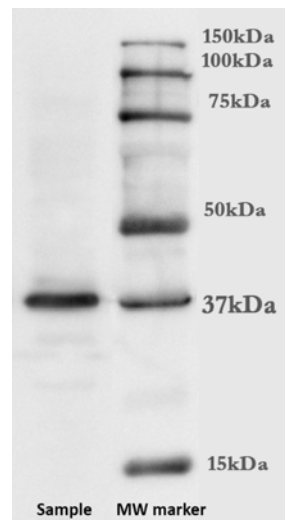
Figure 4.1.1. Mouse monoclonal anti-human GAPDH antibody specificity. Anti-GAPDH antibody (sc-47724, Santa Cruz Biotechnology, Santa Cruz, CA, USA) specificity was proven by Western blot, staining a single band at 37 kDa.

Specific and significant labelling was observed in primary tumours incubated with anti-GAPDH antibody, while control samples did not present any unspecific labelling (Figure 4.1.2). GAPDH expression was quantified using ImageJ software (NIH Imaging, USA) as described in Section 3.23, measuring relative intensity per area and interpolating into a calibration curve plotted using a grey scale. The homoscedasticity for GAPDH expression for all the studied groups was positively assessed using Levene's test ($p = 0.7046$). Having confirmed the normal distribution of our data applying the Shapiro-Wilk test, we performed parametric statistic tests to evaluate the significance of the differences observed. It is worth noting that GAPDH expression was confirmed not to be age ($p = 0.9599$) or gender dependent ($p = 0.8091$). Clinicopathological and immunohistochemical data are summarised in Table 4.1.2.
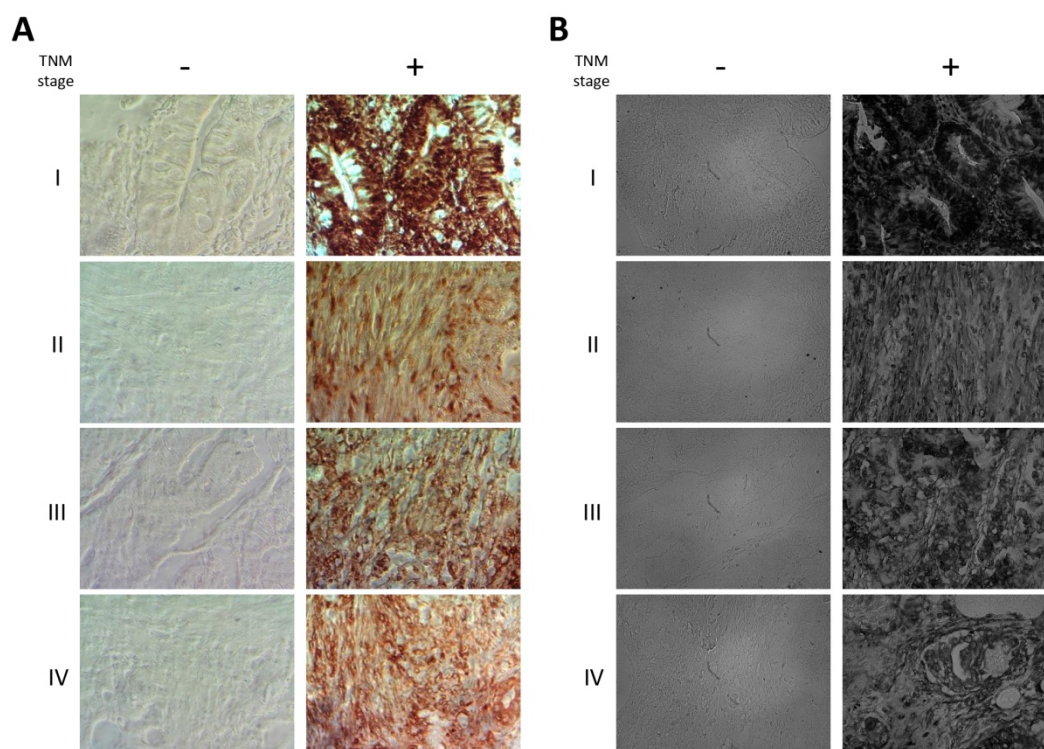
Figure 4.1.2. GAPDH expression in colorectal tumours in different stage of progression. (A) Representative colour photomicrographs presenting immunohistochemical staining (brown) for GAPDH in colorectal tumours (x200). Stained tissues at different stages of progression are displayed in the right column and homologous areas in negative controls in the left column. **(B)** Representative monochromatic photomicrographs were analysed with ImageJ software to quantify immunostaining and assess GAPDH expression (x150). Stained tissues at different stages of progression are portrayed in the right column and homologous areas in negative controls in the left column. For both **(A)** and **(B)**, representative photomicrographs used were from sample 7058 for stage I, sample 7020 for stage II, sample 7112 for stage III and sample 7104 for stage IV.

Table 4.1.2. Clinicopathological and immunohistochemical data. Sample 7107 was identified as an outlier by Dixon's Q-test at the 95% confidence level. Id, arbitrary number used to preserve the privacy of patients; a.u., arbitrary units; M, male; F, female; TNM staging system: T, primary tumour extent; N, regional lymph node involvement; M, absence or presence of distant metastasis.

Id	Stage	Gender	Age	GAPDH (a.u.)	T	N	M	Mean	SD
7001	I	M	70	289.3	2	0	0		
7002	I	M	80	254.6	2	0	0		
7012	I	F	79	219.1	1	0	0		
7023	I	M	78	189.1	2	0	0		
7058	I	M	58	238.8	1	0	0	229.0	± 65.0
7116	I	F	66	212.2	1	0	0		
7160	I	F	45	180.5	1	0	0		
7165	I	M	75	350.2	1	0	0		
7168	I	M	61	127.2	2	0	0		

4. Results and discussion

Id	Stage	Gender	Age	GAPDH (a.u.)	T	N	M	Mean	SD
7004	II	M	56	219.1	3	0	0		
7010	II	F	78	138.7	3	0	0		
7020	II	F	86	63.0	3	0	0		
7026	II	M	60	208.3	4	0	0		
7030	II	F	93	241.3	3	0	0		
7052	II	M	84	65.4	3	0	0		
7053	II	F	76	110.8	4	0	0		
7062	II	M	53	176.4	3	0	0		
7084	II	M	79	122.8	3	0	0		
7115	II	M	67	43.0	3	0	0		
7117	II	M	55	45.8	3	0	0	116.1	± 70.4
7122	II	M	81	17.0	3	0	0		
7123	II	M	70	171.0	3	0	0		
7126	II	F	81	183.3	3	0	0		
7130	II	M	87	81.6	3	0	0		
7135	II	F	79	81.4	3	0	0		
7139	II	M	60	220.5	3	0	0		
7148	II	F	73	46.1	3	0	0		
7151	II	F	68	99.3	3	0	0		
7152	II	M	74	60.7	3	0	0		
7169	II	M	70	42.4	3	0	0		
7005	III	M	67	22.5	4	2	0		
7011	III	F	76	81.7	3	1	0		
7028	III	M	76	125.9	2	1	0		
7042	III	M	74	195.7	3	2	0		
7048	III	F	61	195.3	3	2	0		
7051	III	M	68	143.0	3	1	0		
7056	III	F	76	75.1	3	1	0		
7092	III	M	73	165.3	3	2	0	125.0	± 58.9
7096	III	F	83	103.5	3	1	0		
7109	III	M	41	86.5	3	1	0		
7111	III	M	73	252.3	3	1	0		
7112	III	M	76	122.8	3	2	0		
7119	III	M	65	101.1	3	1	0		
7146	III	M	51	47.7	3	2	0		
7147	III	M	76	145.3	3	2	0		
7167	III	M	69	136.7	3	1	0		
7006	IV	M	33	16.5	3	2	1		
7018	IV	M	74	26.6	3	2	1		
7021	IV	M	73	67.6	3	0	1		
7037	IV	M	67	55.0	3	1	1		
7055	IV	M	77	34.4	3	2	1		
7061	IV	F	60	34.1	4	1	1		
7095	IV	M	64	142.8	3	0	1		
7099	IV	M	67	69.2	3	1	1	92.0	± 62.2
7104	IV	M	86	80.7	-	-	1		
7107	IV	M	69	317.9	3	2	1		
7118	IV	M	64	160.1	3	2	1		
7121	IV	M	73	140.6	4	2	1		
7125	IV	M	77	206.1	3	1	1		
7128	IV	M	74	158.2	3	0	1		
7131	IV	F	67	156.7	2	0	1		
7144	IV	M	57	30.9	4	2	1		

126

4.1.2.3. GAPDH expression in relation to tumour stage

Results summarised in Table 4.1.2 and Figure 4.1.3 show that GAPDH expression ranges from 127.2 to 350.2 a.u. (mean, 229.0 ± 65.0) in stage I tumours, from 17.0 to 241.3 a.u. (mean, 116.1 ± 70.4) in stage II, from 22.5 to 252.3 a.u. (mean, 125.0 ± 58.9) in stage III and 16.5 to 206.1 a.u. (mean, 92.0 ± 62.2) in stage IV (Figure 4.1.3). These results showed a significant overexpression of GAPDH in stage I compared to the other three stages (ANOVA mean comparison, p = 0.0001). An outlier was identified (sample 7107, stage IV) using Dixon's Q-test, presenting an abnormal high value (317.9 a.u.) compared with the rest of its group at the 95% confidence level.
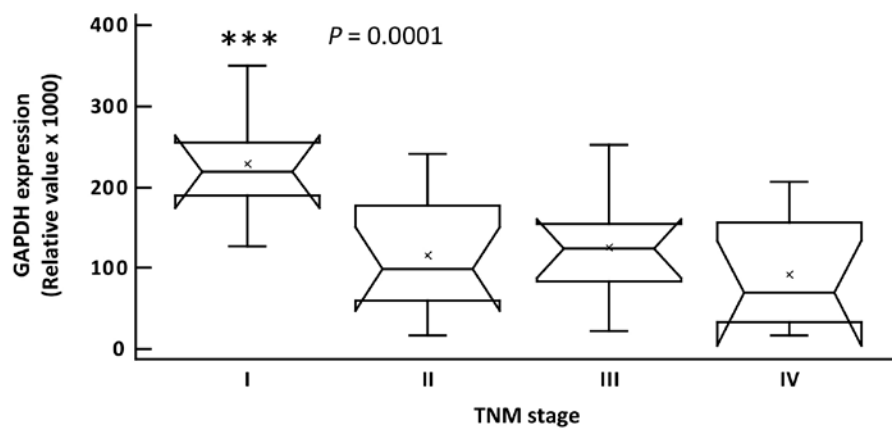
Figure 4.1.3. GAPDH expression in relation to tumour stage. Box and whiskers plot illustrates GAPDH overexpression observed in stage I primary tumours. Mean values are represented by a cross and median values by horizontal lines in each group.

Interestingly, GAPDH expression in stage I tumours was significantly higher than in any other stage of progression. In addition, patients who presented with a more advanced disease stage (stages II, III and IV) displayed similar GAPDH expression levels without any significant differences between them.

4.1.2.4. GAPDH expression according to primary tumour extent

Considering primary tumour transmural progression extent, early stage tumours (T1 and T2) presented significantly enhanced GAPDH expression values, ranging from 125.9 to 350.2 a.u. (mean 213.1 ± 68.4; mean comparison by Student's t-test, p = 0.00003), compared to more advanced primary tumour (T3 and T4) which ranged from 16.5 to 252.3 a.u. (mean 111.3 ± 66.3) (Figure 4.1.4A). This statement is also applicable when only considering non-metastatic primary tumours (Figure 4.1.4B). These data reveal a significant decrease in GAPDH expression when the depth of invasion into the wall of the intestine and the extension to adjacent structures are greater.
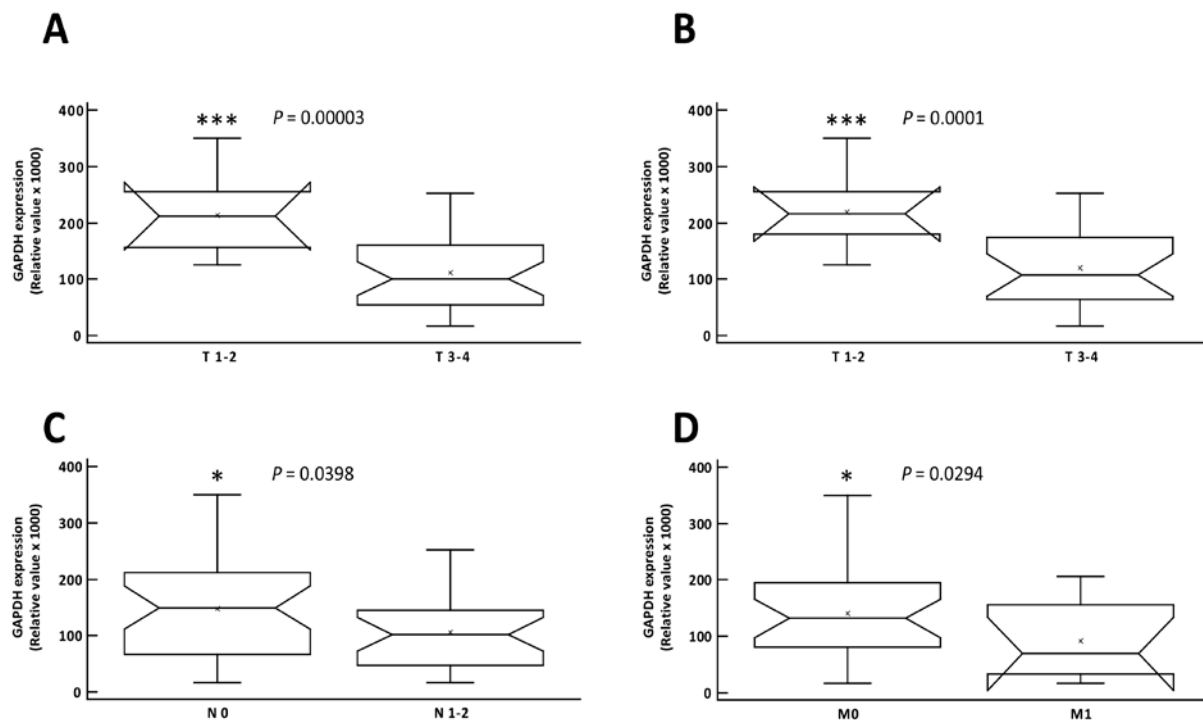
Figure 4.1.4. Correlation between GAPDH expression and TNM classifications. (A) GAPDH expression in relation to the primary tumour extent in all 62 patients and **(B)** in patients who had not developed distant metastasis. In both cases, GAPDH expression is significantly higher in tumours that have only affected the most external layers of the colonic wall (submucosa and muscularis propria) than in tumours in more invasive stages (invasion into the subserosa, non-peritonealised pericolic or perirectal tissues, other organs and/or perforation of visceral peritoneum). **(C)** The presence of metastases in regional lymph nodes is correlated with a significant decrease in primary tumour GAPDH expression. **(D)** In the absence of distant metastasis, tumours express significantly higher levels of GAPDH.

4.1.2.5. GAPDH levels in primary tumours involving regional lymph nodes

GAPDH expression in patients without regional lymph node involvement (N0) (mean 147.8 ± 81.6 a.u.) is statistically superior (Student's t-test, p = 0.0398) than in patients with metastasis in 1 to 3 (N1) and 4 or more (N2) regional lymph nodes (mean 106.7 ± 65.2 a.u.) (Figure 4.1.4C).

4.1.2.6. Influence of distant metastasis in GAPDH expression

Samples from patients who had not developed distant metastasis (M0) displayed an average value for GAPDH expression of 141.3 ± 77.7 a.u. while the corresponding value for those patients who presented with distant metastasis (M1) was 92.0 ± 62.2 a.u. These results depicted a significant decrease in GAPDH expression (Student's t-test, p = 0.0294) with presence of distant metastasis (Figure 4.1.4D).

4.1.2.7. GAPDH expression and survival in colorectal cancer

To assess the relationship between tumour GAPDH expression and patient survival and disease-free survival in colorectal cancer, we used univariate Kaplan-Meier analysis and Mantel-Cox log rank test. We found that there is no significant association between GAPDH expression levels and survival in colorectal cancer (Mantel-Cox log rank test, p = 0.609 considering all stages of tumour progression and p = 0.773 for stages without distant metastasis) (Figures 4.1.5A and 4.1.5B). On the other hand, results suggest a not statistically significant correlation between overexpression of GAPDH and increased disease-free survival (mean values 63.11 ± 3.06 and 52.77 ± 3.97 months for patients with high and lower GAPDH expression levels, respectively; Mantel-Cox log rank test, p = 0.051 considering all stages of tumour progression and p = 0.064 for stages without distant metastasis) (Figures 4.1.5C and 4.1.5D).
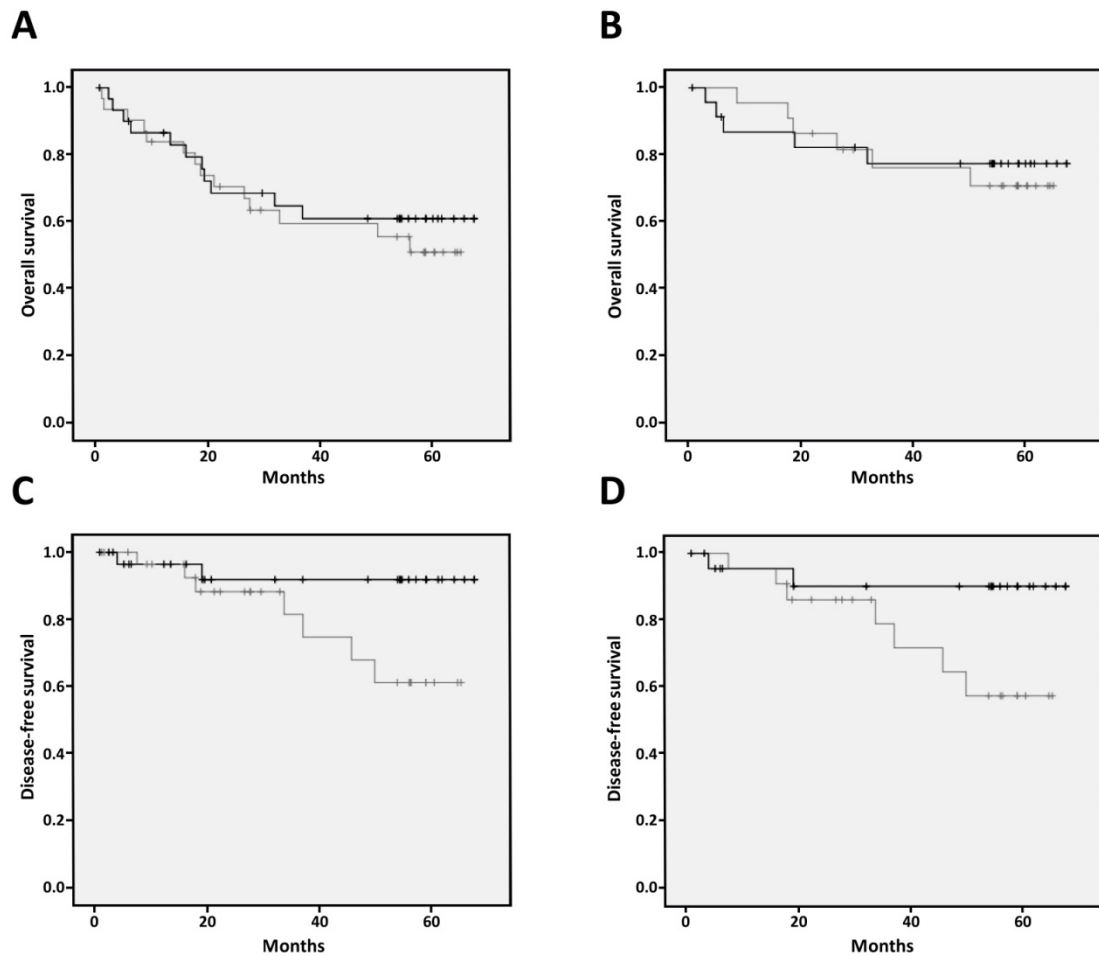
Figure 4.1.5. Correlation between GAPDH expression and patient survival. A. Kaplan-Meier plot correlating GAPDH expression and survival in patients with colorectal cancer (p = 0.609). **B.** In patients with non-metastatic colorectal cancer (p = 0.773). **C.** Kaplan-Meier plot correlating GAPDH expression and disease-free survival in patients with colorectal cancer (p = 0.051). **D.** In patients with non-metastatic colorectal cancer (p = 0.064). Black line represents the group of patients whose GAPDH expression is higher than de median levels, and grey line represents those with GAPDH expression lower than the median levels.

4.1.3. Discussion

In tumour cells, upregulation of aerobic glycolysis with elevated lactate production generates an acidic and hypoxic extracellular microenvironment which gives a selective growth advantage to malignant cells and facilitates invasion through destruction of adjacent normal populations, degradation of the extracellular matrix by metalloproteases and promotion of angiogenesis [486]. Hypoxia and glycolytic products such as lactate and pyruvate can stimulate hypoxia-inducible factor 1 (HIF1)

accumulation in solid tumours leading to upregulation of survival genes, angiogenic factors and glycolytic enzymes, including GAPDH [487-489]. Overexpression of almost every glycolytic enzyme has been described in prostate and brain cancers [113]. However, GAPDH, enolase and pyruvate kinase are the only genes of glycolysis whose expression has been described to be upregulated in colorectal cancer [113]. According to our results, GAPDH is increased in all stages of colorectal tumour progression, reaching its maximum in stage I and moderating its overexpression in the subsequent stages. These findings suggest that GAPDH may be playing a key role in glycolysis but also may be involved in non-glycolytic processes during tumour onset.

In fact, GAPDH is a multifunctional protein implicated not only in glycolysis but also in many other highly relevant non-glycolytic processes in cell such as the cellular response to oxidative stress and DNA damage, transcriptional and post-transcriptional gene regulation, intracellular membrane trafficking, cell cycle regulation, receptor mediated cell signalling, autophagy and apoptosis [112]. All these multiple activities interconnect GAPDH expression and tumourigenesis.

In colon carcinogenesis the selective repression of mitochondrial β-F1-ATPase expression which reduces oxidative phosphorylation leads to an increase in GAPDH expression [490] that may explain the rise of GAPDH levels observed in the initial stages of tumourigenesis. Moreover, reduction of β-F1-ATPase expression limits electron flux through electron transport chain, which is the main endogenous source of oxidative stress, causing the diminution of free radical generation and the risk of apoptosis. Therefore, this could be a mechanism by which cells simultaneously acquire high levels of GAPDH and protect themselves against oxidative stress.

GAPDH is a redox-sensitive enzyme whose activity is affected by oxidation of the cysteine residue located in its catalytic site [491, 492]. The oxidation of GAPDH depends on the intracellular reactive oxygen species (ROS) concentration. Interestingly, a dual modulation of GAPDH activity has been described in cells exposed to sub-apoptogenic and apoptogenic oxidative stresses levels. Under mild oxidative stress conditions, such as that induced by the repression of mitochondrial β-F1-ATPase, GAPDH is strongly hyperactivated while apoptogenic stress levels inhibit

GAPDH activity [110, 493]. In advanced stages of tumour progression, oxidative stress is higher than in early phases of carcinogenesis [494-496] which could explain the increased levels of GAPDH in stage I in comparison with later stages of progression. In addition, overexpression of GAPDH has two cooperative roles in protection towards caspase-independent cell death; a high glycolytic ATP production and the induction of autophagy-mediated clearance of damaged mitochondria [115, 116], both favouring tumour onset.

On the other hand, under high oxidative stress circumstances chaperone-mediate autophagy (CMA) is upregulated to selectively remove altered or damaged proteins. As a CMA putative substrate, GAPDH contains a KFERQ-like motif that is recognised by chaperone heat shock cognate 70 (Hsc70) for lysosomal degradation [497]. The abovementioned increase of oxidative stress in advanced stages of tumour progression can trigger GAPDH inactivation and subsequent CMA, resulting in the observed reduction of protein expression compared to early tumour stages.

The capability to sustain proliferative signalling is one of the hallmarks required in tumourigenesis [6]. GAPDH can enhance cell proliferation during tumour onset binding to the SET protein at the same site of cyclin B and reversing the inhibitory effects of SET on Cyclin B-CDK1 complex [498]. As we mentioned before, metabolic reprogramming is another hallmark of cancer that allows tumour cells to fulfil the increased demand of energy and macromolecules required to sustain the accelerated proliferation rates [6]. In fact, glycolysis is a key pathway in the tumour metabolic reprogramming and a potential target for cancer therapy [499]. Non-tumour cells with intact mitochondria are expected to be less sensitive to glycolysis inhibition than malignant cells which are more dependent on this pathway to generate ATP and proliferate [425]. Accordingly, GAPDH, which is overexpressed in 21 cancer classes [113] and involved not only in cell proliferation and glycolysis but also in several other abovementioned mechanisms which are upregulated in tumour cells, emerges as a promising therapeutic target against cancer [484, 500].

Previous studies have correlated GAPDH expression with an overall poor prognosis. However, in these reports tumour samples were obtained from patients who

presented with advanced stages of tumour progression (II-IV) [114, 490, 501, 502], without tumour staging classification [503] or where *GAPDH* gene but not protein expression was quantified [504, 505]. In the present study, we have observed a significant overexpression of GAPDH protein during the tumour onset (stage I) which is associated with patients in the early stages of disease who have a better outcome.

The use of GAPDH as a housekeeping gene or internal standard for gene/protein level normalisation is still widespread even though it is well documented that this use is inappropriate [506]. Our results further support this conclusion as we have observed significant differences in GAPDH expression between stages of tumour progression in colorectal cancer.

In conclusion, we found that GAPDH expression in colorectal cancer is significantly upregulated during tumour onset. These results suggest that GAPDH plays an important role in the initial events of colorectal tumourigenesis and could be used as an early detection biomarker. Monitoring GAPDH in risk population may enable early diagnosis and better recovering rates. The study of the expression of GAPDH-related proteins can further contribute to the knowledge of the mechanisms underlying tumour onset and to the design of more efficient and personalised anti-oncogenic therapies.

Targeting metabolic reprogramming associated to CDK4 and CDK6 inhibition as a combined therapy in cancer treatment

4.2.1. Introduction

Metabolic reprogramming associated to tumour cells is considered a hallmark of cancer [6]. The existence of this metabolic switch offers new avenues for cancer therapy and the discovery of new putative biomarkers. The recent finding that during cell cycle not only cyclins and cyclin-dependent kinases (CDKs) but also some key metabolic enzymes are coordinately synthesised and degraded [197, 202] opens up a new possibility for cancer treatment, that is, targeting the crosstalk between CDKs signal transduction and the metabolic network.

Genes that have a role in the cell cycle control (checkpoints, regulation of transcription or cell cycle progression) are frequently altered in cancer [38, 62]. Cyclin-dependent kinases CDK4 and CDK6 (CDK4/6) are promising targets for inhibiting cell cycle progression since their overexpression is implicated in a wide range of human cancers but little is known about the metabolic consequences associated to their dysregulation [17, 38, 507]. Under the general aim of exploring links between cell cycle and metabolism, we have analysed the metabolic reprogramming associated to the inhibition of CDK4/6 in HCT116 colon tumour-derived cells. In fact, cells are highly homeostatic systems that depend on metabolic and other regulatory networks for cell function and survival. Therefore, the dysregulation of the cell cycle regulatory network through CDK4/6 inhibition should require a large list of homeostatic adaptations which, in turn, emerge as dysregulation-associated cell vulnerabilities. The expected outcome of this study is the development of combination therapies using CDK4/6 inhibitors together with drugs that directly inhibit the metabolic adaptation exhibited by tumour cells with CDK4/6 downregulation, and their validation as putative therapeutic strategies allowing for a selective lethality to tumour cells.

To this end, we used as a model the human colorectal carcinoma HCT116 cell line, which contain one allele of p16[INK4a] with a coding region frameshift mutation and one wild type allele. Due to promoter hypermethylation, the wild type allele is silenced and only the mutant allele is expressed, resulting in full loss of p16[INK4a] tumour suppressor function [508] and activation of CDK4 and CDK6. In consequence, HCT116 cell line is a good model for studying the effects of CDK4 and CDK6 inhibition in cancer cells.

4.2.2. Results

4.2.2.1. Effects of CDK4/6 inhibition on HCT116 cells phenotype, proliferation, apoptosis and cell cycle

With the aim of finding vulnerabilities associated with the metabolic reprogramming derived from the inhibition of the cyclin-dependent kinases CDK4 and CDK6 (CDK4/6) in human colorectal carcinoma HCT116 cells, we inhibited CDK4/6 using small interference (si) RNAs (as detailed in Section 3.4.). In addition, to both validate the results and test whether the observed effects were due to the inhibition of CDK4/6 kinase activity or the suppression of protein expression, we used a selective chemical inhibitor, PD0332991, which is currently under clinical trials [74] and specifically targets CDK4 and CDK6 (IC_{50} values of 0.011 and 0.015 µM, respectively) with little or no inhibitory activity against a panel of 350 kinases that include other CDKs and a wide variety of serine, threonine and tyrosine kinases [83, 509].

Double CDK4/6 knockdown was validated by Western blot and RT-qPCR (Figure 4.2.1A) (see Sections 3.27 and 3.29, respectively) and proved to be more effective in reducing cell proliferation than inhibiting CDK4 or CDK6 alone (Figure 4.2.1B), confirming that these kinases can play compensatory roles *in vitro* [68]. The inhibition of CDK4/6 caused an increase in cell volume but had no effect on the total cellular protein content (Figures 4.2.1C and 4.2.1D). In association with the reduced viability, knockdown of CDK4/6 promoted early apoptosis (Figure 4.2.1E). As expected, targeting two of the key players in the cell cycle G1 to S phase transition resulted in a G1 cell
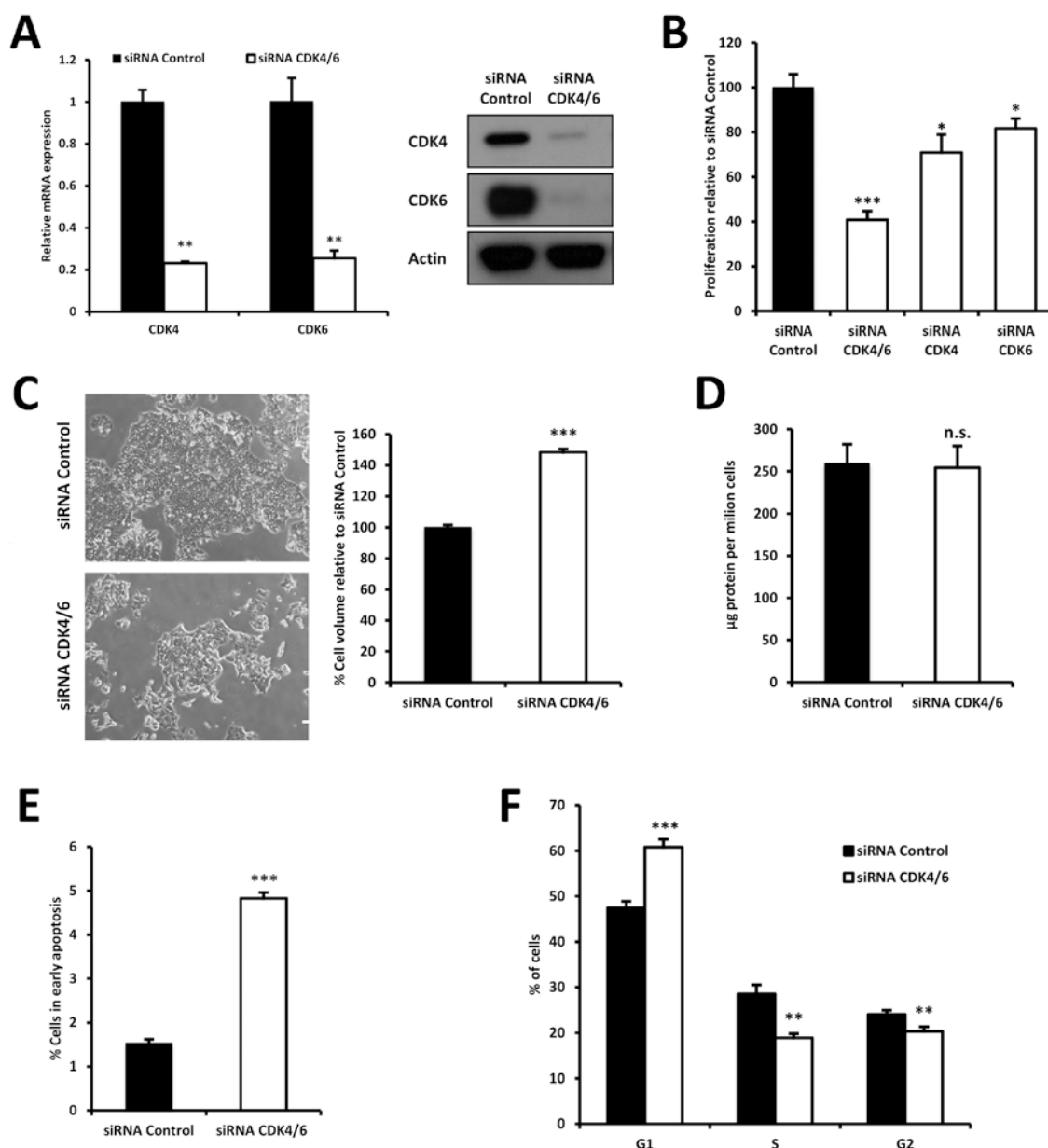
Figure 4.2.1. CDK4/6 knockdown phenotype and effects on cell proliferation, apoptosis and cell cycle. A. CDK4/6 knockdown was validated by RT-qPCR and Western blot 96 h after transfection. **B.** CDK4/6 simultaneous inhibition reduced proliferation by approximately 60%. **C.** Representative micrographs of HCT116 cells transfected with siRNA against CDK4/6 and control siRNA. Cell size and volume were measured with the Scepter^{TM} cell counter (Section 3.5). Bar graph represents the percentage of cell volume relative to control cells. **D.** Protein levels were quantified by the BCA assay. The reported increment in cell volume was not related to an increase in the total protein content. **E.** The percentage of cells in early apoptosis was assessed by flow cytometry analysis of Annexin V-FITC staining and propidium iodide (PI) accumulation (Section 3.10.). **F.** Cell cycle analysis of HCT116 transfected cells. The harvested cells were stained with PI and their DNA content was analysed by flow cytometry (Section 3.9.). Graph bars illustrate the variations in the percentage of cells in each cell cycle phase. All experiments were performed 96 h after siRNA transfection. Data are mean ± SD from at least n=3. Differences between cells transfected with CDK4/6 siRNA and non-targeting siRNA were considered statistically significant when $p < 0.05$ (*), $p < 0.01$ (**) and $p < 0.001$ (***).

cycle arrest (Figure 4.2.1F). The same results were obtained in HCT116 cells treated with PD0332991 (Figures 4.2.2A, 4.2.2B and 4.2.2C). The concentration of PD0332991 selected for the assays was determined by a cell viability dose-response curve with the Hoechst stain system. At 96 h treatment, the concentration that reduced cell viability to a similar extent as siRNA-mediated experiments was 2 μM (Figure 4.2.2D).
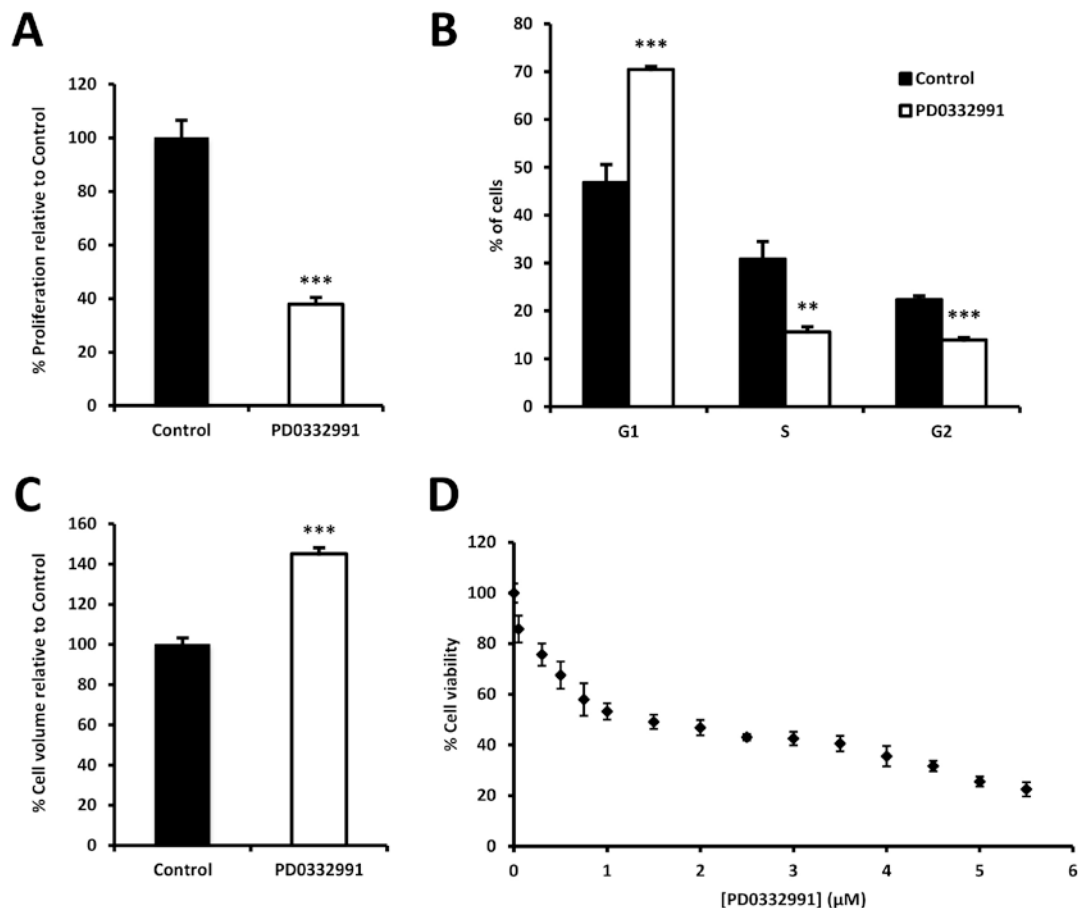
Figure 4.2.2. Effects of CDK4/6 inhibition by PD0332991 treatment. 24 h after seeding, HCT116 cells were incubated with the chemical inhibitor PD0332991 for 96 h. **A.** Effect of 2 μM PD0332991 treatment on cell proliferation determined by flow cytometry combining direct cell counting and PI staining. **B.** Cell cycle analysis of control cells or cells treated with 2 μM PD0332991 for 96 h. Cells were stained with PI and the percentage of cells in each cell cycle phase was assessed by flow cytometry analysis of their DNA content. **C.** Cell size and volume were measured with the Scepter^{TM} cell counter. Bars represent the percentage of cell volume relative to control cells. **D.** Exponentially growing cells were treated with the indicated concentration of PD0332991 for 96 h and cell proliferation was determined by HO33342 staining. Results are represented as percentage of proliferation relative to untreated cells. The concentration of PD0332991 that reduced cell viability to 40% relative to control cells was 2 μM. The assay was carried out using six replicates and repeated three times. Data are shown as mean ± SD. Significant differences between PD0332991 treatment and control were indicated at $p < 0.01$ (**) and $p < 0.001$ (***).

4.2.2.2. CDK4/6 silencing regulates glucose and glutamine metabolism

In order to characterise the metabolic phenotype associated with the inhibition of CDK4/6, we first analysed the glycolytic profile of HCT116 control cells and HCT116 CDK4/6-inhibited cells. Considering that glucose and glutamine represent the two major sources of energy, carbons and nitrogen for the synthesis of macromolecules, we examined glucose, glutamine, lactate and glutamate consumption and production rates (see Sections 3.12 and 3.13). As seen in Figure 4.2.3A, knockdown of CDK4/6 cells enhanced glucose and glutamine consumption and lactate and glutamate production. The same results were obtained using the chemical inhibitor PD0332991 (Figure 4.2.3B). Since we observed the same results either with siRNA knockdown or with the selective chemical inhibitor PD0332991, we performed the experiments employing siRNA techniques, while using PD0332991 for specific assays, as specified in each case.
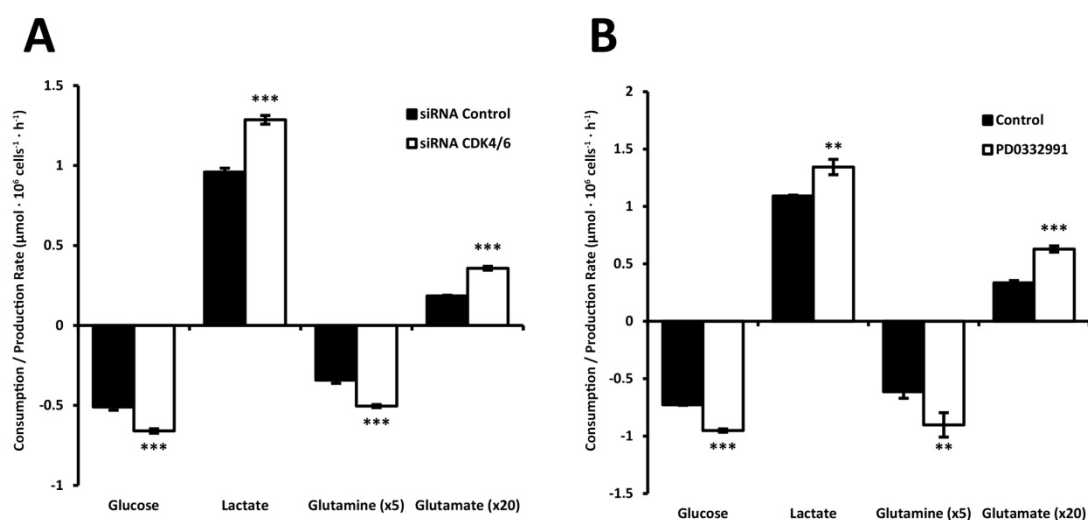
Figure 4.2.3. Comparative extracellular fluxes for control and CDK4/6-inhibited cells. Glucose and glutamine consumption and lactate and glutamate production rates were obtained after 24 h incubation with fresh media and normalised to cell number. Metabolite consumption/production and cell proliferation were determined for **A.** siRNA-transfected cells and **B.** PD0332991-treated cells. Bars represent mean ± SD of n=3. Significant differences between cells with CDK4/6 inhibition and control cells were indicated at $p < 0.01$ (**) and $p < 0.001$ (***).

To confirm the higher glycolytic rate observed in CDK4/6-inhibited cells, we measured the extracellular acidification rate (ECAR) (see Section 3.37), which essentially is a sign of the production of acid lactic (H$^+$, decrease of pH) obtained from glycolysis, with a

small contribution from the CO_2 produced in the tricarboxylic acid (TCA) cycle. As expected, CDK4/6 knockdown generated higher ECAR values than control cells (Figure 4.2.4A). In addition, the measure of ECAR in real time while adding glucose and oligomycin to cells cultured in a glucose-deprived medium allows for the identification of glycolysis (measurement rate of the glycolytic process), glycolytic capacity (maximum response to glycolytic demand from stress) and glycolytic reserve (reserve capacity available to utilise glycolysis beyond the basal rate). Figure 4.2.4B shows the ECAR profiles for control and CDK4/6-inhibited cells, illustrating the increase in glycolysis, glycolytic capacity and glycolytic reserve associated to CDK4/6 knockdown.
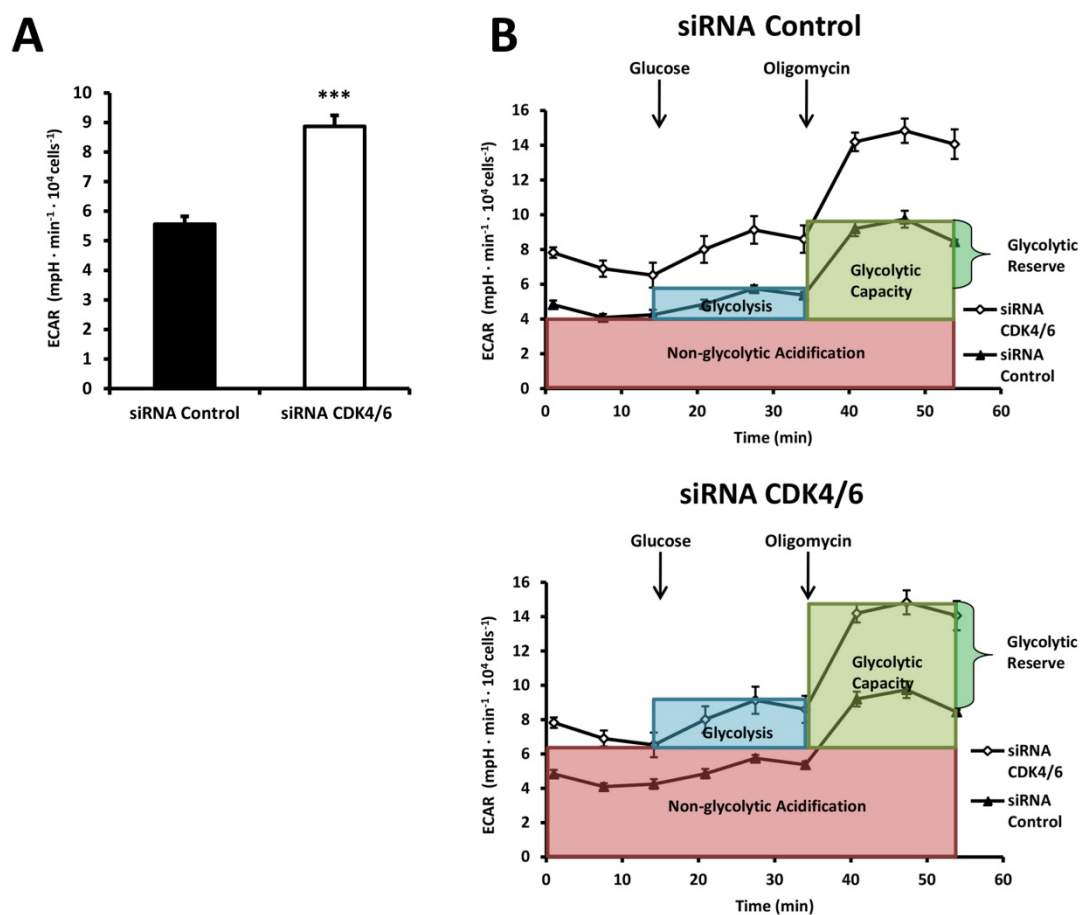
Figure 4.2.4. Comparative glycolytic profile characterisation between control and CDK4/6 knockdown cells. Extracellular acidification rate (ECAR) was determined using the Seahorse XF24 Extracellular Flux Analyser instrument. **A.** The basal ECAR rate was normalised to cell number. **B.** Representation of ECAR profiles for control and CDK4/6-inhibited cells, illustrating the increase in glycolysis, glycolytic capacity and glycolytic reserve observed in CDK4/6 knockdown cells. Cells were incubated in absence of glucose and sequential injections of glucose and oligomycin were performed in order to estimate their glycolytic profile. Data are normalised to cell number and represented as mean ± SD from n=5. Differences between cells transfected with CDK4/6 siRNA and non-targeting siRNA were considered statistically significant when $p < 0.001$ (***).

To examine the contribution of glycolysis, pentose phosphate pathway (PPP) and carbon sources other than glucose (mainly glutamine) to lactate production, we incubated the cells with $[1,2-^{13}C_2]$-glucose and measured the resulting mass isotopomer distribution in lactate (see Appendix I and Section 3.31.2) together with the initial and final lactate concentrations. $[1,2-^{13}C_2]$-glucose metabolised through direct glycolysis produces m2 lactate, whereas its redirection via PPP yields m1 lactate. Then, pathway-specific production of lactate can be calculated based on this fact by using the equations described in Section 3.34.1.

Consistent with the previous results, CDK4/6-inhibited cells presented higher production of lactate through glycolysis, the PPP and using other sources (Figure 4.2.5A). In both control and knockdown cells, direct glycolysis was the principal source of lactate while PPP only accounted for a small proportion of the total produced lactate (Figure 4.2.5A).

In order to evaluate the degree of glycolytic dependence presented by control and CDK4/6-inhibited cells, we explored the effects of glucose deprivation on cell viability. Interestingly, the reduction in cell proliferation in absence of glucose was significantly more pronounced in control cells (Figure 4.2.5B), indicating a higher sensitivity to changes in glucose availability. Despite having an enhanced glycolytic metabolism, cells treated with CDK4/6 siRNA may overcome glucose deprivation by increasing alternative metabolic pathways such as glutaminolysis or glycogenolysis, among others. Glycogen storage forms an energy reserve that can be mobilised through glycogenolysis to fulfil unexpected energetic needs and work as a metabolic survival pathway. Taking into consideration that glycogen accumulation in cancer cells improved survival under hypoxia and glucose deprivation conditions [255], we searched for differences in glycogen levels (methods are detailed in Section 3.31.8) between CDK4/6-inhibited and control cells in normoxic (21% O_2) and hypoxic (1% O_2) conditions. In agreement with their higher glucose consumption rate and better survival under glucose deprivation, cells with CDK4/6 inhibition presented higher glycogen storage than control cells (Figure 4.2.5C). In addition, hypoxia favoured glycogen accumulation only in CDK4/6-deficient cells.
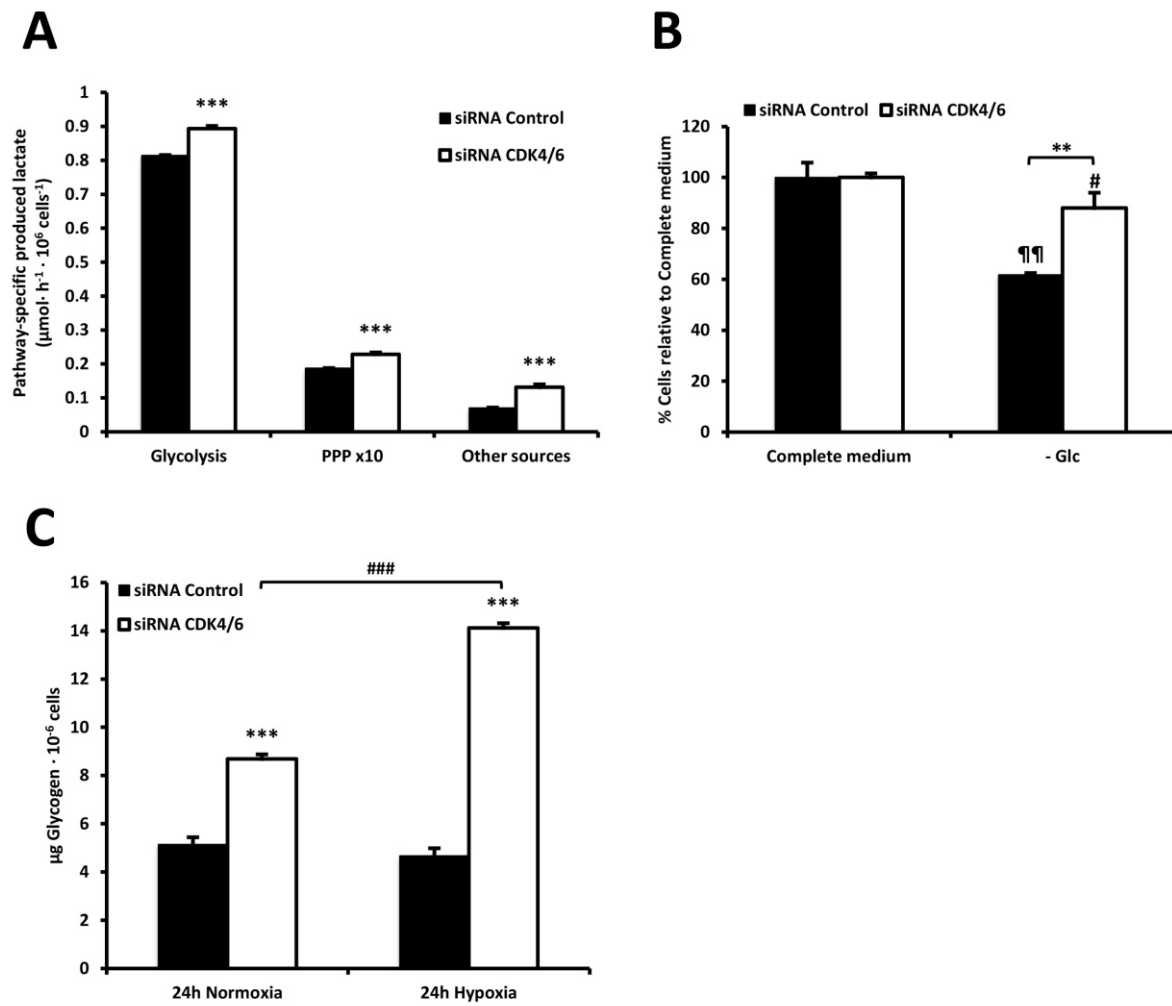
Figure 4.2.5. Glycolytic dependence profiling. A. Cells were incubated in the presence of 10 mM [1,2-^{13}C$_2$]-glucose for 24 h. Pathway-specific lactate fluxes determined by combining lactate mass isotopomer distribution data and lactate production as described in Section 3.34.1 to estimate the lactate produced from glucose through direct glycolysis, diverted through PPP and the lactate obtained from other sources. **B.** Cultures were exposed to glucose deprivation (- Glc) for 72 h and the effect on cell proliferation was determined by cell count analysis. Results are shown as a percentage of proliferation relative to the corresponding control (CDK4/6 siRNA- or non-targeting siRNA- treated cells) grown in complete medium. **C.** Quantification of glycogen in CDK4/6 knockdown and control cells after incubation under normoxic and hypoxic conditions for 24 hours (methods are detailed in Section 3.31.8). All experiments were performed 96 h after siRNA transfection. Data are provided as mean ± SD of n=3. Statistically significant differences between CDK4/6 knockdown and control cells were indicated at p < 0.01 (**) and p < 0.001 (***), while differences between treatment (glucose deprivation or hypoxia) and the corresponding control (CDK4/6 siRNA- or non-targeting siRNA- treated cells in complete medium or normoxia) were shown at p < 0.05 (#) and p < 0.001 (###) for CDK4/6-inhibited cells and at p < 0.01 (¶¶) for control cells.

4.2.2.3. CDK4/6 silencing induces an unbalance between the oxidative and non-oxidative branches of the pentose phosphate pathway

The PPP is an essential biosynthetic pathway fed by the first steps of glycolysis that produces ribose-5-phosphate for nucleotide synthesis, and NADPH for being used in other metabolic pathways and for the maintenance of the reduced glutathione pool to protect against oxidative stress. The PPP includes the non-reversible oxidative and the reversible non-oxidative branches. The oxidative branch generates NADPH and ribose-5-phosphate while the non-oxidative branch recycles pentose phosphates into glycolytic intermediates and produces ribose-5-phosphate.

Since our results indicate that CDK4/6 knockdown was associated with increased lactate production not only through glycolysis but also through PPP (Figure 4.2.5A), the mass isotopomer distribution of ribose after 24 h incubation with $[1,2-^{13}C_2]$-glucose was analysed (see Section 3.31.5). The metabolism of $[1,2-^{13}C_2]$-glucose through the oxidative branch yields m1 labelled ribose (one ^{13}C is released as CO_2), while its metabolism via the non-oxidative branch results in m2 labelled ribose (both ^{13}C are conserved), as detailed in Section 1.6.2.2.2. Accordingly, analysis of mass isotopomer distribution of ribose from RNA revealed that CDK4/6-inhibited cells presented a decrease in m1 and an increase in m2 labelled ribose (Figure 4.2.6A), illustrating an unbalance of the PPP towards the non-oxidative branch, consistent with our previous results [86]. This unbalance can be graphically represented using the isotopomer phase plane analysis of normalised ribose isotopomers m1 and m2, where values for oxidative ribose synthesis are plotted against values for non-oxidative ribose synthesis. As internal controls, we employed siRNA-mediated downregulation of the two key enzymes of the oxidative and non-oxidative branches, glucose-6-phosphate dehydrogenase (G6PD) and transketolase (TKT), respectively (Figure 4.2.6B). Indeed, inhibition of G6PD further increased the glycolytic flux through the non-oxidative branch of the PPP, while TKT inhibition reversed the effect of CDK4/6 knockdown by causing an unbalance of the PPP towards the oxidative branch (Figure 4.2.6B). In addition, TKT enzyme activity was found to be augmented 1.6-fold in CDK4/6-inhibited cells compared to control cells while the increase in G6PD enzyme activity was less pronounced (Figure 4.2.6C) (see Section 3.14 for detailed methods).
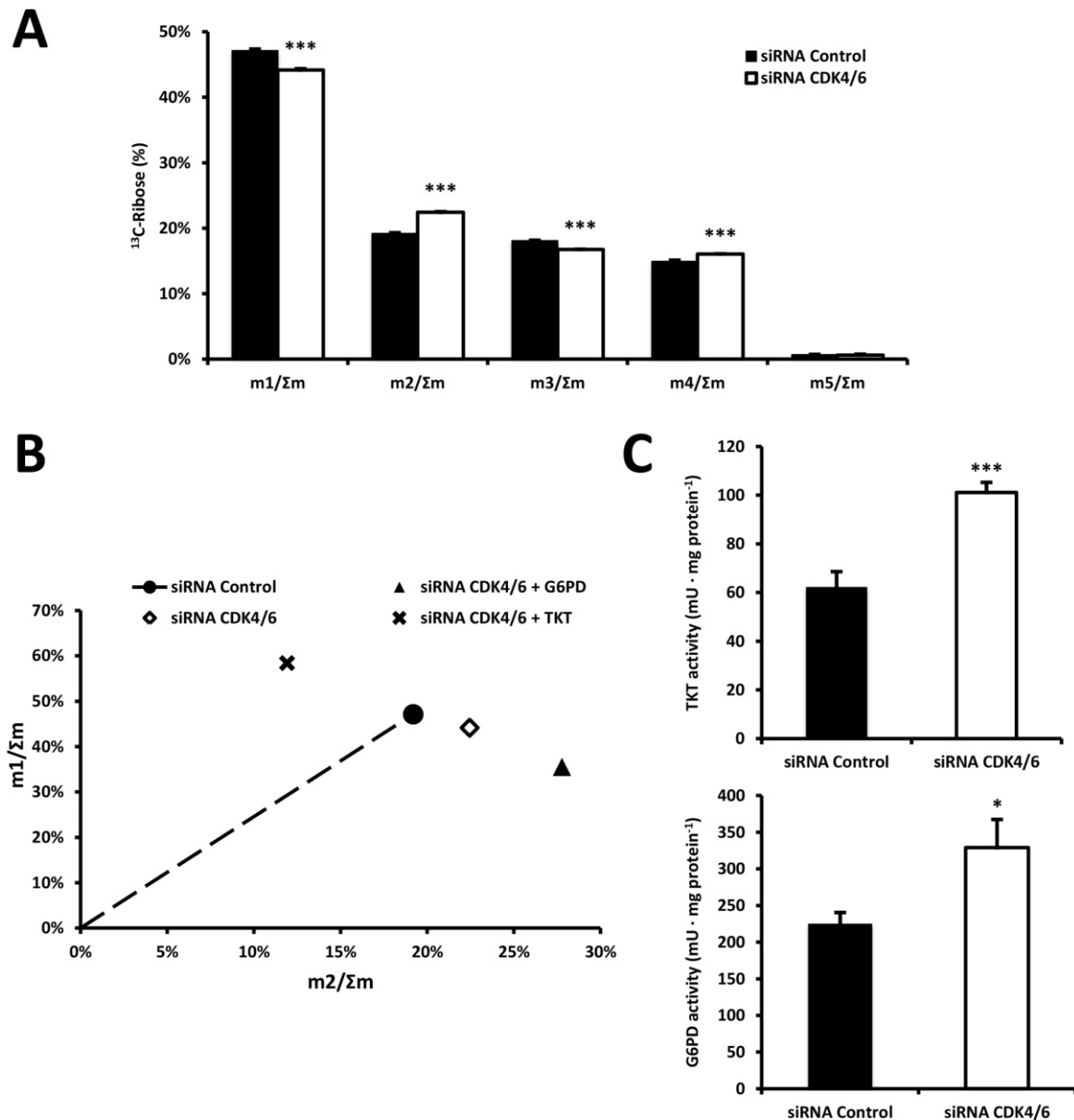
Figure 4.2.6. Pentose phosphate utilisation in CDK4/6 knockdown and control cells. Cells were incubated in the presence of 10 mM [1,2-^{13}C$_2$]-glucose for 24 h. Cell pellets were obtained at this time and ribose was isolated from RNA for mass isotopomer distribution analysis. **A.** Ribose mass isotopomer distribution normalised to total ^{13}C-Ribose label enrichment (Σm). **B.** Isotopomer phase plane analysis for ribose production depicts the contribution of the oxidative and the non-oxidative PPP branches to ribose synthesis. Ribose m1 and m2 were analysed and plotted as percentage of total ^{13}C-Ribose (Σm). The m2 isotopomers of ribose are indicative of the non-oxidative pentose phosphate pathway flux, whereas the m1 isotopomers indicate the oxidative PPP flux producing ribose. For clarity, internal controls with combined CDK4/6 and G6PD or TKT siRNA-mediated knockdown were included. **C.** Total TKT and G6PDH enzyme activities normalised to intracellular protein content. All experiments were performed 96 h after siRNA transfection. Data are represented as mean ± SD of n=3. Statistically significant differences between CDK4/6 knockdown and control cells were indicated at p < 0.05 (*) and p < 0.001 (***).

4.2.2.4. CDK4/6 silencing enhances mitochondrial metabolism

In order to complete the characterisation of the metabolic reprogramming associated to CDK4/6 knockdown, we next examined the mitochondrial metabolism using isotope-based metabolic flux analysis with ^{13}C enriched substrates (see Section 3.31). We used $[1,2\text{-}^{13}C_2]$-glucose and uniformly labelled $[U\text{-}^{13}C_5]$-glutamine tracers in independent parallel experiments. To determine the glucose contribution to the TCA cycle, we incubated the cells with $[1,2\text{-}^{13}C_2]$-glucose for 24 h and analysed the mass isotopomer distribution of the intracellular metabolites citrate, glutamate, α-ketoglutarate, malate, aspartate and pyruvate. We compared the ratios of m2 labelled metabolites to m2 pyruvate, as m2 is the most abundant mass isotopomer obtained from $[1,2\text{-}^{13}C_2]$-glucose, to have an indication of the relative amount of pyruvate that was further oxidised in the TCA cycle [510]. In fact, pyruvate is incorporated to the TCA cycle by either pyruvate dehydrogenase (PDH), pyruvate carboxylase (PC) or malic enzyme (ME2) (Figure 4.2.7A). Interestingly, CDK4/6-inhibited cells presented higher ratios of m2 citrate, glutamate, α-ketoglutarate, malate and aspartate (Figure 4.2.7B), pointing to a greater glucose contribution to the TCA cycle than in control cells.

In addition, glutamine can contribute to a greater extent than glucose to the labelling of the TCA intermediates, as a main substrate of this metabolic pathway [165], thus diluting the labelling from glucose. Having observed that CDK4/6 knockdown cells consumed more glutamine and produced more glutamate than control cells (Figure 4.2.3), we sought to examine the fate of glutamine carbons by monitoring uniformly labelled $[U\text{-}^{13}C_5]$-glutamine incorporation into TCA cycle intermediates (Figure 4.2.8A). Direct glutamine contribution to citrate (m4), glutamate (m5), α-ketoglutarate (αKG) (m5), malate (m4) and aspartate (m4) was significantly increased in CDK4/6-inhibited cells (Figure 4.2.8B), indicating that CDK4/6 knockdown enhances glutamine oxidation and consequent carbon contribution into the oxidative TCA cycle. Several recent studies have demonstrated the importance of glutamine-dependent reductive carboxylation of α-ketoglutarate to isocitrate, especially in tumour cells under hypoxic conditions or mitochondrial impairment [168-171]. The analysis of glutamine contribution to the reductive carboxylation reactions shows that CDK4/6-inhibited cells
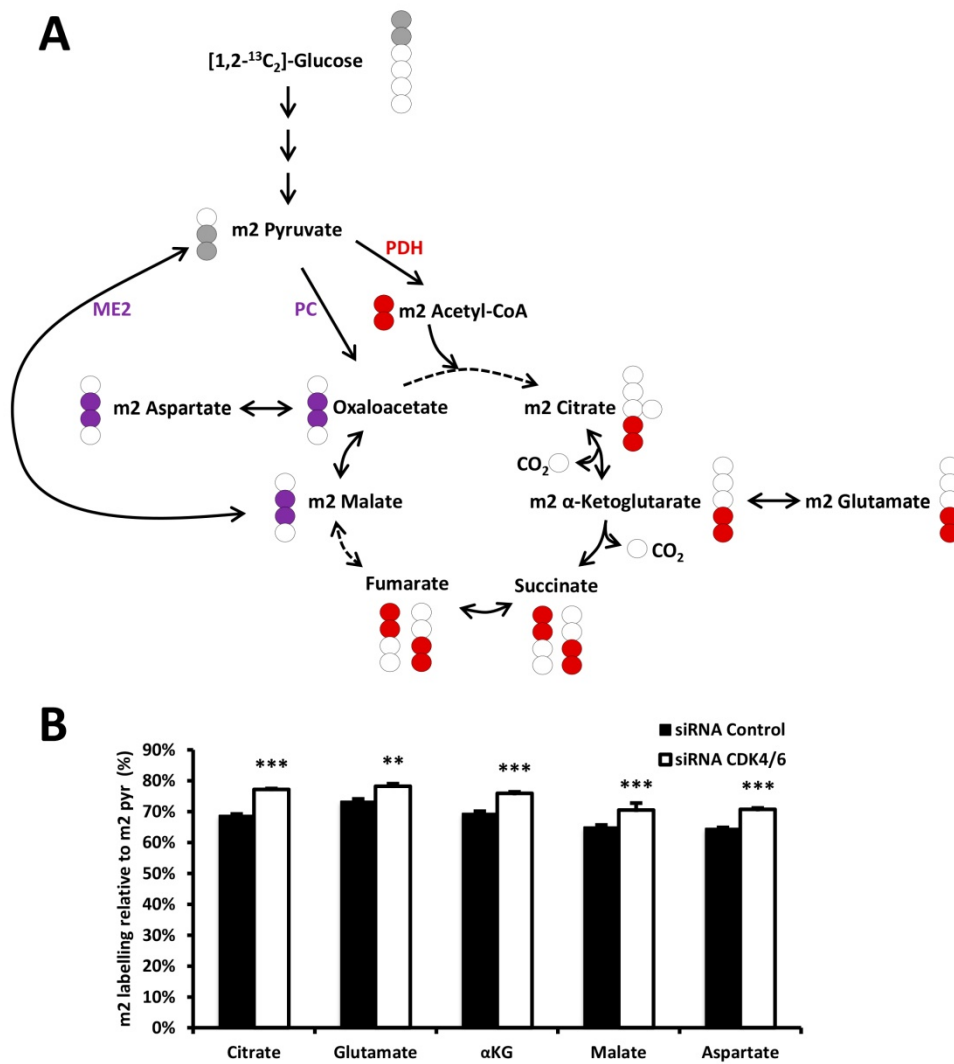
Figure 4.2.7. Glucose contribution to the TCA cycle in CDK4/6 knockdown and control cells. Cells were incubated in the presence of 10 mM [1,2-^{13}C$_2$]-glucose for 24 h and TCA intermediates were isolated from cell pellets for mass isotopomer distribution analysis. **A.** Schematic representation of the labelling distribution in TCA intermediates from [1,2-^{13}C$_2$]-glucose in the first turn of the TCA cycle. The incorporation of ^{13}C-labeling to the TCA intermediates from [1,2-^{13}C$_2$]-glucose is considered to be via pyruvate dehydrogenase (PDH), pyruvate carboxylase (PC) and malic enzyme (ME2). For clarity, only the first turn of the TCA cycle is represented. **B.** Ratio of m2 citrate, glutamate, α-ketoglutarate (α-KG), malate and aspartate normalised to m2 pyruvate (Pyr) labelling. Bars represent the mean ± SD of n=3. Statistically significant differences between CDK4/6 knockdown and control cells were indicated at p < 0.01 (**) and p < 0.001 (***).

presented higher levels of m5 citrate and m3 aspartate and malate (Figure 4.2.8C), which are the mass isotopomers generated from the reductive carboxylation of m5 α-ketoglutarate [168, 169], revealing that this metabolic pathway was more active when
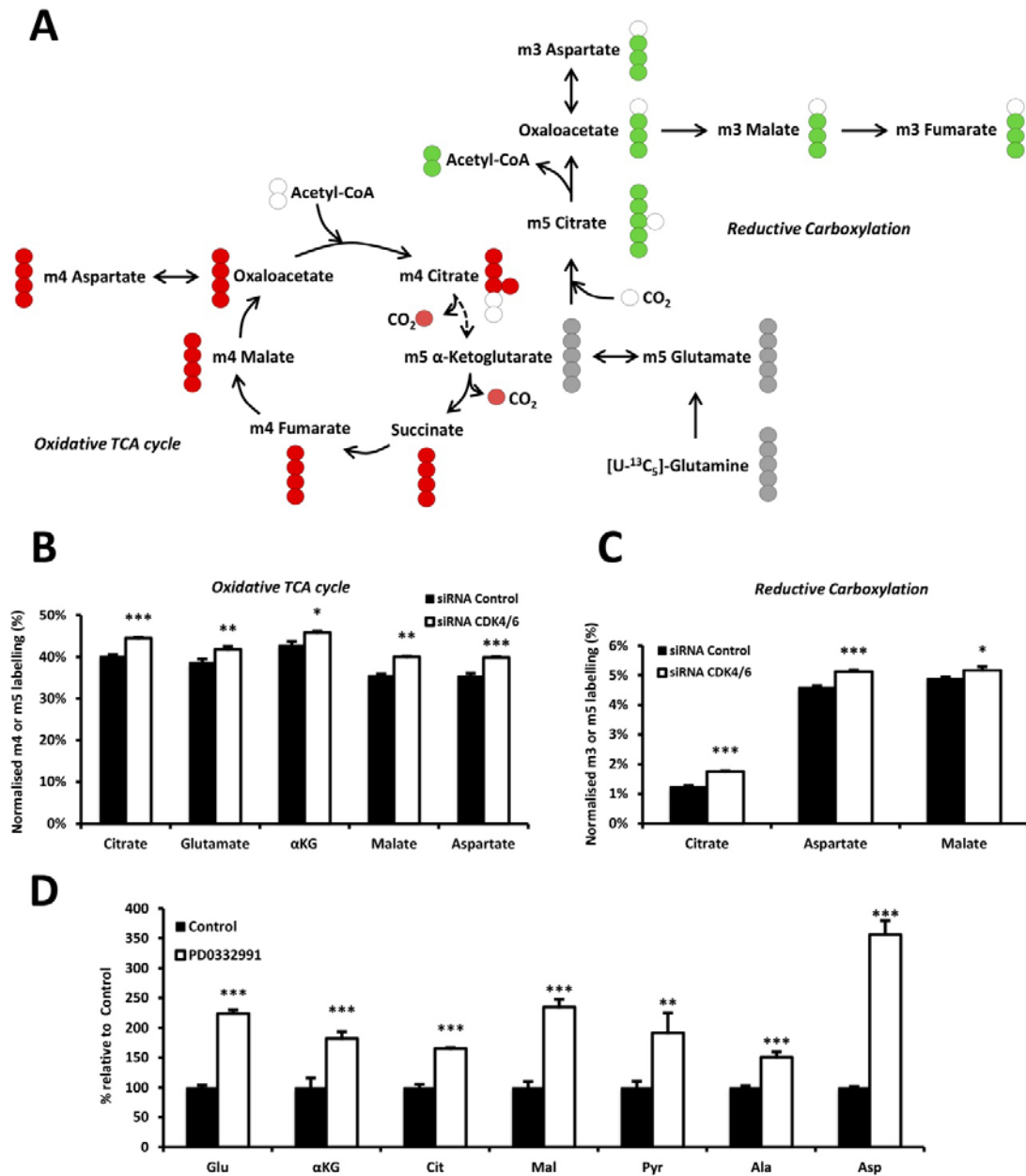
Figure 4.2.8. Glutamine contribution to the TCA cycle in CDK4/6-inhibited and control cells. Cells were incubated in the presence of 2 mM [U-^{13}C$_5$]-glutamine for 24 h and TCA intermediates were isolated from cell pellets for mass isotopomer distribution analysis. **A.** Schematic representation of the labelling distribution in TCA intermediates from [U-^{13}C$_5$]-glutamine in the first turn of the TCA cycle considering the oxidative TCA cycle (red labelling) and the reductive carboxylation (green labelling). The incorporation of ^{13}C-labeling to the TCA intermediates from [U-^{13}C$_5$]-glutamine is considered to be via glutaminase and glutamate dehydrogenase. For clarity purposes, only the first turn of the TCA cycle is depicted. **B.** Normalised m4 citrate, m5 glutamate, m5 α-ketoglutarate (αKG), m4 malate and m4 aspartate labelling are indicative of the oxidative TCA pathway. Values are normalised to total label enrichment (Σm). **C.** Normalised m5 citrate, m3 aspartate and m3 malate are obtained through the reductive carboxylation of [U-^{13}C$_5$]-glutamine. Values are normalised to total label enrichment (Σm). **D.** Quantification of intracellular metabolites per cell related to mitochondrial metabolism by GC/MS (mean ± SD of n=4). Data are represented as a percentage relative to control cells for each metabolite. Bars correspond to mean ± SD of n=3. Statistically significant differences between CDK4/6-inhibited and control cells were indicated at $p < 0.05$ (*), $p < 0.01$ (**) and $p < 0.001$ (***).

CDK4/6 were repressed. These results are consistent with the increased glutamine consumption and glutamate production previously observed in cells with CDK4/6 downregulation. Nevertheless, the relative proportion of m5 citrate, m3 aspartate and m3 malate versus m4 citrate, aspartate and malate labelled species, indicated that oxidative TCA cycle was the main pathway of glutamine metabolism in HCT116 cells (Figures 4.2.8B and 4.2.8C). As CDK4/6 knockdown cells exhibited elevated mitochondrial metabolism compared with control cells, we postulated that the concentration of TCA intermediates and related metabolites would be significantly augmented in CDK4/6-inhibited cells. Using GC/MS analysis (see Section 3.35), we confirmed that cells with CDK4/6 inhibition accumulated per cell from 1.5 to 3.5-fold more intracellular glutamate, αKG, citrate, malate, pyruvate, alanine and aspartate relative to control cells (Figure 4.2.8D).

4.2.2.5. CDK4/6 silencing increases amino acid metabolism

Having observed that CDK4/6 knockdown caused an enhanced metabolism of glucose and glutamine, we measured the consumption and production of the principal amino acids (see Sections 3.12 and 3.13) to reveal changes in their metabolic pathways. As seen in Figure 4.2.9A, cells with CDK4/6 inhibition exhibited greater production rates of aspartate (Asp), asparagine (Asn), proline (Pro), glycine (Gly) and alanine (Ala) and higher consumption rates of serine (Ser), arginine (Arg) and cysteine (Cyst). In agreement with the increased glutamine metabolism, CDK4/6 knockdown produced an enhancement of amino acid metabolism. 24 h incubation with $[1,2-^{13}C_2]$-glucose and $[U-^{13}C_5]$-glutamine allowed the analysis of the mass isotopomer distribution of alanine, aspartate, glycine, proline and serine. We observed that $[1,2-^{13}C_2]$-glucose but not $[U-^{13}C_5]$-glutamine is implicated in glycine and serine synthesis while both substrates contribute to the synthesis of the rest amino acids analysed (Appendix I). On the other hand, we assessed the consumption of some essential amino acids that can be directly degraded to acetyl-CoA and, therefore, enter the TCA cycle. CDK4/6-inhibited cells displayed higher rates of consumption for threonine (Thr), isoleucine (Ile), leucine (Leu) and lysine (Lys) (Figure 4.2.9B), in concurrence with their greater utilisation of

the TCA cycle. The consumption rates of both glucose and glutamine greatly exceeded those of other amino acids (Figures 4.2.3 and 4.2.9), indicating that they are the main substrates for anaplerosis and energy production.
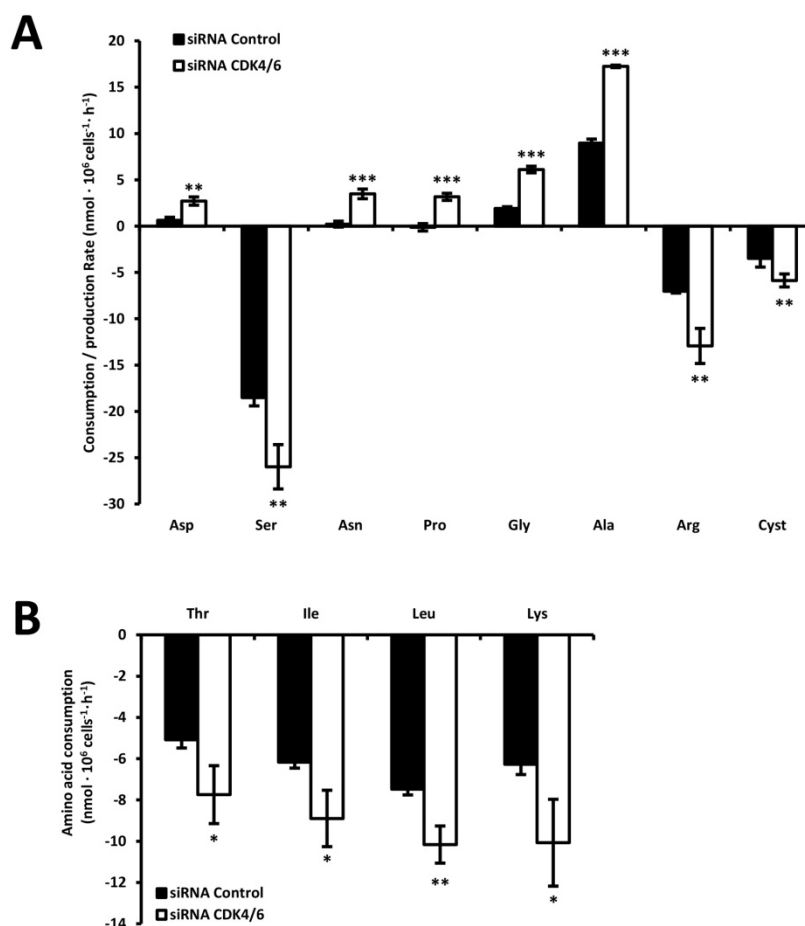
Figure 4.2.9. Amino acid metabolism in CDK4/6 knockdown and control cells. A. Non-essential and **B.** essential amino acids consumption (negative values) and production (positive values) rates. Asp, aspartate; Ser, serine; Asn, asparagine; Pro, proline; Gly, glycine; Ala, alanine; Arg, arginine; Cyst, cysteine; Thr, threonine; Ile, isoleucine; Leu, leucine; Lys, lysine. Data are shown as mean ± SD of n=3. Statistically significant differences between CDK4/6 knockdown and control cells were indicated at $p < 0.05$ (*), $p < 0.01$ (**) and $p < 0.001$ (***).

4.2.2.6. CDK4/6 silencing enhances mitochondrial respiration activity

Having observed an increased TCA cycle metabolism following CDK4/6 knockdown, we analysed whether this inhibition also caused changes in the mitochondrial respiratory capacity. To this aim, we performed a pharmacological profiling of the mitochondrial respiratory function by combining the complex V inhibitor oligomycin, the

protonophoric uncoupler FCCP, the complex III inhibitor antimycin A and the complex I inhibitor rotenone, and measuring the oxygen consumption rate (OCR) and the extracellular acidification rate (ECAR). The design of these experiments is detailed in Section 3.37. First, we analysed the effects of oligomycin addition (1 µM) on cells cultured in complete medium or medium with glucose or glutamine deprivation, since the sensitivity to mitochondrial inhibitors can change as a function of carbon source [511]. Oligomycin inhibits ATP synthase (complex V) preventing oxygen consumption for mitochondrial ATP synthesis. In complete medium, addition of oligomycin similarly decreases OCR in both control and CDK4/6-inhibited cells while in glucose deprivation, cells with CDK4/6 repressed are more sensitive to ATP synthase inhibition, as they have an enhanced mitochondrial metabolism (Figure 4.2.10A). After oligomycin treatment, cells shift their metabolism to obtain ATP through compensatory pathways, which can be detected by an increase in ECAR. However, while in complete medium CDK4/6 knockdown did not affect ECAR, control cells treated with oligomycin under either glucose or glutamine withdrawal conditions dramatically reduced the ECAR levels compared to cells with CDK4/6 inhibition (Figure 4.2.13B). In concordance with a greater dependence of CDK4/6 knockdown cells on ATP synthase and mitochondrial metabolism, sustained oligomycin treatment (72 h, 3 µM) decreased CDK4/6-inhibited cells viability to a greater extent than in control cells (Figure 4.2.10C). These results point out that CDK4/6 knockdown not only increased mitochondrial ATP synthesis, but also sensitised cells to mitochondrial respiration impairment.

The comparison of OCR and ECAR basal profiles in complete medium and in glucose- or glutamine-deprived media is shown in Figures 4.2.10D and 4.2.10E, respectively. In all cases, CDK4/6 knockdown cells exhibit higher OCR and ECAR values, corresponding to augmented mitochondrial respiration and lactate production. Under glutamine deprivation, CDK4/6-inhibited cells almost maintained the levels of basal respiration reported in complete medium and decreased the levels of acidification, evidencing a shift of glucose metabolism into TCA cycle instead of producing lactate. As expected, a drop in ECAR was reported under glucose starvation conditions, while respiration rate was largely increased (2-fold for CDK4/6-inhibited cells) as a result of the enhanced
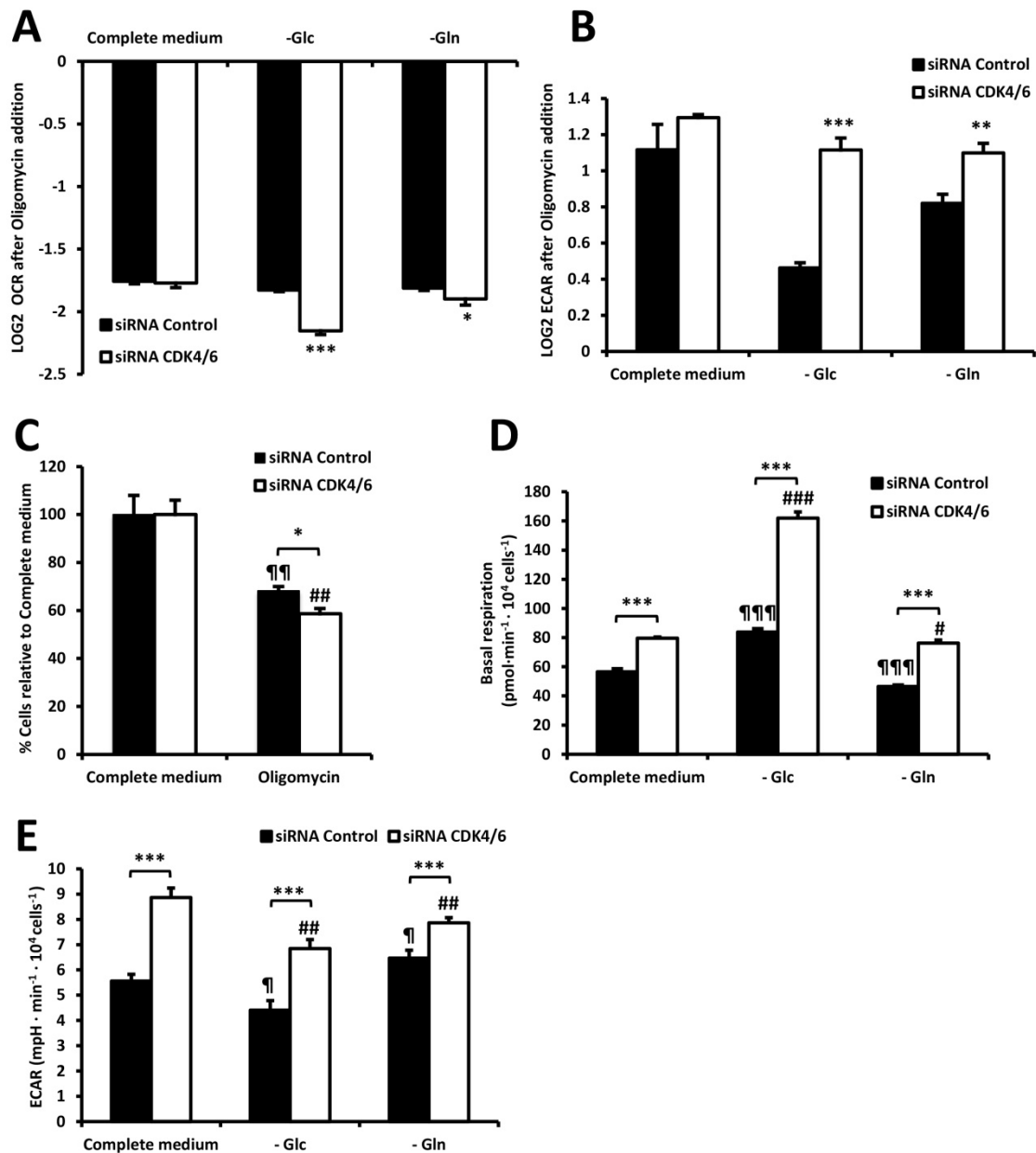
Figure 4.2.10. Characterisation of the mitochondrial function in CDK4/6 knockdown and control cells (I). Oxygen consumption rate (OCR) and extracellular acidification rate (ECAR) were determined with the Seahorse XF24 Extracellular Flux Analyser instrument. LOG2 (Fold change) in **A.** OCR and **B.** ECAR following oligomycin injection (mean ± SD of n=5). **C.** Cells were incubated with 3 μM oligomycin for 72 h and cell proliferation was measured by flow cytometry. Results are shown as percentage of proliferation relative to cells cultured in the absence of oligomycin (Complete medium) (mean ± SD of n=3). **D.** OCR and **E.** ECAR basal levels in complete and restricted media conditions, normalised to cell number (mean ± SD of n=5). Glucose and glutamine deprived media are referred as –Glc and –Gln, respectively. Cells were cultured for 1 h in glucose- or glutamine- deprived media before experimental determinations were made, and these conditions were maintained throughout the experiment. Statistically significant differences between CDK4/6 knockdown and control cells were indicated at $p < 0.05$ (*), $p < 0.01$ (**) and $p < 0.001$ (***), while differences between treatment (oligomycin, glucose or glutamine deprivation) and the corresponding control (CDK4/6 siRNA- or non-targeting siRNA- treated cells in complete medium) were shown at $p < 0.05$ (#), $p < 0.01$ (##) and $p < 0.001$ (###) for CDK4/6-inhibited cells and at $p < 0.05$ (¶), $p < 0.01$ (¶¶) and $p < 0.001$ (¶¶¶) for control cells.

mitochondrial metabolism of glutamine, one of the main sources of carbon in absence of glucose, to compensate for the reduced glycolytic ATP production.
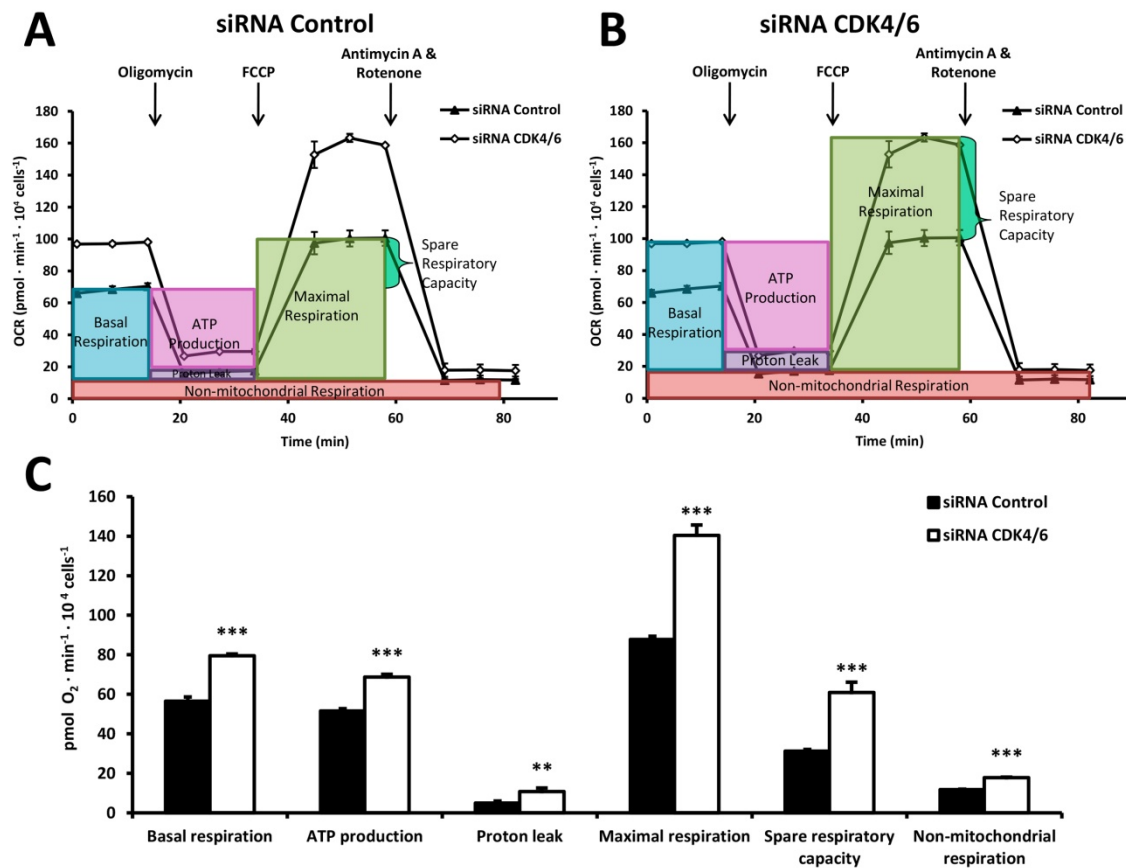
Figure 4.2.11. Characterisation of the mitochondrial function in CDK4/6 knockdown and control cells (II). Schematic representation of the OCR profiles and the subsequent estimation of the mitochondrial respiration defining parameters after the sequential injection of oligomycin (1.5 µM), FCCP (1 µM), antimycin A (1 µM) and rotenone (1 µM) in **A.** control and **B.** CDK4/6-inhibited cells cultured in complete medium. **C.** Quantification of oxygen consumption rates for basal respiration, ATP production-associated respiration, non-ATP linked oxygen consumption (proton leak), maximal respiration, spare respiratory capacity and non-mitochondrial respiration, in complete medium and normalised to cell number. Results are shown as mean ± SD of n=5. Statistically significant differences between CDK4/6 knockdown and control cells were indicated at $p < 0.01$ (**) and $p < 0.001$ (***).

The sequential addition of oligomycin (1.5 µM), FCCP (1 µM), antimycin A (1 µM) and rotenone (1 µM) in cultured cells while measuring OCR in real time, allows for the characterisation of the mitochondrial respiration capacity by estimation of its defining parameters. Figures 4.2.11 and 4.2.12 illustrate the OCR profiles obtained for CDK4/6-
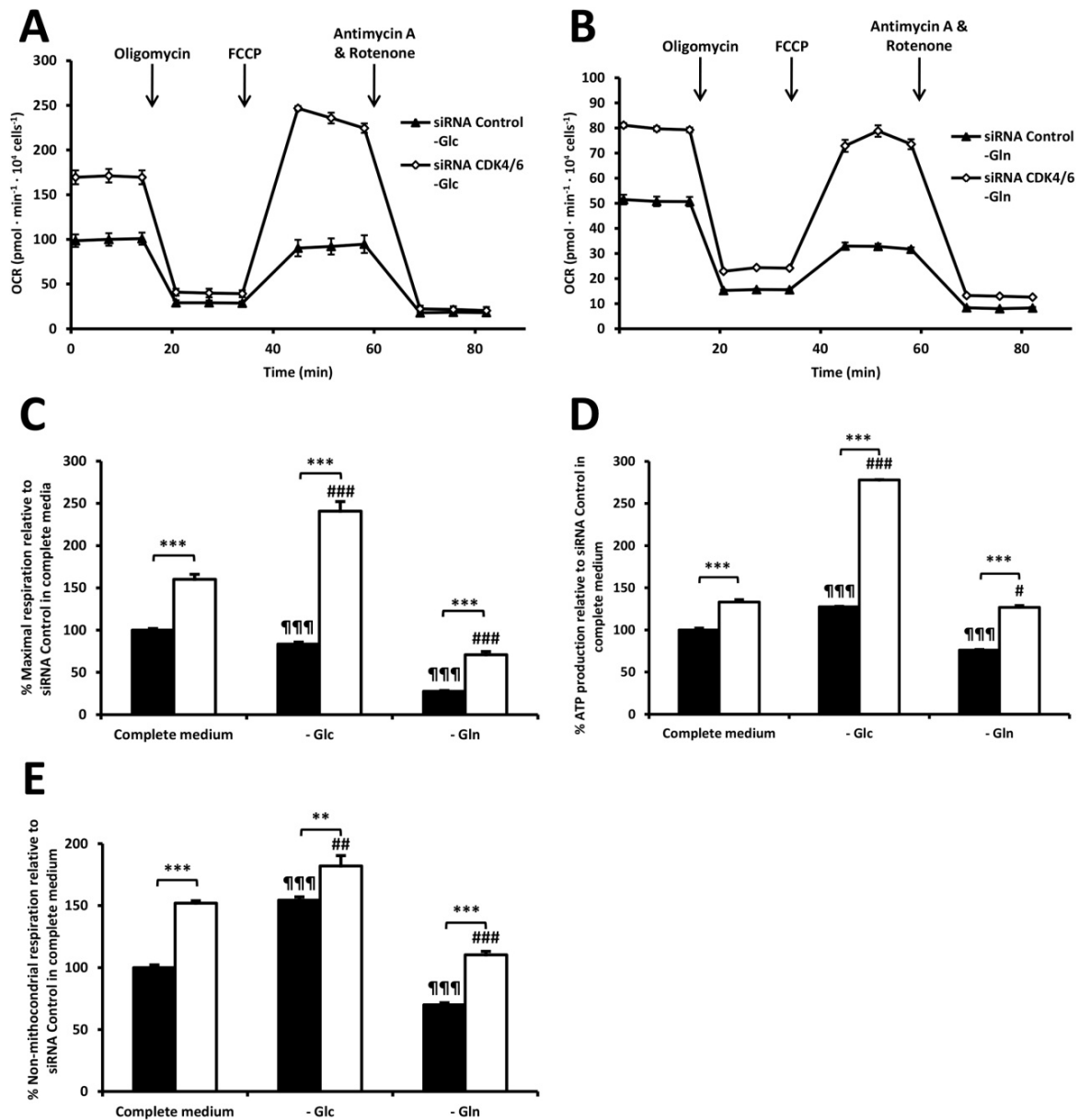
Figure 4.2.12. Effects of glucose and glutamine withdrawal on the mitochondrial function in CDK4/6 knockdown and control cells. Comparison of the OCR profiles under **A.** glucose or **B.** glutamine deprivation conditions following injections of oligomycin (1.5 µM), FCCP (1 µM), antimycin A (1 µM) and rotenone (1 µM) (mean ± SD of n=5). Glucose and glutamine deprivation effects on **C.** maximal respiration, **D.** ATP production-associated respiration and **E.** non-mitochondrial respiration. Results are normalised to cell number and shown as percentage of OCR relative to non-targeting siRNA-treated cells cultured in complete medium (mean ± SD of n=3). Cells were cultured for 1 h in glucose- or glutamine- deprived media (–Glc and –Gln, respectively) before experimental determinations were made, and these conditions were maintained throughout the experiment. Statistically significant differences between CDK4/6 knockdown and control cells were indicated at p < 0.01 (**) and p < 0.001 (***), while differences between treatment (glucose or glutamine deprivation) and the corresponding control (CDK4/6 siRNA- or non-targeting siRNA- treated cells in complete medium) were shown at p < 0.05 (#), p < 0.01 (##) and p < 0.001 (###) for CDK4/6-inhibited cells and at p < 0.001 (¶¶¶) for control cells.

inhibited and control cells in complete medium (Figures 4.2.11A and 4.2.11B) and under glucose (Figure 4.2.12A) or glutamine deprivation (Figure 4.2.12B). Remarkably, cells with CDK4/6 knockdown presented higher basal respiration, ATP production-associated respiration, non-ATP linked oxygen consumption (proton leak), maximal respiration, spare respiratory capacity and non-mitochondrial respiration than control cells, reflecting an general enhanced mitochondrial respiratory capacity (Figure 4.2.11C). Moreover, glucose removal increased the OCR values of the mitochondrial respiration parameters while glutamine deprivation decreased them (Figures 4.2.12C-E), evidencing the essential role for glutamine in supporting oxidative phosphorylation. Interestingly, when CDK4/6 are inhibited, the reduction of oxygen consumption after glutamine withdrawal was smaller and the increase of OCR in glucose starvation was higher than in control cells (Figures 4.2.10D, 4.2.12C and 4.2.12D). These results are in accordance with the increased dependency displayed by control cells on glycolysis, which is linked to the attenuation of mitochondrial oxidative phosphorylation capacity under glucose deprivation [512]. Conversely, the rise of non-mitochondrial respiration after glucose withdrawal was higher in control cells (Figure 4.2.12E), suggesting that control cells increased non-mitochondrial oxygen consuming reactions (e.g. substrate oxidation and cell surface oxygen consumption) in absence of glucose. Finally, addition
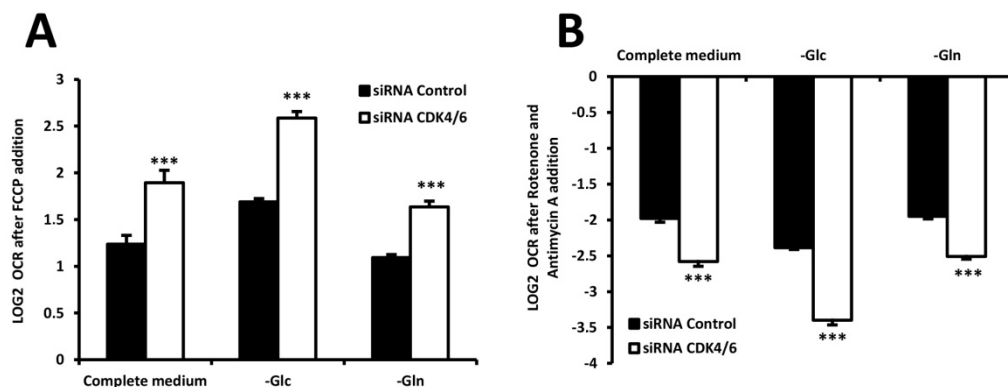
Figure 4.2.13. Effects of mitochondrial uncoupling and mitochondrial complex I and III inhibition on OCR. A. LOG2 (Fold change) in OCR after FCCP addition or **B.** rotenone and antimycin A addition in complete and restricted media. Cells were cultured for 1 h in glucose- or glutamine- deprived media (–Glc and –Gln, respectively) before experimental determinations were made, and these conditions were maintained throughout the experiment. Bars represent mean ± SD of n=3. Statistically significant differences between CDK4/6 knockdown and control cells were indicated at p < 0.001 (***).

of FCCP, rotenone and antimycin A caused significantly more pronounced effects on cells with CDK4/6 inhibition (Figures 4.2.13A and 4.2.13B), further supporting that CDK4/6 knockdown led to a more prominent mitochondrial function and respiration. Taken together, these data confirmed that CDK4/6 knockdown enhanced not only mitochondrial metabolism through elevated utilisation of glutamine, but also mitochondrial respiratory capacity.

4.2.2.7. CDK4/6 silencing increases glutathione, NADPH and ROS levels

Glutathione (GSH) is synthesised through two ATP-requiring enzymatic steps; formation of γ-glutamylcysteine from glutamate and cysteine catalysed by rate-limiting γ-glutamylcysteine synthetase (GCL), and formation of GSH from γ-glutamylcysteine and glycine catalysed by GSH synthetase (GS) [513]. Taking into account that CDK4/6-inhibited cells presented higher levels of extracellular glutamate and glycine, and consumed more cysteine (Figure 4.2.9A), we quantified the content of glutathione (see Section 3.16) and found that CDK4/6 siRNA-treated cells displayed higher intracellular
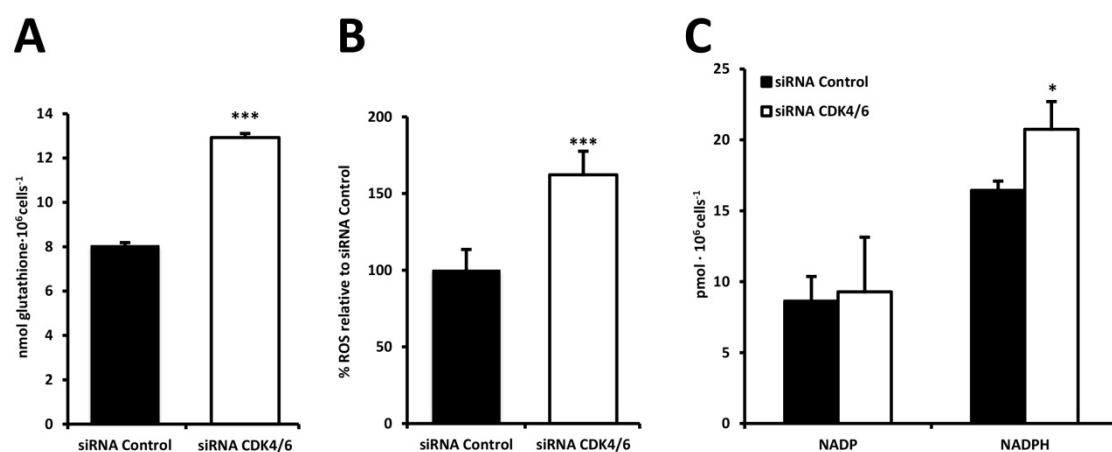
Figure 4.2.14. Intracellular glutathione, ROS and NADPH levels in CDK4/6 knockdown and control cells. A. Total intracellular glutathione content normalised to number of cells. **B.** Intracellular ROS levels determined by flow cytometry. Data are expressed as percentage of mean fluorescent intensity (MnX) relative to control cells. **C.** NADP and NADPH levels quantified in a colorimetric assay using the NADP/NADPH Quantification Kit (Ref. MAK038, Sigma-Aldrich) as described in Section 3.17 and normalised to cell number. Bars correspond to mean ± SD of n=3. Statistically significant differences between CDK4/6-inhibited and control cells were indicated at $p < 0.05$ (*) and $p < 0.001$ (***).

levels of GSH than control cells (Figure 4.2.14A), suggesting that a proportion of the cysteine consumed and the glutamate and glycine produced could be redirected to the synthesis of glutathione. GSH peroxidase (GPx)-catalyses the antioxidant function of GSH, reducing peroxides as GSH is oxidised to GSSG, which in turn is reduced back to GSH by GSSG reductase at the expense of NADPH, forming a redox cycle [513]. The increased presence of glutathione caused by CDK4/6 knockdown could be explained as a protection against generated oxidative stress. To test this hypothesis, NADP/NADPH and reactive oxygen species (ROS) levels were assessed (as described in Sections 3.17 and 3.18, respectively). In agreement, higher amounts of ROS and NADPH were observed in CDK4/6-inhibited cells (Figures 4.2.14B and 4.2.14C).

4.2.2.8. CDK4/6 silencing impairs fatty acid synthesis

Since fatty acid synthesis is essential for cell proliferation, we analysed the mass isotopomer distribution of palmitate, the first fatty acid synthesised in lipogenesis, and stearate, obtained from palmitate by chain elongation, after 24 h incubation with $[1,2\text{-}^{13}C_2]$-glucose or $[U\text{-}^{13}C]$-glutamine (see Section 3.31.6). When cultured with $[1,2\text{-}^{13}C_2]$-glucose, we observed that CDK4/6 knockdown cells presented higher levels of m2 and m4 labelled palmitate and stearate, while control cells displayed increased m6 and m8 labelled fatty acid isotopomers (Figures 4.2.15A and 4.2.15B). Taking into account that the label propagation into fatty acids was not reaching the steady state, and therefore was a dynamic phenomenon, the mass isotopomers m2-m4 and m6-m8 correspond to recent and remote enrichments, respectively. Accordingly, our results suggest that control cells directed a greater amount of glucose-derived carbons into fatty acid synthesis compared to CDK4/6-inhibited cells. To determine the glutamine contribution to fatty acid synthesis, we examined the label incorporation into palmitate and stearate following $[U\text{-}^{13}C]$-glutamine incubation, which mainly derives from reductive metabolism of glutamine [514]. Likewise, cells with CDK4/6 inhibition presented an increase in m2 palmitate and m2 stearate, and a decrease in m4 isotopomers in comparison to control cells (Figures 4.2.15C and 4.2.15D). These results

suggest that fatty acid synthesis may be greater in control cells, which is consistent with the reduced cell proliferation observed in CDK4/6 knockdown cells.
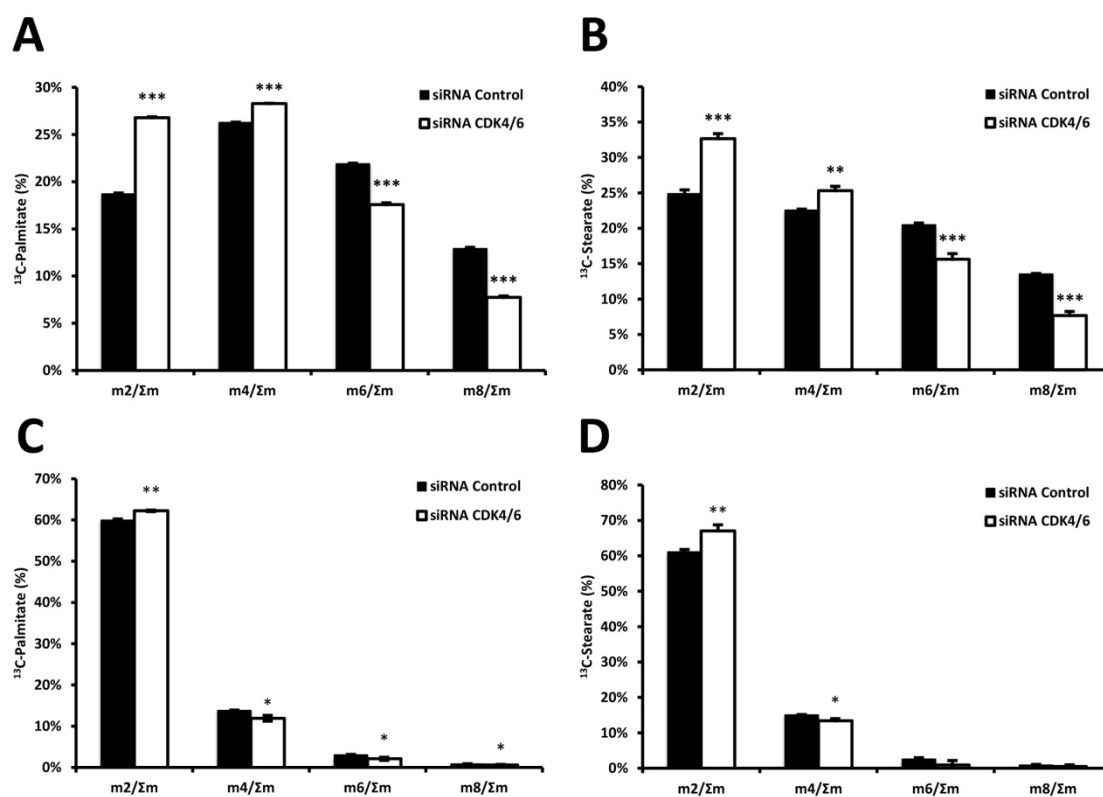
Figure 4.2.15. Fatty acid synthesis in CDK4/6 knockdown and control cells. Mass isotopomer distribution of **A.** palmitate and **B.** stearate after 24 h incubation with 10 mM [1,2-$^{13}C_2$]-glucose. **C.** Mass isotopomer distribution of **C.** palmitate and **D.** stearate after 24 h incubation with 2 mM [U-^{13}C]-glutamine. Bars represent mean ± SD of n=3. Statistically significant differences between CDK4/6 knockdown and control cells were indicated at $p < 0.05$ (*), $p < 0.01$ (**) and $p < 0.001$ (***).

4.2.2.9. Fluxomics and transcriptomics data analysis revealed MYC, HIF1 and mTOR as the key players in CDK4/6 knockdown

4.2.2.9.1. Gene expression profile

To study CDK4/6 knockdown-mediated changes in the robust metabolism of tumour cells, we analysed differences in gene expression between CDK4/6 siRNA- and non-targeting siRNA- treated cells. High-throughput gene expression analysis using *Affymetrix GeneChip* arrays (see Section 3.30) identified 1283 genes whose expression

differed by >1.5-fold between CDK4/6 knockdown and control cells, with 576 and 707 genes down- and upregulated in CDK4/6-inhibited cells, respectively.

We used gene expression to explore the two levels of metabolic reprogramming, namely direct changes in the expression of enzymes and changes in sets of genes revealing the activation or inhibition of key regulatory proteins of cancer and metabolism. In order to identify these proteins, genetic association studies were performed using Gene Set Enrichment Analysis (GSEA) [478] looking for associated gene signatures, which provided the evidence of partially shared mechanisms between CDK4/6 inhibition and other treatments affecting regulatory factors with a key role in cancer and metabolism. A summary with the most interesting results is provided in Figure 4.2.16 and in Appendix II. Likewise, manual examination of the list of significantly enriched genes suggested that several signal transduction networks were affected upon CDK4/6 inhibition. Among the large list of affected components and mechanisms, we focused our attention on a selection of gene sets with a high correlation and derived from components or functions associated with the regulation of metabolism, cancer and/or cell cycle. Accordingly, Figure 4.2.17 and Appendix II highlight GSEA enrichment plots associated with gene signatures for c-MYC (hereafter termed MYC) (HALLMARK_MYC_TARGETS_V1, HALLMARK_MYC_TARGETS_V2, SCHUHMACHER_ MYC_TARGETS_UP [515], DANG_MYC_TARGETS_UP [229] and BILD_MYC_ONCOGENIC_ SIGNATURE [464]), hypoxia (HALLMARK_HYPOXIA, MANALO_ HYPOXIA_UP, MANALO_HYPOXIA_DN [516], ELVIDGE_HYPOXIA_UP, ELVIDGE_ HYPOXIA_DN [245], MENSE_HYPOXIA_UP [517], FARDIN_HYPOXIA_11 [518] and LEONARD_HYPOXIA_UP [519]), hypoxia inducible factor 1α (HIF1α) (ELVIDGE_ HIF1A_TARGETS_UP, ELVIDGE_HIF1A_TARGETS_DN, ELVIDGE_HIF1A_AND_HIF2A_ TARGETS_UP and ELVIDGE_HIF1A_AND_HIF2A_TARGETS_DN) [245], molecular target of rapamycin (mTOR) (PENG_RAPAMYCIN_RESPONSE_DN) [520], FOXO3a (DELPUECH_ FOXO3_TARGETS_UP) [521] and KRAS (HALLMARK_KRAS_SIGNALING_UP). Interestingly, the direction of gene expression changes (increase or decrease) associated with CDK4/6 inhibition was positively correlated with gene sets associated with MYC activity, but negatively with gene sets associated with HIF 1α transcriptional
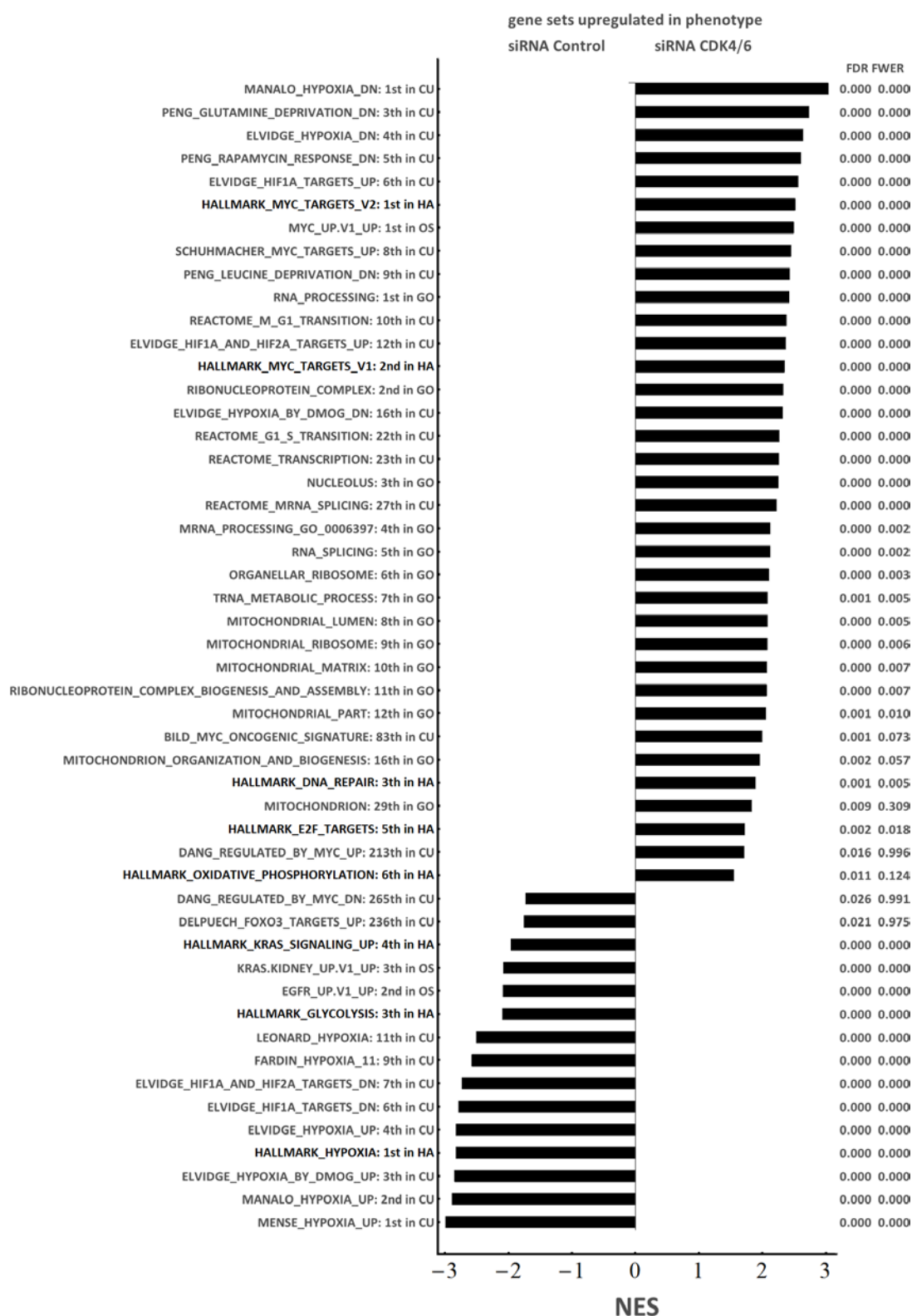
Figure 4.2.16. Associated gene sets. Genetic association studies were performed using Gene Set Enrichment Analysis (GSEA). The specific gene sets from the MSigDB collection [478] that were relevant in our analyses and presented the most significant enrichments according to GSEA's statistics are detailed. Gene sets upregulated in CDK4/6 knockdown cells are represented with positive normalised enrichment score (NES) values, while negative NES values correspond to gene sets downregulated in CDK4/6 knockdown. HA, CU, GO and OS refer to the Hallmark gene sets (in black), Curated gene sets, GO gene sets and Oncogenic signatures collections, respectively.

activity, KRAS signalling or the inhibitor of prolyl hydroxylases (PHD) DMOG (ELVIDGE_ HYPOXIA_BY_DMOG_UP and ELVIDGE_HYPOXIA_BY_DMOG_DN) [245].
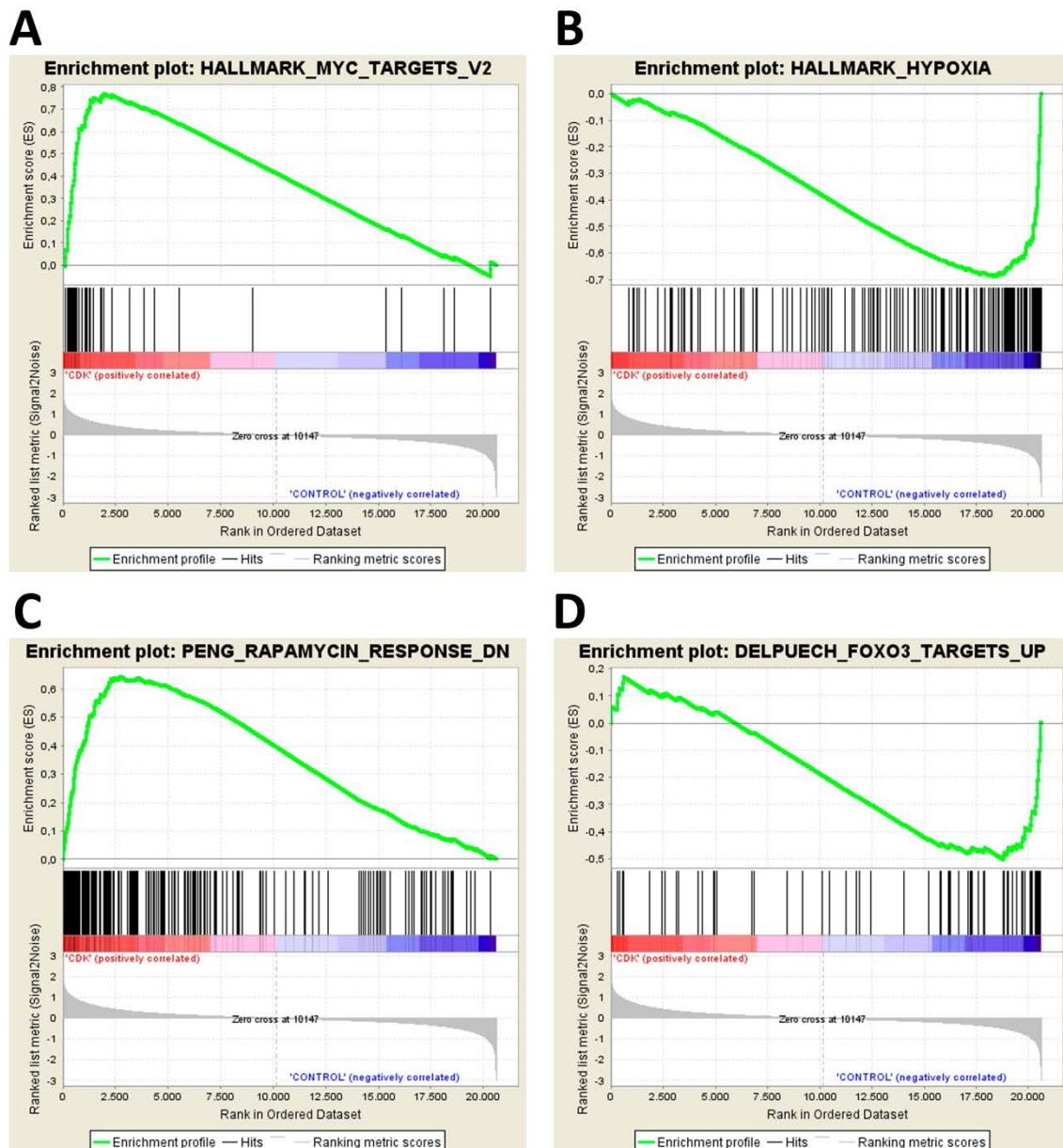
Figure 4.2.17. Examples of GSEA enrichment plots associated with gene signatures for MYC (HALLMARK_MYC_ TARGETS_V2), hypoxia (HALLMARK_HYPOXIA), mTOR (PENG_RAPAMYCIN_RESPONSE_DN) and FOXO3a (DELPUECH_FOXO3_TARGETS_UP). Gene expression changes of cells with CDK4/6 inhibition were positively correlated with gene sets associated with MYC and mTOR activity, since MYC target genes and genes that are downregulated by the mTOR inhibitor rapamycin were found to be upregulated in CDK4/6 knockdown cells in comparison to control cells. Conversely, gene expression changes of CDK4/6-inhibited cells were negatively correlated with gene sets associated with hypoxia and FOXO3a activation, as genes that are upregulated under hypoxia and FOXO3a target genes were found to be downregulated in cells with CDK4/6 knockdown compared to control cells. A summary with the most interesting results is provided in Appendix II.

160

The differentially expressed genes encoding enzymes of the central carbon metabolism were identified using, among others, human genome-scale databases [522, 523], and are listed in Appendix III, together with other key genes differentially expressed and involved in cell cycle and cancer. Importantly, gene set enrichment analysis revealed enrichment of genes associated with MYC among the upregulated genes in CDK4/6 knockdown cells (Appendix II and Figure 4.2.17). Indeed, genes of glutamine and polyamine metabolism or genes with a role in mitochondrial biogenesis and function were found overexpressed compared to control cells, which is in agreement with the experimentally observed increased respiratory activity and mitochondrial function. The increased metabolic activity reported after CDK4/6 knockdown agrees with the hypothesis of an increased activity of MYC as the major metabolic effector affected by inhibition of CDK4/6. Besides, GSEA reveals important correlations with gene sets associated with other key metabolic regulators, as summarised in Appendix II. For example, HIF1α responsive genes were downregulated in CDK4/6-inhibited cells, revealing an opposite correlation with the hypoxic gene signature (Figure 4.2.17 and Appendix II). Likewise, cells with CDK4/6 knockdown displayed a reverse correlation with the expected pattern under glutamine or leucine deprivation (PENG_GLUTAMINE_DEPRIVATION_DN and PENG_LEUCINE_DEPRIVATION_DN) [520] (Appendix II). Hence, the observed transcriptional changes suggested that CDK4/6 knockdown sensitised cells to hypoxia and caused a dependence on MYC and its target genes and/or mTOR pathway.

4.2.2.9.2. Fluxomics analysis revealed an increased metabolism of glucose, glutamine and amino acids in CDK4/6-inhibited cells

To infer intracellular metabolic fluxes, we constructed a quantitative metabolic network model of the central carbon metabolism (glycolysis, TCA cycle, pentose-phosphate pathway (PPP), glycogen metabolism, nucleotide metabolism and fatty acid synthesis) and applied metabolic flux analysis to identify a flux distribution fitting the experimental data obtained. To this end, we combined direct measurements like oxygen consumption or metabolite consumption/production rates with the resulting

mass isotopomer distributions of glucose, lactate and amino acids from incubation media, and glycogen, RNA ribose, fatty acids and glycolytic and TCA intermediates from cells. In order to test the hypotheses regarding flux ratios, the mass isotopomer distribution of each measured metabolite was mathematically predicted by assuming a metabolic network and a particular distribution of fluxes through this network. By comparing measured and predicted mass isotopomer distributions, the reliability of hypotheses regarding flux distributions was evaluated. Thus, a computer programs was developed with Mathematica [524] and applied to predict the ^{13}C enrichments for control and CDK4/6 inhibited cells. A review on the different methods related to estimation of changes in reaction fluxes using ^{13}C-labeling has been recently published [525]. Mass isotopomer distributions were mathematically predicted by assuming a metabolic network and a particular distribution of fluxes through this network. The estimation of the reaction fluxes involved in central carbon metabolism reprogramming was based on the addition of successive constraints. In order to satisfy all constraints, the range of possible values for each flux can be determined using linear programming techniques where each reaction flux is maximised or minimised while leaving all other reaction fluxes free [526-528]. Notes on the selected metabolic network for model analysis and a detailed description of the procedure and results are provided in Appendix IV. The predicted ^{13}C label enrichments are shown as coloured dots on the measured values in Appendix IV, allowing the comparison of the estimated ^{13}C-labeled values with the measured ^{13}C-labeled mass isotopomers.

Then, by integrating the metabolic phenotype with the gene expression profile exhibited by CDK4/6 knockdown cells, we identified suitable candidates for combination therapies from central metabolism enzymes and gene regulators. The integrated picture obtained from all our experiments is in part represented in Figure 4.2.18. This figure provided a metabolic scenario, a network of enzyme-catalysed transformations of chemical species, with each chemical reaction associated with a rate (flux) of transformation, which can be increased, decreased or maintained unchanged. Each reaction is catalysed by an enzyme or block of enzymes, which are regulated as a system by different layers of regulatory circuits, with the effect of the
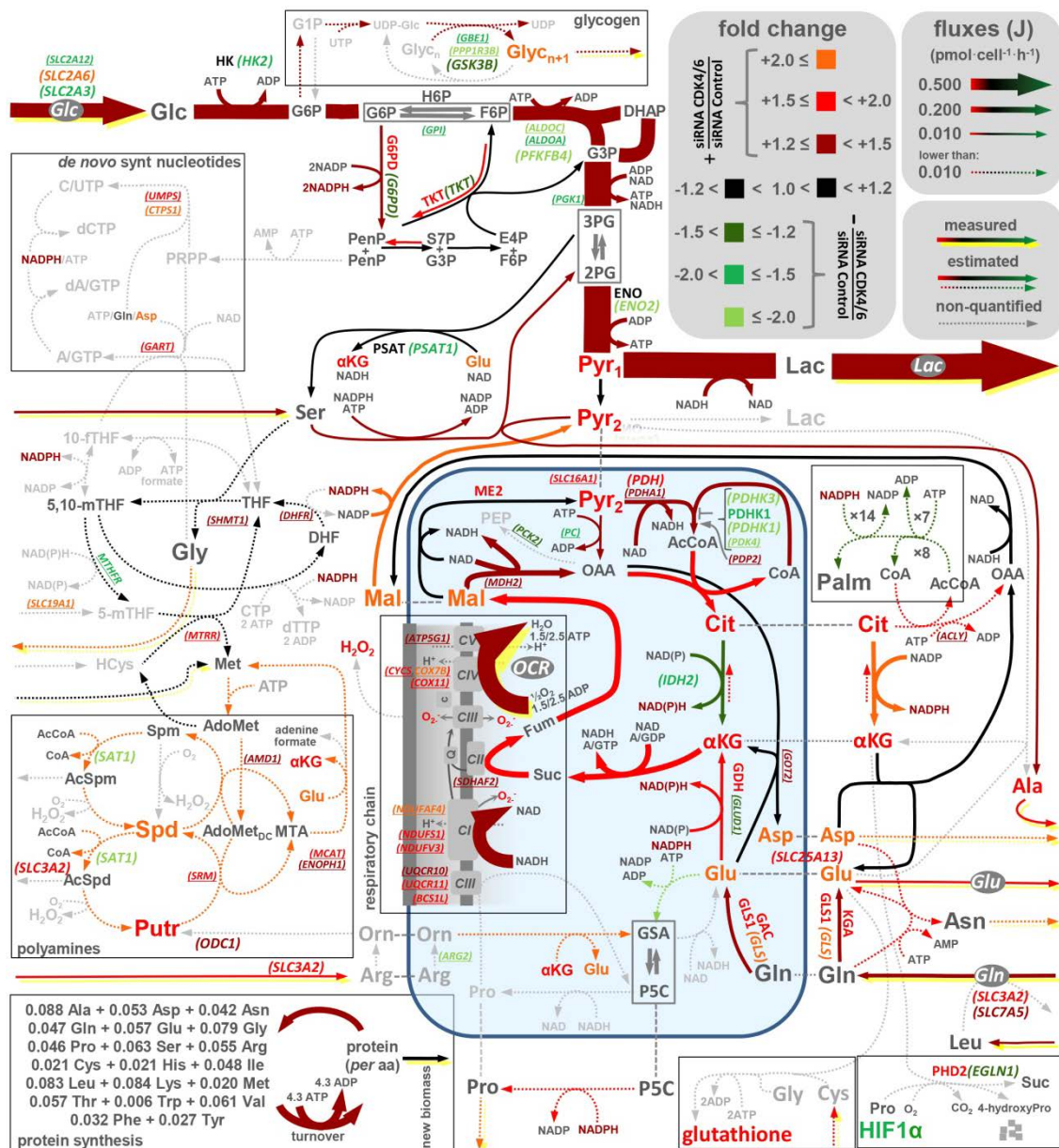
Figure 4.2.18. Integrated picture of metabolic and gene expression changes. The metabolic network contains a graphic description of both reaction and transport processes involved in the conversion or transport of metabolic intermediates. Fold changes refer to CDK4/6 inhibited cells with respect to control cells, providing a measure of the changes in the flux through the metabolic steps (coloured arrows), the expression levels of genes and proteins (coloured abbreviations) and the concentrations of some of the metabolic intermediates (coloured abbreviations). Changes in the expression or enzyme activity of key metabolic and regulatory proteins were assessed by Western blot and enzymatic activity assays, respectively, and are indicated in coloured **bold** letters. Changes in gene expression measured by RT-qPCR are represented in coloured *italic* type between round brackets. Changes in gene expression identified from the normalised RMA expression data obtained from the *Affymetrix GeneChip* arrays are presented in coloured <u>underlined</u> *italic* type between round brackets. The magnitude of the fluxes refers to control cells. Proline and asparagine are only exported in CDK4/6-inhibited cells. 10-fTHF, 10-formyltetrahydrofolate; 2PG, 2-phosphoglycerate; 3PG, 3-phosphoglycerate; 5,10-mTHF, 5,10-methenyltetrahydrofolate; 5-mTHF, 5-methyltetra hydrofolate; αKG, α-ketoglutarate; acCoA, Acetyl-CoA; AcSpd, N^1-acetylspermidine; AcSpn, N^1-acetylspermine;

identified main regulatory actors expected to be the most important. Together, these results allowed for a direct comparison of the changes affecting fluxes, accumulation of metabolic intermediaries and level of expression / activity of the metabolic enzymes catalysing the reactions. An exploration tour of this integrated picture provides a precise assessment of the metabolic adaptations associated with CDK4/6 inhibition.

Therefore, the metabolic reprogramming associated with the inhibition of CDK4/6 rendered cancer cells highly dependent on specific metabolic enzymes or pathways, which were identified as key components of the homeostatic machinery with the double objective to provide cells with the building blocks and energy required for cell function and biomass generation. Accordingly, the identification of central metabolism enzymes or gene regulators changing their activity as a consequence of tumour reprogramming provided the evidence of regulatory components that might be fundamental for the maintenance of the tumour metabolic condition, highlighting potential weaknesses that might be exploited for cancer therapy. Among the dysregulated enzymes, the most promising candidate found for a combined therapy with the inhibition of CDK4/6 was glutaminase 1 (GLS1). Thus, drugs involved in the inhibition of the metabolic reprogramming presented by tumour cells with CDK4/6 downregulation are potential candidates for synergistic interactions in combined therapies with CDK4/6 inhibitors.

AdoMet$_{DC}$, S-adenosyl 3-(methylthio)propylamine; Ala, alanine; Arg, arginine; Asn, asparagine; Asp, aspartate; CoA, Coenzyme A; Cys, cysteine; DHAP, dihydroxyacetone phosphate; DHF, dihydrofolate; E4P, erythrose 4-phosphate; ENO, enolase; Fum, fumarate; G1P, glucose 1-phosphate; G3P, glyceraldehyde 3-phosphate; G6P, glucose 6-phosphate; G6PD, glucose-6-phosphate dehydrogenase; GABA, gamma-amino butyric acid; GDH, glutamate dehydrogenase; Glc, glucose; Gln, glutamine; Glu, glutamate; GLS1, glutaminase 1; Gly, glycine; Glyc, glycogen; GSA, L-glutamate 5-semialdehyde; H6P, hexose 6-phosphate (G6P+F6P); His, histidine; HK, hexokinase; Ile, isoleucine; Lac, lactate; Leu, leucine; Lys, lysine; Mal, malate; ME2, malic enzyme; Met, methionine; MTA, 5'-S-methyl-5'-thioadenosine; OAA, oxaloacetate; OCR, oxygen consumption rate for ATP production; Orn, ornithine; P5C, Δ^1-pyrroline-5-carboxylate; Palm, palmitate; PDH, pyruvate dehydrogenase; PDHK1, pyruvate dehydrogenase kinase 1; PenP, pentose phosphate; PHD2, prolyl hydoxylase 2; Phe, phenylalanine; Phser, o-phospho-L-serine; Pro, proline; PRPP, 5-phospho-α-D-ribose 1-diphosphate; PSAT, phosphoserine transaminase; Put, putrescine; Pyr1, pyruvate (pool 1); Pyr2, pyruvate (pool 2); ROS, reactive oxygen species; Rib, ribose; S7P, Sedoheptulose 7-phosphate; Ser, serine; Spd, spermidine; Spn, spermine; Stear, stearate; Suc, succinate; Thr, threonine; TA, transaldolase; THF, tetrahydrofolate; TKT, transketolase; Trp, tryptophan; Tyr, tyrosine; Val, valine.

It is noteworthy to mention that changes in the capacity of an individual enzyme can be translated in a change in the collective flux of the metabolic pathway when the enzyme affected corresponds to a key regulatory enzyme, such as pyruvate dehydrogenase (PDH). Also, changes in the capacity of an individual enzyme can be translated in a change in the collective flux when there is a simultaneous multisite modulation of the activities of all the enzymes with some control in the flux of the pathway [529]. Accordingly, CDK4/6 knockdown cells exhibited a remarkable collective increase of the expression of genes involved in the respiratory chain and oxidative phosphorylation (MITOCHONDRION, HALLMARK_OXIDATIVE_PHOSPHORYLATION, MITOCHONDRIAL_LUMEN, MITOCHONDRIAL_RIBOSOME, MITOCHONDRIAL_MATRIX, MITOCHONDRIAL_PART and MITOCHONDRION_ORGANIZATION_AND_BIOGENESIS, as detailed in Appendix II) in concordance with the increased mitochondrial activity. However, gene expression analysis also showed that cells with CDK4/6 inhibition presented a notable collective decrease in the expression of genes involved in glycolysis (HALLMARK_GLYCOLYSIS, Appendix II) that was not in correspondence with the enhanced glycolytic metabolism experimentally reported in CDK4/6 knockdown cells (Section 4.2.2.2.). Nevertheless, the downregulation of the expression of these genes can be explained by the opposite correlation with hypoxia and HIF1α responsive genes observed in CDK4/6-inhibited cells (Figure 4.2.17 and Appendix II), as glycolytic genes are also categorised as HIF1α targets [212].

4.2.2.10. CDK4/6 knockdown causes HIF1α degradation, MYC accumulation and activation of mTOR pathway

The integration of data into the informatics system analysis revealed MYC, mTOR and HIF1α as the principal regulators in CDK4/6 knockdown. To validate the conclusions of the system analysis, we examined by Western blot the expression of these proteins under normoxic (21% O_2) and hypoxic (1% O_2) conditions, and in presence of the prolyl hydroxylase (PHD) inhibitor DMOG. We also analysed prolyl hydoxylase 2 (PHD2) levels as it is reported to be the major isoform responsible for the hydroxylation of HIF1α in normoxia [243] and the principal target for the α-ketoglutarate-mediated reduction in

HIF1α expression in hypoxia [248]. It is worth noting that direct phosphorylation of mTOR at Ser2448 by S6 kinase 1 (S6K1) in a feedback loop mechanism is a biomarker for the activation status of mTOR [530]. Glutaminase 1 (GLS1) protein levels were also assessed since this metabolic enzyme is known to be regulated by MYC [214]. In normoxia, MYC, P-mTOR (Ser2448) and GLS1 are highly overexpressed in CDK4/6-inhibited cells while HIF1α expression is significantly decreased along with higher levels of PHD2 (Figure 4.2.19A). On the other hand, hypoxia incubation completely depressed MYC and P-mTOR levels in control cells while CDK4/6 knockdown cells presented at least some degree of protein expression (Figures 4.2.19A and 4.2.26D). Glutaminase was also reduced in hypoxia but CDK4/6-inhibited cells maintained higher expression levels than control cells. Interestingly, CDK4 and CDK6 protein levels were also decreased in hypoxia. Incubation with DMOG, which stabilises HIF1α expression by competitively inhibiting PHD activity, caused a similar effect as hypoxia in MYC expression although GLS1, P-mTOR and PHD2 were increased or unaltered in comparison to normoxic conditions (Figure 4.2.19A). Remarkably, DMOG produced an increase in HIF1α levels of CDK4/6-inhibited cells (Figure 4.2.19A), revealing that the reduction observed in normoxia is mediated by PHD hydroxylation of HIF1α. To further validate these data, we analysed by RT-qPCR the expression of genes related to MYC and glutamine, such as *GLS1* (encoding GLS1), the glutamine transporter genes *SLC7A5* and *SLC7A6*, and the *MYC associated factor X* (*MAX*), which encodes the factor MAX that binds to MYC to activate the transcription of target genes. As expected, CDK4/6 knockdown increased the mRNA levels of *GLS1*, *SLC7A5*, *SLC7A6* and *MAX* (Figure 4.2.19B).

Considering that control cells gene expression correlated with an increased KRAS signalling (HALLMARK_KRAS_SIGNALING_UP, Figure 4.2.16 and Appendix II), we measured KRAS protein levels by Western blot and found a depletion of KRAS expression in CDK4/6 knockdown cells under normoxia, hypoxia and after DMOG treatment (Figure 4.2.19A). Under hypoxic conditions, KRAS protein levels in CDK4/6-inhibited cells were reduced to the greatest extent while DMOG incubation induced KRAS overexpression in both control and CDK4/6 knockdown cells (Figure 4.2.19A). Consistently, recent studies have reported a synthetic lethal interaction between the

RAS oncogene and the absence of CDK4 expression [92, 531]. Moreover, RAS is also reported to inhibit both oxygen consumption and oxidative flux through the TCA cycle [165, 532], which is also in concordance with our results in control cells.
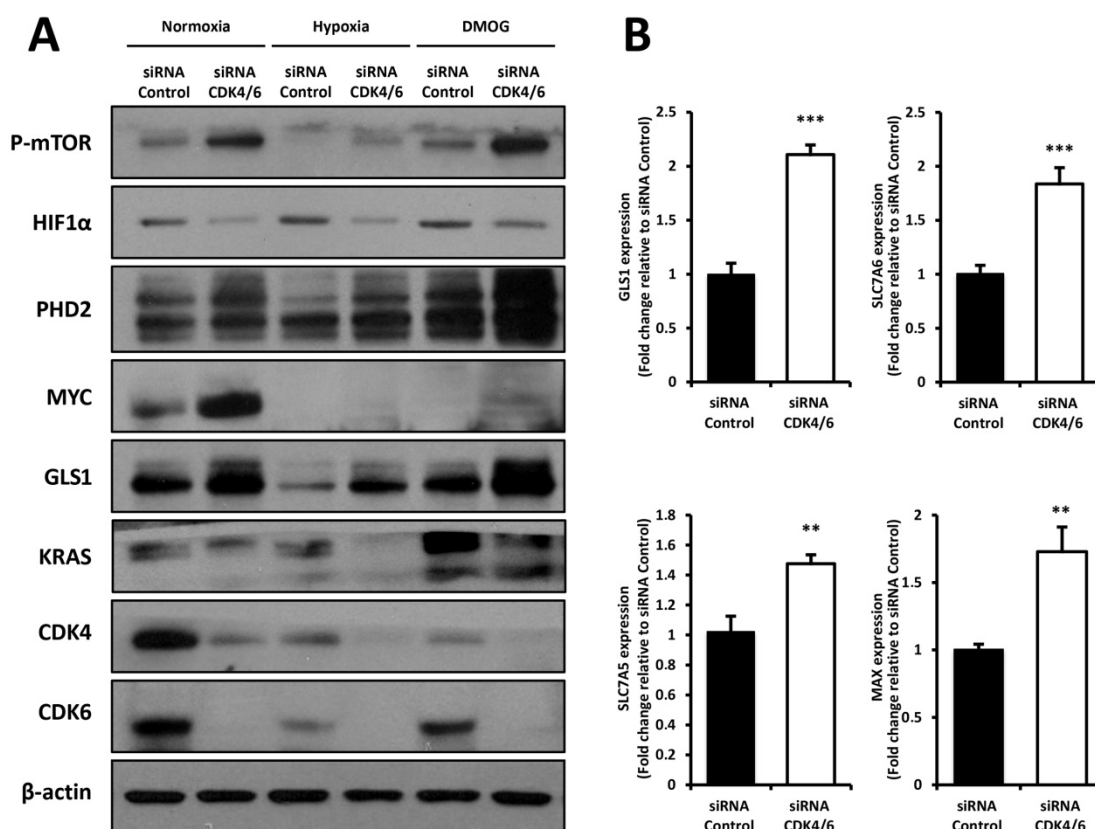
Figure 4.2.19. Effects of CDK4/6 knockdown on signalling pathways. A. Western blot analysis of total protein fractions of CDK4/6 knockdown and control cells under normoxic or hypoxic (1% O_2) conditions, or after DMOG treatment for 24h. β-actin was used as protein loading control. **B.** *GLS1*, *SLC7A6*, *SLC7A5* and *MAX* gene expression was assessed by RT-qPCR. Results are normalised to cyclophilin A and expressed as fold change of mRNA as compared to non-targeting siRNA-treated cells. Data are represented as mean ± SD of n=3. All experiments were performed 96 h after siRNA transfection. Statistically significant differences between CDK4/6 knockdown and control cells were indicated at $p < 0.01$ (**) and $p < 0.001$ (***).

4.2.2.10.1. CDK4/6 silencing increases pyruvate dehydrogenase activity

In order to investigate whether changes in fluxes and gene expression were accompanied by changes at proteomic level, we examined the activity of pyruvate dehydrogenase (PDH), a key enzyme regulating the entry of pyruvate into the TCA

cycle. Consistent with our abovementioned results, PDH activity was incremented in CDK4/6-inhibited cells (Figure 4.2.20A). Considering that PDH is negatively regulated by pyruvate dehydrogenase kinases (PDHK)-mediated phosphorylation, we analysed by Western blot the levels of PDH, P-PDH and PDHK1, which is activated by HIF1α [252]. Accordingly, CDK4/6 knockdown resulted in increased PDH and reduced levels of PDKH1 and P-PDH (Figure 4.2.20B). To further confirm that PDHK were inhibited, we
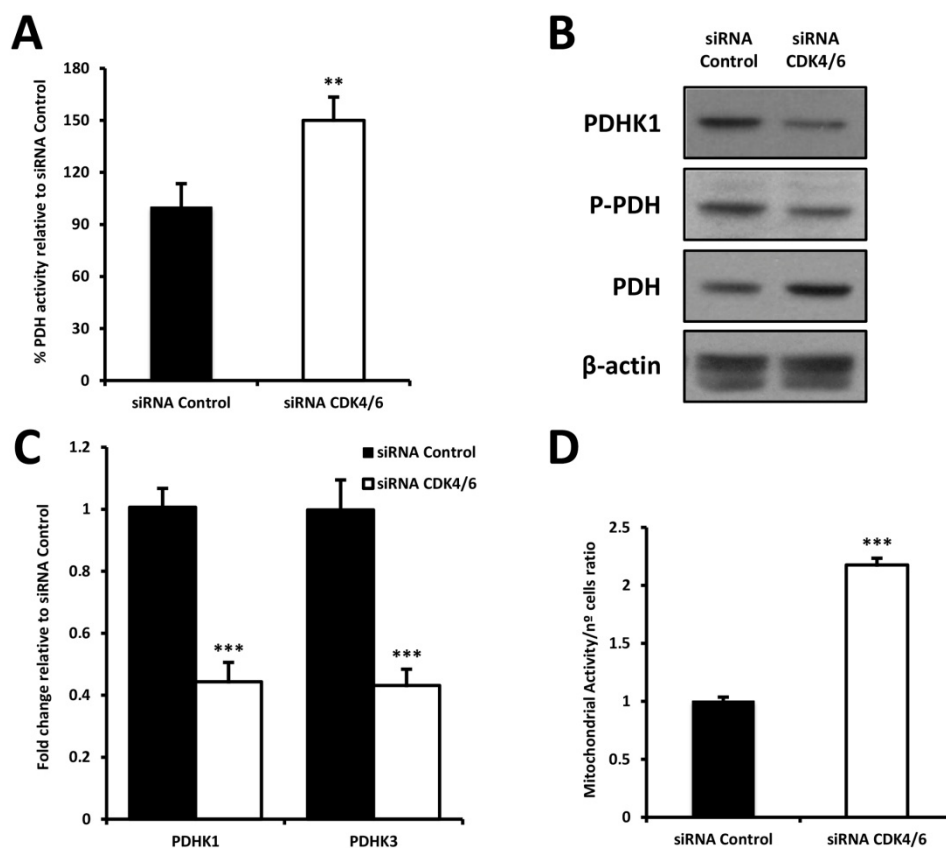
Figure 4.2.20. PDH status in CDK4/6 knockdown and control cells. A. PDH activity assessed with the Pyruvate dehydrogenase (PDH) Enzyme Activity Microplate Assay kit (Abcam) as described in Section 3.15. Results were normalised by protein content in the supernatant. **B.** PDHK1, PDH and P-PDH protein levels were determined by Western blot, using β-actin as a protein loading control. **C.** *PDHK1* and *PDHK3* gene expression was measured by RT-qPCR. Results are normalised to cyclophilin A and expressed as fold change of mRNA relative to non-targeting siRNA-treated cells. **D.** Total mitochondrial activity normalised per number of cells was estimated by the conversion of the tetrazolium salt MTT into formazan crystals as explained in Section 2.5., and the direct cell counting of parallel cultures. Results are expressed as fold change relative to control cells. Bars represent mean ± SD of n=3. All experiments were performed 96 h after siRNA transfection. Statistically significant differences between CDK4/6 knockdown and control cells were indicated at $p < 0.01$ (**) and $p < 0.001$ (***).

checked gene expression levels of *PDHK1* and *PDHK3*, and observed that both kinases were downregulated in CDK4/6-inhibited cells (Figure 4.2.20C). Finally, we estimated the ratio of mitochondrial activity normalised per number of cells to validate our results (as described in Section 3.6). In agreement with our results, CDK4/6 silencing caused a 2-fold increase in the ratio of mitochondrial activity (Figure 4.2.20D). In contrast to MYC, HIF1α blocks pyruvate entry to TCA cycle by inhibiting PDH through PDHK1 upregulation [212]. Indeed, our results can be consistently explained by both the decreased levels of HIF1α and the augmented MYC protein expression observed after CDK4/6 knockdown (Figure 4.2.19A).

4.2.2.10.2. CDK4/6 silencing reveals a new mechanism of MYC regulation

Together, these results suggest that CDK4/6 knockdown caused MYC overexpression which, in turn, is responsible of the metabolic reprogramming observed in these cells. In fact, the mechanism by which MYC is overexpressed in cells with CDK4/6 deficiency could be mediated by CDK4/6 kinase activity and consequent phosphorylation of MYC [533]. Anders et al. performed a systematic screen for CDK4/6 substrates and identified, among others, MYC as a common potential phosphorylation target [533]. To examine if cells with intact CDK4/6 exhibited increased phosphorylation of MYC, we measured MYC phosphorylation levels at Ser62 [235]. In effect, control cells displayed a higher P-MYC/MYC ratio than CDK4/6-inhibited cells (Figure 4.2.21A). In order to test if CDK4/6 phosphorylation of MYC triggered its proteasome-mediated degradation, we incubated the cells with the proteasome inhibitor MG132 for 6 h. As seen in Figure 4.2.21B, the loss of MYC in control cells can be rescued to higher levels than in CDK4/6-inhibited cells by treatment with MG132 indicating that CDK4/6 promote MYC degradation through a ubiquitin/proteasome-dependent mechanism, such as phosphorylation. In addition, using immunoprecipitation analysis (as described in Section 3.28) we confirmed that intact CDK4/6 triggered MYC degradation in control cells since Ub-MYC was principally detectable in the control condition when proteasome was inhibited (Figure 4.2.21C).
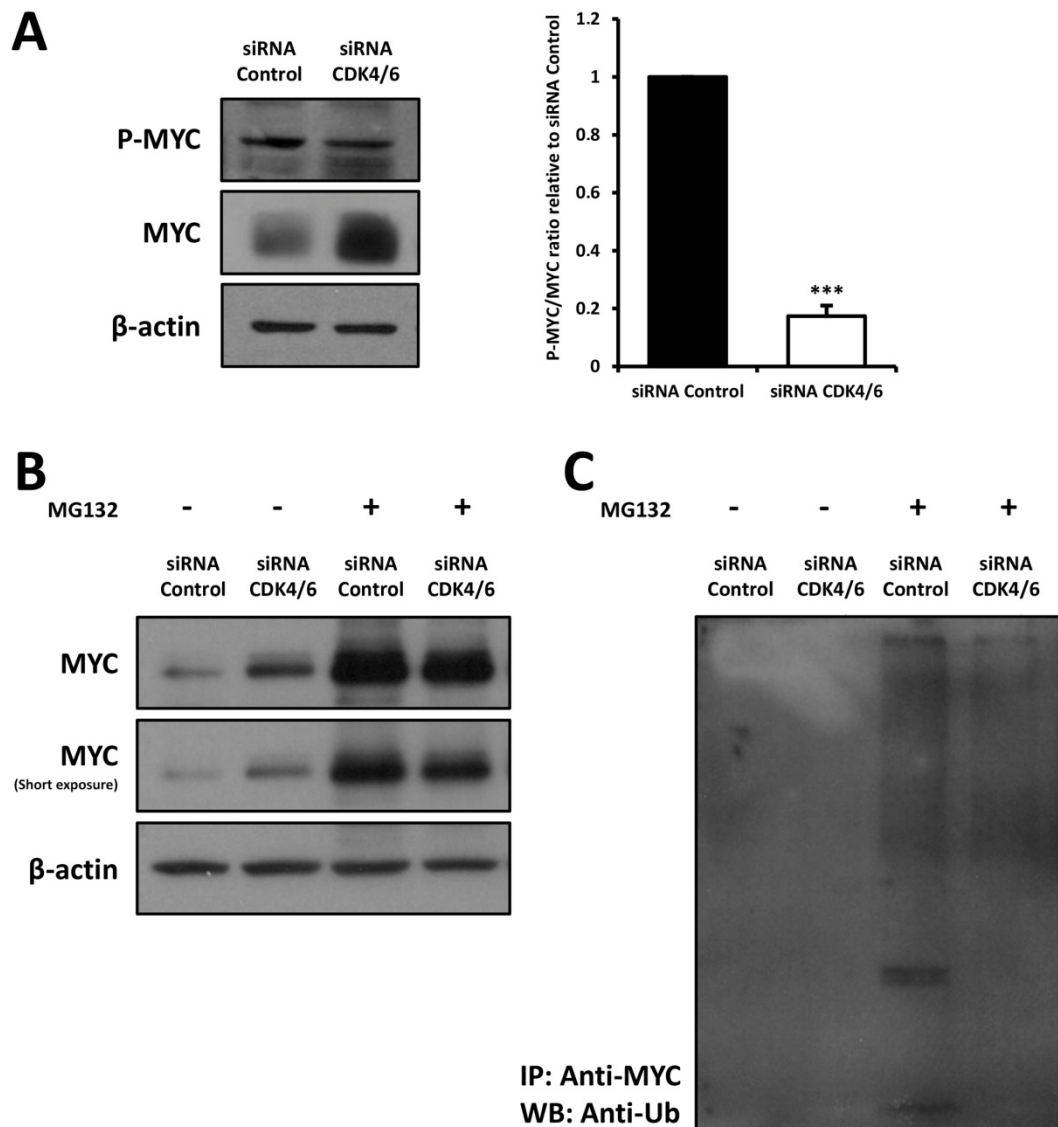
Figure 4.2.21. MYC accumulation after CDK4/6 knockdown. A. MYC and P-MYC (Ser62) protein levels determined by Western blot, using β-actin as a protein loading control. Protein expression was quantified by densitometry analysis using ImageJ software and is represented as mean band intensity of P-MYC/MYC ratio normalised to β-actin and relative to non-targeting siRNA-treated cells. Bars represent mean ± SD of n=3. Statistically significant differences between CDK4/6 knockdown and control cells were indicated at $p < 0.001$ (***). **B.** Western blot analysis of total protein fractions of control and CDK4/6 knockdown cells after incubation with the proteasome inhibitor MG132 or vehicle for 6 h. **C.** Control and CDK4/6 knockdown cells were treated with or without the proteasome inhibitor MG132 for 6 h before collection for immunoprecipitation (IP). Samples were immunoprecipitated with MYC antibody and subjected to immunoblotting using an anti-ubiquitin antibody. All experiments were performed 96 h after siRNA transfection.

4.2.2.10.3. CDK4/6 silencing increases polyamine synthesis

Previous studies have addressed MYC involvement in polyamine metabolism [213]. On the one hand, ornithine decarboxylase (ODC) (the rate-limiting enzyme in polyamine production) [220], S-adenosylmethionine decarboxylase (AMD1) and spermidine synthase (SRM) are transcriptional targets of MYC and, on the other hand, polyamines stimulate MYC transcription in a positive feedback loop [222, 223]. Recent studies
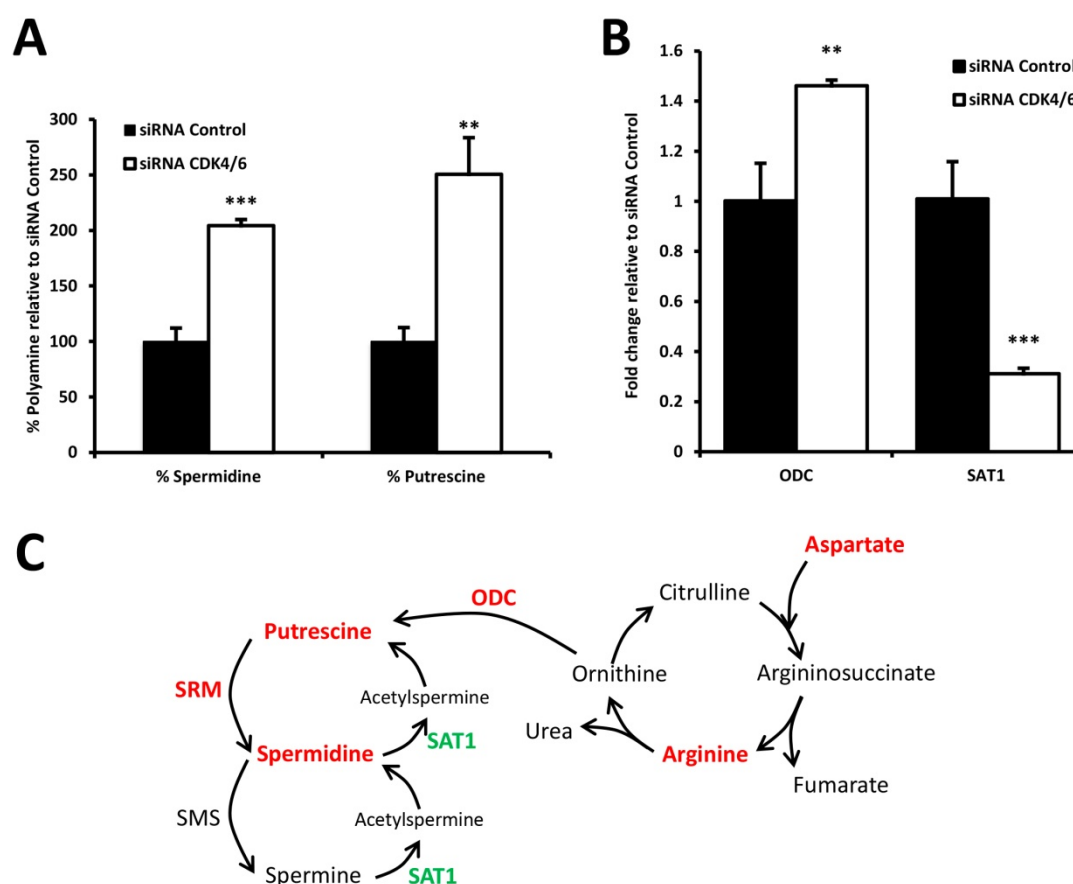
Figure 4.2.22. Polyamine metabolism in CDK4/6 knockdown and control cells. A. Quantification of spermidine and putrescine polyamines by GC/MS as detailed in Section X. Results are shown as percentage of polyamine metabolite relative to control cells. **B.** RT-qPCR measures of *ODC* and *SAT1* gene expression. Data are normalised to cyclophilin A and expressed as fold change of mRNA relative to non-targeting siRNA-treated cells. Bars represent mean ± SD of n=3. All experiments were performed 96 h after siRNA transfection. Statistically significant differences between CDK4/6 knockdown and control cells were indicated at $p < 0.01$ (**) and $p < 0.001$ (***). **C.** Schematic representation of the polyamine metabolism and the urea cycle. This illustration depicts in red the metabolites and enzymes which were observed to be increased and in green the enzymes that were found to be downregulated.

showed that polyamines spermidine and putrescine are downstream of PI3K pathway [534], which is suggested to be upregulated in CDK4/6-inhibited cells since FOXO3a transcriptional activity was repressed in these cells, according to the GSEA (Figure 4.2.17D). To test if CDK4/6 knockdown increased polyamine synthesis, we measured the concentration of putrescine and spermidine (as described in Section 3.36), and *ODC* and *SAT1* gene expression by RT-qPCR. As expected, the production of polyamines putrescine and spermidine were higher in CDK4/6-inhibited cells (Figure 4.2.22A), and ODC was overexpressed while SAT1, the enzyme that catalyses polyamine degradation, was downregulated (Figure 4.2.22B). In addition, transcriptomic analysis showed that SRM expression was increased 1.8-fold in CDK4/6 knockdown cells (Appendix III). The reported augment in arginine consumption (Figure 4.2.9A) and the accumulation of aspartate (Figures 4.2.8D and 4.2.9A) are in agreement with an enhanced polyamine metabolism resulted from CDK4/6 inhibition (Figure 4.2.22C).

4.2.2.10.4. CDK4/6 silencing sensitised cells to MYC inhibition

To ascertain whether MYC is required for the maintenance of CDK4/6-inhibited cells viability, the effect of suppressing MYC using the chemical inhibitor 10058-F4 was examined. Cells were treated with 50 μM 10058-F4 for 24 h and the increase of cell number was calculated. 50 μM 10058-F4 almost depleted MYC protein levels in control cells and caused a reduction of approximately 80% in cells with CDK4/6 knockdown (Figure 4.2.23A), accompanied by a 60% decrease in control cells expansion and a complete abrogation of CDK4/6-inhibited cell proliferation (Figure 4.2.23B).

To determine whether the effect of MYC inhibition on cells with CDK4/6 inhibition is dose-dependent, we incubated the CDK4/6-inhibited cells with vehicle or 50, 75 and 100 μM 10058-F4 for 24 h. As seen in Figures 4.2.23C and 4.2.23D, treatment with 75 and 100 μM 10058-F4 not only suppressed cell proliferation but also caused a dose-dependent diminution of total cell population concomitant with lower MYC protein levels.
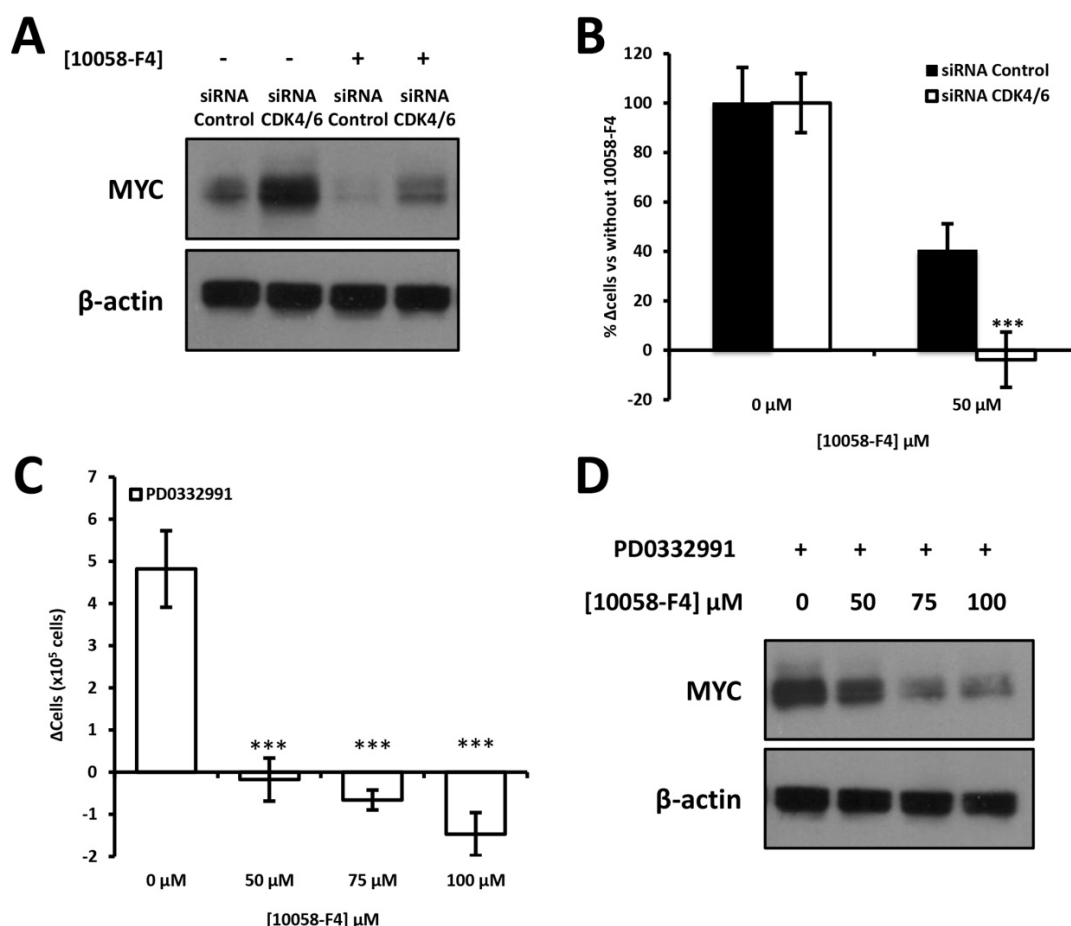
Figure 4.2.23. Inhibition of MYC abrogates CDK4/6 knockdown cell proliferation. CDK4/6 knockdown and control cells were incubated for 24 h either in the presence or the absence of 10058-F4, as indicated. **A.** MYC protein expression was examined by Western blot, using β-actin as a protein loading control. **B.** Cell number was determined by flow cytometry before and after treatment with 50 μM 10058-F4 or vehicle for 24 h. Results are shown as percentage of the increase of cell number relative to untreated CDK4/6 knockdown and control cells. All experiments were performed 96 h after siRNA transfection. Statistically significant differences between CDK4/6 knockdown and control cells were indicated at $p < 0.001$ (***). **C.** Cells treated with the CDK4/6 inhibitor PD0332991 were counted by flow cytometry before and after incubation with vehicle or 50, 75 and 100 μM 10058-F4 for 24 h. Bars represent mean ± SD of n=3. Statistically significant differences between 10058-F4 treatment and untreated cells were indicated at $p < 0.001$ (***). **D.** Western blot analysis of MYC protein expression in CDK4/6-inhibited cells after treatment with the indicated concentrations of 10058-F4 or vehicle for 24 h. β-actin was used as a protein loading control.

4.2.2.10.5. The enhancement of mitochondrial metabolism predicted by integrated data analysis is confirmed through expression changes caused by CDK4/6 silencing

Consistent with our results, MYC overexpression is known to stimulate glutamine metabolism through microRNA-23a/b repression, resulting in GLS1 upregulation [206,

173

214]. In fact, *GLS1* encodes for two alternatively spliced isoforms, known as kidney (k-type) glutaminase or KGA, and glutaminase C or GAC [159]. Using isoform-specific antibodies against KGA and GAC, we confirmed the overexpression of both GLS1 isoforms in CDK4/6 knockdown cells (Figure 4.2.24A), consistent with the increased glutamine consumption rates observed in CDK4/6-inhibited cells (Figure 4.2.3). Furthermore, the mTOR complex 1 (mTORC1) promotes the use of glutamine carbons through TCA anaplerosis by activating glutamate dehydrogenase (GDH) [322]. The augmented levels of TCA intermediates reported in Figure 4.2.8D and the overexpression of GDH validated by Western blot in Figure 4.2.24A, confirmed an enhanced glutamine mitochondrial metabolism. Mitochondrial glutamate uptake was also increased in CDK4/6-inhibited cells, as illustrated by the upregulation of *SLC25A13*
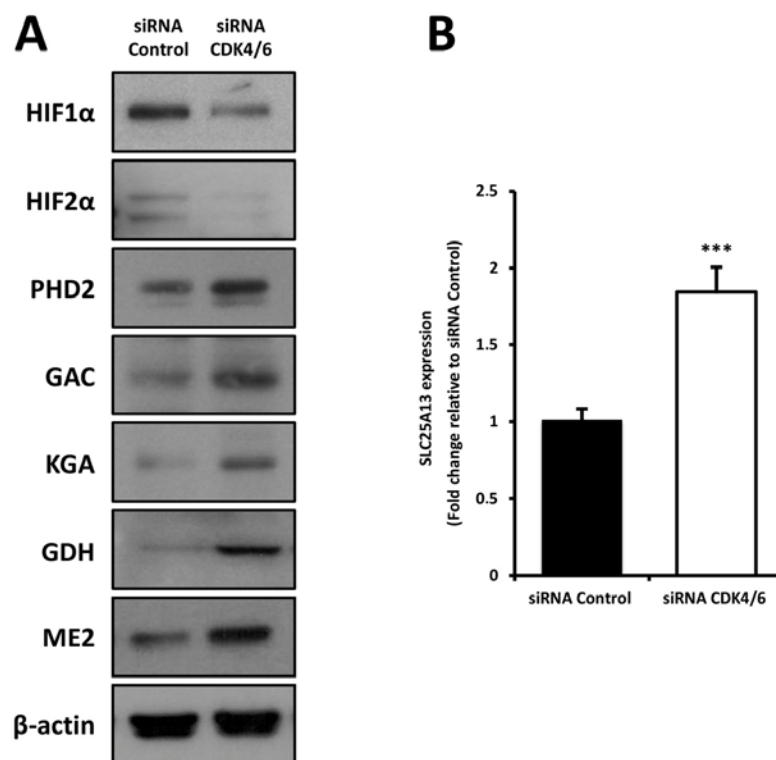
Figure 4.2.24. Expression changes caused by CDK4/6 knockdown lead to an enhanced mitochondrial metabolism. **A.** Western blot analysis of total protein fractions of CDK4/6 knockdown and control cells. β-actin was employed as a protein loading control. **B.** *SLC25A13* gene expression was measured by RT-qPCR. Results are normalised to cyclophilin A and expressed as fold change of mRNA relative to expression of non-targeting siRNA-treated cells. Bars represent mean ± SD of n=3. All experiments were performed 96 h after siRNA transfection. Statistically significant differences between CDK4/6 knockdown and control cells were indicated at $p < 0.001$ (***).

(solute carrier family 25, aspartate/glutamate carrier, member 13) gene expression (Figure 4.2.24B). Moreover, we also observed overexpression of mitochondrial ME2 (Figure 4.2.24A), which can have a regulatory role by recycling malate into pyruvate to match TCA flux to cellular energetic demands, reducing equivalents and biosynthetic precursors [535]. Importantly, the increased glutaminolysis rate generated higher levels of intracellular α-ketoglutarate which, in turn, served as substrate and activated PHD, triggering PHD-dependent HIF1α hydroxylation and proteasome-mediated degradation, even under hypoxic conditions (Figures 4.2.24A and 4.2.19A) [248]. In addition, we also found that HIF2α protein levels were downregulated in CDK4/6-inhibited cells (Figure 4.2.24A). Thus, HIFα subunits degradation caused by CDK4/6 knockdown can explain the opposite correlation with hypoxia and HIFα responsive genes observed in the gene expression analysis (Figure 4.2.17 and Appendix II).

4.2.2.11. CDK4/6 silencing sensitised cells to hypoxia

With the intention of finding vulnerabilities associated to CDK4/6 knockdown, we tested whether the observed depletion of HIF1α sensitised CDK4/6-inhibited cells to hypoxia. Indeed, 24 h incubation under hypoxic conditions (1% O_2) specifically impaired CDK4/6 knockdown cell growth while control cells were not significantly affected (Figure 4.2.25A). The same results were obtained inhibiting CDK4/6 with PD0332991 (Figure 4.2.25B). In addition, incubation with 1 mM DMOG for 24 h also restrained CDK4/6-inhibited cells proliferation to a greater extent than control cells (Figure 4.2.25C).

4.2.2.11.1. Metabolic reprogramming associated to CDK4/6 silencing under hypoxia

As CDK4/6 repression sensitised cells to hypoxia, we next studied the metabolic reprogramming associated to CDK4/6-inhibited cells under hypoxic conditions (1% O_2, 24 h). First, we assessed the consumption rates of the two principal cellular carbon
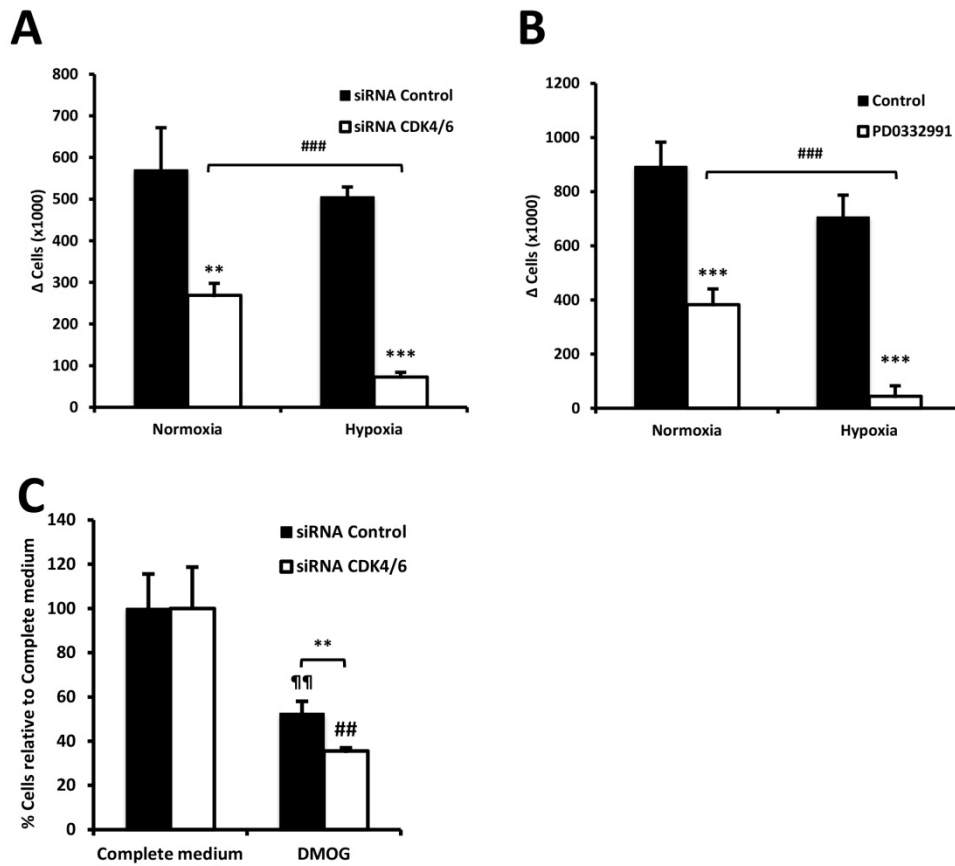
Figure 4.2.25. CDK4/6 knockdown cells are sensitive to hypoxia. A. CDK4/6 knockdown and control cells were incubated for 24 h under normoxic or hypoxic conditions. Cell number was determined by flow cytometry before and after normoxic or hypoxic treatment. Data are represented as increase of cell number. All experiments were performed 96 h after siRNA transfection. **B.** The same results were obtained inhibiting CDK4/6 with PD0332991. **C.** CDK4/6 knockdown and control cell viability after 24 h treatment with 1mM DMOG. Results are shown as the percentage of proliferation relative to CDK4/6 knockdown and control cells cultured with vehicle (100% proliferation). Bars represent mean ± SD of n=3. Statistically significant differences between CDK4/6 knockdown and control cells were indicated at $p < 0.01$ (**) and $p < 0.001$ (***), while differences between treatment (hypoxia or DMOG) and the corresponding control (CDK4/6 siRNA- or non-targeting siRNA- treated cells in normoxia or incubated with vehicle) were shown at $p < 0.01$ (##) and $p < 0.001$ (###) for CDK4/6-inhibited cells and as $p < 0.01$ (¶¶) for control cells.

sources, glucose and glutamine, and the production rate of lactate and glutamate. As expected and in accordance with the described metabolic adaptation to hypoxia [212, 251], the rates of glucose consumption and lactate production were enhanced in both control and CDK4/6 knockdown cells (Figure 4.2.26A as compared to Figure 4.2.3A), in
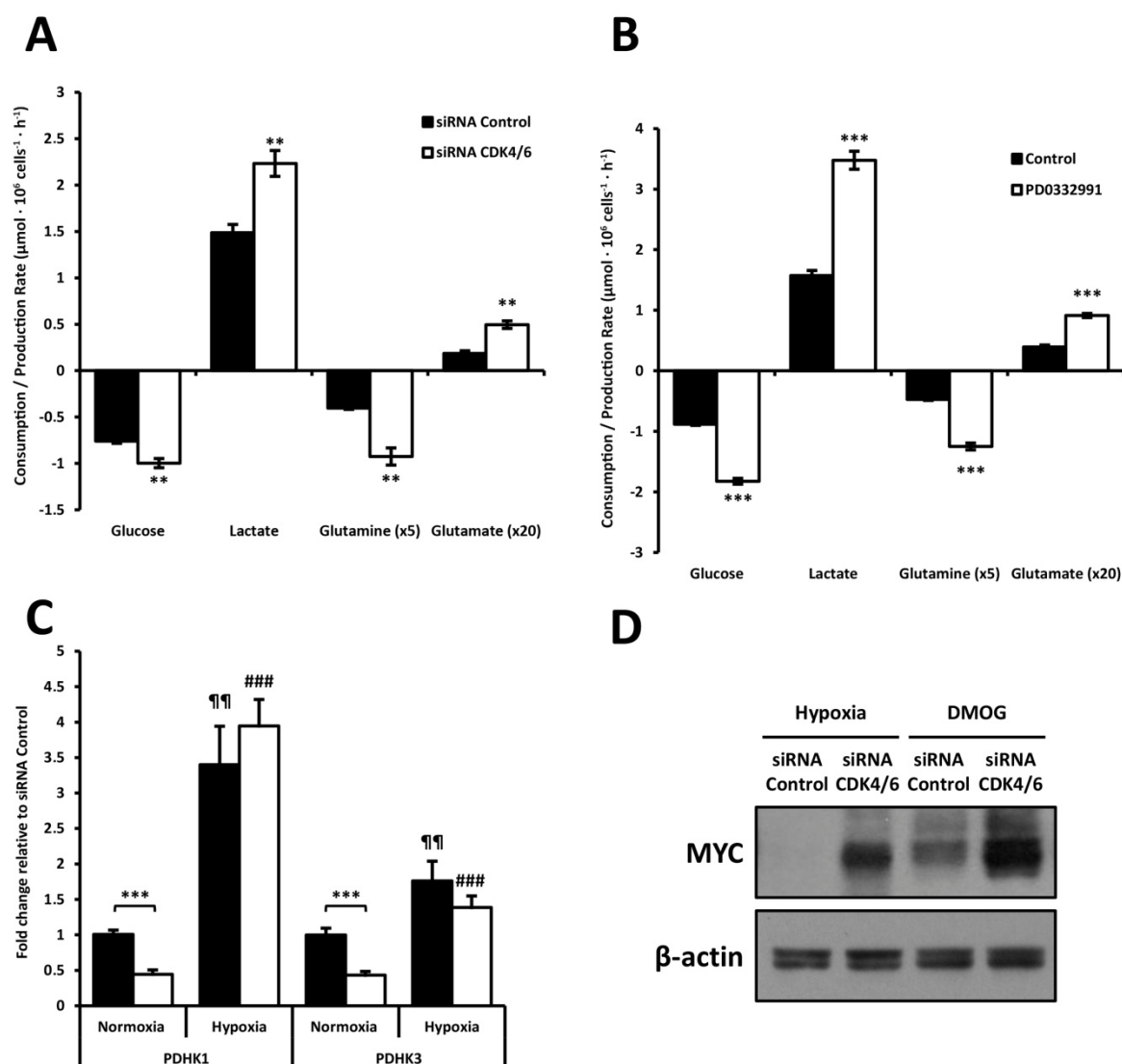
Figure 4.2.26. Metabolic reprogramming associated to CDK4/6-inhibited cells under hypoxia. Glucose and glutamine consumption and lactate and glutamate production rates were obtained after 24 h incubation with fresh media under hypoxia (1% O_2) and normalised to cell number. Metabolite consumption/production and cell proliferation were determined for **A.** siRNA-transfected cells and **B.** PD0332991-treated cells. **C.** *PDHK1* and *PDHK3* gene expression was measured by RT-qPCR after normoxic or hypoxic incubation for 24 h. Results are normalised to cyclophilin A and expressed as fold change of mRNA relative to expression of non-targeting siRNA-treated cells in normoxia. Bars represent mean ± SD of n=3. Statistically significant differences between cells with CDK4/6 inhibition and control cells were indicated at $p < 0.01$ (**) and $p < 0.001$ (***), while differences between treatment (hypoxia) and the corresponding control (CDK4/6 siRNA- or non-targeting siRNA- treated cells in normoxia) were shown at $p < 0.001$ (###) for CDK4/6-inhibited cells and at $p < 0.01$ (¶¶) for control cells. **D.** CDK4/6 knockdown and control cells were incubated in hypoxia or with the prolyl hydroxylase inhibitor DMOG for 24 h. MYC protein levels were determined by Western blot and visualised after a long film exposure to obtain a significant signal. β-actin was employed as a protein loading control.

association with the expected increase in the glycolytic flux reported in hypoxia [240, 536]. However, CDK4/6-inhibited cells always maintained significantly higher consumption and production rates than control cells. Remarkably, only cells with CDK4/6 inhibition exhibited an increase both in glutamine consumption and in glutamate production under hypoxic conditions (Figure 4.2.26A as compared to Figure 4.2.3A). Hypoxic PD0332911 treatment also provided the same results (Figure 4.2.26B). Hypoxia is characterised by an enhanced glycolytic metabolism through the activation of the glycolytic targets of HIF1α, the blockage of pyruvate entry into the TCA cycle via PDH inhibition owing to HIF1α-dependent PDHK1 induction, and the HIF1α-mediated reduction of mitochondrial biogenesis due to induction of the MYC-negative regulator MXI1 [536]. In fact, hypoxia treatment caused 3- up to 8-fold and 1.5- up to 3-fold increases in *PDHK1* and *PDHK3* gene expression, respectively (Figure 4.2.26C). In agreement with PDHK upregulation and consequent PDH inhibition, the proportion of labelled glutamate measured after 24 h incubation with $[1,2-^{13}C_2]$-glucose in hypoxia (1% O_2) was almost non-existent (approximately 0.5-1%). Notably, CDK4/6-inhibited cells presented augmented glucose and glutamine uptake rates under hypoxia despite exhibiting impaired proliferation (Figures 4.2.25A-B and 4.2.26A-B). This phenomenon might be explained by the remaining levels of MYC in CDK4/6 knockdown cells at 1% O_2 observed after long film exposure, whereas hypoxia completely abrogated MYC expression in control cells (Figure 4.2.26D). The results obtained after 1 mM DMOG incubation for 24 h were in the same direction but to a lesser extent (Figure 4.2.26D).

MYC transcriptional activity was reduced under hypoxic conditions, as revealed by the decrease of mRNA expression levels of known MYC target genes such as *ODC* and *CCND1* (encoding cyclin D1) [210], especially in control cells (Figures 4.2.27A and 4.2.27B). *MAX* was exclusively downregulated in control cells (Figure 4.2.27B), consistent with the complete depletion of MYC protein expression presented by control cells under hypoxia (Figure 4.2.26D). These results are in accordance with the decreased HIF1α and HIF2α protein levels observed in cells with CDK4/6 inhibited (Figure 4.2.24A), as HIFs are required for MYC degradation [260]. MYC downregulation also impacted on proline synthesis since the proportion of labelled proline from [U-$^{13}C_5$]-glutamine dramatically decreased from 20-30% in normoxia to approximately 5%

in hypoxia (Appendix I). On the other hand, hypoxia-inducible genes *PFKFB4* (encoding 6-phosphofructo-2-kinase/fructose-2,6-biphosphatase 4), *HK2* (hexokinase II), *ENO2* (enolase II), *SLC2A3* (solute carrier family 2, facilitated glucose transporter member 3) [212, 537] were, as expected, upregulated under hypoxic conditions and overexpressed in control cells compared with CDK4/6-inhibited cells (Figure 4.2.27C), in correlation with increased HIF1α protein levels. In effect, gene expression analysis
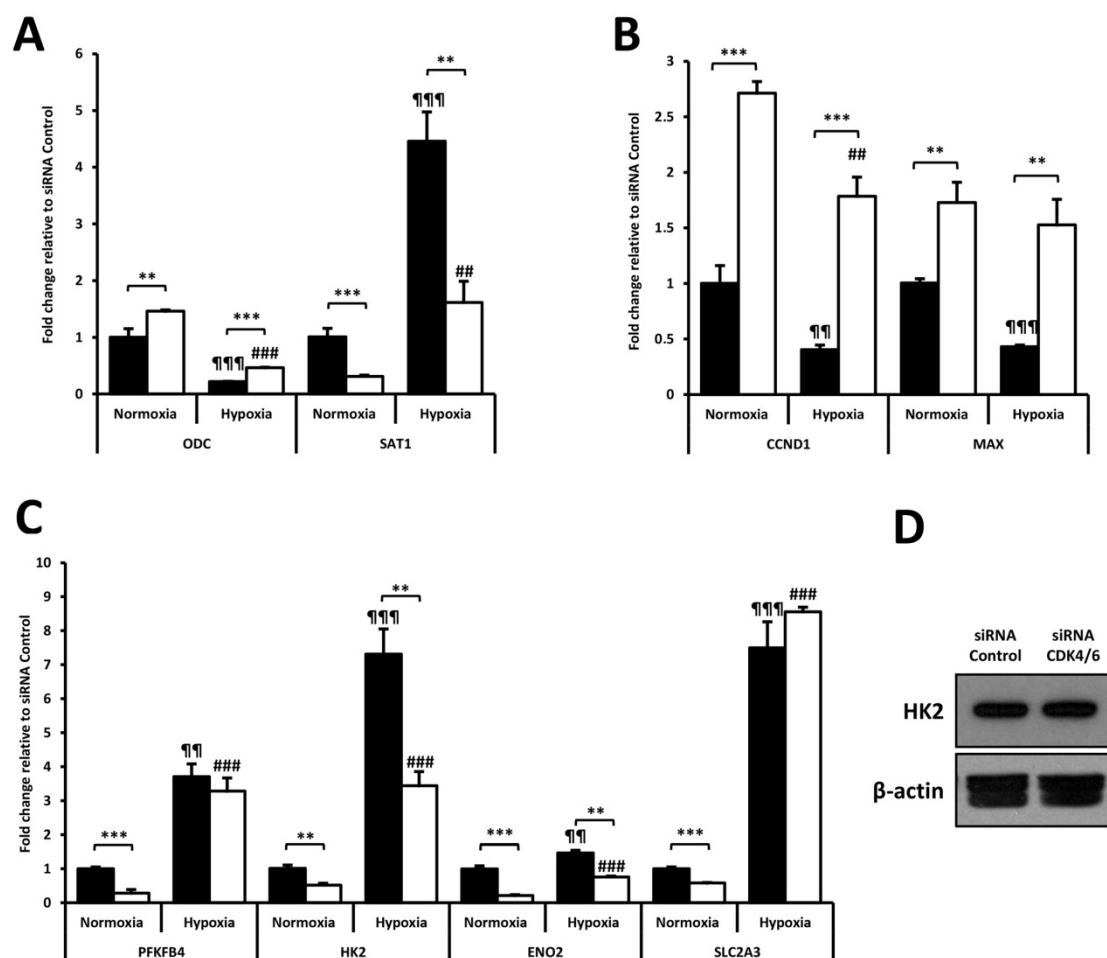
Figure 4.2.27. Expression changes produced by hypoxia in CDK4/6 knockdown and control cells. Cells were incubated in hypoxia (1% O$_2$) for 24 h and the gene expression of **A.** polyamine metabolism enzymes **B.** MYC-related enzymes and **C.** hypoxia-inducible genes was assessed by RT-qPCR. Results are normalised to cyclophilin A and expressed as fold change of mRNA relative to expression of non-targeting siRNA-treated cells in normoxia. Bars represent mean ± SD of n=3. Statistically significant differences between cells with CDK4/6 inhibition and control cells were indicated at $p < 0.01$ (**) and $p < 0.001$ (***), while differences between treatment (hypoxia) and the corresponding control (CDK4/6 siRNA- or non-targeting siRNA- treated cells in normoxia) were shown at $p < 0.01$ (##) and $p < 0.001$ (###) for CDK4/6-inhibited cells and at $p < 0.01$ (¶¶) and $p < 0.001$ (¶¶¶) for control cells. **D.** Western blot analysis of HK2 protein levels in normoxia, using β-actin as a protein loading control.

consistently evidenced the downregulation of HIF1α target genes in CDK4/6 knockdown cells (Appendix II). In addition, we observed that the transcriptional downregulation of glycolytic genes reported in CDK4/6-inhibited cells under normoxic conditions did not affect its protein levels, since hexokinase 2 protein expression was unaltered between CDK4/6 knockdown and control cells (Figure 4.2.27D). Since *ODC* was found downregulated, we assessed *SAT1* gene expression under hypoxic conditions. Surprisingly, hypoxia greatly enhanced SAT1 mRNA expression (Figure 4.2.27A), which in combination with the reduction *ODC* mRNA levels suggested a decrease in polyamine synthesis. It is important to note that CDK4/6 knockdown significantly attenuated the magnitude of these gene expression changes in polyamine metabolism, corroborating the augmented polyamine synthesis observed in normoxia in comparison to control cells (Figure 4.2.22).
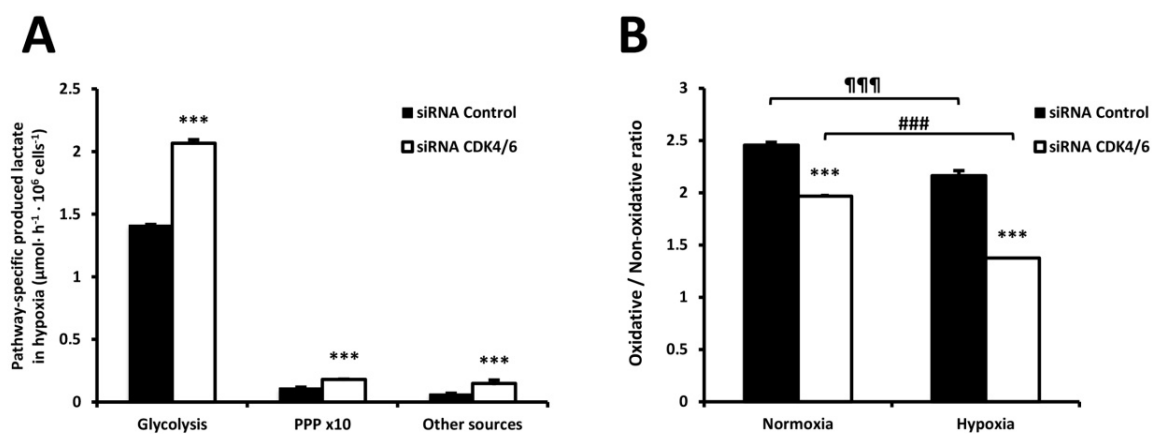
Figure 4.2.28. Hypoxic glucose metabolism in CDK4/6 knockdown and control cells. Cells were incubated in the presence of 10 mM [1,2-^{13}C$_2$]-glucose under hypoxia (1% O$_2$) for 24 h. **A.** Pathway-specific lactate fluxes determined by combining mass isotopomer distribution data and lactate production as described in Section 3.34.1 to estimate the lactate produced from glucose through direct glycolysis, diverted through PPP and the lactate obtained from other sources. **B.** Oxidative versus non-oxidative branch of PPP in normoxia and hypoxia calculated as m1/m2 ribose. Cell pellets were obtained after 24 h normoxic or hypoxic incubation and ribose was isolated from RNA for mass isotopomer distribution analysis. The m1 isotopomers of ribose are indicative of the oxidative pentose phosphate pathway flux, whereas the m2 isotopomers indicate the non-oxidative PPP flux producing ribose. Bars represent mean ± SD of n=3. Statistically significant differences between CDK4/6 knockdown and control cells were indicated at $p < 0.001$ (***), while differences between treatment (hypoxia) and the corresponding control (CDK4/6 siRNA- or non-targeting siRNA- treated cells in normoxia) were shown at $p < 0.001$ (###) for CDK4/6-inhibited cells and at $p < 0.001$ (¶¶¶) for control cells.

Having observed that hypoxic treatment enhanced glycolytic metabolism, we determined the contribution of glycolysis, pentose phosphate pathway (PPP) and carbon sources other than glucose to lactate production. As for normoxia, we incubated the cells with $[1,2-^{13}C_2]$-glucose and measured the mass isotopomer distribution of lactate and the initial and final lactate concentrations. Pathway-specific production of lactate estimation indicated that glycolysis was the major source of lactate with an even greater difference, compared with normoxia, between CDK4/6-inhibited and control cells (Figures 4.2.28A and 4.2.5A). However, PPP produced lower amounts of lactate than in normoxic conditions (Figures 4.2.28A and 4.2.5A) while the quantity of lactate obtained using other sources remained constant. In addition, hypoxic CDK4/6-inhibited cells exhibited a higher decrease in m1 and a greater increase in m2 labelled ribose, depicting a more pronounced unbalance of the PPP towards the non-oxidative branch (Figure 4.2.28B) associated with an augmented redirection of glucose-based PPP intermediates back to glycolysis.

Taking into account that enhanced glutamine consumption and glutamate production under hypoxia was only observed in cells with CDK4/6 inhibition (Figures 4.2.26A and 4.2.26B), we wanted to determine whether glutamine was metabolised oxidatively (through oxidative TCA cycle) or reductively (via reductive carboxylation) by monitoring $[U-^{13}C_5]$-glutamine incorporation into TCA cycle intermediates. Analysis of citrate label distribution shows evidence for glutamine contribution to reductive carboxylation (m5 labelled citrate) or regular TCA cycle (m4 labelled citrate), while m5/m4 citrate gives relative ratio information between both pathways [169]. Label incorporation in fatty acids after $[U-^{13}C_5]$-glutamine incubation also comes from reductive carboxylation (Figure 4.2.8A). As seen in Figure 4.2.29A, CDK4/6-inhibited cells presented a higher contribution of glutamine to reductive carboxylation than control cells in both normoxic and hypoxic conditions. However, under hypoxia, CDK4/6 knockdown caused a greater increase in the reductive glutamine metabolism (Figure 4.2.29A). Likewise, higher levels of m5 citrate and m3 mass isotopomers of aspartate and malate, which are also result of the reductive glutamine conversion, were reported in cells with CDK4/6 inhibition (Figure 4.2.29B). On the other hand,
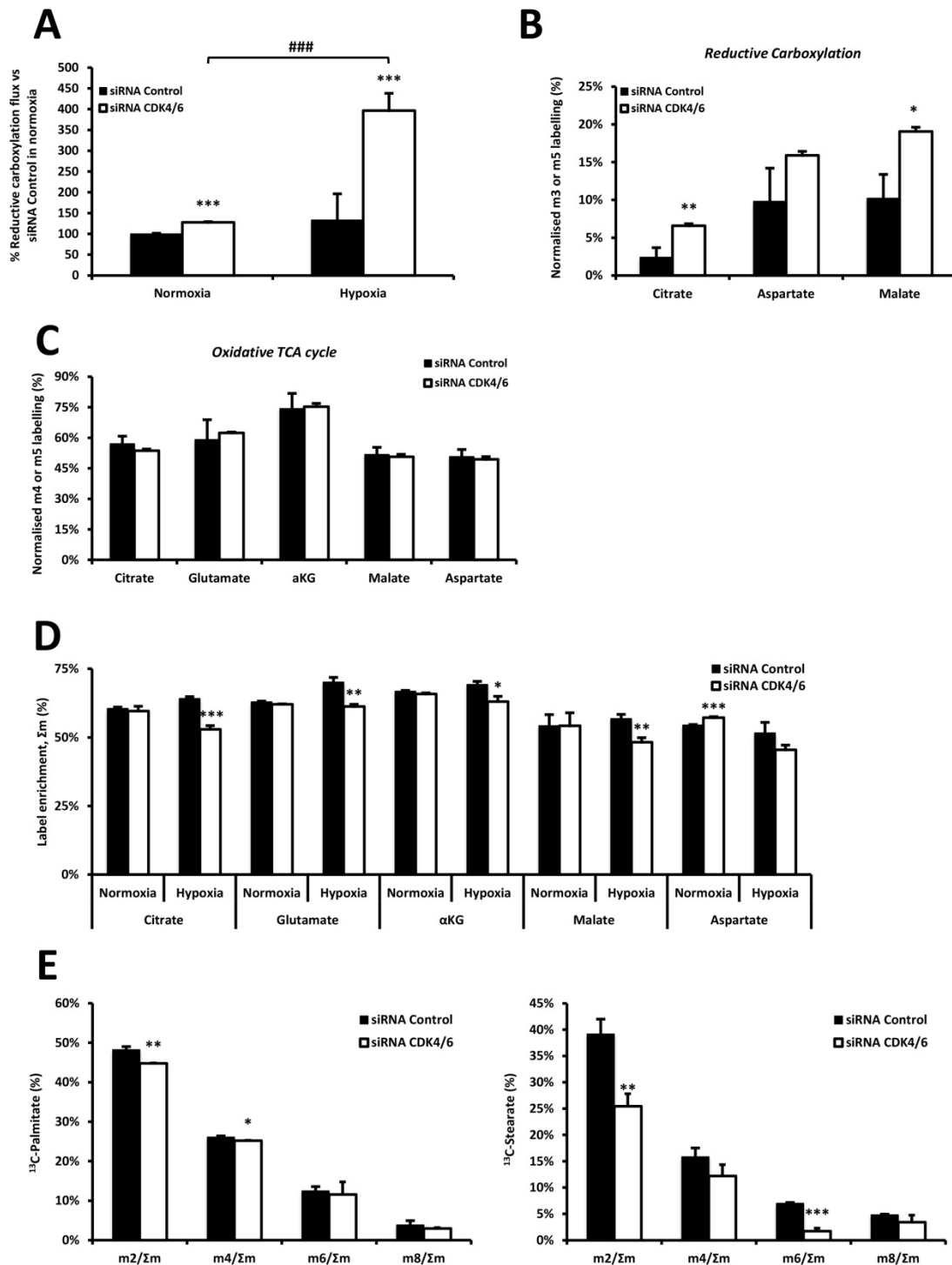
Figure 4.2.29. Hypoxic glutamine metabolism in CDK4/6 knockdown and control cells. Cells were incubated in the presence of 2 mM [U-$^{13}C_5$]-glutamine under hypoxia (1% O_2) for 24 h. Fatty acids and TCA intermediates were isolated from cell pellets for mass isotopomer distribution analysis. **A.** Estimation of the normoxic and hypoxic reductive carboxylation flux obtained from m5/m4 labelled citrate ratio. Data are represented as relative reductive carboxylation flux with control cells in normoxia levels set as 100%. **B.** Normalised m5 citrate, m3 aspartate and m3 malate labelling are characteristic of the reductive carboxylation of [U-$^{13}C_5$]-glutamine. **C.** Normalised m4 citrate, m5 glutamate, m5 α-ketoglutarate (αKG), m4 malate and m4 aspartate are indicative of the oxidative TCA pathway.

oxidative metabolism of glutamine under hypoxia presented no differences between CDK4/6-inhibited and control cells, as observed by comparing m4 citrate, m5 glutamate, m5 α-ketoglutarate (αKG), m4 malate and m4 aspartate labelling levels (Figure 4.2.29C). As reported in normoxia, oxidative TCA cycle was the major pathway in mitochondrial glutamine metabolism as observed by comparison of the relative proportion of the labelled species that are characteristic of the forward reactions of the TCA cycle (Figure 4.2.29C) and reductive carboxylation (Figure 4.2.29B). It is worth noting that glutamine metabolism through the TCA cycle persisted under hypoxic conditions (1% O_2) since glutamine contribution to citrate, glutamate, α-ketoglutarate, malate and aspartate carbons was comparable to normoxia (Figure 4.2.29D), which is in agreement with previous studies [157, 165].

Through reductive carboxylation, glutamine maintains citrate levels by conversion of α-ketoglutarate to isocitrate and citrate by means of mitochondrial isocitrate dehydrogenase 1 (IDH1) and aconitase [168, 538]. The reductive metabolism of glutamine can be accomplished by NADH conversion to NADPH by mitochondrial transhydrogenase, which is used in α-ketoglutarate carboxylation. The citrate exported to the cytosol may in part be cleaved by ATP citrate lyase (ACLY) to oxaloacetate and acetyl-CoA, which in turn is used for lipogenesis, or oxidatively metabolised by IDH1, producing cytosolic NADPH and α-ketoglutarate [95]. Since citrate can stimulate fatty acids biosynthesis [538], we examined the mass isotopomer distribution of palmitate and stearate in HCT116 cells cultured for 24 h in presence of [U-^{13}C]-glutamine and under hypoxia (1% O_2). Despite exhibiting lower levels of reductive carboxylation metabolites, control cells presented higher levels of labelled palmitate and stearate isotopomers (Figure 4.2.29E). These results may be explained by the sustained

D. Total ^{13}C-citrate, ^{13}C-glutamate, ^{13}C-α-ketoglutarate (αKG), ^{13}C-malate and ^{13}C-aspartate label enrichment in normoxia or hypoxia represented as the sum of the labelled isotopomers (Σm). **E.** Mass isotopomer distribution of palmitate and stearate after 24 h incubation with 2 mM [U-^{13}C]-glutamine. Data are shown as mean ± SD of n=3. Statistically significant differences between CDK4/6-inhibited and control cells were indicated at $p < 0.05$ (*), $p < 0.01$ (**) and $p < 0.001$ (***), while differences between treatment (hypoxia) and the corresponding control (CDK4/6 siRNA- or non-targeting siRNA- treated cells in normoxia) were shown at $p < 0.001$ (###) for CDK4/6-inhibited cells.

proliferation of control cells under hypoxia, in contrast to CDK4/6-inhibited cells, which exhibited an impaired proliferation capacity (Figures 4.2.25A and 4.2.25B).

4.2.2.12. CDK4/6 knockdown effects are not a result of cell cycle G1 phase arrest

To examine whether the induction of MYC, GLS1 and P-mTOR, or the repression of HIF1α resulted from the cell cycle G1 phase arrest, we analysed their protein levels in HCT116 cells synchronised with double thymidine block. While treatment with thymidine completely arrested cells in cell cycle G1 phase (Figure 4.2.30A), the protein expression of MYC, GLS1 and P-mTOR was not increased compared to control cells, and the protein level of HIF1α was higher than in CDK4/6-inhibited cells (Figure 4.2.30B). The fact that G1-synchronised cells presented significantly lower MYC levels than CDK4/6-inhibited cells is in accordance with our hypothesis that CDK4/6 can trigger MYC degradation through phosphorylation. Hence, the changes in MYC, GLS1, P-mTOR and HIF1α expression are not a result of G1 arrest but are related to the kinase activity of CDK4 and CDK6.

To further confirm our hypothesis, we assessed the consumption rate of glucose and glutamine and the production rate of lactate and glutamate in G1-synchronised cells. Figure 4.2.30C compares the consumption and production rates of these metabolites between G1-synchronised and asynchronised cells. The absence of significant changes in these rates confirmed that the increase in consumption of glucose and glutamine and in production of lactate and glutamate observed in CDK4/6-inhibited cells are not caused by the G1 cell cycle arrest.

4.2.2.13. Targeting CDK4/6 and GLS1 as a combination therapy

Overexpression of MYC reprograms mitochondrial metabolism, leading to cell dependence on glutamine as a bioenergetic substrate to maintain cellular viability and anaplerosis of the TCA cycle [96]. This dependence results in glutamine addiction for
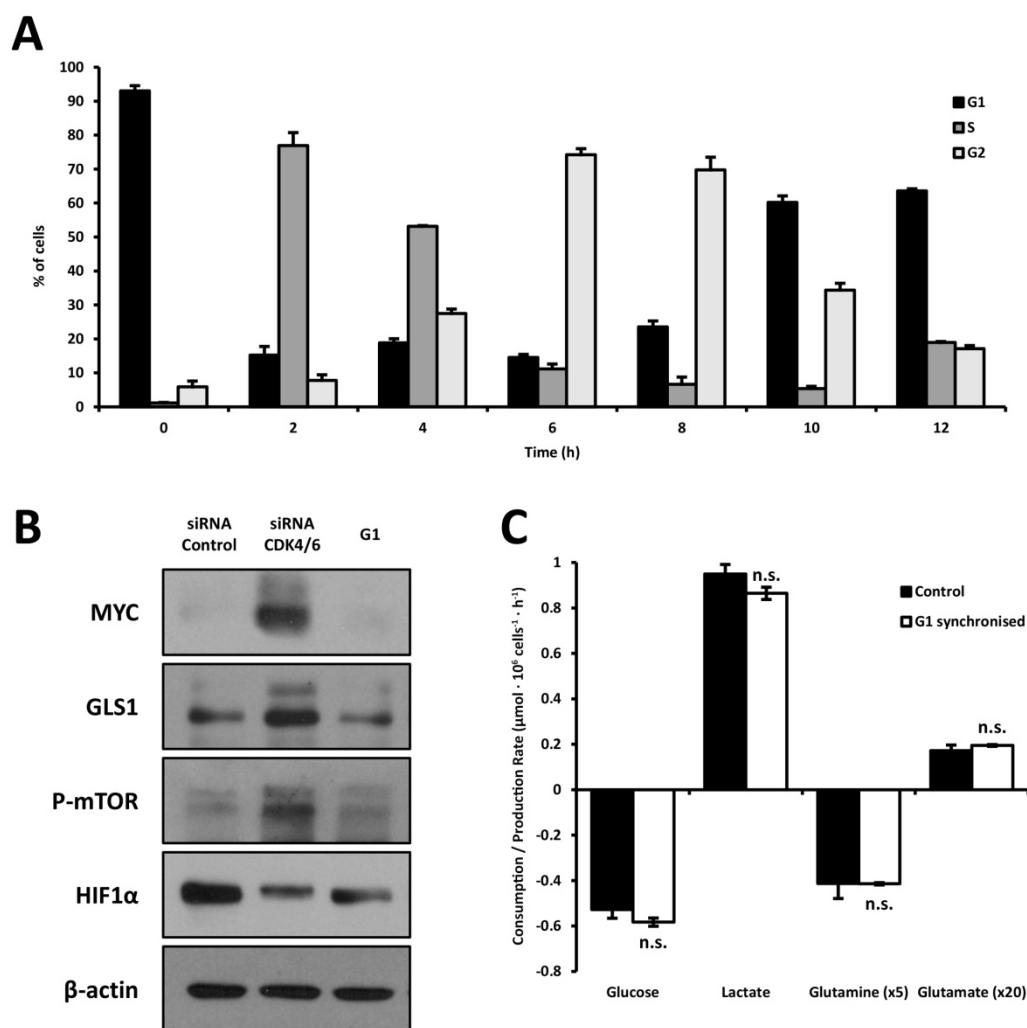
Figure 4.2.30. Characterisation of cell cycle G1 phase arrest. A. After treatment of HCT116 cells with double thymidine block, cells were synchronised in the G1 phase (0 h). **B.** Western blot analysis of total protein fractions of CDK4/6 knockdown, control and G1 synchronised cells. β-actin was employed as a protein loading control. **C.** Glucose and glutamine consumption and lactate and glutamate production rates were obtained after 24 h incubation with fresh media in the presence of thymidine (G1 synchronised) or vehicle (Control) and normalised to cell number. Bars represent mean ± SD of n=3. Non-significant differences between G1 synchronised and control cells were indicated at $p > 0.05$ (n.s.).

the maintenance of mitochondrial integrity and TCA intermediates metabolism. Taking into account that GLS1 is the first essential enzyme for mitochondrial glutamine metabolism whose inhibition limits glutamine flux through the TCA cycle [155], and having observed GLS1 overexpression in CDK4/6 knockdown cells, we treated the cells with the specific GLS1 inhibitor bis-2-(5-phenylacetoamido-1,2,4-thiadiazol-2-yl)ethyl

sulfide (BPTES) [539] for 72 h and compared the results with glutamine-free conditions. Importantly, specific inhibition of GLS1 by 10 μM BPTES selectively reduced CDK4/6-inhibited cells viability without affecting HCT116 control cells population (Figure 4.2.31A). In contrast, complete deprivation of glutamine caused a significant reduction in the viability of both control and CDK4/6-inhibited cells (Figure 4.2.31A).

Figure 4.2.31. Effects of glutaminase inhibition and glutamine deprivation on cell proliferation and apoptosis in CDK4/6 knockdown and control cells. Cells were incubated with 10 μM BPTES or vehicle, or in the absence of glutamine for 72h. Glutamine-deprived and BPTES-treated cells were also cultured with 2 mM dimethyl α-ketoglutarate (indicated as αKG). **A.** Cell proliferation was determined by flow cytometry. Data are shown as percentage of proliferation relative to the corresponding control (CDK4/6 siRNA- or non-targeting siRNA- treated cells) grown in complete medium without BPTES. **B.** The percentage of cells in early apoptosis was measured by flow cytometry analysis of Annexin V-FITC staining and propidium iodide accumulation. The presence of absence of glutamine in the medium is referred as +Gln and –Gln, respectively. Data are represented as mean ± SD of n=3. Statistically significant differences between CDK4/6 knockdown and control cells were indicated at $p < 0.01$ (**) and $p < 0.001$ (***), while differences between treatment (BPTES or glutamine deprivation with or without dimethyl α-ketoglutarate supplementation) and the corresponding control (CDK4/6 siRNA- or non-targeting siRNA- treated cells in complete medium without BPTES nor dimethyl α-ketoglutarate) were shown at $p < 0.05$ (#), $p < 0.01$ (##) and $p < 0.001$ (###) for CDK4/6-inhibited cells and at $p < 0.05$ (¶), $p < 0.01$ (¶¶) and $p < 0.001$ (¶¶¶) for control cells.

186

Remarkably, the addition of the cell-permeable form of α-ketoglutarate (αKG), dimethyl α-ketoglutarate, rescued CDK4/6-inhibited cell viability but does not have any effect on control cells (Figure 4.2.31A). In addition, BPTES induced greater early apoptosis in cells with CDK4/6 inhibition whereas glutamine removal significantly increases early apoptosis in both control and CDK4/6-inhibited cells (Figure 4.2.31B). Addition of dimethyl α-ketoglutarate on cells treated with BPTES caused no effects on control cells while decreased early apoptosis in CDK4/6 knockdown cells (Figure 4.2.31B). Interestingly, under glutamine deprivation, the replacement of glutamine with dimethyl α-ketoglutarate also suppressed early apoptosis in CDK4/6 knockdown cells but not in control cells (Figure 4.2.31B). These findings indicate that MYC-induced glutamine dependence is not caused by the requirement of amide groups and nitrogen for the biosynthesis of nucleotides and non-essential amino acids, respectively, as dimethyl α-ketoglutarate is not able to fulfil these glutamine-dependent reactions. GLS1 catalyses the glutamine entry to the central mitochondrial metabolism of the TCA cycle, only one of the multiple reactions in which glutamine is involved. Our results are in accordance with previous studies showing that glutamine metabolism through the TCA cycle is required for the survival of cells that overexpress MYC [96, 540].

Next, we examined GLS1 inhibition and glutamine deprivation effects on glucose and glutamine consumption and lactate and glutamate production. Interestingly, neither glucose consumption nor lactate production rates were affected by BPTES or glutamine depletion (Figures 4.2.32A and 4.2.32B). On the other hand, dimethyl α-ketoglutarate supplementation decreased glucose consumption and lactate production in both control and CDK4/6-inhibited cells (Figures 4.2.32A and 4.2.32B). As expected, BPTES repressed glutamine consumption in both cases, but a reduction in glutamate production is only seen in control cells (Figures 4.2.32C and 4.2.32D). In addition, glutamine deprivation greatly decreased glutamate production in control cells compared to CDK4/6 knockdown cells (Figure 4.2.32D). Moreover, addition of dimethyl α-ketoglutarate enhanced glutamate production in CDK4/6-inhibited cells and reduced glutamine uptake in both control and CDK4/6-inhibited cells (Figures 4.2.32D and 4.2.32C). Together, these data suggest that cells with CDK4/6 knockdown present an
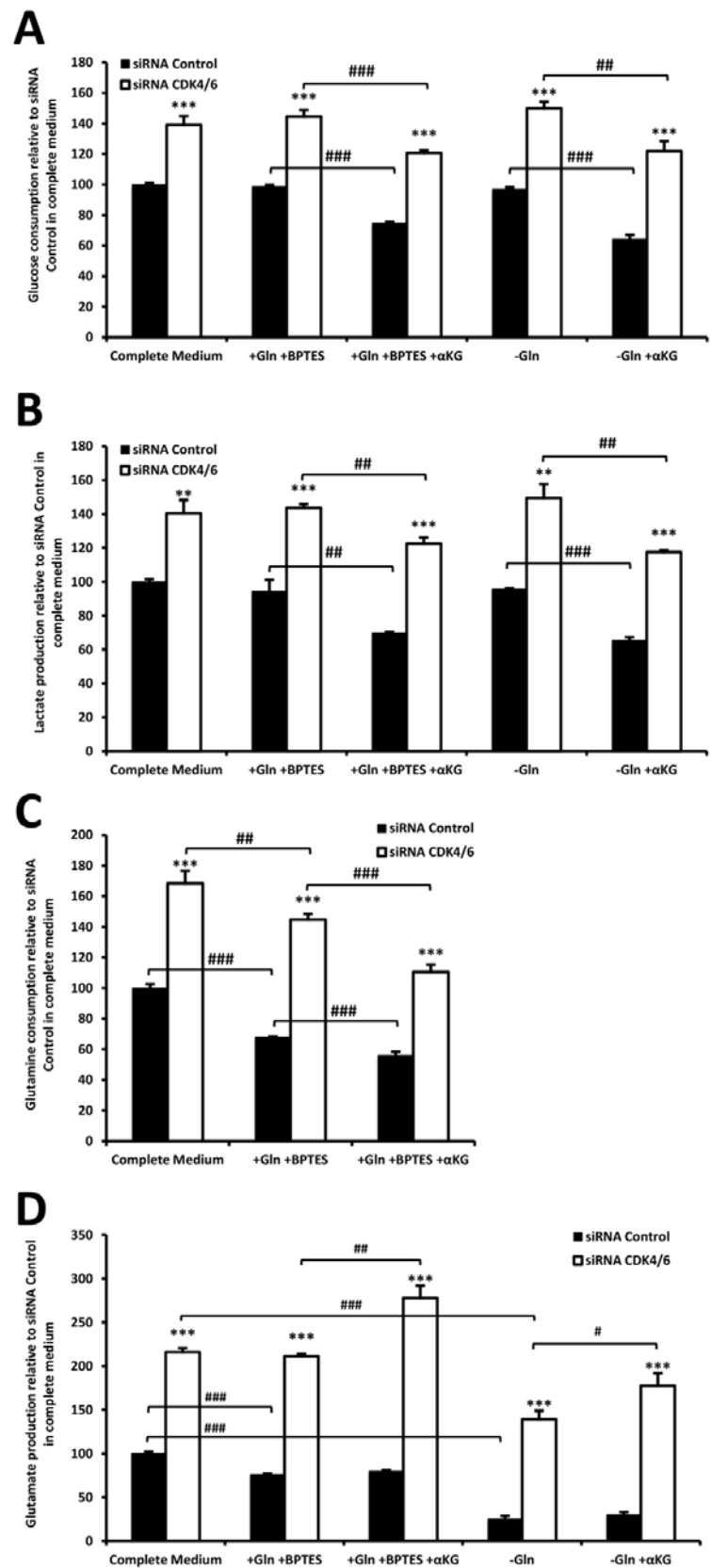
Figure 4.2.32. Effects of glutaminase inhibition and glutamine deprivation on metabolic extracellular fluxes in CDK4/6 knockdown and control cells. Cells were incubated with 10 μM BPTES or vehicle, or in the absence of glutamine for 72h. Glutamine-deprived and BPTES-treated cells were also cultured with 2 mM dimethyl

enhanced mitochondrial metabolism even in the absence of glutamine or with inhibition of GLS1.

As CDK4/6 knockdown cells exhibited both elevated mitochondrial function and ROS production, we hypothesised that glutamine deprivation and BPTES would significantly increase ROS levels in CDK4/6-inhibited cells. Indeed, absence of glutamine enhanced ROS production to a similar extent in both control and CDK4/6 knockdown cells, whereas only cells with CDK4/6 inhibition presented a superior percentage positive for ROS after 72 h of BPTES treatment (Figure 4.2.33A). These results corroborate our theory that cells with reduced levels of CDK4/6 are sensitive to GLS1 inhibition by BPTES. In fact, the increase in ROS production can contribute to the reduced viability of CDK4/6-inhibited cells observed after BPTES incubation. To probe the connection between ROS and cell viability, we tested the effect of an antioxidant, N-acetyl cysteine (NAC), on cells treated with BPTES. Interestingly, incubation with 5 µM NAC completely recovered the basal levels of ROS (Figure 4.2.33A) while partially rescuing BPTES-treated cell viability (Figure 4.2.33B). These results suggested that the augment in ROS is in part responsible of the decreased viability of CDK4/6 knockdown cells. However, addition of dimethyl α-ketoglutarate completely abrogated the reduced proliferation of CDK4/6-inhibited cells under glutamine deprivation or after BPTES treatment (Figure 4.2.31A), suggesting that the suppression of glutamine anaplerosis is playing a greater role in the reduction of proliferation.

Together, these results robustly suggest CDK4/6 and GLS1 inhibition as a potential combination therapy for colon cancer therapy, which is consistent with Yuneva et al.

α-ketoglutarate (indicated as αKG). Glucose and glutamine consumption and lactate and glutamate production rates were obtained after 72 h incubation with the specified media and normalised to cell number. **A.** Glucose consumption rate. **B.** Lactate production rate. **C.** Glutamine consumption rate. **D.** Glutamate production rate. All data are represented as relative consumption/production rate with the rates of non-targeting siRNA-treated cells in complete medium set to 100%. The presence of absence of glutamine in the medium is referred as +Gln and –Gln, respectively. Data are represented as mean ± SD of n=3. Statistically significant differences between CDK4/6 knockdown and control cells were indicated at $p < 0.01$ (**) and $p < 0.001$ (***), while differences between treatments were shown at $p < 0.05$ (#), $p < 0.01$ (##) and $p < 0.001$ (###).
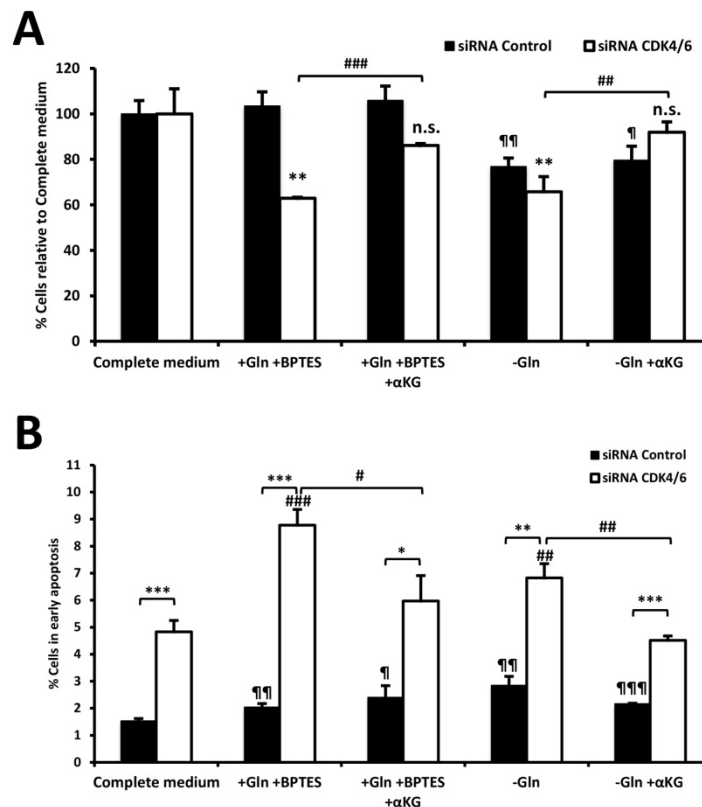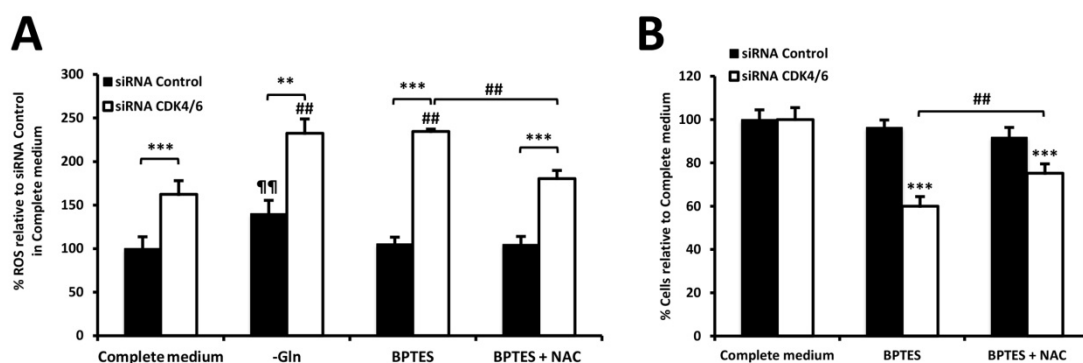
Figure 4.2.33. Effects of glutaminase inhibition and glutamine deprivation on ROS production in CDK4/6 knockdown and control cells. Cells were cultured in complete medium, medium with 10 µM BPTES in presence or absence of 5 µM N-acetyl cysteine (NAC) or glutamine-deprived medium for 72h. **A.** Intracellular ROS levels were determined by flow cytometry. Data are expressed as percentage of mean fluorescent intensity (MnX) relative to control cells in complete medium (mean ± SD of n=3). The absence of glutamine in the medium is referred as –Gln. **B.** Cell proliferation was measured by HO33342 staining (see Section 3.5). Results are represented as percentage of proliferation relative to control cells cultured without BPTES (mean ± SD of n=6). The effect of BPTES treatment is also compared to with BPTES and NAC treatment. Statistically significant differences between CDK4/6 knockdown and control cells were indicated at p < 0.01 (**) and p < 0.001 (***), while differences between treatments (glutamine deprivation or BPTES with or without NAC supplementation) and with the corresponding control (CDK4/6 siRNA- or non-targeting siRNA- treated cells in complete medium without BPTES nor NAC) were shown at p < 0.01 (##) for CDK4/6-inhibited cells and at p < 0.01 (¶¶) for control cells.

hypothesis about a synthetic lethal interaction between cells that overexpressed *MYC* and GLS1 inhibition [155]. Conventional chemotherapeutic treatments for cancer such as cisplatin have its clinical efficacy compromised by acquired resistance and dose-limiting side effects [5]. Therefore, the search for new combination therapies is essential for optimising the chemotherapeutic treatment outcome. Thus, in order to test whether the combined treatment of PD0332991 with BPTES can be a promising new strategy in cancer therapy, we studied the effect on HCT116 cell viability of these two specific inhibitors alone and in constant ratio (1:4) combination (Figure 4.2.34A). To quantify the synergy of dose-dependent effect on cell viability, the Combination Index (CI) equation of Chou and Talalay [483] was used with the CompuSyn software (ComboSyn, Inc., Paramus, NJ, USA). The CI equation determines the additive effect of drug combinations, such that synergism is defined as a greater-than-the-expected-additive effect, and antagonism is defined as less-than-an-expected-additive effect.

Thus, CI=1 indicates an additive effect, CI<1 indicates a synergistic effect, and CI>1 indicates antagonism. CI values are interpreted as follows [541]:

CI value	Agonistic effect
<0.10	Very strong synergism
0.10–0.30	Strong synergism
0.30–0.70	Synergism
0.70–0.90	Moderate to slight synergism
0.90–1.10	Nearly additive
1.10–1.45	Slight to moderate antagonism
1.45–3.30	Antagonism
>3.30	Strong to very strong antagonism

Importantly, the combination of PD0332991 and BPTES treatments in a wide dose range showed a strong synergism in the antiproliferative effect with a CI<1 (Table 4.2.1A). In order to determine if this combination treatment obtained similar growth inhibitory results in other cancer cell lines, we measured the effect of PD0332991 alone or combined with 10 µM BPTES on cell viability in MCF7 (breast cancer ER positive and HER2 negative) and SKBR3 (breast cancer ER negative and HER2 positive) cell lines, since PD0332991 is being used for breast cancer therapy [85, 542]. The $^{96h}IC_{50}$ values obtained for PD0332991 treatment alone were 0.81 ± 0.14 µM and 4.67 ± 0.11 µM for MCF7 and SKBR3 cells, respectively. The addition of 10 µM BPTES significantly reduced $^{96h}IC_{50}$ values for MCF7 and SKBR3 cells to 0.18 ± 0.02 µM and 2.31 ± 0.05 µM, respectively. In addition, we analysed the effect of PD0332991, BPTES and their combined treatment in constant ratio (1:4) on MCF7 (Figure 4.2.34B) and SKBR3 (Figure 4.2.34C) cell viability. To this aim, we also employed the CI equation of Chou and Talalay [483] and the CompuSyn software. In agreement with the effects on HCT116 cells, PD0332991 and BPTES combination in MCF7 cells exhibited a strong synergism (CI<0.3) at low drug concentrations and a synergistic antiproliferative effect (CI<0.7) at a higher dose range (Table 4.2.1B). In the case of SKBR3 cells, the simultaneous treatment of PD0332991 and BPTES exhibited a strong synergistic antiproliferative effect with a CI<0.3 at a wide dose range (Table 4.2.1C).
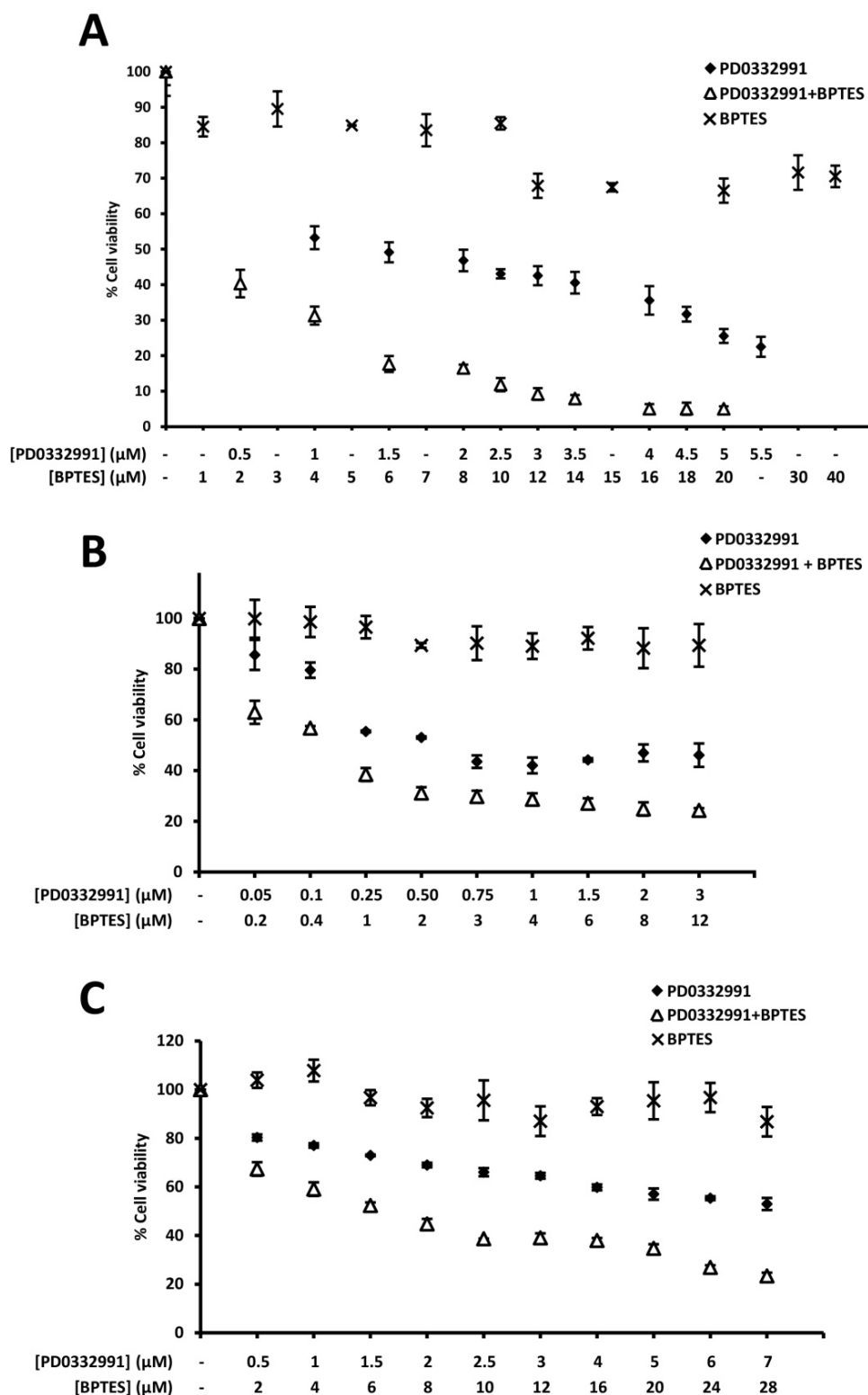
Figure 4.2.34. Synergistic antiproliferative effect of PD0332991 and BPTES combined treatment. Cells were cultured at the indicated concentrations of inhibitors for 96 h and cell proliferation was determined by the Hoechst staining. Cell viability was assessed after incubation with PD0332991, BPTES and a combination the two inhibitors at the indicated concentrations in **A.** HCT116 cells, **B.** MCF7 cells and **C.** SKBR3 cells. In all cases, results are shown as percentage of proliferation relative to untreated cells (mean ± SD of n=6).

192

Table 4.2.1. Synergistic antiproliferative effect of PD0332991 and BPTES combined treatment. A. HCT116, **B.** MCF7 and **C.** SKBR3 cells were treated for 96 h at the indicated concentrations of PD0332991 and BPTES in a constant ratio (1:4). The CI results obtained with CompuSyn software revealed a synergy (CI<1) in the antiproliferative effects of PD0332991 and BPTES at each dose combination tested.

A

HCT116 cells			
PD0332991 (µM)	BPTES (µM)	Viability (%)	CI Value
0.5	2	40.3 ± 3.9	*0.195*
1	4	31.3 ± 2.5	*0.227*
1.5	6	17.7 ± 2.3	*0.122*
2	8	16.5 ± 0.9	*0.146*
2.5	10	11.8 ± 1.9	*0.107*
3	12	9.2 ±1.7	*0.088*
3.5	14	7.9 ± 1.0	*0.082*
4	16	5.1 ± 1.3	*0.049*
4.5	18	5.0 ± 1.7	*0.055*
5	20	5.0 ± 0.7	*0.060*

B

MCF7 cells			
PD0332991 (µM)	BPTES (µM)	Viability (%)	CI Value
0.05	0.2	63.0 ± 4.6	*0.163*
0.1	0.4	56.8 ± 0.8	*0.196*
0.25	1	38.5 ± 2.6	*0.130*
0.5	2	31.1 ± 2.3	*0.161*
0.75	3	29.8 ± 2.3	*0.222*
1	4	28.7 ± 2.4	*0.277*
1.5	6	27.1 ± 2.0	*0.377*
2	8	24.9 ± 2.6	*0.438*
3	12	24.3 ± 1.9	*0.636*

C

SKBR3 cells			
PD0332991 (µM)	BPTES (µM)	Viability (%)	CI Value
0.5	2	67.4 ± 2.8	*0.222*
1	4	59.1 ± 2.8	*0.223*
1.5	6	52.3 ± 1.3	*0.197*
2	8	44.8 ± 2.1	*0.145*
2.5	10	39.0 ± 0.1	*0.112*
3	12	38.7 ± 1.9	*0.138*
4	16	38.0 ± 1.0	*0.169*
5	20	34.7± 1.7	*0.160*
6	24	26.9 ± 0.9	*0.094*
7	28	23.4 ± 1.4	*0.077*

The synergism observed in HCT116, MCF7 and SKBR3 cell lines suggests that PD0332991 and BPTES co-treatment is an efficient strategy to decrease the chemotherapeutic dose required for therapy and consequently, the overall toxicity.

Next, to test the selective cytotoxicity of PD0332991 and BPTES combination treatment for cancer cells, we determined the cell viability dose-response curve of the non-tumour BJ human foreskin fibroblast cell line using the Hoechst stain assay. HCT116 and BJ cells were grown in 96-well plates and incubated for 96 h at the indicated concentrations with PD0332991 alone or with addition of 10 µM BPTES, and the effect on cell proliferation was determined (Figure 4.2.35).
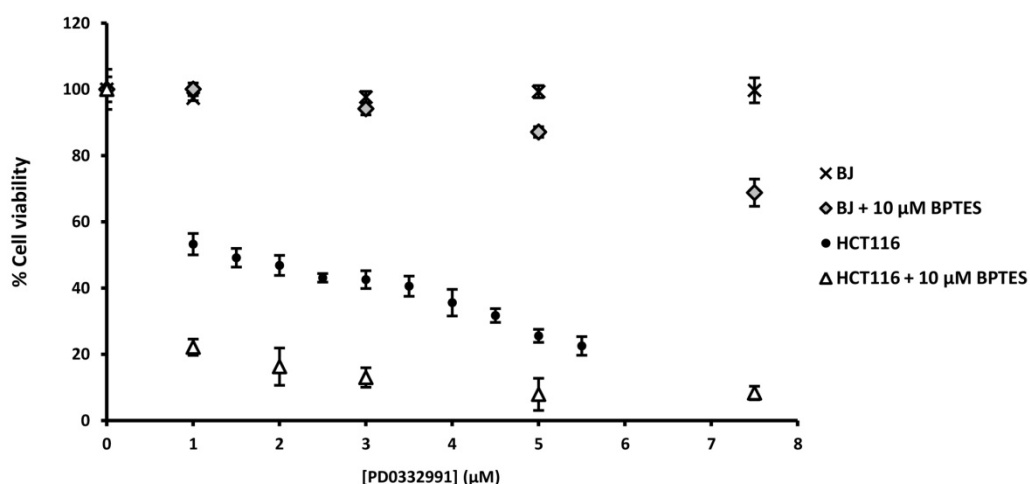
Figure 4.2.35. Selective cytotoxicity of PD0332991 and BPTES combined treatment for cancer cells. Cells were cultured at the indicated concentrations of inhibitors for 96 h and cell proliferation was determined by the Hoechst staining. Cell viability of BJ and HCT116 cells was assessed after incubation with PD0332991 alone or PD0332991 with 10 µM BPTES. In all cases, results are shown as percentage of proliferation relative to untreated cells (mean ± SD of n=6).

As seen in Figure 4.2.35, the simultaneous incubation with PD0332991 and BPTES at all concentrations tested had little or no effect on non-tumour BJ cells viability but greatly impaired proliferation of HCT116 cells. For example, combination treatment with 1 µM PD0332991 and 10 µM BPTES caused no cytotoxic effects on non-tumour BJ cells while producing an approximate 80% reduction in HCT116 cell viability. All together, these

results support the concomitant use of PD0332991 with BPTES as a promising chemotherapeutic therapy with selective antiproliferative effects on cancer cells.

4.2.2.14. Combination therapies involving CDK4/6 inhibition and other metabolic regulators

4.2.2.14.1. Combined treatment with PD0332991 and rapamycin

Gene set enrichment analysis revealed that CDK4/6 knockdown induced an upregulation of mTOR target genes, which was confirmed by the observed increase in P-mTOR protein levels (Figure 4.2.19A). Moreover, Nicklin et al. provided a model in which intracellular glutamine acts upstream of mTORC1 serving as an efflux substrate for SLC7A5/SLC3A2, a plasma membrane heterodimer, to regulate the uptake of extracellular leucine, and leading to mTORC1 activation [133]. Therefore, intracellular glutamine works as an essential and rate-limiting sensor that allows leucine and growth factors to activate mTOR, while SLC7A5/SLC3A2 bidirectional transporter is also required to enable this system to function. According to our results, CDK4/6-inhibited cells exhibited enhanced glutamine (increased intracellular levels) and leucine uptake (Figures 4.2.3 and 4.2.9B), and increased *SLC7A5* gene expression (Figure 4.2.19B). To determine whether this mechanism was activated in CDK4/6 knockdown cells, we analysed the gene expression levels of *SLC3A2*. Consistent with the observed activation of mTOR, CDK4/6 inhibition induced a 1.7-fold upregulation of *SLC3A2* mRNA compared to control cells (Figure 4.2.36A).

Accordingly, we reasoned that rapamycin treatment in combination with CDK4/6 inhibition might be a good therapeutic strategy, since rapamycin is a specific mTOR inhibitor. To test this hypothesis, we studied the effect on HCT116 cell viability of PD0332991 and rapamycin alone and in constant ratio (5:1) combination (Figure 4.2.36B). As in the case of PD0332991 and BPTES treatment, we quantified the dose-dependent synergistic effect on HCT116 cell viability by means of the Combination Index (CI) equation of Chou and Talalay [483].

Notably, the simultaneous treatment of PD0332991 and rapamycin in a wide dose range exhibited a very strong synergistic antiproliferative effect with a CI<0.1 (Table 4.2.2). This synergism endorses PD0332991 and rapamycin co-treatment as an efficient strategy in cancer therapy.

Table 4.2.2. Synergistic antiproliferative effect of PD0332991 and rapamycin combined treatment. HCT116 cells were treated for 96 h at the specified concentrations of PD0332991 and rapamycin in a constant ratio (5:1). The CI results obtained with CompuSyn software revealed a very strong synergism (CI<1) in the antiproliferative activity of PD0332991 and rapamycin at each dose combination tested.

PD0332991 (µM)	Rapamycin (µM)	Viability (%)	CI Value
0.01	0.002	53.9 ± 3.7	*0.008*
0.03	0.006	36.3 ± 3.0	*0.009*
0.05	0.01	31.9 ± 4.9	*0.012*
0.15	0.03	27.1 ± 1.4	*0.026*
0.25	0.05	21.2 ± 2.9	*0.028*
0.4	0.08	21.2 ± 2.4	*0.044*
0.5	0.1	21.2 ± 0.9	*0.055*
1	0.2	17.1 ± 1.7	*0.077*
2	0.4	11.8 ± 1.7	*0.086*
3	0.6	9.9 ± 1.1	*0.097*

To further validate the therapeutic potential of this combined treatment, we tested the selective cytotoxicity of PD0332991 and rapamycin co-treatment for cancer cells. To this end, as previously, we assessed a dose-response curve for cell viability of the non-tumour BJ human foreskin fibroblast cell line using the Hoechst stain assay. HCT116 and BJ cells were grown in 96-well plates and simultaneously incubated with PD0332991 and rapamycin at the specified concentrations maintaining a constant ratio (5:1). After 96 h treatment, the effect on cell proliferation was determined (Figure 4.2.36C). Importantly, the concomitant treatment with PD0332991 and rapamycin at all concentrations tested had no cytotoxic effects on non-tumour BJ cells while drastically reducing HCT116 cell proliferation. These results reassure the combined treatment of PD0332991 and rapamycin as a potential chemotherapeutic therapy with selective antiproliferative activity on tumour cells.
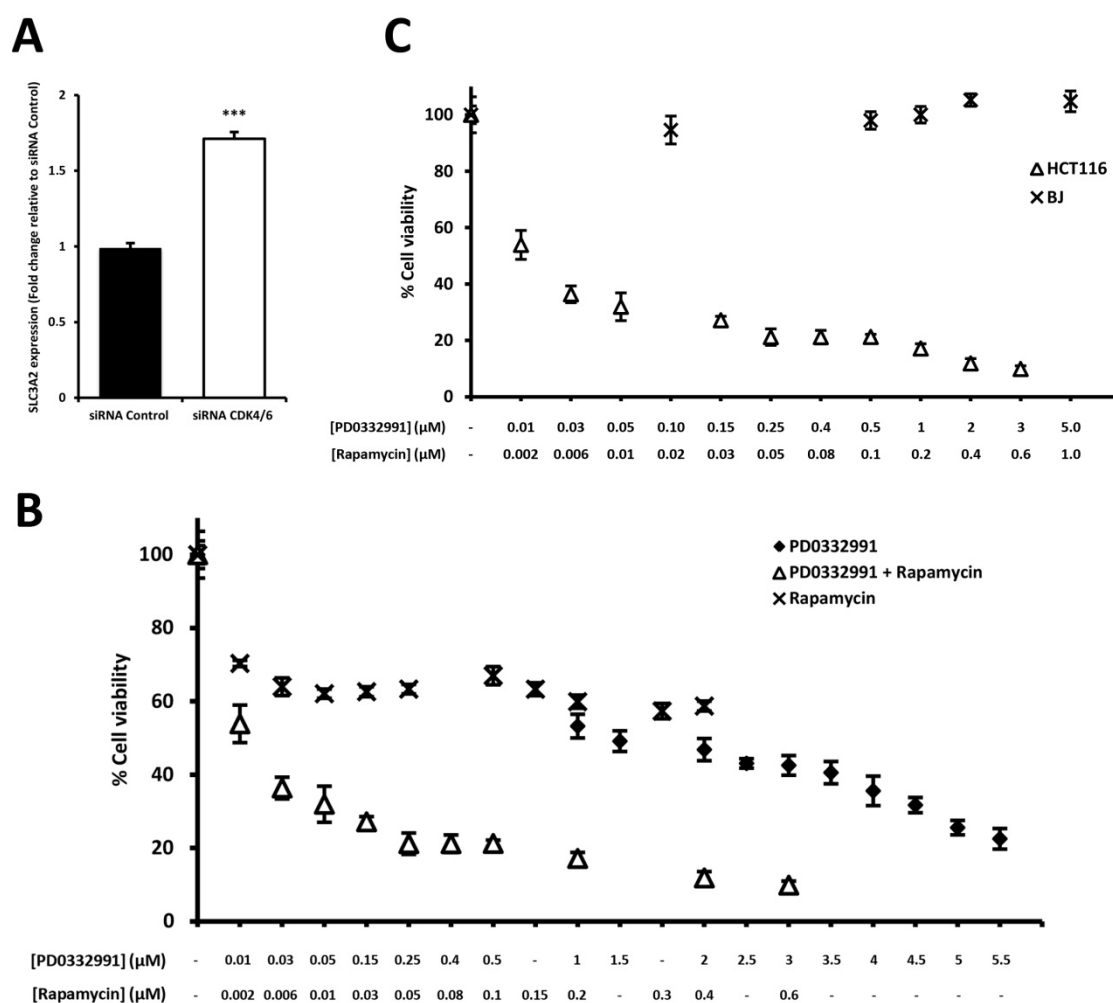
Figure 4.2.36. Synergistic antiproliferative effect of PD0332991 and rapamycin combined treatment. A. *SLC3A2* gene expression was measured by RT-qPCR in CDK4/6 knockdown and control cells 96 h after transfection. Results are normalised to cyclophilin A and expressed as fold change of mRNA relative to expression of non-targeting siRNA-treated cells. Bars represent mean ± SD of n=3. Statistically significant differences between CDK4/6 knockdown and control cells were indicated at $p < 0.001$ (***). **B.** HCT116 cells were cultured at the indicated concentrations of inhibitors for 96 h and cell proliferation was determined by the Hoechst staining. Cell viability was assessed after incubation with PD0332991, rapamycin and their combination at the indicated concentrations **C.** Cell viability of BJ and HCT116 cells assessed with Hoechst staining after incubation with PD0332991 and rapamycin combination (5:1 ratio). Results are shown as percentage of proliferation relative to untreated cells (mean ± SD of n=6).

4.2.2.14.2. Combined treatment with PD0332991 and inhibitors of the PI3K/Akt axis

Searching for other potential candidates for combined treatments with CDK4/6 inhibition, we considered targeting the PI3K/Akt axis since mTOR activation can, in

197

turn, activate PI3K/Akt pathway [307, 315], suggesting that CDK4/6 knockdown cells can also be sensitive to PI3K/Akt pathway inhibition. To this end, we experimentally confirmed that PI3K/Akt signalling was activated in CDK4/6-inhibited cells by increased protein levels of phosphorylated Akt (Ser473) and reduced protein expression of p27[Kip1] (Figure 4.2.37A), which is known to be suppressed by the PI3K/Akt pathway in order to proceed with cell cycle [297]. RT-qPCR analyses reported an upregulation of *PIK3R3* (encoding the PI3K regulatory subunit p55γ) (Figure 4.2.37B) and *CCND1* (cyclin D1) (Figure 4.2.27B), which is induced through FOXO3a inactivation by Akt-mediated phosphorylation [278, 279, 543]. Furthermore, as seen in Figures 4.2.19A and 4.2.36A, the knockdown of CDK4/6 led to increased levels of phosphorylated mTOR at Ser2448 residue, a known Akt phosphorylation site [544, 545]. Collectively, these results suggest that upregulation of the PI3K/Akt axis is associated with the metabolic reprogramming driven by CDK4/6 knockdown. To investigate whether PI3K/Akt inhibition represented a promising vulnerability in CDK4/6-inhibited cells, we examined the effect of PD0332991 and LY294002 (a known PI3K inhibitor [546]) alone and in constant ratio (1:1) combination on HCT116 cell viability (Figure 4.2.37C). As in the other combined treatments tested, we used the Combination Index (CI) equation of Chou and Talalay [483] to estimate the dose-dependent synergistic effect on HCT116 cell viability.

In this case, co-treatment with PD0332991 and LY294002 in a wide dose range showed a synergistic reduction of cell proliferation with a CI<1 (Table 4.2.3). It is noteworthy that the stronger synergistic effects were achieved at low combined doses. Therefore, PD0332991 and LY294002 simultaneous treatment increased the efficiency of the antiproliferative action of these drugs.

To test whether PD0332991 and LY294002 combined treatment was selective to tumour cells, we performed a dose-response analysis of the non-tumour BJ human foreskin fibroblast cells by using the Hoechst stain system. As with the other inhibitor combinations, HCT116 and BJ cells were grown in 96-well plates and treated at the same time with PD0332991 and LY294002 at the indicated concentrations maintaining a constant ratio (1:1 for HCT116 cells and 1:10 for BJ cells). After 96 h incubation, we

Table 4.2.3. Synergistic antiproliferative effect of PD0332991 and LY294002 combined treatment. HCT116 cells were treated for 96 h at the indicated concentrations of PD0332991 and LY294002 in a constant ratio (1:1). Using CompuSyn software, we found synergism (CI<1) in the antiproliferative action of PD0332991 and LY294002 at each combined dose tested.

PD0332991 (µM)	LY294002 (µM)	Viability (%)	CI Value
0.05	0.05	78.3 ± 1.7	*0.191*
0.1	0.1	69.7 ± 3.0	*0.209*
0.5	0.5	49.2 ± 3.7	*0.338*
1	1	42.3 ± 3.6	*0.476*
1.5	1.5	39.3 ± 1.9	*0.613*
2	2	37.5 ± 3.0	*0.743*
2.5	2.5	28.6 ± 2.0	*0.574*
3	3	24.4 ± 2.0	*0.542*
4	4	17.3 ± 1.8	*0.460*
4.5	4.5	14.1 ± 0.8	*0.412*

measured the effect of the combination on cell proliferation (Figure 4.2.37D). Remarkably, the simultaneous treatment with PD0332991 and LY294002 at each dose level tested significantly reduced HCT116 cell viability while had little or no cytotoxic effects on non-tumour BJ cells despite being incubated with a concentration of LY294002 10 times higher than HCT116 cells. Therefore, these data reveal the co-treatment of PD0332991 and LY294002 as a potential combined therapy selective to tumour cells.

To determine if this combined treatment achieved comparable synergistic effects with a different PI3K/Akt inhibitor, we incubated HCT116 cells with PD0332991 and methylseleninic acid (MSA) (Chapter 4.3) alone or in combination at the detailed concentrations and in a constant ratio (1:1) (Figure 4.2.37E). As illustrated in Table 4.2.4, the concomitant treatment with PD0332991 and MSA presented a strong synergism at low concentrations, a moderate to nearly additive synergism at concentrations ranging 1-2 µM and synergistic effects at the rest of the doses tested. Together, these results confirmed the combined inhibition of CDK4/6 and PI3K/Akt axis as a promising tumour therapy approach.
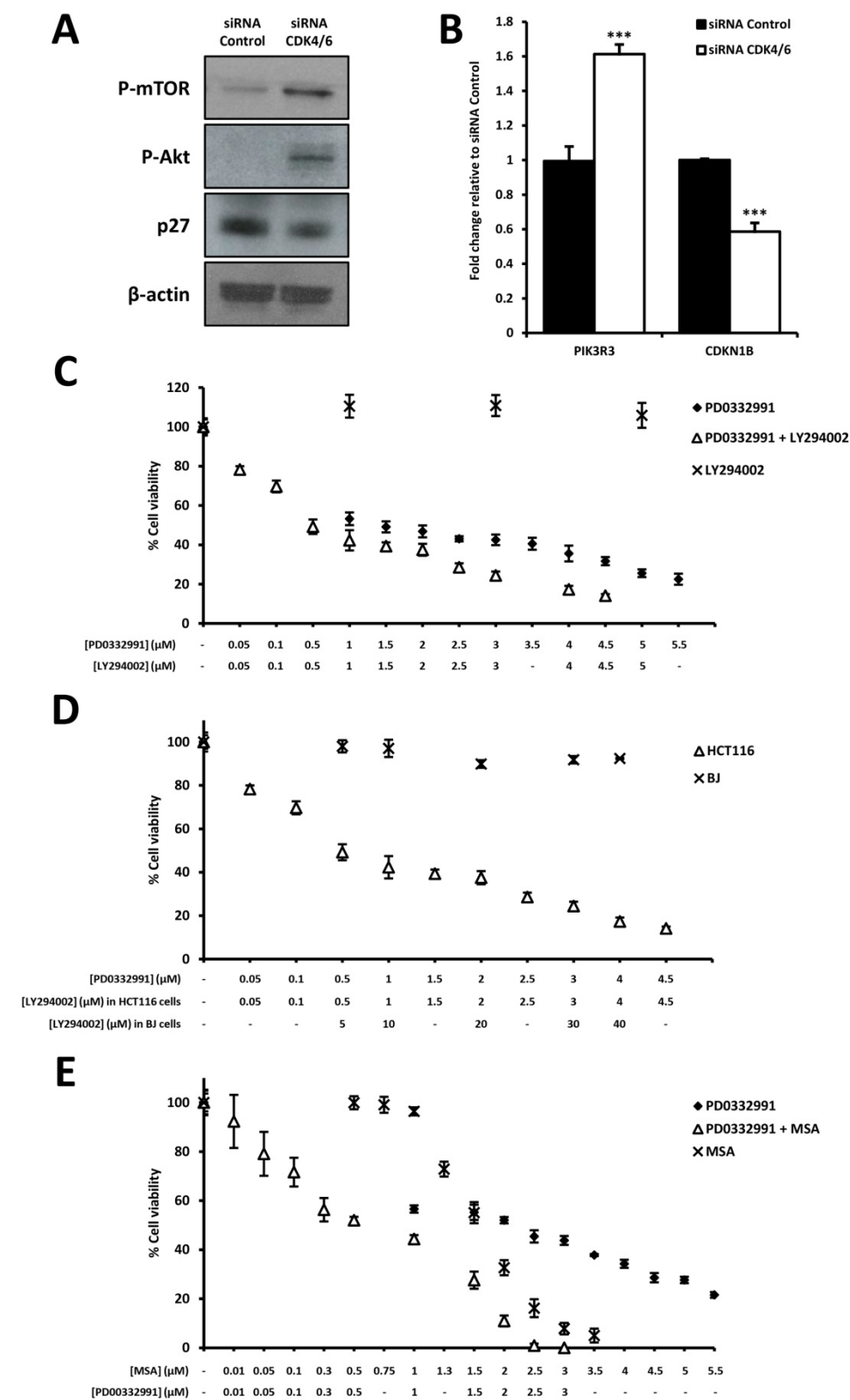
Figure 4.2.37. Synergistic antiproliferative effect of PD0332991 and inhibitors of the PI3K/Akt axis combined treatment. A. Western blot analysis of total protein fractions of CDK4/6 knockdown and control cells 96 h after transfection. β-actin was used as a protein loading control. **B.** *PIK3R3* and *CDKN1B* gene expression was measured by RT-qPCR in CDK4/6 knockdown and control cells 96 h after transfection. Results are normalised to cyclophilin A

Table 4.3.4. Synergistic antiproliferative effect of PD0332991 and MSA combined treatment. HCT116 cells were treated for 96 h at the specified concentrations of PD0332991 and MSA in a constant ratio (1:1). The CI results obtained using CompuSyn software exposed a synergism (CI<1) in the antiproliferative activity of PD0332991 and MSA at each combined dose tested.

PD0332991 (µM)	MSA (µM)	Viability (%)	CI Value
0.01	0.01	92.3 ± 5.2	*0.093*
0.05	0.05	79.1 ± 2.3	*0.155*
0.10	0.10	71.6 ± 3.2	*0.219*
0.30	0.30	56.3 ± 0.4	*0.394*
0.50	0.50	52.0 ± 1.4	*0.584*
1.00	1.00	44.3 ± 1.6	*0.963*
1.50	1.50	27.6 ± 3.5	*0.979*
2.00	2.00	11.0 ± 2.2	*0.852*
2.50	2.50	0.9 ± 0.8	*0.567*
3.00	3.00	0.0 ± 0.0	*0.279*

4.2.2.15. Combination therapies validation in 3D in vitro culture system

To test whether the combined therapies studied here presented similar results in a more physiologically relevant system, we generated spheroids of HCT116 cells (as described in Section 3.7) as an *in vitro* tumour model system of intermediate complexity between standard monolayer cultures and tumours *in vivo* [547]. Indeed, it is worth noting that the spheroid model has been increasingly recognised as a primary tool for positive selection in innovative drug development therapies since it can remarkably reflect the 3D heterogeneous microenvironments as well as the therapeutically relevant pathophysiological gradients of *in vivo* tumours [548].

and expressed as fold change of mRNA relative to expression of non-targeting siRNA-treated cells. Bars represent mean ± SD of n=3. Statistically significant differences between CDK4/6 knockdown and control cells were indicated at $p < 0.001$ (***). **C.** HCT116 cells were cultured with PD0332991, LY294002 or their combination at the indicated concentrations for 96 h and cell proliferation was determined by Hoechst staining. **D.** Cell viability of BJ and HCT116 cells was assessed with Hoechst staining after incubation with PD0332991 and LY294002 combination (1:1 ratio) at the indicated concentrations for 96 h. **E.** HCT116 cell viability was determined by Hoechst staining after incubation with PD0332991, MSA or their combination (1:1 ratio). In **C.**, **D.** and **E.**, results are shown as percentage of proliferation relative to untreated cells (mean ± SD of n=6).
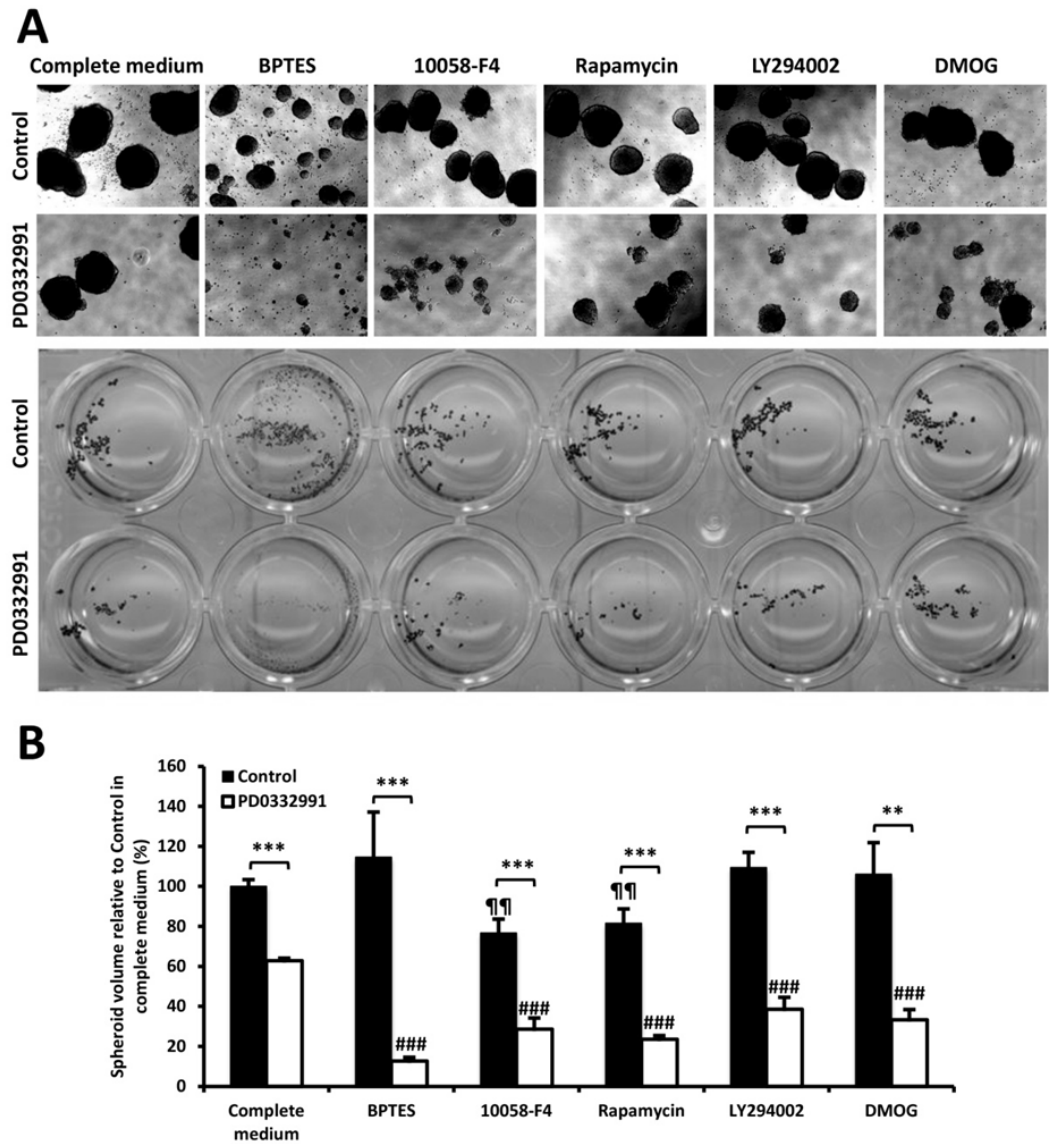
Figure 4.2.38. Combined treatments decreased the formation of spheroids. A. Images of HCT116 spheroids after 10 days of treatment with the indicated inhibitors. **B.** Quantification of the total spheroid volume after treatment with each inhibitor alone or in combination with PD0332991. Spheroids were scored by image acquisition and spheroid area and volume quantification with ImageJ software. Results are shown as percentage of total spheroid volume relative to untreated cells. Data are represented as mean ± SD of n=5. Statistically significant differences between CDK4/6-inhibited and control cells were indicated at $p < 0.01$ (**) and $p < 0.001$ (***), while differences between treatment (BPTES, 10058-F4, rapamycin, LY294002 or DMOG) and the corresponding control (PD0332991-treated cells or untreated cells in complete medium) were shown at $p < 0.001$ (###) for CDK4/6-inhibited cells and at $p < 0.01$ (¶¶) for control cells.

Towards this end, HCT116 cells were grown in ultra low attachment plates (as detailed in Section 3.7) with the specified concentration of inhibitor(s) and were scored for

spheroids after 10 days. Inhibition of CDK4/6 decreased the anchorage-independent colony-forming growth of HCT116 cells (Figure 4.2.38). Moreover, the combination of PD0332991 with the metabolic inhibitors BPTES, 10058-F4, rapamycin, LY294002 and DMOG reduced the formation of spheroids to a greater extent than either therapy alone (Figure 4.2.38). Importantly, PD0332991 and BPTES simultaneous treatment caused the greatest effects. Consistent with our results in monolayer cells, BPTES treatment alone produced no effects on total spheroid volume while, when combined with CDK4/6 inhibition, dramatically abrogated the formation of spheroids, diminishing the overall spheroid volume to 13 ± 2% (Figure 4.2.38). Interestingly, GLS1 inhibition alone caused a significant reduction in spheroid diameter associated with a 5-fold increase in the number of spheroids, maintaining the global spheroid volume (Figure 4.2.38A). On the other hand, the concomitant inhibition of CDK4/6 and mTOR by PD0332991 and rapamycin, respectively, produced a synergic diminution of total spheroid volume to 23 ± 2%. Likewise, spheroids under PD0332991 and 10058-F4 treatment grew to 1/3 relative to control spheroids. In agreement with the viability assays, rapamycin and 10058-F4 single treatments decreased the growth of control cells spheroids but to a lesser extent than in monolayer experiments. On the other hand, both LY294002 and DMOG had no effects on HCT116 spheroid formation by themselves. However, when combined with CDK4/6 repression, a significant reduction in the total spheroid volume is observed (Figure 4.2.38).

4.2.3. Discussion

Cyclin-dependent kinases 4 and 6 (CDK4/6) are pivotal regulators of cell cycle that are frequently altered in cancer, leading to unscheduled proliferation [38, 43]. Due to their essential role in the regulation of cell cycle progression at the G1 restriction point, CDK4/6 have been largely studied as therapeutic drug targets [62, 507]. At the same time, highly selective and potent small-molecule CDK4/6 inhibitors such as PD0332991 have been identified and approved for clinical development [75, 83]. Accordingly, the inhibition of CDK4/6 showed antiproliferative effects in multiple tumour cell lines, human tumour xenografts and clinical trials [83, 84, 381, 542]. However, little is known

about the metabolic reprogramming resulting from the inhibition of CDK4/6. Indeed, the identification of the homeostatic adaptations following CDK4/6 inhibition, such as the dysregulation of transcription factors and their targets, may reveal vulnerabilities that can be therapeutically targeted in combination with CDK4/6 inhibition.

Our study provides an exhaustive characterisation of the biosynthetic and bioenergetic metabolic pathways induced by CDK4/6 inhibition, together with an integrated transcriptomic and fluxomic data analysis as a tool to reveal specific vulnerabilities resulting from CDK4/6 downregulation. Interestingly, CDK4/6 inhibition, through siRNA knockdown or by using the selective inhibitor PD0332991, caused cell cycle arrest, reduced cell proliferation and triggered apoptosis in association with an extensive metabolic reprogramming, as summarised in Figure 4.2.39. In particular, CDK4/6-inhibited cells exhibited an increase of mitochondrial metabolism and function accompanied by an enhanced metabolism of glucose, and especially of glutamine and amino acids.

The association analyses by GSEA correlated our pattern of gene expression with gene sets associated with components that are known to be fundamental for cell growth, cell proliferation and apoptosis. In particular, our analysis suggested that CDK4/6 inhibition correlates with the dysregulated activities of MYC, mTOR and HIF, which are master regulators of metabolism that have a large list of metabolic targets. Specifically, we found that gene expression of CDK4/6 knockdown cells exhibited a positive correlation with genes positively regulated by the transcription factor MYC and the serine/threonine protein kinase mTOR, and a negative correlation with genes upregulated in response to HIF transcription factor.

An integrated picture of the reprogramming of the central carbon metabolism is provided in Figure 4.2.18, combining the results of our fluxomic analysis with the metabolic and transcriptomic data. Interestingly, the reprogramming of the central carbon metabolism is directly associated with an important re-modulation of the expression of genes involved in metabolic activities. Interestingly, the interplay between regulatory proteins and the metabolic status is involved in the coordination

A

B
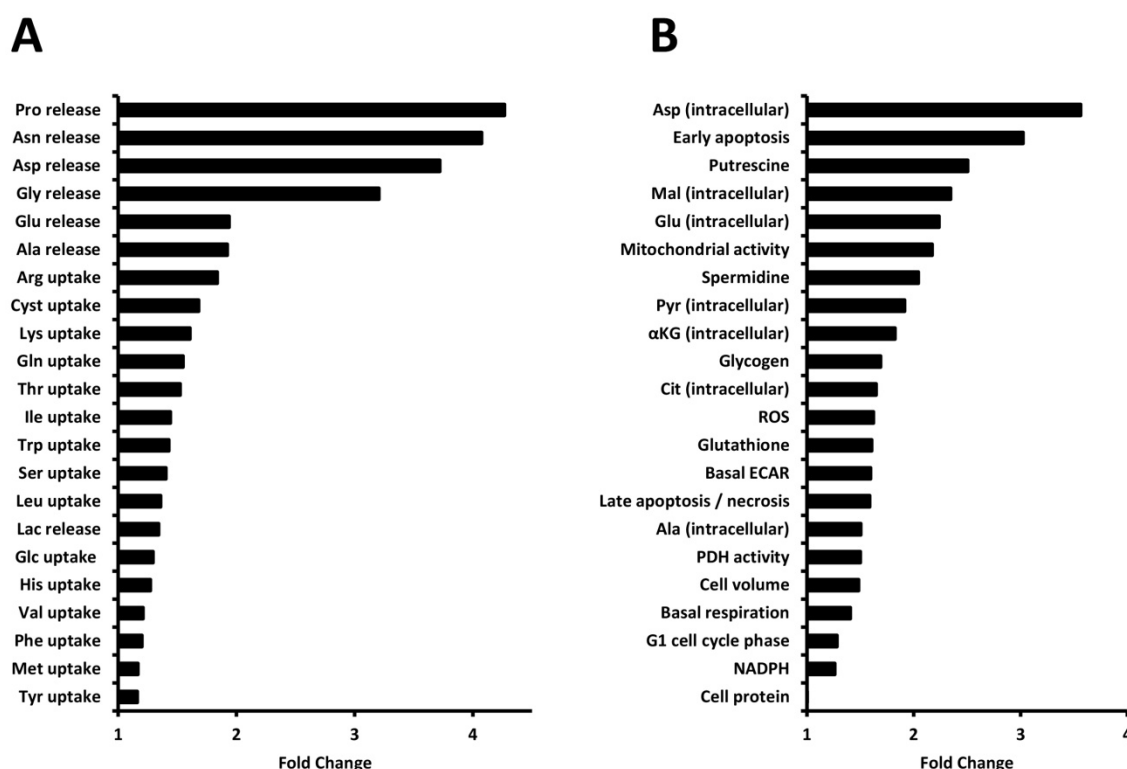
Figure 4.2.39. Changes in the principal measured fluxes, metabolites pools and functional characteristics exhibited by CDK4/6-inhibited cells compared to control cells. Comparisons were based on measures per cell or percentage of cells. Fold changes quantifying the differential measured biological characteristics are defined as the ratio of mean values (per cell or percentage of cells) in CDK4/6-inhibited cells relative to control cells.

of cell growth through sensing mechanisms of extracellular and intracellular conditions [132]. Among others, these sensors include Rag GTPases, which are key transducers between amino acids and mTOR complex 1 (mTORC1) activation, and prolyl hydroxylases that sense molecular oxygen and α-ketoglutarate to signal for the degradation of HIF1α. Therefore, fluxomics and transcriptomics integrated data analysis revealed MYC, mTOR and HIF1 as the principal key players of the metabolic adaptation exhibited by cells with CDK4/6 inhibition.

Importantly, our integrated analysis unambiguously identified MYC as the principal player in the metabolic reprogramming resulting from CDK4/6 inhibition. Overexpression of MYC is at the top of the cascade of events initiated by inhibition of CDK4/6, leading in turn to a dependence on glutaminase and MYC itself (Figures 4.2.31A and 4.2.23). We also have provided experimental evidence supporting that

CDK4/6 can trigger MYC proteasome-mediated degradation by phosphorylation at Ser62 (Figure 4.2.21) [231, 233, 235]. In addition, we have confirmed that CDK4/6 knockdown effects are not a result of cell cycle G1 phase arrest but a consequence of the loss of CDK4/6 kinase activity (Figure 4.2.30). Therefore, our results demonstrate that CDK4/6 inhibition releases MYC from proteasomal degradation and results in MYC accumulation.

Consequently, according to the key regulatory role of MYC, overexpression of MYC leads to a general activation of fundamental processes for cell growth and proliferation [147, 206]. In accordance with our results, it is well established that MYC increases oxygen consumption and promotes mitochondrial biogenesis and function [215, 216]. The enhanced mitochondrial metabolism and oxidative phosphorylation observed in CDK4/6-inhibited cells generate higher amounts of ROS [217] which, in turn, initiate the antioxidant cell machinery, resulting in increased levels of glutathione, NADPH and glutamine consumption. The detected early apoptosis may be a result of the higher levels of oxidative stress reported in cells with CDK4/6 inhibition. MYC involvement with mitochondrial biogenesis and oxidative phosphorylation provides an explanation for the increase in reactive oxygen species (ROS) associated to MYC activation [549], as mitochondrial respiration is a major source of ROS generation [217]. However, MYC is also implicated in oxidative stress protection through transcriptional activation of ɣ-glutamyl-cysteine synthetase (ɣ -GCS), the rate-limiting enzyme catalysing glutathione biosynthesis [550].

The enhancement of glucose, glutamine and amino acid metabolism exhibited by CDK4/6-inhibited cells are also likely to be a result from MYC overexpression. Indeed, MYC is known to enhance glycolysis through the activation of glycolytic and glucose transporters genes [210, 211] and also to promote lactate production and export [207, 212, 213]. However, it is worth noting that this activation of glycolysis is also coordinated with HIF1 [212, 237]. In addition, MYC stimulates the use of the TCA cycle to generate intermediates for macromolecular synthesis using both glucose and glutamine as carbon source [152, 157]. Accordingly, MYC also contributes to increase glutamine uptake by upregulation of the expression of glutamine transporters [147, 214] and enhances glutamine metabolism by transcriptionally repressing microRNA-

23a/b, resulting in a greater expression of glutaminase (GLS1) [214]. In fact, GLS1 can enhance the mitochondrial metabolism by catalysing the conversion of glutamine to glutamate. Therefore, the upregulation of glutamine transporters and GLS1 results in increased levels of glutamate, which is a key substrate for energy and redox processes, including mitochondrial respiration by fuelling the TCA cycle through its conversion to α-ketoglutarate. Glutamate can also transfer amino groups for synthesis of amino acids and nucleotides, and carbons for lipid biosynthesis through acetyl-CoA production or by generating citrate through reductive carboxylation. Furthermore, in line with our observations, high levels of glutamine, proline, alanine and asparagine are reported to stimulate glycogen synthesis in hepatocytes [551]. In particular, the mechanism of stimulation of glycogen synthesis by glutamine has been related to an increase in cell volume as a result of Na^+-dependent amino acid uptake [552], which is also in agreement with our results.

MYC is also involved in the regulation of proline metabolism, not only promoting the expression of GLS1, Δ^1-pyrroline-5-carboxylate synthetase (P5CS), and Δ^1-pyrroline-5-carboxylate reductase 1 (PYCR1), which are the enzymes implicated in proline biosynthesis from glutamine, but also suppressing proline catabolism through inhibition of proline oxidase/proline dehydrogenase (POX/PRODH) and Δ^1-pyrroline-5-carboxylate dehydrogenase (P5CDH) [135, 143]. Therefore, the 3-fold increase in proline production observed in CDK4/6-inhibited cells (Figure 4.2.9A) can be a result of MYC overexpression, causing proline accumulation. In addition, proline metabolism is also connected with polyamine synthesis through glutamic-gamma-semialdehyde (GSA) reversible conversion to ornithine catalysed by ornithine aminotransferase (OAT) [143]. It is worth noting that MYC upregulates polyamine biosynthesis, which in turn stimulate MYC transcription in a positive feedback loop [222, 223], in concordance with the increased levels of spermidine, putrescine and ODC1 observed in cells with inhibited CDK4/6.

Furthermore, MYC is known to activate mTOR signalling pathway through direct repression of tuberous sclerosis 2 (TSC2) [320], since TSC2 is a key component in the negative regulation of cell proliferation via mTOR [308]. Then, mTORC1 promotes the anaplerotic entry of glutamine to the TCA cycle by activating glutamate dehydrogenase

(GDH) through transcriptional repression of SIRT4 [322]. SIRT4 tumour suppressor functions include the regulation of the metabolic response to DNA damage through repression of mitochondrial glutamine metabolism [553]. In addition, the mTORC1 downstream effector S6 Kinase 1 (S6K1) positively controls MYC and, in turn, GLS by enhancing the translation efficiency of *MYC* mRNA which contains a secondary structure in its 5' untranslated region (5'UTR) [321]. Moreover, glutaminolysis and α-ketoglutarate production, in response to glutamine and leucine [133], also mediate mTORC1 activation [161]. Therefore, increased levels of MYC and P-mTOR induce glutamine transporters, GLS1 and GDH overexpression (Figures 4.2.19 and 4.2.24), leading to both an increase of the glutamine uptake and the intracellular concentration of α-ketoglutarate which, in turn, activates the degradation of HIF1α through hydroxylation by PHD2 (Figures 4.2.8D and 4.2.19). This situation sensitises CDK4/6-inhibited cells to hypoxia (Figure 4.2.25) and is in accordance with the observed reduction of HIF1α protein levels (Figure 4.2.19). On the other hand, increased levels of α-ketoglutarate also activate mTORC1, resulting in an increased demand of energy and exchange of amino acids, which correlates with the enhanced amino acid metabolism exhibited by CDK4/6-inhibited cells (Appendix IV) [162].

On the other hand, HIF1α has been reported to suppress mitochondrial biogenesis and oxygen consumption by inhibiting MYC through two mechanisms; the transcriptional induction of the MYC antagonist MXI1 and the promotion of proteasome-dependent MYC degradation [216, 261]. It has been proposed that the hypoxic degradation of MYC is an adaptive strategy to ensure cell survival by reducing proliferation [260]. Moreover, mTOR is also sensitive to oxygen deprivation. In this case, hypoxia inhibition of mTOR complex is mediated through AMP-activated protein kinase (AMPK) and REDD1-dependent activation of TSC2 [318]. Indeed, we experimentally observed the disappearance of MYC and P-mTOR under hypoxic conditions (Figure 4.2.19).

Likewise, FOXO3a transcription factor is upregulated under hypoxic conditions [302, 303] and acts as an important negative regulator of MYC by reducing its protein stability through phosphorylation at Thr58 [299], the MYC phosphodegron motif [235], and inducing MXI1 expression to counteract MYC [300]. As a result, FOXO3a represses MYC target genes and acts as a negative regulator of mitochondrial function through

inhibition of MYC (reviewed in [301]). However, PI3K/Akt pathway activation, high levels of cyclin D and decreased p27^{Kip1} expression observed in CDK4/6-inhibited cells are associated with FOXO3a phosphorylation and inhibition [297, 543, 554, 555], which is in agreement with the observed MYC overexpression.

The identification of the tumour metabolic adaptations associated to CDK4/6 silencing revealed potential metabolic vulnerabilities that can be exploited in combination therapies with CDK4/6 inhibitors. Indeed, combination therapies are a promising strategy to achieve synergistic therapeutic effects, dose and toxicity reduction, and minimise or delay the induction of drug resistance [556]. Accordingly, we have obtained synergistic and selective antiproliferative effects *in vitro* by inhibiting mTOR, PI3K/Akt axis or MYC target genes in combination with CDK4/6 inhibitors.

For instance, the observed increase in glucose consumption, lactate production and ECAR observed in CDK4/6-inhibited cells correlates with the activation of either Akt or MYC [557]. Akt activity determines the ability of mTOR inhibitors such as rapamycin to specifically downregulate both transcription and translation of MYC. Indeed, high levels of P-Akt result in rapamycin-induced downregulation of MYC expression and renders cells rapamycin-sensitive [558]. This is in accordance with our results obtained by combination of PD0332991 with rapamycin. Indeed, CDK4/6 inhibition caused Akt activation and combined therapy with rapamycin greatly affected CDK4/6-inhibited cells compared to control cells, which had lower levels of P-Akt.

Importantly, fluxomics and transcriptomics integrated data analysis revealed glutamine metabolism as the central node in CDK4/6-inhibited cells metabolic reprogramming (Figure 4.2.18). In effect, CDK4/6-inhibited cells increase glutamine uptake to replenish the carbon pool required for enhanced mitochondrial metabolism and function, and to provide for other glutamine- and glutamate-dependent processes, such as the polyamine and glutathione augmented synthesis. In addition, cells with supraphysiological levels of MYC are more sensitive to mitochondrial oxidative metabolism inhibition [218]. As there are no effective small-molecule inhibitors that selectively and directly target MYC [443, 444], we propose that GLS1 inhibition can be a promising strategy in the treatment of human malignancies that overexpress MYC. It

is worth noting that the rates of glutamine utilisation are limited by mitochondrial uptake via GLS1 [155, 157, 438] and that inhibition of GLS1 also prevents mTORC1 activation [161]. In effect, selective inhibition of GLS1 by BPTES reduces the viability of CDK4/6-inhibited cells but has no significant effects on control cells (Figures 4.2.31A and 4.2.34). Importantly, supplementation with dimethyl α-ketoglutarate rescues CDK4/6-inhibited cells treated with BPTES, revealing the pivotal role of glutamine as a substrate for mitochondrial energy production. In addition, BPTES produces a significant increase in early apoptosis in siRNA CDK4/6-treated cells (Figure 4.2.31B). Likewise, glutamine deprivation seems to produce a similar effect in early apoptosis. Gaglio et al. stated that oncogenic KRAS expression decreased overall oxidative flux through the TCA cycle and increased the use of glutamine for anabolic synthetic processes [532], giving a possible explanation for the observed resistance of control cells to BPTES and also for dimethyl α-ketoglutarate inefficiency in rescuing the viability of control cells under glutamine deprivation, as the anaplerotic use of glutamine is not as relevant as its implication in supporting anabolic processes. In addition, our results are in concordance with previous studies that have revealed that *CDK4* loss accelerates the development and increases the tumourigenic potential of *MYC*-driven lymphoma [559]. Remarkably, inhibition of GLS1 may have significant therapeutic implications since increased glutamine metabolism is not critical for normally differentiated cells [321, 418] (Figure 4.2.35). Therefore, our present work demonstrates that combination therapy by simultaneous inhibition of GLS1 and CDK4/6 provides an improved treatment with synergistic antiproliferative effects which are selective to cancer cells.

Methylseleninic acid promotes antitumour effects via nuclear FOXO3a translocation through Akt inhibition

4.3.1. Introduction

In the previous chapter of this thesis we explored the possibility to exploit the crosstalk between metabolic and signal transduction networks in colon cancer therapy, revealing synergies between CDK4/6 inhibitors and PI3K pathway inhibitors as promising combination antitumour therapies for colon cancer. Interestingly, the antiproliferative and pro-apoptotic activities of methylseleninic acid (MSA), one of the compounds we tested in the previous chapter in combination with CDK4/6 inhibition, are considered to be mediated by inhibition of the PI3K pathway [459, 460], although its molecular mechanism of action has not been yet fully elucidated. In fact, MSA has been showing promising *in vitro* and *in vivo* antitumour results [452, 454, 560-562]. Likewise, selenium supplement has been shown in clinical trials to reduce the risk of different cancers [453-455, 563], raising interest in its possible uses in lung carcinoma, the most prevalent cancer worldwide [1]. However, the fact that the molecular mechanism underlying MSA antitumour properties is still not completely understood is a bottleneck in designing combination therapies with MSA.

In this chapter, with the aim to better characterise the molecular mechanisms and downstream targets of MSA, we have analysed the effects of MSA on viability, cell cycle, metabolism, apoptosis, protein expression, and reactive oxygen species production in human lung carcinoma A549 cells. Our results demonstrate that MSA induces FOXO3a nuclear translocation after 1.5 h in A549 cells and in U2OS cells that stably express GFP-FOXO3a. Interestingly, sodium selenite, another selenium compound, did not induce any significant effects on FOXO3a translocation despite inducing apoptosis. Single strand break of DNA, disruption of tumour cell metabolic

adaptations, decrease in ROS production, and cell cycle arrest in G1 accompanied by induction of apoptosis are late events occurring after 24 h of MSA treatment in A549 cells. Our findings suggest that FOXO3a is a relevant mediator of the antiproliferative effects of MSA. This new evidence on the mechanistic action of MSA can open new avenues in exploiting its antitumour properties and in the optimal design of novel combination therapies. Moreover, since it has been reported that the antitumour effects of the conventional chemotherapeutic cisplatin are enhanced when combined with FOXO nuclear export inhibitors [286, 290, 291, 564] and that MSA synergistically sensitised cancer cells in combination with certain chemotherapeutic drugs [565, 566], we present MSA as a promising chemotherapeutic agent with synergistic antiproliferative effects with cisplatin.

4.3.2. Results

4.3.2.1. MSA inhibits cell proliferation and causes G1 arrest in human lung carcinoma A549 cells

The effect of MSA on human lung carcinoma A549 cell proliferation was examined using the MTT (3-[4,5-dimethylthiazol-2-yl]-2,5-diphenyltetrazolium bromide) colorimetric viability assay (as described in Section 3.5). Significant dose-dependent growth inhibition was observed in this cell line after treatment with 10 different concentrations of MSA in a range between 0.1 and 6 µM for 24, 48 and 72 h (Figure 4.3.1A).

The MSA concentrations at which A549 cell proliferation was inhibited by 50% after 24, 48 and 72 h of treatment ($^{24h}IC_{50}$, $^{48h}IC_{50}$ and $^{72h}IC_{50}$) were 2.2 ± 0.3 µM, 1.6 ± 0.2 and 1.3 ± 0.1 µM, respectively.

Flow cytometric analyses of cell cycle distribution (as described at Section 3.9) of A549 cells that had been exposed to $^{72h}IC_{50}$ MSA showed an increase of the G1 population at 24, 48 and 72 h of treatment as compared to control cells (increasing by 41% at 72 h). With the same treatment, a concomitant decrease was also observed in the

percentage of cells in the S phase after 24, 48 and 72 h of treatment with respect to the untreated cells (38% decrease at 72 h), suggesting a G0/G1 arrest (Figure 4.3.1B). A reduction in the percentage of cells in the G2 phase was also observed at all times.

In order to test whether MSA induced cell cycle arrest as a result of negative regulation of CDK4/6-cyclin D complexes, CDK4 and CDK6 protein expression was analysed by Western blot (Section 3.25) after incubating A549 cells with 5 µM MSA for 6 h. Indeed, results depicted in Figure 4.3.1C show that MSA-treated cells exhibited a significant decrease in the protein levels of CDK4/6.
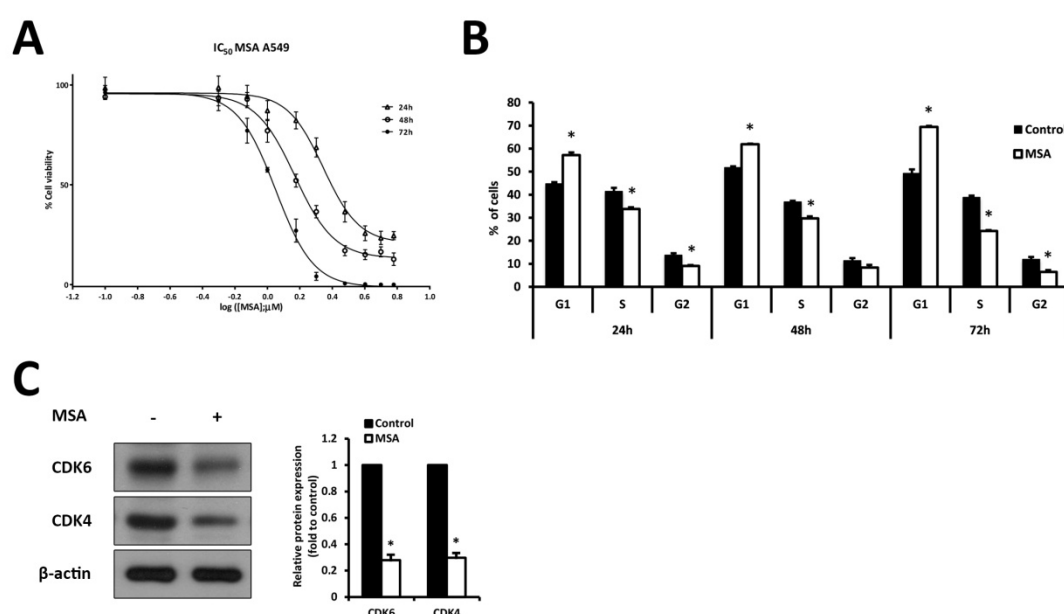
Figure 4.3.1. MSA effects on cell viability and cell cycle in A549 cells. A. Growth inhibition of MSA on A549 lung cancer cells after 24, 48 and 72 h measured by MTT assay. Exponentially growing cells were treated with the indicated concentration of MSA for 24, 48 and 72 h. The assay was carried out using six replicates and repeated three times. Data are represented as mean ± SD. **B**. Cell cycle analysis of MSA-treated cells. A549 cells treated for 24, 48, 72 hours with 1.3 µM MSA presented a G1 arrest. Cell cycle analysis was conducted after propidium iodide staining. Values represent mean ± SD and statistically significant differences between treated and control cells at $p < 0.05$ are indicated with an asterisk (*). **C.** Western blot analysis showed a significant CDK4 and CDK6 inhibition at 6 h treatment with 5 µM MSA. Protein expression levels were quantified using ImageJ software and are expressed as mean band intensity normalised to β-actin and relative to control condition (*, $p < 0.05$).

To determine whether the concentrations of MSA used in the present study can acidify the media, we measured the pH values before and after the addition of MSA at 1.3 and

5 µM final concentrations. We also assessed the pH values after the addition of acetic acid, which is a weak acid with an acid dissociation constant (K_a) of $1.8 \cdot 10^{-5}$ and a similar molecular structure as MSA. While the addition of acetic acid at 5 µM decreased the pH of the medium by 0.5 units, the same concentration of MSA did not cause any significant effects. Therefore, we conclude that the media were not acidified by the doses of MSA used in this study.

4.3.2.2. MSA induces apoptosis in A549 cells

To investigate whether MSA promoted programmed cell death, apoptosis was assessed in A549 cells after 24, 48 and 72 h of treatment with 1.3 µM MSA ($^{72h}IC_{50}$ for growth inhibition). FACS analysis using annexin V-FITC staining and propidium iodide (PI) accumulation was performed as described in Section 3.10 to differentiate non-apoptotic cells (annexin V^- and PI^-), early apoptotic cells (annexin V^+ and PI^-) and late apoptotic/necrotic cells (PI^+). In early apoptosis, cells lose their membrane asymmetry and phosphatidylserine is exposed to the outer membrane, where annexin V-FITC conjugate is able to bind to it. In late apoptotic and necrotic cells, cell membrane integrity is highly compromised and PI can access the nucleus.

To determine if MSA effects were specific or general to other selenium compounds, treatment with $^{72h}IC_{50}$ sodium selenite was included in our analysis (Figure 4.3.2A). Sodium selenite $^{72h}IC_{50}$ in A549 cells was calculated using Graphpad Prism 6 software (La Jolla, CA, USA) and determined to be 5.5 ± 0.4 µM. As shown in Figure 4.3.2A, MSA treatment for 24 h caused no significant effect on A549 cell apoptosis, while at 48 and 72 h, MSA exposure generated an increase in early apoptotic cells. In contrast, the apoptotic effect of sodium selenite was visible at 24 h and greatly enhanced at 48 and 72 h (reaching around 40% for early apoptotic cells) whereas the percentage of late apoptotic and necrotic cells remained constant at the three time points. Therefore, the extent of apoptosis caused by MSA was much reduced compared to that induced by sodium selenite, which can be due to different mechanisms of apoptosis activation.

Apoptotic cells undergo a series of characteristic morphological changes, such as shrinkage of the cell, chromatin condensation, apoptotic body formation and internucleosomal fragmentation of genomic DNA [567]. In order to evaluate DNA integrity, a single-cell gel electrophoresis was performed (Comet assay, Section 3.11). Single strand break of DNA was observed after 24 h treatment with 1.3 µM MSA, while control condition showed no induction of DNA fragmentation (Figure 4.3.2B). Total Comet score of treated and untreated cells were 199 and 74, respectively. In addition, the presence of apoptotic bodies following 72 h MSA treatment at $^{72h}IC_{50}$ concentration was detected by Hoechst 33342 staining (see Section 3.10) (Figure 4.3.2C). Using an inverted phase contrast microscope, we examined the morphology of A549 cells after the incubation with MSA, sodium selenite and LY294002, a known PI3K inhibitor [546], at the indicated concentrations for 24 h (Figure 4.3.2D). As illustrated in Figure 4.3.2D, other typical apoptotic features such as rounding, shrinkage, detachment and loss of contact with adjacent cells were observed in MSA- and sodium selenite-treated cells.

Activation of the caspase pathway plays an important role in apoptosis. Caspases are constitutive cysteine proteases that are normally present as inactive proenzymes. Their enzymatic activity is induced during apoptosis in a self-amplifying cascade. Cleaved upstream caspases (caspases 2, 8, 9 and 10) activate effector caspases (caspases 3, 6 and 7) by proteolysis initiating the apoptotic cascade of events [567]. The intrinsic apoptosis pathway involves the release of cytochrome c into cytosol and the formation of the apoptosome complex by association with APAF-1. This complex activates caspase 9 which in turn cleaves procaspase 3, implicated in the proteolysis of poly (ADP-ribose) polymerase (PARP).

To elucidate the mechanisms involved in MSA or sodium selenite-mediated induction of apoptosis in A549 cells, whole-cell lysates were extracted and Western blot analyses were performed. In order to compare the effects of MSA and sodium selenite, we incubated the cells with both $^{72h}IC_{50}$ concentrations (1.3 µM and 5 µM). The effects of LY294002 were also assessed as a positive control for PI3K pathway inhibition. As shown in Figure 4.3.2E, incubation with 5 µM MSA enhanced the expression of pro-
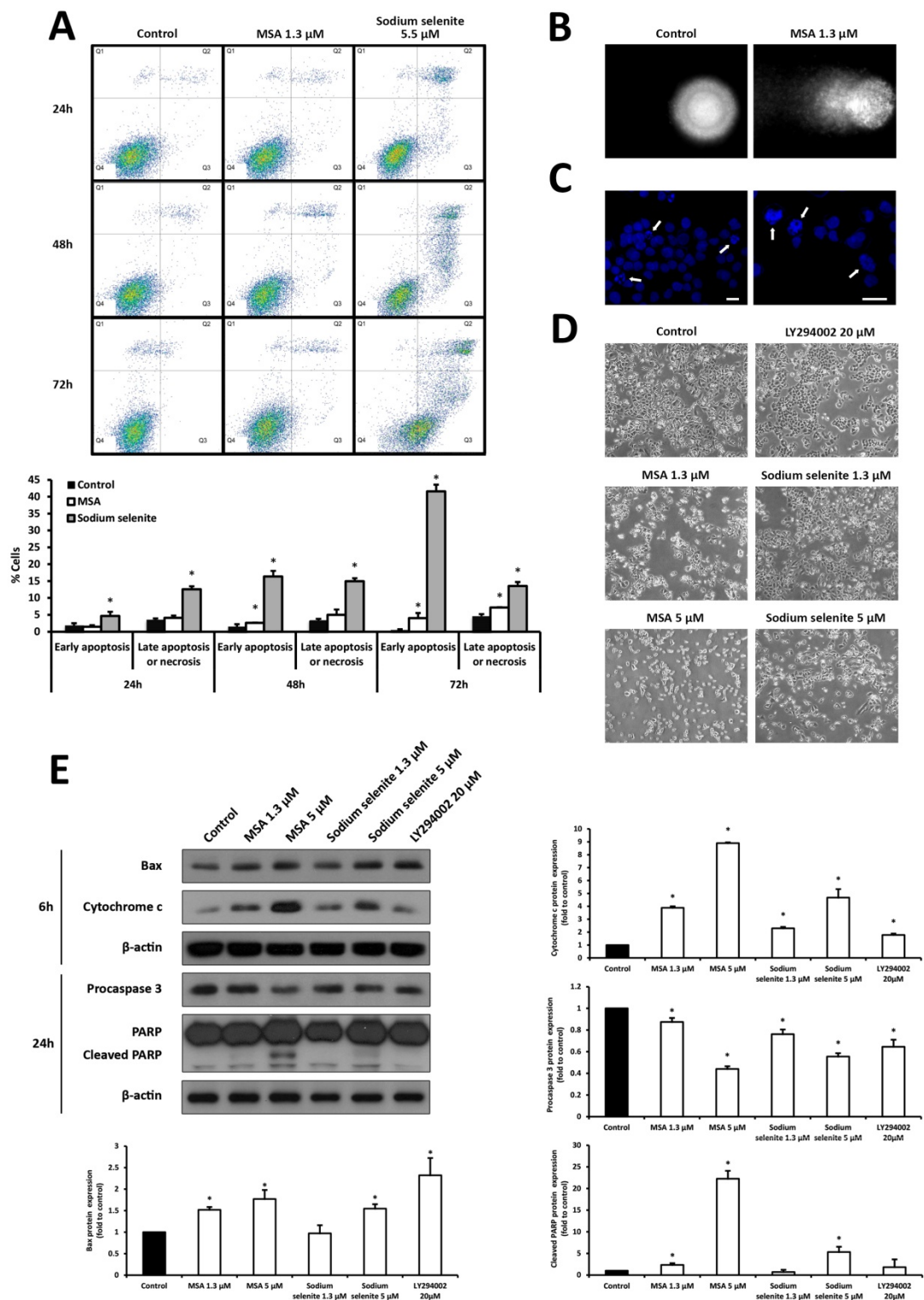
Figure 4.3.2. Apoptosis assays in A549 cells. A. Flow cytometry analysis of Annexin V-FITC staining and propidium iodide accumulation after exposure of A549 cells to MSA and sodium selenite at their respective $^{72h}IC_{50}$ concentrations for 24, 48 and 72 hours. PI staining at 488 nm is represented on the *y* axis and annexin V-FITC staining at 488 nm on the *x* axis. Quadrant 4 (PI$^-$/FITC$^-$) represents non-apoptotic cells, early apoptosis is shown in

apoptotic Bax and cytosolic cytochrome c, decreased the level of procaspase 3 and caused PARP cleavage. Sodium selenite 5 µM treatment induced changes in the same direction but to a significantly lower extent. When comparing the effects of the treatment with the respective $^{72h}IC_{50}$ concentration, 1.3 µM MSA and 5 µM sodium selenite exhibited similar results (Figure 4.3.2E).

4.3.2.3. MSA blocks glycolysis, TCA cycle and nucleotide biosynthesis

The effect of MSA on A549 cell metabolism was examined using the Stable Isotope-Resolved Metabolomics (SIRM) approach [568-570]. A549 cells were treated with uniformly ^{13}C-labeled glucose ([U-^{13}C]-glucose) in the absence (Control) or presence of 5 µM MSA for 24 h (see details in Section 3.30). The glucose transformation products were analysed by 1D HSQC NMR and GC/MS, as shown in Figure 4.3.3. MSA-treated A549 cells had reduced synthesis of ^{13}C labelled lactate (glycolytic product), malate, aspartate, glutamate, citrate (TCA cycle metabolites), as well as adenine and uracil nucleotides (with the ribose unit derived from the pentose phosphate pathway, PPP), relative to untreated A549 cells. These results suggest that MSA attenuates the activity of glycolysis, TCA cycle, PPP and/or nucleotide biosynthesis.

right bottom quadrant (PI$^-$/FITC$^+$) and quadrants 1 and 2 (PI$^+$) depict late apoptotic/necrotic cells. Plots illustrate the percentage of cells in early apoptosis and late apoptosis/necrosis. Values are expressed as mean ± SD of three experiments in triplicate. Differences between treated and control groups were considered statistically significant at p < 0.05 (*). **B.** DAPI staining of A549 cells DNA after electrophoresis in agarose gel (single-cell gel electrophoresis, Comet Assay). Control condition treatment with vehicle showed no induction of single strand breaks while 24 h MSA exposure at $^{72h}IC_{50}$ concentration caused DNA fragmentation in A549 cells. **C.** Morphological changes in nuclei were examined after 72 h MSA treatment at $^{72h}IC_{50}$ concentration. Hoechst stained nuclei were evaluated with a fluorescence microscope (200 and 400X, scale bar 3 µm) to detect increased condensation and margination of chromatin to the nuclear envelope and the formation of apoptotic bodies (indicated with white arrows). Apoptotic bodies were not observed in control condition. **D.** Cells were incubated with MSA, sodium selenite and LY294002 at the specified concentrations for 24 h and observed using an inverted phase contrast microscope. **E.** Western blot analysis of total protein fractions of A549 cells. Protein expression was determined by densitometry analysis using ImageJ software and is represented as mean band intensity normalised to β-actin and related to untreated controls. MSA apoptosis activation is represented by enhancement of Bax and cytosolic cytochrome c expression, decrease of procaspase 3 levels and PARP cleavage (*, p < 0.05). Sodium selenite induced changes in the same direction.
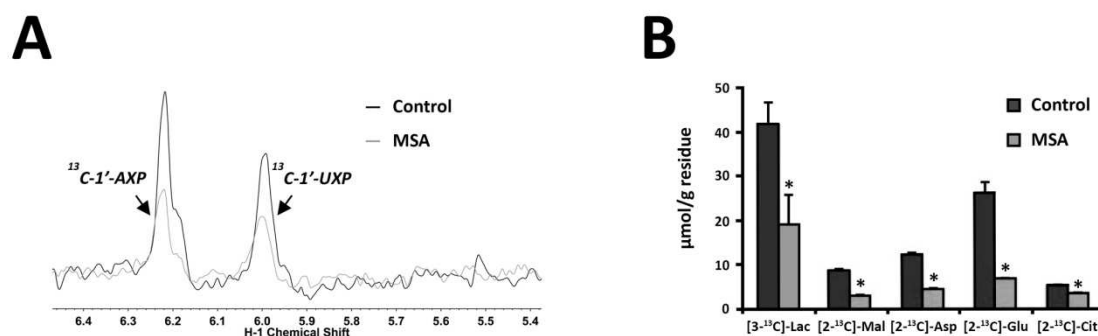
Figure 4.3.3. MSA perturbs glycolysis, TCA cycle and nucleotide biosynthesis. A549 cells were grown in 0.2% [U-^{13}C]-glucose in the presence or absence of 5 µM MSA for 24 h. The polar metabolites were extracted in ice-cold 10% trichloroacetic acid and analysed by 1D HSQC NMR (**A**, acquired at 14.1 T, 20ºC) and GC/MS (**B**). **A.** Representative 1D HSQC NMR spectrum. The abundance of the ribosyl unit of adenine (^{13}C-1'-AXP) and uracil (^{13}C-1'-UXP) nucleotides was significantly attenuated 24 h after MSA treatment, relative to the control treatment. **B.** The GC/MS analysis revealed reduced synthesis of TCA cycle metabolites, [2-^{13}C]-malate (Mal), [2-^{13}C]-aspartate (Asp), [2-^{13}C]-glutamate (Glu) and [2-^{13}C]-citrate (Cit), in addition to the glycolytic product, [3-^{13}C]-lactate (Lac). p values < 0.05 (*) were considered statistically significant.

4.3.2.4. MSA causes nuclear translocation of FOXO3a in U2foxRELOC cells

Taking into account the arrest of cell cycle (G1), apoptosis induction, the metabolic effects of MSA on A549 cells and their correlation with those described for the PI3K inhibition [458], and the observed effects of MSA on PI3K signalling, we evaluated the effect of MSA on FOXO factors known to be the major transcriptional downstream effector proteins of the PI3K/Akt signal transduction pathway [571]. As the activity of FOXO factors is mainly regulated by their subcellular localisation [572], we first investigated if MSA induced FOXO nuclear translocation. To this end we used U2foxRELOC cells, a previously established cell system based on U2OS osteosarcoma cells that stably express a GFP–FOXO3a reporter [468, 573, 574].

In order to select the optimal MSA concentration for analysing its effects on FOXO translocation, the MSA $^{72h}IC_{50}$ in U2foxRELOC cells was determined by incubating the cells with 10 different concentrations of MSA for 72 h and performing colorimetric
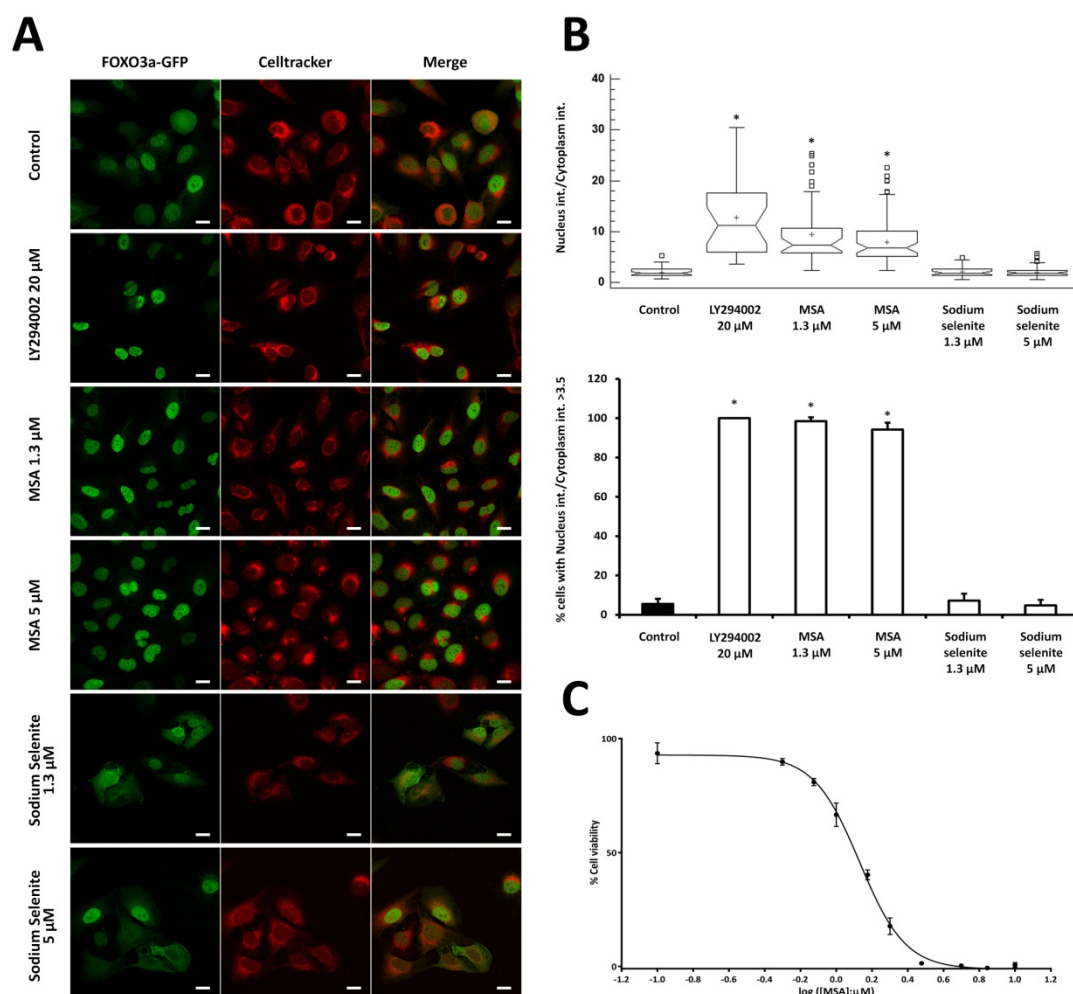
Figure 4.3.4. Nuclear translocation of GFP–FOXO following MSA treatment in U2foxRELOC cells. U2foxRELOC cells stably expressing GFP–FOXO fusion protein were treated with vehicle, LY294002 (PI3K pathway inhibitor), MSA or sodium selenite for 6 hours. **A.** Representative confocal microscopy images for U2foxRELOC cells. Left row (green) indicates the subcellular location of FOXO3a-GFP. Celltracker location (red) identifies the cytoplasm. Scale bar, 5 μm. **B.** Box and whiskers plot for the correlation between the nuclear and cytoplasmic green fluorescence intensity. Higher values represent a higher FOXO3a-GFP presence in the nucleus compared to the cytoplasm. Bar graph shows the percentage of the cells in each condition exhibiting nuclear/cytoplasmic ratios of fluorescence intensity greater than 3.5. MSA and LY294002 treatments display statistically significant differences (*) with the control condition using a multiple rang test (Kruskal-Wallis test) with 99% confidence. **C.** Viability assay with MSA in U2foxRELOC cells at 72 h. Exponentially growing cells were treated with the indicated concentration of MSA for 72 h. The assay was carried out using six replicates and repeated three times. Data are represented as mean ± SD.

viability assay. The values for dose-dependent growth inhibition were similar to the results obtained for A549 cells (Figure 4.3.4C). We next analysed the spatio-temporal kinetics of FOXO nuclear translocation upon MSA treatment (see Section 3.21). We

exposed U2foxRELOC cells to 5 µM MSA for 1.5, 3, 6, 11 and 24 hours and determined the subcellular localisation of the fluorescent FOXO reporter protein. MSA treatment induced GFP-FOXO3a nuclear translocation from 1.5 to 24 h, reaching a maximum effect between 3 and 6 hours (data not shown).

With the assay conditions optimised, U2foxRELOC cells were treated with 1.3 and 5 µM MSA for 6 h and the subcellular localisation of GFP-FOXO3a was monitored by confocal microscopy (as detailed in Section 3.20). Vehicle was used as a negative control and LY294002 (20 µM) as a positive control. As shown in Figure 4.3.4A, GFP-FOXO3a was present in the cytosol of untreated cells as well as in the nucleus, whereas in MSA- and LY294002-incubated cells GFP-FOXO3a was localised almost exclusively in the nuclei. The percentage of cells in which GFP-FOXO3a nuclear intensity was at least 3.5 times higher than GFP-FOXO3a cytoplasmic intensity was less than 6% for control cells, more than 95% for LY294002-treated cells and more than 94% for MSA-treated cells (at both concentrations) (Figure 4.3.4B). To determine whether FOXO3a nuclear translocation was specifically driven by MSA or was a general characteristic of selenium compounds, U2foxRELOC cells were also incubated with sodium selenite at the same concentrations as MSA. The intracellular distribution of GFP-FOXO3a remained unaltered in the presence of sodium selenite (Figure 4.3.4A). These results support our hypothesis that MSA specifically induces FOXO3a nuclear translocation.

4.3.2.5. MSA induces GFP-FOXO3a nuclear translocation and increases nuclear FOXO3a in A549 cells

To further confirm our hypothesis and test if the translocation effect of MSA is also relevant for lung cancer cells, the effect of MSA on FOXO3a in A549 cells was analysed. To this end, we transiently transfected GFP-FOXO into A549 cells (see Section 3.19) and exposed them to MSA. Figures 4.3.5A and 4.3.5B illustrate the results obtained after 6 h incubation with 5 µM MSA, 20 µM LY294002 or vehicle. MSA induced nuclear accumulation of FOXO3a in A549 cells, resulting in over 90% of cells exhibiting nuclear fluorescence intensity at least 1.5 times greater than cytoplasmic fluorescence
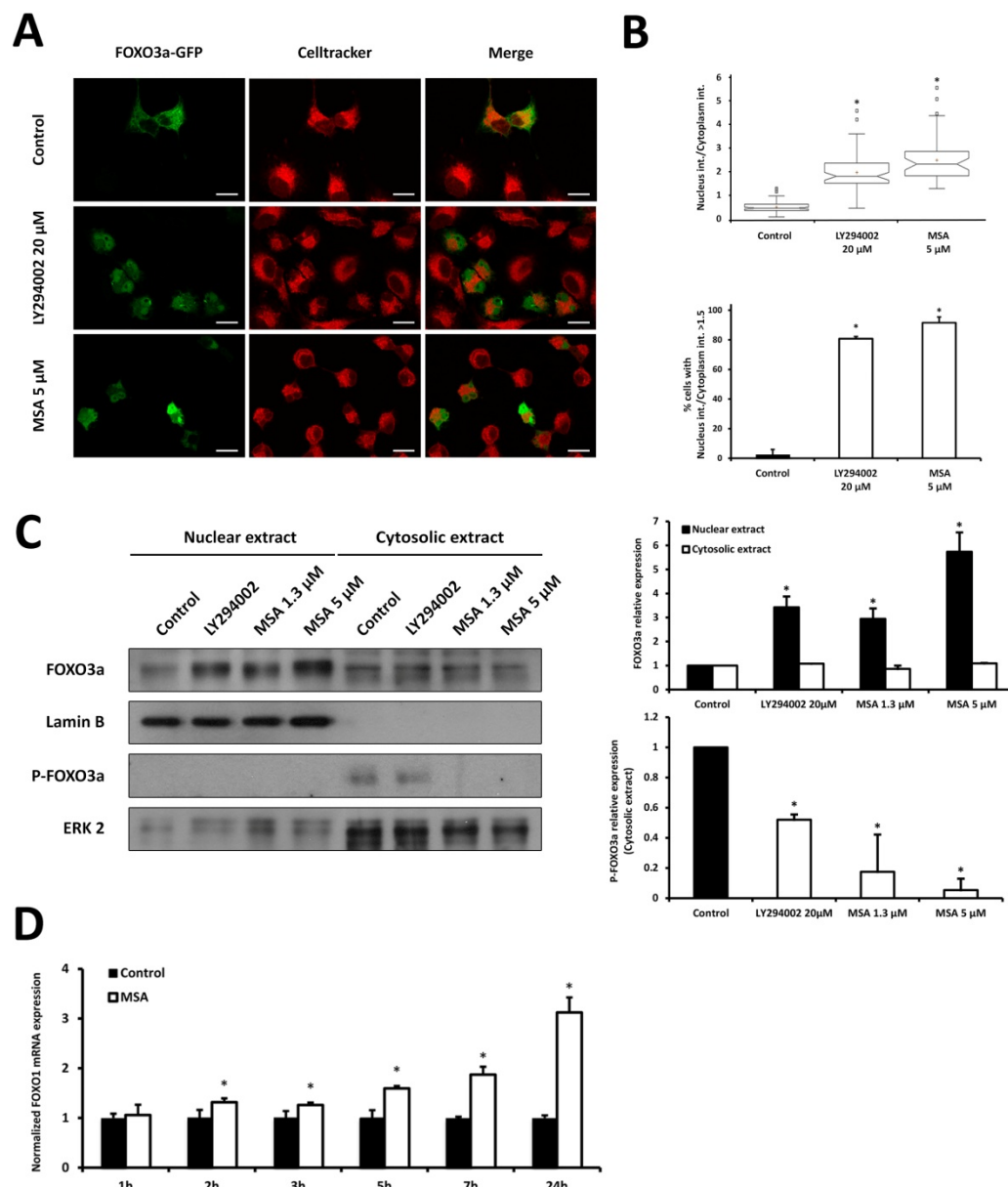
Figure 4.3.5. MSA induces GFP-FOXO3a nuclear translocation and increases endogenous nuclear FOXO3a in A549 cells. A. Representative confocal microscopy images for A549 cells transfected with a FOXO3a-GFP reporter plasmid and treated with vehicle, 20 µM LY294002 or 5 µM MSA for 6 h. Left row (green) indicates the intracellular location of FOXO3a-GFP. Celltracker location (red) identifies the cytoplasm. Scale bar, 5 µm. **B.** Box and whiskers plot for the correlation between the nuclear and cytoplasmic green fluorescence intensity. Higher values indicate a higher FOXO3a-GFP presence in the nucleus compared to the cytoplasm. Bar graph represents the percentage of the cells in each condition displaying nuclear/cytoplasmic ratios of fluorescence intensity greater than 1.5. MSA and LY294002 treatments present statistically significant differences (*) with the control condition using a multiple rang test (Kruskal-Wallis test) with 99% confidence. **C.** Western blots for the nuclear and cytoplasmic fractions of A549 cells. Protein expression levels were quantified using ImageJ software and are expressed as mean band intensity normalised to Lamin B (nuclear extract) or ERK 2 (cytosolic extract) and related to untreated controls. Endogenous nuclear FOXO3a levels increase with 6 h MSA and LY294002 treatments whereas phosphorylated FOXO3a

…/…

intensity, compared to less than 2.5% of cells for the control conditions. To confirm the nuclear translocation of endogenous FOXO3a in non-transfected A549 cells in response to MSA treatment, Western blot assays of cells incubated in the same conditions were performed. As shown in Figure 4.3.5C, MSA causes an increase in nuclear FOXO3a concentration and a decrease in the levels of cytoplasmic phosphorylated FOXO3a at the Ser253 residue (a known Akt phosphorylation site), consistent with our aforementioned results.

Since it is been described that FOXO1 transcription is stimulated by FOXO3a in a positive feedback loop [296, 575], the effect of MSA on FOXO1 mRNA levels was analysed (see Section 3.27). Cells were incubated with 5 µM MSA for different time periods from 1 h up to 24 h. Induction of FOXO1 expression was detected from 2 h to 24 h and increased in a time-dependent manner (Figure 4.3.5D).

To validate the results obtained with confocal microscopy of U2foxRELOC cells treated with either MSA or sodium selenite, the levels of active FOXO3a in non-transfected A549 cells were analysed by Western blot. As shown in Figure 4.3.6, MSA induced FOXO3a expression while sodium selenite caused its inhibition. To confirm this observation, FOXM1 protein expression was examined, as previous studies have reported that FOXO3a is a negative regulator of FOXM1 at the transcriptional level [284, 285]. In agreement with these observations and further supporting MSA's mode of action through FOXO3a activity, MSA treatment significantly decreased FOXM1 expression while sodium selenite enhanced the level of this transcription factor (Figure 4.3.6).

In order to identify the mechanisms involved in FOXO subcellular redistribution, changes in FOXO-regulating signal transduction pathways in response to MSA treatment were studied. It was previously reported that cell cycle arrest induced by

…/…

cytoplasmic levels decrease (*, $p < 0.05$). **D.** mRNA levels of FOXO1 were analysed by qRT-PCR. Cells were incubated with 5 µM MSA from 1 h up to 24 h. The graph bar represents the expression of FOXO1 relative to control, which was assigned a value of 1. FOXO1 expression was significantly (*, $p < 0.05$) and progressively induced from 2 to 24 h.

FOXO proteins is mediated by enhanced transcription and protein expression of the cyclin-dependent kinase inhibitor p27[Kip1] [554, 555] and reduced protein expression of cyclins D1 and D2 [543]. Both cases result in an impaired capacity of CDK4 and CDK6 to hyperphosphorylate the RB protein family, leading to G1 arrest [576]. Moreover, while FOXO3a has been reported to induce the transcription of p27[Kip1], PI3K/Akt pathway is known to suppress its expression in order to proceed with cell cycle [297]. To investigate whether MSA-induced G1 cell cycle arrest is associated with Akt and FOXO signalling, p27[Kip1] and phosphorylation of Akt on Ser 473 status were analysed by Western blot. Six-hour treatment with MSA (at both 1.3 and 5 μM) significantly
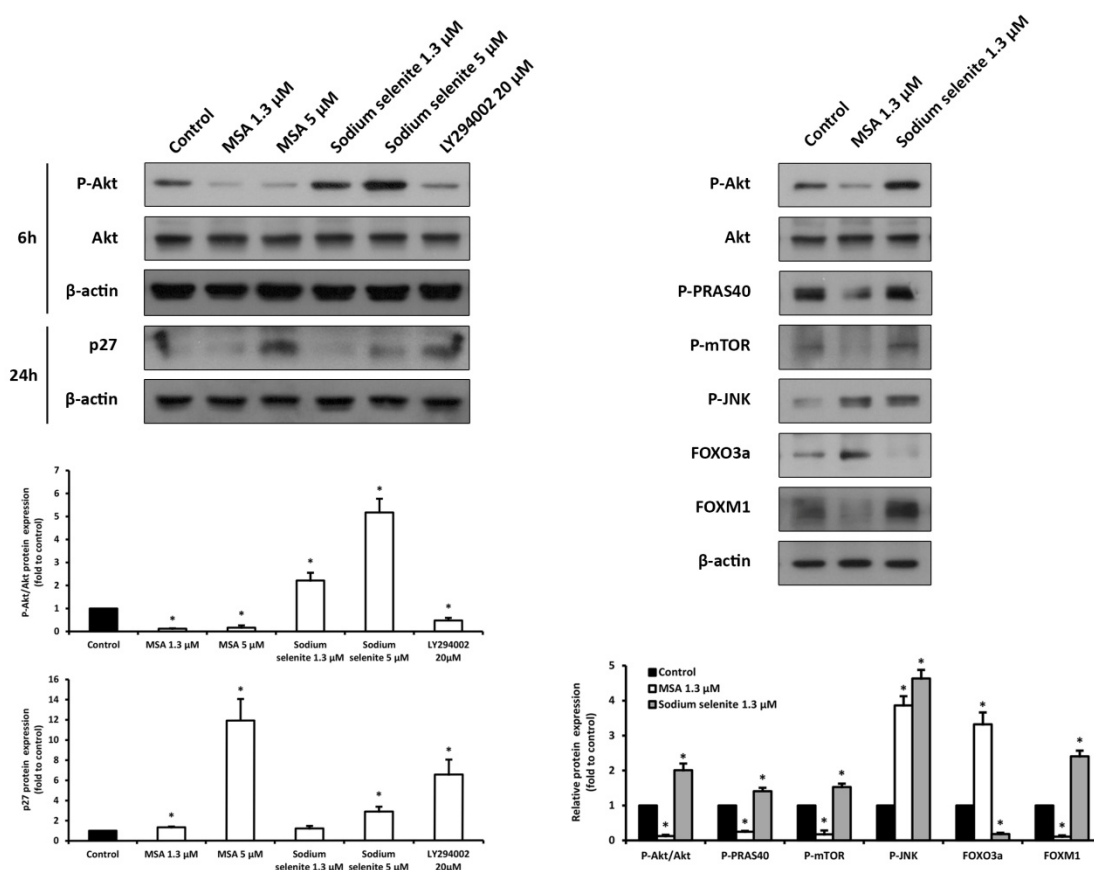
Figure 4.3.6. MSA-induced G1 arrest and apoptosis are associated with Akt inhibition. Total protein fractions of A549 cells were analysed by Western blot. Protein expression was quantified by densitometric analysis using ImageJ software and is represented as mean band intensity normalised to β-actin and related to untreated controls. MSA induces the dephosphorylation of mTOR and Akt and its downstream target PRAS-40, the phosphorylation of JNK, an increase of FOXO3a levels, a reduction of FOXM1 protein expression and a G1 arrest represented by p27 accumulation. Differences between treated and control groups were considered statistically significant at $p < 0.05$ (*).

suppressed Akt phosphorylation without affecting its total protein level (Figure 4.3.6). These results suggest that FOXO3a dephosphorylation and nuclear accumulation in response to MSA are mediated by Akt inactivation. The PI3K inhibitor LY294002 showed the same behaviour as MSA while sodium selenite increased Akt phosphorylation in a dose-dependent manner. The overactivation of Akt mediated by sodium selenite could account for the depletion in FOXO3a levels observed (Figure 4.3.6). PRAS-40, an Akt substrate, followed the same phosphorylation pattern, further supporting our hypothesis (Figure 4.3.6). mTOR pathway was downregulated by MSA as phosphorylated mTOR levels were reduced significantly after MSA treatment while sodium selenite activated this signalling pathway by increasing P-mTOR level.

Dephosphorylation of Akt and FOXO activation preceded the caspase-mediated apoptosis and the transcription of FOXO3a target genes such as p27 (Figure 4.3.6). As expected, p27^{Kip1} levels were notably increased after exposure to 5 μM MSA and 20 μM LY294002 for 24 h, even though p27^{Kip1} levels were only slightly enhanced by exposure to 1.3 μM MSA. These data corroborate with previous results that showed MSA and sodium selenite inducing distinct biochemical and cellular responses [451, 577, 578].

4.3.2.6. MSA elicits ROS detoxification

FOXO proteins have been reported to induce detoxification of reactive oxygen species (ROS) by up-regulating free radical scavenging enzymes, including manganese superoxide dismutase and catalase [295]. FOXO transcription factors regulate two aspects of cellular resistance to stress: repair of damages caused by ROS and detoxification of ROS [270]. Given that MSA causes FOXO3a translocation to the nucleus, we measured ROS levels in A549 cells (see Section 3.18). The results show that 1.3 μM MSA caused a significant decrease in the levels of ROS at 24 and 48 h (Figure 4.3.7). This decrease is consistent with the increased cellular free thiol levels observed by Poerschke et al. [579] after 24 h MSA incubation. Cells incubated with MSA for 72 h had similar ROS level to control cells. In contrast, sodium selenite

inhibited ROS production at 24 h but enhanced it at 48 and 72 h.

Previous studies described the role of JNK as a FOXO activator mediating the phosphorylation of 14-3-3 proteins, thus releasing FOXO factors and trigging their nuclear relocalisation [580-582]. As shown in Figure 4.3.6, MSA incubation resulted in an increase in P-JNK, which is consistent with FOXO activation by Akt dephosphorylation. Sodium selenite enhancement in P-JNK levels (Figure 4.3.6) could be a consequence of selenite-induced ROS production since JNK cascade can be independently activated by environmental stresses [583].
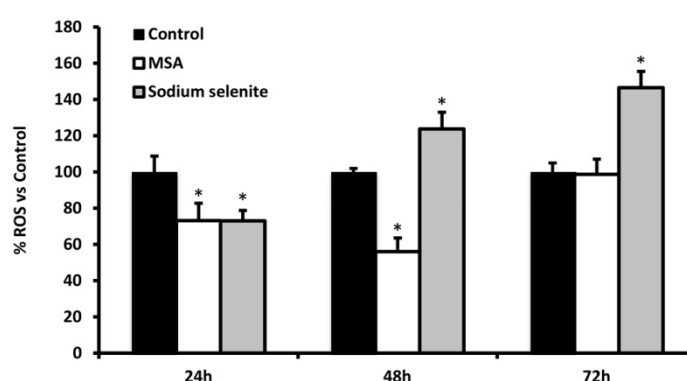
Figure 4.3.7. ROS detoxification by MSA treatment. A decrease in ROS levels was observed in MSA-treated A549 cells. This reduction was only statistically significant after 24 and 48 h (*, p< 0.05). Cells treated with sodium selenite for 24 h presented similar ROS level to MSA-treated cells but significantly enhanced the production of ROS in a time-dependent manner after 48 and 72 h incubations.

4.3.2.7. FOXO3a knockdown attenuates MSA effects

In order to confirm the role of FOXO3a as a mediator of MSA antitumour effects, we stably silenced FOXO3 in two different cell lines using shRNA vectors. We established U2OS and HEK293 cells that stably expressed three different hairpin sequences and validated the efficiency of FOXO3a knockdown by Western blot. The results revealed that FOXO3a KD#1 construct exhibited the strongest knockdown effect, followed by FOXO3a KD#2 (Figure 4.3.8A). Hence, the U2OS cell lines transfected with these two constructs and the FOXO3a KD#1 HEK293 cell line were selected to perform the following experiments.
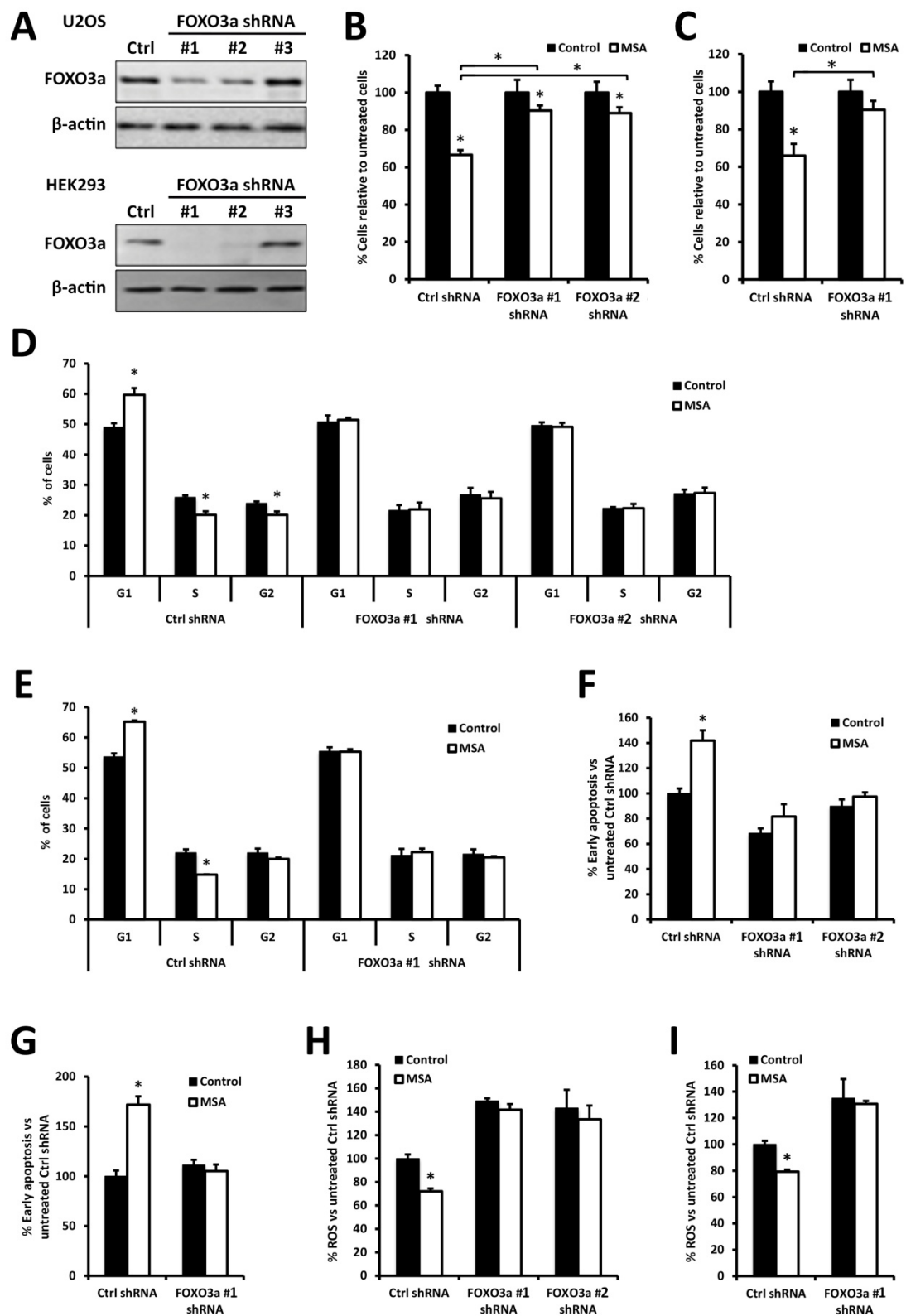
Figure 4.3.8. Effects of FOXO3a knockdown on MSA activity. U2OS and HEK293 cells were stably transfected with control shRNA (Ctrl) or constructs expressing two different FOXO3a-specific shRNA sequences (FOXO3a #1 and FOXO3a #2). **A.** Western blot analysis of total protein fractions of U2OS and HEK293 cells. β-actin was used as a protein loading control. Sequence #1 exhibited the highest knockdown efficiency. **B** and **C.** Viability assays after

We incubated Ctrl (empty vector) and FOXO3a knockdown cells with 1 µM MSA or vehicle (PBS) and measured cell proliferation, cell cycle and apoptosis after 72 h (Figure 4.3.8B-G), and ROS after 48 h treatment (Figure 4.3.8H-I). The results showed that MSA effects were attenuated or even abolished by FOXO3a knockdown. In fact, the observed antiproliferative effect of MSA was significantly reduced after FOXO3a inhibition, while no differences in cell cycle, apoptosis and ROS levels were found between untreated and MSA-treated FOXO3a knockdown cells. These results further confirm that the antitumour response of MSA treatment is mediated by FOXO3a.

4.3.2.8. Combined therapy with MSA and cisplatin

Cisplatin-based therapy is a conventional chemotherapeutic treatment for many cancers, including lung cancer. However, its clinical efficacy is compromised by acquired resistance and dose-limiting side effects [5]. Consequently, the search for combination therapies and chemosensitising agents to cisplatin is essential for improving its treatment outcome. Given that previous studies reported the enhancement of cisplatin's antitumour effects in combination with FOXO nuclear export inhibitors [286, 290, 291, 564], we hypothesised that combined treatment of MSA with cisplatin could be a promising new strategy in cancer therapy.

To quantify the synergy of dose-dependent effect on cell viability, we used the Combination Index (CI) equation of Chou and Talalay [483] (see Section 3.38). We

treatment with 1 µM MSA for 72 h in **B.** U2OS shRNA transfected cells and **C.** HEK293 shRNA transfected cells. Data are expressed as percentage of viability relative to untreated cells. **D** and **E.** Cell cycle analysis of 1 µM MSA-treated cells for 72 h in **D.** U2OS shRNA transfected cells and **E.** HEK293 shRNA transfected cells. Cell cycle analysis was conducted after propidium iodide staining. **F** and **G.** Percentage of early apoptotic cells relative to untreated Ctrl shRNA cells obtained by flow cytometry analysis of Annexin V-FITC staining and propidium iodide accumulation after exposure of **F.** U2OS shRNA transfected cells and **G.** HEK293 shRNA transfected cells to 1 µM MSA for 72 h. **H** and **I.** Intracellular ROS levels determined by flow cytometry after 1 µM MSA incubation for 48 h of **H.** U2OS shRNA transfected cells and **I.** HEK293 shRNA transfected cells. Results are expressed as percentage of mean fluorescent intensity relative to untreated Ctrl shRNA cells. In all cases, values represent mean ± SD and statistically significant differences between treated and control cells at $p < 0.05$ are indicated with an asterisk (*).

examined the synergistic effects of MSA and cisplatin in A549, HCT116 (colorectal carcinoma), MCF7 (breast adenocarcinoma) and OVCAR3 (ovary adenocarcinoma) cells which are considered to present cisplatin-resistance, exhibiting IC50 values higher than 10 µM [584] (*http://www.cancerrxgene.org/translation/Drug/1005*). The combination of MSA and cisplatin treatment in a wide dose range showed a significant synergism in the antiproliferative effects with a CI<1 in each tested cell line (Table 4.3.1). This synergism suggests that MSA co-treatment could be an efficient strategy to decrease the cisplatin dose required for therapy and therefore, its toxicity.

MSA and cisplatin treatment in a wide dose range showed a significant synergism in the antiproliferative effects with a CI<1 in each tested cell line (Table 4.3.1). This synergism suggests that MSA co-treatment could be an efficient strategy to decrease the cisplatin dose required for therapy and therefore, its toxicity.

Table 4.3.1. Synergistic antiproliferative effect of MSA and cisplatin combination treatment. Cells were treated for 72 h at the indicated concentrations of MSA and cisplatin in a constant ratio. **A.** A549 cells, ratio 1:10. **B.** HCT116 cells, ratio 1:5. **C.** MCF7 cells, ratio 1:4. **D.** OVCAR3 cells, ratio 1:5. The CI results obtained with CompuSyn software (ComboSyn, Inc.) revealed a synergy (CI<1) in the antiproliferative effects of MSA and cisplatin at each dose combination tested.

A. A549 cells, ratio 1:10.

MSA (µM)	Cisplatin (µM)	Viability (%)	CI Value
0.1	1	78.9 ± 1.1	*0.447*
0.3	3	56.5 ± 2.0	*0.631*
0.5	5	41.1 ± 3.4	*0.707*
0.75	7.5	27.9 ± 2.6	*0.751*
1	10	17.3 ± 0.5	*0.729*
1.3	13	8.5 ± 0.5	*0.663*
1.5	15	4.2 ± 0.5	*0.578*
2	20	1.8 ± 0.5	*0.595*

B. HCT116 cells, ratio 1:5.

MSA (μM)	Cisplatin (μM)	Viability (%)	CI Value
0.75	3.75	74.5 ± 4.9	*0.717*
1	5	62.8 ± 3.9	*0.667*
1.5	7.5	45.1 ± 3.0	*0.669*
2	10	34.9 ± 3.9	*0.725*
2.5	12.5	26.0 ± 2.4	*0.750*
3	15	16.8 ± 2.1	*0.716*
3.5	17.5	11.0 ± 1.3	*0.695*
4	20	3.6 ± 0.7	*0.517*
5	25	2.6 ± 0.6	*0.579*

C. MCF7 cells, ratio 1:4.

MSA (μM)	Cisplatin (μM)	Viability (%)	CI Value
0.5	2	78.0 ± 1.2	*0.275*
0.75	3	74.6 ± 2.3	*0.363*
1	4	74.1 ± 2.1	*0.476*
1.5	6	70.2 ± 0.5	*0.629*
2	8	66.6 ± 0.1	*0.753*
2.5	10	49.5 ± 2.3	*0.608*
3	12	39.5 ± 3.2	*0.575*
3.5	14	19.9 ± 2.1	*0.392*
4	16	13.5 ± 1.4	*0.350*

D. OVCAR3 cells, ratio 1:5.

MSA (μM)	Cisplatin (μM)	Viability (%)	CI Value
0.75	3.75	49.8 ± 2.9	*0.431*
1	5	36.7 ± 2.6	*0.446*
1.5	7.5	25.5 ± 2.3	*0.523*
2	10	18.4 ± 1.1	*0.573*
2.5	12.5	11.6 ± 0.7	*0.555*
3	15	7.4 ± 0.6	*0.530*
3.5	17.5	6.9 ± 0.4	*0.597*
4	20	4.6 ± 0.2	*0.557*
5	25	2.7 ± 0.6	*0.538*

In addition, we studied the synergism of MSA and carboplatin, a derivative of cisplatin commonly used in conventional chemotherapy with similar efficacy, in the same cell lines. Likewise, the combination of MSA and carboplatin treatment in a wide dose range exhibited a synergistic (CI<1) antiproliferative effect in each tested cell line (Table 4.3.2).

Compared with cisplatin or carboplatin single treatments, dosage of these conventional chemotherapeutics could be remarkably reduced in combination therapy with MSA to gain the same inhibitory effect on cell proliferation. Therefore, the synergism observed in HCT116, MCF7, A549 and OVCAR3 cells suggests the combined MSA / cisplatin or carboplatin treatment as an efficient strategy to decrease the chemotherapeutic doses and consequently, mitigate the overall toxicity.

Table 4.3.2. Synergistic antiproliferative effect of MSA and carboplatin combination treatment. Cells were treated for 72 h at the indicated concentrations of MSA and carboplatin in a constant ratio. **A.** A549 cells, ratio 1:6. **B.** HCT116 cells, ratio 1:10. **C.** MCF7 cells, ratio 1:6. **D.** OVCAR3 cells, ratio 1:6. The CI results obtained with CompuSyn software revealed a synergistic (CI<1) antiproliferative effect of MSA and carboplatin at each dose combination tested.

A. A549 cells, ratio 1:6.

MSA (µM)	Cisplatin (µM)	Viability (%)	CI Value
0.5	3	81.2 ± 4.1	0.408
0.75	4.5	71.3 ± 5.2	0.642
1	6	61.2 ± 0.4	0.637
1.5	9	48.2 ± 1.4	0.775
2	12	30.7 ± 3.2	0.781
2.5	15	19.3 ± 0.9	0.626
3	18	12.8 ± 2.1	0.792
3.5	21	10.5 ± 1.3	0.816
4	24	8.1 ± 0.5	0.887

B. HCT116 cells, ratio 1:10.

MSA (µM)	Cisplatin (µM)	Viability (%)	CI Value
0.25	2.5	89 ± 1.3	*0.306*
0.5	5	77 ± 1.9	*0.398*
1	10	72 ± 0.2	*0.661*
1.5	15	55 ± 0.6	*0.731*
2	20	38 ± 3.4	*0.711*
2.5	25	22 ± 2.0	*0.674*
3	30	14 ± 0.6	*0.692*
3.5	35	12 ± 1.5	*0.752*
4	40	4 ± 2.8	*0.608*
5	50	2 ± 0.6	*0.567*

C. MCF7 cells, ratio 1:6.

MSA (µM)	Cisplatin (µM)	Viability (%)	CI Value
0.5	3	84.9 ± 5.4	*0.295*
0.75	4.5	70.3 ± 3.9	*0.299*
1	6	63.5 ± 5.0	*0.347*
1.5	9	55.2 ± 2.0	*0.445*
2	12	46.7 ± 4.3	*0.510*
2.5	15	36.1 ± 5.0	*0.523*
3	18	15.8 ± 4.2	*0.381*
3.5	21	13.4 ± 1.3	*0.408*
4	24	11.2 ± 0.7	*0.424*
5	30	8.7 ± 0.7	*0.469*

D. OVCAR3 cells, ratio 1:6.

MSA (µM)	Cisplatin (µM)	Viability (%)	CI Value
0.75	4.5	85.1 ± 1.8	*0.668*
1	6	77.5 ± 5.1	*0.697*
1.5	9	66.9 ± 0.5	*0.908*
2	12	44.4 ± 0.0	*0.862*
2.5	15	37.1 ± 1.0	*0.966*
3	18	24.7 ± 0.6	*0.937*
3.5	21	14.9 ± 0.1	*0.874*
4	24	6.5 ± 2.0	*0.719*
5	30	3.2 ± 0.6	*0.686*

4.3.2.9. MSA as a promising chemotherapeutic agent

In order to determine if MSA treatment obtained similar growth inhibitory results in other cancer cell lines, the effect of MSA on cell viability in NCI-H460 (large cell lung cancer) and HCT116 (colorectal carcinoma) cell lines was measured. The $^{72h}IC_{50}$ values obtained were in the same range as for A549 cells, being 1.7 ± 0.2 µM and 1.9 ± 0.2 µM for NCI-H460 and HCT116 cells, respectively (Figure 4.3.9A). To investigate if FOXO activation mediated by MSA is a general mechanism and not cell-dependent, HCT116 cell line was used to evaluate FOXO1 mRNA expression, which showed a significant increase in a time-dependent manner beginning at 2 h with 5 µM MSA treatment (data not shown).
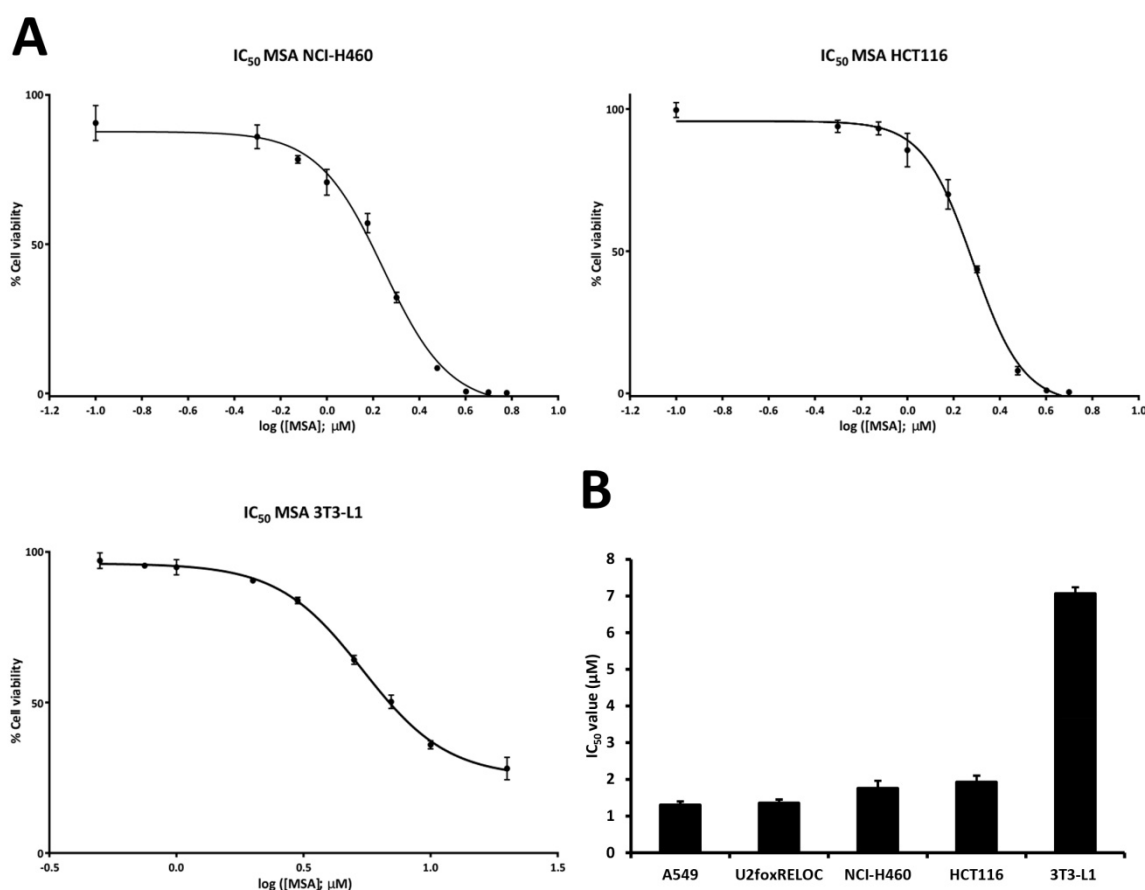
Figure 4.3.9. Effect of MSA on cell viability. A. Viability assays with MSA in NCI-H460, HCT116 and differentiated 3T3-L1 cells. **B.** Comparison between the $^{72h}IC_{50}$ values for the tested cell lines. The MSA concentration that caused 50% of inhibition of cell viability at 72 h of treatment for the 3T3-L1 non-tumour cell line was three to five times the value for all tumour cell lines analysed.

To test the selective cytotoxicity of MSA for cancer cells, a MTT colorimetric viability assay using a non-tumour non-proliferating cell line was performed. Differentiated 3T3-L1 adipocytes (see Section 3.3) were incubated for 72 h with 9 different MSA concentrations and the effect on cell proliferation and the $^{72h}IC_{50}$ value were determined (Figure 4.3.9A). $^{72h}IC_{50}$ for MSA in 3T3-L1 cells was three to five times the value for all tumour cell lines that have been studied (Figure 4.3.9B), supporting MSA as a promising chemotherapeutic agent with selective antiproliferative effects on cancer cells.

4.3.3. Discussion

Selenium is an essential trace element fundamental to human health with pivotal structural and enzymatic functions in selenoproteins. Selenium deficiency has been acknowledged as a contributing factor to a series of distinct pathophysiological conditions, including cancer. Several selenium compounds have shown cancer chemopreventive and chemotherapeutic activities in both animal models and humans [455, 585-587]. It is important to note that both dose and chemical form of selenium are crucial for the antitumour activity. MSA and sodium selenite are among the forms with high anticarcinogenic activity while selenomethionine was concluded to be ineffective in human cancer prevention [455, 588, 589] according to a recent large chemoprevention clinical trial (SELECT) [456].

There are several *in vivo* studies involving dietary selenium supplementation for cancer therapy and prevention. The evaluation of the effects of different diets containing MSA, sodium selenite or selenomethionine in tumour xenografts in mice has led to the conclusion that MSA exhibits a superior in vivo inhibitory efficacy against human prostate and breast cancers over selenomethionine or sodium selenite [452, 454, 560]. Indeed, dietary supplementation with MSA significantly inhibits xenograft tumour growth and reduces angiogenesis and spontaneous metastasis [452, 454, 560-562]. Importantly, supplementation with MSA does not affect neither the animal body weight nor the food consumption when compared with control diet animals, and

histological alterations in organs are not observed, altogether indicating a good tolerance to the used dosage of MSA without adverse side effects [452, 560, 561]. Moreover, MSA supplementation results in less accumulation of selenium both in liver and primary tumour when compared with selenomethionine, while causes no increment in kidney selenium levels relative to controls [452, 454, 560]. These results are consistent with the fact that MSA is efficiently transformed into methylselenol which in turn can be methylated and excreted [590]. Therefore, MSA treatment presents superior *in vivo* antitumour efficacy with good tolerance results over other selenium derivates [452, 454, 560, 561].

The fact that the molecular mechanism underlying MSA's antitumour properties has not been fully elucidated is a bottle neck in designing combination therapies with MSA. In this study, we described that lung carcinoma A549 cells are very sensitive to MSA treatment, in terms of growth inhibition, cell cycle arrest in G1 phase, attenuated intracellular ROS levels and apoptosis. However, some studies have described selenium derivatives as pro-oxidant products at higher doses than those used in this study [457]. This property could be due to dose dependence: at low concentrations MSA could serve as an antioxidant product, while at higher concentrations it could act as a pro-oxidant compound [588]. The antioxidant function could be mediated via the synthesis of selenocysteine, which is an essential residue of important ROS-detoxifying selenoproteins, such as glutathione peroxidases, thioredoxin reductases and possibly selenoprotein P [591]. Our results suggest distinct redox modulations of the two selenocompounds tested and thus different mechanisms of action. Heightened levels of ROS generated by sodium selenite can cause damage to DNA and mitochondria, leading to apoptosis. Considering these and previous results [450], sodium selenite induces apoptosis through generation of ROS while MSA-mediated apoptosis is regulated by a different molecular pathway like FOXO activation.

We have also shown that MSA induces FOXO translocation to the nucleus after 1.5 h of a 5 µM treatment and this localisation is maintained for at least 24 h. In addition, we have demonstrated that FOXO translocation after 1.5 h is the early event that occurs before the observed molecular and metabolic effects of MSA. Moreover, we have shown that the inhibition of the PI3K pathway through Akt and FOXO3a

dephosphorylation could be the molecular mechanism underlying inhibition of cell proliferation, disruption of tumour cell metabolic adaptations, induction of apoptosis, ROS detoxification and cell cycle arrest in A549 cells. Indeed, FOXO3a knockdown attenuated or even abolished the antiproliferative effects of MSA.

FOXO proteins are potentially key targets for new therapeutic strategies for blocking tumourigenesis due to their ability to control cell cycle and promote apoptosis [592]. The tumour suppressor properties of FOXO factors are mostly inhibited by overactivation of their inhibitory signalling, in contrast to other tumour suppressors, whose activities are abrogated by genetic or epigenetic changes [292]. These characteristics call for strategies on rescuing FOXO activity through its reactivation or by targeting its inhibitors [295]. As such, MSA is well-suited to serve as an anticancer agent by inhibiting the PI3K/Akt/mTOR axis and activating JNK signalling pathway, leading to FOXO nuclear relocalisation and restoration of its gene expression. Moreover, combination therapies that target PI3K/Akt pathway and promote nuclear FOXO retention are considered to be a promising approach to treat several tumour types. For example, in recent studies it has been proposed that cytotoxicity of cisplatin in sensitive cells can be enhanced and drug resistance in unresponsive cells reversed by using agents that target the PI3K/Akt/FOXO pathway in combination with cisplatin [286, 290, 291, 564]. Our study supports such hypothesis as MSA both synergised with cisplatin and its derivative carboplatin in blocking A549, HCT116, MCF7 and OVCAR3 cell proliferation. Thus, the combination of MSA with either cisplatin or carboplatin could represent a promising new approach to lung cancer treatment in terms of reducing platinum derivatives dose or toxicity as well as drug resistance.

Our data support a strong antiproliferative action of MSA in the low micromolar range on A549 cells, which is mediated by blocking G1 progression and triggering apoptosis. These MSA effects are associated with the inhibition of the Akt pathway, leading to dephosphorylation of FOXO proteins and their nuclear translocation, which in turn activate the expression of FOXO target genes. The time course data suggest that FOXO dephosphorylation and relocalisation to the nucleus are early events that activate the antiproliferative response of A549 cells to MSA. Moreover, the observed synergism in the antiproliferative effect between MSA and either cisplatin or carboplatin in several

cell lines derived from lung, colon, breast and ovarian tumours, reveal MSA as a very promising candidate for combination therapies for these types of tumours. Moreover, the synergistic effect of MSA and the specific CDK4/6 inhibitor PD0332991 depicted in Chapter 4.2 could also been explained by MSA-mediated inhibition of the Akt pathway (which was observed to be activated in CDK4/6-inhibited cells) and subsequent FOXO3a dephosphorylation, reverting the metabolic reprogramming of cells with CDK4/6 inhibition. In addition, several target genes that are induced by MYC are repressed by FOXO transcription factors. Indeed, when FOXO proteins are in a non-phosphorylated state, they inhibit MYC-mediated cell proliferation and transformation [298] by inducing MXI1 expression and repressing both MYC target genes and mitochondrial respiratory activity [299, 300]. Therefore, the activation of FOXO3a by MSA in CDK4/6-inhibited cells causes the inhibition of MYC target genes and counteracts the metabolic adaptation accompanying CDK4/6 inhibition.

5. General discussion

5. GENERAL DISCUSSION

Cancer is characterised by the lost of physiological control and the malignant transformation of cells that acquire functional and genetic abnormalities, leading to tumour development and progression. In 2012, the most commonly diagnosed cancers were lung (1.82 million), breast (1.67 million), and colorectal (1.36 million) [1]. Since cancer is a leading cause of death worldwide, the understanding of cancer cell biology is of pivotal importance to identify novel biomarkers for early diagnosis and design new therapeutic strategies. Indeed, tumour cells present common biological capabilities sequentially acquired during the development of cancer that are considered essential to drive malignancy [6]. In particular, tumour cells switch their core metabolism to meet the increased requirements of cell growth and division. Accordingly, oncogenic signals converge to reprogram tumour metabolism by enhancing key metabolic pathways such as glycolysis, pentose phosphate pathway (PPP), glutaminolysis and amino acid, lipid and nucleic acid metabolism [95, 130]. Consequently, tumour metabolic reprogramming is a direct result of the re-engineering of intracellular signalling pathways that are altered by activating mutations in oncogenes and loss-of-function mutations in tumour suppressor genes, which finally gives to transformed cells a proliferative advantage over non-malignant cells [9, 10]. Since several oncogenes including MYC, hypoxia inducible factor 1 (HIF1), phosphoinositide-3-kinase (PI3K), protein kinase B (PBK or Akt) and the mechanistic target of rapamycin (mTOR) have been known to be involved in the regulation of tumour metabolic reprogramming [9, 97, 151], the study of the metabolic adaptation of tumour cells and its connection with oncogenic signalling is a key strategy to identify new targets for cancer therapy and diagnosis.

Throughout this thesis, new possibilities for cancer treatment and diagnosis have been explored through the analysis of the links between metabolism and tumour progression (Chapter 4.1), the tumour metabolic reprogramming associated to the dysregulation of cell cycle (Chapter 4.2), and the use of combination therapies for cancer treatment (Chapters 4.2 and 4.3).

Early detection and adequate and efficient treatment of patients with cancer are the ultimate goals in order to reduce the burden of cancer. In fact, early diagnosis is especially relevant when there are no effective screening methods or effective treatment interventions. In addition, early detection allows for timely implementation of treatments and improves the chances of a positive clinical outcome. Screening programmes are designed to identify individuals presenting early signs of a specific cancer and then to provide a reliable method for on-time diagnosis and adequate treatment. Therefore, the identification of new biomarkers that are overexpressed in cancer onset is a key approach to detect early signs of disease in the population. Since cancer cells exhibit a metabolic phenotype that is significantly different from that of non-malignant cells, the study of the expression level of specific metabolic enzymes can lead to the identification of new biomarkers of cancer onset and progression. Accordingly, in Chapter 4.1 we have identified glyceraldehyde-3-phosphate dehydrogenase (GAPDH) as a potential predictive biomarker for tumour staging and prognosis of human colorectal cancer. In addition, our results clearly discourage the use of GAPDH as a housekeeping marker in colorectal cancer. The monitoring of GAPDH in risk population can facilitate early diagnosis and treatment, while studying GAPDH function in malignant transformation can shed new light on the understanding of tumour onset and lead to the design of more efficient personalised therapies.

Personalised medicine in cancer requires the correct diagnosis of cancer to give patients the most appropriate treatment according to their individual circumstances and the molecular characteristics of their tumours. However, personalised medicine is still at a relatively early stage in its development, and therefore the classification of cancers is based on critical molecular targets identified by translational research. Hence, more efforts should be put into understanding the tumour biology in order to identify the involved targets and determine the optimum treatment for each specific tumour. Likewise, the developing of new therapeutic strategies that specifically target the molecular pathways involved in promoting tumour cell proliferation and survival, such as targeted therapies, is a major focus of cancer research today [462]. However, the currently available chemotherapeutic treatments exhibit modest efficacy due to their side effects and drug resistance. In addition, the design of more efficient targeted

therapies requires a better definition of the activated oncogenic pathways in transformed cells and the availability of selective small-molecule inhibitors directed to these pathways. In this context, the search for combined chemotherapies with low systemic toxicity that inhibit two or more molecular targets in a single pathway, or in redundant or compensatory pathways, is a promising strategy for cancer treatment [463]. With this purpose, both metabolic tumour characterisation and gene expression analysis can be used to identify the dysregulated molecular pathways in a specific tumour, providing a potential basis for guiding the use of target-specific drugs and directing combination therapies [464].

To this aim, in Chapter 4.2, we have characterised the metabolic reprogramming associated to the inhibition of cyclin-dependent kinases 4 and 6 (CDK4/6) in HCT116 colon cancer cells, confirming the involvement of CDK4/6 proteins in metabolism regulation. CDK4/6 inhibition causes a shift towards enhanced metabolism of glucose, glutamine and amino acids by increasing mitochondrial metabolism and function as well as glycolytic flux. It is worth noting that oxidative metabolism driven by glutamine is a main energetic source, even under hypoxia, in many cancer cells [163, 165]. Fan et al. predicted that oxidative phosphorylation contributes 70-84% of the total ATP production on average across the NCI-60 cell lines [165]. In agreement with these results, we have found that the contribution of oxidative phosphorylation to total ATP production was around 60% in control cells, and that total contributions are greater when CDK4/6 are inhibited (Annex IV). On the other hand, despite being an inefficient way to generate ATP, aerobic glycolysis is able to endorse tumour proliferation and fulfil its metabolic requirements by providing metabolic intermediates and precursors that are essential to drive biosynthesis of nucleotides, amino acids and lipids, among other, to increase the cell biomass and support oncogenic growth [106]. Importantly, fluxomics and transcriptomics integrated data analysis supported that this metabolic reprogramming is directed by MYC, which is accumulated when CDK4/6 are inhibited. MYC overexpression can upregulate mTOR pathway [320], increasing glutamine metabolism and leading to an augmented production of α-ketoglutarate [321, 322] which, in turn, serves as a substrate for prolyl hydroxylases, triggering HIF1α hydroxylation and degradation [160], and sensitising cells with CDK4/6 inhibition to

hypoxia (Figure 5.1). In addition, mTOR upregulation can activate PI3K/Akt pathway contributing to FOXO3a inhibition and MYC stimulation [298, 306, 315].
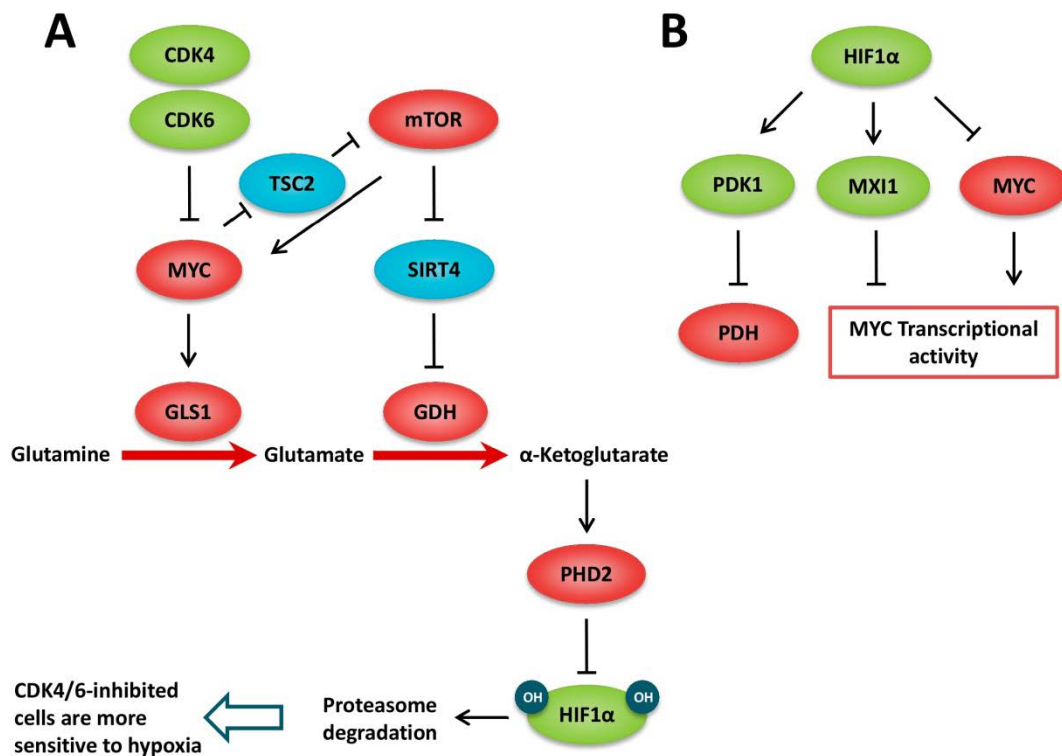
Figure 5.1. Mechanism and consequences of HIF1α degradation. A. MYC and mTOR activation observed in CDK4/6-inhibited cells increase the protein expression of GLS1 and GDH, respectively, resulting in an enhanced glutamine uptake and conversion to α-ketoglutarate. The accumulation of α-ketoglutarate serves as a substrate for PHD2, which triggers HIF1α hydroxylation and consequent proteasomal degradation. The overall result is that CDK4/6 knockdown renders cells sensitive to hypoxic conditions. **B.** Conversely, in control cells, HIF1α is significantly expressed and inhibits mitochondrial metabolism and function through MYC degradation and PDH inhibition. Proteins coloured in green and red correspond to proteins that were measured and found to be down and overexpressed, respectively, in CDK4/6-inhibited cells compared to control cells. Proteins represented in blue were not experimentally measured. Red arrows denote an increase in the metabolic flux of cells with CDK4/6 inhibition relative to control cells.

Consequently, the metabolic adaptation associated to cell cycle dysregulation through CDK4/6 inhibition reveals specific cell vulnerabilities which, in turn, are potential candidates to be therapeutically targeted in combination with CDK4/6 inhibitors. Indeed, the expected outcome of this study was the development of combination therapies using CDK4/6 inhibitors together with drugs that directly inhibit the

metabolic adaptation exhibited by tumour cells with CDK4/6 downregulation, and their validation as putative therapeutic strategies displaying selectivity for tumour cells. The final aim of the proposed combination treatments is to achieve synergistic therapeutic effect, dose and toxicity reduction, and to minimise or delay the induction of drug resistance [556].

In particular, our results reveal that CDK4/6 inhibition affects fundamental regulators of cell metabolism, leading to a change in the cell homeostatic and regulatory balance. Indeed, the identification of central metabolism enzymes or gene regulators changing their activity as a consequence of CDK4/6 inhibition provides the evidence of regulatory components that are suggested to be fundamental for the maintenance of the tumour metabolic condition, accentuating potential weaknesses that can be exploited for cancer therapy. In particular, the principal potential candidates for
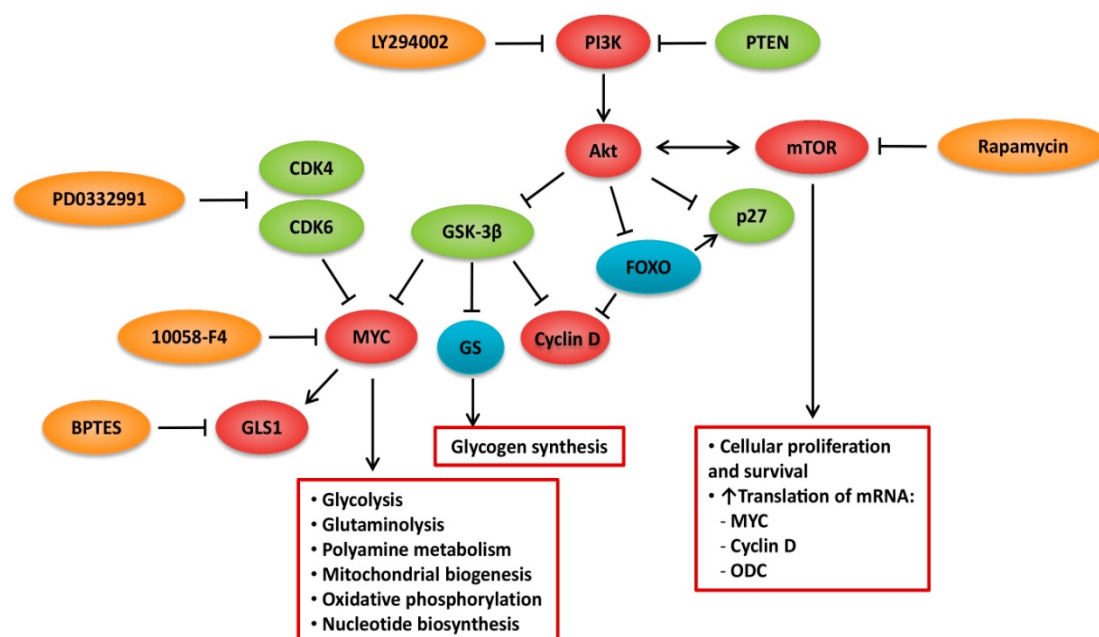
Figure 5.2. Summary of activated pathways underlying the metabolic reprogramming in cells with CDK4/6 inhibition. MYC, mTOR and PI3K/Akt are the key regulators driving the metabolic adaptation associated to CDK4/6 inhibition. Their identification opens up new opportunities for combined therapies with the clinical approved CDK4/6 specific inhibitor PD0332991. Proteins coloured in green and red correspond to proteins that were measured and found to be down and overexpressed, respectively, in CDK4/6-inhibited cells compared to control cells. Proteins represented in blue were not experimentally measured. Chemical inhibitors are represented in orange.

combination therapy were MYC, mTOR, PI3K and Akt. In effect, we have obtained synergistic and selective antiproliferative effects *in vitro* by inhibiting mTOR, PI3K/Akt axis or MYC target genes in combination with CDK4/6 inhibitors. Above all, our system analysis has clearly identified MYC as the main dysregulated regulatory protein responsible for the metabolic re-modulation after CDK4/6 inhibition. Accordingly, from our results glutaminase (GLS1) emerges as the most promising candidate for combination therapies with CDK4/6 inhibitors. Hence, drugs that target the metabolic reprogramming exhibited by CDK4/6-inhibited cells are potential candidates for synergistic interactions in combined cancer therapies with the inhibition of CDK4/6 (Figure 5.2).

In Chapter 4.3, we have determined the molecular mechanism of action of the selenium compound methylseleninic acid (MSA) in order to design efficient combination therapies with traditional chemotherapeutic drugs. Our study shows that MSA effects are associated with the inhibition of the Akt pathway, resulting in the dephosphorylation of FOXO3a transcription factors and their nuclear translocation which, in turn, activates the expression of FOXO3a target genes. Since the tumour suppressor properties of FOXO factors are mostly inhibited by the overactivation of their inhibitory signalling [292], the best therapeutic approach is to rescue FOXO activity through its reactivation or by targeting its inhibitors [295]. Accordingly, MSA has proved to be a promising chemotherapeutic agent by both inhibiting the PI3K/Akt/mTOR axis and activating JNK signalling pathway, inducing FOXO3a nuclear relocalisation and restoration of its transcriptional activity (Figure 5.3). In contrast, sodium selenite, another selenium derivative, causes apoptosis but does not induce either FOXO3a nuclear translocation or Akt inhibition, which reveals different mechanisms of action of the two selenium compounds. It is worth noting that the antitumour effects of some conventional chemotherapeutic agents such as cisplatin are enhanced in combination with drugs that target PI3K/Akt pathway and promote nuclear FOXO3a retention [286, 290, 291, 564]. Accordingly, we have found that MSA synergises with both cisplatin and carboplatin and thus has the potential to be used in
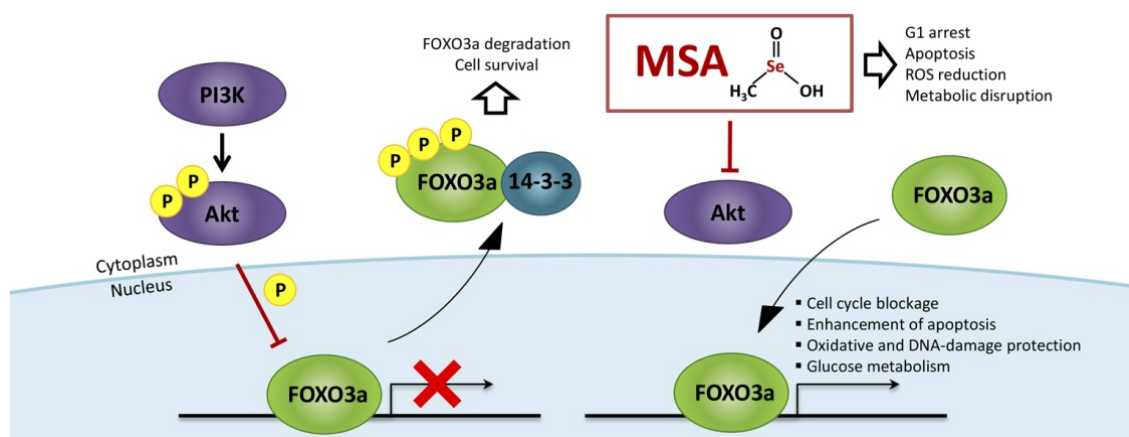
Figure 5.3. Molecular mechanism of action of methylseleninic acid (MSA). MSA is well-suited to serve as an anticancer agent by inhibiting the PI3K/Akt/mTOR axis, leading to FOXO3a nuclear relocalisation and restoration of its transcriptional activity.

combined therapies to reduce the commonly observed toxicity of platinum derivatives as well as overcome the resistance of cancer cells to chemotherapy. In addition, as described in Chapter 4.2, MSA also presents synergistic effects with the specific CDK4/6 inhibitor PD0332991, as a consequence of MSA-mediated inhibition of the Akt pathway, which is one of the metabolic vulnerabilities associated to CDK4/6 inhibition.

Collectively, our results have contributed to the understanding of tumour metabolic reprogramming as well as the mechanisms of action of compounds potentially useful as antitumour agents. We have used this information to develop novel promising molecular-targeted strategies that complement conventional and existing chemotherapies, providing new therapeutic opportunities for improving cancer treatment and diagnosis.

6. Conclusions

6. CONCLUSIONS

1. Glyceraldehyde-3-phosphate dehydrogenase (GAPDH) is overexpressed in early stages of colorectal cancer progression, revealing an important role in cancer onset, which prevents its use as a housekeeping marker in colorectal cancer. Using GAPDH as an early detection biomarker in colorectal cancer and for monitoring high-risk populations is a promising strategy to facilitate early diagnosis and treatment.

2. Inhibition of cyclin-dependent kinases 4 and 6 (CDK4/6) causes a shift towards enhanced metabolism of glucose, glutamine and amino acids by increasing mitochondrial metabolism and function as well as glycolytic flux. Fluxomics and transcriptomics integrated data analysis revealed that this metabolic reprogramming is directed by MYC transcription factor, which is accumulated when CDK4/6 are inhibited.

   MYC upregulates mTOR pathway and increases glutamine metabolism and production of α-ketoglutarate, which serves as a substrate for prolyl hydroxylases, triggering HIF1α hydroxylation and degradation, and sensitising cells with CDK4/6 inhibition to hypoxia. In addition, mTOR upregulation activates PI3K/Akt pathway contributing to FOXO3a inhibition and MYC stimulation.

3. The identification of the tumour metabolic adaptations associated to CDK4/6 inhibition reveals potential metabolic vulnerabilities that can be exploited in combination therapies based on CDK4/6 inhibitors. On the one hand, mTOR and PI3K/Akt axis are potential targets for combination therapies with CDK4/6 inhibitors, resulting in synergistic and selective antiproliferative effects *in vitro*. On the other hand, we have identified glutaminase 1 (GLS1) as a promising target for combination therapy with specific CDK4/6 inhibitors such as PD0332991. The inhibition of GLS1 alone has little effect on colon and breast cancer cells, while its combination with PD0332991 exhibits a strong synergistic antiproliferative effect at a wide dose range which is selective to tumour cells.

4. Methylseleninic acid (MSA) exhibits strong antiproliferative effects in the low micromolar range through cell cycle arrest at G1 phase and apoptosis induction. MSA antitumour activity is mediated by nuclear FOXO3a translocation through Akt inhibition. FOXO3a dephosphorylation and relocalisation to the nucleus are the early events that activate the antiproliferative response of MSA. By targeting the PI3K/Akt/FOXO3a pathway, MSA synergises with cisplatin in combination therapy to reduce the toxicity and overcome the resistance of cisplatin-based chemotherapy.

7. References

7. REFERENCES

[1] Ferlay J, Soerjomataram I, Dikshit R, Eser S, Mathers C, Rebelo M, et al. Cancer incidence and mortality worldwide: sources, methods and major patterns in GLOBOCAN 2012. Int J Cancer. 2015;136:E359-86.

[2] Edge SB BD, Compton CC, Fritz AG, Greene FL, Trotti A. AJCC cancer staging manual (7th ed). New York, NY: Springer; 2010.

[3] Johnson DH, Schiller JH, Bunn PA, Jr. Recent clinical advances in lung cancer management. J Clin Oncol. 2014;32:973-82.

[4] Wheate NJ, Walker S, Craig GE, Oun R. The status of platinum anticancer drugs in the clinic and in clinical trials. Dalton Trans. 2010;39:8113-27.

[5] Dasari S, Tchounwou PB. Cisplatin in cancer therapy: Molecular mechanisms of action. European Journal of Pharmacology. 2014;740:364-78.

[6] Hanahan D, Weinberg RA. Hallmarks of cancer: the next generation. Cell. 2011;144:646-74.

[7] Shortt J, Johnstone RW. Oncogenes in cell survival and cell death. Cold Spring Harb Perspect Biol. 2012;4.

[8] Hanahan D, Weinberg RA. The hallmarks of cancer. Cell. 2000;100:57-70.

[9] Qiu B, Simon MC. Oncogenes strike a balance between cellular growth and homeostasis. Semin Cell Dev Biol. 2015.

[10] Morris LG, Chan TA. Therapeutic targeting of tumor suppressor genes. Cancer. 2015;121:1357-68.

[11] Norbury C, Nurse P. Animal cell cycles and their control. Annu Rev Biochem. 1992;61:441-70.

[12] Pardee AB. A restriction point for control of normal animal cell proliferation. Proceedings of the National Academy of Sciences of the United States of America. 1974;71:1286-90.

[13] Buchakjian MR, Kornbluth S. The engine driving the ship: metabolic steering of cell proliferation and death. Nat Rev Mol Cell Biol. 2010;11:715-27.

[14] Viallard JF, Lacombe F, Belloc F, Pellegrin JL, Reiffers J. [Molecular mechanisms controlling the cell cycle: fundamental aspects and implications for oncology]. Cancer Radiother. 2001;5:109-29.

[15] Strauss M, Lukas J, Bartek J. Unrestricted cell cycling and cancer. Nat Med. 1995;1:1245-6.

[16] Malumbres M, Barbacid M. Cell cycle kinases in cancer. Curr Opin Genet Dev. 2007;17:60-5.

[17] Shapiro GI. Cyclin-dependent kinase pathways as targets for cancer treatment. J Clin Oncol. 2006;24:1770-83.

[18] Meyerson M, Enders GH, Wu CL, Su LK, Gorka C, Nelson C, et al. A family of human cdc2-related protein kinases. Embo J. 1992;11:2909-17.

[19] Sausville EA. Complexities in the development of cyclin-dependent kinase inhibitor drugs. Trends Mol Med. 2002;8:S32-7.

[20] Morgan DO. Cyclin-dependent kinases: engines, clocks, and microprocessors. Annu Rev Cell Dev Biol. 1997;13:261-91.

[21] Sherr CJ. G1 phase progression: cycling on cue. Cell. 1994;79:551-5.

[22] Nurse P. A long twentieth century of the cell cycle and beyond. Cell. 2000;100:71-8.

[23] Arellano M, Moreno S. Regulation of CDK/cyclin complexes during the cell cycle. Int J Biochem Cell Biol. 1997;29:559-73.

[24] Glotzer M, Murray AW, Kirschner MW. Cyclin is degraded by the ubiquitin pathway. Nature. 1991;349:132-8.

[25] Pfleger CM, Kirschner MW. The KEN box: an APC recognition signal distinct from the D box targeted by Cdh1. Genes Dev. 2000;14:655-65.

[26] Vodermaier HC. APC/C and SCF: controlling each other and the cell cycle. Curr Biol. 2004;14:R787-96.

[27] Barford D. Structure, function and mechanism of the anaphase promoting complex (APC/C). Q Rev Biophys. 2011;44:153-90.

[28] Peters JM. The anaphase promoting complex/cyclosome: a machine designed to destroy. Nat Rev Mol Cell Biol. 2006;7:644-56.

[29] Malumbres M, Harlow E, Hunt T, Hunter T, Lahti JM, Manning G, et al. Cyclin-dependent kinases: a family portrait. Nat Cell Biol. 2009;11:1275-6.

[30] Ren S, Rollins BJ. Cyclin C/cdk3 promotes Rb-dependent G0 exit. Cell. 2004;117:239-51.

[31] Ye X, Zhu C, Harper JW. A premature-termination mutation in the Mus musculus cyclin-dependent kinase 3 gene. Proceedings of the National Academy of Sciences of the United States of America. 2001;98:1682-6.

[32] Zhang J, Cicero SA, Wang L, Romito-Digiacomo RR, Yang Y, Herrup K. Nuclear localization of Cdk5 is a key determinant in the postmitotic state of neurons. Proceedings of the National Academy of Sciences of the United States of America. 2008;105:8772-7.

[33] Maestre C, Delgado-Esteban M, Gomez-Sanchez JC, Bolanos JP, Almeida A. Cdk5 phosphorylates Cdh1 and modulates cyclin B1 stability in excitotoxicity. Embo J. 2008;27:2736-45.

[34] Chen HH, Wang YC, Fann MJ. Identification and characterization of the CDK12/cyclin L1 complex involved in alternative splicing regulation. Molecular and cellular biology. 2006;26:2736-45.

[35] Chen HH, Wong YH, Geneviere AM, Fann MJ. CDK13/CDC2L5 interacts with L-type cyclins and regulates alternative splicing. Biochemical and biophysical research communications. 2007;354:735-40.

[36] Malumbres M, Barbacid M. Mammalian cyclin-dependent kinases. Trends Biochem Sci. 2005;30:630-41.

[37] Harbour JW, Dean DC. The Rb/E2F pathway: expanding roles and emerging paradigms. Genes Dev. 2000;14:2393-409.

[38] Malumbres M, Barbacid M. To cycle or not to cycle: a critical decision in cancer. Nat Rev Cancer. 2001;1:222-31.

[39] Wu CL, Zukerberg LR, Ngwu C, Harlow E, Lees JA. In vivo association of E2F and DP family proteins. Molecular and cellular biology. 1995;15:2536-46.

[40] La Thangue NB. E2F and the molecular mechanisms of early cell-cycle control. Biochem Soc Trans. 1996;24:54-9.

[41] Ortega S, Malumbres M, Barbacid M. Cyclin D-dependent kinases, INK4 inhibitors and cancer. Biochimica et biophysica acta. 2002;1602:73-87.

[42] Sherr CJ, Roberts JM. CDK inhibitors: positive and negative regulators of G1-phase progression. Genes Dev. 1999;13:1501-12.

[43] Malumbres M. Physiological relevance of cell cycle kinases. Physiol Rev. 2011;91:973-1007.

[44] Zhang W, Koepp DM. Fbw7 isoform interaction contributes to cyclin E proteolysis. Mol Cancer Res. 2006;4:935-43.

[45] Kitagawa M, Higashi H, Suzuki-Takahashi I, Segawa K, Hanks SK, Taya Y, et al. Phosphorylation of E2F-1 by cyclin A-cdk2. Oncogene. 1995;10:229-36.

[46] Peters JM. The anaphase-promoting complex: proteolysis in mitosis and beyond. Mol Cell. 2002;9:931-43.

[47] Harper JW, Burton JL, Solomon MJ. The anaphase-promoting complex: it's not just for mitosis any more. Genes Dev. 2002;16:2179-206.

[48] Blain SW. Switching cyclin D-Cdk4 kinase activity on and off. Cell Cycle. 2008;7:892-8.

[49] Sheaff RJ, Groudine M, Gordon M, Roberts JM, Clurman BE. Cyclin E-CDK2 is a regulator of p27Kip1. Genes Dev. 1997;11:1464-78.

[50] Massague J. G1 cell-cycle control and cancer. Nature. 2004;432:298-306.

[51] He G, Siddik ZH, Huang Z, Wang R, Koomen J, Kobayashi R, et al. Induction of p21 by p53 following DNA damage inhibits both Cdk4 and Cdk2 activities. Oncogene. 2005;24:2929-43.

[52] Cazzalini O, Scovassi AI, Savio M, Stivala LA, Prosperi E. Multiple roles of the cell cycle inhibitor p21(CDKN1A) in the DNA damage response. Mutat Res. 2010;704:12-20.

[53] Hoeferlin LA, Oleinik NV, Krupenko NI, Krupenko SA. Activation of p21-Dependent G1/G2 Arrest in the Absence of DNA Damage as an Antiapoptotic Response to Metabolic Stress. Genes Cancer. 2011;2:889-99.

[54] Lee IH, Kawai Y, Fergusson MM, Rovira, II, Bishop AJ, Motoyama N, et al. Atg7 modulates p53 activity to regulate cell cycle and survival during metabolic stress. Science (New York, NY. 2012;336:225-8.

[55] Castro A, Bernis C, Vigneron S, Labbe JC, Lorca T. The anaphase-promoting complex: a key factor in the regulation of cell cycle. Oncogene. 2005;24:314-25.

[56] Palframan WJ, Meehl JB, Jaspersen SL, Winey M, Murray AW. Anaphase inactivation of the spindle checkpoint. Science (New York, NY. 2006;313:680-4.

[57] Bartek J, Lukas J. Chk1 and Chk2 kinases in checkpoint control and cancer. Cancer cell. 2003;3:421-9.

[58] Kastan MB, Bartek J. Cell-cycle checkpoints and cancer. Nature. 2004;432:316-23.

[59] Nakayama KI, Nakayama K. Ubiquitin ligases: cell-cycle control and cancer. Nat Rev Cancer. 2006;6:369-81.

[60] Tudzarova S, Colombo SL, Stoeber K, Carcamo S, Williams GH, Moncada S. Two ubiquitin ligases, APC/C-Cdh1 and SKP1-CUL1-F (SCF)-beta-TrCP, sequentially regulate glycolysis during the cell cycle. Proceedings of the National Academy of Sciences of the United States of America. 2011;108:5278-83.

[61] Kramer ER, Scheuringer N, Podtelejnikov AV, Mann M, Peters JM. Mitotic regulation of the APC activator proteins CDC20 and CDH1. Mol Biol Cell. 2000;11:1555-69.

[62] Malumbres M, Barbacid M. Cell cycle, CDKs and cancer: a changing paradigm. Nat Rev Cancer. 2009;9:153-66.

[63] Barbacid M, Ortega S, Sotillo R, Odajima J, Martin A, Santamaria D, et al. Cell cycle and cancer: genetic analysis of the role of cyclin-dependent kinases. Cold Spring Harb Symp Quant Biol. 2005;70:233-40.

[64] Barriere C, Santamaria D, Cerqueira A, Galan J, Martin A, Ortega S, et al. Mice thrive without Cdk4 and Cdk2. Mol Oncol. 2007;1:72-83.

[65] Berthet C, Aleem E, Coppola V, Tessarollo L, Kaldis P. Cdk2 knockout mice are viable. Curr Biol. 2003;13:1775-85.

[66] Ortega S, Prieto I, Odajima J, Martin A, Dubus P, Sotillo R, et al. Cyclin-dependent kinase 2 is essential for meiosis but not for mitotic cell division in mice. Nat Genet. 2003;35:25-31.

[67] Martin A, Odajima J, Hunt SL, Dubus P, Ortega S, Malumbres M, et al. Cdk2 is dispensable for cell cycle inhibition and tumor suppression mediated by p27(Kip1) and p21(Cip1). Cancer cell. 2005;7:591-8.

[68] Malumbres M, Sotillo R, Santamaria D, Galan J, Cerezo A, Ortega S, et al. Mammalian cells cycle without the D-type cyclin-dependent kinases Cdk4 and Cdk6. Cell. 2004;118:493-504.

[69] Santamaria D, Barriere C, Cerqueira A, Hunt S, Tardy C, Newton K, et al. Cdk1 is sufficient to drive the mammalian cell cycle. Nature. 2007;448:811-5.

[70] Ingolia N. Cell cycle: bistability is needed for robust cycling. Curr Biol. 2005;15:R961-3.

[71] Uhlmann F, Bouchoux C, Lopez-Aviles S. A quantitative model for cyclin-dependent kinase control of the cell cycle: revisited. Philos Trans R Soc Lond B Biol Sci. 2011;366:3572-83.

7. References

[72] Gerard C, Goldbeter A. A skeleton model for the network of cyclin-dependent kinases driving the mammalian cell cycle. Interface Focus. 2011;1:24-35.

[73] Tetsu O, McCormick F. Proliferation of cancer cells despite CDK2 inhibition. Cancer cell. 2003;3:233-45.

[74] Casimiro MC, Velasco-Velazquez M, Aguirre-Alvarado C, Pestell RG. Overview of cyclins D1 function in cancer and the CDK inhibitor landscape: past and present. Expert Opin Investig Drugs. 2014;23:295-304.

[75] Sanchez-Martinez C, Gelbert LM, Lallena MJ, de Dios A. Cyclin dependent kinase (CDK) inhibitors as anticancer drugs. Bioorg Med Chem Lett. 2015;25:3420-35.

[76] Bruyere C, Meijer L. Targeting cyclin-dependent kinases in anti-neoplastic therapy. Curr Opin Cell Biol. 2013;25:772-9.

[77] Graf F, Koehler L, Kniess T, Wuest F, Mosch B, Pietzsch J. Cell Cycle Regulating Kinase Cdk4 as a Potential Target for Tumor Cell Treatment and Tumor Imaging. J Oncol. 2009;2009:106378.

[78] Malumbres M, Barbacid M. Is Cyclin D1-CDK4 kinase a bona fide cancer target? Cancer cell. 2006;9:2-4.

[79] Molenaar JJ, Ebus ME, Koster J, van Sluis P, van Noesel CJ, Versteeg R, et al. Cyclin D1 and CDK4 activity contribute to the undifferentiated phenotype in neuroblastoma. Cancer Res. 2008;68:2599-609.

[80] Ely S, Di Liberto M, Niesvizky R, Baughn LB, Cho HJ, Hatada EN, et al. Mutually exclusive cyclin-dependent kinase 4/cyclin D1 and cyclin-dependent kinase 6/cyclin D2 pairing inactivates retinoblastoma protein and promotes cell cycle dysregulation in multiple myeloma. Cancer Res. 2005;65:11345-53.

[81] Landis MW, Pawlyk BS, Li T, Sicinski P, Hinds PW. Cyclin D1-dependent kinase activity in murine development and mammary tumorigenesis. Cancer cell. 2006;9:13-22.

[82] Yu Q, Sicinska E, Geng Y, Ahnstrom M, Zagozdzon A, Kong Y, et al. Requirement for CDK4 kinase function in breast cancer. Cancer Cell. 2006;9:23-32.

[83] Fry DW, Harvey PJ, Keller PR, Elliott WL, Meade M, Trachet E, et al. Specific inhibition of cyclin-dependent kinase 4/6 by PD 0332991 and associated antitumor activity in human tumor xenografts. Mol Cancer Ther. 2004;3:1427-38.

[84] Leonard JP, LaCasce AS, Smith MR, Noy A, Chirieac LR, Rodig SJ, et al. Selective CDK4/6 inhibition with tumor responses by PD0332991 in patients with mantle cell lymphoma. Blood. 2012;119:4597-607.

[85] Vidula N, Rugo HS. Cyclin-Dependent Kinase 4/6 Inhibitors for the Treatment of Breast Cancer: A Review of Preclinical and Clinical Data. Clin Breast Cancer. 2015.

[86] Zanuy M, Ramos-Montoya A, Villacanas O, Canela N, Miranda A, Aguilar E, et al. Cyclin-dependent kinases 4 and 6 control tumor progression and direct glucose oxidation in the pentose cycle. Metabolomics. 2012;8:454-64.

[87] Ray D, Terao Y, Fuhrken PG, Ma ZQ, DeMayo FJ, Christov K, et al. Deregulated CDC25A expression promotes mammary tumorigenesis with genomic instability. Cancer Res. 2007;67:984-91.

[88] Ray D, Terao Y, Christov K, Kaldis P, Kiyokawa H. Cdk2-null mice are resistant to ErbB-2-induced mammary tumorigenesis. Neoplasia. 2011;13:439-44.

[89] Yu Q, Geng Y, Sicinski P. Specific protection against breast cancers by cyclin D1 ablation. Nature. 2001;411:1017-21.

[90] Campaner S, Doni M, Hydbring P, Verrecchia A, Bianchi L, Sardella D, et al. Cdk2 suppresses cellular senescence induced by the c-myc oncogene. Nat Cell Biol. 2010;12:54-9; sup pp 1-14.

[91] Hydbring P, Bahram F, Su Y, Tronnersjo S, Hogstrand K, von der Lehr N, et al. Phosphorylation by Cdk2 is required for Myc to repress Ras-induced senescence in cotransformation. Proceedings of the National Academy of Sciences of the United States of America. 2010;107:58-63.

[92] Puyol M, Martin A, Dubus P, Mulero F, Pizcueta P, Khan G, et al. A synthetic lethal interaction between K-Ras oncogenes and Cdk4 unveils a therapeutic strategy for non-small cell lung carcinoma. Cancer cell. 2010;18:63-73.

[93] Kops GJ, Weaver BA, Cleveland DW. On the road to cancer: aneuploidy and the mitotic checkpoint. Nat Rev Cancer. 2005;5:773-85.

[94] Holland AJ, Cleveland DW. Boveri revisited: chromosomal instability, aneuploidy and tumorigenesis. Nat Rev Mol Cell Biol. 2009;10:478-87.

[95] Ward PS, Thompson CB. Metabolic reprogramming: a cancer hallmark even warburg did not anticipate. Cancer cell. 2012;21:297-308.

[96] Wise DR, DeBerardinis RJ, Mancuso A, Sayed N, Zhang XY, Pfeiffer HK, et al. Myc regulates a transcriptional program that stimulates mitochondrial glutaminolysis and leads to glutamine addiction. Proceedings of the National Academy of Sciences of the United States of America. 2008;105:18782-7.

[97] Cairns RA, Harris IS, Mak TW. Regulation of cancer cell metabolism. Nat Rev Cancer. 2011;11:85-95.

[98] Courtnay R, Ngo DC, Malik N, Ververis K, Tortorella SM, Karagiannis TC. Cancer metabolism and the Warburg effect: the role of HIF-1 and PI3K. Mol Biol Rep. 2015;42:841-51.

[99] DeBerardinis RJ, Sayed N, Ditsworth D, Thompson CB. Brick by brick: metabolism and tumor cell growth. Curr Opin Genet Dev. 2008;18:54-61.

[100] Warburg O, Posener K, Negelein E. Über den Stoffwechsel der Karzinomzellen. Biochemische Zeitschrift. 1924;152:309-44.

[101] Warburg O. On the origin of cancer cells. Science (New York, NY. 1956;123:309-14.

[102] Semenza GL, Artemov D, Bedi A, Bhujwalla Z, Chiles K, Feldser D, et al. 'The metabolism of tumours': 70 years later. Novartis Found Symp. 2001;240:251-60; discussion 60-4.

[103] Gogvadze V, Zhivotovsky B, Orrenius S. The Warburg effect and mitochondrial stability in cancer cells. Mol Aspects Med. 2010;31:60-74.

[104] Kroemer G, Pouyssegur J. Tumor cell metabolism: cancer's Achilles' heel. Cancer cell. 2008;13:472-82.

[105] Salway JG. Metabolism at a Glance. 2nd ed. Oxford: Blackwell Science; 2000.

[106] Vander Heiden MG, Cantley LC, Thompson CB. Understanding the Warburg effect: the metabolic requirements of cell proliferation. Science (New York, NY. 2009;324:1029-33.

[107] Som P, Atkins HL, Bandoypadhyay D, Fowler JS, MacGregor RR, Matsui K, et al. A fluorinated glucose analog, 2-fluoro-2-deoxy-D-glucose (F-18): nontoxic tracer for rapid tumor detection. J Nucl Med. 1980;21:670-5.

[108] Yeung SJ, Pan J, Lee MH. Roles of p53, MYC and HIF-1 in regulating glycolysis - the seventh hallmark of cancer. Cell Mol Life Sci. 2008;65:3981-99.

[109] Levine AJ, Puzio-Kuter AM. The control of the metabolic switch in cancers by oncogenes and tumor suppressor genes. Science (New York, NY. 2010;330:1340-4.

[110] Cerella C, Dicato M, Diederich M. Modulatory roles of glycolytic enzymes in cell death. Biochem Pharmacol. 2014;92:22-30.

[111] Kim JW, Dang CV. Multifaceted roles of glycolytic enzymes. Trends Biochem Sci. 2005;30:142-50.

[112] Sirover MA. On the functional diversity of glyceraldehyde-3-phosphate dehydrogenase: biochemical mechanisms and regulatory control. Biochimica et biophysica acta. 2011;1810:741-51.

[113] Altenberg B, Greulich KO. Genes of glycolysis are ubiquitously overexpressed in 24 cancer classes. Genomics. 2004;84:1014-20.

[114] Tang Z, Yuan S, Hu Y, Zhang H, Wu W, Zeng Z, et al. Over-expression of GAPDH in human colorectal carcinoma as a preferred target of 3-bromopyruvate propyl ester. J Bioenerg Biomembr. 2012;44:117-25.

7. References

[115] Colell A, Green DR, Ricci JE. Novel roles for GAPDH in cell death and carcinogenesis. Cell Death Differ. 2009;16:1573-81.

[116] Colell A, Ricci JE, Tait S, Milasta S, Maurer U, Bouchier-Hayes L, et al. GAPDH and autophagy preserve survival after apoptotic cytochrome c release in the absence of caspase activation. Cell. 2007;129:983-97.

[117] Patra KC, Hay N. The pentose phosphate pathway and cancer. Trends Biochem Sci. 2014;39:347-54.

[118] Li D, Zhu Y, Tang Q, Lu H, Li H, Yang Y, et al. A new G6PD knockdown tumor-cell line with reduced proliferation and increased susceptibility to oxidative stress. Cancer Biother Radiopharm. 2009;24:81-90.

[119] Jiang P, Du W, Wang X, Mancuso A, Gao X, Wu M, et al. p53 regulates biosynthesis through direct inactivation of glucose-6-phosphate dehydrogenase. Nat Cell Biol. 2011;13:310-6.

[120] Qiu Z, Guo W, Wang Q, Chen Z, Huang S, Zhao F, et al. MicroRNA-124 Reduces Pentose Phosphate Pathway and Proliferation by Targeting PRPS1 and RPIA mRNAs in Human Colorectal Cancer Cells. Gastroenterology. 2015.

[121] Boros LG, Puigjaner J, Cascante M, Lee WN, Brandes JL, Bassilian S, et al. Oxythiamine and dehydroepiandrosterone inhibit the nonoxidative synthesis of ribose and tumor cell proliferation. Cancer Res. 1997;57:4242-8.

[122] Boren J, Montoya AR, de Atauri P, Comin-Anduix B, Cortes A, Centelles JJ, et al. Metabolic control analysis aimed at the ribose synthesis pathways of tumor cells: a new strategy for antitumor drug development. Mol Biol Rep. 2002;29:7-12.

[123] Comin-Anduix B, Boren J, Martinez S, Moro C, Centelles JJ, Trebukhina R, et al. The effect of thiamine supplementation on tumour proliferation. A metabolic control analysis study. European journal of biochemistry / FEBS. 2001;268:4177-82.

[124] Vizan P, Alcarraz-Vizan G, Diaz-Moralli S, Solovjeva ON, Frederiks WM, Cascante M. Modulation of pentose phosphate pathway during cell cycle progression in human colon adenocarcinoma cell line HT29. Int J Cancer. 2009;124:2789-96.

[125] Cardozo T, Pagano M. The SCF ubiquitin ligase: insights into a molecular machine. Nat Rev Mol Cell Biol. 2004;5:739-51.

[126] Santos CR, Schulze A. Lipid metabolism in cancer. FEBS J. 2012;279:2610-23.

[127] Huang C, Freter C. Lipid metabolism, apoptosis and cancer therapy. Int J Mol Sci. 2015;16:924-49.

[128] Swinnen JV, Brusselmans K, Verhoeven G. Increased lipogenesis in cancer cells: new players, novel targets. Curr Opin Clin Nutr Metab Care. 2006;9:358-65.

[129] Icard P, Poulain L, Lincet H. Understanding the central role of citrate in the metabolism of cancer cells. Biochimica et biophysica acta. 2012;1825:111-6.

[130] Phan LM, Yeung SC, Lee MH. Cancer metabolic reprogramming: importance, main features, and potentials for precise targeted anti-cancer therapies. Cancer Biol Med. 2014;11:1-19.

[131] Menendez JA, Lupu R. Fatty acid synthase and the lipogenic phenotype in cancer pathogenesis. Nat Rev Cancer. 2007;7:763-77.

[132] Yuan HX, Xiong Y, Guan KL. Nutrient sensing, metabolism, and cell growth control. Molecular cell. 2013;49:379-87.

[133] Nicklin P, Bergman P, Zhang B, Triantafellow E, Wang H, Nyfeler B, et al. Bidirectional transport of amino acids regulates mTOR and autophagy. Cell. 2009;136:521-34.

[134] Lamb RF. Amino acid sensing mechanisms: an Achilles heel in cancer? FEBS J. 2012;279:2624-31.

[135] Liu W, Le A, Hancock C, Lane AN, Dang CV, Fan TW, et al. Reprogramming of proline and glutamine metabolism contributes to the proliferative and metabolic responses regulated by oncogenic transcription factor c-MYC. Proceedings of the National Academy of Sciences of the United States of America. 2012;109:8983-8.

[136] Tsun ZY, Possemato R. Amino acid management in cancer. Semin Cell Dev Biol. 2015.

[137] Bhutia YD, Babu E, Ramachandran S, Ganapathy V. Amino Acid transporters in cancer and their relevance to "glutamine addiction": novel targets for the design of a new class of anticancer drugs. Cancer Res. 2015;75:1782-8.

[138] Locasale JW. Serine, glycine and one-carbon units: cancer metabolism in full circle. Nat Rev Cancer. 2013;13:572-83.

[139] Tedeschi PM, Markert EK, Gounder M, Lin H, Dvorzhinski D, Dolfi SC, et al. Contribution of serine, folate and glycine metabolism to the ATP, NADPH and purine requirements of cancer cells. Cell Death Dis. 2013;4:e877.

[140] Jain M, Nilsson R, Sharma S, Madhusudhan N, Kitami T, Souza AL, et al. Metabolite profiling identifies a key role for glycine in rapid cancer cell proliferation. Science (New York, NY. 2012;336:1040-4.

[141] di Salvo ML, Contestabile R, Paiardini A, Maras B. Glycine consumption and mitochondrial serine hydroxymethyltransferase in cancer cells: the heme connection. Med Hypotheses. 2013;80:633-6.

[142] Phang JM, Liu W, Hancock CN, Fischer JW. Proline metabolism and cancer: emerging links to glutamine and collagen. Curr Opin Clin Nutr Metab Care. 2015;18:71-7.

[143] Liu W, Phang JM. Proline dehydrogenase (oxidase) in cancer. Biofactors. 2012;38:398-406.

[144] Daye D, Wellen KE. Metabolic reprogramming in cancer: unraveling the role of glutamine in tumorigenesis. Semin Cell Dev Biol. 2012;23:362-9.

[145] Wallace DC. Mitochondria and cancer. Nat Rev Cancer. 2012;12:685-98.

[146] Weinberg F, Hamanaka R, Wheaton WW, Weinberg S, Joseph J, Lopez M, et al. Mitochondrial metabolism and ROS generation are essential for Kras-mediated tumorigenicity. Proceedings of the National Academy of Sciences of the United States of America. 2010;107:8788-93.

[147] Dang CV. MYC, metabolism, cell growth, and tumorigenesis. Cold Spring Harb Perspect Med. 2013;3.

[148] Gaude E, Frezza C. Defects in mitochondrial metabolism and cancer. Cancer Metab. 2014;2:10.

[149] Acin-Perez R, Enriquez JA. The function of the respiratory supercomplexes: the plasticity model. Biochimica et biophysica acta. 2014;1837:444-50.

[150] Desideri E, Vegliante R, Ciriolo MR. Mitochondrial dysfunctions in cancer: genetic defects and oncogenic signaling impinging on TCA cycle activity. Cancer letters. 2015;356:217-23.

[151] Chen J-Q, Russo J. Dysregulation of glucose transport, glycolysis, TCA cycle and glutaminolysis by oncogenes and tumor suppressors in cancer cells. Biochimica et Biophysica Acta (BBA) - Reviews on Cancer. 2012;1826:370-84.

[152] DeBerardinis RJ, Cheng T. Q's next: the diverse functions of glutamine in metabolism, cell biology and cancer. Oncogene. 2010;29:313-24.

[153] Wise DR, Thompson CB. Glutamine addiction: a new therapeutic target in cancer. Trends Biochem Sci. 2010;35:427-33.

[154] Kim MH, Kim H. Oncogenes and tumor suppressors regulate glutamine metabolism in cancer cells. J Cancer Prev. 2013;18:221-6.

[155] Yuneva MO, Fan TW, Allen TD, Higashi RM, Ferraris DV, Tsukamoto T, et al. The metabolic profile of tumors depends on both the responsible genetic lesion and tissue type. Cell metabolism. 2012;15:157-70.

[156] Gross MI, Demo SD, Dennison JB, Chen L, Chernov-Rogan T, Goyal B, et al. Antitumor activity of the glutaminase inhibitor CB-839 in triple-negative breast cancer. Mol Cancer Ther. 2014;13:890-901.

7. References

[157] Le A, Lane AN, Hamaker M, Bose S, Gouw A, Barbi J, et al. Glucose-independent glutamine metabolism via TCA cycling for proliferation and survival in B cells. Cell metabolism. 2012;15:110-21.

[158] Thangavelu K, Chong QY, Low BC, Sivaraman J. Structural basis for the active site inhibition mechanism of human kidney-type glutaminase (KGA). Sci Rep. 2014;4:3827.

[159] Mates JM, Segura JA, Martin-Rufian M, Campos-Sandoval JA, Alonso FJ, Marquez J. Glutaminase isoenzymes as key regulators in metabolic and oxidative stress against cancer. Curr Mol Med. 2013;13:514-34.

[160] Boulahbel H, Duran RV, Gottlieb E. Prolyl hydroxylases as regulators of cell metabolism. Biochem Soc Trans. 2009;37:291-4. doi: 10.1042/BST0370291.

[161] Duran RV, Oppliger W, Robitaille AM, Heiserich L, Skendaj R, Gottlieb E, et al. Glutaminolysis activates Rag-mTORC1 signaling. Mol Cell. 2012;47:349-58.

[162] DeBerardinis RJ, Mancuso A, Daikhin E, Nissim I, Yudkoff M, Wehrli S, et al. Beyond aerobic glycolysis: transformed cells can engage in glutamine metabolism that exceeds the requirement for protein and nucleotide synthesis. Proceedings of the National Academy of Sciences of the United States of America. 2007;104:19345-50.

[163] Zu XL, Guppy M. Cancer metabolism: facts, fantasy, and fiction. Biochemical and biophysical research communications. 2004;313:459-65.

[164] Shoemaker RH. The NCI60 human tumour cell line anticancer drug screen. Nat Rev Cancer. 2006;6:813-23.

[165] Fan J, Kamphorst JJ, Mathew R, Chung MK, White E, Shlomi T, et al. Glutamine-driven oxidative phosphorylation is a major ATP source in transformed mammalian cells in both normoxia and hypoxia. Mol Syst Biol. 2013;9:712.

[166] Yang C, Sudderth J, Dang T, Bachoo RM, McDonald JG, DeBerardinis RJ. Glioblastoma cells require glutamate dehydrogenase to survive impairments of glucose metabolism or Akt signaling. Cancer Res. 2009;69:7986-93.

[167] Cheng T, Sudderth J, Yang C, Mullen AR, Jin ES, Mates JM, et al. Pyruvate carboxylase is required for glutamine-independent growth of tumor cells. Proceedings of the National Academy of Sciences of the United States of America. 2011;108:8674-9.

[168] Metallo CM, Gameiro PA, Bell EL, Mattaini KR, Yang J, Hiller K, et al. Reductive glutamine metabolism by IDH1 mediates lipogenesis under hypoxia. Nature. 2012;481:380-4.

[169] Fendt SM, Bell EL, Keibler MA, Olenchock BA, Mayers JR, Wasylenko TM, et al. Reductive glutamine metabolism is a function of the alpha-ketoglutarate to citrate ratio in cells. Nat Commun. 2013;4:2236.

[170] Mullen AR, Wheaton WW, Jin ES, Chen PH, Sullivan LB, Cheng T, et al. Reductive carboxylation supports growth in tumour cells with defective mitochondria. Nature. 2012;481:385-8.

[171] Gameiro PA, Yang J, Metelo AM, Perez-Carro R, Baker R, Wang Z, et al. In vivo HIF-mediated reductive carboxylation is regulated by citrate levels and sensitizes VHL-deficient cells to glutamine deprivation. Cell metabolism. 2013;17:372-85.

[172] Kobayashi CI, Suda T. Regulation of reactive oxygen species in stem cells and cancer stem cells. J Cell Physiol. 2012;227:421-30.

[173] Liu W, Phang JM. Proline dehydrogenase (oxidase) in cancer. Biofactors. 2012.

[174] Sauer H, Wartenberg M, Hescheler J. Reactive oxygen species as intracellular messengers during cell growth and differentiation. Cell Physiol Biochem. 2001;11:173-86.

[175] Jones DP. Radical-free biology of oxidative stress. Am J Physiol Cell Physiol. 2008;295:C849-68.

[176] Burhans WC, Heintz NH. The cell cycle is a redox cycle: linking phase-specific targets to cell fate. Free Radic Biol Med. 2009;47:1282-93.

[177] Veal EA, Day AM, Morgan BA. Hydrogen peroxide sensing and signaling. Mol Cell. 2007;26:1-14.

[178] D'Autreaux B, Toledano MB. ROS as signalling molecules: mechanisms that generate specificity in ROS homeostasis. Nat Rev Mol Cell Biol. 2007;8:813-24.

[179] Antico Arciuch VG, Elguero ME, Poderoso JJ, Carreras MC. Mitochondrial regulation of cell cycle and proliferation. Antioxid Redox Signal. 2012;16:1150-80.

[180] Tedeschi PM, Markert EK, Gounder M, Lin H, Dvorzhinski D, Dolfi SC, et al. Contribution of serine, folate and glycine metabolism to the ATP, NADPH and purine requirements of cancer cells. Cell Death and Disease. 2013;4:e877.

[181] Fan J, Ye J, Kamphorst JJ, Shlomi T, Thompson CB, Rabinowitz JD. Quantitative flux analysis reveals folate-dependent NADPH production. Nature. 2014;510:298-302.

[182] Caputo F, Vegliante R, Ghibelli L. Redox modulation of the DNA damage response. Biochemical pharmacology. 2012.

[183] Burch PM, Yuan Z, Loonen A, Heintz NH. An extracellular signal-regulated kinase 1- and 2-dependent program of chromatin trafficking of c-Fos and Fra-1 is required for cyclin D1 expression during cell cycle reentry. Molecular and cellular biology. 2004;24:4696-709.

[184] Hwang JH, Hwang IS, Liu QH, Woo ER, Lee DG. (+)-Medioresinol leads to intracellular ROS accumulation and mitochondria-mediated apoptotic cell death in Candida albicans. Biochimie. 2012;94:1784-93.

[185] Bajad SU, Lu W, Kimball EH, Yuan J, Peterson C, Rabinowitz JD. Separation and quantitation of water soluble cellular metabolites by hydrophilic interaction chromatography-tandem mass spectrometry. J Chromatogr A. 2006;1125:76-88.

[186] Burch PM, Heintz NH. Redox regulation of cell-cycle re-entry: cyclin D1 as a primary target for the mitogenic effects of reactive oxygen and nitrogen species. Antioxid Redox Signal. 2005;7:741-51.

[187] Havens CG, Ho A, Yoshioka N, Dowdy SF. Regulation of late G1/S phase transition and APC Cdh1 by reactive oxygen species. Molecular and cellular biology. 2006;26:4701-11.

[188] Sarsour EH, Kumar MG, Chaudhuri L, Kalen AL, Goswami PC. Redox control of the cell cycle in health and disease. Antioxid Redox Signal. 2009;11:2985-3011.

[189] Gartel AL, Radhakrishnan SK. Lost in transcription: p21 repression, mechanisms, and consequences. Cancer Res. 2005;65:3980-5.

[190] Borriello A, Cucciolla V, Oliva A, Zappia V, Della Ragione F. p27Kip1 metabolism: a fascinating labyrinth. Cell Cycle. 2007;6:1053-61.

[191] Fujikawa M, Katagiri T, Tugores A, Nakamura Y, Ishikawa F. ESE-3, an Ets family transcription factor, is up-regulated in cellular senescence. Cancer Sci. 2007;98:1468-75.

[192] Menon SG, Sarsour EH, Spitz DR, Higashikubo R, Sturm M, Zhang H, et al. Redox regulation of the G1 to S phase transition in the mouse embryo fibroblast cell cycle. Cancer Res. 2003;63:2109-17.

[193] Hoffman A, Spetner LM, Burke M. Ramifications of a redox switch within a normal cell: its absence in a cancer cell. Free Radic Biol Med. 2008;45:265-8.

[194] Mitra K, Wunder C, Roysam B, Lin G, Lippincott-Schwartz J. A hyperfused mitochondrial state achieved at G1-S regulates cyclin E buildup and entry into S phase. Proceedings of the National Academy of Sciences of the United States of America. 2009;106:11960-5.

[195] Laoukili J, Stahl M, Medema RH. FoxM1: at the crossroads of ageing and cancer. Biochimica et biophysica acta. 2007;1775:92-102.

[196] Nilsson I, Hoffmann I. Cell cycle regulation by the Cdc25 phosphatase family. Prog Cell Cycle Res. 2000;4:107-14.

[197] Moncada S, Higgs EA, Colombo SL. Fulfilling the metabolic requirements for cell proliferation. The Biochemical journal. 2012;446:1-7.

[198] Morrish F, Isern N, Sadilek M, Jeffrey M, Hockenbery DM. c-Myc activates multiple metabolic networks to generate substrates for cell-cycle entry. Oncogene. 2009;28:2485-91.

[199] Lee IH, Finkel T. Metabolic regulation of the cell cycle. Current Opinion in Cell Biology. 2013;25:724-9.

[200] Almeida A, Bolanos JP, Moncada S. E3 ubiquitin ligase APC/C-Cdh1 accounts for the Warburg effect by linking glycolysis to cell proliferation. Proceedings of the National Academy of Sciences of the United States of America. 2010;107:738-41.

[201] Bolanos JP, Almeida A, Moncada S. Glycolysis: a bioenergetic or a survival pathway? Trends Biochem Sci. 2010;35:145-9.

[202] Colombo SL, Palacios-Callender M, Frakich N, De Leon J, Schmitt CA, Boorn L, et al. Anaphase-promoting complex/cyclosome-Cdh1 coordinates glycolysis and glutaminolysis with transition to S phase in human T lymphocytes. Proceedings of the National Academy of Sciences of the United States of America. 2010;107:18868-73.

[203] Meyer N, Penn LZ. Reflecting on 25 years with MYC. Nat Rev Cancer. 2008;8:976-90.

[204] Gabay M, Li Y, Felsher DW. MYC activation is a hallmark of cancer initiation and maintenance. Cold Spring Harb Perspect Med. 2014;4.

[205] Patel JH, Loboda AP, Showe MK, Showe LC, McMahon SB. Analysis of genomic targets reveals complex functions of MYC. Nat Rev Cancer. 2004;4:562-8.

[206] Wahlstrom T, Arsenian Henriksson M. Impact of MYC in regulation of tumor cell metabolism. Biochimica et biophysica acta. 2015;1849:563-9.

[207] Adhikary S, Eilers M. Transcriptional regulation and transformation by Myc proteins. Nat Rev Mol Cell Biol. 2005;6:635-45.

[208] Herkert B, Eilers M. Transcriptional repression: the dark side of myc. Genes Cancer. 2010;1:580-6.

[209] Eisenman RN. Deconstructing myc. Genes Dev. 2001;15:2023-30.

[210] Dang CV, O'Donnell KA, Zeller KI, Nguyen T, Osthus RC, Li F. The c-Myc target gene network. Seminars in cancer biology. 2006;16:253-64.

[211] Osthus RC, Shim H, Kim S, Li Q, Reddy R, Mukherjee M, et al. Deregulation of glucose transporter 1 and glycolytic gene expression by c-Myc. The Journal of biological chemistry. 2000;275:21797-800.

[212] Gordan JD, Thompson CB, Simon MC. HIF and c-Myc: sibling rivals for control of cancer cell metabolism and proliferation. Cancer cell. 2007;12:108-13.

[213] Rimpi S, Nilsson JA. Metabolic enzymes regulated by the Myc oncogene are possible targets for chemotherapy or chemoprevention. Biochem Soc Trans. 2007;35:305-10.

[214] Gao P, Tchernyshyov I, Chang TC, Lee YS, Kita K, Ochi T, et al. c-Myc suppression of miR-23a/b enhances mitochondrial glutaminase expression and glutamine metabolism. Nature. 2009;458:762-5.

[215] Li F, Wang Y, Zeller KI, Potter JJ, Wonsey DR, O'Donnell KA, et al. Myc stimulates nuclearly encoded mitochondrial genes and mitochondrial biogenesis. Molecular and cellular biology. 2005;25:6225-34.

[216] Zhang H, Gao P, Fukuda R, Kumar G, Krishnamachary B, Zeller KI, et al. HIF-1 inhibits mitochondrial biogenesis and cellular respiration in VHL-deficient renal cell carcinoma by repression of C-MYC activity. Cancer cell. 2007;11:407-20.

[217] Morrish F, Giedt C, Hockenbery D. c-MYC apoptotic function is mediated by NRF-1 target genes. Genes Dev. 2003;17:240-55.

[218] Morrish F, Neretti N, Sedivy JM, Hockenbery DM. The oncogene c-Myc coordinates regulation of metabolic networks to enable rapid cell cycle entry. Cell Cycle. 2008;7:1054-66.

[219] Murphy TA, Dang CV, Young JD. Isotopically nonstationary 13C flux analysis of Myc-induced metabolic reprogramming in B-cells. Metab Eng. 2013;15:206-17.

[220] Bello-Fernandez C, Packham G, Cleveland JL. The ornithine decarboxylase gene is a transcriptional target of c-Myc. Proceedings of the National Academy of Sciences of the United States of America. 1993;90:7804-8.

[221] Liu YC, Li F, Handler J, Huang CR, Xiang Y, Neretti N, et al. Global regulation of nucleotide biosynthetic genes by c-Myc. PloS one. 2008;3:e2722.

[222] Ruiz-Perez MV, Medina MA, Urdiales JL, Keinanen TA, Sanchez-Jimenez F. Polyamine metabolism is sensitive to glycolysis inhibition in human neuroblastoma cells. The Journal of biological chemistry. 2015;290:6106-19.

[223] Celano P, Baylin SB, Casero RA, Jr. Polyamines differentially modulate the transcription of growth-associated genes in human colon carcinoma cells. The Journal of biological chemistry. 1989;264:8922-7.

[224] Vazquez A, Markert EK, Oltvai ZN. Serine biosynthesis with one carbon catabolism and the glycine cleavage system represents a novel pathway for ATP generation. PloS one. 2011;6:e25881.

[225] Vazquez A, Tedeschi PM, Bertino JR. Overexpression of the mitochondrial folate and glycine-serine pathway: a new determinant of methotrexate selectivity in tumors. Cancer Res. 2013;73:478-82.

[226] Bretones G, Delgado MD, Leon J. Myc and cell cycle control. Biochimica et biophysica acta. 2014.

[227] Schuhmacher M, Staege MS, Pajic A, Polack A, Weidle UH, Bornkamm GW, et al. Control of cell growth by c-Myc in the absence of cell division. Curr Biol. 1999;9:1255-8.

[228] Hermeking H, Rago C, Schuhmacher M, Li Q, Barrett JF, Obaya AJ, et al. Identification of CDK4 as a target of c-MYC. Proceedings of the National Academy of Sciences of the United States of America. 2000;97:2229-34.

[229] Zeller KI, Jegga AG, Aronow BJ, O'Donnell KA, Dang CV. An integrated database of genes responsive to the Myc oncogenic transcription factor: identification of direct genomic targets. Genome Biol. 2003;4:R69.

[230] Gregory MA, Hann SR. c-Myc proteolysis by the ubiquitin-proteasome pathway: stabilization of c-Myc in Burkitt's lymphoma cells. Molecular and cellular biology. 2000;20:2423-35.

[231] Sears R. Multiple Ras-dependent phosphorylation pathways regulate Myc protein stability. Genes & Development. 2000;14:2501-14.

[232] Sears R, Leone G, DeGregori J, Nevins JR. Ras enhances Myc protein stability. Mol Cell. 1999;3:169-79.

[233] Yeh E, Cunningham M, Arnold H, Chasse D, Monteith T, Ivaldi G, et al. A signalling pathway controlling c-Myc degradation that impacts oncogenic transformation of human cells. Nat Cell Biol. 2004;6:308-18.

[234] Flinn EM, Busch CM, Wright AP. myc boxes, which are conserved in myc family proteins, are signals for protein degradation via the proteasome. Molecular and cellular biology. 1998;18:5961-9.

[235] Sears RC. The life cycle of C-myc: from synthesis to degradation. Cell Cycle. 2004;3:1133-7.

[236] Gordan JD, Simon MC. Hypoxia-inducible factors: central regulators of the tumor phenotype. Curr Opin Genet Dev. 2007;17:71-7.

[237] Dang CV, Kim JW, Gao P, Yustein J. The interplay between MYC and HIF in cancer. Nat Rev Cancer. 2008;8:51-6.

[238] Guzy RD, Schumacker PT. Oxygen sensing by mitochondria at complex III: the paradox of increased reactive oxygen species during hypoxia. Exp Physiol. 2006;91:807-19.

[239] Semenza GL. Regulation of oxygen homeostasis by hypoxia-inducible factor 1. Physiology (Bethesda). 2009;24:97-106.

[240] Majmundar AJ, Wong WJ, Simon MC. Hypoxia-inducible factors and the response to hypoxic stress. Mol Cell. 2010;40:294-309.

[241] Semenza GL. Defining the role of hypoxia-inducible factor 1 in cancer biology and therapeutics. Oncogene. 2010;29:625-34.

[242] Chan DA, Sutphin PD, Denko NC, Giaccia AJ. Role of prolyl hydroxylation in oncogenically stabilized hypoxia-inducible factor-1alpha. The Journal of biological chemistry. 2002;277:40112-7.

[243] Berra E, Benizri E, Ginouves A, Volmat V, Roux D, Pouyssegur J. HIF prolyl-hydroxylase 2 is the key oxygen sensor setting low steady-state levels of HIF-1alpha in normoxia. EMBO J. 2003;22:4082-90.

[244] Hirsila M, Koivunen P, Gunzler V, Kivirikko KI, Myllyharju J. Characterization of the human prolyl 4-hydroxylases that modify the hypoxia-inducible factor. The Journal of biological chemistry. 2003;278:30772-80.

[245] Elvidge GP, Glenny L, Appelhoff RJ, Ratcliffe PJ, Ragoussis J, Gleadle JM. Concordant regulation of gene expression by hypoxia and 2-oxoglutarate-dependent dioxygenase inhibition: the role of HIF-1alpha, HIF-2alpha, and other pathways. The Journal of biological chemistry. 2006;281:15215-26.

[246] Selak MA, Armour SM, MacKenzie ED, Boulahbel H, Watson DG, Mansfield KD, et al. Succinate links TCA cycle dysfunction to oncogenesis by inhibiting HIF-alpha prolyl hydroxylase. Cancer cell. 2005;7:77-85.

[247] MacKenzie ED, Selak MA, Tennant DA, Payne LJ, Crosby S, Frederiksen CM, et al. Cell-permeating alpha-ketoglutarate derivatives alleviate pseudohypoxia in succinate dehydrogenase-deficient cells. Molecular and cellular biology. 2007;27:3282-9.

[248] Tennant DA, Frezza C, MacKenzie ED, Nguyen QD, Zheng L, Selak MA, et al. Reactivating HIF prolyl hydroxylases under hypoxia results in metabolic catastrophe and cell death. Oncogene. 2009;28:4009-21.

[249] Duran RV, MacKenzie ED, Boulahbel H, Frezza C, Heiserich L, Tardito S, et al. HIF-independent role of prolyl hydroxylases in the cellular response to amino acids. Oncogene. 2013;32:4549-56.

[250] Baek JH, Liu YV, McDonald KR, Wesley JB, Zhang H, Semenza GL. Spermidine/spermine N(1)-acetyltransferase-1 binds to hypoxia-inducible factor-1alpha (HIF-1alpha) and RACK1 and promotes ubiquitination and degradation of HIF-1alpha. The Journal of biological chemistry. 2007;282:33358-66.

[251] Hu CJ, Wang LY, Chodosh LA, Keith B, Simon MC. Differential roles of hypoxia-inducible factor 1alpha (HIF-1alpha) and HIF-2alpha in hypoxic gene regulation. Molecular and cellular biology. 2003;23:9361-74.

[252] Kim JW, Tchernyshyov I, Semenza GL, Dang CV. HIF-1-mediated expression of pyruvate dehydrogenase kinase: a metabolic switch required for cellular adaptation to hypoxia. Cell metabolism. 2006;3:177-85.

[253] Fukuda R, Zhang H, Kim JW, Shimoda L, Dang CV, Semenza GL. HIF-1 regulates cytochrome oxidase subunits to optimize efficiency of respiration in hypoxic cells. Cell. 2007;129:111-22.

[254] Pescador N, Villar D, Cifuentes D, Garcia-Rocha M, Ortiz-Barahona A, Vazquez S, et al. Hypoxia promotes glycogen accumulation through hypoxia inducible factor (HIF)-mediated induction of glycogen synthase 1. PloS one. 2010;5:e9644.

[255] Pelletier J, Bellot G, Gounon P, Lacas-Gervais S, Pouyssegur J, Mazure NM. Glycogen Synthesis is Induced in Hypoxia by the Hypoxia-Inducible Factor and Promotes Cancer Cell Survival. Front Oncol. 2012;2:18.

[256] Brahimi-Horn MC, Bellot G, Pouyssegur J. Hypoxia and energetic tumour metabolism. Curr Opin Genet Dev. 2011;21:67-72.

[257] Huang LE. Carrot and stick: HIF-alpha engages c-Myc in hypoxic adaptation. Cell Death Differ. 2008;15:672-7.

[258] Koshiji M, Kageyama Y, Pete EA, Horikawa I, Barrett JC, Huang LE. HIF-1alpha induces cell cycle arrest by functionally counteracting Myc. Embo J. 2004;23:1949-56. Epub 2004 Apr 8.

[259] Koshiji M, To KK, Hammer S, Kumamoto K, Harris AL, Modrich P, et al. HIF-1alpha induces genetic instability by transcriptionally downregulating MutSalpha expression. Mol Cell. 2005;17:793-803.

[260] Wong WJ, Qiu B, Nakazawa MS, Qing G, Simon MC. MYC degradation under low O2 tension promotes survival by evading hypoxia-induced cell death. Molecular and cellular biology. 2013;33:3494-504.

[261] Li Q, Kluz T, Sun H, Costa M. Mechanisms of c-myc degradation by nickel compounds and hypoxia. PloS one. 2009;4:e8531.

[262] Hubbi ME, Luo W, Baek JH, Semenza GL. MCM proteins are negative regulators of hypoxia-inducible factor 1. Molecular cell. 2011;42:700-12.

[263] Semenza GL. Hypoxia. Cross talk between oxygen sensing and the cell cycle machinery. Am J Physiol Cell Physiol. 2011;301:C550-2.

[264] Zwaans BM, Lombard DB. Interplay between sirtuins, MYC and hypoxia-inducible factor in cancer-associated metabolic reprogramming. Dis Model Mech. 2014;7:1023-32.

[265] Zhdanov AV, Waters AH, Golubeva AV, Papkovsky DB. Differential contribution of key metabolic substrates and cellular oxygen in HIF signalling. Exp Cell Res. 2015;330:13-28.

[266] Okuyama H, Endo H, Akashika T, Kato K, Inoue M. Downregulation of c-MYC protein levels contributes to cancer cell survival under dual deficiency of oxygen and glucose. Cancer Research. 2010;70:10213-23.

[267] Thorpe LM, Yuzugullu H, Zhao JJ. PI3K in cancer: divergent roles of isoforms, modes of activation and therapeutic targeting. Nat Rev Cancer. 2015;15:7-24.

[268] Liu P, Begley M, Michowski W, Inuzuka H, Ginzberg M, Gao D, et al. Cell-cycle-regulated activation of Akt kinase by phosphorylation at its carboxyl terminus. Nature. 2014;508:541-5.

[269] Altomare DA, Testa JR. Perturbations of the AKT signaling pathway in human cancer. Oncogene. 2005;24:7455-64.

[270] Greer EL, Brunet A. FOXO transcription factors at the interface between longevity and tumor suppression. Oncogene. 2005;24:7410-25.

[271] Wątroba M, Maślińska D, Maśliński S. Current overview of functions of FoxO proteins, with special regards to cellular homeostasis, cell response to stress, as well as inflammation and aging. Advances in Medical Sciences. 2012;57.

[272] Eijkelenboom A, Burgering BMT. FOXOs: signalling integrators for homeostasis maintenance. Nature Reviews Molecular Cell Biology. 2013;14:83-97.

[273] Yeo H, Lyssiotis CA, Zhang Y, Ying H, Asara JM, Cantley LC, et al. FoxO3 coordinates metabolic pathways to maintain redox balance in neural stem cells. The EMBO Journal. 2013;32:2589-602.

[274] Shats I, Gatza ML, Liu B, Angus SP, You L, Nevins JR. FOXO transcription factors control E2F1 transcriptional specificity and apoptotic function. Cancer Res. 2013;73:6056-67. doi: 10.1158/0008-5472.CAN-13-0453. Epub 2013 Aug 21.

[275] Nho RS, Hergert P. FoxO3a and disease progression. World J Biol Chem. 2014;5:346-54.

[276] Fu Z, Tindall DJ. FOXOs, cancer and regulation of apoptosis. Oncogene. 2008;27:2312-9.

[277] Lam EW, Brosens JJ, Gomes AR, Koo CY. Forkhead box proteins: tuning forks for transcriptional harmony. Nat Rev Cancer. 2013;13:482-95.

[278] Brunet A, Bonni A, Zigmond MJ, Lin MZ, Juo P, Hu LS, et al. Akt promotes cell survival by phosphorylating and inhibiting a Forkhead transcription factor. Cell. 1999;96:857-68.

[279] Biggs WH, 3rd, Meisenhelder J, Hunter T, Cavenee WK, Arden KC. Protein kinase B/Akt-mediated phosphorylation promotes nuclear exclusion of the winged helix transcription factor FKHR1. Proceedings of the National Academy of Sciences of the United States of America. 1999;96:7421-6.

[280] Calnan DR, Brunet A. The FoxO code. Oncogene. 2008;27:2276-88.

[281] Wang Y, Zhou Y, Graves DT. FOXO transcription factors: their clinical significance and regulation. Biomed Res Int. 2014;2014:925350.

[282] Gomes AR, Zhao F, Lam EW. Role and regulation of the forkhead transcription factors FOXO3a and FOXM1 in carcinogenesis and drug resistance. Chin J Cancer. 2013;32:365-70.

[283] Karadedou CT, Gomes AR, Chen J, Petkovic M, Ho KK, Zwolinska AK, et al. FOXO3a represses VEGF expression through FOXM1-dependent and -independent mechanisms in breast cancer. Oncogene. 2012;31:1845-58.

[284] Yung MM, Chan DW, Liu VW, Yao KM, Ngan HY. Activation of AMPK inhibits cervical cancer cell growth through AKT/FOXO3a/FOXM1 signaling cascade. BMC Cancer. 2013;13:327.

[285] Jiang L, Cao XC, Cao JG, Liu F, Quan MF, Sheng XF, et al. Casticin induces ovarian cancer cell apoptosis by repressing FoxM1 through the activation of FOXO3a. Oncol Lett. 2013;5:1605-10.

[286] Liu H, Yin J, Wang C, Gu Y, Deng M, He Z. FOXO3a mediates the cytotoxic effects of cisplatin in lung cancer cells. Anticancer Drugs. 2014;25:898-907.

[287] Kwok JM, Peck B, Monteiro LJ, Schwenen HD, Millour J, Coombes RC, et al. FOXM1 confers acquired cisplatin resistance in breast cancer cells. Mol Cancer Res. 2010;8:24-34.

[288] McGovern UB, Francis RE, Peck B, Guest SK, Wang J, Myatt SS, et al. Gefitinib (Iressa) represses FOXM1 expression via FOXO3a in breast cancer. Mol Cancer Ther. 2009;8:582-91.

[289] Fernandez de Mattos S, Villalonga P, Clardy J, Lam EWF. FOXO3a mediates the cytotoxic effects of cisplatin in colon cancer cells. Molecular Cancer Therapeutics. 2008;7:3237-46.

[290] Cortés R, Tarrado-Castellarnau M, Talancón D, López C, Link W, Ruiz D, et al. A novel cyclometallated Pt(ii)–ferrocene complex induces nuclear FOXO3a localization and apoptosis and synergizes with cisplatin to inhibit lung cancer cell proliferation. Metallomics. 2014;6:622.

[291] Fang L, Wang H, Zhou L, Yu D. FOXO3a reactivation mediates the synergistic cytotoxic effects of rapamycin and cisplatin in oral squamous cell carcinoma cells. Toxicology and Applied Pharmacology. 2011;251:8-15.

[292] Dansen TB, Burgering BM. Unravelling the tumor-suppressive functions of FOXO proteins. Trends in cell biology. 2008;18:421-9.

[293] Reagan-Shaw S. RNA Interference-Mediated Depletion of Phosphoinositide 3-Kinase Activates Forkhead Box Class O Transcription Factors and Induces Cell Cycle Arrest and Apoptosis in Breast Carcinoma Cells. Cancer Research. 2006;66:1062-9.

[294] de Keizer PL, Packer LM, Szypowska AA, Riedl-Polderman PE, van den Broek NJ, de Bruin A, et al. Activation of forkhead box O transcription factors by oncogenic BRAF promotes p21cip1-dependent senescence. Cancer Res. 2010;70:8526-36.

[295] Zhang X, Tang N, Hadden TJ, Rishi AK. Akt, FoxO and regulation of apoptosis. Biochimica et Biophysica Acta (BBA) - Molecular Cell Research. 2011;1813:1978-86.

[296] Fang L, Wang H, Zhou L, Yu D. Akt-FOXO3a signaling axis dysregulation in human oral squamous cell carcinoma and potent efficacy of FOXO3a-targeted gene therapy. Oral Oncology. 2011;47:16-21.

[297] Liang J, Slingerland JM. Multiple Roles of the PI3K/PKB (Akt) Pathway in Cell Cycle Progression. Cell Cycle. 2003;2:336-42.

[298] Bouchard C, Marquardt J, Bras A, Medema RH, Eilers M. Myc-induced proliferation and transformation require Akt-mediated phosphorylation of FoxO proteins. Embo J. 2004;23:2830-40.

[299] Ferber EC, Peck B, Delpuech O, Bell GP, East P, Schulze A. FOXO3a regulates reactive oxygen metabolism by inhibiting mitochondrial gene expression. Cell Death Differ. 2012;19:968-79.

[300] Delpuech O, Griffiths B, East P, Essafi A, Lam EW, Burgering B, et al. Induction of Mxi1-SR alpha by FOXO3a contributes to repression of Myc-dependent gene expression. Molecular and cellular biology. 2007;27:4917-30.

[301] Peck B, Ferber EC, Schulze A. Antagonism between FOXO and MYC Regulates Cellular Powerhouse. Front Oncol. 2013;3:96.

[302] Jensen KS, Binderup T, Jensen KT, Therkelsen I, Borup R, Nilsson E, et al. FoxO3A promotes metabolic adaptation to hypoxia by antagonizing Myc function. Embo J. 2011;30:4554-70.

[303] Bakker WJ, Harris IS, Mak TW. FOXO3a is activated in response to hypoxic stress and inhibits HIF1-induced apoptosis via regulation of CITED2. Mol Cell. 2007;28:941-53.

[304] Lin A, Yao J, Zhuang L, Wang D, Han J, Lam EW, et al. The FoxO-BNIP3 axis exerts a unique regulation of mTORC1 and cell survival under energy stress. Oncogene. 2014;33:3183-94.

[305] Mori S, Nada S, Kimura H, Tajima S, Takahashi Y, Kitamura A, et al. The mTOR Pathway Controls Cell Proliferation by Regulating the FoxO3a Transcription Factor via SGK1 Kinase. PloS one. 2014;9:e88891.

[306] Masui K, Tanaka K, Akhavan D, Babic I, Gini B, Matsutani T, et al. mTOR complex 2 controls glycolytic metabolism in glioblastoma through FoxO acetylation and upregulation of c-Myc. Cell metabolism. 2013;18:726-39.

[307] Laplante M, Sabatini DM. mTOR signaling in growth control and disease. Cell. 2012;149:274-93.

[308] Sabatini DM. mTOR and cancer: insights into a complex relationship. Nat Rev Cancer. 2006;6:729-34.

[309] Efeyan A, Sabatini DM. mTOR and cancer: many loops in one pathway. Curr Opin Cell Biol. 2010;22:169-76.

[310] Inoki K, Li Y, Xu T, Guan KL. Rheb GTPase is a direct target of TSC2 GAP activity and regulates mTOR signaling. Genes Dev. 2003;17:1829-34.

[311] Hay N, Sonenberg N. Upstream and downstream of mTOR. Genes Dev. 2004;18:1926-45.

[312] Laplante M, Sabatini DM. An emerging role of mTOR in lipid biosynthesis. Curr Biol. 2009;19:R1046-52.

[313] Cunningham JT, Rodgers JT, Arlow DH, Vazquez F, Mootha VK, Puigserver P. mTOR controls mitochondrial oxidative function through a YY1-PGC-1alpha transcriptional complex. Nature. 2007;450:736-40.

[314] Laplante M, Sabatini DM. Regulation of mTORC1 and its impact on gene expression at a glance. J Cell Sci. 2013;126:1713-9.

[315] Sarbassov DD, Guertin DA, Ali SM, Sabatini DM. Phosphorylation and regulation of Akt/PKB by the rictor-mTOR complex. Science (New York, NY. 2005;307:1098-101.

[316] Arsham AM, Howell JJ, Simon MC. A novel hypoxia-inducible factor-independent hypoxic response regulating mammalian target of rapamycin and its targets. The Journal of biological chemistry. 2003;278:29655-60.

[317] Brugarolas J, Lei K, Hurley RL, Manning BD, Reiling JH, Hafen E, et al. Regulation of mTOR function in response to hypoxia by REDD1 and the TSC1/TSC2 tumor suppressor complex. Genes Dev. 2004;18:2893-904.

[318] Wouters BG, Koritzinsky M. Hypoxia signalling through mTOR and the unfolded protein response in cancer. Nat Rev Cancer. 2008;8:851-64.

[319] Li Y, Wang Y, Kim E, Beemiller P, Wang CY, Swanson J, et al. Bnip3 mediates the hypoxia-induced inhibition on mammalian target of rapamycin by interacting with Rheb. The Journal of biological chemistry. 2007;282:35803-13.

[320] Ravitz MJ, Chen L, Lynch M, Schmidt EV. c-myc Repression of TSC2 contributes to control of translation initiation and Myc-induced transformation. Cancer Research. 2007;67:11209-17.

[321] Csibi A, Lee G, Yoon SO, Tong H, Ilter D, Elia I, et al. The mTORC1/S6K1 pathway regulates glutamine metabolism through the eIF4B-dependent control of c-Myc translation. Curr Biol. 2014;24:2274-80.

[322] Csibi A, Fendt SM, Li C, Poulogiannis G, Choo AY, Chapski DJ, et al. The mTORC1 pathway stimulates glutamine metabolism and cell proliferation by repressing SIRT4. Cell. 2013;153:840-54.

[323] Fan TWM, Higashi RM, Lane AN. Integrating Metabolomics and Transcriptomics for Probing Se Anticancer Mechanisms*. Drug Metabolism Reviews. 2006;38:707-32.

[324] Cascante M, Marin S. Metabolomics and fluxomics approaches. Essays Biochem. 2008;45:67-81.

[325] Borodina I, Nielsen J. From genomes to in silico cells via metabolic networks. Curr Opin Biotechnol. 2005;16:350-5.

[326] Zhang T, Zhang A, Qiu S, Yang S, Wang X. Current Trends and Innovations in Bio-Analytical Techniques of Metabolomics. Crit Rev Anal Chem. 2015:0.

[327] Cortassa S, Caceres V, Bell LN, O'Rourke B, Paolocci N, Aon MA. From metabolomics to fluxomics: a computational procedure to translate metabolite profiles into metabolic fluxes. Biophys J. 2015;108:163-72.

[328] Garcia Sanchez CE, Torres Saez RG. Comparison and analysis of objective functions in flux balance analysis. Biotechnol Prog. 2014;30:985-91.

[329] Orth JD, Thiele I, Palsson BO. What is flux balance analysis? Nat Biotechnol. 2010;28:245-8.

[330] Antoniewicz MR. Methods and advances in metabolic flux analysis: a mini-review. J Ind Microbiol Biotechnol. 2015;42:317-25.

[331] Antoniewicz MR. 13C metabolic flux analysis: optimal design of isotopic labeling experiments. Curr Opin Biotechnol. 2013;24:1116-21.

[332] Walther JL, Metallo CM, Zhang J, Stephanopoulos G. Optimization of 13C isotopic tracers for metabolic flux analysis in mammalian cells. Metab Eng. 2012;14:162-71.

[333] Paul Lee WN, Wahjudi PN, Xu J, Go VL. Tracer-based metabolomics: concepts and practices. Clin Biochem. 2010;43:1269-77.

[334] Metallo CM, Walther JL, Stephanopoulos G. Evaluation of 13C isotopic tracers for metabolic flux analysis in mammalian cells. J Biotechnol. 2009;144:167-74.

[335] Ahn WS, Antoniewicz MR. Parallel labeling experiments with [1,2-(13)C]glucose and [U-(13)C]glutamine provide new insights into CHO cell metabolism. Metab Eng. 2013;15:34-47.

[336] Crown SB, Antoniewicz MR. Parallel labeling experiments and metabolic flux analysis: Past, present and future methodologies. Metab Eng. 2013;16:21-32.

[337] Antoniewicz MR. Parallel labeling experiments for pathway elucidation and C metabolic flux analysis. Curr Opin Biotechnol. 2015;36:91-7.

[338] Ramos-Montoya A, Lee W-NP, Bassilian S, Lim S, Trebukhina RV, Kazhyna MV, et al. Pentose phosphate cycle oxidative and non-oxidative balance: A new vulnerable target for overcoming drug resistance in cancer. Int J Cancer. 2006;119:2733-41.

[339] Marin S, Lee WN, Bassilian S, Lim S, Boros LG, Centelles JJ, et al. Dynamic profiling of the glucose metabolic network in fasted rat hepatocytes using [1,2-13C2]glucose. The Biochemical journal. 2004;381:287-94.

[340] Davies TG, Bentley J, Arris CE, Boyle FT, Curtin NJ, Endicott JA, et al. Structure-based design of a potent purine-based cyclin-dependent kinase inhibitor. Nat Struct Biol. 2002;9:745-9.

[341] Collins I, Garrett MD. Targeting the cell division cycle in cancer: CDK and cell cycle checkpoint kinase inhibitors. Curr Opin Pharmacol. 2005;5:366-73.

[342] Lapenna S, Giordano A. Cell cycle kinases as therapeutic targets for cancer. Nat Rev Drug Discov. 2009;8:547-66.

[343] Cicenas J, Valius M. The CDK inhibitors in cancer research and therapy. J Cancer Res Clin Oncol. 2011;137:1409-18.

[344] Meijer L, Borgne A, Mulner O, Chong JP, Blow JJ, Inagaki N, et al. Biochemical and cellular effects of roscovitine, a potent and selective inhibitor of the cyclin-dependent kinases cdc2, cdk2 and cdk5. European journal of biochemistry / FEBS. 1997;243:527-36.

[345] Sedlacek HH. Mechanisms of action of flavopiridol. Crit Rev Oncol Hematol. 2001;38:139-70.

[346] Alessi F, Quarta S, Savio M, Riva F, Rossi L, Stivala LA, et al. The cyclin-dependent kinase inhibitors olomoucine and roscovitine arrest human fibroblasts in G1 phase by specific inhibition of CDK2 kinase activity. Exp Cell Res. 1998;245:8-18.

[347] McClue SJ, Stuart I. Metabolism of the trisubstituted purine cyclin-dependent kinase inhibitor seliciclib (R-roscovitine) in vitro and in vivo. Drug Metab Dispos. 2008;36:561-70.

[348] Siemeister G, Luecking U, Wagner C, Detjen K, Mc Coy C, Bosslet K. Molecular and pharmacodynamic characteristics of the novel multi-target tumor growth inhibitor ZK 304709. Biomed Pharmacother. 2006;60:269-72.

[349] Lin TS, Ruppert AS, Johnson AJ, Fischer B, Heerema NA, Andritsos LA, et al. Phase II study of flavopiridol in relapsed chronic lymphocytic leukemia demonstrating high response rates in genetically high-risk disease. J Clin Oncol. 2009;27:6012-8.

[350] Luke JJ, D'Adamo DR, Dickson MA, Keohan ML, Carvajal RD, Maki RG, et al. The cyclin-dependent kinase inhibitor flavopiridol potentiates doxorubicin efficacy in advanced sarcomas: preclinical investigations and results of a phase I dose-escalation clinical trial. Clin Cancer Res. 2012;18:2638-47.

[351] Bible KC, Peethambaram PP, Oberg AL, Maples W, Groteluschen DL, Boente M, et al. A phase 2 trial of flavopiridol (Alvocidib) and cisplatin in platin-resistant ovarian and primary peritoneal carcinoma: MC0261. Gynecol Oncol. 2012;127:55-62.

[352] Garrofe-Ochoa X, Cosialls AM, Ribas J, Gil J, Boix J. Transcriptional modulation of apoptosis regulators by roscovitine and related compounds. Apoptosis. 2011;16:660-70.

[353] Le Tourneau C, Faivre S, Laurence V, Delbaldo C, Vera K, Girre V, et al. Phase I evaluation of seliciclib (R-roscovitine), a novel oral cyclin-dependent kinase inhibitor, in patients with advanced malignancies. Eur J Cancer. 2010;46:3243-50.

[354] Shafiq MI, Steinbrecher T, Schmid R. Fascaplysin as a specific inhibitor for CDK4: insights from molecular modelling. PloS one. 2012;7:e42612.

[355] Johnson N, Bentley J, Wang LZ, Newell DR, Robson CN, Shapiro GI, et al. Pre-clinical evaluation of cyclin-dependent kinase 2 and 1 inhibition in anti-estrogen-sensitive and resistant breast cancer cells. Br J Cancer. 2010;102:342-50.

[356] Johnson AJ, Yeh YY, Smith LL, Wagner AJ, Hessler J, Gupta S, et al. The novel cyclin-dependent kinase inhibitor dinaciclib (SCH727965) promotes apoptosis and abrogates microenvironmental cytokine protection in chronic lymphocytic leukemia cells. Leukemia. 2012;26:2554-7.

[357] Shirsath NP, Manohar SM, Joshi KS. P276-00, a cyclin-dependent kinase inhibitor, modulates cell cycle and induces apoptosis in both in vitro and in vivo mantle cell lymphoma cell lines. Mol Cancer. 2012;11:77.

[358] Graf F, Wuest F, Pietzsch J. Cyclin-Dependent Kinases (Cdk) as Targets for Cancer Therapy and Imaging, Advances in Cancer Therapy. In: (Ed.) HG-M, editor. Advances in Cancer Therapy. 1st ed: InTech; 2011. p. 25.

[359] Lincet H, Poulain L, Remy JS, Deslandes E, Duigou F, Gauduchon P, et al. The p21(cip1/waf1) cyclin-dependent kinase inhibitor enhances the cytotoxic effect of cisplatin in human ovarian carcinoma cells. Cancer letters. 2000;161:17-26.

[360] Chopin V, Toillon RA, Jouy N, Le Bourhis X. P21(WAF1/CIP1) is dispensable for G1 arrest, but indispensable for apoptosis induced by sodium butyrate in MCF-7 breast cancer cells. Oncogene. 2004;23:21-9.

[361] Kang KH, Kim WH, Choi KH. p21 promotes ceramide-induced apoptosis and antagonizes the antideath effect of Bcl-2 in human hepatocarcinoma cells. Exp Cell Res. 1999;253:403-12.

[362] Kraljevic Pavelic S, Cacev T, Kralj M. A dual role of p21waf1/cip1 gene in apoptosis of HEp-2 treated with cisplatin or methotrexate. Cancer Gene Ther. 2008;15:576-90.

[363] Swords R, Mahalingam D, O'Dwyer M, Santocanale C, Kelly K, Carew J, et al. Cdc7 kinase - a new target for drug development. Eur J Cancer. 2010;46:33-40.

7. References

[364] Montagnoli A, Moll J, Colotta F. Targeting cell division cycle 7 kinase: a new approach for cancer therapy. Clin Cancer Res. 2010;16:4503-8.

[365] Rivest P, Renaud M, Sanderson JT. Proliferative and androgenic effects of indirubin derivatives in LNCaP human prostate cancer cells at sub-apoptotic concentrations. Chem Biol Interact. 2011;189:177-85.

[366] Heath EI, Bible K, Martell RE, Adelman DC, Lorusso PM. A phase 1 study of SNS-032 (formerly BMS-387032), a potent inhibitor of cyclin-dependent kinases 2, 7 and 9 administered as a single oral dose and weekly infusion in patients with metastatic refractory solid tumors. Invest New Drugs. 2008;26:59-65.

[367] Tong WG, Chen R, Plunkett W, Siegel D, Sinha R, Harvey RD, et al. Phase I and pharmacologic study of SNS-032, a potent and selective Cdk2, 7, and 9 inhibitor, in patients with advanced chronic lymphocytic leukemia and multiple myeloma. J Clin Oncol. 2010;28:3015-22.

[368] Mahadevan D, Plummer R, Squires MS, Rensvold D, Kurtin S, Pretzinger C, et al. A phase I pharmacokinetic and pharmacodynamic study of AT7519, a cyclin-dependent kinase inhibitor in patients with refractory solid tumors. Ann Oncol. 2011;22:2137-43.

[369] Zhong W, Lalovic B, Zhan J. Characterization of in vitro and in vivo metabolism of AG-024322, a novel cyclin-dependent kinase (CDK). Health. 2009;1:249-62.

[370] Berkofsky-Fessler W, Nguyen TQ, Delmar P, Molnos J, Kanwal C, DePinto W, et al. Preclinical biomarkers for a cyclin-dependent kinase inhibitor translate to candidate pharmacodynamic biomarkers in phase I patients. Mol Cancer Ther. 2009;8:2517-25.

[371] DePinto W, Chu XJ, Yin X, Smith M, Packman K, Goelzer P, et al. In vitro and in vivo activity of R547: a potent and selective cyclin-dependent kinase inhibitor currently in phase I clinical trials. Mol Cancer Ther. 2006;5:2644-58.

[372] Graham JS, Plummer R, McCoy C, Kowal K, Wiesinger H, Detjen K, et al. Open-label, non-randomised, inter-individual dose escalation of ZK 304709 with the evaluation of safety, tolerability, pharmacokinetics, oral bioavailability and orientating efficacy after daily administration in patients with advanced cancer (7 d treatment and 14 d recovery). Eur J Cancer. 2008;44:2162-8.

[373] Scott EN, Thomas AL, Molife LR, Ahmed S, Blagden S, Fong PC, et al. A phase I dose escalation study of the pharmacokinetics and tolerability of ZK 304709, an oral multi-targeted growth inhibitor (MTGI), in patients with advanced solid tumours. Cancer Chemother Pharmacol. 2009;64:425-9.

[374] Siemeister G, Lucking U, Wengner AM, Lienau P, Steinke W, Schatz C, et al. BAY 1000394, a novel cyclin-dependent kinase inhibitor, with potent antitumor activity in mono- and in combination treatment upon oral application. Mol Cancer Ther. 2012;11:2265-73.

[375] Ryu CK, Kang HY, Lee SK, Nam KA, Hong CY, Ko WG, et al. 5-Arylamino-2-methyl-4,7-dioxobenzothiazoles as inhibitors of cyclin-dependent kinase 4 and cytotoxic agents. Bioorg Med Chem Lett. 2000;10:461-4.

[376] Hikita T, Oneyama C, Okada M. Purvalanol A, a CDK inhibitor, effectively suppresses Src-mediated transformation by inhibiting both CDKs and c-Src. Genes Cells. 2010;15:1051-62.

[377] Kazmierczak A, Czapski GA, Adamczyk A, Gajkowska B, Strosznajder JB. A novel mechanism of non-Abeta component of Alzheimer's disease amyloid (NAC) neurotoxicity. Interplay between p53 protein and cyclin-dependent kinase 5 (Cdk5). Neurochem Int. 2011;58:206-14.

[378] Uchiyama H, Sowa Y, Wakada M, Yogosawa M, Nakanishi R, Horinaka M, et al. Cyclin-dependent kinase inhibitor SU9516 enhances sensitivity to methotrexate in human T-cell leukemia Jurkat cells. Cancer Sci. 2010;101:728-34.

[379] Schwartz GK, LoRusso PM, Dickson MA, Randolph SS, Shaik MN, Wilner KD, et al. Phase I study of PD 0332991, a cyclin-dependent kinase inhibitor, administered in 3-week cycles (Schedule 2/1). Br J Cancer. 2011;104:1862-8.

[380] Flaherty KT, Lorusso PM, Demichele A, Abramson VG, Courtney R, Randolph SS, et al. Phase I, dose-escalation trial of the oral cyclin-dependent kinase 4/6 inhibitor PD 0332991, administered using a 21-day schedule in patients with advanced cancer. Clin Cancer Res. 2012;18:568-76.

[381] Beaver JA, Amiri-Kordestani L, Charlab R, Chen W, Palmby T, Tilley A, et al. FDA Approval: Palbociclib for the Treatment of Postmenopausal Patients with Estrogen Receptor-Positive, HER2-Negative Metastatic Breast Cancer. Clin Cancer Res. 2015.

[382] Zhang D, Mita M, Shapiro GI, Poon J, Small K, Tzontcheva A, et al. Effect of aprepitant on the pharmacokinetics of the cyclin-dependent kinase inhibitor dinaciclib in patients with advanced malignancies. Cancer Chemother Pharmacol. 2012;70:891-8.

[383] Gorlick R, Kolb EA, Houghton PJ, Morton CL, Neale G, Keir ST, et al. Initial testing (stage 1) of the cyclin dependent kinase inhibitor SCH 727965 (dinaciclib) by the pediatric preclinical testing program. Pediatr Blood Cancer. 2012;59:1266-74.

[384] Boss DS, Schwartz GK, Middleton MR, Amakye DD, Swaisland H, Midgley RS, et al. Safety, tolerability, pharmacokinetics and pharmacodynamics of the oral cyclin-dependent kinase inhibitor AZD5438 when administered at intermittent and continuous dosing schedules in patients with advanced solid tumours. Ann Oncol. 2010;21:884-94.

[385] Caporali S, Alvino E, Levati L, Esposito AI, Ciomei M, Brasca MG, et al. Down-regulation of the PTTG1 proto-oncogene contributes to the melanoma suppressive effects of the cyclin-dependent kinase inhibitor PHA-848125. Biochem Pharmacol. 2012;84:598-611.

[386] Albanese C, Alzani R, Amboldi N, Avanzi N, Ballinari D, Brasca MG, et al. Dual targeting of CDK and tropomyosin receptor kinase families by the oral inhibitor PHA-848125, an agent with broad-spectrum antitumor efficacy. Mol Cancer Ther. 2010;9:2243-54.

[387] Brasca MG, Amboldi N, Ballinari D, Cameron A, Casale E, Cervi G, et al. Identification of N,1,4,4-tetramethyl-8-{[4-(4-methylpiperazin-1-yl)phenyl]amino}-4,5-dihydro-1H-py razolo[4,3-h]quinazoline-3-carboxamide (PHA-848125), a potent, orally available cyclin dependent kinase inhibitor. J Med Chem. 2009;52:5152-63.

[388] Grossman SA, Ye X, Peereboom D, Rosenfeld MR, Mikkelsen T, Supko JG, et al. Phase I study of terameprocol in patients with recurrent high-grade glioma. Neuro Oncol. 2012;14:511-7.

[389] Khanna N, Dalby R, Connor A, Church A, Stern J, Frazer N. Phase I clinical trial of repeat dose terameprocol vaginal ointment in healthy female volunteers. Sex Transm Dis. 2008;35:577-82.

[390] Terret C, Zanetta S, Roche H, Schellens JH, Faber MN, Wanders J, et al. Phase I clinical and pharmacokinetic study of E7070, a novel sulfonamide given as a 5-day continuous infusion repeated every 3 weeks in patients with solid tumours. A study by the EORTC Early Clinical Study Group (ECSG). Eur J Cancer. 2003;39:1097-104.

[391] Talbot DC, von Pawel J, Cattell E, Yule SM, Johnston C, Zandvliet AS, et al. A randomized phase II pharmacokinetic and pharmacodynamic study of indisulam as second-line therapy in patients with advanced non-small cell lung cancer. Clin Cancer Res. 2007;13:1816-22.

[392] Jani JP, Arcari J, Bernardo V, Bhattacharya SK, Briere D, Cohen BD, et al. PF-03814735, an orally bioavailable small molecule aurora kinase inhibitor for cancer therapy. Mol Cancer Ther. 2010;9:883-94.

[393] Meulenbeld HJ, Mathijssen RH, Verweij J, de Wit R, de Jonge MJ. Danusertib, an aurora kinase inhibitor. Expert Opin Investig Drugs. 2012;21:383-93.

[394] Arkenau HT, Plummer R, Molife LR, Olmos D, Yap TA, Squires M, et al. A phase I dose escalation study of AT9283, a small molecule inhibitor of aurora kinases, in patients with advanced solid malignancies. Ann Oncol. 2012;23:1307-13.

[395] Matulonis UA, Lee J, Lasonde B, Tew WP, Yehwalashet A, Matei D, et al. ENMD-2076, an oral inhibitor of angiogenic and proliferation kinases, has activity in recurrent, platinum resistant ovarian cancer. Eur J Cancer. 2012.

7. References

[396] How J, Yee K. ENMD-2076 for hematological malignancies. Expert Opin Investig Drugs. 2012;21:717-32.

[397] Lowenberg B, Muus P, Ossenkoppele G, Rousselot P, Cahn JY, Ifrah N, et al. Phase 1/2 study to assess the safety, efficacy, and pharmacokinetics of barasertib (AZD1152) in patients with advanced acute myeloid leukemia. Blood. 2011;118:6030-6.

[398] Ma WW, Messersmith WA, Dy GK, Weekes CD, Whitworth A, Ren C, et al. Phase I study of Rigosertib, an inhibitor of the phosphatidylinositol 3-kinase and Polo-like kinase 1 pathways, combined with gemcitabine in patients with solid tumors and pancreatic cancer. Clin Cancer Res. 2012;18:2048-55.

[399] Hikichi Y, Honda K, Hikami K, Miyashita H, Kaieda I, Murai S, et al. TAK-960, a novel, orally available, selective inhibitor of polo-like kinase 1, shows broad-spectrum preclinical antitumor activity in multiple dosing regimens. Mol Cancer Ther. 2012;11:700-9.

[400] Frost A, Mross K, Steinbild S, Hedbom S, Unger C, Kaiser R, et al. Phase i study of the Plk1 inhibitor BI 2536 administered intravenously on three consecutive days in advanced solid tumours. Curr Oncol. 2012;19:e28-35.

[401] Olmos D, Barker D, Sharma R, Brunetto AT, Yap TA, Taegtmeyer AB, et al. Phase I study of GSK461364, a specific and competitive Polo-like kinase 1 inhibitor, in patients with advanced solid malignancies. Clin Cancer Res. 2011;17:3420-30.

[402] Jordan MA, Wilson L. Microtubules as a target for anticancer drugs. Nat Rev Cancer. 2004;4:253-65.

[403] Ma Z, Yao G, Zhou B, Fan Y, Gao S, Feng X. The Chk1 inhibitor AZD7762 sensitises p53 mutant breast cancer cells to radiation in vitro and in vivo. Mol Med Report. 2012;6:897-903.

[404] Riesterer O, Matsumoto F, Wang L, Pickett J, Molkentine D, Giri U, et al. A novel Chk inhibitor, XL-844, increases human cancer cell radiosensitivity through promotion of mitotic catastrophe. Invest New Drugs. 2011;29:514-22.

[405] Ludwig H, Khayat D, Giaccone G, Facon T. Proteasome inhibition and its clinical prospects in the treatment of hematologic and solid malignancies. Cancer. 2005;104:1794-807.

[406] Lansdell TA, Hurchla MA, Xiang J, Hovde S, Weilbaecher KN, Henry RW, et al. Non-competitive modulation of the proteasome by imidazoline scaffolds overcome bortezomib resistant and delay MM tumor growth in vivo. ACS Chem Biol. 2012.

[407] Vassilev LT, Vu BT, Graves B, Carvajal D, Podlaski F, Filipovic Z, et al. In vivo activation of the p53 pathway by small-molecule antagonists of MDM2. Science (New York, NY. 2004;303:844-8.

[408] Shangary S, Wang S. Small-molecule inhibitors of the MDM2-p53 protein-protein interaction to reactivate p53 function: a novel approach for cancer therapy. Annu Rev Pharmacol Toxicol. 2009;49:223-41.

[409] Zeng X, Sigoillot F, Gaur S, Choi S, Pfaff KL, Oh DC, et al. Pharmacologic inhibition of the anaphase-promoting complex induces a spindle checkpoint-dependent mitotic arrest in the absence of spindle damage. Cancer cell. 2010;18:382-95.

[410] Bowles DW, Diamond JR, Lam ET, Weekes CD, Astling DP, Anderson RT, et al. Phase I study of oral rigosertib (ON 01910.Na), a dual inhibitor of the PI3K and Plk1 pathways, in adult patients with advanced solid malignancies. Clin Cancer Res. 2014;20:1656-65.

[411] Li Y, Sun X, LaMont JT, Pardee AB, Li CJ. Selective killing of cancer cells by beta - lapachone: direct checkpoint activation as a strategy against cancer. Proceedings of the National Academy of Sciences of the United States of America. 2003;100:2674-8.

[412] Park EJ, Choi KS, Kwon TK. beta-Lapachone-induced reactive oxygen species (ROS) generation mediates autophagic cell death in glioma U87 MG cells. Chem Biol Interact. 2011;189:37-44.

[413] Huang HC, Shi J, Orth JD, Mitchison TJ. Evidence that mitotic exit is a better cancer therapeutic target than spindle assembly. Cancer cell. 2009;16:347-58.

272

[414] Manchado E, Guillamot M, de Carcer G, Eguren M, Trickey M, Garcia-Higuera I, et al. Targeting mitotic exit leads to tumor regression in vivo: Modulation by Cdk1, Mastl, and the PP2A/B55alpha,delta phosphatase. Cancer cell. 2010;18:641-54.

[415] Ling YH, Liebes L, Jiang JD, Holland JF, Elliott PJ, Adams J, et al. Mechanisms of proteasome inhibitor PS-341-induced G(2)-M-phase arrest and apoptosis in human non-small cell lung cancer cell lines. Clin Cancer Res. 2003;9:1145-54.

[416] Warburg O, Posener K, Negelein E. Über den Stoffwechsel der Carcinomzelle. Biochem Z. 1924;152:309–44.

[417] Warburg O, Wind F, Negelein E. The Metabolism of Tumors in the Body. The Journal of general physiology. 1927;8:519-30.

[418] Zhao Y, Butler EB, Tan M. Targeting cellular metabolism to improve cancer therapeutics. Cell Death Dis. 2013;4:e532.

[419] Farber S, Diamond LK. Temporary remissions in acute leukemia in children produced by folic acid antagonist, 4-aminopteroyl-glutamic acid. N Engl J Med. 1948;238:787-93.

[420] Heidelberger C, Chaudhuri NK, Danneberg P, Mooren D, Griesbach L, Duschinsky R, et al. Fluorinated pyrimidines, a new class of tumour-inhibitory compounds. Nature. 1957;179:663-6.

[421] Sun Y, Zhao X, Zhou Y, Hu Y. miR-124, miR-137 and miR-340 regulate colorectal cancer growth via inhibition of the Warburg effect. Oncol Rep. 2012;28:1346-52.

[422] Zhou CF, Li XB, Sun H, Zhang B, Han YS, Jiang Y, et al. Pyruvate kinase type M2 is upregulated in colorectal cancer and promotes proliferation and migration of colon cancer cells. IUBMB Life. 2012;64:775-82.

[423] Chaneton B, Gottlieb E. Rocking cell metabolism: revised functions of the key glycolytic regulator PKM2 in cancer. Trends Biochem Sci. 2012;37:309-16.

[424] Scatena R, Bottoni P, Pontoglio A, Mastrototaro L, Giardina B. Glycolytic enzyme inhibitors in cancer treatment. Expert Opin Investig Drugs. 2008;17:1533-45.

[425] Pelicano H, Martin DS, Xu RH, Huang P. Glycolysis inhibition for anticancer treatment. Oncogene. 2006;25:4633-46.

[426] Deepa PR, Vandhana S, Jayanthi U, Krishnakumar S. Therapeutic and toxicologic evaluation of anti-lipogenic agents in cancer cells compared with non-neoplastic cells. Basic Clin Pharmacol Toxicol. 2012;110:494-503.

[427] Hatzivassiliou G, Zhao F, Bauer DE, Andreadis C, Shaw AN, Dhanak D, et al. ATP citrate lyase inhibition can suppress tumor cell growth. Cancer Cell. 2005;8:311-21.

[428] Zaidi N, Swinnen JV, Smans K. ATP-citrate lyase: a key player in cancer metabolism. Cancer Res. 2012;72:3709-14.

[429] Xiang X, Saha AK, Wen R, Ruderman NB, Luo Z. AMP-activated protein kinase activators can inhibit the growth of prostate cancer cells by multiple mechanisms. Biochemical and biophysical research communications. 2004;321:161-7.

[430] Swinnen JV, Beckers A, Brusselmans K, Organe S, Segers J, Timmermans L, et al. Mimicry of a cellular low energy status blocks tumor cell anabolism and suppresses the malignant phenotype. Cancer Res. 2005;65:2441-8.

[431] Rattan R, Giri S, Singh AK, Singh I. 5-Aminoimidazole-4-carboxamide-1-beta-D-ribofuranoside inhibits cancer cell proliferation in vitro and in vivo via AMP-activated protein kinase. The Journal of biological chemistry. 2005;280:39582-93.

[432] Van Den Neste E, Van den Berghe G, Bontemps F. AICA-riboside (acadesine), an activator of AMP-activated protein kinase with potential for application in hematologic malignancies. Expert Opin Investig Drugs. 2010;19:571-8.

[433] Rais B, Comin B, Puigjaner J, Brandes JL, Creppy E, Saboureau D, et al. Oxythiamine and dehydroepiandrosterone induce a G1 phase cycle arrest in Ehrlich's tumor cells through inhibition of the pentose cycle. FEBS Lett. 1999;456:113-8.

[434] Papandreou I, Goliasova T, Denko NC. Anticancer drugs that target metabolism: Is dichloroacetate the new paradigm? Int J Cancer. 2011;128:1001-8.

[435] Michelakis ED, Sutendra G, Dromparis P, Webster L, Haromy A, Niven E, et al. Metabolic modulation of glioblastoma with dichloroacetate. Sci Transl Med. 2010;2:31ra4.

[436] Dunbar EM, Coats BS, Shroads AL, Langaee T, Lew A, Forder JR, et al. Phase 1 trial of dichloroacetate (DCA) in adults with recurrent malignant brain tumors. Invest New Drugs. 2014;32:452-64.

[437] Ishiguro T, Ishiguro M, Ishiguro R, Iwai S. Cotreatment with dichloroacetate and omeprazole exhibits a synergistic antiproliferative effect on malignant tumors. Oncol Lett. 2012;3:726-8.

[438] Wang JB, Erickson JW, Fuji R, Ramachandran S, Gao P, Dinavahi R, et al. Targeting mitochondrial glutaminase activity inhibits oncogenic transformation. Cancer cell. 2010;18:207-19.

[439] Xiang Y, Stine ZE, Xia J, Lu Y, O'Connor RS, Altman BJ, et al. Targeted inhibition of tumor-specific glutaminase diminishes cell-autonomous tumorigenesis. The Journal of clinical investigation. 2015;125:2293-306.

[440] Olver IN, Green M, Millward MJ, Bishop JF. Phase II study of acivicin in patients with recurrent high grade astrocytoma. J Clin Neurosci. 1998;5:46-8.

[441] Seltzer MJ, Bennett BD, Joshi AD, Gao P, Thomas AG, Ferraris DV, et al. Inhibition of glutaminase preferentially slows growth of glioma cells with mutant IDH1. Cancer Res. 2010;70:8981-7.

[442] Jacque N, Ronchetti AM, Larrue C, Meunier G, Birsen R, Willems L, et al. Targeting glutaminolysis has antileukemic activity in acute myeloid leukemia and synergizes with BCL-2 inhibition. Blood. 2015;126:1346-56.

[443] Li B, Simon MC. Molecular Pathways: Targeting MYC-induced metabolic reprogramming and oncogenic stress in cancer. Clin Cancer Res. 2013;19:5835-41.

[444] Goga A, Yang D, Tward AD, Morgan DO, Bishop JM. Inhibition of CDK1 as a potential therapy for tumors over-expressing MYC. Nat Med. 2007;13:820-7.

[445] Yang D, Liu H, Goga A, Kim S, Yuneva M, Bishop JM. Therapeutic potential of a synthetic lethal interaction between the MYC proto-oncogene and inhibition of aurora-B kinase. Proceedings of the National Academy of Sciences of the United States of America. 2010;107:13836-41.

[446] Ganther HE. Selenium metabolism, selenoproteins and mechanisms of cancer prevention: complexities with thioredoxin reductase. Carcinogenesis. 1999;20:1657-66.

[447] Schrauzer GN. Selenium and selenium-antagonistic elements in nutritional cancer prevention. Critical reviews in biotechnology. 2009;29:10-7.

[448] Muecke R, Schomburg L, Buentzel J, Kisters K, Micke O. Selenium or No Selenium- That Is the Question in Tumor Patients: A New Controversy. Integrative Cancer Therapies. 2010;9:136-41.

[449] An JJ, Shi KJ, Wei W, Hua FY, Ci YL, Jiang Q, et al. The ROS/JNK/ATF2 pathway mediates selenite-induced leukemia NB4 cell cycle arrest and apoptosis in vitro and in vivo. Cell Death and Disease. 2013;4:e973.

[450] Park SH. Induction of apoptosis and autophagy by sodium selenite in A549 human lung carcinoma cells through generation of reactive oxygen species. Toxicology Letters. 2012;212:252-61.

[451] Jiang C, Wang Z, Ganther H, Lü J. Distinct effects of methylseleninic acid versus selenite on apoptosis, cell cycle, and protein kinase pathways in DU145 human prostate cancer cells. Molecular Cancer Therapeutics. 2002;1:1059-66.

[452] Li GX, Lee HJ, Wang Z, Hu H, Liao JD, Watts JC, et al. Superior in vivo inhibitory efficacy of methylseleninic acid against human prostate cancer over selenomethionine or selenite. Carcinogenesis. 2008;29:1005-12.

[453] Patrick L. Selenium biochemistry and cancer: a review of the literature. Altern Med Rev. 2004;9:239-58.

[454] Chen YC, Prabhu KS, Das A, Mastro AM. Dietary selenium supplementation modifies breast tumor growth and metastasis. Int J Cancer. 2013;133:2054-64.

[455] Sharma AK, Amin S. Post SELECT: selenium on trial. Future Med Chem. 2013;5:163-74.

[456] Lippman SM, Klein EA, Goodman PJ, Lucia MS, Thompson IM, Ford LG, et al. Effect of selenium and vitamin E on risk of prostate cancer and other cancers: the Selenium and Vitamin E Cancer Prevention Trial (SELECT). JAMA. 2009;301:39-51.

[457] Fan TW, Higashi RM, Lane AN. Integrating metabolomics and transcriptomics for probing SE anticancer mechanisms. Drug Metab Rev. 2006;38:707-32.

[458] Robey RB, Hay N. Is Akt the "Warburg kinase"?-Akt-energy metabolism interactions and oncogenesis. Seminars in cancer biology. 2009;19:25-31.

[459] Wang Z, Jiang C, Ganther H, Lu J. Antimitogenic and proapoptotic activities of methylseleninic acid in vascular endothelial cells and associated effects on PI3K-AKT, ERK, JNK and p38 MAPK signaling. Cancer Res. 2001;61:7171-8.

[460] Wu Y. Delineating the mechanism by which selenium deactivates Akt in prostate cancer cells. Molecular Cancer Therapeutics. 2006;5:246-52.

[461] Hu H, Jiang C, Li G, Lu J. PKB/AKT and ERK regulation of caspase-mediated apoptosis by methylseleninic acid in LNCaP prostate cancer cells. Carcinogenesis. 2005;26:1374-81.

[462] Narang A, Desai D. Anticancer Drug Development. In: Lu Y, Mahato RI, editors. Pharmaceutical Perspectives of Cancer Therapeutics: Springer US; 2009. p. 49-92.

[463] Li F, Zhao C, Wang L. Molecular-targeted agents combination therapy for cancer: developments and potentials. Int J Cancer. 2014;134:1257-69.

[464] Bild AH, Yao G, Chang JT, Wang Q, Potti A, Chasse D, et al. Oncogenic pathway signatures in human cancers as a guide to targeted therapies. Nature. 2006;439:353-7.

[465] Mosmann T. Rapid colorimetric assay for cellular growth and survival: application to proliferation and cytotoxicity assays. J Immunol Methods. 1983;65:55-63.

[466] Stein G, Stein J, Lian J, Last T, Owen T, McCabe L. Synchronization of normal diploid and transformed mammalian cells. Cell biology: a laboratory handbook. 1994;1:282-7.

[467] Tice RR, Agurell E, Anderson D, Burlinson B, Hartmann A, Kobayashi H, et al. Single cell gel/comet assay: guidelines for in vitro and in vivo genetic toxicology testing. Environ Mol Mutagen. 2000;35:206-21.

[468] Zanella F, Rosado A, Garcia B, Carnero A, Link W. Chemical genetic analysis of FOXO nuclear-cytoplasmic shuttling by using image-based cell screening. Chembiochem. 2008;9:2229-37.

[469] Rosado A, Zanella F, Garcia B, Carnero A, Link W. A dual-color fluorescence-based platform to identify selective inhibitors of Akt signaling. PloS one. 2008;3:e1823.

[470] Berns K, Hijmans EM, Mullenders J, Brummelkamp TR, Velds A, Heimerikx M, et al. A large-scale RNAi screen in human cells identifies new components of the p53 pathway. Nature. 2004;428:431-7.

[471] Diaz-Moralli S, Tarrado-Castellarnau M, Alenda C, Castells A, Cascante M. Transketolase-like 1 expression is modulated during colorectal cancer progression and metastasis formation. PloS one. 2011;6:e25323.

[472] Noorden Cv, Frederiks W. Enzyme histochemistry. A laboratory manual of current methods: Oxford [etc.]: Oxford University Press; 1992.

[473] Kawashima Y, Kodera Y, Singh A, Matsumoto M, Matsumoto H. Efficient extraction of proteins from formalin-fixed paraffin-embedded tissues requires higher concentration of tris(hydroxymethyl)aminomethane. Clin Proteomics. 2014;11:4.

[474] Irizarry RA, Bolstad BM, Collin F, Cope LM, Hobbs B, Speed TP. Summaries of Affymetrix GeneChip probe level data. Nucleic Acids Res. 2003;31:e15.

[475] Wilson CL, Miller CJ. Simpleaffy: a BioConductor package for Affymetrix Quality Control and data analysis. Bioinformatics. 2005;21:3683-5.

[476] Smyth GK. Linear models and empirical bayes methods for assessing differential expression in microarray experiments. Stat Appl Genet Mol Biol. 2004;3:Article3.

[477] Benjamini Y, Drai D, Elmer G, Kafkafi N, Golani I. Controlling the false discovery rate in behavior genetics research. Behav Brain Res. 2001;125:279-84.

[478] Subramanian A, Tamayo P, Mootha VK, Mukherjee S, Ebert BL, Gillette MA, et al. Gene set enrichment analysis: a knowledge-based approach for interpreting genome-wide expression profiles. Proc Natl Acad Sci U S A. 2005;102:15545-50.

[479] Fan TW. Considerations of Sample Preparation for Metabolomics Investigation. The Handbook of Metabolomics. New York2012. p. 7-27.

[480] Lane AN, Fan TW, Higashi RM. Isotopomer-based metabolomic analysis by NMR and mass spectrometry. Methods Cell Biol. 2008;84:541-88.

[481] Selivanov VA, Meshalkina LE, Solovjeva ON, Kuchel PW, Ramos-Montoya A, Kochetov GA, et al. Rapid simulation and analysis of isotopomer distributions using constraints based on enzyme mechanisms: an example from HT29 cancer cells. Bioinformatics. 2005;21:3558-64.

[482] Lee WN, Boros LG, Puigjaner J, Bassilian S, Lim S, Cascante M. Mass isotopomer study of the nonoxidative pathways of the pentose cycle with [1,2-13C2]glucose. Am J Physiol. 1998;274:E843-51.

[483] Chou TC, Talalay P. Quantitative analysis of dose-effect relationships: the combined effects of multiple drugs or enzyme inhibitors. Adv Enzyme Regul. 1984;22:27-55.

[484] Krasnov GS, Dmitriev AA, Snezhkina AV, Kudryavtseva AV. Deregulation of glycolysis in cancer: glyceraldehyde-3-phosphate dehydrogenase as a therapeutic target. Expert Opin Ther Targets. 2013;17:681-93.

[485] Castellvi-Bel S, Ruiz-Ponte C, Fernandez-Rozadilla C, Abuli A, Munoz J, Bessa X, et al. Seeking genetic susceptibility variants for colorectal cancer: the EPICOLON consortium experience. Mutagenesis. 2012;27:153-9.

[486] Gatenby RA, Gillies RJ. Why do cancers have high aerobic glycolysis? Nat Rev Cancer. 2004;4:891-9.

[487] Dang CV, Semenza GL. Oncogenic alterations of metabolism. Trends Biochem Sci. 1999;24:68-72.

[488] Graven KK, Troxler RF, Kornfeld H, Panchenko MV, Farber HW. Regulation of endothelial cell glyceraldehyde-3-phosphate dehydrogenase expression by hypoxia. The Journal of biological chemistry. 1994;269:24446-53.

[489] Graven KK, Bellur D, Klahn BD, Lowrey SL, Amberger E. HIF-2alpha regulates glyceraldehyde-3-phosphate dehydrogenase expression in endothelial cells. Biochimica et biophysica acta. 2003;1626:10-8.

[490] Cuezva JM, Krajewska M, de Heredia ML, Krajewski S, Santamaria G, Kim H, et al. The bioenergetic signature of cancer: a marker of tumor progression. Cancer Res. 2002;62:6674-81.

[491] Hwang NR, Yim SH, Kim YM, Jeong J, Song EJ, Lee Y, et al. Oxidative modifications of glyceraldehyde-3-phosphate dehydrogenase play a key role in its multiple cellular functions. The Biochemical journal. 2009;423:253-64.

[492] Sirover MA. Structural analysis of glyceraldehyde-3-phosphate dehydrogenase functional diversity. Int J Biochem Cell Biol. 2014;57C:20-6.

[493] Cerella C, D'Alessio M, Cristofanon S, De Nicola M, Radogna F, Dicato M, et al. Subapoptogenic oxidative stress strongly increases the activity of the glycolytic key enzyme glyceraldehyde 3-phosphate dehydrogenase. Annals of the New York Academy of Sciences. 2009;1171:583-90.

[494] Panis C, Victorino VJ, Herrera AC, Freitas LF, De Rossi T, Campos FC, et al. Differential oxidative status and immune characterization of the early and advanced stages of human breast cancer. Breast Cancer Res Treat. 2012;133:881-8.

[495] Acquaviva R, Iauk L, Sorrenti V, Lanteri R, Santangelo R, Licata A, et al. Oxidative profile in patients with colon cancer: effects of Ruta chalepensis L. Eur Rev Med Pharmacol Sci. 2011;15:181-91.

[496] Reuter S, Gupta SC, Chaturvedi MM, Aggarwal BB. Oxidative stress, inflammation, and cancer: how are they linked? Free Radic Biol Med. 2010;49:1603-16.

[497] Cuervo AM, Terlecky SR, Dice JF, Knecht E. Selective binding and uptake of ribonuclease A and glyceraldehyde-3-phosphate dehydrogenase by isolated rat liver lysosomes. The Journal of biological chemistry. 1994;269:26374-80.

[498] Carujo S, Estanyol JM, Ejarque A, Agell N, Bachs O, Pujol MJ. Glyceraldehyde 3-phosphate dehydrogenase is a SET-binding protein and regulates cyclin B-cdk1 activity. Oncogene. 2006;25:4033-42.

[499] Ganapathy-Kanniappan S, Geschwind JF. Tumor glycolysis as a target for cancer therapy: progress and prospects. Mol Cancer. 2013;12:152.

[500] Ganapathy-Kanniappan S, Kunjithapatham R, Geschwind JF. Glyceraldehyde-3-phosphate dehydrogenase: a promising target for molecular therapy in hepatocellular carcinoma. Oncotarget. 2012;3:940-53.

[501] Hjerpe E, Egyhazi Brage S, Carlson J, Frostvik Stolt M, Schedvins K, Johansson H, et al. Metabolic markers GAPDH, PKM2, ATP5B and BEC-index in advanced serous ovarian cancer. BMC Clin Pathol. 2013;13:30.

[502] Barbazan J, Muinelo-Romay L, Vieito M, Candamio S, Diaz-Lopez A, Cano A, et al. A multimarker panel for circulating tumor cells detection predicts patient outcome and therapy response in metastatic colorectal cancer. Int J Cancer. 2014;135:2633-43.

[503] Revillion F, Pawlowski V, Hornez L, Peyrat JP. Glyceraldehyde-3-phosphate dehydrogenase gene expression in human breast cancer. Eur J Cancer. 2000;36:1038-42.

[504] Puzone R, Savarino G, Salvi S, Dal Bello MG, Barletta G, Genova C, et al. Glyceraldehyde-3-phosphate dehydrogenase gene over expression correlates with poor prognosis in non small cell lung cancer patients. Mol Cancer. 2013;12:97.

[505] Wang D, Moothart DR, Lowy DR, Qian X. The expression of glyceraldehyde-3-phosphate dehydrogenase associated cell cycle (GACC) genes correlates with cancer stage and poor survival in patients with solid tumors. PloS one. 2013;8:e61262.

[506] Rubie C, Kempf K, Hans J, Su T, Tilton B, Georg T, et al. Housekeeping gene variability in normal and cancerous colorectal, pancreatic, esophageal, gastric and hepatic tissues. Mol Cell Probes. 2005;19:101-9.

[507] Peyressatre M, Prevel C, Pellerano M, Morris MC. Targeting cyclin-dependent kinases in human cancers: from small molecules to Peptide inhibitors. Cancers (Basel). 2015;7:179-237.

[508] Myohanen SK, Baylin SB, Herman JG. Hypermethylation can selectively silence individual p16ink4A alleles in neoplasia. Cancer Res. 1998;58:591-3.

[509] Baker SJ, Reddy EP. CDK4: A Key Player in the Cell Cycle, Development, and Cancer. Genes Cancer. 2012;3:658-69.

[510] Grassian AR, Metallo CM, Coloff JL, Stephanopoulos G, Brugge JS. Erk regulation of pyruvate dehydrogenase flux through PDK4 modulates cell proliferation. Genes & Development. 2011;25:1716-33.

[511] Zhdanov AV, Waters AHC, Golubeva AV, Dmitriev RI, Papkovsky DB. Availability of the key metabolic substrates dictates the respiratory response of cancer cells to the mitochondrial uncoupling. Biochimica et Biophysica Acta (BBA) - Bioenergetics. 2014;1837:51-62.

[512] Wu M, Neilson A, Swift AL, Moran R, Tamagnine J, Parslow D, et al. Multiparameter metabolic analysis reveals a close link between attenuated mitochondrial bioenergetic function and enhanced glycolysis dependency in human tumor cells. Am J Physiol Cell Physiol. 2007;292:C125-36.

[513] Lu SC. Glutathione synthesis. Biochimica et biophysica acta. 2013;1830:3143-53.

[514] Yoo H, Antoniewicz MR, Stephanopoulos G, Kelleher JK. Quantifying reductive carboxylation flux of glutamine to lipid in a brown adipocyte cell line. The Journal of biological chemistry. 2008;283:20621-7.

[515] Schuhmacher M, Kohlhuber F, Holzel M, Kaiser C, Burtscher H, Jarsch M, et al. The transcriptional program of a human B cell line in response to Myc. Nucleic Acids Res. 2001;29:397-406.

[516] Manalo DJ, Rowan A, Lavoie T, Natarajan L, Kelly BD, Ye SQ, et al. Transcriptional regulation of vascular endothelial cell responses to hypoxia by HIF-1. Blood. 2005;105:659-69.

[517] Mense SM, Sengupta A, Zhou M, Lan C, Bentsman G, Volsky DJ, et al. Gene expression profiling reveals the profound upregulation of hypoxia-responsive genes in primary human astrocytes. Physiol Genomics. 2006;25:435-49.

[518] Fardin P, Barla A, Mosci S, Rosasco L, Verri A, Versteeg R, et al. A biology-driven approach identifies the hypoxia gene signature as a predictor of the outcome of neuroblastoma patients. Mol Cancer. 2010;9:185.:10.1186/476-4598-9-185.

[519] Leonard MO, Cottell DC, Godson C, Brady HR, Taylor CT. The role of HIF-1 alpha in transcriptional regulation of the proximal tubular epithelial cell response to hypoxia. J Biol Chem. 2003;278:40296-304. Epub 2003 Jul 28.

[520] Peng T, Golub TR, Sabatini DM. The immunosuppressant rapamycin mimics a starvation-like signal distinct from amino acid and glucose deprivation. Molecular and cellular biology. 2002;22:5575-84.

[521] Delpuech O, Griffiths B, East P, Essafi A, Lam EWF, Burgering B, et al. Induction of Mxi1-SR by FOXO3a Contributes to Repression of Myc-Dependent Gene Expression. Molecular and Cellular Biology. 2007;27:4917-30.

[522] Duarte NC, Becker SA, Jamshidi N, Thiele I, Mo ML, Vo TD, et al. Global reconstruction of the human metabolic network based on genomic and bibliomic data. Proc Natl Acad Sci U S A. 2007;104:1777-82.

[523] Schellenberger J, Park JO, Conrad TM, Palsson BO. BiGG: a Biochemical Genetic and Genomic knowledgebase of large scale metabolic reconstructions. BMC Bioinformatics. 2010;11:213.

[524] Wolfram S. The Mathematica Book. Fifth ed: Wolfram Media; 2003.

[525] Buescher JM, Antoniewicz MR, Boros LG, Burgess SC, Brunengraber H, Clish CB, et al. A roadmap for interpreting C metabolite labeling patterns from cells. Curr Opin Biotechnol. 2015;34C:189-201.

[526] Mahadevan R, Schilling CH. The effects of alternate optimal solutions in constraint-based genome-scale metabolic models. Metab Eng. 2003;5:264-76.

[527] Llaneras F, Pico J. An interval approach for dealing with flux distributions and elementary modes activity patterns. J Theor Biol. 2007;246:290-308.

[528] Orman MA, Arai K, Yarmush ML, Androulakis IP, Berthiaume F, Ierapetritou MG. Metabolic flux determination in perfused livers by mass balance analysis: effect of fasting. Biotechnol Bioeng. 2010;107:825-35. doi: 10.1002/bit.22878.

[529] Rodríguez-Prados JC, de Atauri P, Maury J, Ortega F, Portais JC, Chassagnole C, et al. In silico strategy to rationally engineer metabolite production: A case study for threonine in Escherichia coli. Biotechnol Bioeng. 2009;103:609-20.

[530] Chiang GG, Abraham RT. Phosphorylation of mammalian target of rapamycin (mTOR) at Ser-2448 is mediated by p70S6 kinase. The Journal of biological chemistry. 2005;280:25485-90.

[531] Mao CQ, Xiong MH, Liu Y, Shen S, Du XJ, Yang XZ, et al. Synthetic lethal therapy for KRAS mutant non-small-cell lung carcinoma with nanoparticle-mediated CDK4 siRNA delivery. Mol Ther. 2014;22:964-73.

[532] Gaglio D, Metallo CM, Gameiro PA, Hiller K, Danna LS, Balestrieri C, et al. Oncogenic K-Ras decouples glucose and glutamine metabolism to support cancer cell growth. Mol Syst Biol. 2011;7:523.

[533] Anders L, Ke N, Hydbring P, Choi Yoon J, Widlund Hans R, Chick Joel M, et al. A Systematic Screen for CDK4/6 Substrates Links FOXM1 Phosphorylation to Senescence Suppression in Cancer Cells. Cancer cell. 2011;20:620-34.

[534] Rajeeve V, Pearce W, Cascante M, Vanhaesebroeck B, Cutillas PR. Polyamine production is downstream and upstream of oncogenic PI3K signalling and contributes to tumour cell growth. The Biochemical journal. 2013;450:619-28.

[535] Jiang P, Du W, Mancuso A, Wellen KE, Yang X. Reciprocal regulation of p53 and malic enzymes modulates metabolism and senescence. Nature. 2013;493:689-93.

[536] Denko NC. Hypoxia, HIF1 and glucose metabolism in the solid tumour. Nat Rev Cancer. 2008;8:705-13.

[537] Mobasheri A, Richardson S, Mobasheri R, Shakibaei M, Hoyland JA. Hypoxia inducible factor-1 and facilitative glucose transporters GLUT1 and GLUT3: putative molecular components of the oxygen and glucose sensing apparatus in articular chondrocytes. Histol Histopathol. 2005;20:1327-38.

[538] Iacobazzi V, Infantino V. Citrate--new functions for an old metabolite. Biol Chem. 2014;395:387-99.

[539] Robinson MM, McBryant SJ, Tsukamoto T, Rojas C, Ferraris DV, Hamilton SK, et al. Novel mechanism of inhibition of rat kidney-type glutaminase by bis-2-(5-phenylacetamido-1,2,4-thiadiazol-2-yl)ethyl sulfide (BPTES). The Biochemical journal. 2007;406:407-14.

[540] Yuneva M, Zamboni N, Oefner P, Sachidanandam R, Lazebnik Y. Deficiency in glutamine but not glucose induces MYC-dependent apoptosis in human cells. The Journal of cell biology. 2007;178:93-105.

[541] Reynolds CP, Maurer BJ. Evaluating response to antineoplastic drug combinations in tissue culture models. Methods Mol Med. 2005;110:173-83.

[542] Finn RS, Dering J, Conklin D, Kalous O, Cohen DJ, Desai AJ, et al. PD 0332991, a selective cyclin D kinase 4/6 inhibitor, preferentially inhibits proliferation of luminal estrogen receptor-positive human breast cancer cell lines in vitro. Breast Cancer Research. 2009;11:R77.

[543] Schmidt M, Fernandez de Mattos S, van der Horst A, Klompmaker R, Kops GJPL, Lam EWF, et al. Cell Cycle Inhibition by FoxO Forkhead Transcription Factors Involves Downregulation of Cyclin D. Molecular and cellular biology. 2002;22:7842-52.

[544] Nave BT, Ouwens M, Withers DJ, Alessi DR, Shepherd PR. Mammalian target of rapamycin is a direct target for protein kinase B: identification of a convergence point for opposing effects of insulin and amino-acid deficiency on protein translation. The Biochemical journal. 1999;344 Pt 2:427-31.

[545] Hassan B, Akcakanat A, Holder AM, Meric-Bernstam F. Targeting the PI3-kinase/Akt/mTOR signaling pathway. Surg Oncol Clin N Am. 2013;22:641-64.

[546] Vlahos CJ, Matter WF, Hui KY, Brown RF. A specific inhibitor of phosphatidylinositol 3-kinase, 2-(4-morpholinyl)-8-phenyl-4H-1-benzopyran-4-one (LY294002). The Journal of biological chemistry. 1994;269:5241-8.

[547] Sutherland R, Carlsson J, Durand R, Yuhas J. Spheroids in Cancer Research. Cancer Research. 1981;41:2980-4.

[548] Hirschhaeuser F, Menne H, Dittfeld C, West J, Mueller-Klieser W, Kunz-Schughart LA. Multicellular tumor spheroids: an underestimated tool is catching up again. J Biotechnol. 2010;148:3-15.

[549] Vafa O, Wade M, Kern S, Beeche M, Pandita TK, Hampton GM, et al. c-Myc can induce DNA damage, increase reactive oxygen species, and mitigate p53 function: a mechanism for oncogene-induced genetic instability. Mol Cell. 2002;9:1031-44.

[550] Benassi B, Fanciulli M, Fiorentino F, Porrello A, Chiorino G, Loda M, et al. c-Myc phosphorylation is required for cellular response to oxidative stress. Mol Cell. 2006;21:509-19.

[551] Baquet A, Lavoinne A, Hue L. Comparison of the effects of various amino acids on glycogen synthesis, lipogenesis and ketogenesis in isolated rat hepatocytes. Biochem J. 1991;273:57-62.

[552] Plomp PJ, Boon L, Caro LH, van Woekom GM, Meijer AJ. Stimulation of glycogen synthesis in hepatocytes by added amino acids is related to the total intracellular content of amino acids. European journal of biochemistry / FEBS. 1990;191:237-43.

[553] Jeong SM, Xiao C, Finley LW, Lahusen T, Souza AL, Pierce K, et al. SIRT4 has tumor-suppressive activity and regulates the cellular metabolic response to DNA damage by inhibiting mitochondrial glutamine metabolism. Cancer cell. 2013;23:450-63.

[554] Medema RH, Kops GJPL, Bos JL, Burgering BMT. AFX-like Forkhead transcription factors mediate cell-cycle regulation by Ras and PKB through p27kip1. Nature. 2000;404:782-7.

[555] Li CJ, Chang JK, Chou CH, Wang GJ, Ho ML. The PI3K/Akt/FOXO3a/p27Kip1 signaling contributes to anti-inflammatory drug-suppressed proliferation of human osteoblasts. Biochemical Pharmacology. 2010;79:926-37.

[556] Chou TC. Drug Combination Studies and Their Synergy Quantification Using the Chou-Talalay Method. Cancer Research. 2010;70:440-6.

[557] Fan Y, Dickman KG, Zong WX. Akt and c-Myc differentially activate cellular metabolic programs and prime cells to bioenergetic inhibition. The Journal of biological chemistry. 2010;285:7324-33.

[558] Gera JF, Mellinghoff IK, Shi Y, Rettig MB, Tran C, Hsu JH, et al. AKT activity determines sensitivity to mammalian target of rapamycin (mTOR) inhibitors by regulating cyclin D1 and c-myc expression. The Journal of biological chemistry. 2004;279:2737-46.

[559] Lu Y, Wu Y, Feng X, Shen R, Wang JH, Fallahi M, et al. CDK4 deficiency promotes genomic instability and enhances Myc-driven lymphomagenesis. The Journal of clinical investigation. 2014;124:1672-84.

[560] Yan L, DeMars LC. Dietary supplementation with methylseleninic acid, but not selenomethionine, reduces spontaneous metastasis of Lewis lung carcinoma in mice. Int J Cancer. 2012;131:1260-6.

[561] Zeng H, Wu M. The Inhibitory Efficacy of Methylseleninic Acid Against Colon Cancer Xenografts in C57BL/6 Mice. Nutrition and cancer. 2015:1-8.

[562] Wang Z, Hu H, Li G, Lee HJ, Jiang C, Kim SH, et al. Methylseleninic acid inhibits microvascular endothelial G1 cell cycle progression and decreases tumor microvessel density. Int J Cancer. 2008;122:15-24.

[563] Zhuo H, Smith AH, Steinmaus C. Selenium and lung cancer: a quantitative analysis of heterogeneity in the current epidemiological literature. Cancer Epidemiol Biomarkers Prev. 2004;13:771-8.

[564] Fernandez de Mattos S, Villalonga P, Clardy J, Lam EW. FOXO3a mediates the cytotoxic effects of cisplatin in colon cancer cells. Mol Cancer Ther. 2008;7:3237-46.

[565] Yin S, Dong Y, Li J, Fan L, Wang L, Lu J, et al. Methylseleninic acid potentiates multiple types of cancer cells to ABT-737-induced apoptosis by targeting Mcl-1 and Bad. Apoptosis. 2011;17:388-99.

[566] Hu H, Jiang C, Ip C, Rustum YM, Lu J. Methylseleninic acid potentiates apoptosis induced by chemotherapeutic drugs in androgen-independent prostate cancer cells. Clin Cancer Res. 2005;11:2379-88.

[567] Saraste A, Pulkki K. Morphologic and biochemical hallmarks of apoptosis. Cardiovasc Res. 2000;45:528-37.

[568] Fan TW, Lane AN, Higashi RM, Farag MA, Gao H, Bousamra M, et al. Altered regulation of metabolic pathways in human lung cancer discerned by (13)C stable isotope-resolved metabolomics (SIRM). Mol Cancer. 2009;8:41.

[569] Fan TW, Lane AN, Higashi RM, Yan J. Stable isotope resolved metabolomics of lung cancer in a SCID mouse model. Metabolomics. 2011;7:257-69.

[570] Fan TW, Yuan P, Lane AN, Higashi RM, Wang Y, Hamidi AB, et al. Stable isotope-resolved metabolomic analysis of lithium effects on glial-neuronal metabolism and interactions. Metabolomics. 2010;6:165-79.

[571] Zanella F, Link W, Carnero A. Understanding FOXO, new views on old transcription factors. Curr Cancer Drug Targets. 2010;10:135-46.

[572] Zanella F, dos Santos NR, Link W. Moving to the Core: Spatiotemporal Analysis of Forkhead Box O (FOXO) and Nuclear Factor-κB (NF-κB) Nuclear Translocation. Traffic. 2013;14:247-58.

[573] Link W, Oyarzabal J, Serelde BG, Albarran MI, Rabal O, Cebria A, et al. Chemical Interrogation of FOXO3a Nuclear Translocation Identifies Potent and Selective Inhibitors of Phosphoinositide 3-Kinases. Journal of Biological Chemistry. 2009;284:28392-400.

[574] Zanella F, Rosado A, Garcia B, Carnero A, Link W. Using multiplexed regulation of luciferase activity and GFP translocation to screen for FOXO modulators. BMC Cell Biology. 2009;10:14.

[575] Essaghir A, Dif N, Marbehant CY, Coffer PJ, Demoulin JB. The Transcription of FOXO Genes Is Stimulated by FOXO3 and Repressed by Growth Factors. Journal of Biological Chemistry. 2009;284:10334-42.

[576] Diaz-Moralli S, Tarrado-Castellarnau M, Miranda A, Cascante M. Targeting Cell Cycle Regulation in Cancer Therapy. Pharmacol Ther. 2013;138:255-71.

[577] Li GX, Hu H, Jiang C, Schuster T, Lü J. Differential involvement of reactive oxygen species in apoptosis induced by two classes of selenium compounds in human prostate cancer cells. International Journal of Cancer. 2007;120:2034-43.

[578] de Miranda JX, Andrade FD, Conti AD, Dagli ML, Moreno FS, Ong TP. Effects of selenium compounds on proliferation and epigenetic marks of breast cancer cells. J Trace Elem Med Biol. 2014;28:486-91.

[579] Poerschke RL, Franklin MR, Moos PJ. Modulation of redox status in human lung cell lines by organoselenocompounds: Selenazolidines, selenomethionine, and methylseleninic acid. Toxicology in Vitro. 2008;22:1761-7.

[580] Wang X, Chen WR, Xing D. A pathway from JNK through decreased ERK and Akt activities for FOXO3a nuclear translocation in response to UV irradiation. Journal of Cellular Physiology. 2012;227:1168-78.

[581] Sunayama J. JNK antagonizes Akt-mediated survival signals by phosphorylating 14-3-3. The Journal of cell biology. 2005;170:295-304.

[582] Sunters A. Paclitaxel-Induced Nuclear Translocation of FOXO3a in Breast Cancer Cells Is Mediated by c-Jun NH2-Terminal Kinase and Akt. Cancer Research. 2006;66:212-20.

[583] Zou Y, Niu P, Yang J, Yuan J, Wu T, Chen X. The JNK signaling pathway is involved in sodium-selenite-induced apoptosis mediated by reactive oxygen in HepG2 cells. Cancer Biol Ther. 2008;7:689-96.

[584] Garnett MJ, Edelman EJ, Heidorn SJ, Greenman CD, Dastur A, Lau KW, et al. Systematic identification of genomic markers of drug sensitivity in cancer cells. Nature. 2012;483:570-5.

[585] Micke O, Schomburg L, Buentzel J, Kisters K, Muecke R. Selenium in oncology: from chemistry to clinics. Molecules (Basel, Switzerland). 2009;14:3975-88.

[586] Rayman MP. Selenium in cancer prevention: a review of the evidence and mechanism of action. The Proceedings of the Nutrition Society. 2005;64:527-42.

[587] Christensen MJ. Selenium and Prostate Cancer Prevention: What Next--If Anything? Cancer Prevention Research. 2014;7:781-5.

[588] Drake EN. Cancer chemoprevention: selenium as a prooxidant, not an antioxidant. Med Hypotheses. 2006;67:318-22.

[589] Vinceti M, Dennert G, Crespi CM, Zwahlen M, Brinkman M, Zeegers MP, et al. Selenium for preventing cancer. Cochrane Database Syst Rev. 2014;3:CD005195.

[590] Ganther HE. Pathways of Selenium Metabolism Including Respiratory Excretory Products. International Journal of Toxicology. 1986;5:1-5.

[591] Steinbrenner H, Sies H. Protection against reactive oxygen species by selenoproteins. Biochimica et biophysica acta. 2009;1790:1478-85.

[592] Link W. FOXO proteins as potential targets for anticancer therapy. Current Drug Targets. 2011;12:1232-4.

Appendix I

Measured ^{13}C label enrichments

Table AI.1: Measured isotopomer enrichments using [1,2-^{13}C$_2$]-D-glucose. Internal ribose, glycogen, palmitate and stearate

		normoxia				hypoxia			
		control		CDK4/6 inh		control		CDK4/6 inh	
		mean	SD	mean	SD	mean	SD	mean	SD
Rib-256	m0	0.556	0.008	0.569	0.005	0.621	0.018	0.695	0.002
	m1	0.209	0.004	0.190	0.003	0.161	0.008	0.107	0.001
	m2	0.085	0.002	0.097	0.001	0.075	0.004	0.078	0.000
	m3	0.080	0.001	0.072	0.001	0.072	0.003	0.050	0.000
	m4	0.066	0.002	0.069	0.001	0.068	0.003	0.068	0.001
	m5	0.003	0.000	0.003	0.001	0.003	0.000	0.003	0.000
Glyc-328	m0	0.294	0.033	0.433	0.049	0.221	0.023	0.268	0.025
	m1	0.046	0.001	0.034	0.003	0.011	0.001	0.013	0.001
	m2	0.565	0.028	0.464	0.039	0.723	0.020	0.662	0.023
	m3	0.034	0.001	0.023	0.003	0.008	0.000	0.010	0.000
	m4	0.061	0.003	0.046	0.004	0.037	0.001	0.047	0.002
Palm-270	m0	0.647	0.061	0.803	0.083	0.886	0.008	0.935	0.007
	m1	0.008	0.001	0.007	0.001	0.003	0.002	0.004	0.002
	m2	0.066	0.012	0.052	0.023	0.055	0.004	0.028	0.003
	m3	0.019	0.003	0.013	0.005	0.004	0.000	0.004	0.002
	m4	0.093	0.016	0.055	0.024	0.030	0.002	0.016	0.002
	m5	0.025	0.004	0.012	0.005	0.001	0.001	0.001	0.001
	m6	0.077	0.013	0.035	0.015	0.014	0.000	0.008	0.002
	m7	0.020	0.003	0.007	0.003	0.002	0.001	0.001	0.000
	m8	0.046	0.008	0.015	0.007	0.004	0.001	0.002	0.001
	m9					0.001	0.001	0.001	0.000
	m10					0.000	0.000	0.000	0.000
Stear-298	m0	0.871	0.027	0.944	0.021	0.915	0.013	0.936	0.013
	m1	0.003	0.001	0.003	0.001	0.007	0.004	0.009	0.005
	m2	0.032	0.006	0.018	0.007	0.033	0.007	0.016	0.003
	m3	0.006	0.001	0.003	0.001	0.005	0.004	0.008	0.004
	m4	0.029	0.006	0.014	0.005	0.014	0.004	0.008	0.003
	m5	0.008	0.002	0.003	0.001	0.002	0.001	0.003	0.001
	m6	0.026	0.006	0.009	0.004	0.006	0.001	0.001	0.000
	m7	0.007	0.002	0.001	0.001	0.013	0.004	0.012	0.003
	m8	0.017	0.004	0.004	0.002	0.004	0.001	0.005	0.003
	m9					0.001	0.000	0.002	0.001
	m10					0.000	0.000	0.000	0.000

Abbreviations according to Materials and Methods: Rib-256, C1-C5 ribose in the range 256-261 m/z; Glyc-328, recorded abundance of C1-C6 glycogen in the range 327-334 m/z; Palm-270, palmitate in the range 269-278 m/z; Stear-298, sterarate in the range 297-306 m/z..

Table AI.2: Measured isotopomer enrichments using [U-^{13}C$_5$]-L-glutamine. Internal ribose, glycogen, palmitate and stearate

		normoxia			
		control		CDK4/6 inh	
		mean	SD	mean	SD
Palm-270	m0	0.868	0.018	0.915	0.020
	m1	0.020	0.003	0.014	0.002
	m2	0.079	0.011	0.053	0.013
	m3	0.008	0.001	0.005	0.001
	m4	0.018	0.002	0.010	0.003
	m5	0.001	0.000	0.001	0.000
	m6	0.004	0.001	0.002	0.001
	m7	0.000	0.000	0.000	0.000
	m8	0.001	0.000	0.000	0.000

		normoxia			
		control		CDK4/6 inh	
		mean	SD	mean	SD
	m0	0.936	0.012	0.969	0.011
	m1	0.009	0.002	0.005	0.001
	m2	0.039	0.007	0.020	0.007
	m3	0.003	0.001	0.002	0.001
Stear-298	m4	0.010	0.002	0.004	0.002
	m5	0.001	0.000	0.000	0.000
	m6	0.002	0.000	0.000	0.000
	m7	0.000	0.000	0.000	0.000
	m8	0.001	0.000	0.000	0.000

See Table AI.1 for abbreviations

Table AI.3: Measured isotopomer enrichments using [1,2-^{13}C$_2$]-D-glucose. External glucose

		normoxia			
		control		CDK4/6 inh	
		mean	SD	mean	SD
	m0	0.035	0.000	0.032	0.000
	m1	0.015	0.000	0.015	0.002
	m2	0.930	0.000	0.933	0.001
Glc-328	m3	0.004	0.000	0.003	0.000
	m4	0.015	0.000	0.016	0.000
	m5	0.000	0.000	0.001	0.000
	m6	0.000	0.000	0.000	0.000

Abbreviations according to Materials and Methods: Glc-328, C1-C6 glucose in the range 327-336 m/z.

Table AI.4: Measured isotopomer enrichments using [1,2-^{13}C$_2$]-D-glucose. External glucose, lactate, alanine, glutamate/glutamine, and aspartate/asparagine

		normoxia				hypoxia			
		control		CDK4/6 inh		control		CDK4/6 inh	
		mean	SD	mean	SD	mean	SD	mean	SD
	m0	0.542	0.001	0.562	0.004	0.542	0.003	0.551	0.006
Lac-328	m1	0.030	0.000	0.031	0.001	0.011	0.001	0.011	0.000
	m2	0.419	0.001	0.396	0.004	0.442	0.002	0.431	0.006
	m3	0.009	0.000	0.011	0.000	0.006	0.000	0.007	0.000
	m0	0.639	0.001	0.755	0.003	0.690	0.005	0.803	0.009
Ala-242	m1	0.025	0.001	0.018	0.000	0.003	0.001	0.004	0.000
	m2	0.348	0.001	0.233	0.003	0.304	0.005	0.191	0.009
	m3	0.000	0.000	0.000	0.000	0.003	0.001	0.003	0.000
	m0	0.952	0.003	0.984	0.000	0.996	0.000	0.996	0.000
	m1	0.010	0.001	0.004	0.000	0.000	0.000	0.000	0.000
Glu+Gln-384	m2	0.029	0.001	0.010	0.000	0.004	0.000	0.003	0.000
	m3	0.006	0.000	0.001	0.000	0.000	0.000	0.000	0.000
	m4	0.003	0.000	0.001	0.000	0.000	0.000	0.000	0.000
	m5	0.001	0.001	0.000	0.000	0.000	0.000	0.000	0.000
	m0	0.953	0.003	0.985	0.002	0.991	0.001	0.991	0.000
Glu+Gln-152	m1	0.035	0.002	0.012	0.001	0.007	0.001	0.007	0.000
	m2	0.010	0.001	0.003	0.000	0.001	0.000	0.002	0.000
	m3	0.003	0.000	0.001	0.000	0.001	0.000	0.001	0.000
	m0	0.951	0.002	0.984	0.000	0.995	0.000	0.996	0.000
	m1	0.013	0.001	0.005	0.000	0.001	0.000	0.001	0.000
Glu+Gln-198	m2	0.028	0.001	0.009	0.000	0.004	0.000	0.003	0.000
	m3	0.006	0.000	0.002	0.000	0.000	0.000	0.000	0.000
	m4	0.002	0.001	0.000	0.000	0.000	0.000	0.000	0.000

		normoxia				hypoxia			
		control		CDK4/6 inh		control		CDK4/6 inh	
		mean	SD	mean	SD	mean	SD	mean	SD
Asp+Asn-342	m0	0.891	0.004	0.955	0.000	0.987	0.001	0.990	0.002
	m1	0.030	0.001	0.013	0.000	0.001	0.000	0.001	0.001
	m2	0.063	0.002	0.027	0.000	0.011	0.001	0.008	0.001
	m3	0.012	0.001	0.004	0.000	0.000	0.000	0.000	0.000
	m4	0.003	0.000	0.001	0.000	0.000	0.000	0.000	0.000

Abbreviations according to Materials and Methods: Lac-328, C1-C3 lactate in the range 327-332 m/z; Ala-242, C1-C3 alanine in the range 241-246 m/z; Glu+Gln-384, C1-C5 glutamate and glutamine in the range 383-390 m/z; Glu+Gln-152, C2-C4 glutamate and glutamine in the range 151-157 m/z; Glu+Gln-198, C2-C5 glutamate and glutamine in the range 197-203 m/z; Asp+Asn-342, C1-C4 aspartate and asparagine in the range 341-348 m/z.

Table AI.5: Measured isotopomer enrichments using [U-^{13}C$_5$]-L-glutamine. External lactate, alanine, glutamate/glutamine, and aspartate/asparagine

		normoxia				hypoxia			
		control		CDK4/6 inh		control		CDK4/6 inh	
		mean	SD	mean	SD	mean	SD	mean	SD
Lac-328	m0	0.978	0.001	0.976	0.001	0.995	0.001	0.995	0.000
	m1	0.006	0.001	0.006	0.001	0.000	0.000	0.001	0.000
	m2	0.004	0.000	0.004	0.001	0.001	0.000	0.001	0.000
	m3	0.012	0.000	0.013	0.000	0.004	0.001	0.003	0.000
Ala-242	m0	0.967	0.003	0.971	0.004	0.990	0.002	0.994	0.000
	m1	0.009	0.001	0.008	0.001	0.002	0.000	0.001	0.000
	m2	0.005	0.001	0.004	0.001	0.002	0.000	0.001	0.000
	m3	0.019	0.001	0.016	0.002	0.006	0.001	0.003	0.000
Glu+Gln-384	m0	0.113	0.001	0.115	0.001	0.090	0.007	0.097	0.000
	m1	0.018	0.000	0.008	0.001	0.000	0.000	0.000	0.000
	m2	0.012	0.000	0.006	0.000	0.000	0.000	0.000	0.000
	m3	0.048	0.000	0.029	0.001	0.020	0.001	0.019	0.000
	m4	0.021	0.001	0.021	0.001	0.040	0.000	0.040	0.000
	m5	0.787	0.002	0.822	0.003	0.851	0.007	0.845	0.000
Glu+Gln-152	m0	0.134	0.001	0.129	0.004	0.079	0.001	0.089	0.001
	m1	0.041	0.002	0.024	0.002	0.009	0.004	0.011	0.001
	m2	0.046	0.001	0.027	0.001	0.024	0.003	0.022	0.001
	m3	0.779	0.002	0.821	0.007	0.889	0.003	0.878	0.001
Glu+Gln-198	m0	0.091	0.004	0.100	0.002	0.069	0.004	0.076	0.001
	m1	0.021	0.000	0.009	0.000	0.002	0.000	0.002	0.000
	m2	0.044	0.001	0.023	0.001	0.012	0.002	0.010	0.000
	m3	0.000	0.000	0.000	0.000	0.013	0.013	0.008	0.002
	m4	0.844	0.005	0.868	0.001	0.904	0.019	0.904	0.003
Asp+Asn-342	m0	0.639	0.011	0.819	0.010	0.908	0.018	0.951	0.004
	m1	0.057	0.001	0.028	0.002	0.003	0.001	0.003	0.000
	m2	0.093	0.001	0.047	0.002	0.010	0.003	0.008	0.001
	m3	0.024	0.000	0.012	0.001	0.037	0.001	0.016	0.001
	m4	0.182	0.004	0.096	0.005	0.042	0.015	0.022	0.002

See Table AI.4 for abbreviations

Table AI.6: Measured isotopomer enrichments using [1,2-^{13}C$_2$]-D-glucose. External proline, serine, glycine and methionine

| | | normoxia | | | | hypoxia | | | |
| | | control | | CDK4/6 inh | | control | | CDK4/6 inh | |
		mean	SD	mean	SD	mean	SD	mean	SD
Pro-296	m0	0.917	0.002	0.950	0.001	0.994	0.000	0.993	0.002
	m1	0.016	0.001	0.012	0.000	0.000	0.000	0.001	0.000
	m2	0.053	0.001	0.032	0.001	0.004	0.000	0.006	0.001
	m3	0.008	0.000	0.004	0.000	0.000	0.000	0.000	0.000
	m4	0.006	0.000	0.002	0.000	0.001	0.000	0.000	0.000
	m5	0.001	0.000	0.000	0.000	0.000	0.000	0.000	0.000
Ser-354	m0	0.925	0.003	0.933	0.001	0.920	0.001	0.957	0.002
	m1	0.052	0.002	0.052	0.001	0.068	0.001	0.031	0.000
	m2	0.022	0.001	0.015	0.001	0.011	0.001	0.011	0.001
	m3	0.001	0.000	0.000	0.000	0.001	0.000	0.001	0.001
Gly-228	m0	0.975	0.000	0.987	0.000	0.988	0.002	0.997	0.000
	m1	0.027	0.000	0.013	0.000	0.012	0.002	0.003	0.001
	m2	0.000	0.000	0.000	0.000	0.000	0.000	0.000	0.000
Met-330	m0	0.961	0.002	0.981	0.002	0.987	0.002	0.996	0.001
	m1	0.015	0.001	0.007	0.000	0.004	0.001	0.001	0.001
	m2	0.012	0.002	0.006	0.001	0.004	0.001	0.001	0.001
	m3	0.011	0.000	0.006	0.000	0.003	0.001	0.001	0.001
	m4	0.000	0.000	0.001	0.001	0.002	0.004	0.000	0.000
	m5	0.000	0.000	0.000	0.000	0.001	0.001	0.000	0.000
Met-254	m0	0.963	0.000	0.979	0.001	0.995	0.002	0.997	0.001
	m1	0.013	0.000	0.008	0.000	0.002	0.000	0.002	0.002
	m2	0.013	0.001	0.006	0.001	0.001	0.001	0.001	0.001
	m3	0.010	0.000	0.006	0.000	0.002	0.000	0.000	0.001
	m4	0.000	0.000	0.000	0.000	0.000	0.000	0.000	0.000

Abbreviations according to Materials and Methods: Pro-296, C1-C5 proline in the range 295-302 m/z; Ser-354, C1-C3 serine in the range 353-358 m/z; Gly-228, C1-C2 glycine in the range 227-231 m/z; Met-330, C1-C4SC5 methionine in the range 329-336 m/z; Met-254, C1-C4 methionine in the range 253-259 m/z.

Table AI.7: Measured isotopomer enrichments using [U-^{13}C$_5$]-L-glutamine. External proline, serine, glycine and methionine

| | | normoxia | | | | hypoxia | | | |
| | | control | | CDK4/6 inh | | control | | CDK4/6 inh | |
		mean	SD	mean	SD	mean	SD	mean	SD
Pro-296	m0	0.719	0.005	0.799	0.012	0.942	0.012	0.956	0.005
	m1	0.034	0.000	0.025	0.001	0.000	0.000	0.002	0.000
	m2	0.022	0.001	0.016	0.003	0.001	0.001	0.001	0.001
	m3	0.071	0.001	0.052	0.002	0.008	0.002	0.009	0.001
	m4	0.004	0.000	0.003	0.000	0.002	0.001	0.001	0.000
	m5	0.149	0.003	0.105	0.006	0.047	0.008	0.031	0.003
Ser-354	m0	0.999	0.000	0.997	0.002	0.996	0.002	0.999	0.001
	m1	0.000	0.001	0.002	0.001	0.002	0.001	0.000	0.000
	m2	0.000	0.000	0.000	0.000	0.001	0.000	0.000	0.000
	m3	0.000	0.000	0.000	0.000	0.001	0.001	0.000	0.000
Gly-228	m0	0.999	0.000	0.999	0.000	1.000	0.000	1.000	0.000
	m1	0.000	0.000	0.000	0.000	0.000	0.000	0.000	0.000
	m2	0.000	0.000	0.000	0.000	0.000	0.000	0.000	0.000
Met-330	m0	0.998	0.002	0.994	0.005	0.998	0.001	0.994	0.006
	m1	0.000	0.000	0.003	0.002	0.000	0.000	0.001	0.001
	m2	0.001	0.001	0.000	0.000	0.000	0.000	0.001	0.000
	m3	0.000	0.000	0.001	0.001	0.001	0.000	0.001	0.001
	m4	0.000	0.001	0.001	0.001	0.000	0.000	0.002	0.003
	m5	0.000	0.000	0.001	0.001	0.000	0.000	0.001	0.001

	m0	0.988	0.010	0.980	0.032	0.997	0.004	0.998	0.001
	m1	0.001	0.001	0.001	0.001	0.000	0.000	0.001	0.002
Met-254	m2	0.010	0.008	0.017	0.028	0.002	0.004	0.000	0.000
	m3	0.000	0.000	0.000	0.000	0.000	0.000	0.000	0.000
	m4	0.001	0.001	0.002	0.003	0.000	0.000	0.000	0.000

See Table AI.6 for abbreviations

Table AI.8: Measured isotopomer enrichments using [1,2-^{13}C$_2$]-D-glucose. Internal glutamate and α-ketoglutarate

		normoxia			
		control		CDK4/6 inh	
		mean	SD	mean	SD
	m0	0.709	0.013	0.751	0.003
	m1	0.089	0.004	0.081	0.001
Glu-330	m2	0.154	0.006	0.135	0.002
	m3	0.041	0.002	0.027	0.000
	m4	0.008	0.000	0.006	0.000
	m0	0.733	0.013	0.757	0.007
	m1	0.036	0.003	0.045	0.004
Glu-432	m2	0.167	0.007	0.151	0.003
	m3	0.039	0.002	0.028	0.000
	m4	0.023	0.001	0.017	0.000
	m5	0.002	0.000	0.001	0.000
	m0	0.700	0.004	0.749	0.004
	m1	0.057	0.003	0.051	0.002
αKG-346	m2	0.178	0.001	0.152	0.002
	m3	0.037	0.001	0.027	0.000
	m4	0.025	0.001	0.017	0.000
	m5	0.004	0.001	0.004	0.000

Abbreviations according to Material and Methods: Glu-330, C2-C5 glutamate in the range 329-338 m/z; Glu-432, C1-C5 glutamate in the range 431-442 m/z; αKG-346, C1-C5 α-ketoglutarate in the range 345-356 m/z..

Table AI.9: Measured isotopomer enrichments using [U-^{13}C$_5$]-L-glutamine. Internal glutamate and α-ketoglutarate

		normoxia				hypoxia			
		control		CDK4/6 inh		control		CDK4/6 inh	
		mean	SD	mean	SD	mean	SD	mean	SD
	m0	0.345	0.003	0.349	0.002	0.280	0.012	0.366	0.007
	m1	0.165	0.003	0.144	0.001	0.059	0.028	0.047	0.002
Glu-330	m2	0.202	0.002	0.202	0.001	0.188	0.043	0.150	0.003
	m3	0.013	0.000	0.013	0.000	0.019	0.001	0.017	0.000
	m4	0.275	0.006	0.292	0.003	0.453	0.063	0.421	0.002
	m0	0.371	0.003	0.379	0.001	0.299	0.017	0.387	0.008
	m1	0.106	0.002	0.088	0.001	0.038	0.019	0.033	0.001
Glu-432	m2	0.067	0.001	0.060	0.000	0.041	0.013	0.039	0.000
	m3	0.198	0.002	0.198	0.001	0.182	0.045	0.135	0.003
	m4	0.015	0.000	0.015	0.000	0.026	0.003	0.024	0.000
	m5	0.244	0.005	0.259	0.002	0.413	0.061	0.382	0.002
	m0	0.332	0.003	0.342	0.003	0.312	0.004	0.393	0.007
	m1	0.122	0.002	0.104	0.005	0.010	0.010	0.004	0.003
αKG-346	m2	0.061	0.002	0.054	0.003	0.018	0.005	0.029	0.007
	m3	0.192	0.001	0.193	0.001	0.150	0.033	0.122	0.002
	m4	0.006	0.000	0.006	0.000	0.001	0.001	0.001	0.001
	m5	0.286	0.006	0.301	0.004	0.515	0.060	0.475	0.018

See Table AI.8 for abbreviations

Table AI.10: Measured isotopomer enrichments using [1,2-^{13}C$_2$]-D-glucose. Internal citrate

| | | normoxia | | | |
| | | control | | CDK4/6 inh | |
		mean	SD	mean	SD
	m0	0.441	0.003	0.520	0.004
	m1	0.079	0.001	0.078	0.001
	m2	0.328	0.001	0.295	0.003
Cit-459	m3	0.066	0.001	0.047	0.000
	m4	0.070	0.000	0.051	0.001
	m5	0.014	0.000	0.008	0.000
	m6	0.003	0.000	0.002	0.000
	m0	0.464	0.003	0.543	0.004
	m1	0.062	0.002	0.062	0.000
	m2	0.322	0.003	0.287	0.003
Cit-591	m3	0.070	0.002	0.052	0.001
	m4	0.065	0.001	0.047	0.001
	m5	0.014	0.000	0.008	0.000
	m6	0.002	0.000	0.001	0.000

Abbreviations according to Material and Methods: Cit-459 and Cit-591, C1-C6 citrate in the ranges 458-469 and 590-599 m/z, respectively.

Table AI.11: Measured isotopomer enrichments using [U-^{13}C$_5$]-L-glutamine. Internal citrate

| | | normoxia | | | | hypoxia | | | |
| | | control | | CDK4/6 inh | | control | | CDK4/6 inh | |
		mean	SD	mean	SD	mean	SD	mean	SD
	m0	0.395	0.005	0.404	0.018	0.358	0.007	0.471	0.013
	m1	0.148	0.002	0.122	0.004	0.055	0.020	0.041	0.003
	m2	0.166	0.001	0.152	0.004	0.147	0.028	0.101	0.004
Cit-459	m3	0.036	0.000	0.040	0.001	0.049	0.013	0.060	0.001
	m4	0.243	0.003	0.265	0.008	0.366	0.021	0.284	0.011
	m5	0.008	0.000	0.010	0.000	0.015	0.008	0.035	0.003
	m6	0.005	0.000	0.006	0.000	0.009	0.001	0.008	0.000
	m0	0.423	0.006	0.433	0.018	0.373	0.007	0.489	0.015
	m1	0.131	0.002	0.105	0.004	0.052	0.020	0.039	0.005
	m2	0.165	0.001	0.152	0.005	0.153	0.026	0.104	0.002
Cit-591	m3	0.038	0.001	0.042	0.001	0.054	0.013	0.064	0.001
	m4	0.223	0.002	0.244	0.007	0.341	0.018	0.263	0.010
	m5	0.015	0.001	0.018	0.001	0.022	0.010	0.036	0.001
	m6	0.004	0.000	0.005	0.000	0.007	0.001	0.006	0.001

See Table AI.10 for abbreviations.

Table AI.12: Measured isotopomer enrichments using [1,2-^{13}C$_2$]-D-glucose. Internal malate and aspartate

| | | normoxia | | | |
| | | control | | CDK4/6 inh | |
		mean	SD	mean	SD
	m0	0.712	0.004	0.760	0.001
	m1	0.088	0.002	0.077	0.001
Mal-419	m2	0.159	0.001	0.135	0.001
	m3	0.034	0.001	0.023	0.000
	m4	0.006	0.000	0.005	0.000
	m0	0.723	0.004	0.762	0.001
	m1	0.084	0.001	0.076	0.001
Asp-418	m2	0.153	0.002	0.134	0.001
	m3	0.034	0.001	0.023	0.000
	m4	0.006	0.000	0.005	0.000

Abbreviations according to Material and Methods: Mal-419, C1-C4 malate in the range 418-428 m/z; Asp-418, C1-C4 aspartate in the range 417-428 m/z.

Table AI.13: Measured isotopomer enrichments using [U-^{13}C$_5$]-L-glutamine. Internal malate and aspartate

| | | normoxia | | | | hypoxia | | | |
| | | control | | CDK4/6 inh | | control | | CDK4/6 inh | |
		mean	SD	mean	SD	mean	SD	mean	SD
	m0	0.458	0.041	0.458	0.047	0.432	0.015	0.518	0.017
	m1	0.150	0.012	0.129	0.012	0.062	0.020	0.041	0.003
Mal-419	m2	0.173	0.014	0.168	0.015	0.155	0.025	0.105	0.005
	m3	0.027	0.002	0.028	0.002	0.058	0.017	0.092	0.006
	m4	0.193	0.013	0.217	0.018	0.294	0.012	0.245	0.012
	m0	0.455	0.002	0.428	0.004	0.484	0.039	0.545	0.017
	m1	0.148	0.004	0.132	0.003	0.043	0.026	0.043	0.002
Asp-418	m2	0.179	0.001	0.182	0.001	0.132	0.050	0.114	0.005
	m3	0.025	0.000	0.029	0.000	0.080	0.052	0.072	0.005
	m4	0.193	0.003	0.228	0.001	0.261	0.013	0.225	0.013

See Table AI.12 for abbreviations.

Table AI.14: Measured isotopomer enrichments using [1,2-^{13}C$_2$]-D-glucose. Internal lactate, pyruvate and alanine

| | | normoxia | | | |
| | | control | | CDK4/6 inh | |
		mean	SD	mean	SD
	m0	0.644	0.011	0.809	0.033
Lac-261	m1	0.029	0.002	0.019	0.003
	m2	0.320	0.009	0.168	0.029
	m3	0.007	0.000	0.004	0.001
	m0	0.652	0.007	0.721	0.020
Pyr-174	m1	0.040	0.004	0.044	0.009
	m2	0.296	0.007	0.227	0.019
	m3	0.012	0.001	0.008	0.003
	m0	0.675	0.003	0.763	0.004
Ala-232	m1	0.029	0.003	0.024	0.001
	m2	0.296	0.000	0.212	0.003
	m0	0.647	0.005	0.737	0.004
Ala-260	m1	0.021	0.005	0.021	0.001
	m2	0.330	0.001	0.238	0.004
	m3	0.003	0.002	0.005	0.000

Abbreviations according to Material and Methods: Lac-261, C1-C3 lactate in the range 260-269 m/z; Pyr-174, C1-C3 pyruvate in the range 173-181 m/z; Ala-232, C2-C3 alanine in the range 231-239 m/z; Ala-260, C1-C3 alanine in the range 259-268 m/z.

Table AI.15: Measured isotopomer enrichments using [U-^{13}C$_5$]-L-glutamine. Internal lactate, pyruvate and alanine

| | | normoxia | | | | hypoxia | | | |
| | | control | | CDK4/6 inh | | control | | CDK4/6 inh | |
		mean	SD	mean	SD	mean	SD	mean	SD
	m0	0.987	0.000	0.987	0.001	0.992	0.002	0.990	0.000
Lac-261	m1	0.004	0.000	0.004	0.000	0.003	0.000	0.003	0.000
	m2	0.002	0.000	0.003	0.000	0.002	0.001	0.005	0.000
	m3	0.007	0.000	0.006	0.001	0.003	0.001	0.002	0.000
	m0	0.939	0.011	0.918	0.029	0.976	0.005	0.983	0.004
Pyr-174	m1	0.021	0.005	0.027	0.007	0.000	0.000	0.000	0.000
	m2	0.009	0.001	0.007	0.003	0.010	0.002	0.013	0.002
	m3	0.031	0.004	0.049	0.020	0.014	0.003	0.004	0.002
	m0	0.978	0.000	0.976	0.001	0.885	0.003	0.899	0.003
Ala-232	m1	0.007	0.001	0.009	0.001	0.109	0.003	0.098	0.003
	m2	0.014	0.000	0.014	0.000	0.007	0.001	0.003	0.000
	m0	0.981	0.001	0.976	0.001	0.897	0.007	0.912	0.005
Ala-260	m1	0.003	0.000	0.007	0.001	0.095	0.006	0.080	0.003
	m2	0.005	0.000	0.004	0.000	0.000	0.000	0.002	0.004
	m3	0.012	0.000	0.012	0.000	0.007	0.001	0.005	0.000

See Table AI.14 for abbreviations.

Appendix II

Gene Set Enrichment Analysis (GSEA)

II.1 Summary of the results

Genetic association studies were performed using Gene Set Enrichment Analysis (GSEA) [1] looking for associated gene signatures, which provided the evidence of partially shared mechanisms between the analysed treatment - here CDK4/6 inhibition - and the control condition affecting regulatory factors with a key role in cancer and metabolism. To generate hypotheses, the sole analysis of the "hallmark gene sets" collection, envisioned as a starting point of the GSEA analysis, is sufficient to suggest that CDK4/6 inhibition correlates with genes associated with several key regulators involved in cancer and metabolism. Statistics associated with GSEA provide a selection of gene sets upregulated in CDK4/6 knockdown cells (CDK) and control cells (CONTROL) are shown:

	data sets	filtered out gene sets (*)	significant gene sets			
			CDK4/6-inhibited cells		Control cells	
			FDR < 5%	FWER < 1%	FDR < 5%	FWER < 1%
MSigDB v5.0	*hallmark gene sets*	0 / 50	8	4	19	6
	curated gene sets	1043 / 4530	293	49	412	56
	GO gene sets	462 / 1454	51	12	0	0
	oncogenic signatures	2 / 189	15	4	56	10

(*) Gene set size filters (min=15, max=500) resulted in filtering out gene sets. The remaining gene sets were used in the analyses

The figures in this Appendix summarises specific gene sets from the MSigDB collection [1] that appear to be relevance in our analyses and among those with the most significant enrichments according to GSEA's statistics:

ASSOCIATED GENE SETS
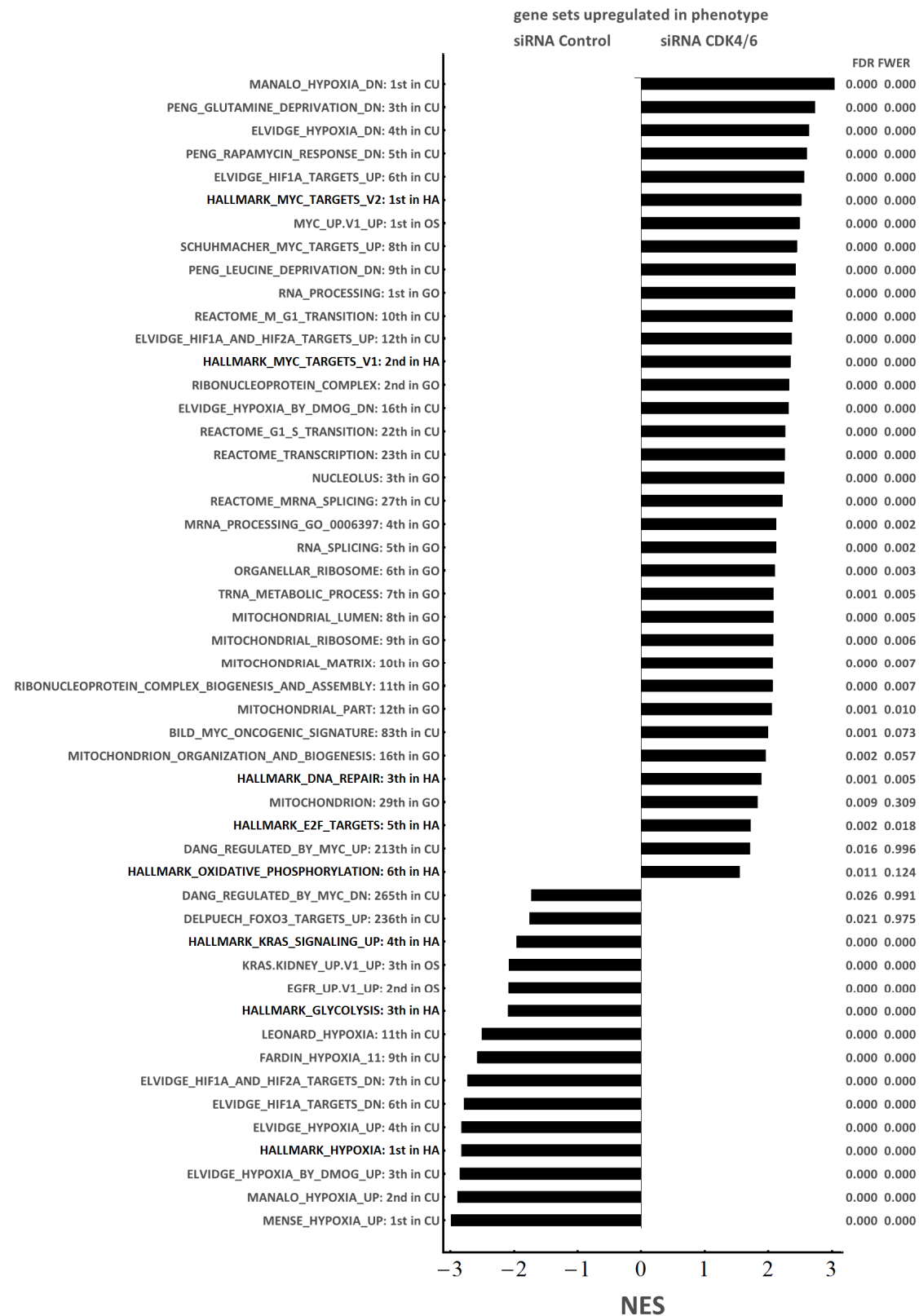
HA, CU, GO and OS refer to the "hallmark gene sets" (in black), "Curated gene sets", "GO gene sets" and "Oncogenic signatures" collections, respectively.

II.2 Enrichment plots

Figures below are GSEA enrichment plots showing the correlation of the expression profiles of CDK4/6 knockdown cells (CDK) *versus* control cells (CONTROL) with gene expression signatures from specific gene sets from the MSigDB collection [1]. See instructions in Materials and Methods for interpretation of the plots. Gene sets with a distinct peak at the beginning or end of the ranked list are the most interesting. For example, on the one hand, the positive peak toward the start of the gene set HALLMARK_MYC_TARGETS_V1 indicates a significant enrichment of the analysed gene set in CDK4/6-inhibited phenotype; on the other hand, the negative peak towards the end of the gene set HALLMARK_HYPOXIA indicates a significant enrichment of the analysed gene set in CONTROL phenotype.

II.2.1 Gene sets associated with MYC

HALLMARK_MYC_TARGETS_V1
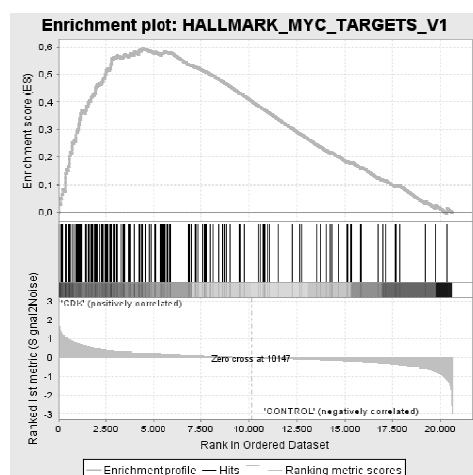
SCHUHMACHER_MYC_TARGETS_UP
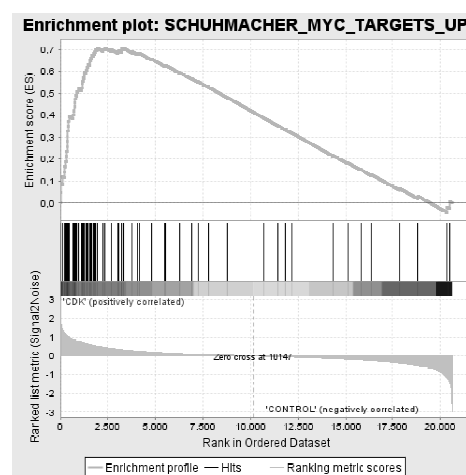
Genes up-regulated in P493-6 cells (Burkitt's lymphoma) induced to express MYC [2].

HALLMARK_MYC_TARGETS_V2
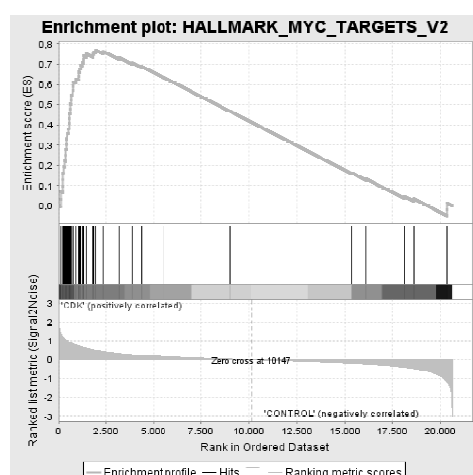
A subgroup of genes regulated by MYC - version 1 (v1) and version 2 (v2). Response to CDK4/6 inhibition follows the same direction than response to MYC activity.

BILD_MYC_ONCOGENIC_SIGNATURE
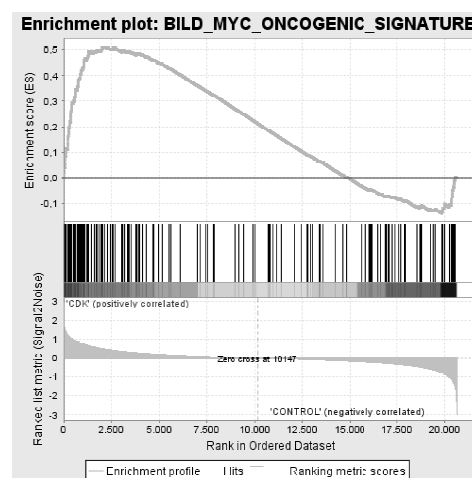
Genes selected in supervised analyses to discriminate cells expressing MYC from control cells expressing GFP [3].

299

DANG_REGULATED_BY_MYC_UP/DN
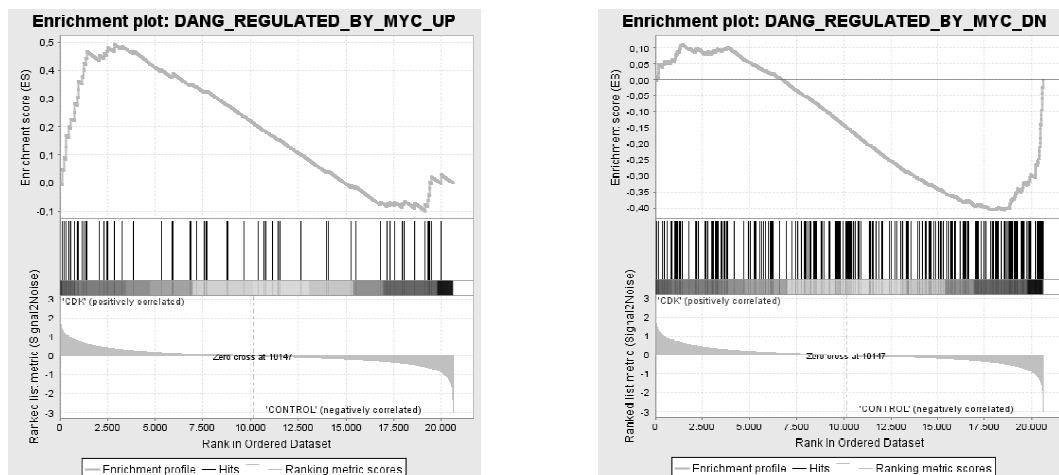
Genes up-regulated (UP) and down-regulated (DN) by MYC, according to the MYC Target Gene Database [4].

According to these enrichment plots, response to CDK4/6 inhibition follows the same direction than response to MYC activity.

II.2.2 Gene sets associated with hypoxia

HALLMARK_HYPOXIA
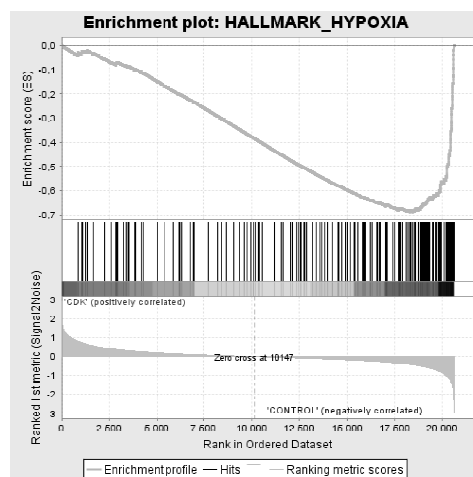
Genes up-regulated in response to low oxygen levels (hypoxia). The market negative peak toward the final indicates a significant enrichment of the analysed gene set in CONTROL phenotype.

MANALO_HYPOXIA_UP/DN
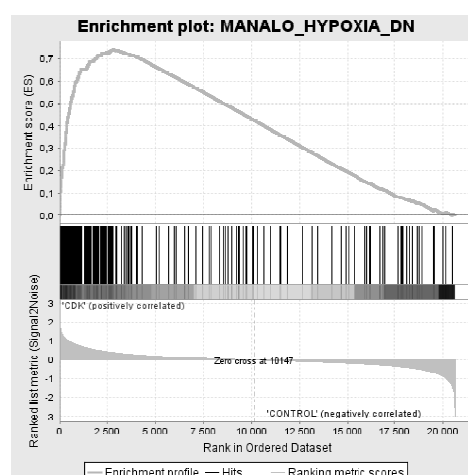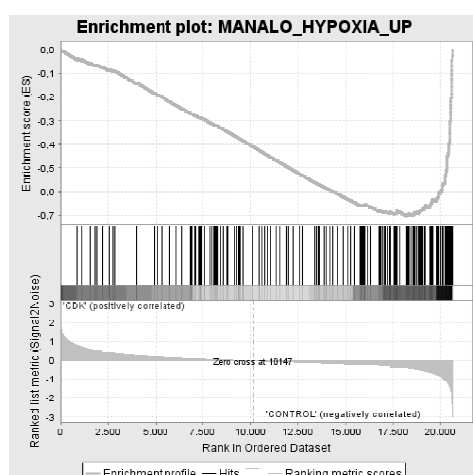
Genes up-regulated (UP) and down-regulated (DN) in response to both hypoxia and overexpression of an active form of HIF1A [5].

ELVIDGE_HYPOXIA_UP/DN
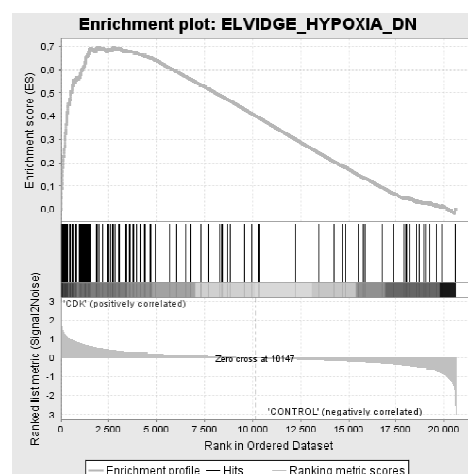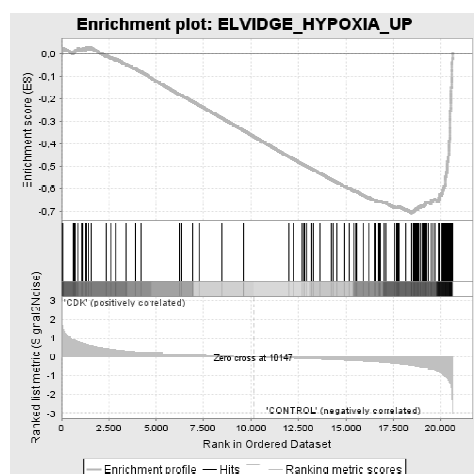
Genes up-regulated (UP) and down-regulated (DN) in MCF7 cells (breast cancer) under hypoxia conditions [6].

ELVIDGE_HIF1A_TARGETS_UP/DN
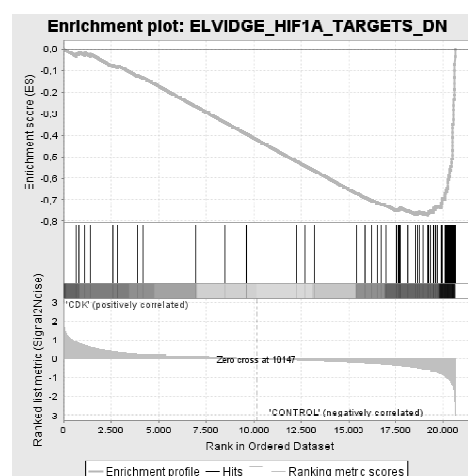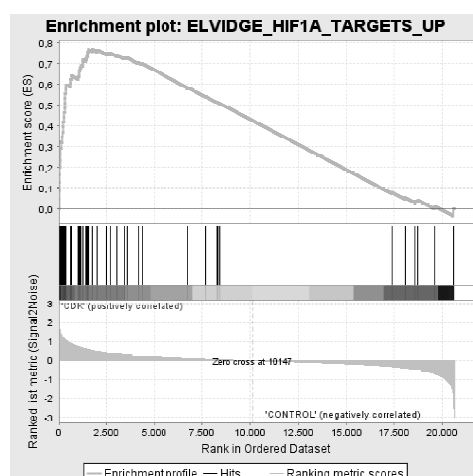
Genes up-regulated (UP) and down-regulated (DN) in MCF7 cells (breast cancer) after knockdown of HIF1α by RNAi [6].

ELVIDGE_HIF1A_AND_HIF2A_TARGETS_UP/DN
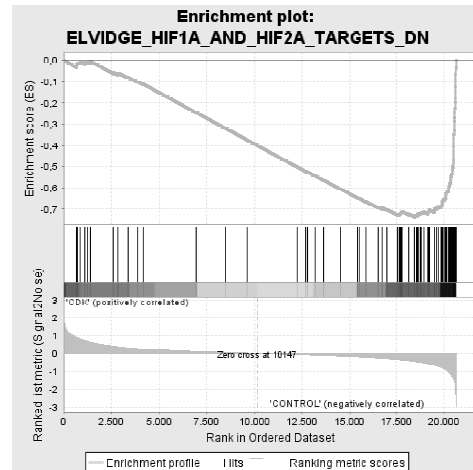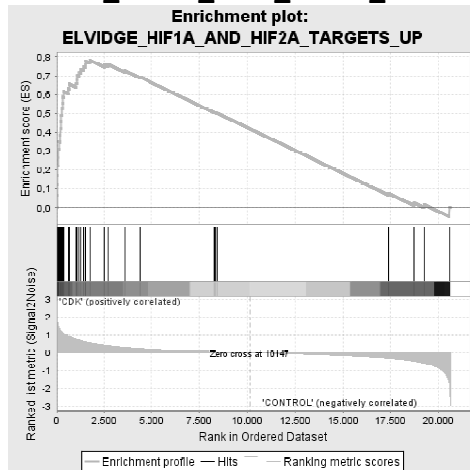
Genes up-regulated (UP) and down-regulated (DN) in MCF7 cells (breast cancer) after knockdown of both HIF1A and HIF2A by RNAi [6].

ELVIDGE_HYPOXIA_BY_DMOG_UP/DN
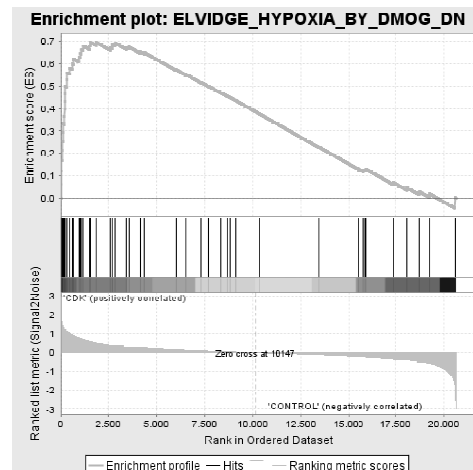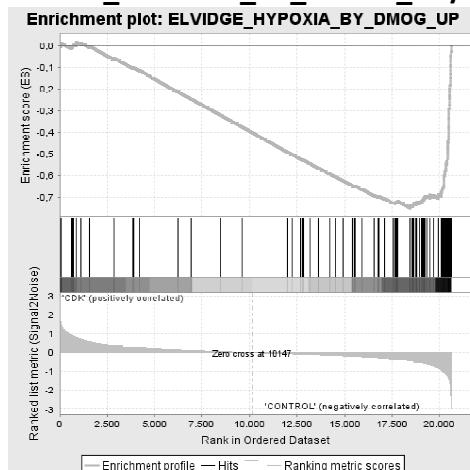
Genes up-regulated (UP) and down-regulated (DN) in MCF7 cells (breast cancer) treated with hypoxia mimetic DMOG [6]. DMOG (dimethyloxalylglycine) is a cell permeable competitive inhibitor of prolyl hydroxylase leading to the stabilisation of HIF1α.
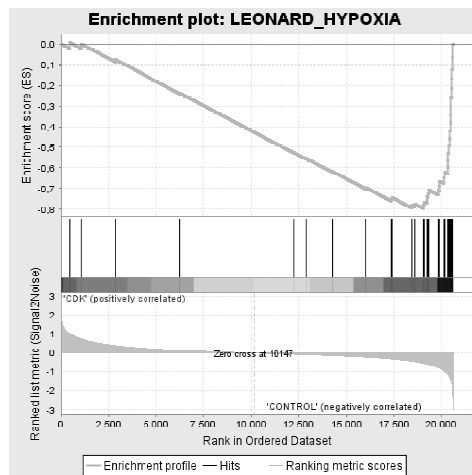
MENSE_HYPOXIA_UP
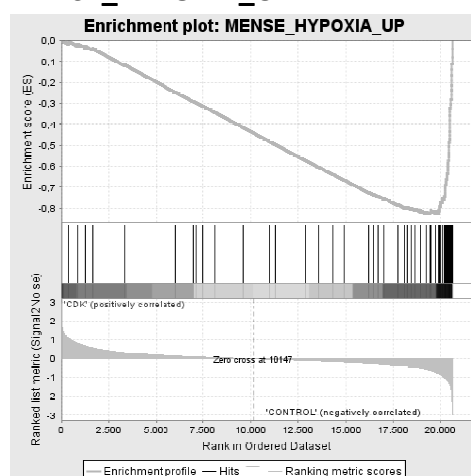
Hypoxia response genes up-regulated in both astrocytes and HeLa cell line [7].

FARDIN_HYPOXIA_11
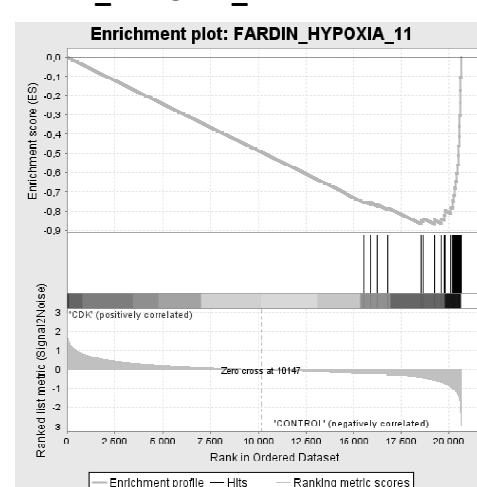
Genes in the hypoxia signature, based on analysis of 11 neuroblastoma cell lines in hypoxia and normal oxygen conditions [8].

LEONARD_HYPOXIA

Genes up-regulated in HK-2 cells kidney tubular epithelium under hypoxia and down-regulated on re-oxygenation [9].

According to these enrichment plots, response to CDK4/6 inhibition follows the opposite direction than response to hypoxia or HIF1α stabilisation. Here, the comparison of pairs of gene sets that separately describe up-regulated and down-regulated genes provide a nice example of opposite direction. On the one hand, genes up-regulated in CDK4/6-inhibited cells are down-regulated under hypoxia or treatment with hypoxia mimetic DMOG, and vice versa. On the other hand, genes up-regulated in CDK4/6 inhibited cells are up-regulated after knockdown of hypoxia mediator HIF1α, and genes down-regulated in CDK4/6-inhibited cells are down-regulated after knockdown of hypoxia mediator HIF1α.

II.3 Gene sets associated with mTOR

PENG_RAPAMYCIN_RESPONSE_DN
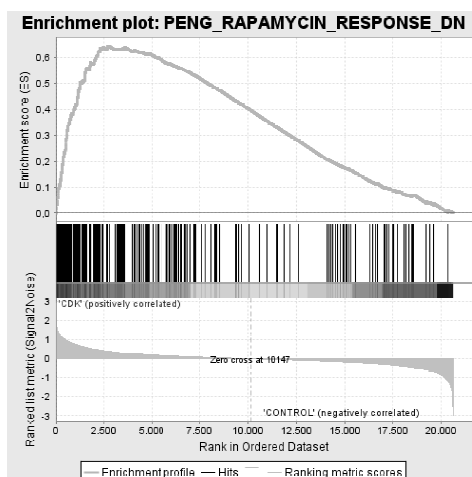
Genes down-regulated in BJUB cells (B-lymphoma) in response to rapamycin (clinically known as sirolimus) treatment [10]. Rapamycin is an inhibitor of mTOR.

According to these enrichment plots, response to CDK4/6 inhibition follows the opposite direction than response to mTOR inhibition by rapamycin.
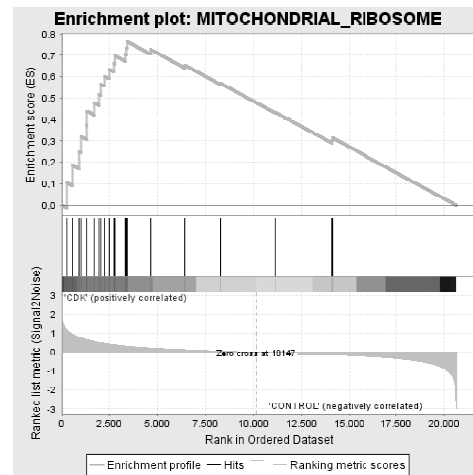
II.4 Gene sets associated with mitochondrial activity
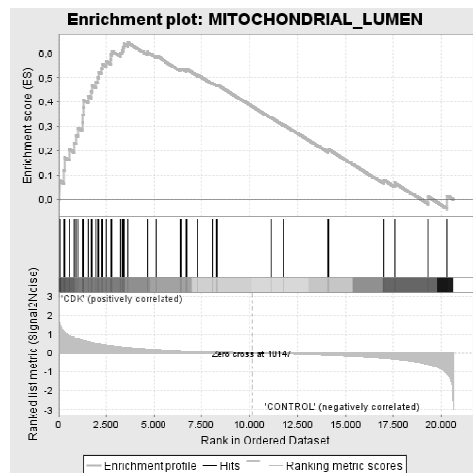
HALLMARK_OXIDATIVE_PHOSPHORY-LATION
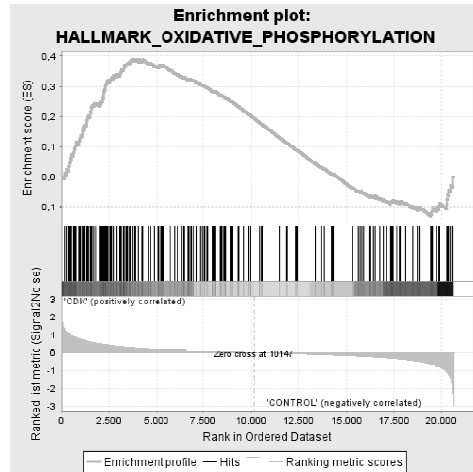
Genes encoding proteins involved in oxidative phosphorylation.
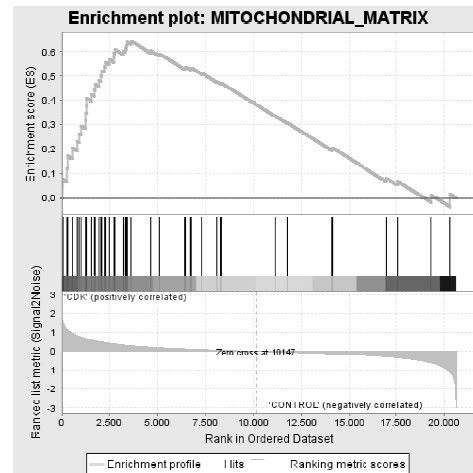
MITOCHONDRIAL_RIBOSOME

Genes annotated by the GO term GO:0005761. A ribosome found in the mitochondrion of a eukaryotic cell; contains a characteristic set of proteins distinct from those of cytosolic ribosomes.

MITOCHONDRIAL_LUMEN

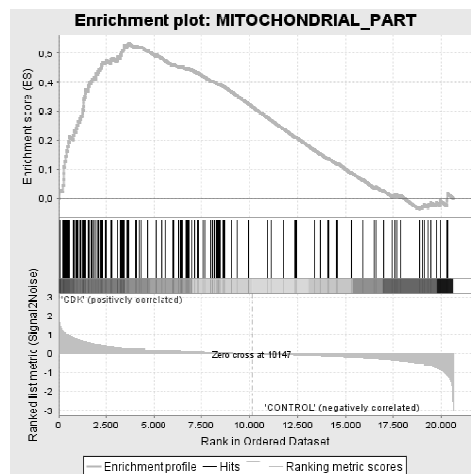Genes annotated by the GO term GO:0031980. The volume enclosed by the mitochondrial inner membrane.
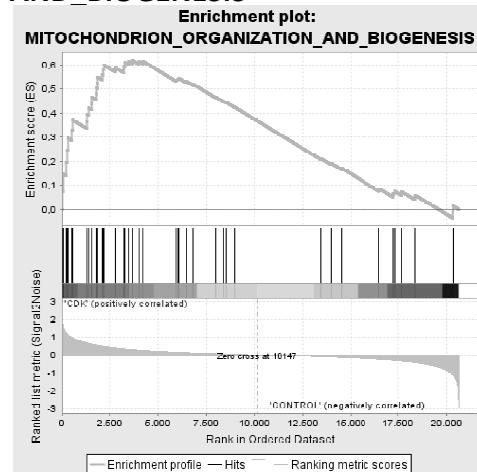
MITOCHONDRIAL_MATRIX

Genes annotated by the GO term GO:0005759. The gel-like material, with considerable fine structure, that lies in the matrix space, or lumen, of a mitochondrion. It contains the enzymes of the tricarboxylic acid cycle and, in some organisms, the enzymes concerned with fatty-acid oxidation.

MITOCHONDRIAL_PART

Genes annotated by the GO term GO:0044429. Any constituent part of a mitochondrion, a semiautonomous, self-replicating organelle that occurs in varying numbers, shapes, and sizes in the cytoplasm of virtually all eukaryotic cells. It is notably the site of tissue respiration.

MITOCHONDRION_ORGANIZATION_ AND_BIOGENESIS

Genes annotated by the GO term GO:0007005. A process that is carried out at the cellular level which results in the formation, arrangement of constituent parts, or disassembly of a mitochondrion; includes mitochondrial morphology and distribution, and replication of the mitochondrial genome as well as synthesis of new mitochondrial components.

MITOCHONDRION
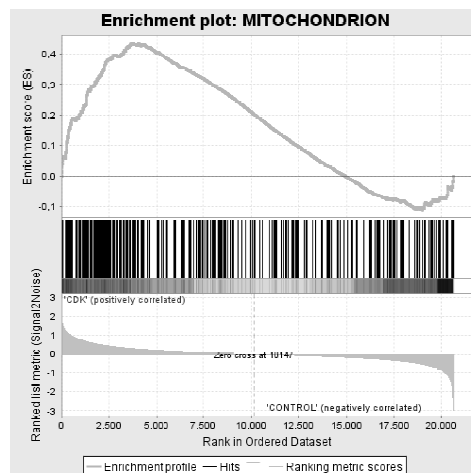
Genes annotated by the GO term GO:0005739. A semiautonomous, self replicating organelle that occurs in varying numbers, shapes, and sizes in the cytoplasm of virtually all eukaryotic cells. It is notably the site of tissue respiration.

According to these enrichment plots, response to CDK4/6 inhibition up-regulates genes associated with oxidative phosphorylation and other mitochondrial components and processes.

II.5 Other gene sets relevant to our analyses

HALLMARK_GLYCOLYSIS
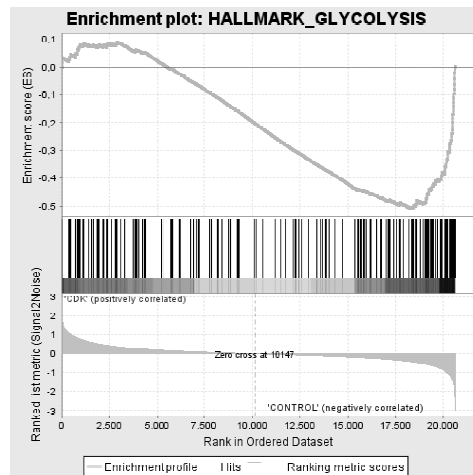
Genes encoding proteins involved in glycolysis and gluconeogenesis. Accordingly, response to CDK4/6 inhibition down-regulates these genes.

HALLMARK_E2F_TARGETS
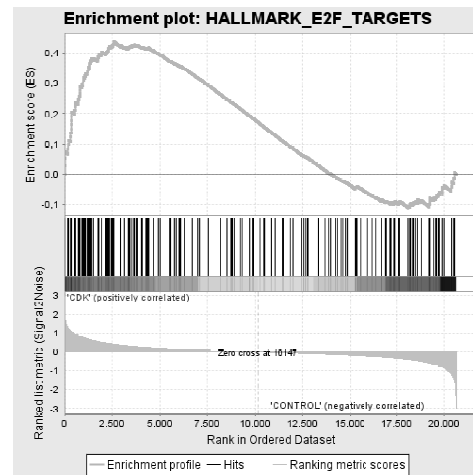
Genes encoding cell cycle related targets of E2F transcription factors. Accordingly, response to CDK4/6 inhibition mainly up-regulates these genes.

HALLMARK_DNA_REPAIR
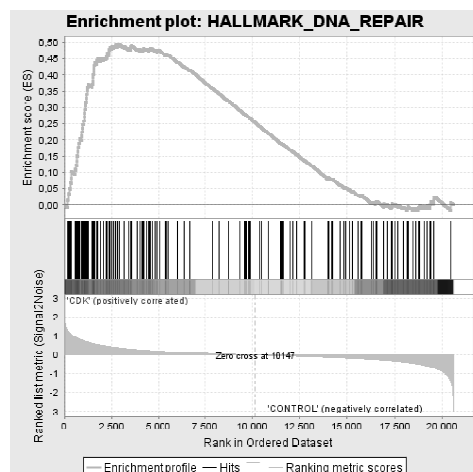
Genes involved in DNA repair. Accordingly, response to CDK4/6 inhibition up-regulates these genes.

HALLMARK_KRAS_SIGNALING_UP
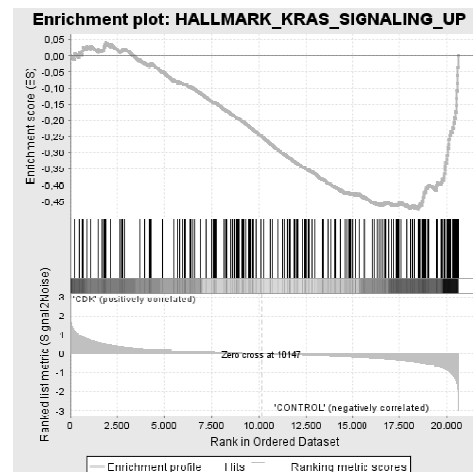
Genes up-regulated by KRAS activation. Accordingly, response to CDK4/6 inhibition mainly down-regulates these genes.

PENG_GLUTAMINE_DEPRIVATION_DN
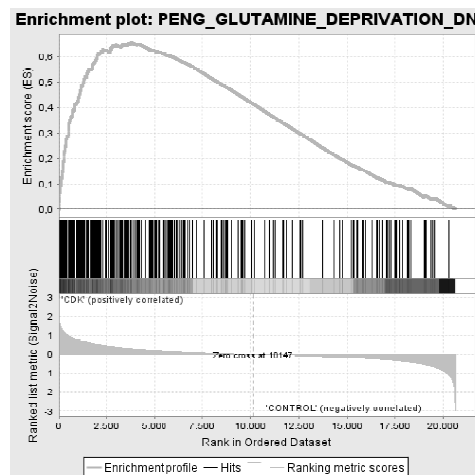
Genes down-regulated in BJAB cells (B-lymphoma) after glutamine deprivation [10]. Accordingly, response to CDK4/6 inhibition follows the opposite direction than response to glutamine deprivation.

REACTOME_M_G1_TRANSITION
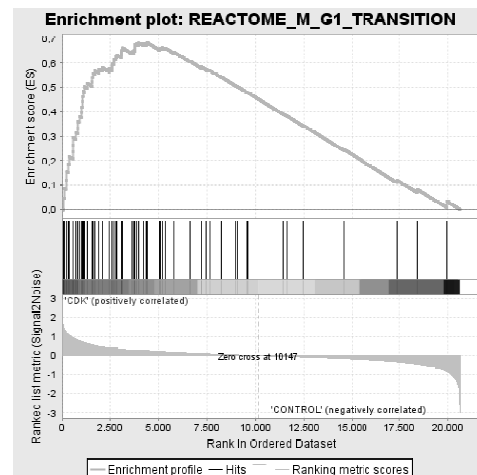
Genes involved in M/G1 Transition. Accordingly, response to CDK4/6 inhibition mainly up-regulates these genes.

PENG_LEUCINE_DEPRIVATION_DN
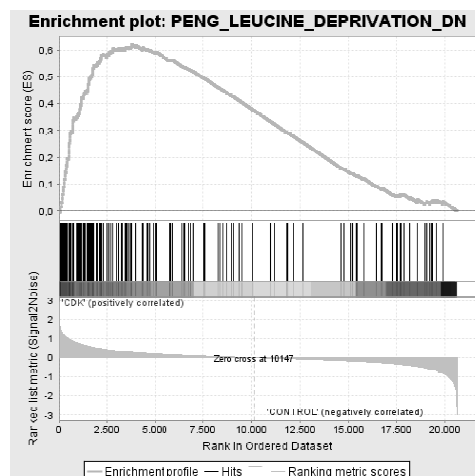
Genes down-regulated in BJAB cells (B-lymphoma) after leucine deprivation [10]. Accordingly, response to CDK4/6 inhibition follows the opposite direction than response to leucine deprivation.

REACTOME_G1_S_TRANSITION
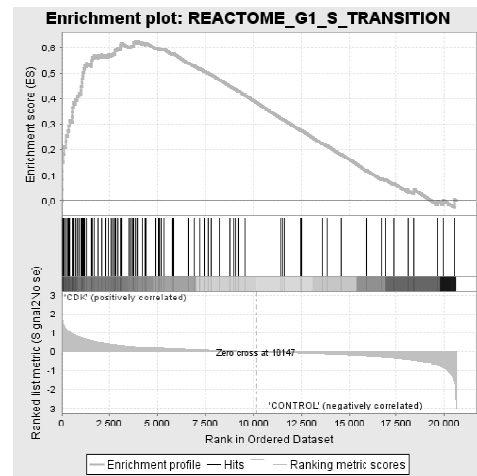
Genes involved in G1/S Transition. Accordingly, response to CDK4/6 inhibition mainly up-regulates these genes.

REACTOME_TRANSCRIPTION
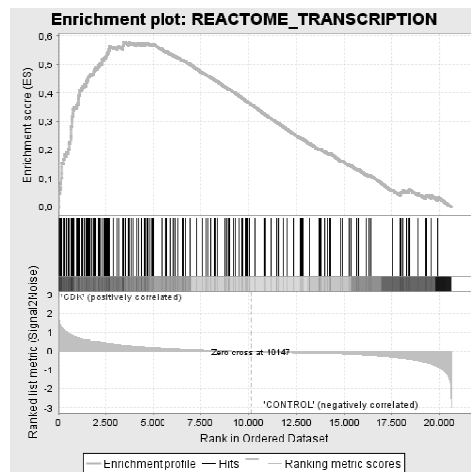
Genes involved in transcription. Accordingly, response to CDK4/6 inhibition mainly up-regulates these genes.

REACTOME_MRNA_SPLICING
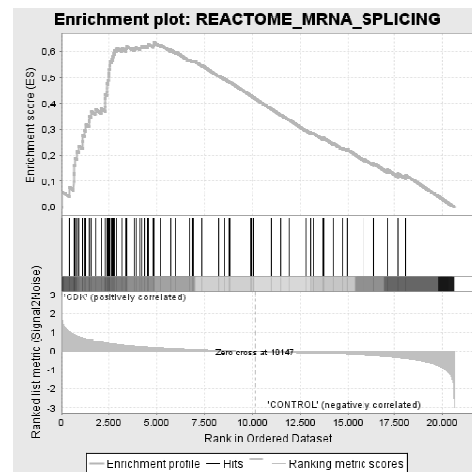
Genes involved in mRNA Splicing. Accordingly, response to CDK4/6 inhibition mainly upregulates these genes.

DELPUECH_FOXO3_TARGETS_UP
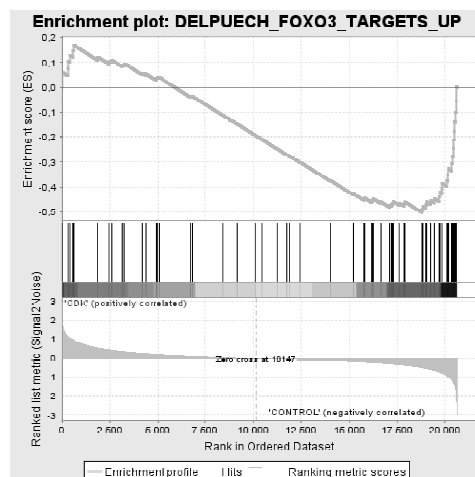
Genes up-regulated in DL23 cells (colon cancer) upon expression of an activated form of FOXO3 [11]. Accordingly, FOXO3a target gens are downregulated in CDK4/6-inhibited cells.

II.6 References

1. Subramanian A, Tamayo P, Mootha VK, Mukherjee S, Ebert BL, et al. (2005) Gene set enrichment analysis: a knowledge-based approach for interpreting genome-wide expression profiles. Proc Natl Acad Sci U S A 102: 15545-15550.
2. Schuhmacher M, Kohlhuber F, Holzel M, Kaiser C, Burtscher H, et al. (2001) The transcriptional program of a human B cell line in response to Myc. Nucleic Acids Res 29: 397-406.
3. Bild AH, Yao G, Chang JT, Wang Q, Potti A, et al. (2006) Oncogenic pathway signatures in human cancers as a guide to targeted therapies. Nature 439: 353-357. Epub 2005 Nov 2006.
4. Zeller KI, Jegga AG, Aronow BJ, O'Donnell KA, Dang CV (2003) An integrated database of genes responsive to the Myc oncogenic transcription factor: identification of direct genomic targets. Genome Biol 4: R69. Epub 2003 Sep 2011.
5. Manalo DJ, Rowan A, Lavoie T, Natarajan L, Kelly BD, et al. (2005) Transcriptional regulation of vascular endothelial cell responses to hypoxia by HIF-1. Blood 105: 659-669.
6. Elvidge GP, Glenny L, Appelhoff RJ, Ratcliffe PJ, Ragoussis J, et al. (2006) Concordant regulation of gene expression by hypoxia and 2-oxoglutarate-dependent dioxygenase inhibition: the role of HIF-1alpha, HIF-2alpha, and other pathways. J Biol Chem 281: 15215-15226.
7. Mense SM, Sengupta A, Zhou M, Lan C, Bentsman G, et al. (2006) Gene expression profiling reveals the profound upregulation of hypoxia-responsive genes in primary human astrocytes. Physiol Genomics 25: 435-449.
8. Fardin P, Barla A, Mosci S, Rosasco L, Verri A, et al. (2010) A biology-driven approach identifies the hypoxia gene signature as a predictor of the outcome of neuroblastoma patients. Mol Cancer 9:185.: 10.1186/1476-4598-1189-1185.
9. Leonard MO, Cottell DC, Godson C, Brady HR, Taylor CT (2003) The role of HIF-1 alpha in transcriptional regulation of the proximal tubular epithelial cell response to hypoxia. J Biol Chem 278: 40296-40304. Epub 42003 Jul 40228.
10. Peng T, Golub TR, Sabatini DM (2002) The immunosuppressant rapamycin mimics a starvation-like signal distinct from amino acid and glucose deprivation. Mol Cell Biol 22: 5575-5584.
11. Delpuech O, Griffiths B, East P, Essafi A, Lam EWF, et al. (2007) Induction of Mxi1-SR by FOXO3a Contributes to Repression of Myc-Dependent Gene Expression. Molecular and Cellular Biology 27: 4917-4930.

Appendix III

Gene Expression
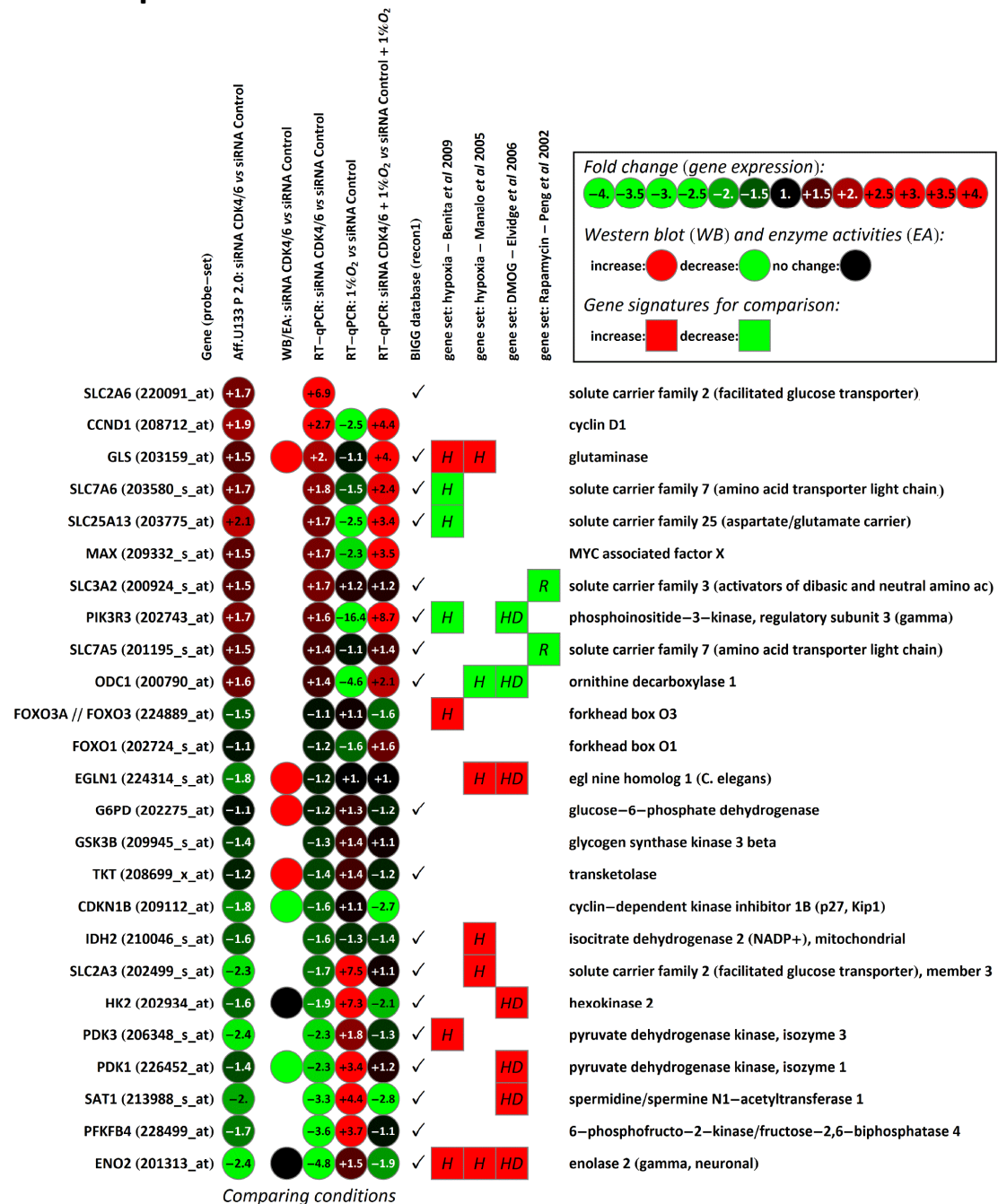
Figure A.III.1.
1st column, subset of genes differentially expressed identified from *Affymetrix GeneChips*. The encircled numbers are fold changes measuring differential gene expression / protein level / enzyme activity with respect to control cells. **2nd column**, effect of CDK4/6 inhibition (CDK4/6$^-$) in gene expression measured from *Affymetrix GeneChips*. **3rd column**, effect of CDK4/6 inhibition in protein levels by Western blot or enzyme activities. **4th column**, effect of CDK4/6 inhibition in gene expression measured by RT-qPCR. **5th column**, effect of hypoxia (1%O$_2$) in gene expression by RT-qPCR. **6th column**, effect of combination of CDK4/6 inhibition and hypoxia in gene expression by RT-qPCR. **7th column**, genes encoding metabolic enzymes or transporters identified according to BIGG database [12]. Colored squares identify the direction of changes (up-regulated or down-regulated) of some of the genes as described in four gene sets: 1) Hypoxia Inducible Factor-1 (HIF-1)-target genes that form the core response to hypoxia [13] (gene set: hypoxia – Benita et al 2009) (**8th column**); "MANALO_HYPOXIA_UP+DN" [5] (gene set: hypoxia – Manalo et al 2005), "ELVIDGE_HYPOXIA_BY_DMOG_UP+DN" [6] (gene set: DMOG – Elvidge et al 2006) (**9th column**); and PENG_RAPAMYCIN_RESPONSE_UP+DN" [10] (gene set: Rapamycin – Peng et al 2002) (**10th column**).

References

1. Schellenberger J, Park JO, Conrad TM, Palsson BO (2010) BiGG: a Biochemical Genetic and Genomic knowledgebase of large scale metabolic reconstructions. BMC Bioinformatics 11: 213.
2. Benita Y, Kikuchi H, Smith AD, Zhang MQ, Chung DC, et al. (2009) An integrative genomics approach identifies Hypoxia Inducible Factor-1 (HIF-1)-target genes that form the core response to hypoxia. Nucleic Acids Res 37: 4587-4602.
3. Manalo DJ, Rowan A, Lavoie T, Natarajan L, Kelly BD, et al. (2005) Transcriptional regulation of vascular endothelial cell responses to hypoxia by HIF-1. Blood 105: 659-669.
4. Elvidge GP, Glenny L, Appelhoff RJ, Ratcliffe PJ, Ragoussis J, et al. (2006) Concordant regulation of gene expression by hypoxia and 2-oxoglutarate-dependent dioxygenase inhibition: the role of HIF-1alpha, HIF-2alpha, and other pathways. J Biol Chem 281: 15215-15226.
5. Peng T, Golub TR, Sabatini DM (2002) The immunosuppressant rapamycin mimics a starvation-like signal distinct from amino acid and glucose deprivation. Mol Cell Biol 22: 5575-5584.

Appendix IV

Integrated Picture

VI.1 Integrated picture

An integrated picture is provided below in Figure SII.1 of observed and estimated changes in the metabolic and gene and protein expression profiles resulting from CDK4/6 inhibition. The scope of this graphical network covers all species involved in our metabolic profile and analysis of ^{13}C propagation. Each arrow identifies a metabolic step, which corresponds to one chemical transformation – catalysed by an enzyme or a group of enzymes – or transport process. This picture is based on data bases of human metabolism – BIGG database [1] (includes the human genome scale network reconstruction, *recon 1* [2]), metacyc database [3], ExPASy [4] and KEGG [5] – and generic [6] and specific literature for polyamine [7-14] [15-18], methionine salvage cycle [19-23], proline [24-27] and glycine, serine and folate metabolisms [28-31]. Reactions are included to emphasise parts of the metabolism that are modulated as a consequence of CDK4/6 inhibition. These modulations are reflected in changes in the levels of metabolic intermediaries (polyamines), label propagation (fatty acids) and gene expression. Although the direction of transcriptional or translational changes is not necessarily in correspondence with the direction of changes in the fluxes, they are likely to reflect modulated parts of the metabolism. Genes and proteins differentially expressed are associated with their encoded enzymes or transporters.

Quantified fluxes in Figure SII.1 correspond to measured values (underlined in yellow) or estimated according to a ^{13}C-metabolic flux analysis strategy [32, 33]. Our applied procedure for ^{13}C-based model-based estimation of fluxes is explained in this annex and the resulting flux distributions are listed in Table SII.8.

Regarding measured values, net fluxes (rates) per cell of uptake and release of different metabolites (J_{met}) – glucose, lactate, and all amino acids – were estimated from the experimental variation of concentrations in media and the changes in the number of cells measured during 24 hours, as detailed in Materials and Methods. Analogously, we estimated the net flux of glycogen accumulation and protein synthesis (for new biomass) per cell and per glucose residue or amino acid, respectively. The difference is that we used the content of glycogen in the pellet or the estimated protein per cell instead of medium concentrations. These net fluxes of glycogen accumulation and protein synthesis are equivalent to output

fluxes, which must not be confused with the turnover rates. Uptake of essential amino acids for protein synthesis is in a quasi-perfect proportion with their relative abundances in proteins, as previously reported [29] (Figure SII.2). Measured rates of O_2 consumption for ATP production by mitochondrial respiration (J_{OCR}) were also considered.
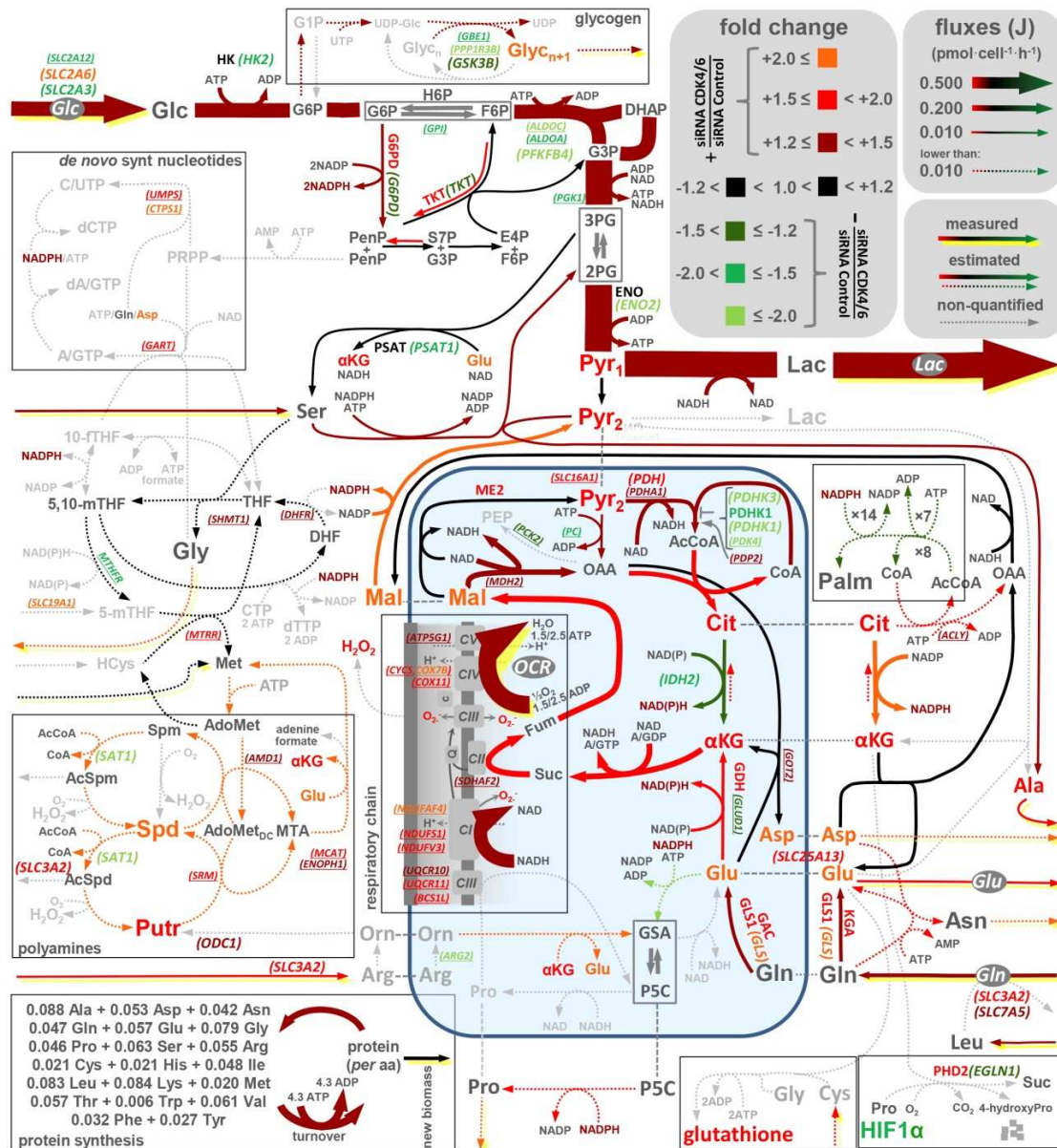
Figure SII.1 Integrated picture

Bold letters refer to metabolites, proteins or enzyme activities, italic letters refer to genes measured by RT-qPCR, and underlined letters refer to genes identified from the normalised RMA expression data obtained from the *Affymetrix GeneChip* arrays). Fold changes refer to CDK4/6-inhibited cells with respect to control cells. The magnitude of the fluxes refers to control cells. Fold changes for fluxes and concentrations are based on a comparison per cell, while fold changes for protein or gene expression are based on different criteria as detailed in Materials and Methods. See abbreviations in the List of abbreviations in this annex.
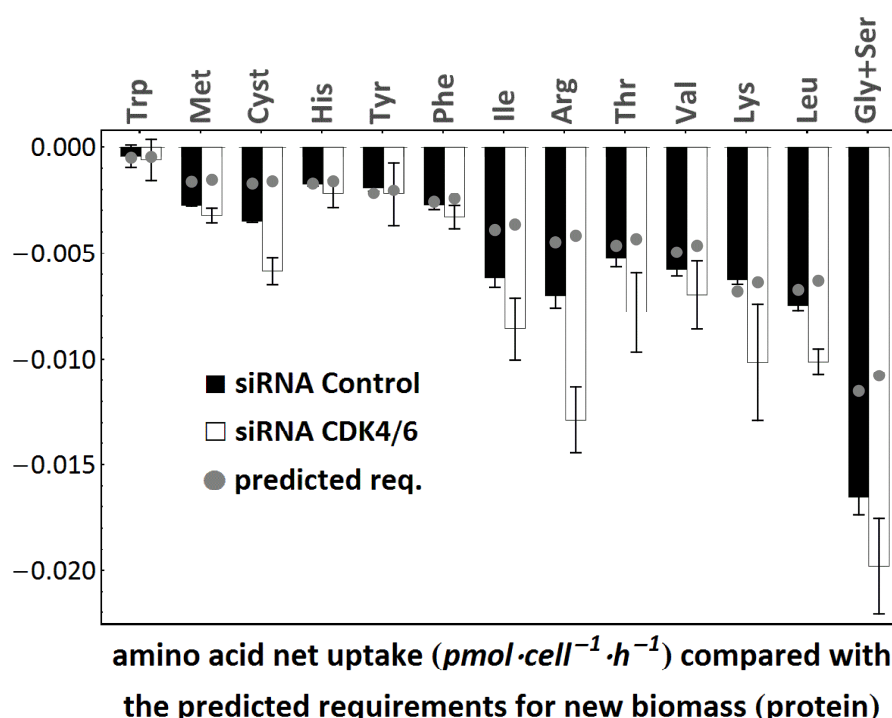
Figure SII.2 Amino acid exchange and demand for protein.

Bars represent the experimental measurements for uptake or release of all amino acids. Gray dots represent demands for protein synthesis estimated for each amino acid and the calculated from the estimated rates of protein synthesis per amino acid (J_{Prot}) and the relative abundance of these amino acids in proteins [34]. The calculated demands for protein production matched the measured uptakes of essential amino acids in control cells, supporting the hypothesis [29] that the import rate of an essential amino acid is proportional to the demand protein synthesis, with a coefficient of proportionality matching its relative abundance in the proteome. The validity of this assumption for tumour-derived cell lines has been tested [29] using the measured metabolic cell-medium exchange fluxes reported for the NCI-60 panel [28]. Also, the sum of serine and glycine exchange rates results in a net import that matches the overall serine and glycine requirements for protein synthesis, as previously noted for all NCI60 cell lines [29]. In CDK4/6 inhibited cells, there is an extra uptake of these amino acids with respect to the value required for protein synthesis.

VI.2 ^{13}C-based model-based estimation of fluxes

VI.2.1 Methods

Procedure description

With the aim to solve hypotheses regarding flux distributions, by comparing measured and predicted mass isotopomer distributions, the reliability of hypotheses regarding flux distributions can be evaluated. A computer programme was developed with Mathematica [35] and applied to predict the ^{13}C enrichments. The estimation of the reaction fluxes was based on the addition of successive constraints. In order to satisfy all constraints and taking advantage of the linear nature of the problem to be solved, the range of possible values for each flux was determined using linear programming where each flux is maximised or minimised while leaving all other fluxes free [36-38].

A detailed description of such procedure and results is provided using a simple model for only three dependent variables:

1. Setting mass balance equations around metabolites. The assumed model (see model scheme in Figure SII.3) is a network of enzyme-catalysed transformations of chemical species. Each chemical reaction is associated with a rate (flux) of transformation, which is a numerical value. The estimation of the values of the fluxes is based on the addition of successive constraints. At steady state, a mass balance can be set around each internal metabolite (B, C and D), while taking all internal metabolites together constitutes a system of linear equations.
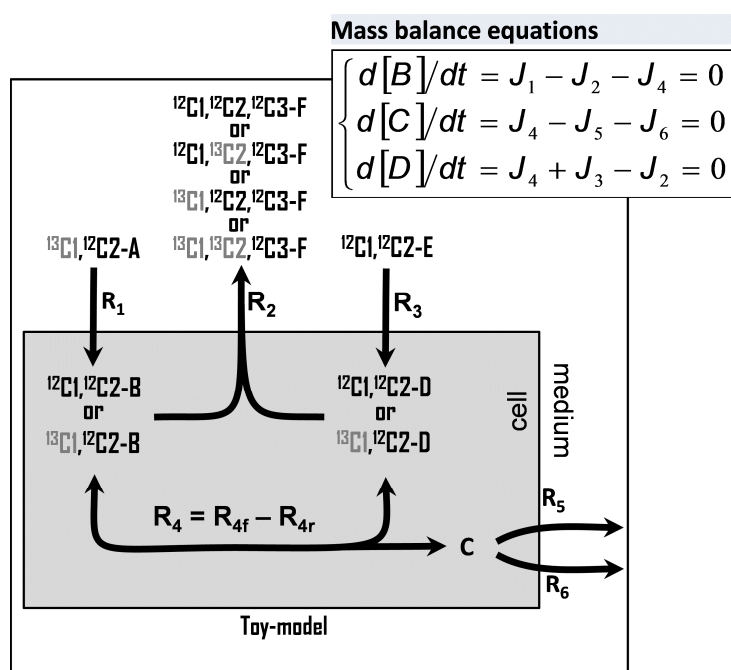
Figure SII.3 Model scheme (toy model)

Mass balance equations

$$\begin{cases} d[B]/dt = J_1 - J_2 - J_4 = 0 \\ d[C]/dt = J_4 - J_5 - J_6 = 0 \\ d[D]/dt = J_4 + J_3 - J_2 = 0 \end{cases}$$

2. Setting reaction stoichiometry and assumed values . Each mass balance equation is a linear constraint, where each term in the summation is a reaction flux scaled by a stoichiometric coefficient (all 1 in the example). Also, all reaction fluxes are subjected to numerical boundaries, which can be represented as domains of possible values (intervals). All irreversible reactions have fluxes with positive values ($J_i \geq 0$). For reversible reactions (R_4 in toy-model), both   forward J_{if} and reverse J_{ir} reactions are positive ($J_i = J_{if} - J_{ir}$; J_{if}, $J_{ir} \geq 0$). Also, the domains of some reactions are additionally fixed from experimental evidence. These are in general reactions involved in the uptake from the media or release to the media of external metabolites. Table SII.1 shows both reaction stoichiometry and numerical boundaries (assumed values):

Table SII.1 Model scheme (toy model)

ID	substrates	products	assumed values
R_1	$_{c1,c2\text{-}}A$	$_{c1,c2\text{-}}B$	$1.00 \leq J_1 \leq 1.00$
R_2	$_{c1,c2\text{-}}B + _{c3,c4\text{-}}D$	$_{c1,c3,c4\text{-}}F$	$0.00 \leq J_2$
R_3	$_{c1,c2\text{-}}E$	$_{c1,c2\text{-}}D$	$0.50 \leq J_3 \leq 1.00$
R_{4f}	$_{c1,c2\text{-}}B$	$_{c1,c2\text{-}}D$	$0.00 \leq J_{4f}$
R_{4r}	$_{c1,c2\text{-}}D$	$_{c1,c2\text{-}}B$	$0.00 \leq J_{4r}$
R_5	C	-	$0.00 \leq J_5$
R_6	C	-	$0.00 \leq J_6$
	net reactions		
R_4	$R_4 = R_{4f} - R_{4r}$	-	

3. Flux solution. All previous constraints are limiting a solution space, where a solution is such a complete assignation of flux values that all the constraints are simultaneously satisfied. In order to satisfy all constraints and taking advantage of the linear nature of the problem to be solved, the range of possible values for each flux can be determined using linear programming where each flux is maximised or minimised while leaving all other fluxes free. The resulting solution in Table SII.2 was not a unique solution but a solution space that can be reduced:

Table SII.2 Flux solution (toy-model)

ID	solution
R_1	$1.00 \leq J_1 \leq 1.00$
R_2	$0.75 \leq J_2 \leq 1.00$
R_3	$0.50 \leq J_3 \leq 1.05$
R_{4f}	$0.00 \leq J_{4f} \leq M$
R_{4r}	$0.00 \leq J_{4r} \leq M$
R_5	$0.00 \leq J_5 \leq 0.25$
R_6	$0.00 \leq J_6 \leq 0.25$
R_{4f}	$0.00 \leq J_6 \leq 0.25$

4. Flux solution refinement. The solution space is refined to a unique numerical solution instead of intervals, as shown in Table SII.4, by addition of linear constraints and subsequent application of linear programming maximising and minimising each flux value. These linear constraints can be flux ratios, as shown in Table SII.3, which could be associated to particular hypotheses about flux distribution.

Table SII.3: additional constraints (toy-model)

constraint		resulting lineal constraint
J_{4r} $/J_1$	10	$-10 \times J_1 + J_{4r} = 0$
J_{4f} $/J_3$	12	$-13 \times J_3 + J_{4r} = 0$

Table SII.4: refined flux solution (toy-model)

ID	refined solution
R_1	1
R_2	0.92
R_3	0.84
R_{4f}	10.08
R_{4r}	10
R_5	$0 \leq J_5 \leq 0.08$
R_6	$0 \leq J_6 \leq 0.08$
R_{4f}	0.08

5. Predicted ^{13}C label enrichments. Under isotopic steady state, isotopomer and mass isotopomer abundances reach a steady value and can be predicted by solving a system of balance equations around isotopomers, which take into account label transitions and the refined solution for fluxes in Table SII.4. These equations describe the dependency of isotopomer abundances on fluxes and isotopomer abundances of other metabolites, and satisfy all topological and stoichiometric constraints. Thus, balance equations around isotopomers of B, D and F are set taking into account the labelled status of the substrate (100%[1-^{13}C$_1$]-A) and the appropriate carbon transitions as shown in Table SII.5, which depends on the reaction as described in Table SII.1. Solving this system of equations, the resulting ^{13}C label enrichments are shown in Table SII.6.

Table SII.5: setting balance equations around isotopomers (toy model)

	isotopomer		constraint
B	$^{12}c_1,^{12}c_2$-B/B	=	$(J_{4r} \times ^{12}c_1,^{12}c_2$-D/D$) / (J_1 + J_{4r})$
	$^{13}c_1,^{12}c_2$-B/B	=	$((J_1 \times ^{13}c_1,^{12}c_2$-A/A$) + (J_{4r} \times ^{13}c_1,^{12}c_2$-D/D$)) / (J_1 + J_{4r})$
D	$^{12}c_1,^{12}c_2$-D/D	=	$((J_{4f} \times ^{12}c_1,^{12}c_2$-B/B$) + (J_3 \times ^{12}c_1,^{12}c_2$-E/E$)) / (J_{4f} + J_3)$
	$^{13}c_1,^{12}c_2$-D/D	=	$(J_{4f} \times ^{13}c_1,^{12}c_2$-B/B$) / (J_{4f} + J_3)$
F	$^{12}c_1,^{12}c_2,^{12}c_3$-F/F	=	$(^{12}c_1,^{12}c_2$-B/B$) \times (^{12}c_1,^{12}c_2$-D/D$)$
	$^{13}c_1,^{12}c_2,^{12}c_3$-F/F	=	$(^{13}c_1,^{12}c_2$-B/B$) \times (^{12}c_1,^{12}c_2$-D/D$)$
	$^{12}c_1,^{13}c_2,^{12}c_3$-F/F	=	$(^{12}c_1,^{12}c_2$-B/B$) \times (^{13}c_1,^{12}c_2$-D/D$)$
	$^{13}c_1,^{13}c_2,^{12}c_3$-F/F	=	$(^{13}c_1,^{12}c_2$-B/B$) \times (^{13}c_1,^{12}c_2$-D/D$))$

The relative abundance of product mass isotopomers depends on the labelled status of the substrates and the flux distribution throughout the metabolic network. Notice that the level of enrichment and label distribution depends on input fluxes – not on outputs – and on relative contributions, but not on absolute values.

Table SII.6: predicted label enrichments (toy-model)

constraint	descriptio	mass isotopomers	isotopomers	%

$_{c1,c2-}$A	fixed	m0	$^{12}c_1, ^{12}c_2$-A	0
		m1	$^{12}c_1, ^{13}c_2$-A	0
			$^{13}c_1, ^{12}c_2$-A	100
		m2	$^{13}c_1, ^{13}c_2$-A	0
$_{c1,c2-}$B	simulate	-	-	-
$_{c1,c2-}$D	simulate	-	-	-
$_{c1,c2-}$E	simulate	-	-	-
$_{c1,c2,c3-}$F	simulated	m0	$^{12}c_1, ^{12}c_2, ^{12}c_3$-F	21
		m1	$^{13}c_1, ^{12}c_2, ^{12}c_3$-F	27
			$^{12}c_1, ^{13}c_2, ^{12}c_3$-F	23
			$^{12}c_1, ^{12}c_2, ^{13}c_3$-F	0
		m2	$^{13}c_1, ^{13}c_2, ^{12}c_3$-F	29
			$^{13}c_1, ^{12}c_2, ^{13}c_3$-F	0
			$^{12}c_1, ^{13}c_2, ^{13}c_3$-F	0
		m3	$^{13}c_1, ^{13}c_2, ^{13}c_3$-F	0

VI.2.2 Results

The same procedure described above was applied to estimate two flux distributions (one for CDK4/6 inhibited cells and another for control cells) predicting each one the label distribution in two separate experiments using either 100% $[1,2-^{13}C_2]$-D-glucose as the labelled substrate or 100% $[U-^{13}C_5]$-L-glutamine as the labelled substrate. A set of flux ratios (accounting for specific enzyme activities and ratios among different reaction fluxes) was first selected as this providing a constrained space for flux distributions and affecting ^{13}C label enrichments. For each flux distribution, the enrichment in ^{13}C-labeled products can be predicted and then compared with the measured enrichments, where comparisons were made at the mass isotopomer level. The selected ratios among fluxes were iteratively fitted until the difference among predicted and measured label enrichments was reduced. This process constrained most of the reaction fluxes. The final predicted flux distributions are shown in Table SII.7, together with a complete description of reaction stoichiometry and carbon transitions, initially assumed values, and fitted ratios among fluxes. The predicted ^{13}C label enrichments (associated with these specific flux distributions) are provided as gray dots over the bars for measured values in Figures SII.4 – SII.9.

The following conclusions were reached:

- The hypotheses regarding an increase of the non-oxidative PPP with respect to the oxidative PPP, discussed in Chapter 4.2, were shown to be compatible in the context of a complete model of central carbon metabolism.

- The model agrees with two different pools of glucose 6-phosphate (G6P) and pyruvate (Pyr), according to previously published reports [39, 40]. The different pools for G6P explain the label enrichment in glycogen. The different pools for Pyr explain the higher total ^{13}C label enrichment in medium lactate (Σm of among 15% and 35 %) compared with internal lactate (Σm around 45%) using labelled glucose.

- Measured rates of O_2 consumption for ATP production by mitochondrial respiration (J_{OCR}) constrained largely the flux distributions. This take advantage of the redox balanced nature of the designed model i.e., the high energy electron (NADH or $FADH_2$) production rate matches the consumption rate by oxidative phosphorylation [41]. As stated by Fan et al [41] for cancer cells, oxidative phosphorylation was the major ATP source and was driven by glutamine. On the one hand, ATP produced *via* glycolysis (J_{ATPGlc} in Table SII.7) was around 40% and ATP produced *via* oxidative phosphorylation (J_{ATPOCR} in Table SII.7) was around 60%. Interestingly, total contributions were greater when CDK4/6 were inhibited: J_{ATPGlc} = 1.01 pmol·cell^{-1}·h^{-1} and J_{ATPOCR} = 1.53 pmol·cell^{-1}·h^{-1} for control cells, and J_{ATPGlc} = 1.29 pmol·cell^{-1}·h^{-1} and J_{ATPOCR} = 2.04 pmol·cell^{-1}·h^{-1} for CDK4/6-inhibited cells. On the other hand, the more important contribution *per* carbon to produce α-ketoglutarate (αKG) was from glutamine (Gln).

- OCR values and redox balanced model were 100% compatible with all measured exchanges regarding glucose, lactate and amino acids, and also with the requirement of amino acids for protein synthesis. Interestingly, in CDK4/6 inhibited cells, this perfect compatibility required an extra uptake of essential amino acids in addition with the quantities required for protein synthesis. This extra uptake corresponded to the uptakes measured in these CDK4/6-inhibited cells (Figure SII.2).

- The requirement of ATP for the synthesis of protein, including synthesis for new biomass and protein turnover, was assumed to be associated to the rate of ATP produced by glycolysis as suggested by [29], with higher value for CDK4/6 inhibited cells. The resulting values for protein turnover were in tune with previously reported values [42].

However, the most relevant conclusion from this integrated analysis supports the hypothesis of increased MYC activity leading to a remodelling of central carbon metabolism, with a relevant increase of glutamine-driven mitochondrial respiratory activity. This major mitochondrial activity leads to a major glutamine demand (and dependence) resulting in increased uptake of glutamine and accordingly, a lower availability of glutamine for other processes – i.e, major dependence and sensitivity to glutamine.

The adjustment of flux distributions described above constrained most of the reaction fluxes – those with higher magnitudes (glycolysis, Krebs cycle), pentose phosphate pathway (PPP), serine to glycine, etc. – although maintained a level of uncertainty for fluxes with reduced magnitudes – as those through pyruvate dehydrogenase (PDH), pyruvate carboxylase (PC) and those leading to synthesis of lipids and polyamines. Additional fitting of ratios among these unconstrained fluxes can be performed in order to test if other hypotheses discussed in the main text (and regarding these unconstrained fluxes) are compatible with the integrated picture of all observed exchanges, OCR, label propagation and model scheme. Accordingly, first the suggested increase in the flux through the pyruvate dehydrogenase was satisfied by slightly decreasing the production of lactate in CDK4/6 inhibited cells. Second, the suggested decrease in fatty acid synthesis and increase in polyamine synthesis was satisfied playing with the ratios among citrate synthase and citrate lyase, and fatty acid and polyamine synthesis. This adjustment was supported by the proposed competition between fatty acids and polyamines for cytoplasmic acetyl-CoA [16, 43].

Table SII.7: ^{13}C-based estimated reaction fluxes

Predicted values in control or CDK4/6 inhibited cells correspond to two separate experiments using either 100% [1,2-^{13}C$_2$]-D-glucose as the labelled substrate or 100% [U-^{13}C$_5$]-L-glutamine as the labelled substrate. However, the label enrichment was corrected to 90% according to measured values enrichments for glucose and glutamine. Ri refers to the global chemical transformation or transport process through the *ith* metabolic step and J_i refers to the rate (flux) through it. When reversibility is explicitly assumed, J_{if} and J_{ir} refer to forward and reverse reactions, respectively. Additional reactions – not included in **Figure SII.1** – are included for NADPH and ATP utilization, and also for amino acid uptake and utilization. UTP to UDP, GTP to GDP and ATP to AMP are simplified for ATP to ADP conversions. Also, mitochondrial NADPH and NADP are assumed as NADH and NAD respectively. Stoichiometry for amino acid incorporation into protein and turnover is based on the relative abundance of these amino acids in proteins [34]. See abbreviations in the List of abbreviations in this annex.

	reaction stoichiometry and carbon transitions		assumed values (pmol·cell^{-1}·h^{-1})		fitted ratios		resulting values (pmol·cell^{-1}·h^{-1})	
ID	substrates	products	siControl	siCDK4/6	siControl	siCDK4/6	siControl	siCDK4/6
R$_{Ala}$	Ala		0.00896694 ≤ J ≤ 0.00896694	0.0172325 ≤ J ≤ 0.0172325			0.008967 ≤ J ≤ 0.008967	0.017233 ≤ J ≤ 0.017233
R$_{Argi}$	C1,C2,C3,C4,C5-extArgi	C1,C2,C3,C4,C5-Argi	0.00700593 ≤ J ≤ 0.00700593	0.0128823 ≤ J ≤ 0.0128823			0.007006 ≤ J ≤ 0.007006	0.012882 ≤ J ≤ 0.012882

	reaction stoichiometry and carbon transitions		assumed values (pmol·cell⁻¹·h⁻¹)		fitted ratios		resulting values (pmol·cell⁻¹·h⁻¹)	
ID	substrates	products	siControl	siCDK4/6	siControl	siCDK4/6	siControl	siCDK4/6
R_{Asn}	Asn		$0.000402363 \leq J \leq 0.000402363$	$0.00346088 \leq J \leq 0.00346088$			$0.000402 \leq J \leq 0.000402$	$0.003461 \leq J \leq 0.003461$
R_{Asp}	Asp		$0.000647706 \leq J \leq 0.000647706$	$0.00270108 \leq J \leq 0.00270108$			$0.000648 \leq J \leq 0.000648$	$0.002701 \leq J \leq 0.002701$
R_{Cys}	$_{C1,C2,C3}$-extCys	$_{C1,C2,C3}$-Cys	$0.00348494 \leq J \leq 0.00348494$	$0.00585242 \leq J \leq 0.00585242$			$0.003485 \leq J \leq 0.003485$	$0.005852 \leq J \leq 0.005852$
R_{Glc}	$_{C1,C2,C3,C4,C5,C6}$-extGlc	$_{C1,C2,C3,C4,C5,C6}$-Glc	$0.509635 \leq J \leq 0.509635$	$0.659947 \leq J \leq 0.659947$			$0.509635 \leq J \leq 0.509635$	$0.659947 \leq J \leq 0.659947$
R_{Gln}	$_{C1,C2,C3,C4,C5}$-extGln	$_{C1,C2,C3,C4,C5}$-Gln	$0.0682803 \leq J \leq 0.0682803$	$0.100875 \leq J \leq 0.100875$			$0.06828 \leq J \leq 0.06828$	$0.100875 \leq J \leq 0.100875$
R_{Glu}	Glu		$0.00925057 \leq J \leq 0.00925057$	$0.0178881 \leq J \leq 0.0178881$			$0.009251 \leq J \leq 0.009251$	$0.017888 \leq J \leq 0.017888$
R_{Gly}	Gly		$0.00190306 \leq J \leq 0.00190306$	$0.00610001 \leq J \leq 0.00610001$			$0.001903 \leq J \leq 0.001903$	$0.0061 \leq J \leq 0.0061$
R_{His}	$_{C1,C2,C3,C4,C5}$-extHis	$_{C1,C2,C3,C4,C5}$-His	$0.00173453 \leq J \leq 0.00173453$	$0.00220178 \leq J \leq 0.00220178$			$0.001735 \leq J \leq 0.001735$	$0.002202 \leq J \leq 0.002202$
R_{Ile}	$_{C1,C2,C3,C4,C5,C6}$-extIle	$_{C1,C2,C3,C4,C5,C6}$-Ile	$0.00616882 \leq J \leq 0.00616882$	$0.00857362 \leq J \leq 0.00857362$			$0.006169 \leq J \leq 0.006169$	$0.008574 \leq J \leq 0.008574$
R_{Lac}	Lac		$0.958813 \leq J \leq 0.958813$	$(1.28558 \cdot 0.97) \leq J \leq (1.28558 \cdot 0.97)$			$0.958813 \leq J \leq 0.958813$	$1.24701 \leq J \leq 1.24701$
R_{Leu}	$_{C1,C2,C3,C4,C5,C6}$-extLeu	$_{C1,C2,C3,C4,C5,C6}$-Leu	$0.00746987 \leq J \leq 0.00746987$	$0.0101292 \leq J \leq 0.0101292$			$0.00747 \leq J \leq 0.00747$	$0.010129 \leq J \leq 0.010129$
R_{Lys}	$_{C1,C2,C3,C4,C5,C6}$-extLys	$_{C1,C2,C3,C4,C5,C6}$-Lys	$0.00624903 \leq J \leq (0.00624903 \cdot 1.1)$	$0.0101456 \leq J \leq 0.0101456$			$0.006871 \leq J \leq 0.006874$	$0.010146 \leq J \leq 0.010146$
R_{Met}	$_{C1,C2,C3,C4,C5}$-extMet	$_{C1,C2,C3,C4,C5}$-Met	$0.00276546 \leq J \leq 0.00276546$	$0.00322802 \leq J \leq 0.00322802$			$0.002765 \leq J \leq 0.002765$	$0.003228 \leq J \leq 0.003228$
R_{Phe}	$_{C1,C2,C3,C4,C5,C6,C7,C8,C9}$-extPhe	$_{C1,C2,C3,C4,C5,C6,C7,C8,C9}$-Phe	$0.0027453 \leq J \leq (0.0027453 \cdot 1.07)$	$0.00330047 \leq J \leq 0.00330047$			$0.002916 \leq J \leq 0.002937$	$0.0033 \leq J \leq 0.0033$
R_{Pro}	Pro		$0.00141227 \leq J \leq 0.00141227$	$0.00595744 \leq J \leq 0.00595744$			$0.001412 \leq J \leq 0.001412$	$0.005957 \leq J \leq 0.005957$
R_{Ser}	$_{C1,C2,C3}$-extSer	$_{C1,C2,C3}$-Ser	$0.01848 \leq J \leq 0.01848$	$0.0259168 \leq J \leq 0.0259168$			$0.01848 \leq J \leq 0.01848$	$0.025917 \leq J \leq 0.025917$
R_{Thr}	$_{C1,C2,C3,C4}$-extThr	$_{C1,C2,C3,C4}$-Thr	$0.00524434 \leq J \leq 0.00524434$	$0.00779097 \leq J \leq 0.00779097$			$0.005244 \leq J \leq 0.005244$	$0.007791 \leq J \leq 0.007791$
R_{Trp}	$_{C1,C2,C3}$-extTrp	$_{C1,C2,C3}$-Trp	$0.000418068 \leq J \leq (0.000418068 \cdot 1.18)$	$0.000594384 \leq J \leq 0.000594384$			$0.000491 \leq J \leq 0.000493$	$0.000594 \leq J \leq 0.000594$
R_{Tyr}	$_{C1,C2,C3,C4,C5,C6,C7,C8,C9}$-extTyr	$_{C1,C2,C3,C4,C5,C6,C7,C8,C9}$-Tyr	$0.00191047 \leq J \leq 0.00191047$	$0.00221605 \leq J \leq 0.00221605$			$0.00191 \leq J \leq 0.00191$	$0.002216 \leq J \leq 0.002216$
R_{Vali}	$_{C1,C2,C3,C4}$-extVali	$_{C1,C2,C3,C4}$-Vali	$0.00577229 \leq J \leq 0.00577229$	$0.00697533 \leq J \leq 0.00697533$			$0.005772 \leq J \leq 0.005772$	$0.006975 \leq J \leq 0.006975$
R_{Glyc}	G6P + ATP	ADP ($+ _{gly}$GP1)	$0 \leq J \leq 100000$	$0 \leq J \leq 100000$			$0.001 \leq J \leq 0.001$	$0.0012 \leq J \leq 0.0012$

	reaction stoichiometry and carbon transitions		assumed values (pmol·cell⁻¹·h⁻¹)		fitted ratios		resulting values (pmol·cell⁻¹·h⁻¹)	
ID	substrates	products	siControl	siCDK4/6	siControl	siCDK4/6	siControl	siCDK4/6
$R_{synProt}$	0.088 Ala + 0.055 Argi + 0.042 Asn + 0.053 Asp + 0.047 Gln + 0.057 Glu + 0.079 Gly + 0.021 His + 0.046 Pro + 0.063 Ser + 0.057 Thr + 0.006 Trp + 0.021 Cys + 0.084 Lys + 0.048 Ile + 0.083 Leu + 0.027 Tyr + 0.032 Phe + 0.020 Met + 0.061 Vali + 4.3 ATP	0.088 prAla + 0.055 prArgi + 0.042 prAsn + 0.053 prAsp + 0.047 prGln + 0.057 prGlu + 0.079 prGly + 0.021 prHis + 0.046 prPro + 0.063 prSer + 0.057 prThr + 0.006 prTrp + 0.021 prCys + 0.084 prLys + 0.048 prIle + 0.083 prLeu + 0.027 prTyr + 0.032 prPhe + 0.020 prMet + 0.061 prVali + 4.3 ADP + 4.3 pATPProt	0 ≤ J ≤ 100000	0 ≤ J ≤ 100000			0.234369 ≤ J ≤ 0.234369	0.300789 ≤ J ≤ 0.300789
$R_{degProt}$	0.088 $_{C1,C2,C3}$-prAla + 0.042 $_{C4,C5,C6,C7}$-prAsn + 0.053 $_{C8,C9,C10,C11}$-prAsp + 0.047 $_{C12,C13,C14,C15,C16}$-prGln + 0.057 $_{C17,C18,C19,C20,C21}$-prGlu + 0.079 $_{C22,C23}$-prGly + 0.046 $_{C24,C25,C26,C27,C28}$-prPro + 0.063 $_{C29,C30,C31}$-prSer + 0.055 $_{C32,C33,C34,C35,C36}$-prArgi + 0.021 $_{C37,C38,C39,C40,C41}$-prHis + 0.057 $_{C42,C43,C44,C45}$-prThr + 0.006 $_{C46,C47,C48}$-prTrp + 0.021 $_{C49,C50,C51}$-prCys + 0.084 $_{C52,C53,C54,C55,C56,C57}$-prLys + 0.048 $_{C59,C60,C61,C62,C63,C64}$-prIle + 0.083 $_{C65,C66,C67,C68,C69,C70}$-prLeu + 0.027 $_{C71,C72,C73,C74,C75,C76,C77,C78,C79}$-prTyr + 0.032 $_{C80,C81,C82,C83,C84,C85,C86,C87,C88}$-prPhe + 0.020 $_{C89,C90,C91,C92,C93}$-prMet + 0.061 $_{C94,C95,C96,C97}$-prVali	0.088 $_{C1,C2,C3}$-Ala + 0.042 $_{C4,C5,C6,C7}$-Asn + 0.053 $_{C8,C9,C10,C11}$-Asp + 0.047 $_{C12,C13,C14,C15,C16}$-Gln + 0.057 $_{C17,C18,C19,C20,C21}$-Glu + 0.079 $_{C22,C23}$-Gly + 0.046 $_{C24,C25,C26,C27,C28}$-Pro + 0.063 $_{C29,C30,C31}$-Ser + 0.055 $_{C32,C33,C34,C35,C36}$-Argi + 0.021 $_{C37,C38,C39,C40,C41}$-His + 0.057 $_{C42,C43,C44,C45}$-Thr + 0.006 $_{C46,C47,C48}$-Trp + 0.021 $_{C49,C50,C51}$-Cys + 0.084 $_{C52,C53,C54,C55,C56,C57}$-Lys + 0.048 $_{C59,C60,C61,C62,C63,C64}$-Ile + 0.083 $_{C65,C66,C67,C68,C69,C70}$-Leu + 0.027 $_{C71,C72,C73,C74,C75,C76,C77,C78,C79}$-Tyr + 0.032 $_{C80,C81,C82,C83,C84,C85,C86,C87,C88}$-Phe + 0.020 $_{C89,C90,C91,C92,C93}$-Met + 0.061 $_{C94,C95,C96,C97}$-Vali	0 ≤ J ≤ 100000	0 ≤ J ≤ 100000			0.152569 ≤ J ≤ 0.152569	0.224989 ≤ J ≤ 0.224989
R_{Prot}	0.088 prAla + 0.055 prArgi + 0.042 prAsn + 0.053 prAsp + 0.047 prGln + 0.057 prGlu + 0.079 prGly + 0.021 prHis + 0.046 prPro + 0.063 prSer + 0.057 prThr + 0.006 prTrp +		0.0818 ≤ J ≤ 0.0818	0.0758 ≤ J ≤ 0.0758			0.0818 ≤ J ≤ 0.0818	0.0758 ≤ J ≤ 0.0758

ID	substrates	products	assumed values (pmol·cell^{-1}·h^{-1}) siControl	siCDK4/6	fitted ratios siControl	siCDK4/6	resulting values (pmol·cell^{-1}·h^{-1}) siControl	siCDK4/6
	0.021 prCys + 0.084 prLys + 0.048 prIle + 0.083 prLeu + 0.027 prTyr + 0.032 prPhe + 0.020 prMet + 0.061 prVali							
R_{OCR}	$J_{OCR} = J_{36} + J_{37}$		$0.6192 \leq J \leq 0.6192$	$0.8244 \leq J \leq 0.8244$			$0.6192 \leq J \leq 0.6192$	$0.8244 \leq J \leq 0.8244$
R_{01}	$_{C1,C2,C3,C4,C5,C6}$-Glc + ATP	$_{C1,C2,C3,C4,C5,C6}$-G6P + ADP	$0 \leq J \leq 100000$	$0 \leq J \leq 100000$			$0.509635 \leq J \leq 0.509635$	$0.659947 \leq J \leq 0.659947$
R_{02f}	$_{C1,C2,C3,C4,C5,C6}$-G6P	$_{C1,C2,C3,C4,C5,C6}$-H6P	$0 \leq J \leq 100000$	$0 \leq J \leq 100000$			$1.14443 \leq J \leq 1.14443$	$1.48218 \leq J \leq 1.48218$
R_{02r}	$_{C1,C2,C3,C4,C5,C6}$-H6P	$_{C1,C2,C3,C4,C5,C6}$-G6P	$0 \leq J \leq 100000$	$0 \leq J \leq 100000$	$J_{02r} / J_{02} = 125 / 100$		$0.635794 \leq J \leq 0.635794$	$0.823434 \leq J \leq 0.823434$
R_{02}	$J_{02} = J_{02f} - J_{02r}$		$0 \leq J \leq 100000$	$0 \leq J \leq 100000$			$0.508635 \leq J \leq 0.508635$	$0.658747 \leq J \leq 0.658747$
R_{03}	$_{C1,C2,C3,C4,C5,C6}$-H6P + ATP	$_{C1,C2,C3}$-DHAP + $_{C4,C5,C6}$-G3P + ADP	$0 \leq J \leq 100000$	$0 \leq J \leq 100000$			$0.497766 \leq J \leq 0.497766$	$0.64042 \leq J \leq 0.64042$
R_{04}	$_{C1,C2,C3}$-DHAP	$_{C3,C2,C1}$-G3P	$0 \leq J \leq 100000$	$0 \leq J \leq 100000$			$0.497766 \leq J \leq 0.497766$	$0.64042 \leq J \leq 0.64042$
R_{05}	$_{C1,C2,C3}$-G3P + cNAD + ADP	$_{C1,C2,C3}$-3PG + cNADH + ATP	$0 \leq J \leq 100000$	$0 \leq J \leq 100000$			$1.00539 \leq J \leq 1.00539$	$1.29147 \leq J \leq 1.29147$
R_{06}	$_{C1,C2,C3}$-3PG + ADP	$_{C1,C2,C3}$-Pyr1 + ATP	$0 \leq J \leq 100000$	$0 \leq J \leq 100000$			$1.0098 \leq J \leq 1.0098$	$1.30229 \leq J \leq 1.30229$
R_{07}	$_{C1,C2,C3}$-Pyr1 + cNADH	$_{C1,C2,C3}$-Lac + cNAD	$0 \leq J \leq 100000$	$0 \leq J \leq 100000$			$0.958813 \leq J \leq 0.958813$	$1.24701 \leq J \leq 1.24701$
R_{08f}	$_{C1,C2,C3}$-Pyr1	$_{C1,C2,C3}$-Pyr2	$0 \leq J \leq 100000$	$0 \leq J \leq 100000$			$1.32566 \leq J \leq 1.32568$	$1.4371 \leq J \leq 1.4371$
R_{08r}	$_{C1,C2,C3}$-Pyr2	$_{C1,C2,C3}$-Pyr1	$0 \leq J \leq 100000$	$0 \leq J \leq 100000$	$J_{08r} / J_{08} = 2500 / 100$		$1.27467 \leq J \leq 1.2747$	$1.38182 \leq J \leq 1.38182$
R_{08}	$J_{08} = J_{08f} - J_{08r}$		$0 \leq J \leq 100000$	$0 \leq J \leq 100000$			$0.050987 \leq J \leq 0.050988$	$0.055273 \leq J \leq 0.055273$
R_{11}	$_{C1,C2,C3,C4,C5,C6}$-H6P + 2 cNADP	$_{C2,C3,C4,C5,C6}$-PenP + 2 cNADPH	$0 \leq J \leq 100000$	$0 \leq J \leq 100000$	$J_{11} / J_{Glc} = 6 / 100$		$0.030578 \leq J \leq 0.030578$	$0.039597 \leq J \leq 0.039597$
R_{12f}	$_{C1,C2,C3,C4,C5}$-PenP + $_{C6,C7,C8,C9}$-E4P	$_{C3,C4,C5}$-G3P + $_{C1,C2,C6,C7,C8,C9}$-H6P	$0 \leq J \leq 100000$	$0 \leq J \leq 100000$			$0.016887 \leq J \leq 0.016888$	$0.021722 \leq J \leq 0.021722$
R_{12r}	$_{C3,C4,C5}$-G3P + $_{C1,C2,C6,C7,C8,C9}$-H6P	$_{C1,C2,C3,C4,C5}$-PenP + $_{C6,C7,C8,C9}$-E4P	$0 \leq J \leq 100000$	$0 \leq J \leq 100000$	$J_{12r} / J_{11} = 23 / 100$	$J_{12r} / J_{11} = 28 / 100$	$0.007033 \leq J \leq 0.007033$	$0.011087 \leq J \leq 0.011087$
R_{12}	$J_{12} = J_{12f} - J_{12r}$		$0 \leq J \leq 100000$	$0 \leq J \leq 100000$			$0.009854 \leq J \leq 0.009855$	$0.010635 \leq J \leq 0.010635$
R_{13f}	$_{C1,C2,C3,C4,C5}$-PenP + $_{C6,C7,C8,C9,C10}$-PenP	$_{C1,C2,C6,C7,C8,C9,C10}$-S7P + $_{C3,C4,C5}$-G3P	$0 \leq J \leq 100000$	$0 \leq J \leq 100000$			$0.016887 \leq J \leq 0.016888$	$0.021722 \leq J \leq 0.021722$
R_{13r}	$_{C1,C2,C6,C7,C8,C9,C10}$-S7P + $_{C3,C4,C5}$-G3P	$_{C1,C2,C3,C4,C5}$-PenP + $_{C6,C7,C8,C9,C10}$-PenP	$0 \leq J \leq 100000$	$0 \leq J \leq 100000$	$J_{13r} / J_{11} = 23 / 100$	$J_{13r} / J_{11} = 28 / 100$	$0.007033 \leq J \leq 0.007033$	$0.011087 \leq J \leq 0.011087$
R_{13}	$J_{13} = J_{13f} - J_{13r}$		$0 \leq J \leq$	$0 \leq J \leq$			$0.009854 \leq J$	0.010635

ID	reaction stoichiometry and carbon transitions		assumed values (pmol·cell^{-1}·h^{-1})		fitted ratios		resulting values (pmol·cell^{-1}·h^{-1})	
	substrates	products	siControl	siCDK4/6	siControl	siCDK4/6	siControl	siCDK4/6
			100000	100000			≤ 0.009855	≤ J ≤ 0.010635
R_{14f}	$_{C1,C2,C3,C4,C5,C6,C7}$-S7P + $_{C8,C9,C10}$-G3P	$_{C4,C5,C6,C7}$-E4P + $_{C1,C2,C3,C8,C9,C10}$-H6P	0 ≤ J ≤ 100000	0 ≤ J ≤ 100000			0.774307 ≤ J ≤ 0.774307	1.00056 ≤ J ≤ 1.00056
R_{14r}	$_{C4,C5,C6,C7}$-E4P + $_{C1,C2,C3,C8,C9,C10}$-H6P	$_{C1,C2,C3,C4,C5,C6,C7}$-S7P + $_{C8,C9,C10}$-G3P	0 ≤ J ≤ 100000	0 ≤ J ≤ 100000	$J_{14r} / J_{11} = 2500 / 100$		0.764452 ≤ J ≤ 0.764452	0.989921 ≤ J ≤ 0.989921
R_{14}	$J_{14} = J_{14f} - J_{14r}$		0 ≤ J ≤ 100000	0 ≤ J ≤ 100000			0.009854 ≤ J ≤ 0.009855	0.010635 ≤ J ≤ 0.010635
R_{21}	$_{C1,C2,C3}$-C3PG + $_{C4,C5,C6,C7,C8}$-Glu + cNAD	$_{C1,C2,C3}$-Ser + $_{C4,C5,C6,C7,C8}$-αKG + cNADH	0 ≤ J ≤ 100000	0 ≤ J ≤ 100000			0.011749 ≤ J ≤ 0.011752	0.012952 ≤ J ≤ 0.012952
R_{22}	$_{C1,C2,C3}$-Ser + $_{C4,C5,C6}$-Pyr2 + cNADPH + ATP	$_{C1,C2,C3}$-C3PG + $_{C4,C5,C6}$-Ala + cNADP + ADP	0 ≤ J ≤ 100000	0 ≤ J ≤ 100000			0.016163 ≤ J ≤ 0.016165	0.023763 ≤ J ≤ 0.023763
R_{24f}	$_{C1,C2,C3}$-Ser + THF	$_{C1,C2}$-Gly + $_{C3}$-5,10-mTHF	0 ≤ J ≤ 100000	0 ≤ J ≤ 100000			0.076823 ≤ J ≤ 0.076823	0.147624 ≤ J ≤ 0.147624
R_{24r}	$_{C1,C2}$-Gly + $_{C3}$-5,10-mTHF	$_{C1,C2,C3}$-Ser + THF	0 ≤ J ≤ 100000	0 ≤ J ≤ 100000	$J_{24r} / J_{24} = 887 / 100$	$J_{24r} / J_{24} = 1613 / 100$	0.06904 ≤ J ≤ 0.06904	0.139006 ≤ J ≤ 0.139006
R_{24}	$J_{24} = J_{24f} - J_{24r}$		0 ≤ J ≤ 100000	0 ≤ J ≤ 100000			0.007784 ≤ J ≤ 0.007784	0.008618 ≤ J ≤ 0.008618
R_{25}	5,10-mTHF	DHF	0 ≤ J ≤ 100000	0 ≤ J ≤ 100000			0.007413 ≤ J ≤ 0.007413	0.008207 ≤ J ≤ 0.008207
R_{26}	DHF	THF	0 ≤ J ≤ 100000	0 ≤ J ≤ 100000			0.007413 ≤ J ≤ 0.007413	0.008207 ≤ J ≤ 0.008207
R_{27}	$_{C1}$-5,10-mTHF	$_{C1}$-5-mTHF	0 ≤ J ≤ 100000	0 ≤ J ≤ 100000			0.000371 ≤ J ≤ 0.000371	0.00041 ≤ J ≤ 0.00041
R_{28}	$_{C1,C2,C3,C4}$-HCys + $_{C5}$-5-mTHF	$_{C1,C2,C3,C4,C5}$-Met + THF	0 ≤ J ≤ 100000	0 ≤ J ≤ 100000	$J_{28} / J_{25} = 5 / 100$		0.000371 ≤ J ≤ 0.000371	0.00041 ≤ J ≤ 0.00041
R_{29}	$_{C1,C2,C3,C4,C5,C6,C7,C8,C9,C10}$-AdoMet	$_{C1,C2,C3,C4}$-HCys	0 ≤ J ≤ 100000	0 ≤ J ≤ 100000			0.000371 ≤ J ≤ 0.000371	0.00041 ≤ J ≤ 0.00041
R_{31}	$_{C1,C2,C3}$-Pyr2 + mCoA + mNAD	$_{C2,C3}$-mAcCoA + mNADH	0 ≤ J ≤ 100000	0 ≤ J ≤ 100000			0.080923 ≤ J ≤ 0.080947	0.109145 ≤ J ≤ 0.109145
R_{32}	$_{C1,C2,C3}$-Pyr2 + $_{C4}$-extCO2 + ATP	$_{C1,C2,C3,C4}$-mOAA + ADP	0 ≤ J ≤ 100000	0 ≤ J ≤ 100000	$J_{32} / J_{31} = 15 / 100$		0.012139 ≤ J ≤ 0.012142	0.016372 ≤ J ≤ 0.016372
R_{33}	$_{C1,C2,C3,C4}$-mOAA + $_{C5,C6}$-mAcCoA	$_{C4,C3,C2,C1,C6,C5}$-Cit + mCoA	0 ≤ J ≤ 100000	0 ≤ J ≤ 100000			0.085789 ≤ J ≤ 0.085861	0.13871 ≤ J ≤ 0.13871
R_{34cf}	$_{C1,C2,C3,C4,C5,C6}$-Cit + cNADP	$_{C1,C2,C3,C5,C6}$-αKG + cNADPH	0 ≤ J ≤ 100000	0 ≤ J ≤ 100000			0.002545 ≤ J ≤ 0.021238	0.076085 ≤ J ≤ 0.132372
R_{34cr}	$_{C1,C2,C3,C5,C6}$-αKG + $_{C4}$-extCO2 + cNADPH	$_{C1,C2,C3,C4,C5,C6}$-Cit + cNADP	0 ≤ J ≤ 100000	0 ≤ J ≤ 100000	$J_{34cr} / J_{35} = 2 / 100$		0.002545 ≤ J ≤ 0.002546	0.004066 ≤ J ≤ 0.004066
R_{34c}	$J_{34c} = J_{34cf} - J_{34cr}$		0 ≤ J ≤ 100000	0 ≤ J ≤ 100000			0. ≤ J ≤ 0.018692	0.07202 ≤ J ≤ 0.128306
R_{34mf}	$_{C1,C2,C3,C4,C5,C6}$-Cit + mNAD	$_{C1,C2,C3,C5,C6}$-αKG + mNADH	0 ≤ J ≤ 100000	0 ≤ J ≤ 100000			0.063275 ≤ J ≤ 0.081968	0.004066 ≤ J ≤ 0.060352
R_{34mr}	$_{C1,C2,C3,C5,C6}$-αKG + $_{C4}$-extCO2 + mNADH	$_{C1,C2,C3,C4,C5,C6}$-Cit + mNAD	0 ≤ J ≤ 100000	0 ≤ J ≤ 100000	$J_{34mr} / J_{35} = 2 / 100$		0.002545 ≤ J ≤ 0.002546	0.004066 ≤ J ≤ 0.004066

ID	reaction stoichiometry and carbon transitions		assumed values (pmol·cell⁻¹·h⁻¹)		fitted ratios		resulting values (pmol·cell⁻¹·h⁻¹)	
	substrates	products	siControl	siCDK4/6	siControl	siCDK4/6	siControl	siCDK4/6
R_{34m}	$J_{34m} = J_{34mf} - J_{34mr}$		$0 \leq J \leq 100000$	$0 \leq J \leq 100000$			$0.060729 \leq J \leq 0.079422$	$0. \leq J \leq 0.056287$
R_{34}	$J_{34} = J_{34c} - J_{34m}$		$0 \leq J \leq 100000$	$0 \leq J \leq 100000$			$0.079355 \leq J \leq 0.079422$	$0.128306 \leq J \leq 0.128306$
R_{35}	$_{C1,C2,C3,C4,C5}$-αKG + mNAD + ADP	$0.5\ _{C2,C3,C4,C5}$-Suc + $0.5\ _{C5,C4,C3,C2}$-Suc + mNADH + ATP	$0 \leq J \leq 100000$	$0 \leq J \leq 100000$			$0.127226 \leq J \leq 0.127293$	$0.203289 \leq J \leq 0.203289$
R_{36}	$_{C1,C2,C3,C4}$-Suc + 1.5 ADP	$_{C1,C2,C3,C4}$-Fum + 1.5 ATP	$0 \leq J \leq 100000$	$0 \leq J \leq 100000$			$0.13138 \leq J \leq 0.131447$	$0.212288 \leq J \leq 0.212288$
R_{37}	mNADH + 2.5 ADP	mNAD + 2.5 ATP	$0 \leq J \leq 100000$	$0 \leq J \leq 100000$			$0.487753 \leq J \leq 0.48782$	$0.612112 \leq J \leq 0.612112$
R_{38}	$_{C1,C2,C3,C4}$-Fum	$_{C1,C2,C3,C4}$-Mal	$0 \leq J \leq 100000$	$0 \leq J \leq 100000$			$0.13138 \leq J \leq 0.131469$	$0.213332 \leq J \leq 0.213332$
R_{39c}	$_{C1,C2,C3,C4}$-cOAA + cNADH	$_{C1,C2,C3,C4}$-Mal + cNAD	$0 \leq J \leq 100000$	$0 \leq J \leq 100000$			$0.058322 \leq J \leq 0.058326$	$0.057413 \leq J \leq 0.057413$
R_{39mf}	$_{C1,C2,C3,C4}$-Mal + mNAD	$_{C1,C2,C3,C4}$-mOAA + mNADH	$0 \leq J \leq 100000$	$0 \leq J \leq 100000$			$27.0069 \leq J \leq 27.0192$	$36.7249 \leq J \leq 36.7249$
R_{39mr}	$_{C1,C2,C3,C4}$-mOAA + mNADH	$_{C1,C2,C3,C4}$-Mal + mNAD	$0 \leq J \leq 100000$	$0 \leq J \leq 100000$	$J_{39mr} / J_{39m} = 20000 / 100$		$26.8725 \leq J \leq 26.8848$	$36.5421 \leq J \leq 36.5421$
R_{39m}	$J_{39m} = J_{39mf} - J_{39mr}$		$0 \leq J \leq 100000$	$0 \leq J \leq 100000$			$0.134363 \leq J \leq 0.134424$	$0.182711 \leq J \leq 0.182711$
R_{41f}	$_{C1,C2,C3,C4,C5}$-Gln	$_{C1,C2,C3,C4,C5}$-Glu	$0 \leq J \leq 100000$	$0 \leq J \leq 100000$			$0.081537 \leq J \leq 0.081538$	$0.102147 \leq J \leq 0.102147$
R_{41r}	$_{C1,C2,C3,C4,C5}$-Glu	$_{C1,C2,C3,C4,C5}$-Gln	$0 \leq J \leq 100000$	$0 \leq J \leq 100000$	$J_{41r} / J_{41} = 36 / 100$	$J_{41r} / J_{41} = 22.5 / 100$	$0.021583 \leq J \leq 0.021584$	$0.018762 \leq J \leq 0.018762$
R_{41}	$J_{41} = J_{41f} - J_{41r}$		$0 \leq J \leq 100000$	$0 \leq J \leq 100000$			$0.059954 \leq J \leq 0.059954$	$0.083386 \leq J \leq 0.083386$
R_{42f}	$_{C1,C2,C3,C4,C5}$-Glu + mNAD	$_{C1,C2,C3,C4,C5}$-αKG + mNADH	$0 \leq J \leq 100000$	$0 \leq J \leq 100000$			$5.86143 \leq J \leq 5.86203$	$10.0699 \leq J \leq 10.0699$
R_{42r}	$_{C1,C2,C3,C4,C5}$-αKG + mNADH	$_{C1,C2,C3,C4,C5}$-Glu + mNAD	$0 \leq J \leq 100000$	$0 \leq J \leq 100000$	$J_{42r} / J_{42} = 20000 / 100$		$5.83226 \leq J \leq 5.83287$	$10.0198 \leq J \leq 10.0198$
R_{42}	$J_{42} = J_{42f} - J_{42r}$		$0 \leq J \leq 100000$	$0 \leq J \leq 100000$			$0.029161 \leq J \leq 0.029164$	$0.050099 \leq J \leq 0.050099$
R_{51c}	$_{C1,C2,C3,C4}$-Asp + $_{C5,C6,C7,C8,C9}$-αKG	$_{C1,C2,C3,C4}$-cOAA + $_{C5,C6,C7,C8,C9}$-Glu	$0 \leq J \leq 100000$	$0 \leq J \leq 100000$			$0.051883 \leq J \leq 0.051892$	$0.04701 \leq J \leq 0.04701$
R_{51m}	$_{C1,C2,C3,C4}$-mOAA + $_{C5,C6,C7,C8,C9}$-Glu	$_{C1,C2,C3,C4}$-Asp + $_{C5,C6,C7,C8,C9}$-αKG	$0 \leq J \leq 100000$	$0 \leq J \leq 100000$			$0.060704 \leq J \leq 0.060713$	$0.060373 \leq J \leq 0.060373$
R_{52}	Asp + $_{C1,C2,C3,C4,C5}$-Gln + 2 ATP	Asn + $_{C1,C2,C3,C4,C5}$-Glu + 2 ADP	$0 \leq J \leq 100000$	$0 \leq J \leq 100000$			$0.003838 \leq J \leq 0.003838$	$0.006644 \leq J \leq 0.006644$
R_{53}	$_{C1,C2,C3,C4,C5,C6}$-Cit + cCoA + ATP	$_{C4,C3,C2,C1}$-cOAA + $_{C6,C5}$-cAcCoA + ADP	$0 \leq J \leq 100000$	$0 \leq J \leq 100000$	$J_{53} / J_{33} = 7.5 / 100$		$0.006434 \leq J \leq 0.00644$	$0.010403 \leq J \leq 0.010403$
R_{54}	8 cAcCoA + 14 cNADPH + 7 ATP	8 cCoA + 14 cNADP + 7 ADP	$0 \leq J \leq 100000$	$0 \leq J \leq 100000$			$0.000724 \leq J \leq 0.000724$	$0.00039 \leq J \leq 0.00039$
R_{55c}	$_{C1,C2,C3,C4}$-Mal + cNADP	$_{C1,C2,C3}$-Pyr2 + cNADPH	$0 \leq J \leq 100000$	$0 \leq J \leq 100000$			$0. \leq J \leq 0.018692$	$0.031748 \leq J \leq 0.088035$

	reaction stoichiometry and carbon transitions		assumed values (pmol·cell⁻¹·h⁻¹)		fitted ratios		resulting values (pmol·cell⁻¹·h⁻¹)	
ID	**substrates**	**products**	**siControl**	**siCDK4/6**	**siControl**	**siCDK4/6**	**siControl**	**siCDK4/6**
R_{55m}	$_{C1,C2,C3,C4}$-Mal + mNAD	$_{C1,C2,C3}$-Pyr2 + mNADH	0 ≤ J ≤ 100000	0 ≤ J ≤ 100000			0.036676 ≤ J ≤ 0.055368	0. ≤ J ≤ 0.056287
R_{61}	$_{C1,C2,C3,C4,C5}$-Glu + ATP + mNADH	$_{C1,C2,C3,C4,C5}$-P5C + ADP + mNAD	0 ≤ J ≤ 100000	0 ≤ J ≤ 100000			0.002668 ≤ J ≤ 0.002668	0.000731 ≤ J ≤ 0.000731
R_{62}	$_{C1,C2,C3,C4,C5}$-P5C + cNADPH	$_{C1,C2,C3,C4,C5}$-Pro + cNADP	0 ≤ J ≤ 100000	0 ≤ J ≤ 100000			0.005175 ≤ J ≤ 0.005175	0.009444 ≤ J ≤ 0.009444
R_{63}	$_{C1,C2,C3,C4,C5}$-Argi + $_{C6,C7,C8,C9,C10}$-αKG	$_{C1,C2,C3,C4,C5}$-P5C + $_{C6,C7,C8,C9,C10}$-Glu	0 ≤ J ≤ 100000	0 ≤ J ≤ 100000			0.002507 ≤ J ≤ 0.002507	0.008713 ≤ J ≤ 0.008713
R_{65}	$_{C1,C2,C3,C4,C5}$-His	$_{C1,C2,C3,C4,C5}$-Glu	0 ≤ J ≤ 100000	0 ≤ J ≤ 100000			0.000017 ≤ J ≤ 0.000017	0.00061 ≤ J ≤ 0.00061
R_{72}	$_{C1,C2,C3,C4,C5}$-Met + $_{C6,C7,C8,C9,C10}$-PenP	$_{C1,C2,C3,C4,C5,C6,C7,C8,C9,C10}$-AdoMet	0 ≤ J ≤ 100000	0 ≤ J ≤ 100000			0.001014 ≤ J ≤ 0.001015	0.007693 ≤ J ≤ 0.007693
R_{73}	$_{C1,C2,C3,C4,C5,C6,C7,C8,C9,C10}$-AdoMet	$_{C2,C3,C4,C5,C6,C7,C8,C9,C10}$-AdoMet$_{DC}$	0 ≤ J ≤ 100000	0 ≤ J ≤ 100000			0.000643 ≤ J ≤ 0.000644	0.007282 ≤ J ≤ 0.007282
R_{74}	$_{C1,C2,C3,C4,C5,C6}$-MTA + $_{C7,C8,C9,C10,C11}$-Gln	$_{C2,C3,C4,C5,C6}$-Met + $_{C7,C8,C9,C10,C11}$-αKG	0 ≤ J ≤ 100000	0 ≤ J ≤ 100000			0.000643 ≤ J ≤ 0.000644	0.007282 ≤ J ≤ 0.007282
R_{75a}	$_{C1,C2,C3,C4,C5,C6,C7,C8,C9}$-AdoMet$_{DC}$ + Putr	$_{C5,C6,C7,C8,C9,C4}$-MTA + Spd	0 ≤ J ≤ 100000	0 ≤ J ≤ 100000			0. ≤ J ≤ 0.000644	0. ≤ J ≤ 0.007282
R_{75b}	$_{C1,C2,C3,C4,C5,C6,C7,C8,C9}$-AdoMet$_{DC}$ + Spd	$_{C5,C6,C7,C8,C9,C4}$-MTA + Spn	0 ≤ J ≤ 100000	0 ≤ J ≤ 100000			0. ≤ J ≤ 0.000644	0. ≤ J ≤ 0.007282
R_{75}	$J_{75} = J_{75a} + J_{75b}$		0 ≤ J ≤ 100000	0 ≤ J ≤ 100000			0.000643 ≤ J ≤ 0.000644	0.007282 ≤ J ≤ 0.007282
R_{76a}	cAcCoA + Spd	cCoA + AcSpd	0 ≤ J ≤ 100000	0 ≤ J ≤ 100000			0. ≤ J ≤ 0.000644	0. ≤ J ≤ 0.007282
R_{76b}	cAcCoA + Spn	cCoA + AcSpn	0 ≤ J ≤ 100000	0 ≤ J ≤ 100000			0. ≤ J ≤ 0.000644	0. ≤ J ≤ 0.007282
R_{76}	$J_{76} = J_{76f} + J_{76r}$		0 ≤ J ≤ 100000	0 ≤ J ≤ 100000	J_{76} / J_{53} = 10 / 100	J_{76} / J_{53} = 70 / 100	0.000643 ≤ J ≤ 0.000644	0.007282 ≤ J ≤ 0.007282
R_{78a}	AcSpd	Putr	0 ≤ J ≤ 100000	0 ≤ J ≤ 100000			0. ≤ J ≤ 0.000644	0. ≤ J ≤ 0.007282
R_{78b}	AcSpn	Spd	0 ≤ J ≤ 100000	0 ≤ J ≤ 100000			0. ≤ J ≤ 0.000644	0. ≤ J ≤ 0.007282
R_{78}	$J_{78} = J_{78a} - J_{78b}$		0 ≤ J ≤ 100000	0 ≤ J ≤ 100000			0.000643 ≤ J ≤ 0.000644	0.007282 ≤ J ≤ 0.007282
R_{81}	$_{C1,C2,C3,C4,C5,C6}$-Ile + mCoA + $_{C7}$-extCO2	$_{C6,C5}$-mAcCoA + 0.5 $_{C7,C4,C3,C2}$-Suc + 0.5 $_{C2,C3,C4,C7}$-Suc	0 ≤ J ≤ 100000	0 ≤ J ≤ 100000			0.002242 ≤ J ≤ 0.002242	0.004935 ≤ J ≤ 0.004935
R_{82}	$_{C1,C2,C3,C4,C5,C6}$-Leu + 3 mCoA + $_{C7}$-extCO2	$_{C2,C3}$-mAcCoA + $_{C4,C7}$-mAcCoA + $_{C6,C5}$-mAcCoA	0 ≤ J ≤ 100000	0 ≤ J ≤ 100000			0.00068 ≤ J ≤ 0.00068	0.003838 ≤ J ≤ 0.003838
R_{83}	$_{C1,C2,C3,C4,C5,C6}$-Lys + 2 mCoA + mNAD	$_{C2,C3}$-mAcCoA + $_{C5,C4}$-mAcCoA + mNADH	0 ≤ J ≤ 100000	0 ≤ J ≤ 100000			0. ≤ J ≤ 0.	0.003778 ≤ J ≤ 0.003778
R_{84}	$_{C1,C2,C3,C4}$-Thr + mCoA + mNAD	$_{C1,C2}$-mAcCoA + mNADH + $_{C4,C3}$-Gly	0 ≤ J ≤ 100000	0 ≤ J ≤ 100000			0.000582 ≤ J ≤ 0.000582	0.00347 ≤ J ≤ 0.00347
R_{85}	$_{C1,C2,C3,C4,C5,C6,C7,C8,C9}$-Tyr + 2 mCoA	$_{C4,C5,C6,C7}$-Fum + $_{C3,C2}$-mAcCoA + $_{C8,C9}$-mAcCoA	0 ≤ J ≤ 100000	0 ≤ J ≤ 100000			0. ≤ J ≤ 0.000022	0.001044 ≤ J ≤ 0.001044
R_{86}	$_{C1,C2,C3}$-Trp	$_{C1,C2,C3}$-Ala	0 ≤ J ≤ 100000	0 ≤ J ≤ 100000			0. ≤ J ≤ 0.	0.00014 ≤ J ≤ 0.00014
R_{87}	$_{C1,C2,C3}$-Cys	$_{C1,C2,C3}$-Pyr2	0 ≤ J ≤ 100000	0 ≤ J ≤ 100000			0.002897 ≤ J ≤ 0.002897	0.005973 ≤ J ≤ 0.005973

| ID	reaction stoichiometry and carbon transitions		assumed values (pmol·cell⁻¹·h⁻¹)		fitted ratios		resulting values (pmol·cell⁻¹·h⁻¹)	
	substrates	products	siControl	siCDK4/6	siControl	siCDK4/6	siControl	siCDK4/6
R_{88}	$_{C1,C2,C3,C4,C5}$-Met + $_{C6,C7,C8}$-Ser + $_{C9}$-extCO2 + mNAD	$_{C6,C7,C8}$-Cys + 0.5 $_{C9,C4,C3,C2}$-Suc + 0.5 $_{C2,C3,C4,C9}$-Suc + mNADH	$0 \leq J \leq 100000$	$0 \leq J \leq 100000$			$0.001129 \leq J \leq 0.001129$	$0.001712 \leq J \leq 0.001712$
R_{89}	$_{C1,C2,C3,C4}$-Vali + $_{C5}$-extCO2 + mNAD	$0.5\ _{C5,C4,C3,C2}$-Suc + $0.5\ _{C2,C3,C4,C5}$-Suc + mNADH	$0 \leq J \leq 100000$	$0 \leq J \leq 100000$			$0.000782 \leq J \leq 0.000782$	$0.002352 \leq J \leq 0.002352$
R_{90}	$_{C1,C2,C3,C4,C5,C6,C7,C8,C9}$-Phe	$_{C1,C2,C3,C4,C5,C6,C7,C8,C9}$-Tyr	$0 \leq J \leq 100000$	$0 \leq J \leq 100000$			$0.000298 \leq J \leq 0.00032$	$0.000875 \leq J \leq 0.000875$
R_{conATP}	ATP	ADP	$0 \leq J \leq 100000$	$0 \leq J \leq 100000$			$1.49268 \leq J \leq 1.4927$	$1.98351 \leq J \leq 1.98351$
$R_{conNADPH}$	cNADPH	cNADP	$0 \leq J \leq 100000$	$0 \leq J \leq 100000$			$0.04806 \leq J \leq 0.048368$	$0.200579 \leq J \leq 0.200579$
R_{ATPGlc}	$J_{ATPGlc} = J_{05} + J_{06} - J_{01} - J_{03}$		$0 \leq J \leq 100000$	$0 \leq J \leq 100000$	$J_{ATPGlc} / J_{synProt} = 4.3 / 1$		$1.00779 \leq J \leq 1.00779$	$1.29339 \leq J \leq 1.29339$
R_{ATPOCR}	$J_{ATPOCR} = 1.5\ J_{36} + 2.5\ J_{37} + J_{35} - J_{32}$		$0 \leq J \leq 100000$	$0 \leq J \leq 100000$			$1.53170 \leq J \leq 1.53171$	$2.03563 \leq J \leq 2.03563$
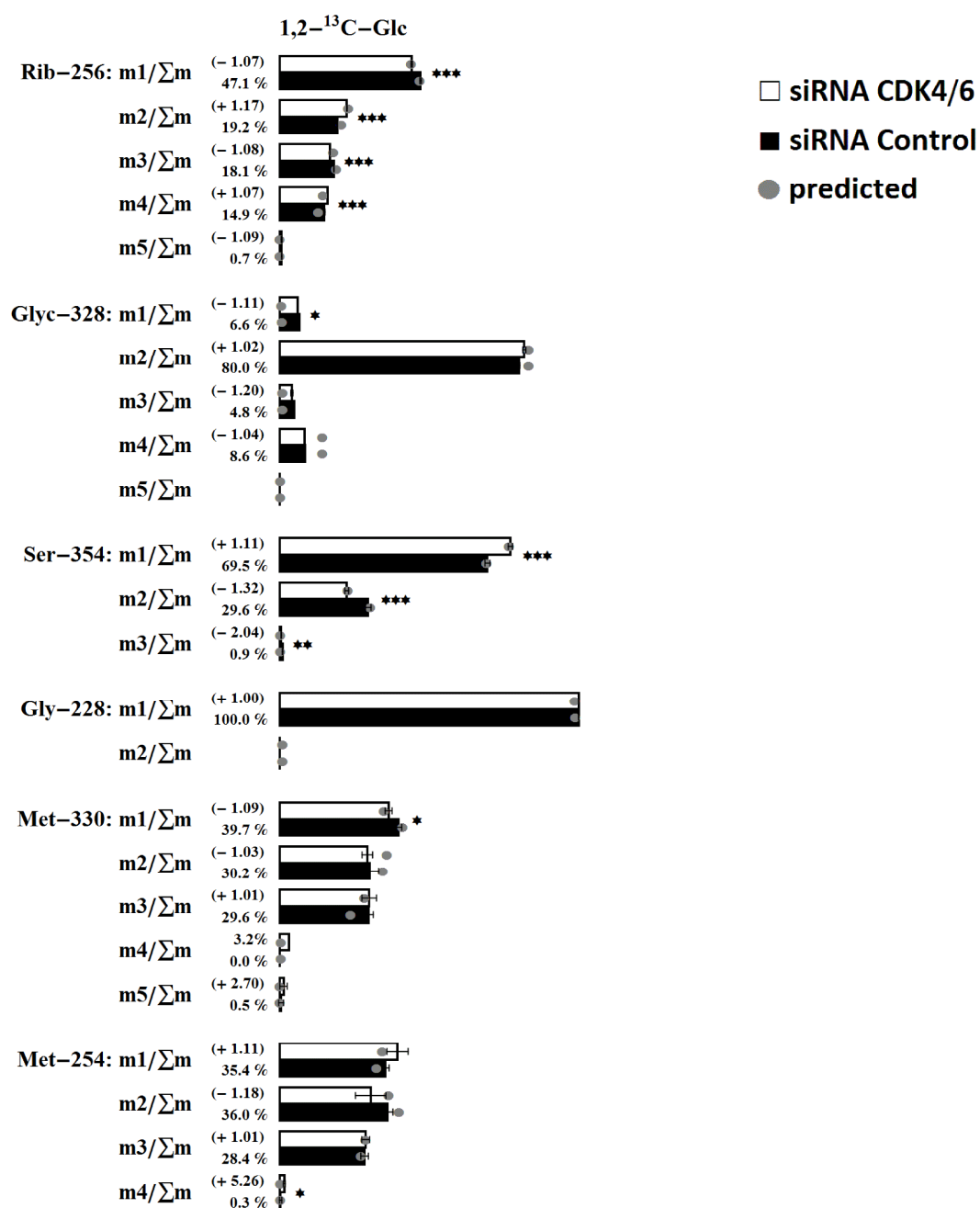
Figure SII.4: Measured and predicted isotopomer enrichments. Ribose, glycogen, and external serine, glycine and methionine
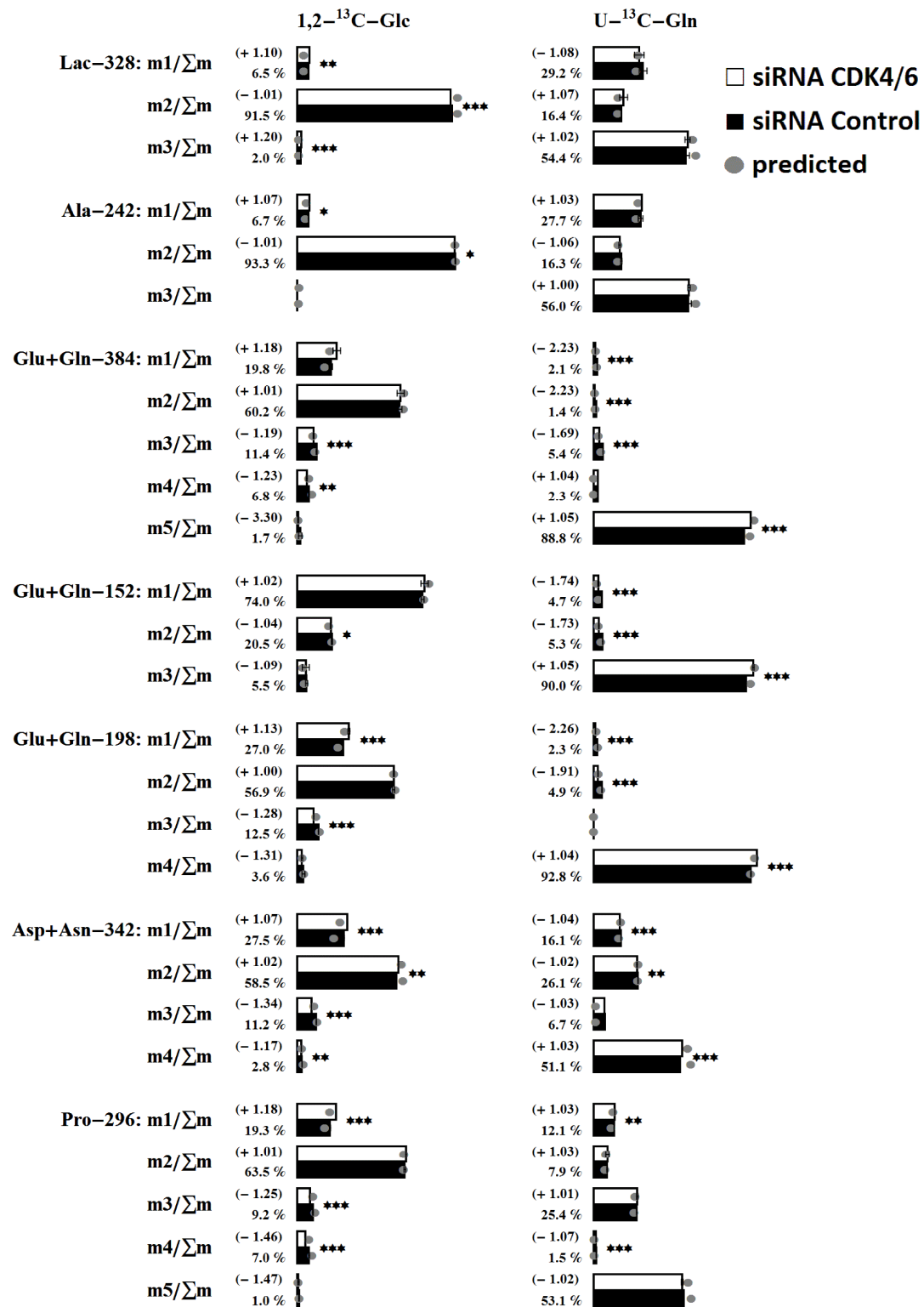
See appendix I for abbreviations.

Figure SII.5: Measured and predicted isotopomer enrichments. External lactate, alanine, glutamate/glutamine, aspartate/asparagine, and proline
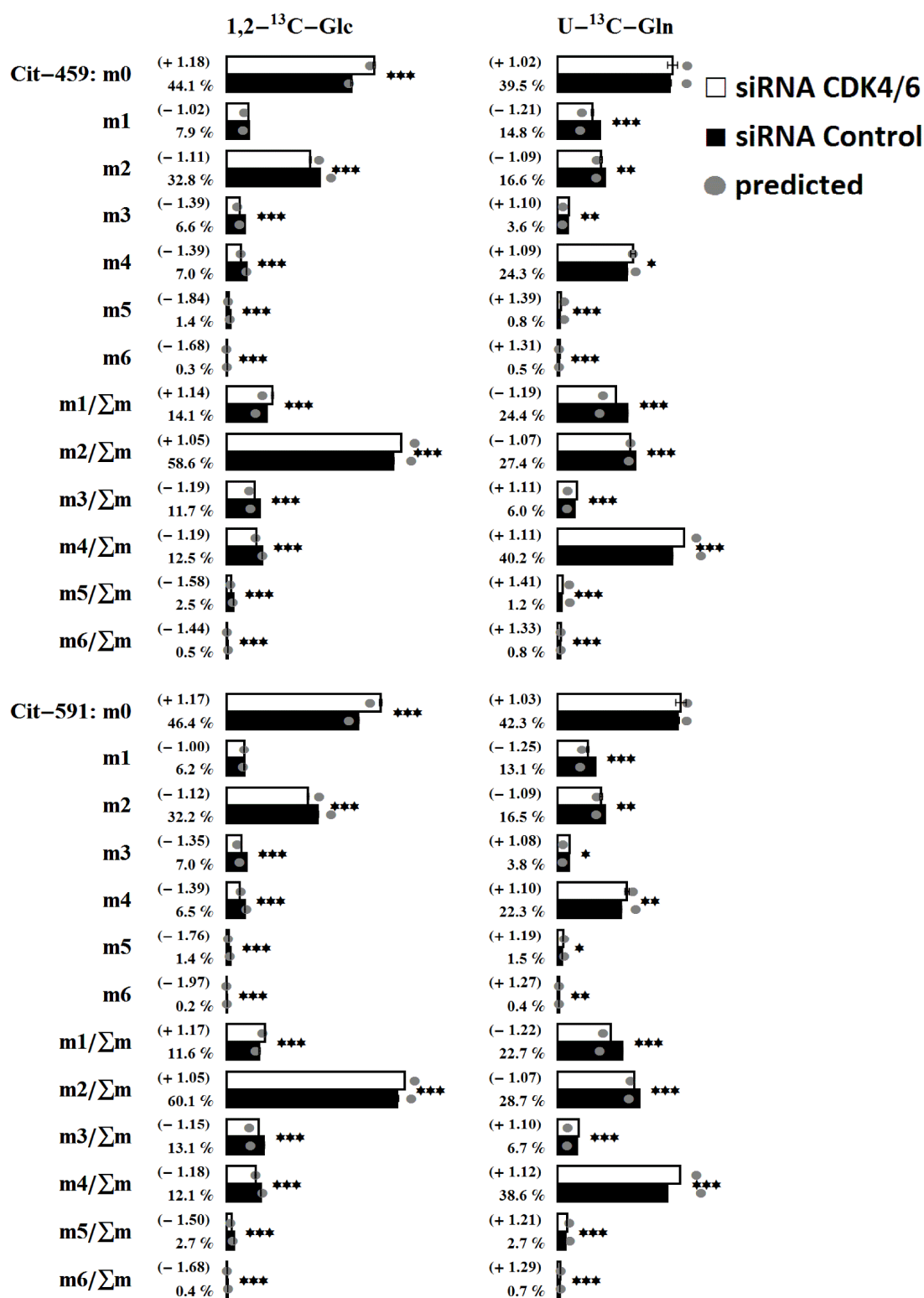
See appendix I for abbreviations.

Figure SII.6: Measured and predicted isotopomer enrichments. Internal citrate
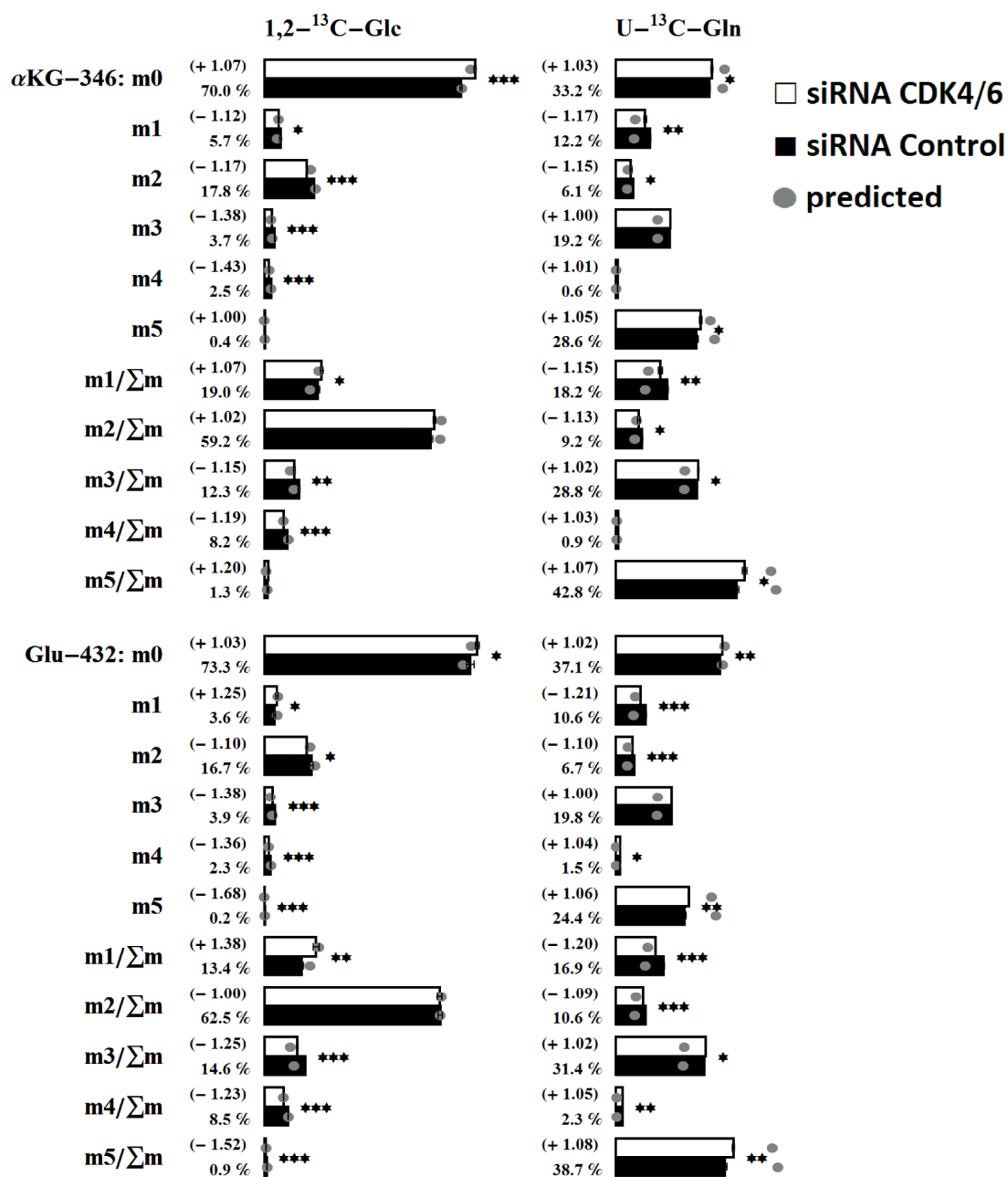See appendix I for abbreviations.

Figure SII.7: Measured and predicted isotopomer enrichments. Internal α-ketoglutarate and glutamate.
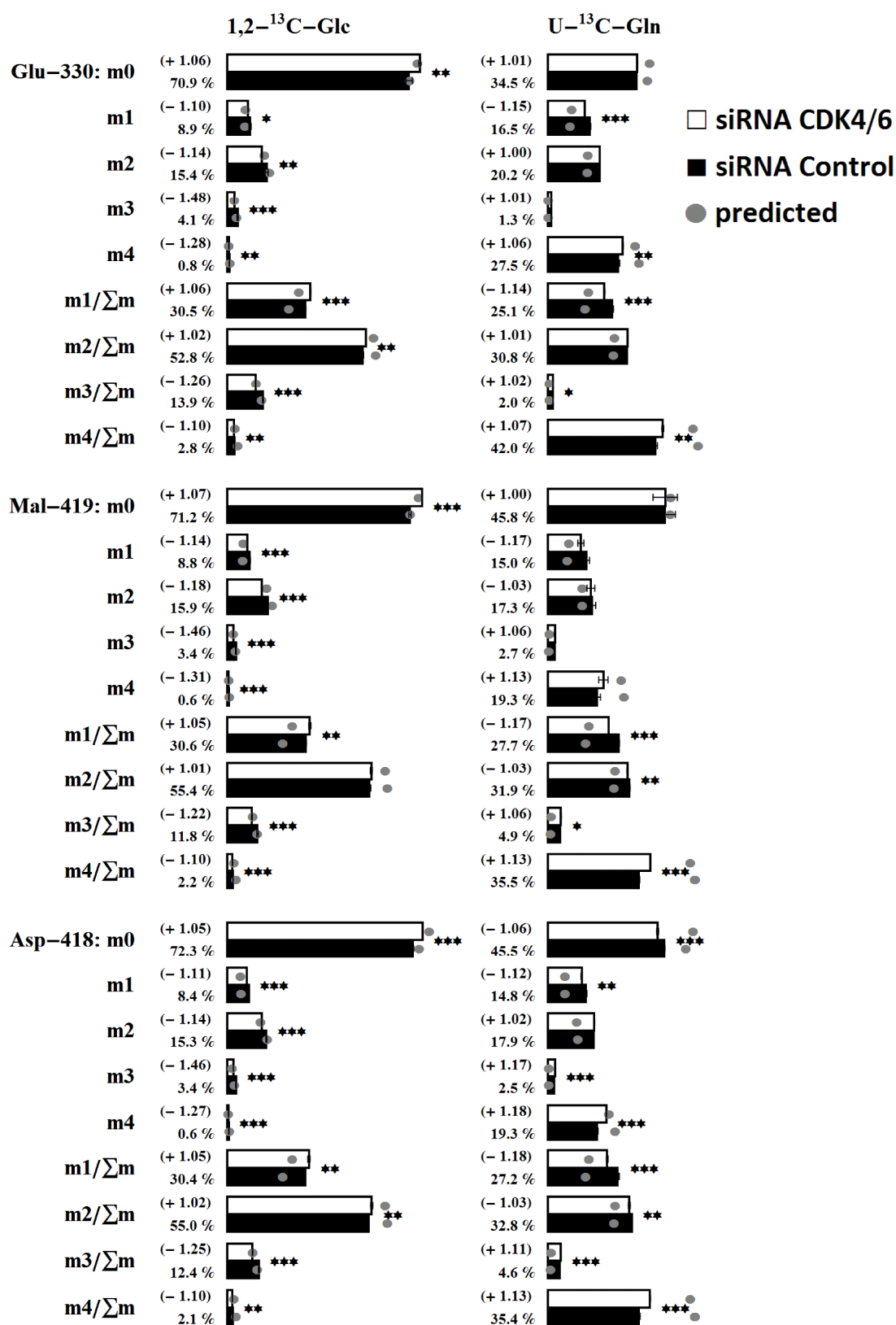See appendix I for abbreviations

Figure SII.8: Measured and predicted isotopomer enrichments. Internal glutamate, malate, and aspartate.
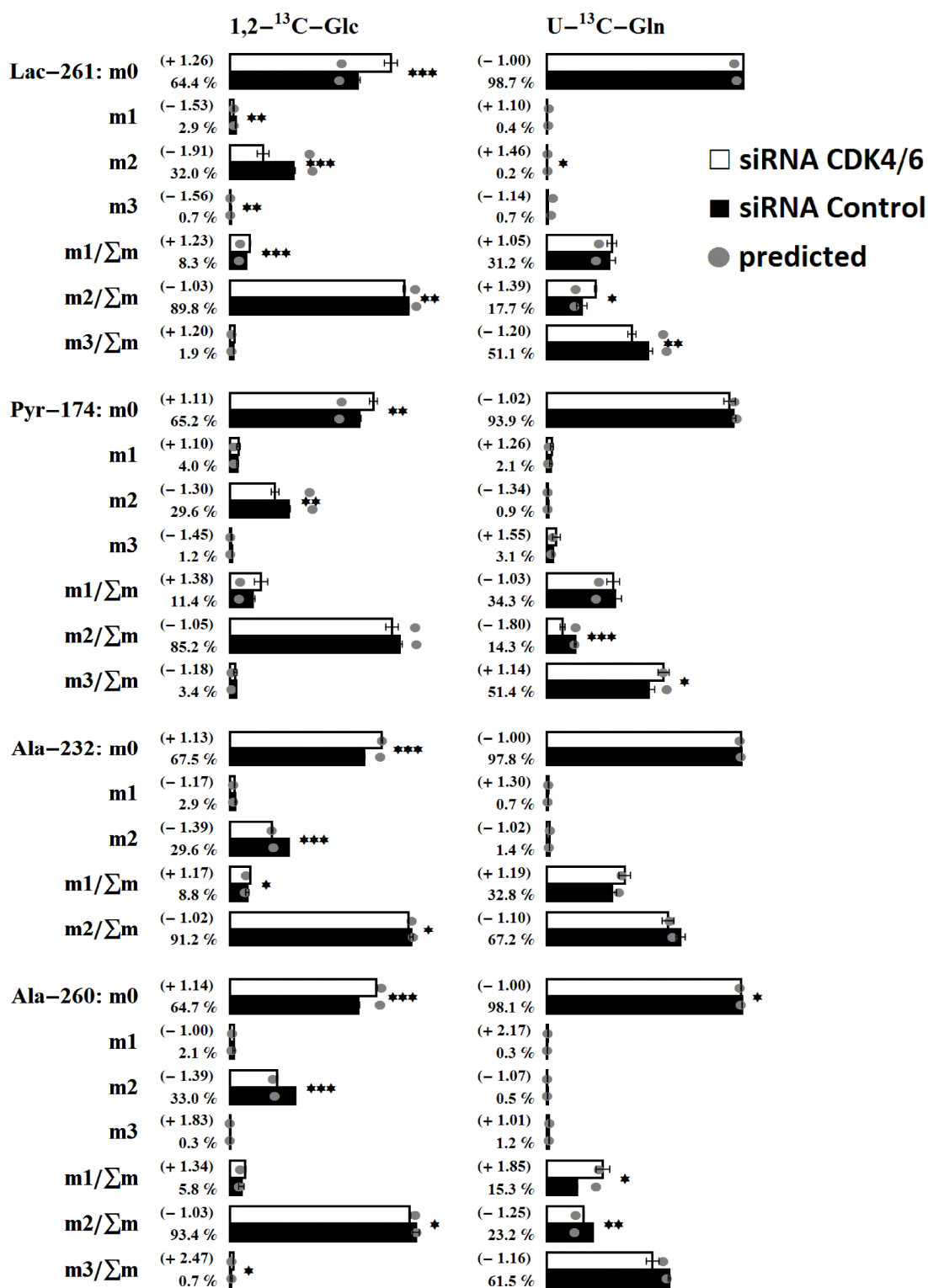See appendix I for abbreviations.

Figure SII.9: Measured and predicted isotopomer enrichments. Internal lactate, pyruvate and alanine
See appendix I for abbreviations.

VI.2.3 List of abbreviations:

10-fTHF (10-formyltetrahydrofolate); 2PG (2-Phosphoglycerate); 3PG (3-Phosphoglycerate); 5,10-mTHF (5,10-Methenyltetrahydrofolate); 5-mTHF (5-methyltetrahydrofolate); AcCoA (Acetyl-CoA); AcSpd (N^1-acetylspermidine); AcSpm (N^1-acetylspermine); AdoMet$_{DC}$ (S-adenosyl 3-(methylthio)propylamine); Ala (Alanine); Arg (Arginine); Asn (Asparagine); Asp (Aspartate); Cit (Citrate); CoA (Coenzyme A); Cys (Cysteine); DHAP (Dihydroxyacetone phosphate); DHF (Dihydrofolate); E4P (Erythrose 4-phosphate); ENO (Enolase); extArg (external arginine); extCO$_2$ (external CO2); extCys (external cysteine); extGlc (external glucose); extGln (external glutamine); extHis (external histidine); extIle (external isoleucine); extLeu (external leucine); extLys (external lysine); extMet (external methionine); extPhe (external phenylalanine); extSer (external serine); extThr (external Threonine); extTyr (external Tyrosine); extVal (external Valine); Fum (Fumarate); G3P (Glyceraldehide 3-phosphate); G6P (Glucose 6-phosphate); G6PD (Glucose-6-phosphate dehydrogenase); GABA (Gamma-Amino Butyric Acid); GDH (Glutamate dehydrogenase); Glc (Glucose l-phosphate); Gln (Glutamine); GLS1 (Glutaminase 1); Glu (Glucose); Gly (Glycine); Glyc (Glycogen); glyGP1 (Glucose 1-phosphate from glycogen); GSA (L-glutamate 5-semialdehyde); H6P (Hexose phosphate (G6P+F6P)); HCys (Homocysteine); His (Histidine); HK (Hexokinase); Ile (Isoleucine); Lac (Lactate); Leu (Leucine); Lys (Lysine); Mal (Malate); ME2 (Malic enzyme (NAD+, mitochondrial)); Met (Methionine); MTA (5'-S-methyl-5'-thioadenosine); OAA (oxaloacetate); OCR (Oxygen consumption rate (ATP production)); Orn (Ornithine); P5C (Glucose 5-phosphate); Palm (Palmitate); PDHK1 (pyruvate dehydrogenase kinase 1); PenP (Pentose phosphate); PHD2 (Prolyl hydroxylase 2); Phe (Phenylalanine); prAla (Alanine in protein); prArg (Arginie in protein); prAsn (Asparagine in protein); prAsp (Aspartate in protein); prCys (Cysteine in protein); prGln (Glutamine in protein); prGlu (Glutamate in protein); prGly (Glycine in protein); prHis (Histidine in protein); prIle (Isoleucine in protein); prLeu (Leucine in protein); prLys (Lysine in protein); prMet (Methionine in protein); Pro (Proline); prPhe (Phenylalanine in protein); PRPP (5-phospho-α-D-ribose 1-diphosphate); prPro (Proline in protein); prSer (Serine in protein); prThr (Threonine in protein); prTrp (Triptophan in protein); prTyr (Tyrosine in protein); prVal (Valine in protein); PSAT (Phosphoserine transaminase); Put (Putrescine); Pyr1 (Pyruvate (pool 1)); Pyr2 (Pyruvate (pool 2)); S7P (Sedoheptulose 7-phosphate); Ser (Serine); Spd (spermidine); Spn (Spermine); Suc (Succinate); THF (Tetrahydrofolate); Thr (Threonine); TKT (Transketolase); Trp (Triptophan); Tyr (Tyrosine); Val (Valine); αKG (alpha-Ketoglutarate).

VI.3 References

[1] Schellenberger J, Park JO, Conrad TM, Palsson BO. BiGG: a Biochemical Genetic and Genomic knowledgebase of large scale metabolic reconstructions. BMC Bioinformatics. 2010;11:213.

[2] Duarte NC, Becker SA, Jamshidi N, Thiele I, Mo ML, Vo TD, et al. Global reconstruction of the human metabolic network based on genomic and bibliomic data. Proc Natl Acad Sci U S A. 2007;104:1777-82.

[3] Caspi R, Altman T, Billington R, Dreher K, Foerster H, Fulcher CA, et al. The MetaCyc database of metabolic pathways and enzymes and the BioCyc collection of Pathway/Genome Databases. Nucleic Acids Research. 2013;42:D459-D71.

[4] Artimo P, Jonnalagedda M, Arnold K, Baratin D, Csardi G, de Castro E, et al. ExPASy: SIB bioinformatics resource portal. Nucleic Acids Research. 2012;40:W597-W603.

[5] Kanehisa M, Goto S, Sato Y, Furumichi M, Tanabe M. KEGG for integration and interpretation of large-scale molecular data sets. Nucleic Acids Research. 2011;40:D109-D14.

[6] Nelson DL, Cox MM. Lehninger. Principles of Biochemistry. fifth ed2008.

[7] Ignatenko NA, Gerner EW, Besselsen DG. Defining the role of polyamines in colon carcinogenesis using mouse models. J Carcinog. 2011;10:10.

[8] Alm K, Oredsson S. Cells and polyamines do it cyclically. Essays Biochem. 2009;46:63-76.

[9] Wallace HM, Caslake R. Polyamines and colon cancer. Eur J Gastroenterol Hepatol. 2001;13:1033-9.

[10] Wallace HM, Fraser AV, Hughes A. A perspective of polyamine metabolism. Biochem J. 2003;376:1-14.

[11] Pegg AE. Spermidine/spermine-N1-acetyltransferase: a key metabolic regulator. Am J Physiol Endocrinol Metab. 2008;294:E995-E1010.

[12] Casero RA, Pegg AE. Polyamine catabolism and disease. Biochem J. 2009;421:323-38. doi: 10.1042/BJ20090598.

[13] Roy UK, Rial NS, Kachel KL, Gerner EW. Activated K-RAS increases polyamine uptake in human colon cancer cells through modulation of caveolar endocytosis. Mol Carcinog. 2008;47:538-53. doi: 10.1002/mc.20414.

[14] Pledgie A, Huang Y, Hacker A, Zhang Z, Woster PM, Davidson NE, et al. Spermine oxidase SMO(PAOh1), Not N1-acetylpolyamine oxidase PAO, is the primary source of cytotoxic H2O2 in polyamine analogue-treated human breast cancer cell lines. J Biol Chem. 2005;280:39843-51.

[15] Cerrada-Gimenez M, Pietila M, Loimas S, Pirinen E, Hyvonen MT, Keinanen TA, et al. Continuous oxidative stress due to activation of polyamine catabolism accelerates aging and protects against hepatotoxic insults. Transgenic Res. 2011;20:387-96.

[16] Kramer DL, Diegelman P, Jell J, Vujcic S, Merali S, Porter CW. Polyamine Acetylation Modulates Polyamine Metabolic Flux, a Prelude to Broader Metabolic Consequences. Journal of Biological Chemistry. 2008;283:4241-51.

[17] Pirinen E, Kuulasmaa T, Pietila M, Heikkinen S, Tusa M, Itkonen P, et al. Enhanced polyamine catabolism alters homeostatic control of white adipose tissue mass, energy expenditure, and glucose metabolism. Molecular and Cellular Biology. 2007;27:4953-67.

[18] Jell J, Merali S, Hensen ML, Mazurchuk R, Spernyak JA, Diegelman P, et al. Genetically altered expression of spermidine/spermine N1-acetyltransferase affects fat metabolism in mice via acetyl-CoA. The Journal of biological chemistry. 2007;282:8404-13.

[19] Shlomi T, Fan J, Tang B, Kruger WD, Rabinowitz JD. Quantitation of cellular metabolic fluxes of methionine. Anal Chem. 2014;86:1583-91.

[20] Ko DC, Gamazon ER, Shukla KP, Pfuetzner RA, Whittington D, Holden TD, et al. Functional genetic screen of human diversity reveals that a methionine salvage enzyme regulates inflammatory cell death. Proceedings of the National Academy of Sciences. 2012;109:E2343-E52.

[21] Sauter M, Moffatt B, Saechao Maye C, Hell R, Wirtz M. Methionine salvage andS-adenosylmethionine: essential links between sulfur, ethylene and polyamine biosynthesis. Biochemical Journal. 2013;451:145-54.

[22] Cavuoto P, Fenech MF. A review of methionine dependency and the role of methionine restriction in cancer growth control and life-span extension. Cancer Treat Rev. 2012;38:726-36. doi: 10.1016/j.ctrv.2012.01.004. Epub Feb 17.

[23] Kang W, Hong SH, Lee HM, Kim NY, Lim YC, Le le TM, et al. Structural and biochemical basis for the inhibition of cell death by APIP, a methionine salvage enzyme. Proc Natl Acad Sci U S A. 2014;111:E54-61. doi: 10.1073/pnas.1308768111. Epub 2013 Dec 23.

[24] Phang JM, Liu W, Hancock CN, Fischer JW. Proline metabolism and cancer. Current Opinion in Clinical Nutrition and Metabolic Care. 2015;18:71-7.

[25] Liu W, Le A, Hancock C, Lane AN, Dang CV, Fan TWM, et al. Reprogramming of proline and glutamine metabolism contributes to the proliferative and metabolic responses regulated by oncogenic transcription factor c-MYC. Proceedings of the National Academy of Sciences. 2012;109:8983-8.

[26] Phang JM, Pandhare J, Zabirnyk O, Liu Y. PPARgamma and Proline Oxidase in Cancer. PPAR Res. 2008;2008:542694.

[27] Liu W, Phang JM. Proline dehydrogenase (oxidase) in cancer. Biofactors. 2012;38:398-406.

[28] Jain M, Nilsson R, Sharma S, Madhusudhan N, Kitami T, Souza AL, et al. Metabolite profiling identifies a key role for glycine in rapid cancer cell proliferation. Science (New York, NY. 2012;336:1040-4.

[29] Dolfi SC, Chan LL, Qiu J, Tedeschi PM, Bertino JR, Hirshfield KM, et al. The metabolic demands of cancer cells are coupled to their size and protein synthesis rates. Cancer Metab. 2013;1:20.

[30] Tedeschi PM, Markert EK, Gounder M, Lin H, Dvorzhinski D, Dolfi SC, et al. Contribution of serine, folate and glycine metabolism to the ATP, NADPH and purine requirements of cancer cells. Cell Death and Disease. 2013;4:e877.

[31] Fan J, Ye J, Kamphorst JJ, Shlomi T, Thompson CB, Rabinowitz JD. Quantitative flux analysis reveals folate-dependent NADPH production. Nature. 2014;510:298-302.

[32] Antoniewicz MR. Methods and advances in metabolic flux analysis: a mini-review. J Ind Microbiol Biotechnol. 2015;42:317-25. doi: 10.1007/s10295-015-1585-x. Epub 2015 Jan 23.

[33] Antoniewicz MR. 13C metabolic flux analysis: optimal design of isotopic labeling experiments. Curr Opin Biotechnol. 2013;24:1116-21. doi: 10.016/j.copbio.2013.02.003. Epub Feb 28.

[34] Sheikh K, Forster J, Nielsen LK. Modeling hybridoma cell metabolism using a generic genome-scale metabolic model of Mus musculus. Biotechnol Prog. 2005;21:112-21.

[35] Wolfram S. The Mathematica Book. Fifth ed: Wolfram Media; 2003.

[36] Mahadevan R, Schilling CH. The effects of alternate optimal solutions in constraint-based genome-scale metabolic models. Metab Eng. 2003;5:264-76.

[37] Llaneras F, Pico J. An interval approach for dealing with flux distributions and elementary modes activity patterns. J Theor Biol. 2007;246:290-308.

[38] Orman MA, Arai K, Yarmush ML, Androulakis IP, Berthiaume F, Ierapetritou MG. Metabolic flux determination in perfused livers by mass balance analysis: effect of fasting. Biotechnol Bioeng. 2010;107:825-35. doi: 10.1002/bit.22878.

[39] Nicolae A, Wahrheit J, Bahnemann J, Zeng AP, Heinzle E. Non-stationary 13C metabolic flux analysis of Chinese hamster ovary cells in batch culture using extracellular labeling highlights metabolic reversibility and compartmentation. BMC Syst Biol. 2014;8:50.:10.1186/752-0509-8-50.

[40] de Mas IM, Selivanov VA, Marin S, Roca J, Oresic M, Agius L, et al. Compartmentation of glycogen metabolism revealed from 13C isotopologue distributions. BMC Syst Biol. 2011;5:175.:10.1186/752-0509-5-175.

[41] Fan J, Kamphorst JJ, Mathew R, Chung MK, White E, Shlomi T, et al. Glutamine-driven oxidative phosphorylation is a major ATP source in transformed mammalian cells in both normoxia and hypoxia. Mol Syst Biol. 2013;9:712.

[42] Eden E, Geva-Zatorsky N, Issaeva I, Cohen A, Dekel E, Danon T, et al. Proteome half-life dynamics in living human cells. Science. 2011;331:764-8. doi: 10.1126/science.1199784. Epub 2011 Jan 13.

[43] Casero RA, Pegg AE. Polyamine catabolism and disease. The Biochemical journal. 2009;421:323-38.